UNIVERSITATEA MARITIMA CONSTANŢA

CONSTANTA MARITIME UNIVERSITY

ANNALS

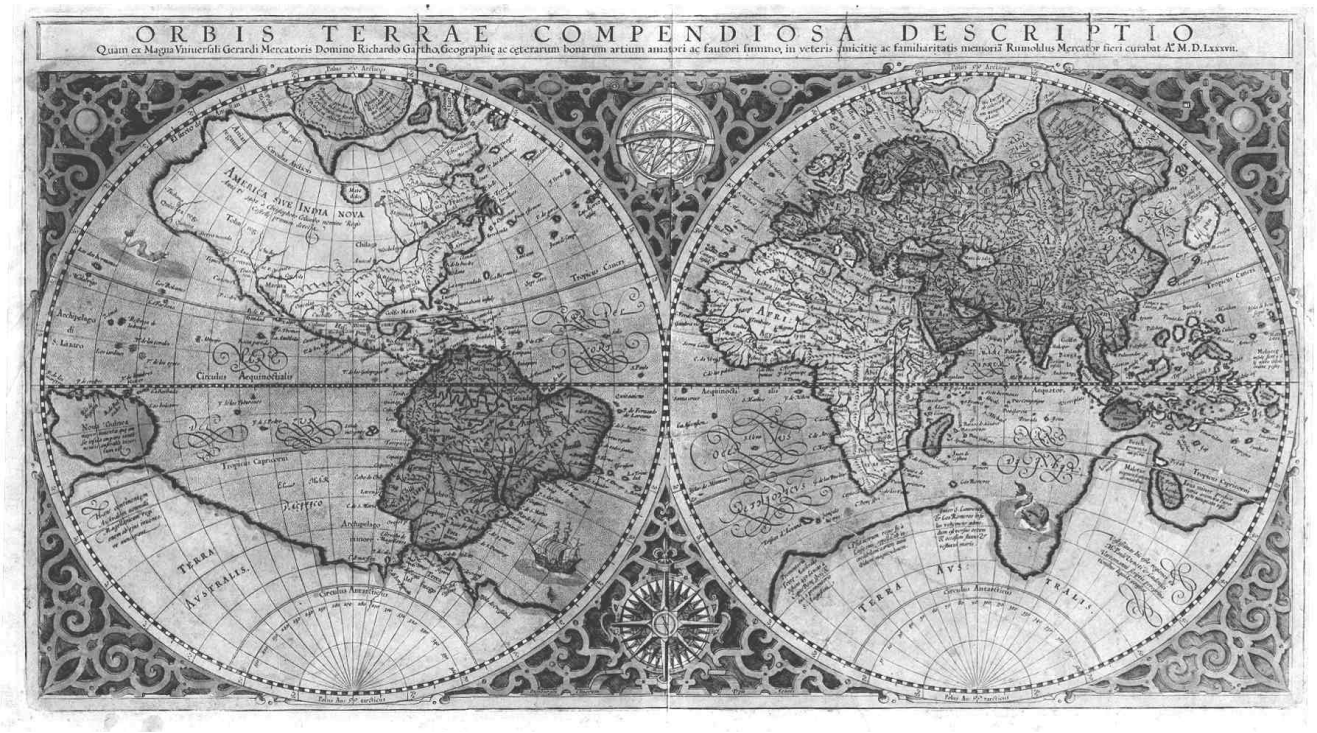

YEAR XI, 14th issue

Editura NAUTICA

CONSTANŢA 2010

SCIENTIFIC COMMITTEE

President:

Cornel Panait	**Rector, Constanta Maritime University**

Members:

Mihail Alexandrescu	**Dean, Transport Faculty, Politehnica University of Bucharest**
Toader Munteanu	**Professor, "Dunarea de Jos" University, Galati**
Mariana Jurian	**Professor, Faculty of Electronics, Communications and Computers, University of Pitesti**
Alexandru Jipa	**Dean, Physics Faculty, University of Bucharest**
Corneliu Burileanu	**Vice-rector, Politehnica University of Bucharest**
Silviu Ciochină	**Chair of Telecommunications, Faculty of Electronics, Telecommunications and Information Technology, Politehnica University of Bucharest**
Mircea Covrig	**Professor, Politehnica University of Bucharest**
Dan Stoichescu	**Professor, Chair of Applied Electronics and Informatics Engineering, Faculty of Electronics, Telecommunications and Information Technology, Politehnica University of Bucharest**
Teodor Petrescu	**Dean, Faculty of Electronics, Telecommunications and Information Technology, Politehnica University of Bucharest**
Marin Drăgulinescu	**Professor, Faculty of Electronics, Telecommunications and Information Technology, Politehnica University of Bucharest**
Cornel Ioana	**Associate Professor - Researcher, Grenoble INP/ENSE3, GIPSA-lab, Department Images-Signal, France**
Ovidiu Dragomirescu	**Professor, Faculty of Electronics, Telecommunications and Information Technology, Politehnica University of Bucharest**
Ricardo Rodríguez-Martos	**Director, Department of Nautical Sciences and Engineering, Polytechnical University of Catalonia**
Donna J. Nincic	**Professor and Chair, Department of Maritime Policy and Management, California Maritime Academy, California State University**
Anto Raukas	**Professor, Estonia Maritime Academy**
Wang Zuwen	**President of Dalian Maritime University**
De Melo German	**Professor, Faculty of Nautical Studies - Polytechnical University of Catalonia**
Mykhaylo V. Miyusov	**President, Odessa National Maritime Academy**
Güler Nil	**Dean, Maritime Faculty, Istanbul Technical University, Turkey**
Cwilewicz Romuald	**President, Gdynia Maritime University, Poland**
Sag Osman Kamil	**Rector, Piri Reis Maritime University, Turkey**
Gruenwald Norbert	**Rector, Hochschule Wismar, University of Technology, Business and Design, Germany**
Dimitar Angelov	**Captain (Navy), N.Y. Vaptsarov Naval Academy**
Oh Keo-Don	**President of Korea Maritime University, Korea**
Eisenhardt William	**President, California Maritime Academy, USA**
Laczynski Bogumil	**Professor, Faculty of Navigation - Gdynia Maritime University, Poland**
Malek Pourzanjani	**President, Australian Maritime College**
Yu Schicheng	**President of Shanghai Maritime University, China**
Jessen Torben	**President of Danish Maritime University, Denmark**

CONTENTS

SECTION III – ELECTRICAL ENGINEERING AND COMPUTER SCIENCE

SECTION I

NAVIGATION AND MARITIME TRANSPORT

FROM THE BARGAIN/BARGAINING "AGREEMENT" TO THE SHIPPING AGREEMENT (I)

[1]COJOC MARIANA, [2]CORNEL GRIGORUT, [3]ANECHITOAE CONSTANTIN, [4]LAVINIA-MARIA GRIGORUT

[1,2,3]University "Ovidius", Constanta, [4]National Institute of Economic Research "Costin Kirițescu", Bucuresti, Romania

ABSTRACT

The analysis of the legal components of the boarding agreement shows that this contract, in fact, is an individual employment contract concluded for a fixed period, with a particular suite of elements determined by very specific of the sailor profession.

The individual boarding agreement is an undefined legal concept, which incidentally regulates the meaning of "individual employment contract concluded for a fixed period" by employees who are part of the crew

Keywords: *Embarking, embarking, Collective Work, boarding personnel*

1. HISTORY

It is inconceivable to specify the time period when navigation began, as the science and art of driving a vessel from one point to another in the world. Failure comes from the fact that man has felt the need to pass a course or a stretch of water early in his existential adventure. It is a known fact that monkeys use, in order to survive, the floating logs in the event of flooding or simply to pass on the other side of a river.

An important step was made when there emerged the idea of keeping the trunk for later use. The archaic tree trunk hollowed inside used in order to float on rivers and seas, described in the Polynesian cosmogonist tales [1] is at the origin of a new occupation in the civilizing race of humanity [2].

The "initiation" into the mysteries of the journey on rivers, lakes and seas was done in several places, separately, due to the isolation of human communities [3]. Thus the movement on rivers, faster than the terrestrial one, created an alternative to human existence, firstly by satisfying the need for food, when people stood still their hunger by cultivating plants, raising animals, or fishing on the shore. The movement on water firstly created a richer source of fishing and also led the man to new shores where he was able to change what they overflowed with what they lacked.

Some tribes moved quickly from monoxides and rafts to boats with superposed rows of paddles able to fish offshore or to sail around islands, and even continents [4]. Over time, the insurmountable obstacles due to the increasing demands of civilization, have turned in factors of progress both in what concerns the means of water transport and the coastal shipping development [5], at first, and then maritime shipping and development.

Subsequently, the modernization of these nautical means shifted from their peaceful use which generated wealth through maritime trade [6], to the conquest or invasion of other territories through the organization of military fleets [7] able to suppress and plunder, to organize maritime blockades in order to control large stretches of water [8].

In these circumstances, besides the quality of grower, farmer, hunter, etc, a new occupation appears – the one of rafter [9], boater [10], oarsman, steersman, seaman or adventurer at first [11], then the sailor, pirate, Viking, corsair [12], sea dog, seafarer or legendary names such as the Argonaut [13].

For a long period of time, the floating means used as the main way of propulsion – the paddle, driven by human force [14], recruited from among the prisoners or slaves [15] whose minimal rights were limited to food and summary equipment. Navigation has evolved, however, and the entire manpower used precisely for vessel propulsion was partially replaced by wind power, respectively by the art of taming the wind and driving the boat as needed - regardless of its direction.

1.1. Bargaining for the ship personnel

After the discovery of the steam engine and the diesel engine, bold seamen have become the masters of the sea. The means of traveling on water required a corresponding qualified service staff followed by a contract of employment between the sailors- employees and the vessel commander, directly, when he was also the owner of the vessel or, in other situations, together with the owner of the respective vessel, who drew the crew list.

An exceptional situation is the bargaining for a crew list on a pirate ship. After taking notice of its contents, the pirates swore with their hands on a Bible that they would comply. The content of the "bargaining agreement" provided for constitutional (the equal right to vote), administrative, criminal (death penalty), civil, religious dispositions and labor standards etc, which provided both for the rights and obligations and prohibitions for all crew members in relation to the positions they held [16].

The harsh life at sea imposed even to pirate crews special measures of labor safety. "The presence of young boys and women is strictly prohibited. The one who will be found guilty of having seduced a person of the opposite sex and of having convinced her to navigate disguised, will be sentenced to death." [17].

Sailors bargaining for the merchant marine knew hard times at first. The owner's interest was to send ships to sail full speed and often face unfavorable weather, in extremely unfavorable working conditions for the crew, and which were unspecified in the bargaining agreement. Underpaid, always living half-wet with their hands rammed by rough ropes, forced to climb all the time on masts, on strong winds and waves (that overburdened the ship in pitch and reeling over 30-40 degrees), on rain or snowstorm, not a few were those who disappeared in the waves [18]. For the ship owners, the cargo was the important one and not the sailors.

The burden of service included different obligatory exercises (of salvation, vitality etc.), but the excesses of some commanders, brought the crew to physical and mental exhaustion, by timed workouts, similar to the imposed military exercises [19]. Fear of the unknown and of the inevitable unknown was a particular obstacle in the selection of the personnel from among those who dreamed of an immediate enrichment.

Every storm at sea could let behind new wrecks, further loss of life and other names of missing vessels – this was the anticipatory picture of each sailor, before deciding to go at sea.

1.2. Crew Enrollment

During the thirteenth and fourteenth centuries, a galley crew consisted of approx. 150-400 people, depending on the voyage, the ship's mission or the ship capacity. The share was represented by the oarsmen and the sailors were around 40-50; they handled the sails and the helm [20]. Their number was completed by the armed personnel - up to approx. 50 people; they constituted what today is called the "marines." The leadership of such a ship usually consisted of a commander who could even be the ship owner, 2-3 under-officers and the commander of the soldiers on board or a commit, two under-commits, the pilot (if applicable) and a scribe. The staff plan of the ship also included the so-called experts: chefs (one or two), thumpers, carpenters, the doctor who also had the attribution of barber and a priest who, when needed, was also a notary.

Before leaving for the voyage, the captain received from the Senate a list of instructions (*commissio*). In these instructions there were contained all the rules governing the navigation, the rights and the obligations of the captain, of the owner and of crew members, drafted on the basis of Senate decisions related to the *muda* of the respective year, either on the basis of current shipping practices, or based on legal practice on the preparation of line galleys.

The choice of captain was subject to fulfilling the minimum age of 30 years and to belonging to a noble caste. He was elected by the Senate, and during the voyage he represented the power of the republic to which he was belonging. The captain had a large number of legal and administrative rights [21], similar to a Venetian consul, or even to a governor.

The Venetian experience presents us a specific way of the employment of seafarers. The enrollment of the crew was made among volunteers, on a day fixed by the Senate, an operation which was held in Piazza San Marco, where there were settled banks for enrollment, where the owners [22] were proceeding to hiring the employers: steersmen, rowers; a cook, a suffrage and a cabin attendant. The captain was also choosing his people, with the exception of the Admiral [23], who was elected by the Council. The carpenters were nominated by the Arsenal.

The conditions of employment were included in the book that was on board, in the care of the ship scribe.

The exigency in the crew recruitment was different in relation to the capacity of the ship, the different situation of the armed ships - which required more severe conditions than those of a commercial vessel.

According to the Venetian documents, need for rowers increased in the early fourteenth century, exacerbated by the Black Plague, which led to their decrease in number. Thus, they started to use as rowers convicted persons, former smugglers, pagan slaves who were promised freedom in exchange for conversion – their fidelity and faith was proven by their work on the galley.

Faced with the challenge of finding volunteers for such an exhausting work, they also passed to illegal methods of recruitment. Agents were sent to cabarets and bars with the task of organizing gambling games. The mission was that those who lost and could not pay their debts to be brought to the galleys in order to be used as oarsmen.

The Eastern policy used the ballot as a means of recruitment and those who escaped were required to contribute, however, with certain expenses for equipping the ships.

During stopovers, which were, most times, very long, the owners were trying to minimize the navigation crew in order to reduce costs; they would hire a new crew when the ship was on the point of leaving the port.

1.3. The Development of Romanian river and maritime transport

In the international trade of goods and services, a higher comparative advantage is the ship transport - with the lowest cost reported to the ton / ton or freight / gauge [24]. A country may be more effective than any other country, in terms of its shipping activity even for the simple reason that it geographically benefits of a sea or ocean gateway.

The development of the Romanian river and maritime transportation imposed the creation of national shipping companies. Thus, in 1888, there was adopted the Law on the Establishment of a river and maritime navigation service, the legal framework providing the basis for the establishment by the State, in 1890, of the company of "Romanian River Navigation (NFR)", and, in 1895, of the company of "Romanian Maritime Service (RMS)", the latter operating initially within the CFR, and, subsequently, becoming independent [25].

In 1903 there was established the Company of the Russian Navigation on the Danube, which held the monopoly of freight and passenger traffic on the Danube and the Prut River. After 1900, the port activity within the Cetatea Alba, Reni, Chilia, Vâlcov centers has known significant increases. Permanent courses tied, by

Ismail, the Galati city to Odessa, while Austrian shipping companies were serving the route Odessa-Vienna [26].

In 1938, there was issued the Decree-Law establishing the National Navy Fund and in 1939 there was adopted a new navy program according to which the Royal Navy was going to be equipped with 180 ships - made partly because of the outbreak of World War II.

In 1939, the sea and river fleet under the Romanian flag consisted of: 26 maritime vessels, including 15 cargo ships, 6 passengers ships and five mixed ships; 807 river vessels, of which 23 of passengers and the rest of the tugs, boats, barges, docks, elevators etc.; 152 service vessels and coastal and river police vessels. The capacity of the maritime vessels was of 58,214 tons of naval registry, the capacity of river vessels was of 519,938 metric tons of river and the capacity of service and police vessels was of 21,340 metric tons [27].

The great loss suffered by the Romanian economy during World War I [28], followed by those produced during World War II (1940-1944), considerably decreased the capacity of maritime and river transport; in most cases, these losses had been caused by air raids. This situation is worsened by the end of World War II, due to the provisions of art. 11 of the Armistice Convention, signed in Moscow on 12 September 1944 [29], when Romania was obliged to pay in products [30], payment spread over six years; 355 maritime and river vessels had to be delivered [31]. To these, there must be added a total of 110 warships seized without any negotiation, and which have been moved to the Caucasus ports, where their Romanian names and flags have been changed with Soviet ones [32].

The future economic relations between Romania and the Soviet Union have continued with the establishment of 16 Soviet-Romanian joint ventures, such as S SOVROMTRANSPORT (19 July 1945) [33] and SOVROMNAVAL (15 August 1952) Soviet-Romanian Shipping Company - returned to Romanian State property after 18 September 1954. The river and maritime navigation of Romanian ships as well as shipbuilding returned again under the full jurisdiction of the Romanian state; this represents a landmark to the alignment to the international legal framework and the beginning of new development projects, in accordance to the need of the Romanian economy.

2. THE SAILOR PROFESSION

The shipping companies with great reputation and financial stability have invested in the construction of commercial and passenger ships, the largest ever. Basically, in terms of passenger ships, there were built real floating cities, with cinemas, dance halls, swimming pools, tennis courts, basketball, fitness centers etc., with the transport capacity of around 1500 - 2000 passengers and a huge number of service personnel, whose number exceeds 400 employees, of which about 30-50 are sailors (about 10 to 15 – able-bodied personnel and the difference – unable-bodied personnel) [34].

These impressive passenger ships that were crossing the Atlantic in 5-6 days, received a heavy blow after the '50s [35], with the advent of passenger jet aircraft, which shortened the time, on the same distance, to 5-6 hours.

In these situations, the sailors together with the service personnel employed on passenger ships, highlighted in the classification of occupations, often reach several pages. They are proposed different ways of employment with the fulfillment of specific training stands obtained under the minimum courses required by the International Maritime Organization and provided for in the contents of international conventions.

Nowadays passenger ships are used only for travel, cruise and leisure [36].

The profession of sailor has become an occupation like any other, only nowadays [37] when there has been obtained, legally, the recognition of certain functions in a functional hierarchy of management and execution, specific to the working conditions on vessels, with jobs recognized after the acquisition of knowledge obtained through training, based on rules imposed by the provisions of international conventions to which most maritime and non-maritime states have acquiesced.

The Ministry of Labor, under the Government Decision no. 575/bis/1992, on the establishment of uniform lists of general interest, provided in the general conception of informatization in Romania has enlisted the sailor profession within the Minor Group 834. According to this classification, sailors, navigators and assimilated personnel fulfill vessel operation tasks, according to navigation instructions.

Lately, it is reminded more and more of a new profession: that of "Community seaman" [38].

3. THE CONCEPT OF "CREW"

Any maritime or river ship, public or private property, which is engaged in the transportation of goods or passengers for commercial ends and which is registered within a country, has hired a specialized staff in order to insure for involvement of the ship in the transport and navigation activities, according to the destination assigned by its construction.

Any vessel flying the Romanian flag is served by a crew operating the vessel safely, meeting the environmental protection conditions and fulfilling other activities on board [39].

The personnel consist of sailing crew and auxiliary staff, and its composition is determined according to ship type and destination [40].

In what concerns the crew, the positions on board (when speaking about ships flying the Romanian flag) can only be occupied by the sailing crew, possessing licenses or certificates for their corresponding competence.

The auxiliary personnel perform activities on board for which no licenses or certificates of competence are issued.

All crew members must demonstrate that they meet minimum age and health conditions laid down in national regulations and international agreements and conventions to which Romania is party.

3.1. The concept of "crew"

ILO Convention no. 22 of 24.06.1926 on the seafarers' employment agreement [41] defines the term

"seafarer" in art. 2 letter a), as being any person employed or used in any capacity on board of a ship and enlisted in the contract of employment on the ship. The term excludes the commanders, pilots, cadets, students on board of school-ships and apprentices with special contracts of apprenticeship; the term excludes crews of the military Navy and other persons in the permanent service of the state.

According to Art. 52 of Government Ordinance no. 42 / 1997 (r) on maritime and inland waterways transport, the Romanian sailing crew consists of all persons, regardless of nationality, who possess a license or a certificate of competence obtained or recognized in accordance with legal provisions which entitle them to perform functions on board of ships.

The record of the Romanian sailing crew is held by the Romanian Naval Authority in the registries of the sailing crew.

The form and content of the Register of Romanian seafarers are approved by the order of the Minister of Transport, Construction and Tourism.

Each crew member must have, necessarily, an identity document.

Crew members on vessels operating at sea may also use the seaman's book as identity document.

The seaman's book is issued on behalf of the Government, by the Ministry of Labor, Family and Equal Opportunities, through the Romanian Naval Authority.

Crew members on vessels operating on inland waterways must have a service card which proves the service skills, medical skills, the navigation times and the sectors covered.

The form and content of the seaman's book and the service card is approved by the Ministry of Transport, Constructions and Tourism.

The service card is issued by the Romanian Naval Authority.

During marching tests of newly built ships or out of repair, the specialized staff of dockyards may also be on board. During this period, the specialized personnel of dockyards have the same rights as seafarers, their salary being paid under the law.

The port captain sets the minimum safety crew which must be embarked on newly constructed vessels or out of repair, during marching tests.

On board of the ships flying the Romanian flag, in addition to the crew, other persons may also be embarked, within the limit of the salvage means existing on board, with the consent and responsibility of the owner / operator of the ship and with the approval of the boarding port captain [art. 57, G. O. 42/1997 (r)].

4. THE BOARDING AGREEMENT, THE ENLISTMENT AGREEMENT, THE CREW ROLLAND THE GENERAL SHIP ROLL

4.1. The Boarding Agreement

In Romania, the boarding conditions are those stipulated in the collective employment agreement, the individual employment agreement concluded under the labor code, and service duties are contained in the regulations and instructions on the service on board of maritime and river ships.

The boarding agreement is defined as that convention which governs the employment relations of crew members, of the ships flying the Romanian flag, with their employers [42].

4.2. The Enlistment Agreement

We will offer additional explanations to those revealed in the "History" Section, Subsection 1.2., in order to eliminate the confusion between several terms of marine life with the same terms accepted by the laws in force today, but which sometimes have a different meaning.

In the English-Romanian maritime lexicon, the employment / enrollment agreement (or the role of crew) is defined as a written document concluded between the commander or the owner and any member of the crew, setting out the conditions of employment: the office, service duties, the rights to salary, food and onboard service, the duration of employment, the termination clauses (to a date stipulated in the contract, at the completion of a specific voyage or at any time by mutual consent in cases of serious damage or loss of the vessel or in case of the loss of the work capacity of the sailor etc.). The agreement in concluded in the presence of an authority (Captain or other organized service). Under the contract, the employed seamen are enlisted within the roll of the ship crew. When employment is made without an express written contract, the enlistment into the roll of the crew (Muster roll) [43] was the legal presumption of the existence of the contract. Thus, the roll of the crew is sometimes confused as notion with the enlistment agreement.

Article 532 et seq. C. com, regarding "the enlistment agreement" and its legal regime have been implicitly repealed and, at present, it is inapplicable [44].

4.3. The Crew Roll

The crew roll is a document almost similar to the nominal list of the crew of a ship, which is one of the main documents without which a ship can not leave the port and can not navigate legally [45].

This document is an official document issued by the competent maritime authority (in Romania, by the port captain), where there is inscribed the entire crew of the ship. It includes: the surname, the forename, the age, the address and the professional qualifications of each member of the crew, the function they fulfill on board, the main obligations of the cart service, rights to salary, food and maintenance etc.

In this document there are mentioned the positions of every man of the crew and passengers under different names in different situations: the roll at crash, roll at leak, roll at maneuver, roll at boat [46]; roll at fire; roll at conflict; roll at cleaning. In such a roll, there are inserted all the duties they have to fulfill in various situations (daily service, in an emergency; failure, etc.).

The crew roll is at the basis of the establishment of the general roll of the ship with which it must not to be confused. Also, in comparison to the crew list [47], it has

different goals and contents. In the absence of an employment / boarding contract, the crew roll replaces it, producing all the legal effects of the contract.

4.4. The General Ship Roll (the Muster)

The general ship roll is an internal organizational document, including the nominal allocation of crew members to the intervention position in cases of fire, damage, ship abandonment, which requires urgent action for the safety of the ship or for saving people. The general ship roll must be made at the ship's entry into service and it is kept up to date, operating whenever changes occur in personnel cases. For each post there are fixed the duties and the procedure regarding: the closing of watertight doors and bottom valves, pipes leak checking axle damper and fire protection installation, putting down fires, preparing the boats and the other life saving equipment on board in order to abandon the ship, announcing the passengers in case of evacuation of the ship, driving them to boarding stations, boarding supervision etc. The general ship roll nominally allocated the entire crew in rescue craft, in accordance with the "International Convention for the Safety of Human Life at Sea" relating to: the maximum capacity, the appointment of a boat chief, assuring a sufficient number of certificated sailors etc. For the cases of fire and ship abandonment, the general roll provides for the special signals that are transmitted on the ship by means of whistle, buzzer or ringtones.

The partial rolls derive from the general roll: of fire, damage, boats, abandonment etc. on which there are conducted training exercises with the crew.

5. REFERENCES

[1] See the legend on Goddess Hina, Maori mythology (New Zeeland). KERNBACH, V. *Mituri esențiale,* Editura Ştiințifică şi Enciclopedică, Bucureşti, 1978, pp. 209-210.
[2] CRĂCINOIU, C.; NEAGU, A. *Dialogul omului cu marea*, Editura Albatros, Bucureşti, 1988, p. 90.
[3] ACSAN, I. *Odiseea primilor corăbieri. Pe urmele vechilor expediții maritime. Homo Navcticvs în antichitate*. Editura Historia, Bucureşti, 2007, p. 26.
[4] Idem, p. 42.
[5] In the past, navigation was extremely difficult and the navigators encountered threats at every step he made; they did not have adequate navigation instruments and they were accompanied by prestigious foretellers whose advice they were strictly respecting. For a very long time, navigation had depended on weather and on winds and their prognosis was difficult to approximate.
[6] From voyages and maritime expeditions to long voyages which are at the basis of the creation of maritime and trade routes. Nowadays it is spoken about the "Sea Highway".
[7] Since the time of Vespasian (69-79 d. Hr.), the Roman military fleet „Classis Flavia Moesica" patrolled under the command of a *praefectus; at* Noviodunum (Isaccea) there was its headquarters. These maritime units had *naves amnicae* - „river vessels", and *musculi Scythici*. Idem p. 65.
[8] See the chronicle of Eusebiu din Cesareea (260-340 d. Hr.) Idem p. 200.
[9] The Roman rafters were called *Ratiari* (ratis, ratiariae = raft). Idem, p. 62.
[10] Epigraphic sources confirm the existence of a *collegium nautarum* = rafters' college. Idem p. 63.
[11] The first transport of slaves in 1444, by the Portuguese Lanzarote; LECA, A. *Atlanticul*, Editura Ştiințifică, Bucureşti, 1969, p. 38-39.
[12] The kings of England and France gave the Corsars „commissions", i.e. plunder authorizations in the mane of the Crown.
[13] Character from the Greek mythology; BEJAN, A. coordonator, *Dicționar enciclopedic de marină*, Editura Societății Scriitorilor Militari, Bucureşti, 2006, p. 31.
[14] The first "navigators" were traveling by water, using the current speed and their hands; later, they used masts, poles, oars and paddles.
[15] See RETINSCKI, A. *Fascinația şi comorile mărilor*, Editura Albatros, Bucureşti, 1988, p. 64 and LECA, A.op. cit., p. 35.
[16] See CRĂCINOIU, C.; NEAGU, A. op.cit. pp. 220-221.
[17] Idem p. 220.
[18] The sailors' slogan: "A hand for you and the other for the ship" (XIXth century).
[19] CRĂCINOIU, C.; NEAGU, A. op. cit. p. 113-114.
[20] ATANASIU, A. *Condițiile salariale, de igienă şi hrana personalului navigant la bordul unui bastiment medieval* în Anuarul Muzeului Marinei Române, Tom X, 2007, Editura Companiei Administrația Porturilor Maritime Constanța, Constanța, 2008, pp. 29-35. See also: ATANASIU, A. *Componența echipajelor italiene din bazinul pontic (secolele XII-XIV)* în Anuarul Muzeului Marinei Române, Tom IX, 2006, Editura Companiei Administrația Porturilor Maritime Constanța, Constanța, 2007, pp. 73-88.
[21] In case of subordination or revolt, the captain had to arrest the responsible persons and to deliver them to the Venetian authorities, in the neighboring harbor; if the ship was off-shore, in full march, the captain himself could judge the case and he could not change his sentence thereafter.
[22] Then patron was the person who represented the interest of the owners and he was organizing the voyage.
[23] The Admiral was the first hand of the captain.
[24] Ships with technical characteristics were very advantageous.
[25] See MUREŞAN, M.; MUREŞAN, D. *Istoria economiei*, ediția a II-a, Editura Economică, Bucureşti, 2003, p. 227.
[26] In1924 The Commercial Marine on Danube under Romanian flag had 637 vessels with a movement force of 34345 C.P. and a capacity of 449,1 thousand tons. Idem, p. 227.
[27] See the data on the maritime traffic of goods in Romanian harbors in 1938; MUREŞAN, M.; MUREŞAN, D. op. cit. p. 293.
[28] See: „*Poziția României în problema generală a reparațiilor"* în: *TITULESCU, T. Discursuri.* Editura Ştiințifică, Bucureşti, 1967, pp. 243-255.
[29] The Armistice Convention between the Romanian government and the governments of URSS, UK and

USA, published in the Official Gazette, Part I, nr. 219 din 22 September 1944.

[30] The amount of compensation is of 300 millions dollars, the parity of 35 de dollars/ 1 ounce of gold, and the prices of Romanian goods that would be delivered were the world ones 1938, with an increase of 15% for the rolling material and of 10% for the others, although, in fact, on the world market, these prices had increased with 33% in comparison with those from 1938; the 300 millions dollars meant over 55% of the Romanian national revenue, evaluated in 1945 to 519 millions dollars.

[31] See: MUREŞAN, M.; MUREŞAN, D. op. cit. p. 35 and ALEXANDRESCU, I. *Economia României în primii ani postbelici (1945-1947)*, Editura Ştiinţifică şi Enciclopedică, Bucureşti, 1986, 38.

[32] MOŞNEAGU, M. *Politica navală postbelică a României (1944-1958)*, Editura „Mica Valahie", Bucureşti, 2005, p.12.

[33] PREDA, G.; PREDA, O.M. *O mărturie privitoare la înfiinţarea Societăţii „SOVROMTRANSPORT"*, în: Document, Anul VI, nr. 1 (23)/2004, p. 16.

[34] See the data on Titanic presented in the article of G. Negru, *Dezastrul transatlanticului Titanic*.

[35] See the situations of the passenger transatlantic vessels *Queen Mary, Queen Elisăbeth, France, Raffaelo United States,* which left the "water scene". CRĂCINOIU, C.; Neagu, A. op. cit. p. 96.

[36] For instance, the vessel „Norwegian Dawn", with a length of 294 m; it can embark over 2500 passengers plus de necessary of 1100 crew members. www.evz.ro/art.679943.

[37] The ancient Greeks used to say that people were of three types the living ones, the dead ones and those off-shore.

[38] CARAIANI, G.; Ambrozie, D.; HORIA, G.A. [et. al.], *Acquis-ul comunitar şi politica sectorială din domeniul transporturilor în Uniunea Europeană,* Editura Pinguin Book, Bucureşti, 2006 p.179.

[39] See the definition of Crew (ship's crew) in BIBICESCU, G.; TUDORICĂ, A.; SCURTU, G.; CHIRIŢĂ, M. *Lexicon maritim englez-român (cu termeni corespondenţi în limbile franceză, germană, spaniolă, rusă),* Editura Ştiinţifică, Bucureşti, 1971, p. 167.

[40] ANECHITOAE, C. *Introducere în drept maritim*, Editura Bren, 2007, p. 167.

[41] The Convention was ratified by Romania by G.O. NO. 16/2000, published in the Official Gazette, Part I, nr. 34 din 28/01/2000.

[42] MIHAELA, T. *Dreptul muncii. Suport de curs pentru anul univ. 2006/2007*.

[43] BIBICESCU G. [et. al], Lexicon maritim englez român, Editura Ştiinţifică, Bucureşti, 1971, p. 462.

[44] PIPEREA, G. *Dreptul transporturilor. Ediţia 2*, Editura All Beck, Bucureşti 2005, p. 153.

[45] Dicţionarul enciclopedic de marină, Coordonator: BEJAN, A. Editura Societăţii Scriitorilor Militari, Bucureşti, Bucureşti, 2006, p. 436. Vezi şi: MANOLE, I.; IONESCU, G. Dicţionar marinăresc, Editura Albatros, Bucureşti, 1982, p. 389Dicţionarul Explicativ Ilustrat al Limbii Române, Editura ARC & GUNIVAS, Chişinău, 2007, p. 1696.

[46] Internal Organizational document on board, which includes the nominal distribution of the entire crew in life boats, in case of ship abandonment.

[47] Nominal list of the embarked crew. It is one of the on board documents that must be presented to the control authorities when arriving and leaving the harbor. It includes: forename and surname of the person, the position on board, the qualification document, date and place of birth, nationality, the embarking date; it has to correspond with the crew roll.

FROM THE BARGAIN/BARGAINING "AGREEMENT" TO THE SHIPPING AGREEMENT (II)

[1]ANECHITOAE CONSTANTIN, [2]COJOC MARIANA [3]CORNEL GRIGORUT, [4]LAVINIA-MARIA GRIGORUT

[1,2,3]University "Ovidius", Constanta, [4]National Institute of Economic Research "Costin Kirițescu", Bucuresti, Romania

ABSTRACT

The analysis of the legal components of the boarding agreement shows that this contract, in fact, is an individual employment contract concluded for a fixed period, with a particular suite of elements determined by very specific of the sailor profession.

The individual boarding agreement is an undefined legal concept, which incidentally regulates the meaning of "individual employment contract concluded for a fixed period" by employees who are part of the crew

Keywords: *Embarking, embarking, Collective Work, boarding personnel*

6. THE INDIVIDUAL BOARDING AGREEMENT

6.1. The definition of terms: "ambarcare" – "îmbarcare" (embarking)

The conventions of maritime law use the term "ambarcare" when speaking of goods and the term "imbarcare" when speaking about persons. However, other conventions from the same field use these two terms the other way around (i.e. "ambarcare" when speaking about persons and the term "imbarcare when speaking of goods"). The International Maritime Organization did not interfered in order to clarify these two terms.

6.1.1. "Imbarcarea" (Embarking)

The Regulation of 2007 regarding minimum training criteria and certification of maritime pilots, other than deep-sea pilots, requires a license and a "minimum embarking period"[1].

In a 1997 methodology [2] issued by the Romanian Government, there is provided that "the crew will present to the port captain an embarking certificate" (art. 12). In another methodology issued in 2003 by the Romanian Naval Authority [3], it is stated that the agency of the crew may place the crew only on the basis of firm job offers made by the ship owners or by their alternates. The firm offer of employment on board made by ship owners or by their alternates means specifying certain minimum data, including "the embarking duration and nature", "the duration of the embarking contract" [4]. Furthermore, crew agencies are required to submit assurances that "embarking contracts" are consistent with the applicable law and collective agreements. The sailing staff must be informed of their rights and obligations conferred by legislation and by the "embarking contract", and after signing it by the parties, the sailing staff receives copies of the individual employment agreement and of the "embarking contract" [5].

The Law no. 17 / 1990 (r) [6] provides for: "boarding on ships of any kind of aircraft," "boarding of military equipment", "embarking or disembarking of goods, narcotics and psychotropic substances, cash or people, "embarking or disembarking passengers or cargo"

The G.D. no. 83/2003 stipulates that, on board, the sailing staff must conclude with the ship owner or with his representative an "embarking contract contract", which sets out specific working and living conditions on board [art. 3. (3)]. It also reminds of "the individual embarking contract" [art. 7 para. (2)] "for two months of embarking contract " (art. 10) and the " embarking contract periods of the staff" [art. 13 para. (2)].

In 1993, an agreement [7] mentioned the term of "the quay for the embarkation/disembarkation of passengers" [art. 1 letter. g), j) - l)]. Another Agreement of 2000 [8] speak about "the embarkation and disembarkation for passengers transportation" [art. 2 letters. a). 5], "passengers boarding" (Article 4 Section 3).

The 2003 instructions of the Minister of Public Works, Transportation and Housing [9] speak about "the Romanian sailing staff on board of Romanian or foreign-flagged vessels" [art. 9 para. (5)].

6.1.2. "Ambarcarea" (Embarking)

The Romanian Government Agreement of 1976 [10] speaks about: "embarking and disembarking passengers" (art. IV).

The Romanian Government Protocol of 1991 [11] defines the term "transit transport": the transport of passengers and/ or goods by a ship of a party on inland waterways in the territory of the other contracting party without "ambarcarea"- embarking or disembarking passengers, i.e. without loading or unloading the gods during the transition (section 1 par. (2)).

The Law no. 138/1999 [12] reminded of the Navy crew from the ship and submarines units and subunits, which is "embarked" (art. 22), and the right to "an embarking allowance" paid to the military and civilian personnel from the units and subunits of "embarked" ships (Annex IV, section 1).

In G.D. no. 245/2003 [13] both terms are used. Although in Chapter III, Section 1 is entitled " 'Imbarcarea'-Embarking and disembarking of crew",

subsequently there is used the term of “ambarcat”- embarked: "the embarked time of the crew "[art. 46 para. (3)], "data on ‘ambarcare’- embarking" [art. 49 para. (A)], "‘ambarcare’- embarking periods" [art. 50 para. (A)], " ‘ambarcare’ -embarking operations" mentioned within the seaman's book, " ‘ambarcare’- embarking certificate" [art. 50 para. (2). a and b], "the ‘ambarcat’- embarked crew" (art. 51), "the individual ‘ambarare’- boarding agreement [art. 51 points. b)]

Section 2, of G.D no. 245/2003 mentions: "If the loading, unloading, transshipment of goods or “imbarcarea”- embarking or disembarking of passengers" [art. 74 para. (A)], for passenger ships, the “imbarcarea”- embarking / disembarking of passengers (art. 86).

This deed uses the term "imbarcarea" or "ambarcarea" in order to define only the crew and for the cargo operations the terms “loading” (“incarcare”) and “unloading” (“descarcare”) are used.

The G.O. no. 42/1997(r) [14], also uses both terms: "In addition to the crew, other persons can be “imbarcate” ... with the approval of “imbarcare” port captain" (art. 57), "the chief engineer “imbarcat” on board a vessel" [art. 73 para. (A)], "the number of the passengers “imbarcati” " [art. 131 points. i)]; "the minimum safety crew which must be “ambarcat” on ships" [art. 56 (2)], "all those persons “ambarcate” on the ship" [art. 72 para. (A)].

We can say that, according to the Romanian legislation in force, there are not given definitions of the terms "ambarcare" and "imbarcare", and the legislator often uses both terms as synonymous.

6.2. Defining the individual boarding agreement

6.2.1. International sources

The boarding agreement is governed within the international law, by international conventions of the International Labor Organization, ratified in successive stages by the States concerned. The sailing river and maritime personnel is characterized as a professional group with certain particularities, which operates under contracts manifestly containing international norms. Thus, it was natural that their rights and obligations be regulated in a uniform manner throughout the world.

The large number of conventions that contain legal rules applicable in what concerns the contractual terms of boarding, which we list below, justify the particular nature of this category of staff.

1. The Convention no. 7/1920 concerning the minimum age of employment at sea.
2. The Convention no. 8/1920 relative to the allowance for lack of work in the case of loss by shipwreck [15];
3. The Convention no. 9 / 1921 regarding the placement of sailors [16];
4. The Convention no. 16/1921 on compulsory medical examination of children employed on board ships [17];
5. The Convention no. 7 / 1922. The draft Convention adopted by the International Labor Conference in the second annual session (15 June - 10 July 1922), which sets the minimum age for admission of children in maritime labor [18];
6. ILO Convention no. 22 of 24.06.1926 on the employment agreement of sailors from 24.06.1926 [19];
7. The Convention no. 27/1929 relative to the indication of the weight on large parcels carried by ships [19];
8. The Convention no. 29/1930, on forced or compulsory labor [20];
9. The Convention no. 53/1936 on capability certificates of officers.
10. The Convention no. 55/1936 on the obligations of ship owners in case of the illness or injury of seamen.
11. The Convention relative to sickness, adopted at the International Labor Conference in Geneva (May 25-June 16, 1927) [21];
12. The Convention no. 56/1936 on the insurance in case of the disease of seafarers;
13. The Convention no. 58/1936 concerning the Minimum Age for the Admission to maritime labor;
14. ILO Convention no. 68 of 1946 on food and dining on board [22];
15. ILO Convention no. 92 of 1949 on the Accommodation of Crews (Revised) [23];
16. ILO Convention no. 105 of 25 June 1957 on the abolition of forced labor[24];
17. ILO Convention no. 108 of 13.05.1958 on national identity documents for seafarers [25];
18. ILO Convention no. 127/1967 on the maximum weight of the cargo that can be carried by one worker [26], at Geneva on 28 iunie1967 (It will be called the "Convention on the maximum weight, 1967);
19. ILO Convention no. 133 of 1970 on crew accommodation [27];
20. ILO Convention no. 134/1970 on preventing the labor accidents of seafarers [28];
21. ILO Convention no. 137 of 25 June 1973 on the social repercussions of the new working methods in ports [29];
22. ILO Convention no. 138 of 26 June 1973 on the minimum age of employment [30];
23. The Convention no. 145/1976 on employment continuity (of the sailors);
24. The Convention no. 147/1976 on the minimum standards on board of merchant ships, adopted by the General Conference of the International Labor Organization in Geneva, on October 29, 1976, and the Protocol to this Convention, adopted by the General Conference of the International Labor Organization in Geneva on October 22, 1996 [31];
25. ILO Convention no. 163 of 1987 on the welfare of seafarers at sea and in port;
26. The detailed rules for implementing the ILO Convention no. 163/1987 regarding the welfare of seafarers at sea and in port [32];
27. ILO Convention no. 166/1987 on the repatriation of seafarers (revised) [33];
28. ILO Convention no. 180 of 1996 on the working time of seafarers and ships crew [34].
29. The Convention no. 186/2006 on maritime labor.

In international law the employment relationships of seafarers are expressly provided for in the Convention no. 22 of 24 June 1926 concerning the employment contracts of seafarers [35] and they apply to all ships registered in the Member State which has ratified this Convention and to the ship owners, commanders [36] and seafarers [37] of these vessels.

The Convention does not apply to:

a) warships;

b) government vessels not engaged in commercial purposes;

c) vessels engaged in the coastal trade;

d) pleasure yachts;

e) Indian craft;

f) fishing vessels;

g) ships below 100 gross registered tons or 300 square meters or vessels engaged in the national transportation, with the tonnage under the tonnage limit prescribed by the national legislation for the special regime of these vessels, in force upon the adoption of this Convention.

According to art. 3 of the Convention, the names and conditions of the employment contract must be provided for in domestic law, so as to ensure the control of the competent public authority.

Andrei Popescu believes that the International Labor Organization rules on sailors, presents a certain originality in comparison with those relating to workers, generally being adopted in special session - called maritime and coming into force in specific circumstances [38].

The International Labor Organization's interest is to develop a new instrument bringing together all maritime conventions; it has been concretized by the adoption of Convention No. 186/2006 on maritime labor. The Convention, described by some analysts as a charter of the fundamental rights of seafarers, provides for clear rules, but also flexible enough for Member States to establish the rights and obligations of the seafarers in a unitary uniform.

The new Convention consolidates and updates the 68 maritime conventions and recommendations adopted by the International Labor Organization in 1920. The Convention will enter into force after the ratification by 30 member states of the International Maritime Organization representing at least 33% of world gross tonnage.

7. EFERENCES

[1] Chapter I: art. 1 lit. b), art. 2 lit. b), art. 3 lit. b). Chapter II: art. 4 lit. b), art. 5 lit. b), art. 6 lit. b). Chapter III: art. 7 lit. b), art. 8 lit. b). The Regulation is published in the Official Gazette, Part I nr. 419 of 22/06/2007.

[2] The Methodology of 28/01/1997, on obtaining the authorization for intermediation activities in order to hire Romanian river or maritime crew on ships flying a foreign flag, Published in the Official Gazette, Part I nr. 13 of 31/01/1997.

[3] The Methodology of 23/01/2003 on issuing function authorizations to trade companies which assure services of selection and placement of Romanian maritime and river crew on ships flying a foreign or a Romanian flag and on establishing several financial security measures in case of their abandonment outside Romania, published in the Official Gazette, Part I no. 84 of 11/02/2003.

[4] Art. 1 Punctul B, lit. a) şi g).

[5] Art. 9 alin. (2) lit. b) – e).

[6] Law nr. 17/1990 (r) on the legal regime of Romanian maritime and inland waterways, of the territorial sea, of the contiguous area and of the exclusive economic area, art. 18 alin. 2, lit. e) - g), art. 49 alin. (1) lit. h) Republished in the Official Gazette, Part I nr. 765 of 21/10/2002.

[7] Agreement of 10/11/1993 between the Romanian Government and the Government of Luxemburg on the transportation on navigable routes, published in the Official Gazette, Part I nr. 138 of 01/06/1994.

[8] Agreement of 06/06/2000 between the Romanian Government and the Government Slovakia on international road transportation, published in the Official Gazette, Part I nr. 136 of 20/03/2001.

[9] Instructions of 24/03/2003 on the medical and psychological examination of the transport personnel with responsibilities regarding circulation and navigation safety published in the Official Gazette, Part I nr. 364bis of 28/05/2003.

[10] Agreement of 08/04/1976 between the Socialist Government of the Romanian Republic and the Government of the Chinese Popular Republic on the maritime navigation, published in the Official Bulletin nr. 60 of 28/06/1976.

[11] Protocol of 22/10/1991 the Romanian Government and the Government of the Federal republic Of Germany on inland waterway navigation, published in the Official Gazette, Part I nr. 77 of 29/04/1992.

[12] Law nr. 138/1999 on the salary and other rights of the military personnel in the public institutions of national defense, public order and national security and on granting several salary rights to the civil personnel in these institutions, published in the Official Gazette, Part I nr. 347 of 22/07/1999.

[13] G.D. nr. 245 din 04/03/2003 approving the Implementation Regulation of G.O. nr. 42/1997 on naval transportation, published in the Official Gazette, Part I nr. 185 of 25/03/2003.

[14] O. G. nr. 42/1997 (r) on maritime transportation and the transportation on inland waterways..

[15] Ratified by Romania by Law nr. 73/1930, promulgated by Decree nr. 1.391/1930, published in the Of. G nr. 91 of 26/04/1930.

[16] Ratified by Romania by Law nr. 73/1930, promulgated by Decree nr. 1.391/1930, published in the Of. G nr. 91 of 2/6/04/1930.

[17] Romania ratified the Convention by Law nr. 55/1923, promulgated by Decree nr. 2.541/1923, published in the Of. G nr. 46 of 2/06/1923.

[18] Ratified by Romania by the Decree - Law (royal) nr. 1902/1922, published in the Of. G nr. 11 of 14/04/1922.

[19] Ratified by Romania by Law nr. 194/1932, promulgated by Decree nr. 2.756/1932, published in the Of. G nr. 222 of22/09/1932.

[20] Ratified by the Great National Assembly by Decree nr. 213/1957, published in the Official Bulletin nr. 4 of 18/01/1958.

[21] In published in the Of. G nr. 98 din 06.05.1929.
[22] The Romanian Government ratified the Convention by G.D. nr. 16 of 27.01.2000, published in the Of. G nr. 34 of 28.01.2000, approved by the Romanian Parliament by Law nr. 155 din 26.07.2000 and promulgated by the Decree of the President of Romania nr. 223/2000, both published in the Of. G nr. 360 of 02.08.2000.
[23] The Romanian Government ratified the Convention by G.D. nr. 16 of 27.01.2000, published in the Of. G nr. 34 din 28.01.2000, approved by the Romanian Parliament by Law nr. 155 din 26.07.2000 and promulgated by the Decree of the President of Romania nr. 223/2000, both published in the Of. G nr. 360 of 02.08.2000.
[24] Ratified by Romania by Law nr. 140 of 2906.1998, promulgated by Decree nr. 251/1998, both documents published in the Of. G. nr. 249 of 06/07/1998.
[25] R.S.R. ratified the Convention by the Decree of the State Council nr. 25 of 03.02.1976, published in the Official Bulletin nr. 10 of 09.02.1976.
[26] R.S.R. ratified the Convention by the Decree of the State Council nr. 83 of 23.07.1975, published in the Official Bulletin nr. 86 of 02.08.1975.
[27] The Romanian Government ratified the Convention by G.D. nr. 16 of 27.01.2000, published in the Of. G nr. 34 of 28.01.2000, approved by the Romanian Parliament by Law nr. 155 of 26.07.2000 and promulgated by the Decree of the President of Romania nr. 223/2000, both published in the Of. G nr. 360 of 02.08.2000.
[28] R.S.R. a ratified the Convention by the Decree of the State Council nr. 83 of 23.07.1975, published in the Official Bulletin nr. 86 of 02.08.1975.
[29] Ratified by the Decree of the State Council nr. 83/1975, published in the Official Bulletin nr. 86 of 02/08/1975.
[30] Ratified the Convention by the Decree of the State Council nr. 83/1975, published in the Offficial Bulletin nr. 86 of 02/08/1975.
[31] Both ratified by G.O. nr. 56 of 24/08/1999, published in the Of. G, Part I nr. 208 of 26/08/1999.
32] The Romanian Government approved the Norms by G.D. nr. 672 of 05.06.2003, published in the Of. G nr. 449 of 26.06.2003.
[33] The Romanian Government ratified the Convention by G.D. nr. 16 of 27.01.2000, published in the Of. G nr. 34 of 28.01.2000, approved by the Romanian Parliament by Law nr. 155 of 26.07.2000 and promulgated by the Decree of the President of Romania nr. 223/2000, both published in the Of. G nr. 360 din 02.08.2000.
[34] The Romanian Government ratified the Convention by G.D nr. 16 of 27.01.2000, published in the Of. G nr. 34 of 28.01.2000, approved by the Romanian Parliament by Law nr. 155 of 26.07.2000 and promulgated by the Decree of the President of Romania nr. 223/2000, both published in the Of. G nr. 360 of 02.08.2000.
[35] Published in the Of. G al Romania nr. 34 of 28 January 2000.
[36] The term commander includes any person who has the command and the responsibility of a ship, except the pilots.
[37] The term navigator includes any person hired on ay position on board of a ship and registered in the employment agreement on the ship; it excludes the commanders, the pilots, the cadets, the students of ship-schools and the apprentices with special contracts, the crew in the military navy and other persons in the permanent service of the state.
[38] POPESCU, A. *Drept Internaţional şi european al mucii*. Ediția2, Editura C.H. Beck, Bucureşti, 2008, p. 239-250.

FROM THE BARGAIN/BARGAINING "AGREEMENT" TO THE SHIPPING AGREEMENT (III)

[1]GRIGORUT CORNEL, [2]ANECHITOAE CONSTANTIN, [3]COJOC MARIANA,
[4] GRIGORUT LAVINIA-MARIA

[1,2,3]University "Ovidius", Constanta, [4]National Institute of Economic Research "Costin Kirițescu", Bucuresti, Romania

ABSTRACT

The analysis of the legal components of the boarding agreement shows that this contract, in fact, is an individual employment contract concluded for a fixed period, with a particular suite of elements determined by very specific of the sailor profession.

The individual boarding agreement is an undefined legal concept, which incidentally regulates the meaning of "individual employment contract concluded for a fixed period" by employees who are part of the crew

Keywords: *Embarking, embarking, Collective Work, boarding personnel*

8. THE INDIVIDUAL BOARDING AGREEMENT

8.1. National sources

The work done by natural persons on a maritime or river vessel was regulated by the following acts:

1. Labor Code [1]

2. Art. 531 -556 (contained in Book III, "On maritime trade and navigation", Title III - "On crew recruitment and salaries) of the Commercial Code (published in Booklet no. 0 of 6/27/1997) ;

3. Decree no. 40 of the Merchant Marine 02/14/1950 (Published in Official Gazette no. 11 of 14 February 1950);

4. Decree no. 41 of 14.02.1950 on the supervision, control and order of maritime and river navigation (Published in Official Gazette no. 11 of February 14, 1950). Decree no. 40/1950 and Decree No. 40/1950. 41/1950 were repealed by Decree no. 443/1972;

5. Decision of the Council of Ministers no. 40 of 01/18/1973 approving the Regulation containing rules regarding civil navigation (Published in Official Gazette no. 7 of 25 January 1973).

6. Decree no. 443/1972 regarding civil navigation (published in the Official Gazette, Part I, no. 132 of 23 November 1972). This document provides that the legal rules of labor law are governed by labor law rules. In turn, Decree no. 443/1972 was expressly repealed, except Chapter VI - "Crimes" - and replaced by GO 142/1972;

7. Government Ordinance no. 142/1997 on naval transportation (published in the Official Gazette of Romania, Part I no. 221 of July 21, 1997), approved with amendments and repeals by Act No, 412/2002. The part regarding criminality contained in Decree no. 443/1972 and non-repealed by the Government Ordinance no. 142/1997, was expressly repealed by Law no. 191 / 2003 on the offenses regarding the regime of naval transportation (published in the Official Gazette of Romania, Part I, no. 332 of 16 May 2003);

8. Government Ordinance no. 42 of 28.08.1997 on civil navigation is approved by Law no. 412 of 2002; HCM no. 40/1973 and Decree No. 443/1972 are repealed, except Chapter IV - "Crimes" and, at the same time, the definition of the rules of navigation is updated;

9. Government Ordinance no. 42 of 28.08.1997 on naval transportation. GO no. 42/1997, after the publication in the Law. 412/2002, has been named by the Order on naval transportation, while changing the law in general. The implementing rules are governed by GD. 245/2003[1] for approving the methodological norms on naval transportation. The legal rules of Law no. 412/2002 refer to the institutional system of naval transport, shipping activities, marine transport means, the crew and vessel crew, activities carried out by means of water transport, navigation surveillance and control in ports and inland waterways. There are not, however, specific rules for the Port of Constanta. Government Ordinance no. 42/1997 was amended and supplemented by Government Ordinance no. 48 of 07.29.2003 and the Government Emergency Ordinance no. 74 of 20.09.2006 amending and completing Government Ordinance no. 42/1997 renamed under art. I point 1, as follows: "Ordinance on maritime and inland waterways transport;

10. Government Decision no. 83 of 23/01/2003 regarding the authorization of trade companies providing services of selection and placement of the maritime and river sailing staff on ships flying a Romanian or foreign flag, and establishing several financial security measures in case of their abandonment outside Romania [2];

11. Law no. 130 of 10.16.1996 on the collective employment agreement [3];

12. Law no. 132 of 12.11.1999 on the settlement of labor disputes [4];

13. Law no. 346 of 05.06.2002 on the insurance for work accidents and professional diseases [5];

14. Emergency Ordinance no. 129 of 31.08.2000 on the vocational training of adults [6];

15. Order of the Minister of Public Works, Transportation and Housing no. 1908 of 28.11.2002 on the Methodology for issuing labor cards in ports and the registration of port workers [7];

16. Order of the Minister of Transport, Constructions and Tourism no. 318 of 03/03/2006 regarding the approval of the training standards, competence confirmation and issue of competence

certificates to the sailing staff for inland waterways ships flying the Romanian flag [8];

17. Order of the Minister of Transport no. 509 of 06/20/2007 amending the Order of the Minister of Transport, Constructions and Tourism no. 318 of 03/03/2006 regarding the approval of the training standards, competence confirmation and issue of competence certificates to the sailing staff for inland waterways ships flying the Romanian flag [9]

18. Order of the Minister of Transport, Constructions and Tourism no. 214 of 07/02/2007 approving the minimum criteria for the training of the Romanian maritime and harbor sailing staff who does not fall under the STCW Convention]10];

19. Order of the Minister of Transport, Constructions and Tourism no. 1627 of 07/09/2006 approving the minimum criteria for training the maritime sailing staff and the system of recognition of certificates of competence [11];

20. Order of the Minister of Transports no. 512 of 21/06/2007 amending and supplementing the Order of the Minister of Transport, Constructions and Tourism no. 1627 of 07/09/2006 approving the minimum criteria for training the maritime sailing staff and the system of recognition of certificates of competence [12];

21. Order of the Minister of Public Works, Transportation and Housing no. 1908 of 28/11/2002 approving the Methodology for the issue of labor cards in ports and the registration of port workers [13].

22. Order of the Minister of Economy and Finance no. 822 of 25/07/2007 on the organization of working time for the staff working off-shore [14].

The employment relationships of crew members [15] of ships flying the Romanian flag in relation to their employers are determined by the provisions of the national legislation, international agreements and conventions to which Romania is party, and based on collective employment agreements and on individual boarding agreements.

The Labor Code defines the individual employment agreement as a "the contract under which a natural person, named employee, undertakes to perform work for and under the authority of an employer, natural or legal person, in exchange for remuneration, called salary" (art. 10). Nicolae Voiculescu, claims that the term traditionally used in the literature is that of "subordination", which better reflects the fundamental characteristics of an employment contract which gives employers the opportunity to have three major powers: legislative, organizational and disciplinary [16].

8.2. The legal status of the boarding agreement

In order to establish specific rights and obligations of employees, employment is done upon the individual boarding contract, subject to the provisions of the Collective Work Agreement.

The term "employees" or "boarding personnel" defines all the persons employed under the individual employment contract or the individual boarding contract, no matter the term of employment.

For the boarding personnel on ships that sail beyond national waters, the individual boarding agreement will be concluded as an appendix to the individual employment contract.

According to art. 1 of Government Decision no. 83/2003 on the authorization of the companies providing the selection and placement of crewing personnel for maritime or inland navigation under Romanian or foreign flag , and also referring to the establishment of financial security measures in case of abandonment of the personnel outside the Romanian borders, the companies established under Law no. 31/1990 and the branches of foreign companies established in Romania that are dealing with crewing operations (maritime or inland) that implies Romanian personnel on ships sailing under the Romanian or foreign flag, have the status of *crewing agencies* only upon the operating permit issued by The Romanian Naval Authority. The Law does not require a unique activity object, but requires that crewing agencies have expressly provided in the articles of association, the object of activity - "the selection and placement of labor force".

Ion Traina Stefanescu states that *crewing agencies are similar to temporary work agencies* as it concerns the terms of selection and the placement of the working personnel [17].

The crewing agencies provide services of selection and placement of such personnel on board ships sailing under the Romanian or foreign flag, if one has the minimum age of 16 years and the Romanian citizenship.

The necessary level of education is determined by Order no. 1627/2006 of the Ministry of Transport, Constructions and Tourism approving the minimum criteria for education and training of Romanian seafarers and the system of the recognition of certificates of competence.

Gheorghe Piperea [18] says that an individual boarding contract is, in fact, an individual contract concluded for a fixed term of employment between an employer and an employee who is part of the crew.

The individual boarding contract will be completed in two copies: one for employer and the other one for the employee.

The employee must always have with him the individual boarding contract and he must provide it to those dealing with labor inspection in the country and abroad, when checking is carried out on board.

In order to have their apprenticeship periods and their embarking (on ships flying a Romanian or foreign flag) taken into account, upon their arrive from voyages, the seafarers must submit to the Romanian Naval Authority a certificate issued by the crewing agency that has selected and placed them, showing the name of ship owner of the, the name of vessel, the registration number of the ship at the International Maritime Organization (IMO number), the gross tonnage of the vessel, the vessel's propulsion engine power, his/her position and the embarking period and the characterization issued by the commander / chief engineer of the ship or by the ship owner.

8.3. Complying with the individual boarding agreement in foreign countries

Determining the law applicable to labor migration is not an easy task. In the case of labor migration of seamen, occasioned by the conduct of business in several states, or navigating in the territorial waters of several countries, this problem is usually solved by applying the principle of the law enforcement of the country under whose flag they navigate flies.

This rule is in line with the new EU coordination regulation no. 883/2004 which introduced a new principle: the mutual recognition and assimilation of facts.

The fact that substantial differences still remain between countries demonstrates the complexity of coordination issues regarding security and labor systems.

Current EU coordination rules require member states, in the national social security systems, not to treat the citizens of other Member States differently from their own citizens when they perform activities within a Member State.

The general ship roll is an internal organizational document, including the nominal allocation of crew members to the intervention position in cases of fire, damage, ship abandonment, which requires urgent action for the safety of the ship or for saving people. The general ship roll must be made at the ship's entry into service and it is kept up to date, operating whenever changes occur in personnel cases. For each post there are fixed the duties and the procedure regarding: the closing of watertight doors and bottom valves, pipes leak checking axle damper and fire protection installation, putting down fires, preparing the boats and the other life saving equipment on board in order to abandon the ship, announcing the passengers in case of evacuation of the ship, driving them to boarding stations, boarding supervision etc. The general ship roll nominally allocated the entire crew in rescue craft, in accordance with the "International Convention for the Safety of Human Life at Sea" relating to: the maximum capacity, the appointment of a boat chief, assuring a sufficient number of certificated sailors etc. For the cases of fire and ship abandonment, the general roll provides for the special signals that are transmitted on the ship by means of whistle, buzzer or ringtones.

The partial rolls derive from the general roll: of fire, damage, boats, abandonment etc. on which there are conducted training exercises with the crew.

9. CONCLUSIONS

The sailors having Romanian citizenship can be employed on foreign-flagged vessels only by means of crewing agencies known as agencies (companies) of crewing [19] (which is the guarantee of financial security).

If the Romanian crews are employed, on their own, on ships flying a foreign flag – which is a possible option, according to art. 14 of Government Decree no. 83/2003 – they can not get financial security measures in cases of their abandonment outside Romania.

The analysis of the legal components of the boarding agreement shows that this contract, in fact, is an individual employment contract concluded for a fixed period, with a particular suite of elements determined by very specific of the sailor profession.

Obviously, the boarding contract (of employment) of seafarers is applied common law rules of the Labor Code, if they are not contrary to the specific rules listed above [20].

The individual boarding agreement is an undefined legal concept, which incidentally regulates the meaning of "individual employment contract concluded for a fixed period" by employees who are part of the crew [21].

10. EFERENCES

[1] Labor Code - *Law nr. 53/2003,* published in the Of. G, Part I nr. 72/5.02.2003, modified and completed by *Law nr. 480/2003* (Of. G, nr. 814/18.11.2003), *Law nr. 541/2003* (Of. G, nr. 913/19.12.2003), *Government Emergency Ordinance nr. 65/2005* (M. Of. nr. 576/5.07.2005), approved with modifications, by *Law nr. 371/2005* (Of. G, nr. 1147/19.12.005) and Government Emergency Ordinance *nr. 55/2006* (Of. G, nr. 788/18.09.2006).

[2] published in the Of. G, Part I nr. 84 of 11/02/2003, when it entered in force. Modified by G.D. nr. 2173/2004.

[3] Republished in the Of. G, Part I nr. 184 of 19/05/1998, when it entered in force. Modified by the Labor Code of 2003 and the Emergency Ordinance nr. 9/2004.

[4] Published in the Of. G, Part I nr. 582 of 29/11/1999, the Act entered in force on 01.01.2000. Modified by Emergency Ordinance nr. 138/2000.

[5] Published in the Of. G, Part I nr. 454 of 27/06/2002, the Act entered in force on 01.01.2003. Modified and completed by the Ordinance by: Emergency nr. 107/2003; Emergency Ordinance nr. 129/2004; Emergency Ordinance nr. 171/2005 and by Law nr. 186/2006.

[6] Republished in the Of. G, Part I nr. 711 of 30/09/2002, when it entered in force. Modified by G.O. nr. 76/2004.

[7] Published in the Of. G, Part I nr. 888 of 09/12/2002, when it entered in force.

[8] Published in the Of. G, Part I nr. 315 of 07/04/2006, when it entered in force.

[9] Published in the Of. G, Part I nr. 470 of 12/07/2007, when it entered in force.

[10] Published in the Of. G, Part I nr. 123 of 20/02/2007, when it entered in force.

[11] Published in the Of. G, Part I nr. 917 of 07/09/2006, when it entered in force.

[12] Published in the Of. G, Part I nr. 471 of 12/07/2007, when it entered in force.

[13] published in the Of. G, Part I nr. 888 of 09/12/2002, when it entered in force.

[14] Published in the Of. G, Part I nr. 537 of 08/08/2007, when it entered in force.

[15] The crew is formed by the crew and by the auxiliary personnel and its organization is made according to the type and the destination of the vessel.

[16] VOICULESCU, N. *Dreptul muncii. Reglementări interne şi comunitare*, Ediția a 2-a, Editura Woters Kkuwer, Bucureşti, 2007, p. 9. See also: R. Gidro, *Opinii asupra unor dispoziții din proiectul Codului Muncii cu privire la încheierea şi conținutul contractului individual de muncă,* în Revista Română de Dreptul muncii nr. 1/2002, p. 22.

[17] ŞTEFĂNESCU, I. T. *Tratat de dreptul muncii*, Editura Wolters Kluwer, Bucureşti, 2007, pp. 442-443.
[18] Apud. PIPEREA, G. *Dreptul transporturilor. Ediția 2*, op. cit. p. 153. SAee also: *Octavian Căpățînă, Gh. Stanca,* op. cit., vol. II, p. 322, and *Şerban. Beligrădeanu,* Contractul individual de ambarcare, in: *Şerban Beligrădeanu, lon Traian Ştefănescu,* Dicționar de drept al muncii de Ed. Lumina Lex, Bucureşti, 1997, p. 42-43. Dicționarul de drept al muncii - art. 39 - 40 of G.D. 42/97 (r) which was cancelled by art. I pct. 31 of O.U.G. nr. 74/2006. See also: Şerban Beligrădeanu - "Natura juridică a contractului individual de ambarcare (îmbarcare)", in *Revista Dreptul* nr. 5/2003, p. 29.
[19] Crewing companies are agencies of labor force placement abroad.
[20] See POPOACA, M. *Natura juridică a contractului de ambarcare al marinarilor. Drepturile şi obligaţiile personalului navigant de pe navele comerciale sub pavilion român,* În: Revista Română de drept maritim, anul II, nr. 4/2000, pp. 27-35 şi Revista de Drept Comercial nr. 7-8/2001, p. 149 -158.
[21] Şerban Beligrădeanu - "Natura juridică a contractului individual de ambarcare (îmbarcare)", in *Revista Dreptul* nr. 5/2003, p. 29.

STUDY OF THE DESTRUCTION INFLUENCE OF ELEMENTS FROM OFFSHORE PLATFORM LEG ON STRESS AND VIBRATION MODES

[1]DOBROT OANA-MIRELA, [2]MOCANU COSTEL-IULIAN

[1,2]University "Dunarea de Jos" of Galati, Faculty of Naval Architecture, Romania

ABSTRACT

In this paper, a model of platform leg has been modeled analytically using finite element program. The numerical results were compared with results from experimental test.

The scope was to obtain numerical results witch can lead to conclusions related to the behavior after destruction of some component elements of the foot. The study was also oriented on the influence of links destruction between composing elements of their own pulsations.

Keywords: offshore, stress, finite element method, experimental tests.

1. INTRODUCTION

Since its inception sixty years ago, the offshore structures industry has been growing at a fast rate. The literature on fixed offshore structures is huge. The continuous increase in the water depth for which these structures have to be designed necessitated the use of new modelling approaches to understand how these structures behave under realistic loads.

Among the various types of offshore structures, the steel jacket platform is the most common in use. Over the years, it has assumed a multi-functional role, being used for oil exploration, drilling as well as production.

Conventionally, such platforms are built up to a depth of about 100–150 m, though some of them have exceeded 200 m. Usually, they are built from tubular steel members. These structures have a very low time period ranging between 2 and 8 s. An offshore structure such as a steel jacket platform apart from the operational loads also experiences environmental loads such as wind, wave and earthquake loads.

The interest in damage detection of structures has increased greatly in the last two decades.

Researchers were interested in damage detection in bridges, composite structures, ships, and offshore structures. Several approaches have been suggested to rationalize inspection of offshore platforms using reliability-based methods and damage detection techniques.

1.1 Offshore Platforms

Offshore platform, also referred to as an oil platform or oil rig, is a large structure with facilities to drill wells and extract and process oil and natural gas and export the products to shore.

Depending on the circumstances, the platform may be fixed to the ocean floor, may consist of an artificial island, or may float.

Being among the major European countries holding reserves of oil and natural gas, Romania also, went to detection and exploitation of offshore oil deposits in the Black Sea continental shelf. Need's to expand petroleum and natural gas in Romania determined the starting of prospecting operations in the Black Sea exclusive economic zone.

Offshore drilling platform are divided in: fix and mobile platforms.

1.1.2 Fixed Offshore Platforms

Fixed offshore platforms are placed directly on the sea and can be used for drilling, extracting and production operations.

The drilling platforms support system can be: from tubular steel members, slender flexible towers, concrete caisson structures.

1.1.2 Mobile Offshore Platforms

Extremely high cost price and long lead times for assembling and dismantling a fixed drilling platform lead to the development of mobile structures.

Type of mobile offshore platforms: mobile self-lifting marine platform, semi-submersible mobile platforms, submersible mobile platforms.

In 1972 was developed a program of exploitation of resources from the Black Sea continental shelf, within the Romanian Marine Research Institute from Constanta.

On 9 November 1975 was launched on water from Galatz shipyards, first romanian offshore drilling marine platform „GLORIA" and has started drilling activities on 16 September 1976, at a distance of 72 Mm in the Black Sea at a depth of approximately 90 m.

Were built then and other offshore platforms: Horizon, Prometheus, Fortuna, Atlas, Jupiter and Saturn.

Romanian erecting platforms were built at shipyards in Galatz, was designed and sized for the following conditions: The average water depth of 90 m, wave amplitude of 12 m, 10 s wave period, Maximum wind speed (no more than 1 minute) of 164 km / h, maximum load on one foot of 2300 ft, Maximum penetration is 6m feet in the mud, leg length is 121.9 m.

The basic components of an oil drilling platform are: main body with parallelepiped shape which builds on four legs to the seabed, as is presented in Figure 1.

Figure 1 Gloria Offshore Platform

1.2 Elements component of a platform leg

Gloria offshore drilling platform is a platform that has four legs erecting the tubular lattice.

Trusses are systems consisting of straight bars, on which loads act only applied to nodes. Points which occur in bars are called nodes.

Assumptions allowed the calculation of trusses are: bars have right axis and are centered in knots; the nodes are considered perfect joints (without friction); force structure applies only to nodes.

Lattice beam bars delimiting the upper plate forming the upper beam. The bottom of the beam is called the lower plate. Vertical bars are called diagonal uprights and slopes. The set of diagonals and uprights are lattice beam. In the figure 2 are presents the nomenclature used in general to common trusses.

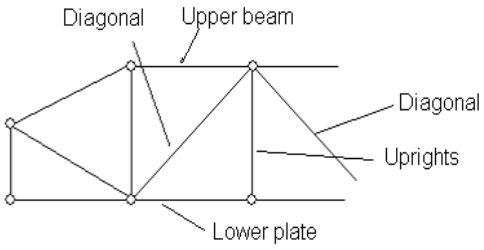

Figure 2 Nomenclature of the trusses

In trusses static structures determined general method for determining the effort is the method of sections. Particularities application of this method depends on the type of structure. In the case of trusses, the method is presented in two forms: process and procedure sections some particular section (isolation nodes).

1. Process of some sections. The process is based on equilibrium expression of a part of structure, driven by external loads forces known and link forces from the bars cut.

2. Isolation process nodes. This process is a special case of the method consists in isolating sections and sections cut through all nodes all the bars around each node. Bars are replaced by efforts suppressed axial unknown. By this, one truss with "n" nodes, leading to "n" independent force systems.

Producing oil and gas from offshore by means of fixed platforms has gained a tremendous momentum in the energy industry in the past ten years. Design of such structures is dependent upon lateral forces applied by environmental conditions such as waves, currents, impacts as well as seismically-induced excitations.

Severe lateral forces may cause considerable damage to load carrying members and endanger overall stability of the structure. To counter this problem, braces are designed to withstand lateral excitations and dissipate earthquake input energy through buckling in compression and yielding in tension. Tubular joints in offshore structures exhibit different failure mechanisms such as joint rupture due to the increase in the size of the affected zone and punching shear failure due to excessive shear forces induced in chord and brace intersection.

Moreover, local cyclic stresses may cause fatigue problems in joints and result in gradual strength deterioration or sudden fracture of connections.

1.3 How to consider leg components

Beam element will be assigned to a straight bar of uniform transversal cross section able to support axial forces, bending moments around the principal axes of sectional transversal plane and torques around the central axis.

Forces acting on the beam are:

- S_1 and S_7: axial forces
- S_2, S_3, S_8 and S_9: shear forces
- S_5, S_6, S_{11} and S_{12}: bending moments
- S_4 and S_{10}: torsion moments

Location and positive direction of these forces is shown in figure 3.

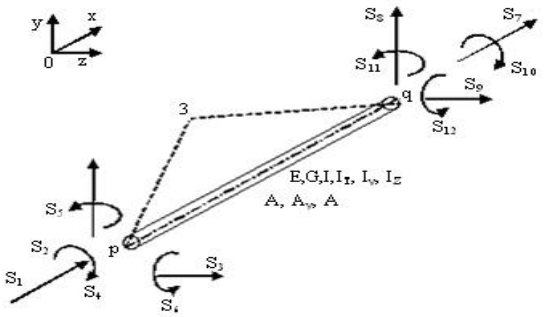

Figure 3 Beam elements in space

Corresponding displacements u_1, u_2, u_3 ... u_{12} will be taken so that to be positive in positive direction of forces.

Stiffness matrix of a beam element is of the order 12x12, but if the axes at local system of coordination are chosen to coincide with the principal axes of the transversal cross section is possible that the order 12x12 stiffness matrix to be constructed from the stiffness of the order sub-matrix 2x2 and 4x4. Forces S_1 and S_7 depend only on their corresponding displacements, the same as moments S_4 and S_{10}. Instead of bending moments and shear forces in the xy plane will not only depend on their corresponding movements but also movements of the forces corresponding xz plane. In case

that the principal axes of the transversal cross section coincide with the planes xy and xz, bending and shearing from this plane can be considered independently of one to another.

2. NUMERICAL ANALYSIS

The Finite Element Method (FEM) knew a quick development in tandem with the increase of the computational capacities and it has enforced as a general numerical method of solving engineering problems from different areas, inclusively the naval domain.

Generally a structural analysis has the following steps: the objectives settlement, the type and the size of the analysis; the modelling of structures and the boundary conditions; the settlement of type and the modelling of the loads; the analysis and the evaluation of the results.

The type and the size of the analysis depend on the nature of the structural response that is to be obtained. Generally to the structural analyses can be obtained the following categories of responses: stresses and deformations for a loading case; eigen vibration modes; the behaviour of structural elements at buckling (stability loss).

At the naval structures the deformations and the stresses can be divided in the following categories, depending on the analyses problem: global deformations and stresses of the ships girder and main structural elements, local deformations and stresses of the main and secondary structural elements, stress hot spot zones in the structural elements.

For the analytic determination of the stresses and deformations, static and dynamic, into the structure, generated by external and thermal loads, it has to be obtained a solution of the elasticity theory equations, with the accomplishment of the boundary conditions enforced to the structure. The structural analysis through the finite element method requires using the same equations of the elasticity theory.

MEF fundamental equation is:

$$[K]\{U\} = \{Q\} \qquad (1)$$

where [K] represent the rigidity matrix and the {U} is displacement vector.

2.1 Leg structure meshing

In ”Dunărea de Jos” University of Galați, in structure laboratory was builded a steel model for a platform leg. In this paper is presented an numerical (using FEM) and experimental test for the model to see the distribution of stress in different loading case.

To determine by calculation the stress was used the COSMOS software, because is easy to work with and provides quick results.

The main leg loads are given by: own weight, body platform weight, wave loads acting on leg structure and wind loads acting on lateral surface of platform body. For FEM analysis we adopt series of calculations which result from composition of the loads outlined above.

Jacket structure was meshed in to 3D elastic beam elements on each node (5193 element). Elements were achieved by rigid nodes.

In figure 4 is presented the mesh structure.

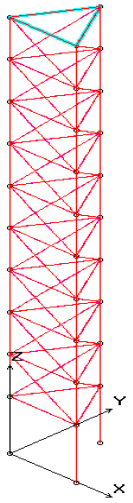

Figure 4 Mesh structure

The stress distribution for model leg charged with 1000N for any element destroyed is present in figure 5. In figure 6 is 1st mode (bending) for model leg, any element destroyed.

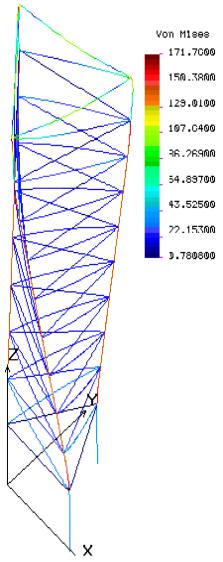

Figure 5 Stress distribution for model leg charged with 1000 N (any element destroyed)

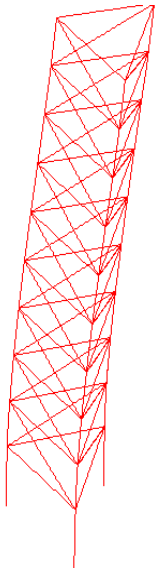

Figure 6 1st mode (bending) for model leg (any element destroyed)

2.2 Results

Frequency for 1st and 2nd mode of vibration variation depending on the number of elements destroyed is present in table 1.

Table 1. Variation of the eigenvalue with number of destroyed elements

Number of elements destroyed	Frequency for 1st mode of vibration [cycle/sec]	Frequency for 2nd mode of vibration [cycle/sec]
0	0.744	1.55
1	0.739	1.543
2	0.736	1.537
3	0.731	1.524
4	0.729	1.519

Numerical stress variation depending on the number of elements destroyed is present in table 2.

Table 2 Variation of stress with number of destroyed elements

Number of elements destroyed	Stress [Pa]
0	171.76
1	174.48
2	174.65
3	175.27
4	184.92

3. EXPERIMENTAL ANALYSIS

3.1 Model description

Of experimental methods for determinate the state of stress with remarkable result as accurate and provides good yield and relatively low cost is the Electrical Tensometry (ET) using strain gauge.

ET is the method of measuring deformation and elongation of a solid body, by means of transducers which transform mechanical deformation changes in variations of electrical quantities.

The resistor is bonded to a substrate or embedded in the medium (plastic or paper). Because it has dimensions small, resistive transducer is called strain gauges or stamp strain gauges.

The transducer is glued piece of research in order to follow its deformations. To achieve an accurate measurements, in electrical strain gauges is used to bridge the transducer assembly, is difficult to measure with sufficient precision with ohmmeter resistance. The simplest type of assembly is the Wheatstone bridge.

The stand represents a platform leg reduced to 1:15 scale, keeping also the ratio between element diameter / wall element thickness. At the bottom, to simulate connection leg - bottom water has built a very rigid structure that simulates fixity.

Locations trademarks strain gauges are shown in figure 7.

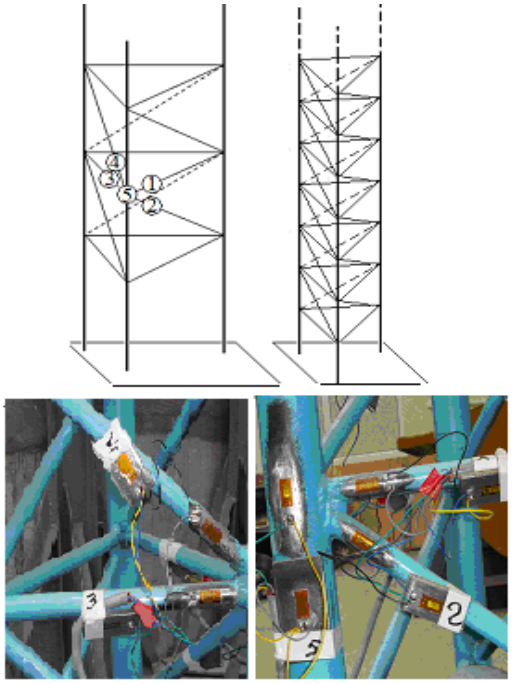

Figure 7 Locations of strain gauges on the leg

The system of data registration is composed by strain gauges posed as is represented in Figure 8; a tensometric acquisition equipment Spider8 (Hottinger); laptop with a soft of acquisition Catman professional.

Figure 8 Stand with acquisition system

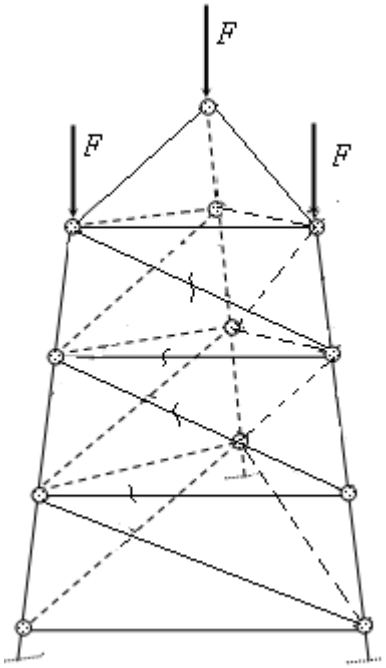

Figure 9 Locations of destroyed elements on the leg

3.2 Results

Experimental frequency variation for 1st and 2nd mode of vibration is present in table 3 and in table 4 is present stress variation for any elements destroyed.

Table 4 Stress for elements destroyed

Number of elements destroyed	Stress [N/mm^2]	Error [%]
0	168.32	2.00
1	171.86	1.5
2	169.59	2.9
3	174.57	0.4
4	183.26	0.9

4. CONCLUSIONS

There aren't experimental results for the variation own pulsation with number of elements destroyed because there was no way to measure them.In figure 10 is presented the numerical of frequency for 1st mode with number of element destroyed for model leg.

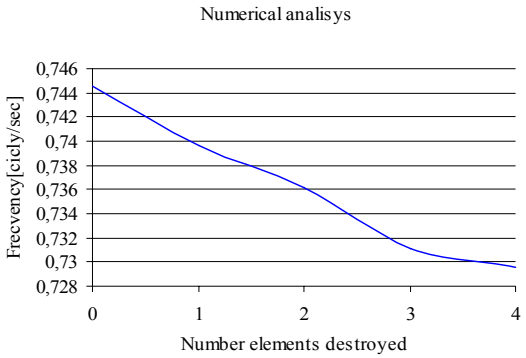

Figure 10 Frequency for 1st mode/ number element destroyed

In figure 11 is presented the numerical of frequency for 2nd mode with number of element destroyed for model leg.

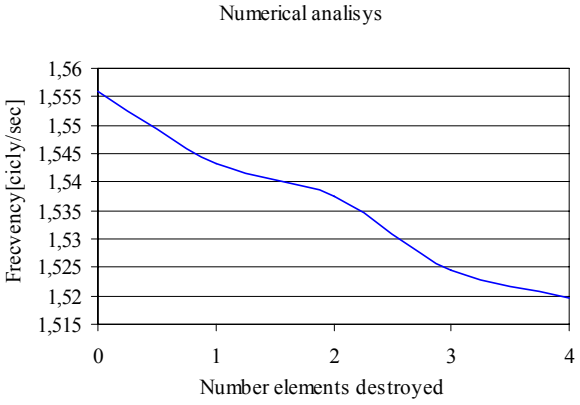

Figure 11 Frequency for 2nd mode/ number element destroyed

In figure 12 is comparison of experiment and numeric result with stress / number element destroyed

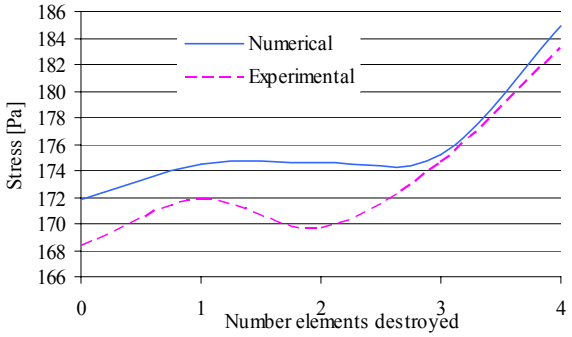

Figure 12 Variation stress depending on the number element destroyed

As it can be seen from the tables and graphics, the major conclusions of this study are summarized below:
1. destroyed of some elements of the structure of an oil rig leg leads to:
- Lowering the own pulsation. This is explained by the fact that the leg stiffness has been decreased.

- Increasing the stress on leg structure of the elements. This is explained by the fact that fewer components participate at the leg solicitation.
2. As a result of the conclusion 1 the destroyed of elements of the drilling platform leg structure has consequences that could be harmful to both increasing the number of elements destroyed.

ACKNOWLEDGEMENTS

The present study has been performed in the frame of the PhD program POSDRU 88/15/S ID-61445– EFICIENT grant of the „Maritime" University of Constanta, 2010.

6. REFERENCES

[1] MOCANU, C.I.**,** *Strenght of materials*, Press Foundation „Dunarea de Jos" University, Galati 2006.
[2] MOCANU, D.R, others: *Experimental stress analysis*, ED. TEHNICA, Bucuresti , 1977.
[3] BUZDUGAN GH., *Vibratii mecanice*, Ed. Didactica si Pedagogica , Bucuresti, 1982.Kuwahara, K et al., *"Direct Simulation of a Flow around an Airfoil",* JSCFD Jones , D.A., 2000.
[4] DOMNISORU L. – *"Finite element method in shipbuilding"*, Engineering Publisher, Bucharest, 2001
[5] DOMNISORU L. – *"Structural analysis and hydroelasticity of ships"*, The University Foundation „Dunarea de Jos" Publishing House, Galati -2006.
[6] DOMNISORU L. – *"Local and general vibration on the ships"*, The University Foundation „Dunarea de Jos" Publishing House, Galati -2007

EXECUTION OF MARITIME PILOTAGE

[1]GEORGESCU STEFAN, [2]SIVRIU GEORGIANA, [3]ACOMI NICOLETA

[1.2.3]*Constanta Maritime University, Romania*

ABSTRACT

The essence of a good plan is knowing the limits within which the ship may be navigated in safety. The essential questions which the Navigating Officer must be able to answer at all times during a pilotage passage are:

Is the ship on track?

If not, where is the ship in relation to the track and what steps are being taken to regain it?

How close is the ship to danger?

How far is it to the next alteration of course?

Are the tidal streams and depths of water as predicted?

Keywords:. *headmark, marks, buoys*.

1. EXECUTION OF PILOTAGE

The essence of a good plan is knowing the limits within which the ship may be navigated in safety. The essential questions which the Navigating Officer must be able to answer at all times during a pilotage passage are:

Is the ship on track?

If not, where is the ship in relation to the track and what steps are being taken to regain it?

How close is the ship to danger?

How far is it to the next alteration of course?

Are the tidal streams and depths of water as predicted?

Organisation and records

A team effort is needed to execute a pilotage plan in safety; Table 1 is a recommended organisation for a 150m length ship. Other ships may need to modify this as necessary, dependent on the size of the ship and the team available.

The pilotage team should produce sufficient records for the ship's track to be accurately reconstructed, if required. The fixes and soundings taken through the passage should provide a series of confirmatory checks to support the visual picture and DR/EP times to support 'wheel over' bearings, etc.

Maintaining the track

An estimate of the distance off track may be made by looking along the desired bearing of the headmark and then making a direct assessment of how far the ship is

is '50 yards to *port* of track'. Remember that 1° off the track is equivalent to a distance of about 100 feet at 1 mile, ½ cable at 3 miles.

When running a mark on a cross-tidal stream, the course steered is bound to differ from the planned bearing of the mark. If the correct bearing is not being maintained, the ship is off track; it must be regained by a bold alteration. When the track has been regained, a course must be steered which will counteract the tidal stream more adequately than the original one.

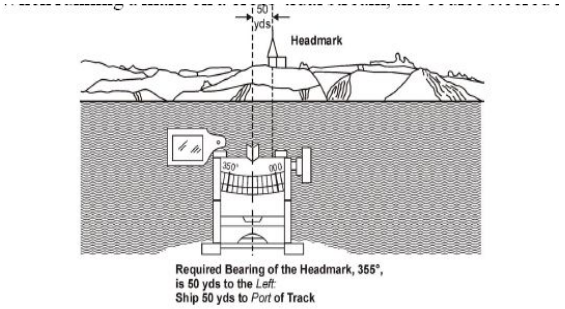

Fig. 1. Running a headmark: ship to port of track

Table 1. Pilotage organisation

CAPTAIN	In command, overall responsibility for ship safety.
NAVIGATING OFFICER (NO)	Acts as the pilot and takes over as necessary from the OOW. Executes the plan at the pelorus from the Note Book. Has ready access to the chart. Keeps the Captain fully informed on the progress of the plan. May take the bearings for his assistant to plot fixes on the chart.
OFFICER OF THE WATCH (OOW)	Filters shipping situation and informs Navigating Officer of ships which may hinder execution of the plan. Takes bearings and gyro checks as directed by the Navigating Officer. Runs the ship's routine and ceremonial and deals with matters of internal safety (of the ship). Maintains liaison with the blind safety team in the operations room.
NAVIGATING OFFICER'S ASSISTANT	Carries out the Navigating Officer's chartwork. Calls for fixes at regular and frequent intervals in order to confirm the ship's position and cross-checks the EP. Plots fixes and generates fresh DR and EP. Reports after each fix: its reliability: 'Good', 'Bad', or 'No fix' as the case may be; its distance from the planned track, and course required to regain; whether the echo sounder reports correlate with charted depth; ETA at next 'wheel over' position.
BLIND SAFETY OFFICER (BSO) AND BLIND SAFETY TEAM (*see* Chapter 15)	Monitors ship's position using blind pilotage techniques as a check on the ship's navigational safety; passes navigational and anti-collision information.
NAVIGATOR'S YEOMAN	Records wheel and engine orders. A tape recorder on the bridge may be found useful.
ECHO SOUNDER OPERATOR	Makes standard reports

Do not nibble at course corrections to maintain the track and avoid making successive alterations of 1° or 2°. Alter 10° or 15° to get back on the correct track quickly, but do not overshoot. Radar is often a useful aid in confirming whether the ship is on track or not.

Running a transit

The rule for running a transit is 'Follow the front mark'. In Fig. 3(b) the front mark (the beacon) is to *port* of the rear mark (the monument). Therefore the alteration of course to get back on track must also be to *port*.

If the transit is *astern*, the alteration must be in the *reverse* direction, e.g. in Fig. 3(b) the beacon is to the *left* of the monument, therefore the alteration must be to *starboard*.

Running a line of bearing

Altering course the wrong way when running a line of bearing is a frequent cause of mistakes in pilotage. This can be avoided by the following simple rules:

1. Look down the bearing on which the headmark should be.
2. The headmark will be: On the mark (Fig. 4) *or* to starboard of the bearing (Fig. 2) *or* to port of the bearing .
3. If the headmark is off the bearing, alter course in its direction: If the headmark is to *starboard* of the correct bearing alter course to *starboard* to regain track (Fig. 2).

If the headmark is to *port* of the correct bearing, alter course to *port* to regain track (Fig. 3).

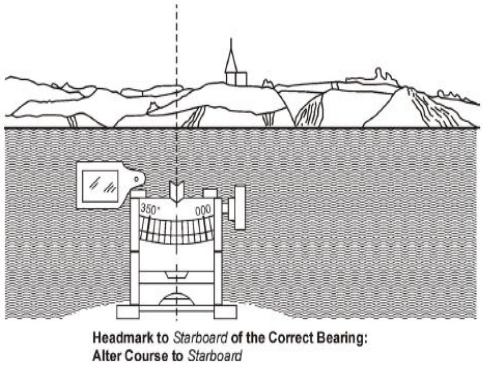

Fig. 2. Running a headmark: headmark to starboard of the correct bearing

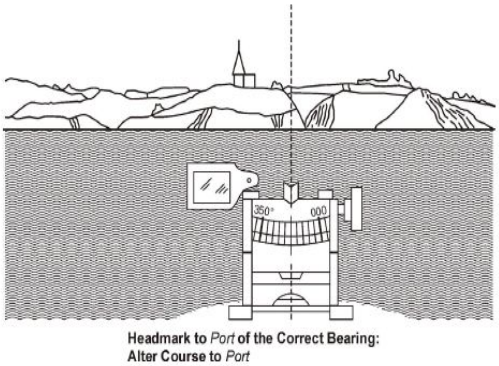

Fig. 3. Running a headmark: headmark to port of the correct bearing

If the mark is *astern* and the ship is running a *back bearing*, the alteration of course must be in the *reserve* direction; e.g. if the mark in is astern and appears to the right of the required bearing, the alteration of course must be to port; if the stern mark appears as shown in Fig. 4, the alteration required must be to starboard.

When the mark is on the correct bearing, note a point on the landscape which is in transit with it (either in front or behind). By using this transit, it is possible to see immediately without reference to the compass whether or not the ship is being set off line.

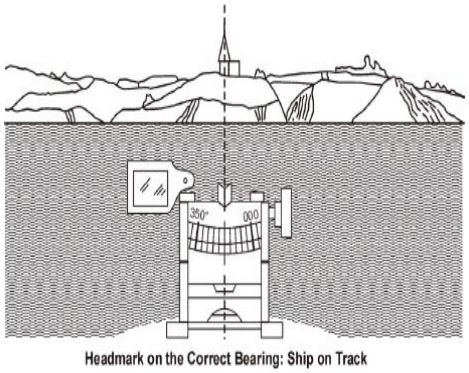

Fig. 4. Running a headmark: ship on track

Fix and run

Having chosen a suitable object on which to run, obtain another one in transit with it in precisely the same way as when running a line of bearing. Radar can often be of great assistance in confirming the track.

Assessment of danger

Always be alert to the nearest and most immediate danger. This could be a ship at anchor or a buoy towards which own ship is being set by wind or tidal stream. The most immediate danger could be a ship approaching down the next leg of the route which, if she does not alter course as expected, could present a collision risk.

The chart gives warning of navigational dangers but there are other hazards ships, yachts and small craft, emergencies such as steering gear or main machinery breakdown.

The navigator must be alert to all of these matters, and be constantly thinking ahead and anticipating possible eventualities.

Identification of marks

In pilotage work, there are two quick and simple methods immediately available for the identification of shore marks.

1. A straightforward comparison of the chart with what is actually visible.

Such a comparison will frequently reveal the marks to be used, without having to take a single bearing. If there is any possibility of confusion between adjacent marks (such as churches, chimneys, blocks of flats, etc.) this may have to be clarified by taking bearings.

2. Identification by means of the transits which shore marks make with the buoys marking the channel. Even if a buoy differs from its charted position by as much as 100 yards, the expected bearing of the mark to be identified will probably not vary by more than 2° or 3°; this is usually sufficient for identification purposes.

Buoys or beacons can be identified by combining single visual bearing with a radar range of the mark.

Shipping

When altering course for shipping, take the necessary action in plenty of time.
If action is delayed, the Officer of the Watch in the other ship may become alarmed and may do something unexpected and dangerous.
Do not pass too close across the bow (upstream) of anchored shipping; if possible, pass astern. The position of ships at anchor near own ship's track can be established by combining a fix with a visual bearing and radar range of the ship at anchor. With the position of the other ship on the chart, a decision can then be made to pass ahead or astern, or take some alternative action such as stopping if, for example, the anchored ship is blocking the channel.

Use of the echo sounder

The intelligent use of the echo sounder is essential to the safe conduct of pilotage. The predicted height of tide must be taken into account at all times.
Reports from the echo sounder operator or the reading on the bridge display unit must be given proper attention. If the reported depths are different from those predicted, the reasons must be considered and the appropriate action taken, particularly if the depths are close to the limiting depth. It may be necessary to stop the ship and clarify the situation before proceeding further.

Altering course and speed

When turning on to a new headmark, the wheel must be put over in plenty of time. If it is put over too soon, it can be quickly eased; if it is put over too late, more wheel may not be effective.
The use of excessive wheel may bring the ends of the ship closer to the clearing bearing than planned. Excessive wheel also reduces ship's speed more than originally intended and this may create problems particularly in strong winds or when in company with other ships.
When about to turn, make sure that the ship is not tending to swing in the opposite direction to that intended. Keep the bows in hand ('smell' the turn) by using small amounts of wheel in the appropriate direction just before the turn, so that the ship 'wants to go the desired way as soon as the wheel is put over for the turn itself. When making a large turn in a big ship, it is often advisable to use plenty of wheel initially to get the ship swinging in the right direction and then ease the wheel, otherwise the ship may 'hang' in the original direction, particularly in shallow water or when turning out of wind.
Remember that, as a general rule, ships going ahead turn more easily into wind than away from it, and allowance should be made for this.
Watch the progress of the ship during the turn to ensure that the planned track is being followed.
Are objects coming up ahead on the right bearing? Does the turn look right? This is particularly important with large turns in big ships.
The monitoring of a large turn is illustrated in Fig. 5.

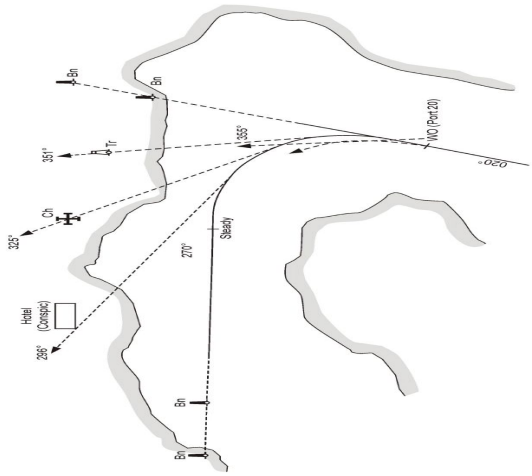

Fig. 5. Monitoring a large turn in pilotage waters

A ship entering harbour on a course of 020° is required to turn 110° to port to the next leg (270°). The courses of 020° and 270° both run on a pair of beacons in transit.
The track of the ship between 'wheel over' and steady is plotted using the ship's turning data. It will be seen that, once the turn has begun, the tower should come up *right ahead* on a bearing of 351°, the church on 325° and the of the hotel (conspic) on 296°, as the ship's head swings through those particular bearings. If these bearings do not come up right ahead, the rate of turn must be adjusted.
For example if, in the early part of the turn, the tower comes up right ahead on a bearing of 355°, the ship is to port of track, and is turning too fast. The wheel must be eased to bring the ship back on to track.
Before altering course, check to see that the track is clear of shipping and other obstructions. Look out on the appropriate quarter for any ship overtaking from that direction.
Always check that the wheel is put over the right way by watching the rudder angle indicator. If the wheel is put the wrong way, order 'Midships' and repeat the original order.
When altering speed, check from the shaft speed indicators or the pitch angle repeaters that speed has been altered correctly. If the shafts have been put the wrong way (e.g. astern instead of ahead), order 'Stop' and repeat the original order.
In ships where the Quartermaster is sited at the QM's console on the bridge, it is important that the above procedure should be followed and that all conning orders and replies are made in a formal manner.

Buoys

Buoys are an essential aid in pilotage, especially in narrow channels, but their positions can vary from that charted with the state of the tide. Buoys can drag, particularly if in an exposed position; they can also be repositioned to mark an extending shoal or altered channel, without immediate notification.
Use but do not trust buoys implicitly. Check the characteristics by night, and the name, number, colour or

topmark by day. Fix from charted shore objects in preference to buoys, using the EP as a check. Take care in areas where it is known that channels shift and the buoys are repositioned accordingly. The charts and *Sailing Directions* may give warning of such areas, for example the channels in the vicinity of the Goodwin Sands and in the Thames Estuary.
When passing a buoy, its position may be checked by transits with two, preferably three, charted shore marks. Radar can help in the identification of buoys and in checking their positions.
Take care if the planned track leads the 'wrong side' of a buoy marking the leg of the channel, e.g. the deep-draught route for heavy ships approaching Smeaton Pass (Fig. 11) from Plymouth Sound which leads east of the West Mallard Buoy. It may on occasion, for example in strong winds, be preferable to aim off 2° or 3° as necessary to get the buoy on the 'correct' bow. Otherwise the ship could be set dangerously close to the buoy concerned if she is slow to turn.
The height of the tide may permit a ship to pass outside the line of buoys yet still be safe. A ship may be forced the wrong side of a buoy by other shipping. It may be better to take this course if collision cannot otherwise be avoided. In certain circumstances, it may even be better to ground than risk a collision.

Tides, tidal streams and wind

For a number of reasons, the predicted height of tide may be different from that actually experienced, perhaps by as much as 1 or even 2 metres. This is particularly dependent on the weather.
Tidal streams experienced may not always agree with the predictions, particularly at springs, and the actual time of a change of direction can be as much as 1 to 2 hours different. Always check the direction and rate by noting the heading of the ships at anchor and the wash of the tidal stream past moored objects such as buoys.
The eye tends to deceive; the actual strength of the stream in knots is not always as great as it appears to be.
Make an adequate allowance for cross-tidal stream and wind, because it is difficult to recover the track having been set downstream of it, especially when speed is reduced. The less the distance to the next 'wheel over' position, the larger must be the correction to regain track. If the ship is upstream of the line, there is no difficulty in regaining it.
An adequate allowance must be made for tidal streams and wind when turning; the 'wheel over' point may have to be adjusted. Wind direction and strength affect not only the leeway but also the turning circle itself. A turn may have to be started early or late, using more or less wheel as appropriate, depending on the combined effects of stream and leeway on the turning circle.

Service to the Command

The Navigating Officer must anticipate the Captain's requirements and provide him with relevant information and situation report. Such information should include:

The headmark and its correct bearing.
Whether on or off track. If off track, by how much, and the course required to regain.
Distance and time to 'wheel over'.
The minimum depth expected.
The tidal stream and the likely effect of wind.
Advice on the shipping situation.

Action on making a mistake

If a mistake has been made, report it immediately. If this leads to uncertainty about the ship's position, consider stopping the ship at once. The Navigating Officer must always be scrupulously honest and never try to bluff his way out of an uncertain situation. His Captain may not find him out, but the rocks and shoals will.

Checks before departure or arrival

Always observe the situation in the vicinity of the ship before leaving harbour. If alongside, the best way is to walk down the jetty checking the catamarans, the positions of adjacent ships, etc. The actual height of tide, the strength and direction of the tidal stream and the wind can be noted, and all these may lead to an adjustment of the plan.
Such a detailed check cannot be done on entering harbour, but the situation needs to be observed as accurately as possible.

2. CONCLUSIONS

The pilotage plan must be complete in every detail. Pre-planned data are essential for a passage in confined waters. The track must be drawn on the chart, using headmarks, if possible. The position along the track must be instantaneously available from cross bearings. The safe limits each side of the track must be defined by clearing bearings. With appropriate details transcribed into a properly prepared Note Book, the Navigating Officer can give his whole attention to the conning and safety of the ship without having to consult the chart. Reports from the navigator's assistant, the echo sounder operator, the blind (safety) and/or visual fixing teams, serve to confirm (or deny) the accuracy of the navigation. If time has to be spent poring over the charts and publications during pilotage instead of conning the ship, it will be evident either that the plan has not been fully prepared, or that the Navigating Officer does not have confidence in it.
The plan must be so organised that, at each stage, the Navigating Officer recognises those factors demanding his attention with sufficient time to deal with them. For example, the plan will need to include the selection of 'wheel over' points and the observation of transits to determine the gyro error.
Neither of these operations should interfere with the other. These points concern the execution of the plan rather than the planning, but consideration of such details at the planning stage will ensure a sounder plan, simpler to execute.

3. REFERENCES

[1] NAUTICAL INSTITUTE, Admiralty manual of navigation, vol. I - *The principles of navigation*, 2008
[2] COJOCARU, S - *Tratat de navigație maritimă*, editura ARSS Academica Bucuresti, 2008
[3] BALABAN, GH. I- *Tratat de navigație maritimă*

PLANNING AND EXECUTION OF BLIND PILOTAGE AND ANCHORAGE

[1]SIVRIU GEORGIANA, [2]GEORGESCU STEFAN, ARSENIE C. PAULICA

[1,2]Constanta Maritime University, Romania

ABSTRACT

Blind pilotage means the navigation of the ship through restricted waters in low visibility with little or no recourse to the visual observation of objects outside the ship. The principal non-visual aid to navigation that enables this to be done is high-definition warning-surface radar, but all available nonvisual aids are employed. The organisation to achieve this is called the blind pilotage organisation, comprising a BP team, led by a BP Officer (BPO).

Keywords: *blind pilotage, blind anchorage.*

1. INTRODUCTION

Assessment of the risk involved in a blind pilotage passage

Although normally the accuracy of blind pilotage is such that a ship can be taken to an open anchorage and anchored within 50 yards of the desired place, the degree of risk involved, particularly in restricted waters, must be carefully assessed. Congestion due to other shipping, the consequences of failure of radar or other vital aids once the ship has been committed to her passage, and the number and quality of fixing marks must be taken into account.

Parallel index technique

The key to blind pilotage is the principle of the parallel index. The running of a parallel index line provides real-time information on the ship's lateral position relative to the planned track. On the chart (Fig. 1), a line is drawn from the edge of a radar-conspicuous object, parallel to the planned track.

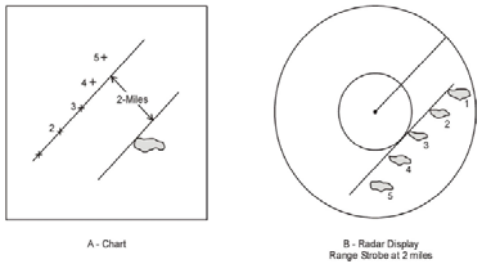

Fig. 1. Parallel index

The perpendicular distance (or cross-index range) from the object to the track is then measured. The range strobe on the radar is then set to this range, and a solid chinagraph line drawn on the display parallel to the planned course on a scale appropriate to the range in use. Positions 1, 2 and 3 on the chart and radar display show the ship on track at various instances up to the time that the island is abeam to starboard.
Positions 4 and 5 show the ship off track to port. The exact distance off track can be measured by dividers from the radar echo of the island to the nearest point of the chinagraphed parallel index line at the scale of the display. This can be made easier by constructing scales for each range setting, as shown below, and mounting them adjacent to the display. (The crosses on the chart do not represent fixes and only appear in order to illustrate the example.)

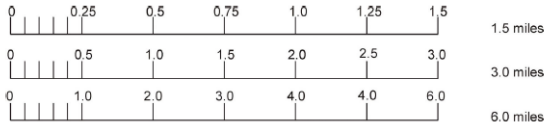

Radar clearing ranges

Radar clearing ranges (Fig. 2) are similarly drawn at the maximum or minimum distances from the radar-conspicuous objects to keep the ship clear of dangers. These are drawn as broken lines:_ _ _ _ _ _ _ _ _ .

Course alterations

'Wheel over' positions are calculated and plotted on the chart as for visual pilotage. A radar-conspicuous mark is selected as close as possible to the 'wheel over' position. A pecked line - - - - - - - - - - - is then drawn through the 'wheel over' position (Fig. 2A) parallel to the new course, and the cross-index range measured. This 'wheel over' range is plotted on the display as a pecked line parallel to the new course. When the selected mark reaches this line, the wheel should be put over and the ship brought round to the new course, by which time the mark should be on the firm line denoting the parallel index for the new course.

Responsibilities

In normal circumstances, the Navigating Officer is the pilot of the ship although, if he
is not a navigation sub-specialist, the duty of pilotage devolves on the Captain, who may either perform it himself or, at his discretion, depute any officer of the ship's complement to do so.
No matter what the blind pilotage organisation may be, the sub-specialist Navigating Officer (NO) is always the pilot of the ship, and thus he should also be the Blind Pilotage Officer (BPO).

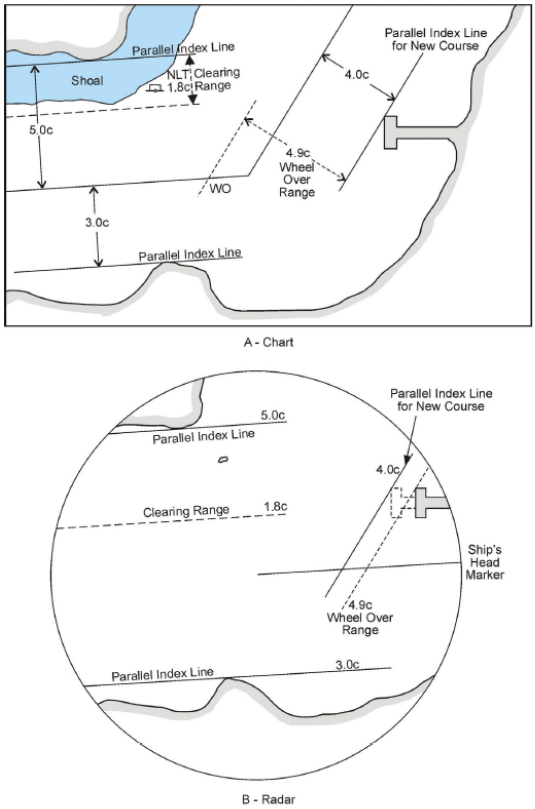

Fig. 2. Clearing and 'wheel over' ranges on the chart and the radar display

Where no navigating sub-specialist is borne, the officer appointed for navigating duties should also be the Blind Pilotage Officer in normal circumstances. However, as responsibility for pilotage is clearly vested in the Captain, he may wish to delegate the blind pilotage duty to some other officer. If so, the Captain must also clearly set out in his standing orders the circumstances envisaged, to ensure that it is absolutely clear who is
responsible and when. These orders must also take into account the organisation for blind pilotage in various circumstances envisaged; the organisation described below may have to be modified.
It must also be decided who is responsible for informing the Captain of the collision risk with other ships. The NO/BPO will be fully employed navigating the ship; therefore it is essential that the officer in charge of the operations room, who already has an anti-collision plot running, should be made responsible for advising the Captain and OOW on this aspect of safety.

The conduct of blind pilotage

The Navigating Officer should remain on the bridge in poor visibility and conduct the blind pilotage from there. It is essential to have another officer, who is suitable by training and experience, as a Blind Safety Officer (BSO) in the operations room, where he can monitor the blind pilotage and back up the Navigating Officer on the bridge. The BSO will need to be in touch with the surface plot to assist with the identification of radar contacts.
The essence of this arrangement is that members of the team do not change position if the visibility changes. The Navigating Officer conducts the pilotage from the bridge whatever the weather or visibility. In good visibility, the BSO acts as a useful check on the visual plan and builds up confidence in his team and the Command. In marginal visibility, the bridge team continues to make use of any visual information to supplement information from the radar.
In nil visibility, the NO conducts the blind pilotage from the bridge radar display, monitored by the BSO. If reports from the NO and BSO disagree, immediate action to stop the ship may be necessary until the position has been accurately determined.
The Navigating Officer should not move from the bridge to the operations room in order to conduct the pilotage from there. This will cause delay and perhaps confusion, and can be particularly undesirable in marginal visibility, when a mixture of visual and blind techniques is required.
There may well be circumstances, particularly in large ships, where the Navigating Officer has already taken or wishes to take the con and therefore charge of the ship from the Officer of the Watch, in order to conduct the pilotage where a blind pilotage situation has already arisen or arises subsequently. In such a situation, it may be undesirable for the NO to move to the bridge radar display as indicated above. The composition and duties of the blind pilotage team must therefore have sufficient flexibility built in to cope with such circumstances. The NO may continue to con the ship from the pelorus, taking full account of the navigational and collision avoidance information he is receiving from the operations room, the bridge radar display (which should be manned by a competent officer such as the NO's assistant) and other sources, e.g. the bearing lattice team, lookouts, etc. Despite being at the con, the NO is still the pilot and the Blind Pilotage Officer of the ship and retains full responsibility for these.

Blind pilotage team and duties

Blind pilotage requires a high degree of organisation and team work, so that not only are the responsibilities of individuals clearly defined but also all relevant factors may be considered while assessing the ship's position and her future movements. Suitable arrangements to achieve this are set out in Table 1; these may have to be adjusted depending on the class of ship, the personnel available, and the above comments.

PLACE	PERSONNEL	DUTY
Operations room	Blind Safety Officer (BSO)	Monitors ship's position as a check on the ship's navigational safety, using the most suitable display. Co-ordinates navigational and anti-collision information to bridge. Although he does not supervise surface plot, he must keep an eye on shipping situation.
Operations room	Blind Safety Officer's assistant	Plots radar fixes and other radio aids (e.g. Decca) as appropriate. Generates DR/EP. Assists in identification of marks, ships. Checks E/S reports with charted depths.
Operations room	Anti-collision plot	A suitably experienced officer or the most experienced Ops(R) Senior Rate in charge. Passes anti-collision information to bridge, co-ordinated by BSO.
Sonar control room	Sonar controller	Reports sonar information as ordered.

Table 1. Blind pilotage organisation

Planning and execution of blind pilotage

General principles

To ensure success, the ship must be accurately navigated along a pre-arranged track. In comparatively unrestricted waters, this is best done by constant fixing using radar in conjunction with other aids such as Decca and echo sounder.

In narrow waters and during the final stages of an anchorage, the delays inherent in fixing are unacceptable to the BPO. It is therefore necessary, for anti-collision and navigation in these conditions, to work directly from the radar display using a prepared Note Book; but it is still necessary to pass radar information for fixing at regular intervals as a safety check and as an insurance against radar failure.

The following principles apply:

1. The Navigating Officer should navigate or pilot the ship.
2. The Captain should have easy access to the blind pilotage position and the NO.
3. The ship should be conned from the compass platform because it is only on the bridge that the 'feel of the ship' can be retained.
4. The Captain, Blind Safety Officer, OOW and the officer in charge of the anti-collision plot should all be carefully briefed before the passage by the NO, so that they are all entirely familiar with the visual/blind plan.
5. Navigational charts with the NO's prepared visual/blind plan must be available on the bridge and in the operations room.
6. The whole pilotage team should be exercised as frequently as possible in clear weather in visual and blind techniques. Only in this way can the necessary confidence in the system be built up which will allow runs of some complexity to be conducted safely in blind conditions.
7. The BSO should be closed up on all occasions of entering and leaving harbour and passages through narrow waters when special sea dutymen are closed up; the BP team should be regarded as part of special sea dutymen.
8. There should be good communication between the blind pilotage position and the BSO and personnel manning navigational aids fitted elsewhere.
9. All members of the team should be encouraged to admit any doubts they may have regarding the information acquired from sensors.

Blind pilotage planning

1. Normal planning considerations for selection of tracks apply. Blind and visual tracks should be the same, to enable the transition from visual to blind or vice versa to be made at any time and also to allow one plan to be used to cross-check the other.
2. The number of course alterations should be kept to a minimum to reduce the work load in redrawing parallel and 'wheel over' lines.
3. Always try to have two parallel index lines where possible, one on each side of the track. These provide a check on measurement, mark identification and can reveal index or linearity errors.
4. Objects to be used both for parallel index lines and for fixing must be carefully selected. They should be radar-conspicuous and unchanged by varying heights of tide. Clearly mark on the chart the objects to be used for fixing and brief the assistant. Avoid if possible fixing by radar range and bearing on a single mark.
5. The range scales to be used require careful consideration. Accuracy is greater at shorter ranges but marks pass more quickly than at a distance, requiring more lines to be drawn. When operating on short-range scales, it is essential that the BPO frequently switches to longer ranges to keep aware of developing situations. Changes of range scales and parallel index marks should be pre-planned and marked in the Note Book. The stage at which charts will be changed must also be carefully considered.
6. Tidal streams and currents should be worked out and noted for calculation of courses to steer and for the calculation of EP. These should be displayed on the chart and recorded in the Note Book.
7. Expected soundings (allowing for height of tide and calibration of echo sounder) should be noted for each leg. The possibility of being early or late should also be borne in mind.
8. All hazards along the track should be boxed in by clearing ranges and their
cross-index ranges listed in the Note Book.
9. Details of all lights and fog signals should be taken from the Admiralty List of Lights/chart and entered in the Note Book.
10. The chart should be drawn up using standard symbols, see Table 2.

Blind pilotage chartwork	Symbol
Parallel index lines to stay on track	———
Clearing ranges	– – – – –
'Wheel over' (WO) ranges	.....

Table 2. Blind pilotage symbols

Use the same conventions as above for cross-index ranges.
The term dead range (Figs. 4, 5) is used to describe the range of a mark ahead when anchoring in a chosen position. The term may also be used when measuring the progress of a radar-conspicuous object along a parallel line, as shown in Fig. 25.

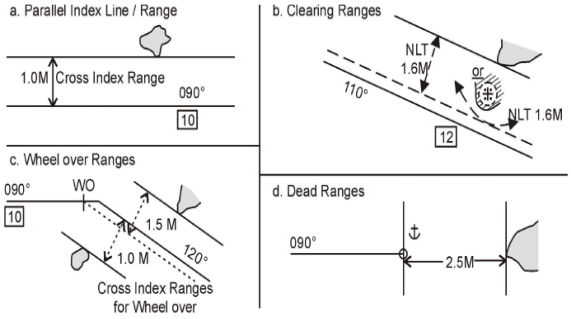

Fig. 4. Blind pilotage symbols

Radar-conspicuous objects such as buoys should be highlighted to enable the BPO to have a clear mental picture of what he expects to see on the display.
11. The Note Book should contain the full plan, neatly and legibly recorded in chronological order. Sketches of both chart and radar display (Fig. 23) can be of great assistance to the BPO in evaluating the picture. A suitable Note Book layout supplementing Fig. 23 is shown in Fig. 24 as a guide to blind pilotage planning.
12. Tracks plotted for entering and leaving harbour should not appear on the same chart simultaneously, otherwise confusion will arise.
13. Clearing range should be simple, safe and easily interpreted.
14. Objects used for 'wheel overs' should be conspicuous, easily identifiable and suitably located adjacent to the track.

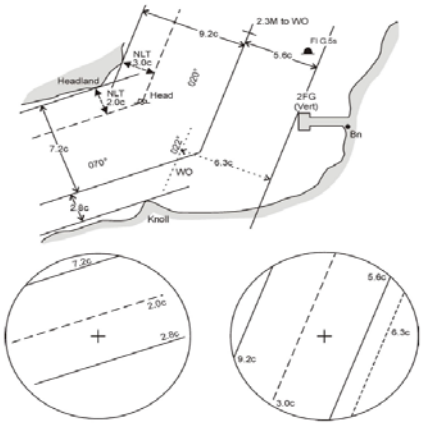

Fig. 3. Blind pilotage: preparation of the chart and displays

Blind pilotage execution

1. Carry out a time check to synchronise clocks and watches.
2. On the radar display, keep one set of parallel index lines drawn up ahead of those in use. Any more will clutter the display excessively. Rub out lines as soon as they are finished with.
3. Identify contacts early (by range and bearing from charted object). An accurate EP is a most useful aid in identification.
4. Fix at frequent intervals and immediately after a change of course. DR/EP ahead. A suitable fixing procedure is:

BPO assistant 'Stand by fix in 1 minute'
BPO 'Roger using points A, B, C'
BPO assistant writes these in Note Book.

Course	Remarks Approach Speed 12 knots	Distance to Wheel-over (W.O.) Miles	Minimum Depth (metres)

070°	on Pier Root Beacon
	// Port Headland 7.2c
	// Stbd. Headland 2.8c
	Head Buoy ⊥ Port 5.2c
		0.1M to W.O.	14m

W.O to 020° (15° port Helm)	Headmak 022° // Stbd. Jetty 6.3c		

020°	on Headmark
	// Port Headland 9.2c
	// Stbd. Jetty 5.6c
	Stbd. Hand Buoy ⊥ stbd. 5c
		2.3M to W.O.	15.6m

	Change to 6 M range scale // Stbd. New Head 6.7c		

Fig. 4. Blind pilotage: layout of Navigating Officer's Note Book

BPO/BPO assistant 'Fix now.' BPO marks the point on face of the display.
BPO assistant notes the time.
BPO then ranges off the marks drawn on display and passes these to BPO assistant.

BPO assistant Records the ranges, plots the fix and generates fresh DR and EP.

This procedure cuts the time to take a fix and reduces the risk of a 'cocked hat' due to ship movement. It may be quicker to interpolate from the range rings rather than use the range strobe, although the latter will be more accurate.

5. Ship's speed. One of the factors affecting the choice of ship's speed will be the rate at which the BPO and his assistant are capable of dealing with the radar information.

6. Commentary and conning advice. Maintain a steady, unhurried and precise flow of information to the Command:

Distance off track/on track/course to maintain or regain.

Distance and time to next 'wheel over', new course.

Present/new course clear of shipping.

Adjacent marks or hazards, expected lights and sound signals.

Expected depth and echo sounding. Minimum depths.

When fixing and result of fix. EP to next alteration.

Manoeuvring limits (e.g. 5 cables clear to stbd, 1 cable to port).

If in any doubt, say so and if necessary stop the ship.

7. It must be appreciated that, whatever the technique employed, a drift off line is likely to be detected less readily by radar than by visual methods.

8. It is vital to pay attention to the echo sounder and the least depth expected. The nearest land is usually the bottom.

Blind pilotage exercise

To improve the reality of BP exercises in clear weather, the following points should not be forgotten:

Safe speed should be maintained.

Fixes should be recorded and plotted at the same frequency as for actual blind pilotage.

A full de-brief should take place on completion of the practice.

Blind anchorages

A blind anchorage should be planned in the same way as a visual anchorage but remember to allow 'stem to radar' instead of 'stem to standard' when plotting the 'let go' position. As shown in Fig. 25, parallel index lines should be used to guide the ship to the anchorage position and she must stay boxed in by clearing ranges. Distances to run can be obtained by using a dead range on a suitable object ahead, or by measuring the progress of a radar-conspicuous object along a parallel index line. Full details must be shown on the chart and in the Note Book. Distances to run must be marked on the face of the display.

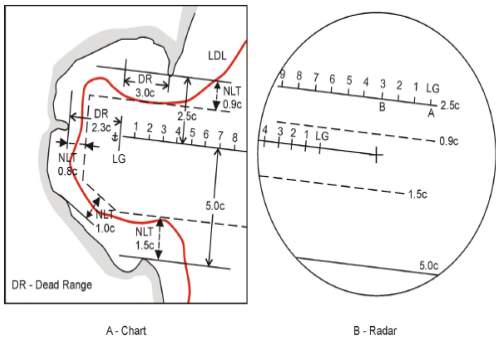

Fig. 5. Blind anchorage execution

These can be backed up by the range strobe, but reliance on the strobe alone is dangerous because the reference is lost as soon as the strobe is required for any other measurement.

In Fig. 25, the dead range of the point of land ahead when anchoring is 2.3 cables. The distance to run to the anchorage position may be obtained by subtracting the dead range from the actual range of the point. For example, if the range of the point is 7.3 cables, the distance to the anchorage is 7.3 - 2.3 = 5 cables.

Fig. 25 also shows that the dead range of the point of land on the starboard side when anchoring is 3 cables. On the radar display, this point of land should 'move' along the parallel index line drawn 2½ cables to starboard of the approach track. When the ship reaches the 'let go' position, the point of land should have reached point A, 3 cables beyond the abeam position B. The distance AB equals the dead range (3 cables).

Navigational records

When carrying out a blind pilotage passage, the Navigating Officer/BPO will be too busy to maintain a continuous written record. It is essential that such a record should be kept, and in comparatively unrestricted waters it is normally sufficient for this record to be kept on the chart itself by plotting fixes and noting the positions and times of alterations of course and speed and other relevant data, in addition to the record in the Navigational Record Book.

This procedure, involving thorough and methodical chartwork, is in fact no different from that which should be practised during any pilotage passage.

In more restricted conditions, however, the Navigating Officer/BPO's running commentary to the Captain should be recorded on tape if possible, for example:

'No. 7 buoy fine on port bow, 8 cables ship 50 yards to port of track steer 136 to regain.'

In conjunction with the Navigating Officer/BPO's prepared Note Book, the chart, the recorded fixes and courses and speeds, this record should suffice for any subsequent analysis required.

Horizontal displays

Where horizontal displays are available in the operations room, the whole passage may be prepared in advance on a series of overlays, the BSO's assistant changing these at appropriate times. The drawback of this method is that all tracking and other additional marks made by the BSO are lost at each change. With most horizontal displays in use in the Royal Navy, the picture is not sufficiently precise for accurate blind pilotage and should not be used.

2. CONCLUSIONS

For merchant ships, the regulations for pilotage are laid down by the national authority or the shipping company, and in the orders for the port concerned. Recommendations on pilotage are also made from time to time by IMO.

Regulations for merchant ships frequently require compulsory pilotage, although Masters who have considerable knowledge of a particular port may be exempted for that port, as may be certain ships regularly trading on the coast concerned. In most ports, it is the usual practice for the pilot to take full control of the handling of the ship between the pilot boarding place (usually shown on the chart) and the berth. Despite the duties and obligations of a pilot, his presence on board does not relieve the Master or the Officer of the Watch from his duties and obligations for the safety of the ship.

The general aim of the Master should be to ensure that the expertise of the pilot is fully supported by the ship's bridge team. The Officer of the Watch is required to co-operate closely with the pilot and keep an accurate check on the vessel's position and movements. If there is any doubt as to the pilot's actions and intentions, these should be clarified immediately. If any doubt still remains, it is up to the Master and/or the Officer of the Watch to take the appropriate action to ensure the safety of the ship.

3. REFERENCES

[1] NAUTICAL INSTITUTE, Admiralty manual of navigation, vol. I - *The principles of navigation*, 2008

[2] COJOCARU, S - *Tratat de navigaţie maritimă*, editura ARSS Academica Bucuresti, 2008

[3] BALABAN, GH. I- *Tratat de navigaţie maritimă*

SECTION II

MECHANICAL ENGINEERING AND ENVIRONMENT

CORROSION MEASUREMENTS AND ULTIMATE STRENGTH OF A BULK CARRIER

[1]ANDREAS IOANNOU, [2]MODIGA MIRCEA

[1]Member of Royal Institute of Naval Architect (R.I.N.), [2]"Dunărea de Jos" University of Galati, Romania

ABSTRACT

For steel construction and marine structure in particular, the corrosion can be one of the collapse causes, due to excessive diminution of strengths areas and implicit increasing of internal stresses. At present, corrosion rate is estimated on the basis of measurements on real ships, which permits to obtain the simplified empirical models. In the paper is presented some results of extensive thickness measurement that was made for a 25 year old bulk carrier and their use for determining of initial yielding, fully plastic (according Prandtl) and ultimate bending moment - in hogging and sagging conditions. The results where compare with those obtained for the newly built ship and for ship at different ages. There have also been determined the same moments for the ship having maximum corrosion according Common Structural Rules (CSR) for bulk-carriers.

Keywords: *corrosion, bulk carrier, ultimate longitudinal strength*

1. INTRODUCTION. IMPORTANCE OF THE SHIP'S AGE AND CORROSION

Over the years, many bulk carriers have suffered serious structural accident, many of them catastrophic. Subsequently, several research programs have identified corrosion and fatigue as weakening the structures of aged bulk carriers. Although lately there is overall decrease in the number of ship losses and associated loss of life, in 2009 there were more accidents than in 2008, an explanation is offered and the increasing number of bulk carriers built (Table 1). A total of 39 lives were lost on nine vessels in 2009 ([2]). The average age of bulk carriers lost in 2009 more than 25 years against a world-wide trading average age of 12.85 years (Table 2).

Table 1 Total loss in 2008 and 2009

	2008	2009	999-2008	2000-2009
Lives	15	39	242	246
Ship losses	4	9	66	71

Table 2 Age of casualty in 2008 and 2009

	2008	2009	1999-2008
0 - 4 years	0	0	1
5 - 9 years	0	0	6
10 - 14 years	0	0	2
20 - 24 years	0	0	11
15 - 19 years	1	2	19
25 + years	3	7	27

There is no doubt that the ship accidents and the ship age are closely related. The main reason why age is so relevant to shipping casualties is that corrosion and general fatigue increases as ships grow older. This is partly because of the stresses to which the ship is inevitably subjected by routine operations, cargo handling, weather/waves and partly due to the effect of water on the steel. Corrosion of metallic structure is likely to be more extensive and work faster than on other structures simply because the ship is in continual contact with water, usually sea-water. Although any type of water tends to cause metals to rust, sea-water is much more harmful than fresh water because it contains much salt. It can also be accelerated by the effects of some cargoes, especially those carried in bulk. The interior of cargo holds can be affected by the humidity resulting from the moisture contained in some cargoes.

Partly as a result of the continued tendency for structural failures to occur on older vessels and partly as a result of the aging worldwide fleet, the remaining life assessment of bulk carriers has assumed greater interest in recent years. Remaining life assessment constitutes a specific area of structural engineering involving a future structural resistance. Structural resistance means the capability of a structure to withstand a loading pattern. As implied, it is time-dependent. This is due to the effect of deterioration caused by corrosion and/or fatigue. It is useful in practice to be able to predict when, where, and to what extent, both fatigue and corrosion will affect the structural integrity of a vessel at future times.

Longitudinal ship strength is directly related to the thickness of longitudinal members, which decreases in time due to the inevitable corrosion process. Statistics show that the bulkers have been and remain exposed to break; therefore ensuring proper longitudinal resistance under all conditions is one of the most important concerns of the owners, designers and builders.

2. CORRODED THICKNESS MEASUREMENT ON A SINGLE SKIN BULK CARRIER

There are various ways of preventing corrosion - or at least of preventing it from becoming a problem. Tanks can be painted with special coatings and can be carefully washed out. Above all, the condition of the hull and other structures can be constantly checked for signs of corrosion or fatigue. This, however, is much easier said

than done, because of the size of the ships themselves and the difficulties involved in assessing the actual plate thickness and implicit corrosion. So, a bulk carrier of 254,000 *tdw* (roughly equal with the cargo it could carry) might be 320 *m* long, 54 *m* in breadth and 26 *m* deep. The total hull area to be examined could thus have in excess 54,000 m^2 and that does not include the interior bulkheads, hopper tanks, brackets and other features. The loss of a few millimetres by corrosion can be disastrous for a bulk carrier with 20 to 29 *mm* thick of side plates. Recognizing that corrosion is one of the main reasons which create the biggest problems for a bulk carrier, Classification societies and International Maritime Organization (IMO) continue to seek acceptable standards for structural integrity of aging ships with respect to the repair and maintenance over the ship life cycle. It was proposed that the plate elements be inspected every five years and whenever a plate is detected with diminution more that 20% of plate's original value to be substituted.

The thickness measurements were made for a bulk carrier with single skin, built in 1982 under Lloyd's Rules and classified under Lloyd's Register. It was sailing under Cyprus Flag. Classification Society of the vessel requested from the owner to carry out a special survey and thickness measurements in order to discover the condition of the plates as their vessel was completing 25 years old. The measurements have taken a while, during which period the vessel was on dry dock 05-28/11/2007 in Fuian Hanhai Shipbuilding Co. in China.

The Equipments which have been used were a KRAUTKRAMER. The Model DM4 gauge is standard unit for basic thickness gauging. It benefits from being very lightweight and compact, but it is also capable of through-coating measurements, eliminating the error caused by paint and other coatings.

These instruments operate on the ultrasonic pulse-echo principle, similar to the sonar one. A short ultrasonic pulse is transmitted into the specific part by a probe. The pulse travels through the material under test and encounters an interface that is a material with substantially different physical characteristics and back at the surface of the part. At the interface, the pulse is reflected back to the probe. The time needed for the pulse to make this round trip is divided by two and multiplied by the velocity of sound in the material under test. The result is the thickness of the material.

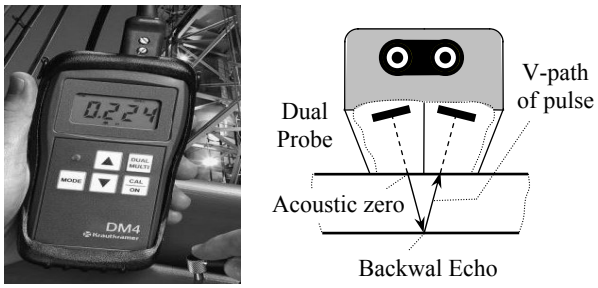

Fig. 1 Dual Element Thickness Measurement

Considering the extent of thickness measurements as required in CSR for bulk carriers, the locations of the points to be measured are given for the most important items of the structure. The ship has been separated in sections in order to be easier to take all necessary measurements for: hull shell plating, main deck plating, forecastle deck and poop deck, hatch coaming structural members, inner bottom plating in cargo holds (CH), transverse watertight bulkhead in CH, side shell frame, inside longitudinal bulkheads in cargo holds, watertight bulkheads in side water ballast tank. These sections were in turn divided into zones. Thus, for example, splitting the deck in zones is shown in figure 2.

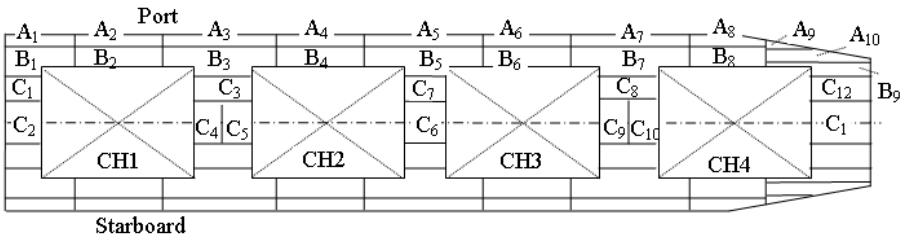

Fig. 2 Zones in main deck plating

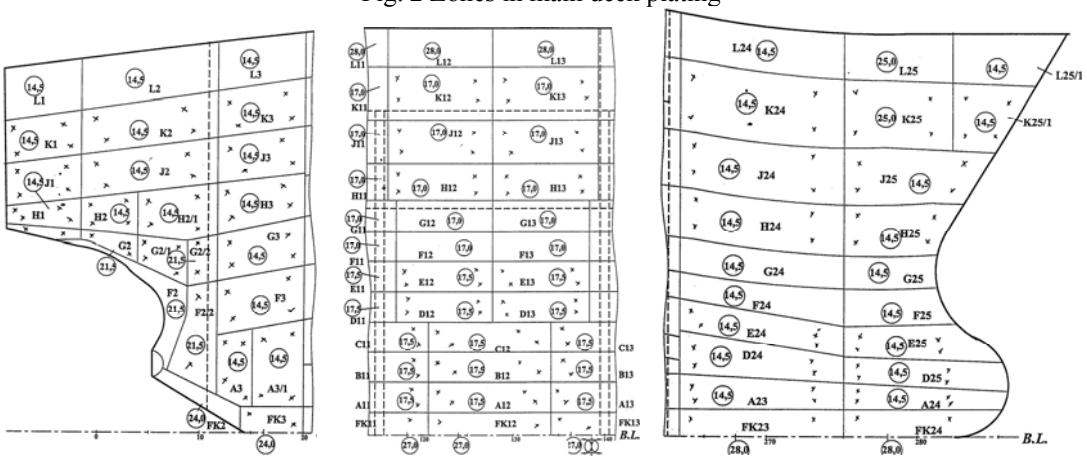

Fig. 3 Zones in side plating

The side was divided into 12 sub-areas on the port and 12 sub-areas on starboard. In Figure 3 shows three such sub-area of the shell. Each sub-area were subdivided into fields marked with a letter and number. For all the fields in each sub-area, in the tables were noted the original thickness, measurement thickness, absolute and percentage thickness reductions, as shown in Table 3. One value in the table is the average of 4-5 measurements. In all, were made thousands thickness measurements.

Table 3 Example of tables filling with measurement results

Field	Original thickness, *mm*		Measurement thickness, *mm*		Thickness diminishing			
					Port		Starboard	
	Port	Starboard	Port	Starboard	*mm*	%	*mm*	%
...	...	...	...	...	...	...	...	...
D13	17.5	17.5	15.7	15.7	1.8	10.3	1.8	10.3
...	...	...	...	...	...	...	...	...

Table 4 presents percentage side plating thickness reductions on three longitudinal strips, appropriate to wing tank - upper strip, middle and lower part of the side. In the longitudinal direction, are considered the frames 50, 70, ..., 250. Values in the table are plotted in Fig. 4. It sees a slight corrosion increase in the side plates of wing-tanks, due to temperature variations.

Table 4 Side plating thickness reductions

	Side plating thickness reductions %		
Frame No.	upper strip	middle strip	lower strip
50	4.50	6.50	6.45
70	3.80	4.10	3.80
90	4.40	4.40	5.60
110	5.00	6.20	6.45
130	4.10	5.00	6.55
150	3.80	5.80	4.40
170	5.00	6.80	5.30
190	2.90	5.00	7.35
210	5.95	5.60	8.15
230	4.85	5.80	6.15
250	3.65	5.70	9.70

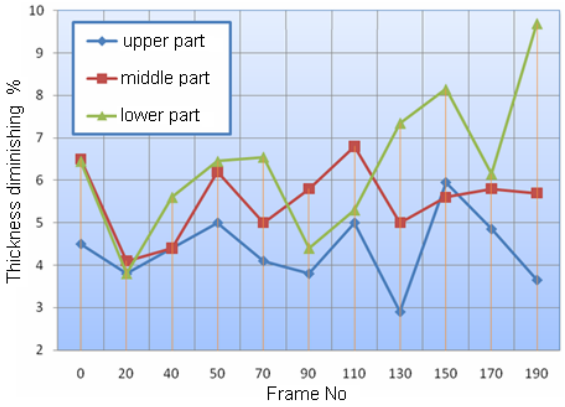

Fig. 4 Side thickness reductions at different frames

3. LIMIT AND ULTIMATE LONGITUDINAL BENDING MOMENTS OF A CORRODED BULK CARRIER

The plating and stiffeners corrosion affects the ship's general strength capability, leading to ultimate resistance worsening, which is a serious concern of the Classification Societies Rules ([5]). To assess the ship's hull general bending strength, the initial yielding bending moment (M_Y), the full plastic bending moment (M_P) and the ultimate bending moments in sagging and hogging conditions (M_{UH} ,M_{US})) may be used. These moments can be defining as follows:

$$M_Y = \sigma_Y . W_D \,, \qquad (1)$$

where W_D is strength modulus at deck's level, where appear the yielding stress σ_Y ; in the other section elements, the stresses remain in elastic range (Fig. 5, *a*);

Selecting the appropriate thickness measurements values for the structural members from the middle transverse section of the ship was made transverse section draw with the original thickness and with the reduced by corrosion measured thickness. This transverse section will be used in the calculation of the longitudinal limit and ultimate bending moments of a corroded bulk carrier.

$$M_P = \sigma_Y . W_{pl} \,, \qquad (2)$$

where W_{pl} is the plastic strength modulus. In achieving the M_P, the Prandtl material constitutive law is assumed (recommended also by Classification Societies Rules).

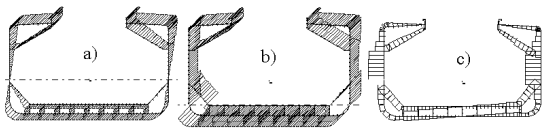

Fig. 5 a), b) Stress distribution due to yielding and plastic moments ; c) Shear stresses distribution

M_{UH} and M_{US} are defined as the maximum values on diagrams of bending moment M versus the curvature χ of the transverse section (Fig. 6); until the general collapse station the ship is achieved, the Transverse section elements are successively attaining limit states such as buckling/plastic deformations, subse-

quently the approach being named as the ship section's progressive collapse.

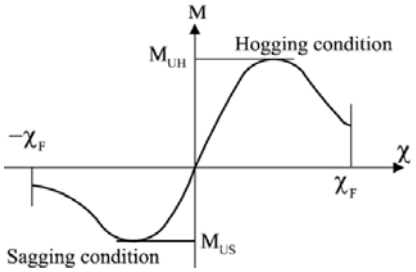

Fig. 6 Ultimate hogging/sagging ultimate moments

It is to be checked that the hull girder ultimate bending moments are in compliance with the formulas

$$\frac{M_U/\gamma_m}{\gamma_S M_{SW}+\gamma_W M_{WV}} \geq \gamma_U \ , \qquad (3)$$

where M_{SW} and M_{WV} are the design still water and wave bending moments. The (3) inequality must be verified in both hogging and sagging conditions. Relevant values for partial safety factors on still water bending moments (γ_S) and on environmental loads (γ_W) and also material factor (γ_m) are listed in Table 5. Ultimate design margin γ_U must be no less than 1.10.

Table 5 Factors γ_S, γ_W, and γ_m

	γ_S	γ_W	γ_m
Normal conditions	1,0	1,1	1,15
Damage conditions	1,1	0,67	1,0

The results were obtained using the software ULTIM, which follows a methodology similar to that recommended by Smith and the CSR. This soft presents a high degree of confidence, confirmed by tests carried out under the European project MARSTRUCT (Network of Excellence on Marine Structure) ([4]) The software takes into account shear, by reduction of the material yield strength depending on the values of shear stress in each element of the section. Shear stresses (Fig. 5, *b*) are calculated with a module that is part of this software.

There are three types of models for corrosion progress: a) corrosion wastage linearly increases with time (line a, Fig. 7); this is perhaps the most common and most widely used assumption in structural strength analyses; b) corrosion increases and accelerates over time (line b); this occurs when rust build-up is disturbed if a structure flexes; c) the rate of corrosion wastage slows down with time (line c), when the steel is gradually covered by scale and rust, preventing further exposure of new steel to corrosive environment.

The analyses based on a recent corrosion wastage database show that corrosion rates scatter in wide ranges. The standard deviations are comparable to or even higher than the averages and the maximum corrosion rate is much higher than the average. Due to the high variability of corrosion rates associated with each database, it is a questionable issue the extent to which different empirical models can be used to make tight estimates of corrosion rates for different structural elements of a bulk carrier.

It is noted that in the first time period (*T*o) of ship operation, corrosion is very low due to coating efficiency. Usually, it is assumed that there is no corrosion during the first five years of service. So, the simplest corrosion model, frequently adopted, assumed no corrosion for 5 years, and a constant corrosion rate for the remaining life of the steel.

But, in the Bulk carriers Guidelines for Surveys and Assessment and Repair of the Hull Structure established by IACS in 1994 ([5]), it is proposed that the structural elements to be inspected every five years and whenever they are detected reduced plate thickness more than 20% of the original, they are replaced. Thus, in ultimate strength checking, the section is composed of a mixture of plates; original plates having thickness less than the initial due to corrosion and new plates results by replacing excessive corroded plates. In this way is obtained a model of corrosion in the form of saw teeth, as shown in figure 8, defined not only by the sizes of the corrosion rates (which are the slopes in linear corrosion model), but also the thickness jumps at each revision.

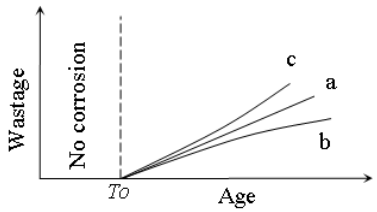

Fig. 7 Types of corrosion models

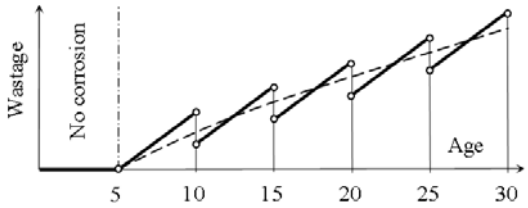

Fig. 8 The simplest corrosion model for Bulk carriers

For approximately same values of these quantities (rate of corrosion and jumps) in different intervals and on periodic inspections, is obtaining a quasi-linear corrosion model having somewhat lower corrosion rate than the linear model in each interval (Fig. 8).
In absence of any information on previous revisions, thickness measurement and eventual plate replacements, we considered the average corrosion rate obtained on the basis of the measurement we obtained. Therefore, using the ULTIM software, were obtained moment-curvature diagrams in figures 9. They allow determining of the moments M_P, M_{UH}, M_{US} for different ages between 6 and 30 years. For the ages between 6 and 26, the results are presented in Table 6, and also in figure 10. There were calculated also the limit and ultimate moments for the transverse section that occurs when the actual values of corroded plate thickness and

the maximum corroded values (according to CSR for B/C) are applied.

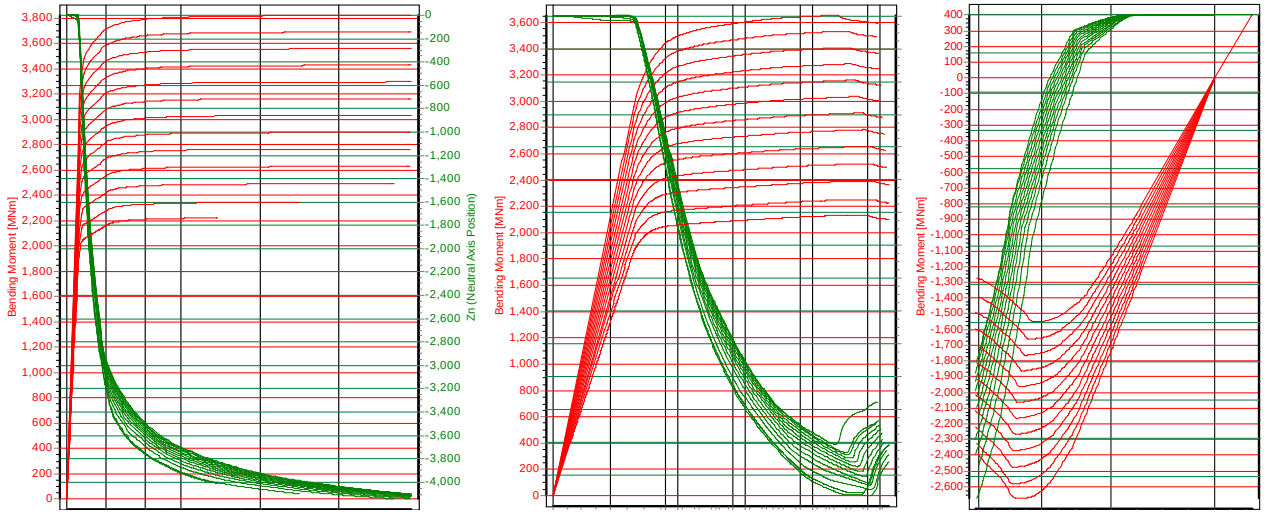

Fig. 9 Moment-curvature diagrams for M_P, M_{UH} and M_{US} at different ages, from 6 to 30 years

Table 6 Limit and ultimate moments at different ages

Age [*Year*]	M_Y [*MNm*]	M_P [*MNm*]	M_{UH} [*MNm*]	M_{US} [*MNm*]
6	2777.898	3825.748	3655.865	-2662.239
8	2690.774	3692.991	3531.851	-2581.781
10	2604.349	3561.586	3407.295	-2475.823
12	2517.960	3429.921	3283.106	-2371.068
14	2431.607	3297.939	3158.645	-2267.771
16	2345.289	3165.562	3033.831	-2165.766
18	2259.007	3032.683	2908.630	-2080.963
20	2172.759	2899.136	2782.592	-1981.813
22	2086.544	2764.657	2655.994	-1884.250
24	1988.363	2628.750	2524.779	-1786.562
26	1809.124	2490.267	2391.176	-1691.038
New Built Ship	2777.90	3825.75	3655.87	-2662.24
Corroded Ship with Measured thicknesses	2489.86	3425.33	3270.95	-2364.11
Maximum Corroded ship (according to CSR for B/C)	2212.65	2882.226	2762.63	-1905.14

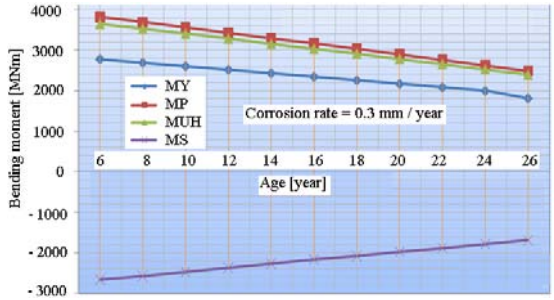

Fig. 10 Change of limit/ultimate moments with age

4. CONCLUSIONS

The obtained results on longitudinal strength of bulk carriers in both intact and corroded states allow us to make a number of important observations and conclusions.

Due to the high variability of corrosion rates associated with the existing database, for each case it may be useful to make thickness measurements at the periodic reviews of the ship. The checking of ultimate ship strengths before and after each revision requires efficiently software.

Nowadays, the limit state of the hull girder is assessed using ultimate moments M_{US} and M_{UH}, determined after proposed by Smith scheme. The full plastic bending moment M_P, used a few years ago as a limit state of hull girder, is substantially higher than ultimate moments. It is currently used as a reference value, for obtaining of some non-dimensional parameters.

Due to a greater concentration of strengths elements of transverse section to its extremities (deck and wing tank on one hand and double bottom and hopper tank on the other hand), at bulk carriers, the difference between M_P and M_Y significantly increases compared with about 1.15, existing to other types of ships.

Compared with other types of ships, the difference between M_{US} and M_{UH} is greater at bulk carriers. This occurs because the double bottom and hopper tank structure are greater strength in compression with than deck and wing tank.

The time decreases of limit/ultimate moments due to corrosion thickness reduction are approximately linear (Fig. 10). Ultimate moments have the decrease rate per year (R_M) of about 3.5 %, and plastic moment has about 4.5 % decrease rate. For a quick assessment of these moments at a certain age (T) can be used a simple relationship, such as $M(T) = M(To)\ (1 - R_M\ (T - To))$.

7. REFERENCES

[1] ANDREAS IOANNOU, *Rezistența Longitudinală ultimă a vrachierelor corodate şi avariate, Ph.D. Thesis in prep*., Galatzi "Dunărea de Jos" University

[2] *** MARITIME SAFETY COMMITTEE (IMO), *Bulk carrier casualty report*, 2009

[3] *** *Common Structural Rules* for Bulk Carriers, Adopted by International Association of Classification Societies (IACS), July, 2010

[4] GUEDES SOARES C., LUÍS R. M., NIKOLOV P., DOWNES J., TACZALA M., MODIGA M., QUESNEL T., TODERAN C., SAMUELIDES M., *Benchmark study on the use of simplified structural codes to predict the ultimate strength of a damaged ship hull*, Int. Shipbuilding Progress, IOS Press, ISSN 0020-868X, vol. 55, No. 1-2/2008, pg. 87-107

[5] *** IACS, *Bulk carriers Guidelines for Surveys. Assessment and Repair of the Hull Structure*, 1994

.

AXIAL THRUST BEARING INFLUENCE ON THE DYNAMIC BEHAVIOUR OF AN ELASTIC SHAFT

[1]BUZBUCHI NICOLAE, [2]STAN LIVIU-CONSTANTIN

[1,2]*Constanta Maritime University, Romania*

ABSTRACT

This paper presents the nonlinear dynamic behavior of a flexible shaft. The shaft is mounted in two journal bearings and the axial load is supported by a hydrodynamic thrust bearing. The coupling between the axial thrust bearing behavior and the bending vibrations of the shaft is studied in particular. The shaft is modeled with typical beam finite elements. The dynamic behaviors of the fluid supports are considered as nonlinear. The dynamic behavior is analyzed using an unsteady time integration procedure. The paper shows the coupling between the axial dynamic behavior and the bending vibrations of the shaft.

Keywords: *Thrust bearing, axial and bending vibration, flexible shafts*

1. INTRODUCTION

In many industrial applications, mechanisms such as turbines or pumps are used in more and more difficult conditions: higher operating speeds, pressures and loads. Engineers must design these types of rotating machinery with very high accuracy. The dynamic behavior of the shaft strongly depends on shaft surrounding elements: squeeze film dampers, journal bearings and thrust bearings. The influence of these fluid elements is often introduced in rotordynamics with dynamic coefficients (linear model. Frêne et al. [1]). In many cases, however the fluid elements have to be modeled with higher accuracy. In particular, Bonneau et al. [2] have shown that the nonlinear dynamic behavior calculation is required when a flexible shaft is mounted on a squeeze film damper. Moreover, Bonneau and Frêne [3] have shown that a defective journal bearing can create a dynamic perturbation of an unpredictable frequency through linear calculations.

The influence of thrust bearing on shaft dynamic behavior, and more especially the effect on lateral shaft vibration have not been extensively studied. Some studies have been carried out on the analysis of the dynamic characteristics of hydrodynamic thrust bearings and their action on axial motion (Someya and Fukuda) [4] - Jeng and Szeri [5] - Zhu [6]). The influence of thrust bearings on lateral shaft vibrations has been studied by Jiang and Yu [7]. They have shown that the thinner the film of the thrust bearing, the more important its action. In addition, it may prevent the shaft from deflecting and the first critical speed and the threshold speed increase.

N. Mittwollen et al. [8] have shown that a reduction of the total axial clearance in hydrodynamic thrust bearing or an increase in the axial load can lead to a significant increase in the first critical speed, in the whirl amplitude at the first critical speed and the threshold speed of instability. In these studies, the influence of hydrodynamic thrust bearing on the shaft dynamic behavior has been assumed to be linear. Berger et al. [9] have studied the effect of thrust bearing on a flexible shaft. The dynamic behavior of the thrust bearing has been assumed to be nonlinear. The authors have shown that a defect in the thrust bearing rotor can excite a critical speed.

The aim of the following paper is to study the nonlinear influence of the thrust bearing on the dynamic behavior of a flexible shaft and, in particular, to analyze the coupling between the axial motion and the bending vibrations of the shaft.

2. THEORY

2.1 Thrust bearing Model

Figure 1 represents the hydrodynamic thrust bearing model. (o_0 ,x_0 ,$y0$,z_0) is the fixed reference. (o_1 ,x_1 ,y_1 ,z_1) and (o_2 ,x_2 ,y_2 ,z_2) are respectively fixed to the center $o1$ of the stator and the center $o2$ of the rotor. The rotor has three translations in the directions x_0 , y_0 and z_0 and two misalignment angles (axis x_2 and y_2). The rotor has z_2 as the axis of rotation.

In the cylindrical reference (o_0 ,r,t,z_0), the thin film equation is defined by:

$$\frac{\partial}{\partial r}\left(rh^3\frac{\partial p}{\partial r}\right)+\frac{\partial}{\partial \theta}\left(\frac{h^3}{r}\frac{\partial p}{\partial \theta}\right)=-6\mu r U_2\frac{\partial h}{\partial r}-6\mu r V_2\frac{\partial h}{\partial \theta}-12\mu r U_2 \tag{1}$$

$$\frac{\partial H_1}{\partial r}$$

$$-12\mu r V_2\frac{\partial H_1}{\partial \theta}+6\mu hr\frac{\partial U_2}{\partial r}+6\mu h\frac{\partial U_2}{\partial \theta}+6\mu hU_2+12\mu rW_2$$

The equation is solved using finite difference with the Gauss Seidel method. The boundary conditions are the following:

- the feed pressure in each groove (atmospheric pressure);
- the Christopherson assumption, i.e., negative pressures are set to zero at each iteration.

The force components and the moment components are calculated by integrating the pressure field into the surface $S2$ of the rotor.

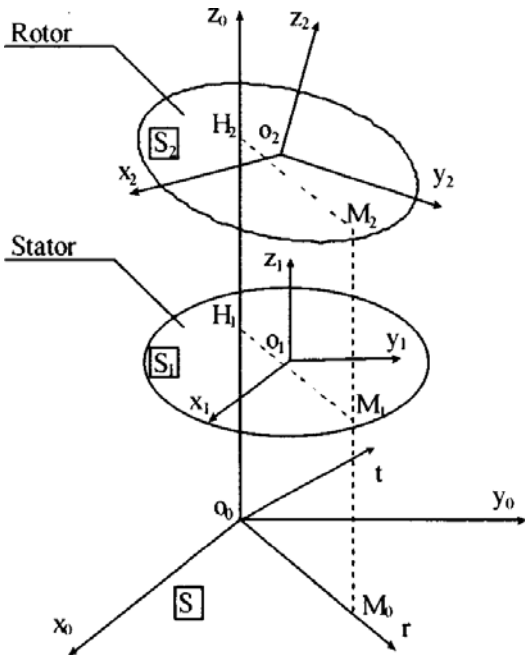

Figure 1. Thrust bearing scheme

$$\vec{F}_b = \iint_{S_2} \vec{r} p ds \tag{2}$$

$$\vec{M}_b(O_2) = \iint_{S_2} O_2\vec{M} \wedge \vec{r} p ds \tag{3}$$

2.2 Journal Bearing Model

The shaft is mounted in two identical hydrodynamic bearings whose dynamic behavior can be modeled with dynamic coefficients. Nevertheless, the dynamic coefficients are valid for a constant speed and in simulations, the rotational speed increases from 3000 rpm to 20000 rpm. Thus, in order to calculate the bearing force, the thin film behavior is assumed to be nonlinear and then, the film equation can be solved using finite differences. However, the nonlinear analysis of the shaft implies heavy numerical calculation. Thus the solution of the short bearing has been chosen. This assumption helps simplification of the differential equation; the circumferential flow is neglected. The force components are obtained by integrating the pressure field with the following boundary conditions: the feed pressure on both sides of the bearing (atmospheric pressure) and the Gumbel assumption (π film), i.e., the negative pressure, are set to zero (Bonneau and Frêne) [3]). It must be noticed that the finite length journal bearings can be used and the same phenomenon should occur.

2.3 Shaft Model

2.3.1 Lateral Dynamic Behavior. The rotor is modeled with typical beam finite elements including gyroscopic effects, (Bonneau et al. [2]). Each element has four degrees of freedom: two translations in the directions $x0$ and $y0$, and two axes of rotations (x_0 and y_0).

The differential system with {δ} as the node displacement vector is:

$$[M]\{\ddot{\delta}\} + [C]\{\dot{\delta}\} + [K]\{\delta\} = \{F_{unb}\} + \{F_{nl}\} + \{F_{gr}\} \tag{4}$$

This system has 4*n* degrees of freedom (*n* is the number of nodes). To reduce the degrees of freedom a modal approach is used by Lacroix [10], and Lalanne and Ferraris [11]. The journal bearings are first modelled by a linear stiffness [$K_{Journal\ Bearing}$] and then the fundamental principle of mechanics on the rotor could be written:

$$[M]\{\ddot{\delta}\} + \left([K_r] + [K_{Journ\ Bearing}]\right)\{\delta\} = 0 \tag{5}$$

The solution has the form: $\{\delta\} = \{\delta_0\}e^{rt}$ and the first 6 modes are calculated. Lacroix [10] has shown that 6 modes are enough to obtain the acceptable precision. A change of variable is done in the form: $\{\delta\} = \{\psi\}\{q\}$ with $\{\psi\}$ the matrix obtained with modal vectors $\{\psi_i\}$ and $\{q\}$ is the modal vector of displacement. A new system is written where the journal bearing effect appears in the modal stiffness matrix.

$$[m]\{\ddot{q}\} + [c]\{\dot{q}\} + [k']\{q\} = \{f\}$$

with

$$\begin{aligned} [m] &= [\psi]^t[M][\psi]; [c] = [\psi]^t[C][\psi] \\ [k'] &= [\psi]^t\left[K + K_{Journ\ Bearing}\right][\psi] \\ [f] &= [\psi]^t[\{F_{unb}\} + \{F_{nlTB}\}][\psi] \end{aligned} \tag{6}$$

To do a nonlinear calculation the linear journal bearings effect [$K_{Journal\ Bearing}$] must be subtracted from modal stiffness [k'] and must be introduced as nonlinear effect. Then

$$[m]\{\ddot{q}\} + [c]\{\dot{q}\} + [k]\{q\} = \{Ff\} + \{F_{nlTB}\} \tag{7}$$

with

$$[k] = [k'] - [\psi]^t\left[K_{Journ\ Bearing}\right][\psi]$$

2.3.2 Axial Dynamic Behavior. In the axial direction (z_0), the shaft is considered rigid. Its dynamic behavior is described by the following equation:

$$m\ddot{z} = F_{b_z} + F_a \tag{8}$$

2.4 Nonlinear Simulation

The simulations of the axial dynamic behavior and the lateral dynamic behavior of the flexible rotor are independent. The only relation between these models is the thrust bearing. Thus, it allows to isolate and to enhance a possible coupling between the axial dynamic behavior and the lateral dynamic behavior of the rotor due to the only thrust bearing.

The simulation of the lateral behavior is obtained by a nonlinear calculation in the modal basis. The flow chart is the following:

1. Start with initial values of modal positions and velocities
2. Calculation of external modal forces (unbalance, weight…)
3. Calculation of physical displacements and velocities in bearings and thrust bearing (through modal basis change)
4. Calculation of nonlinear bearing forces, nonlinear thrust bearing forces and moments (in the real basis)
5. Computation of all forces in the modal basis (through modal basis change)
6. Calculation of modal accelerations (differential system)
7. Time integration (using the variable step Euler method)
8. Shaft speed incremented and the process restarts from 2.

The simulation of the axial behavior is obtained with a similar process in the real basis (direction z_0):

1. Start with initial values of axial position and velocity
2. Calculation of axial external forces (*Fa*) and nonlinear axial thrust bearing force (*Fbz*)
3. Calculation of axial acceleration (differential equation)
4. Time integration (using the variable step Euler method)
5. Shaft speed incremented and the process restarts from 2.

3. RESULTS

3.1 Data

The data of the shaft are [1]: the length which is equal to 1 m and the radius which is equal to 0.03 m. The data of the bearings are: the length L=0.015 m, the radius R=0.03 m, the radial clearance C=3.0E-05 m, the dynamic viscosity μ=0.05 Pas. The thrust bearing has four pads. The data of each pad are the angle β=80 deg, the outer radius R_2=0.04 m, the inner radius R_1=0.02 m. The entry thickness *hse* , the exit thickness h_s of each pad and the axial clearance of the thrust bearing are defined in relation to a virtual surface $S=(o,x_0,y_0)$ (Fig. 2). This surface *S* doesn't represent a real surface and it is used just as a position reference. The entry thickness h_e is equal to 55 μm and the exit thickness h_s is equal to 75 μm. The axial clearance is defined as the distance h_c between the center of the surface S_2 and the surface *S* of the thrust bearing.

3.2 Unbalance Response of Shaft

This part deals with the nonlinear unbalance response of the shaft. In the middle of the rotor, an unbalance force excites the system and a static load is applied in order to stabilize it. More, the thrust bearing supports an axial static force (Fig. 3).

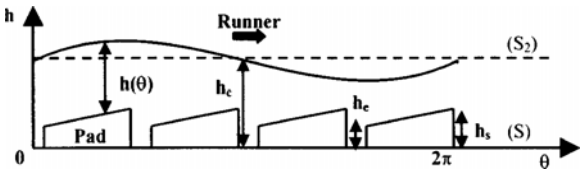

Figure 2. Film circumferential thickness in the thrust bearing

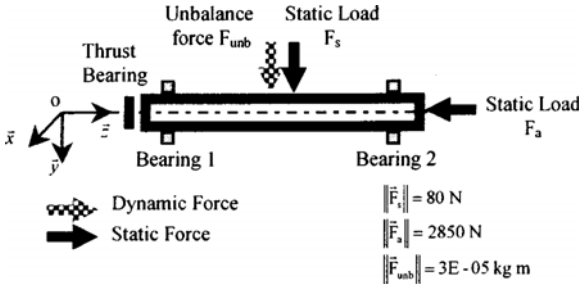

Figure 3. Rotating system

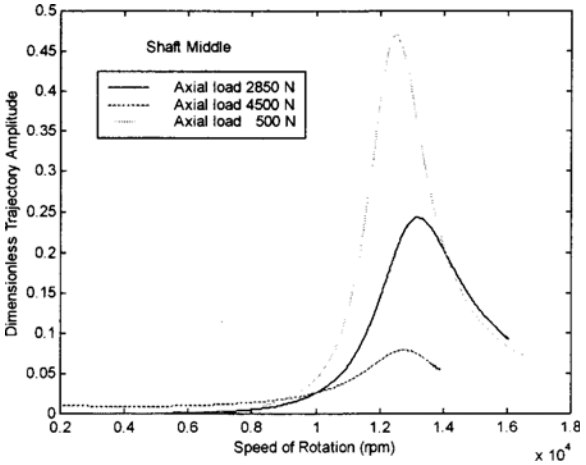

Figure 4. Lateral unbalance response of the shaft middle

3.2.1 Lateral Response of the Shaft. The bending vibrations of the shaft are studied. The rotational speed increases from 4000 rpm to 18000 rpm in 9 s. The shaft response is presented for three different axial loads. Figure 4 displays the nonlinear response of the rotor in the middle of the rotor. The trajectory amplitude of the shaft is plotted in the plane (x_0, y_0).

Note: All the amplitudes given in this paper are nondimensional (amplitude/Bearing radial clearance ratio).

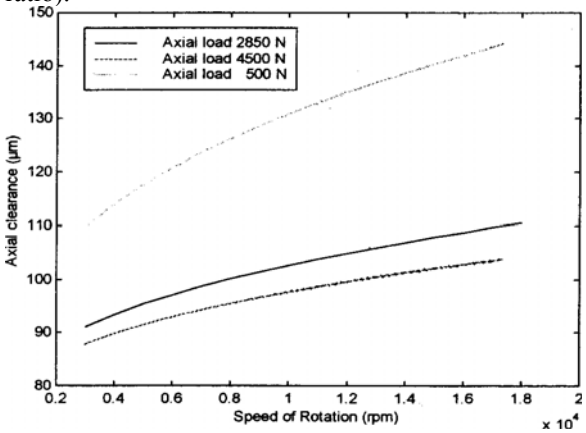

Figure 5. Axial unbalance response of the shaft

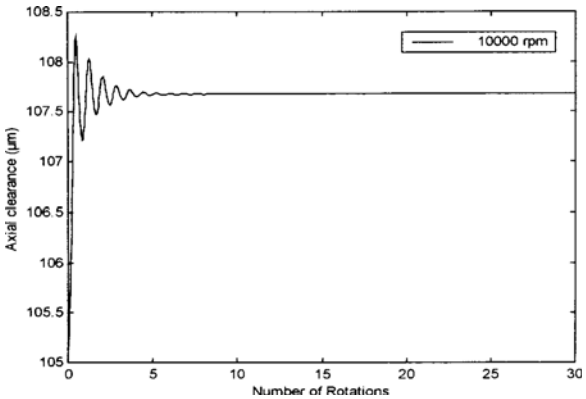

Figure 6. Axial behavior of the shaft for a constant rotational speed

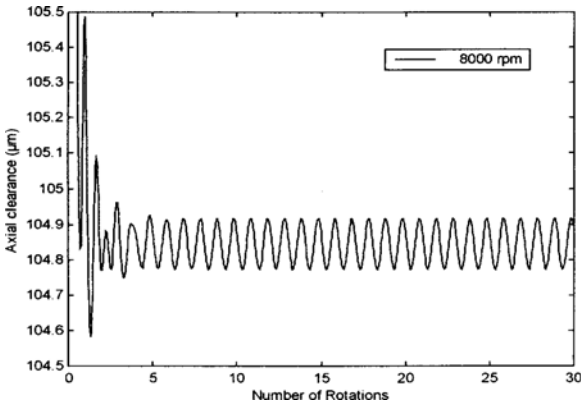

Figure 7. Axial unbalance response of the shaft for a constant rotational speed

A critical speed appears at about 12400 rpm. For an axial load equal to 2850 N, the peak amplitude is equal to 0.25 times the bearing radial clearance. These unbalance responses are usual results. It must be added that the heavier the axial load, the higher the critical speed with a decrease in peak amplitude. The heavier the axial load, the smaller the thrust bearing axial clearance (Fig. 5); the influence of the thrust bearing on the shaft is strong, that is, the thrust bearing applies more and more stiffness and damping on the flexible shaft.

3.2.2 Axial Response of the Shaft. The axial behavior of the shaft is analyzed when the rotational speed increases from 4000 rpm to 18000 rpm in 9 s. Figure 5 displays the axial clearance of the thrust bearing according to the rotational speed.

The axial clearance of the thrust bearing oscillates around a value which increases with the rotational speed and the heavier the axial load, the smaller the axial clearance. In order to analyze the axial response accurately, the axial dynamic behavior of the shaft is studied for a constant rotational speed. Figures 6 and 7 present the axial clearance when the unbalance force is respectivelynil and equal to 3E-05 kgm. When the rotor is not excited, the shaft oscillates and stabilizes in a steady state. Otherwise, when the unbalance force is applied, the shaft oscillates at a frequency equal to the rotational shaft frequency. Thus, a lateral dynamic force can excite the axial dynamic behavior of the shaft through the thrust bearing. In these cases, it must be noticed that the influence of the lateral force on the axial dynamic behavior is very slight and no axial critical frequency is excited.

3.3 Axial Excitation of the Shaft

An axial dynamic force $\vec{F}_a$ excites the shaft at one end: $\vec{F}_a = (1000 + 800\sin(2\pi N_a t))\vec{z}$ with *Na* the rotational shaft frequency. No unbalance force is applied on the shaft. In the middle of the rotor, a static load is used to stabilize it. The rotational speed increases from 4000 rpm to 20000 rpm in 9 s.

3.3.1 Axial Response of the Shaft. This part considers the axial behavior of the shaft. Figure 8 displays the axial clearance of the thrust bearing according to the rotational speed. The axial clearance oscillates around a value which increases with the rotational speed. No axial critical frequency is excited.

3.3.2 Lateral Response of the Shaft. The bending vibrations of the shaft are analyzed. Figure 9 shows the trajectory amplitude of the shaft in the middle of the rotor. A critical speed appears at 14400 rpm. The peak amplitude is equal to 0.09 times the bearing radial clearance. Thus, an axial dynamic force can excite the lateral dynamic behavior of the shaft through the thrust bearing. An axial dynamic load can excite the first bending critical frequency. The Axial Excitation frequency/Rotational Shaft Frequency ratio is about one. The shaft is now excited by an axial dynamic force *Fa* whose frequency is equal to 6 times the rotational shaft frequency. This axial excitation can be generated, for example, by a six-blade turbine fixed on the shaft. The critical speed logically appears at a lower value (2600 rpm). This critical speed is about the critical shaft speed divided by the number of blades (Fig. 10).

In comparison with the previous case, the peak amplitude is much lower because the rotational speed is slower. Thus, the amplitude peaks generated by the turbines at a slow rotational speed
are lower.

4. CONCLUSIONS

The influence of a hydrodynamic thrust bearing on the dynamic behavior of a flexible shaft can be significant. The thrust bearing generates a coupling between the axial motion and the bending vibrations of a flexible shaft.

A lateral dynamic force ~unbalance force! can influence the axial dynamic behavior of the shaft. Nevertheless, in this study, the influence is slight and no axial critical frequency is excited. It must be added that the heavier the axial load, the higher the critical speed and the peak amplitude decreases because the thrust bearing applies more and more stiffness and damping on the flexible shaft.

The ‘‘axial excitation & lateral response’’ coupling can be important. An axial dynamic load can excite the first critical bending frequency of a flexible shaft. The Axial Excitation frequency/Rotational Shaft Frequency ratio is about one. Thus, a turbine with nb blades which generates an axial perturbation can excite the first critical

bending frequency when the rotational shaft frequency is equal to the first bending critical frequency n_b ratio.

In this paper, the coupling between the axial dynamic behavior and the lateral dynamic behavior of the rotor is required to be due only to the thrust bearing. Nevertheless, a coupling can occur between the axial behavior and the lateral behavior of the rotor without any reference to thrust bearing. Mc Lachlan [12] and Ehrich [13] suggest that parametric instability in lateral response is possible when the amplitude of the axial excitation is a nonnegligible fraction of the compressive buckling load of the rotor. It must be pointed out that theses two phenomena are different and independent. It would be interesting to take into account theses two phenomena together.

At this point in the study, the effects of thrust bearing location on the shaft can be studied, in particular, the influence of the thrust bearing on the shaft dynamic behavior can be analyzed, on whether the thrust bearing is on a node or an antinode.

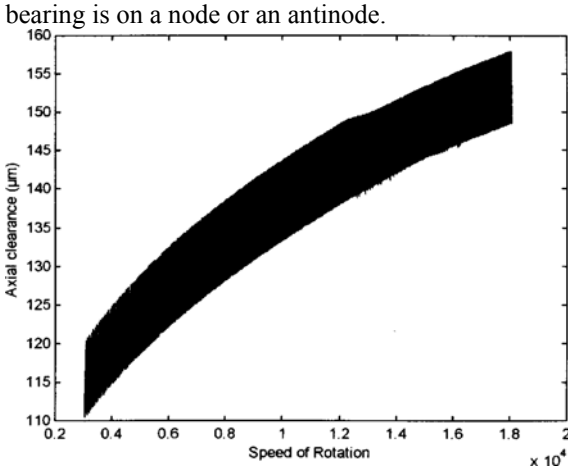

Figure 8 Axial unbalance response of the shaft

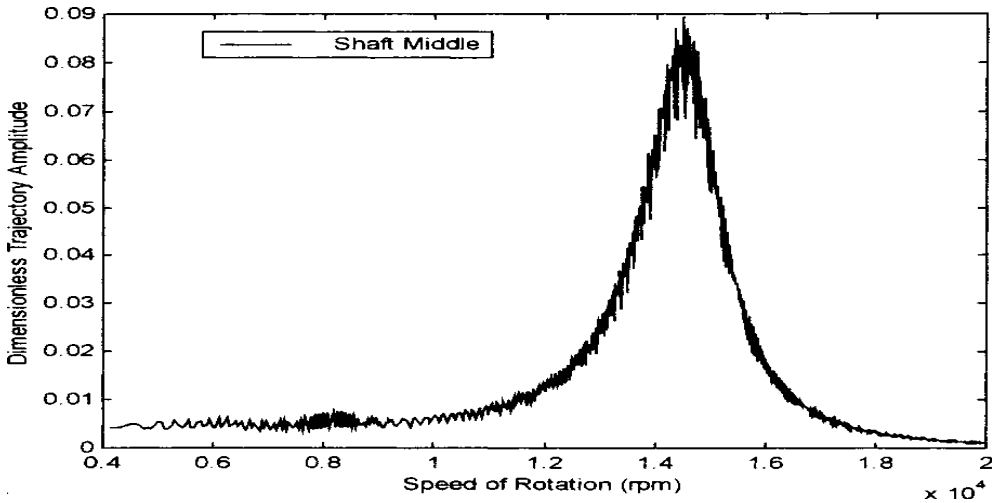

Figure 9 Lateral response of the shaft middle due to axial excitation of the shaft

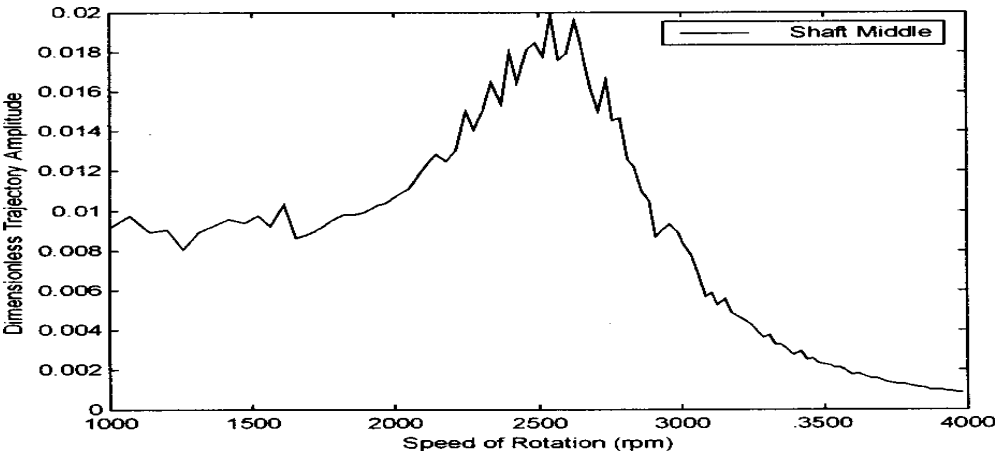

Figure 10 Lateral response of the shaft middle due to axial excitation of the shaft

Nomenclature

(o_0, x_0, y_0, z_0) = fixed reference
(o_0, r, t, z_0) = local reference
(o_1, x_1, y_1, z_1) = reference fixed to the thrust bearing rotor
(o_2, x_2, y_2, z_2) = reference fixed to the thrust bearing stator
p = pressure field (Pa)
$h=H_2-H_1$ = film thickness (m)
U_2, V_2, W_2 = velocity components of the thrust bearing rotor in the reference (o_0, r, t, z_0) (m/s)
μ = dynamic viscosity (Pa.s)
r = radial parameter (m)
θ = angular parameter being its origin one the axis x_0
β = angle of each thrust bearing pad (deg)
R_1 = inner radius of pad thrust bearing (m)
R_2 = outer radius of pad thrust bearing (m)
h_e = entry thickness of pad thrust bearing (m)
h_s = exit thickness of pad thrust bearing (m)
h_c = axial clearance of thrust bearing (m)
$\dot{F}_b$ = thrust bearing force (N)
Fbz = axial component of thrust bearing force (N)
$\dot{M}_b$ = thrust bearing moment (N.m)
C = radial clearance (m)
L = bearing length (m)
R = bearing radial clearance (m)
m = shaft mass
n = number of nodes
$\{\delta\}$ = node displacement (m)
$[C]$ = damping and gyroscopic matrix (N.s/m)
$[K]$ = stiffness matrix (N/m)
$[K_{Journal\ Bearing}]$ = bearing stiffness (N/m)
$[M]$ = mass matrix (kg)
$[\psi]$ = modal matrix
$[F_{unb}]$ = unbalance forces (N)
$\{F_{nl}\} = \{F_{nlTB}\} + \{F_{nlJB}\}$ = nonlinear thrust bearing and journal bearings forces (N)
$\{F_{gr}\}$ = gravity forces (N)
F_s = static lateral axial load (N)
F_a = external axial force (N)
N_a = rotational shaft frequency (Hz)

5. REFERENCES

[1] FRÊNE, J., NICOLAS, D., DEGUEURCE, B., BERTHE, D., AND GODET, M., 1997, *Hydrodynamic Lubrication-Bearings and Thrust Bearings,* Elsevier Science, New York, ISBN-0-444-82366-2.

[2] BONNEAU, O., KASSAI, A., FREÊNE, J., AND DER HAGOPIAN, J., 1989, ‘‘Dynamical Behavior of an Elastic Rotor with a Squeeze Film Damper,’’ *Proceedings EUROTRIB*, Helsinki, Finland, June, 4, pp. 145–149.

[3] BONNEAU, O., AND FREÊNE, J., 1996, ‘‘Influence of Bearing Defects on Dynamical Behavior of an Elastic Shaft,’’ Int. J. Rotating Mach., 2, pp. 281–287.

[4] SOMEYA, T., AND FUKUDA, M., 1972, ‘‘Analysis and Experimental Verification of Dynamic Characteristics of Oil Film Thrust Bearings,’’ Bull. JSME, 15, pp. 1004–1015.

[5] JENG, M. C., SZERI, A. S., 1986, ‘‘A Thermohydrodynamic Solution of Pivoted Thrust Pads,’’ ASME J. Tribol., 108, pp. 195–218.

[6] ZHU, Q., XIE, Y. B., YU, L., 1990, ‘‘Axial Transient Forces of Thrust Bearing Rotor System in a Turbo-expander,’’ *Proceedings of International Conference on Hydrodynamic Bearing-Rotor System Dynamics*, China.

[7] JIANG, P. L., YU, L., 1998, ‘‘Effect of a Hydrodynamic Thrust Bearing on the Statics and Dynamics of a Rotor-Bearing System,’’ Mech. Res. Commun., 25, No. 2, pp. 219–224.

[8] MITTWOLLEN, N., HEGEL, T., GLIENICKE, J., 1991, ‘‘Effect of Hydrodynamic Thrust Bearings on Lateral Shaft Vibrations,’’ ASME J. Tribol., October, 113, pp. 881–818.

[9] BERGER, S., BONNEAU, O., FRÊˆNE, J., 1998, ‘‘Influence of Axial Thrust Bearing Defects on the Dynamic Behavior of an Elastic Shaft,’’ *Proceedings of the 5th International Tribology Conference Austrib’98*, Brisbane, December 6-9, pp. 389–394.

[10] LACROIX, J., 1988, ‘‘Comportement Dynamique d’un Rotor au Passage des Vitesses Critiques,’’ The`se de Doctorat de l’INSA de Lyon.

[11] LALANNE, M., FERRARIS, G., 1990, *Rotordynamics Prediction in Engineering*, Wiley, Chichester.

[12] MC LACHLAN, N. W., 1947, *Theory and Applications of Mathieu Functions*, Oxford University Press, New York, p. 40.

[13] EHRICH, F. F., ed., 1999, *Handbook of Rotordynamics*, Krieger, Malabar, FL, p. 102.

ANALYSIS OF COMPLEXE VIBRATION OF THE HIGH POWER DIESWL ENGINE SHAFTING SYSTEM

[1]BUZBUCHI NICOLAE, [2]STAN LIVIU-CONSTANTIN

[1,2]*Constanta Maritime University, Romania*

ABSTRACT

The development of new marine engine generation for minimum fuel consumption involving greater stroke/bore ratios, lower running speeds and higher combustion pressures, for lower installation and operating costs as well as for higher reliability and a very large spectrum of different shaft line arrangements largely influences the vibration analysis of a modern ship installation. The studies involved in the present paper started with the calculation for axial and torsional shaft line vibration, carried out independently from each other. In reality, these two forms of vibration are linked, since twisting the crankshaft will induce an axial deflection, phenomenon observed only with two-stroke engines. The coupling effect between torsional and axial vibration is thus subject of our research in order to be able to take it more into account in nowadays projects. An axial detuner will be then applied in order to control this coupling effect.

Keywords: *Marine engine, shaft line, coupled vibration analysis, experimental results*

1. INTRODUCTION

Low levels of vibration are generally expected or requested by ship owners, because comfort of personnel on board ship is today a common concern. On the other hand, if the level of vibration is too high, the safety of machinery, electronic equipment and even the ship structure may be threatened.

Thus vibration is subject of continuous research in terms of developing new computer software, analytical methods and measuring techniques for dealing with complex vibration problems.

The vibration of ship machinery is well understood and can be predicted with sufficient accuracy. This confidence in the calculations is needed to be sure that the vibration levels will remain below the corresponding admissible limits.

It is important that vibration aspects are considered at the earliest stage possible in the ship design process to find a cost-effective installation with the best combination of countermeasures against vibration. It is also calls for close collaboration between the shipyard, the engine and propeller suppliers and other suppliers.

As main component of diesel two-stroke marine engine, the design of the crankshaft included in the shaft line system is quite different to those in the past: masses and inertias are larger, so are elasticities.

The common way to find optimal plant design consists today in calculating separately the torsional and axial vibrations (natural frequencies, critical speeds and forced vibrations) in order to determine, if necessary, which kind of torsional damper, flywheel, free-end flywheel, elastic couplings and axial detuner have to be fitted to the engine.

The same mathematical model is used for both vibrations: the shaft line is separated into discrete elements with equivalent inertias and elasticities for torsional vibration, or equivalent masses and stifnesses for axial vibration. The dynamic behavior of each equivalent inertia or mass can be described through the following linear differential equation:

$$[M]\ddot{x}+[D]\dot{x}+[K]x=F(t), \tag{1}$$

where: $[M]$-the matrix of the equivalent inertias or masses, $[D]$-the matrix of the equivalent damping, $[K]$-the matrix of the equivalent stifnesses, $F(t)$-vector of the periodic excitation torque or force, t - time, x -vector of the torsional amplitudes or displacements, $\dot{x}=dx/dt$.

Only one degree of freedom is thus taken into account in this model. The calculation of the torsional and axial vibration is made separately and no coupling effect between these two kinds of vibration can appear in the results of the forced vibration.

However, the comparison between calculation and measurement of these vibrations shows the following:

- the axial displacements are influenced by the torsional vibrations: an increase of displace-ment is observed for the speed range in the neighborhood of any torsional critical speed;
- the torsional amplitudes are not influenced by the axial vibration;
- the coupling effect is larger if torsional and axial critical speeds are closer together.

2. THEORY

Instead of separating the shaft line into separete, discrete elements with equivalent inertias and masses connected through spring elements with damping, as is usually done in standard methods of calculation, a computer finite element (FE) model is used [16]. Figure 1 shows an example of such kind of three-dimensional FE modeling for the crankshaft of a Sulzer 6RND90 engine.

This structure may be simplified [6], [8] for the study, each crank part being reduced to an element containing all the stiffness, mass and inertia characteristics, but we preferred a more accurate model (so called "solid model"). The comparison between calculated and measured natural frequencies is very good despite the fact that the oscillating masses and bearing stiffness have been reduced to a constant mean value. Table 1 indicates these values, for each individual vibration type (bending vibration included, even more significant for two-stroke stiff crankshaft). On the basis of this complete structure, it was then possible to start the calculation of the forced vibration; for this purpose, the tangential and radial excitation forces acting on each crank for each harmonic are calculated according to the tangential forces obtained from the gas forces, after geometrical transformation and Fourier analysis.

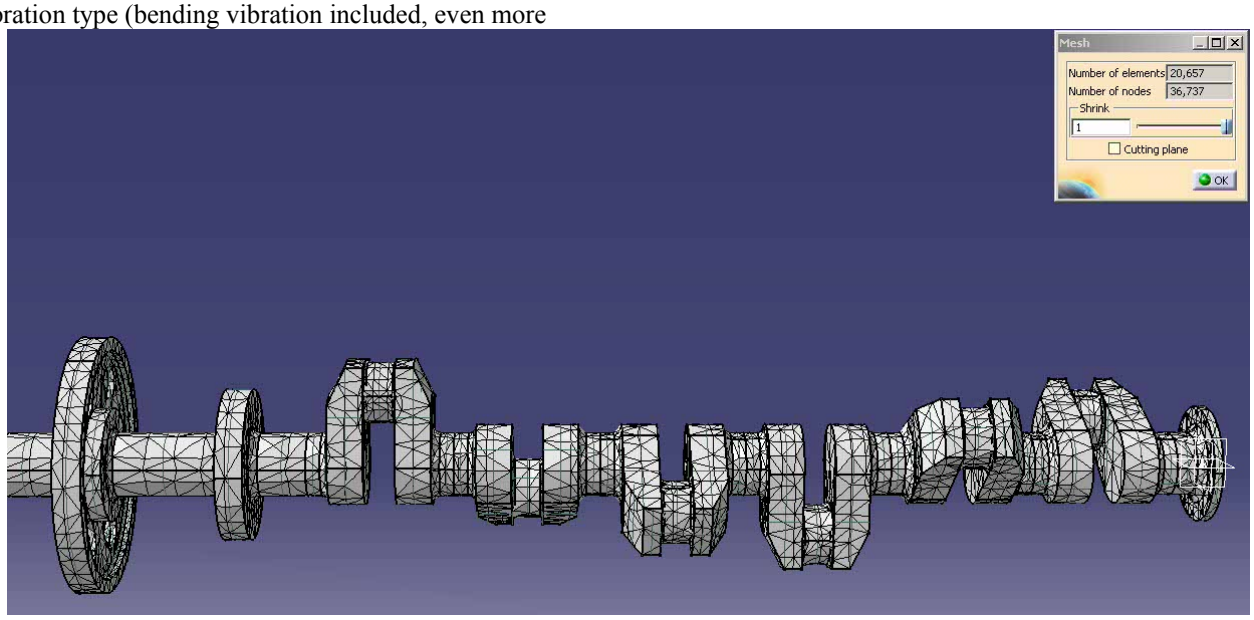

Figure 1 Three-dimensional finite element model for a six-throw shaft line

Figure 2 shows, on the same example of the installation described before, these forces with their locations and directions. The calculation of the forced vibrations is carried out harmonic by harmonic. The backward Fourier transformation should be done by an auxiliary program in order to determinate a synthesis [6]. For the harmonic analysis of the propeller excitation on the shafting system, an original method and computer code have been developed and experimentally confirmed [2], for steady-state conditions. The harmonic coefficients of the propeller torque and the corresponding phases, as well as the thrust harmonic coefficients and their respective phases are presented in [12].

In any case, it is possible to compare the calculated amplitudes with the measured ones, harmonic by harmonic.

Table 1. Natural Frequencies

Frequency order	Torsion $[s]^{-1}$	Bending $[s]^{-1}$	Axial $[s]^{-1}$	Coupled (FEM) $[s]^{-1}$
I	83.287	20.054	31.559	36.014
II	201.405	68.426	77.892	79.238

3. EXPERIMENTAL

The propeller excitation on the shafting system of the engine was experimentally confirmed in [2]. It was easy to verify that values lie within the limits set by the regulations [14].

Subsequently, after having run the FEM code, measurements of the axial vibrations of the shafting system were carried out on a ship equipped with the engine, because of the ship owner's complaints. After the measurements, an axial damper was fitted at the free shafting system.

The set of Brüel & Kjaer instruments required is presented in [6]. The lower branch of this set is used for the measurements on board the ship and the upper part in the analysis in the laboratory. The results were presented and compared with the regulations [14], as shown in Table 2. The frequency analysis for different engine speeds: 100 RPM, corresponding to the beginning of the critical speed area, 115 RPM corresponding to the end of the critical speed area, and 140 RPM corresponding to the cruise engine speed have been carried out.

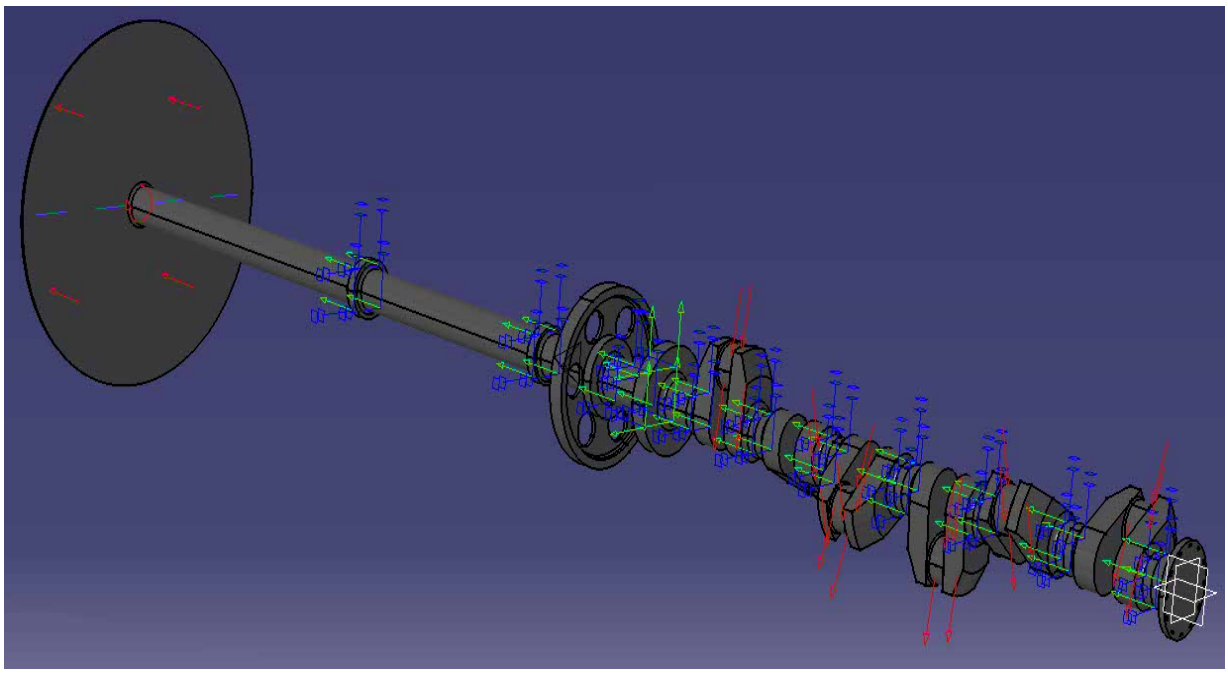

Figure 2 The loads of the shaft line

Table 2. Measured Axial Vibration Amplitudes

Marine Engine Rating [RPM]	Measured Parameters			
	Frequency [Hz]	Amplitudes [mm]		
		Axial Without Damper	Axial With Damper	Admissible
100	10.25	0.865	0.065	0.318
115	11.75	2.740	0.288	0.318
140	14.00	0.726	0.082	0.318
* Recommended by Bureau Veritas				

Table 3. Comparison between Measured and Calculated Axial Vibration Amplitudes

Marine Engine Rating [RPM]	Parameters			
	Frequency [Hz]	Amplitudes [mm]		
		Axial, Without Damper		
		Measured	Calculated	Admissible *
100	10.25	0.865	-	0.318
115	11.75	2.740	-	0.318
140	14.00	0.726	0.793	0.318
* Recommended by Bureau Veritas			approx 8% error	

4. EXPERIMENTAL

As can be seen from Table 1, the first order (I) torsional natural frequency is closer to the second order (II) axial one suggesting a coupling between the two modes. The natural frequencies of the coupled vibrations are even closer to the values of the natural frequencies of the individual axial vibrations indicating an important influence of the latter in the coupled phenomenon. A much weaker influence of the bending vibrations on the coupled phenomenon can also be seen.

As mentioned in [6], the first order torsional vibrations mode shape is very similar to the second order axial one, both of them having a single node. The first order axial vibration mode shape has no sign change; the vibration of the relative axial amplitudes is reduced mainly due to the influence of the thrust bearing. The most dangerous resonance occurs with the order 6, while the influence of the harmonic order 4 (the first order at blade frequency) is much lower. Therefore, the predominant influence on the axial vibration level is

exercised by the torsional vibration conforming to the aforementioned coupling phenomenon and not by the propeller thrust fluctuations.

The computer code allows us to analyze the stresses of the single crank (Fig. 3), the free vibration of this element and its corresponding natural frequencies (Fig. 4) and the deformed shaft line shape (Fig. 5).

The measured values without the axial damper were as presented in Section 3, compared with the numerical results in Table 3. It can be seen that a critical engine speed occurs around 115 RPM. In fact the critical speed corresponding the second order natural frequency of Table 1 will be: $n_0 \cong 9.55$; $\omega_0 = 9.55 \times 79.238 = 756.723$ RPM, while the resonance speed corresponding to the sixth order harmonic will be: $n_6 = 6 \times 115 = 690$ RPM and n6/n0 = 0.91, i.e. inside the critical speed area.

We can also observe that 140 RPM the difference between the theoretical results and the measured values is approximately 8.4% which is considered acceptable.

Therefore, the influence of the damping, which was neglected here, is minimal.

5. CONCLUSIONS

It is very interesting that the main axial excitation of the marine Diesel engine shafting systems, in the frame of the coupling vibrations phenomena is due to the torsional vibrations and not to the propeller thrust fluctuations.

The methods proposed are experimentally validated and may consist a good prediction tool for determining if an axial damper is necessary.

Our computation methods have taken into account only the steady-state operation. Therefore, the damping matrix determination was not necessary. However, we need further experimentation towards this goal and this will be part of our future research.

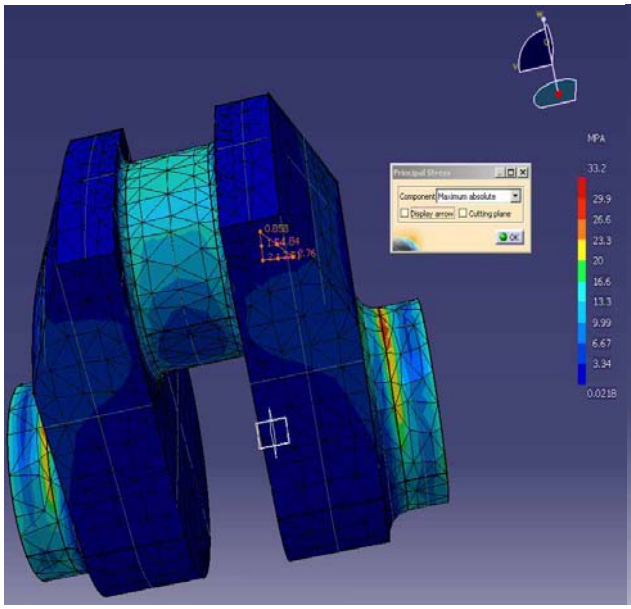

Figure 3 Single crank stresses

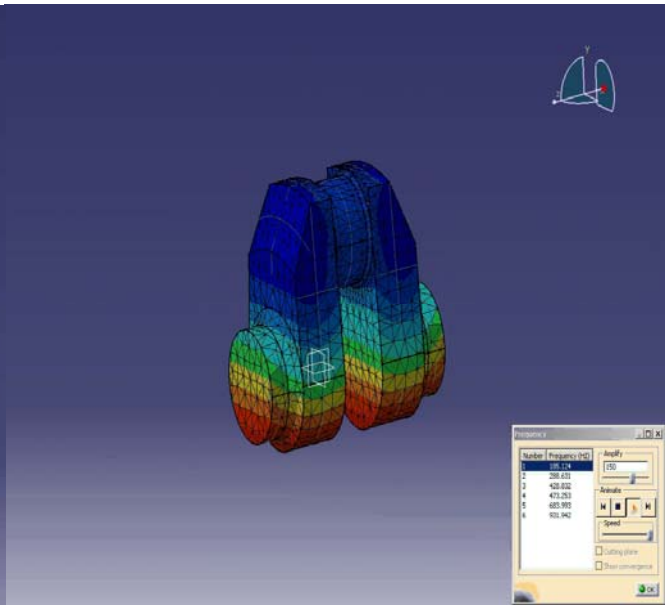

Figure 4 Single crank natural frequencies

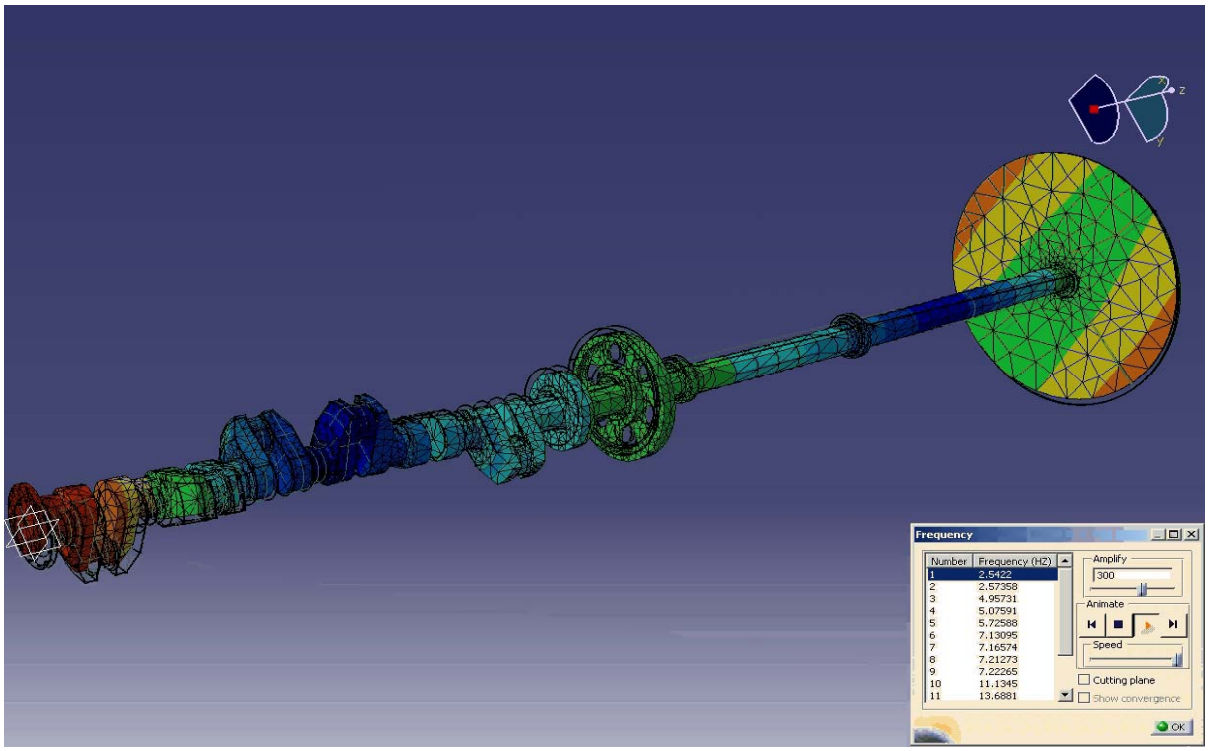

Figure 5 The deformed shape of the engine shaft line

6. REFERENCES

[1] BRYNDUM, L., JAKOBSEN, S.B. *Vibration Characteristics of Two-Stroke Low Speed Diesel Engines*, MAN B&W, Copenhagen, 1987.

[2] BUZBUCHI, N. *Validation Among Theoretical Calculation of the Propeller Harmonic Excitation and Experiments*, Bulletin of the Marine Engineering Society in Japan (MESJ), the Sixth International Sym posium on Marine Engineering ISME-2000, Tokyo, 2000.

[3] BUZBUCHI, N., ŞOLOIU, V.A., DINESCU, C., LYRIDIS, D.V., *Motoare navale. Vol. 2: Supraalimentare *Dinamică*, Editura Didactică şi Pedagogică, Bucureşti, 1998.

[4] BUZBUCHI, N., *Torsional Vibration of Marine Diesel Engines Shafting Systems. Software Reference Manual*, National Technical University of Athens Publishing House, Greece, 1995.

[5] BUZBUCHI, N., OANŢĂ, E., *Matrix Methods in Studying the Torsional Vibration of the Marine Engines Shafting Systems. Software Reference Manual*, National Technical University of Athens Publishing House, Greece, 1996.

[6] BUZBUCHI, N., TARAZA, D., LYRIDIS, D., *Theoretical and Experimental Study of the Torsional, Bending and Axial Coupled Vibration of Marine Diesel Engine Shafting System"*, Bulletin of the Marine Engineering Society in Japan (MESJ), the Fifth International Symposium on Marine Engineering ISME, Yokohama, 1995.

[7] BUZBUCHI, N., TARAZA, D., *On Vibration Analysis in Ship Installations with Two-Stroke Diesel Engines*, the Transaction Volume of the Motor and Motor Vehicle Engines, Izmir, 1993.

[8] JENZER, J., WELTE, Y,. *Coupling Effect between Torsional and Axial Vibration in Installations with Two-Stroke Diesel Engines*, New Sulzer Diesel, Winterthur, Switzerland, 1991.

9] JENZER, J., *Vibration Analysis for Modern Ship Machinery*, New Sulzer Diesel, Winterthur, Switzerland, 1991.

[10] JENZER, J., FROSSARD DE SAUGNY, H., *On the Dynamics of Diesel Power Plant*, New Sulzer Diesel, Winterthur, Switzerland, 1991.

[11] TARAZA, D., *Dinamica motoarelor cu ardere internă*, Editura Didactică şi Pedagogică, Bucureşti, 1985.

[12] TARAZA, D., BUZBUCHI, N., POPOVICI, J.S., *Calculation of the Harmonic Structure of Marine Propeller Torque and Thrust*, International Off-Highway & Powerplant Congress & Exposition, Milwaukee, Wisconsin, 1994.

[13] WAKABAYASHI, K., SHIMOYAMADA, K., KODAMA, T., HONDA, Y., IWAMOTO, S., *A Numerical Computation for Vibration Displacements and Stresses of Crankshaft with a Shear Rubber Torsional Damper* International Congress and Exposition, Detroit, Michigan, 1993.

[14] *** *Reccomandations en vue de limiter les effets des vibrations à bord des navires*, Bureau Veritas, N.I., Juin, 1979.

[15] *** *Master Catalogue-Electronic Instruments*, Brüel & Kjaer, Larsen & Son, Glodstrup, Denmark, 1989.

[16] *** CATIA *Software Reference Manual*.

NUMERICAL INVESTIGATION OF THE INFLUENCE OF INLET PRESSURE ON THE CAVITATING CONDITIONS INTO CENTRIFUGAL PUMPS

[1]CALIMANESCU IOAN, [2]GRIGORESCU LUCIAN

[1]Saipem SpA Italy, [2] Constanta Maritime University, Romania

ABSTRACT

Numerical and experimental results were presented in this study, concerning a test impeller of a centrifugal pump. From the experimental point of view, the cavitation was visualized at different Inlet Pressure values. Image processing and statistical treatment of the photographs taken at given impeller position allowed to quantify the attached and cloud cavitation extent.

A numerical model of 3D cavitating flows, based on the CFD code Fluent 6.1, has been developed to predict the cavitation behavior in our model which is considering the entire pump, the impeller and also the casing of the pump, with all its complex geometry and flow parameters. Non-cavitating and cavitating conditions were investigated. Calculations were found to be in good agreement with experimental measurements and visualisations. Experimental and numerical results concerning the pump parameters were investigated.

The overall conclusion is the obvious knowledge that the NPSH is indeed affecting the cavitation condition in the centrifugal pumps, having direct impact on the magnitude of static pressures in various locations inside the pump, but is not altering too much the velocities distributions of fluid. The results obtained show the ability of the model to simulate the main features of 3D cavitating flows in rotating machinery. The rich palette of results shown below is thoroughly investigating the flow parameters of the model.

Keywords: *FEA, CFD, Pump, Cavitation, Impeller.*

1. INTRODUCTION

Cavitation is a common occurrence but is the least understood of all pumping problems. Cavitation means different things to different people. Some say when a pump makes a rattling or knocking sound along with vibrations, it is cavitating. Some call it slippage as the pump discharge pressure slips and flow becomes erratic. When cavitating, the pump not only fails to serve its basic purpose of pumping the liquid but also may experience internal damage, leakage from the seal and casing, bearing failure, etc.

The term 'cavitation' comes from the Latin word "cavus", which means a hollow space or a cavity. Webster's Dictionary defines the word 'cavitation' as the rapid formation and collapse of cavities in a flowing liquid in regions of very low static pressure.

In any discussion on centrifugal pumps various terms like vapor pockets, gas pockets, holes, bubbles, etc. are used in place of the term cavities. These are one and the same thing and need not be confused. The term bubble shall be used hereafter in the discussion.

In the context of centrifugal pumps, the term cavitation implies a dynamic process of formation of bubbles inside the liquid, their growth and subsequent collapse as the liquid flows through the pump.

Generally, the bubbles that form inside the liquid are of two types: Vapor bubbles or Gas bubbles.

1. Vapor bubbles are formed due to the vaporisation of a process liquid that is being pumped. The cavitation condition induced by formation and collapse of vapor bubbles is commonly referred to as Vaporous Cavitation.

2. Gas bubbles are formed due to the presence of dissolved gases in the liquid that is being pumped (generally air but may be any gas in the system). The cavitation condition induced by the formation and collapse of gas bubbles is commonly referred to as Gaseous Cavitation.

Both types of bubbles are formed at a point inside the pump or in the impeller blades area, where the local static pressure is less than the vapor pressure of the liquid (vaporous cavitation) or saturation pressure of the gas (gaseous cavitation).

The vaporous cavitation is the most common form of cavitation found in process plants. Generally it occurs due to insufficiency of the available NPSH or internal recirculation phenomenon. It generally manifests itself in the form of reduced pump performance, excessive noise and vibrations and wear of pump parts. The extent of the cavitation damage can range from a relatively minor amount of pitting after years of service to catastrophic failure in a relatively short period of time.

Vapor pressure, (p_v)-Vapor pressure is the pressure required to keep a liquid in a liquid state. If the pressure applied to the surface of the liquid is not enough to keep the molecules pretty close together, the molecules will be free to separate and roam around as a gas or vapor. The vapor pressure is dependent upon the temperature of the liquid. Higher the temperature, higher will be the vapor pressure. The bubbles form inside the liquid when it vaporises i.e. phase change from liquid to vapor.

Vaporization of any liquid inside a closed container can occur if either pressure on the liquid surface decreases such that it becomes equal to or less than the liquid vapor pressure at the operating temperature, or the temperature of the liquid rises, raising the vapor pressure such that it becomes equal to or greater than the operating pressure at the liquid surface. For example, if water at room temperature (about 20^0C) is kept in a

closed container and the system pressure is reduced to its vapor pressure (about 3585 Pa (a)), the water quickly changes to a vapor. Just like in a closed container, vaporization of the liquid can occur in centrifugal pumps when the local static pressure reduces below that of the vapor pressure of the liquid at the pumping temperature.

The vaporisation accomplished by addition of heat or the reduction of static pressure without dynamic action of the liquid is excluded from the definition of cavitation. For the purposes of this article, only pressure variations that cause cavitation shall be explored. Temperature changes must be considered only when dealing with systems that introduce or remove heat from the fluid being pumped. To understand vaporization, two important points to remember are:

1. We consider only the static pressure and not the total pressure when determining if the system pressure is less than or greater than the liquid vapor pressure. The total pressure is the sum of the static pressure and dynamic pressure (due to velocity).

2. The terms pressure and head have different meanings and they should not be confused. Thus, the key concept is - vapor bubbles form due to vaporization of the liquid being pumped when the local static pressure at any point inside the pump becomes equal to or less than the vapor pressure of the liquid at the pumping temperature.

The reduction in local static pressure at any point inside the pump occur under two conditions:

1. The actual pressure drop in the external suction system is greater than that considered during design. As a result, the pressure available at pump suction is not sufficiently high enough to overcome the design pressure drop inside the pump.

2. The actual pressure drop inside the pump is greater than that considered during the pump design, mainly in the impeller blades region.

For all practical purposes, the total head at the suction flange is the static pressure head at the suction flange. Therefore the pump's external suction system should be designed such that the static pressure available at the suction flange is always positive and higher than the vapor pressure of the liquid at the pumping temperature. For no vaporization at pump suction flange:

$$p_{s2} > p_v$$
$$(h_{ps2} - h_{pv}) > 0 \qquad (1)$$

where: p_{s2} - Absolute static pressure at the suction flange; h_{ps2} - Static pressure head at the suction flange i.e. absolute pressure of the liquid at the suction flange, converted to meters of head; h_{pv}- Vapor Pressure head i.e. absolute vapor pressure.

As the liquid enters the pump, there is a further reduction in the static pressure. If the value of p_{s2} is not sufficiently higher than p_v, at some point inside the pump the static pressure can reduce to the value of p_v. In pumping terminology, the head difference term corresponding to Equation (5) is called the Net Positive Suction Head or NPSH.

Pumps are mechanisms for delivering from a state of lower static pressure to a state of higher static pressure. At the centrifugal pumps the impeller stud with blades transfers mechanical work to the liquid which is in the impeller channels. The liquid is displaced by centrifugal forces from the impeller. The increase in pressure in the impeller is a consequence of centrifugal forces and possibly also the retarded relative flow in the impeller channels. The absolute speed of the delivery medium increased at the same time and is afterwards converted in a system of static and extending channels into static pressure energy.

With the current of a liquid through the channels of a rotary impeller it is to be differentiated between absolute and relative movement. The movement of the liquid particles is called absolute, if they can be noticed by an outside of the impeller standing observer. The relative movement of the liquid particles notices an observer, who moves with the impeller. In Fig.1 speed conditions in the impeller are represented for a backwards curved blading. The current joins with the relative velocity $\vec{\omega}_1$ the blade channel. At this with "A" designated place the impeller has the peripheral speed $\vec{u}_1$. From the vectorial addition of the relative velocity $\vec{\omega}_1$ and the peripheral speed $\vec{u}_1$ the absolute speed $\vec{c}_1$ results.

With flowing through the blade channel the relative velocity generally decreases. At this with "B" designated place the fluid has the peripheral speed $\vec{u}_2$ and the relative speed $\vec{\omega}_2$. As a result, the absolute outgoing speed $\vec{c}_2$ results will be substantially larger due to the transfer of energy than $\vec{c}_1$.The transformation of the kinetic energy happens in the following guidance mechanism. Here the current with the speed $\vec{c}_2$ occurs and is retarded to the speed $\vec{c}_3$.

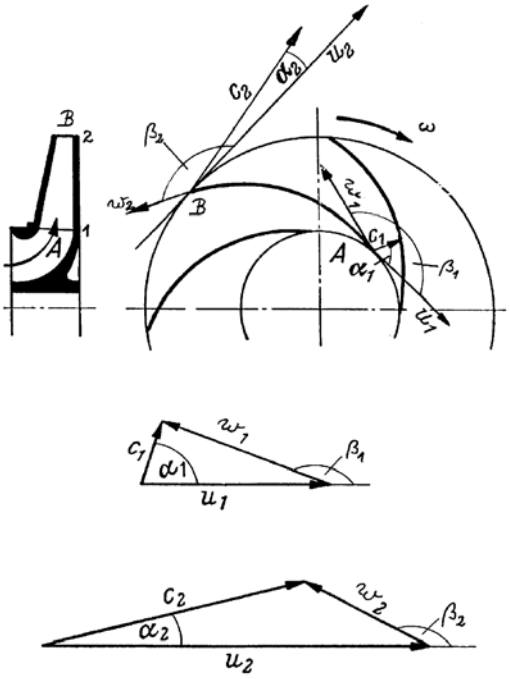

Figure 1. Speed conditions at the impeller

The work transferred in the impeller to the liquid is converted to pressure energy on the one hand by the increase of the circumferential speed from $\vec{u}_1$ to $\vec{u}_2$ and

on the other hand by the delay of the current in impeller and peeler. In order to be able to determine the compression in the impeller and in the peeler, one makes the assumption that all liquid particles follow accurately the course of the rotor blades (Blade-congruent current). Thus the flow conditions (pressure and speed) are alike in each case along concentric circles around the perpendicularly arranged wheel axle. This condition can be fulfilled by the assumption of infinitely many and infinitely thin blades. Further the transformation from speed energy in pressure energy should happen in the blade channels and the repeating-condition ($\vec{c}_3 = \vec{c}_1$) should be fulfilled. The increase in pressure from the work of centrifugal forces can be determined, if a mass particle of the pumping medium is regarded, which is limited by the lateral surfaces of two cylinders with the radii r and r+dr as well as two neighboring blades and the wheel walls of cover and wheel disk (Figure 2).

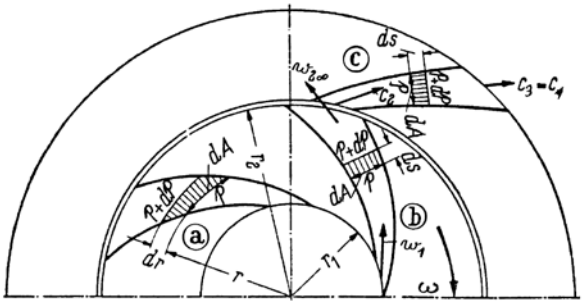

Figure 2. Compression in peeler and impeller

Thus the centrifugal force of the mass particle can be expressed as follows:

$$dF' = dAdr\rho r\omega^2 \tag{2}$$

From this follows for the increase in pressure:

$$dp = \rho r\omega^2 dr \tag{3}$$

If one names with:

$$\frac{dp}{\rho} = dY'_\infty = \omega^2 rdr \tag{4}$$

the specific flow work of centrifugal forces, then the work portion from centrifugal forces can be determined by integration along the radius.

$$Y'_\infty = \frac{1}{\rho}\int_{p1}^{p\infty} dp = \frac{p_\infty - p_1}{\rho} = \omega^2 \int_{r1}^{r2} rdr = \omega^2 \frac{r_2^2 - r_1^2}{2} = \frac{u_2^2 - u_1^2}{2} \tag{5}$$

As a result of the introduction of acceleration due to gravity the delivery head portion arises due to centrifugal forces to:

$$H'_\infty = \frac{Y'_\infty}{g} = \frac{\omega^2}{g}\int_{r1}^{r2} rdr = \omega^2 \frac{r_2^2 - r_1^2}{2g} = \frac{u_2^2 - u_1^2}{2g} \tag{6}$$

The increase in pressure from the delay of the relative velocity w can be derived by Fig. 2 from the dynamic Basic Law:

$$dF'' = -dAds\rho\frac{d\omega}{dt} \tag{7}$$

Thereby dω is negative since ω decreases with rising pressure. With ds/dt = ω and dp =dF´´/dA can be written:

$$dp = -\rho\omega d\omega \tag{8}$$

Names one this time:

$$\frac{dp}{\rho} = dY''_\infty = -\omega d\omega \tag{9}$$

the specific flow work from the delay of the relative velocity, then this work portion can be determined by integration along the entire flow channel:

$$Y''_\infty = \frac{1}{\rho}\int_{p_\infty}^{p_{p\infty}} dp = \frac{p_{p\infty} - p_\infty}{\rho} = \frac{\omega_1^2 - \omega_\infty^2}{2} \tag{10}$$

With acceleration due to gravity the delivery head results:

$$H''_\infty = \frac{\omega_1^2 - \omega_{2\infty}^2}{\rho g} = \frac{c_2^2 - c_1^2}{2g} \tag{11}$$

In simulating the flows in CFD models, the equations of mass, momentum and energy conservation has to be solved and additional transport equations should be considered when the flow is supposed to be turbulent, which is our case too.

The equation for mass conservation is:

$$\frac{\partial\rho}{\partial t} + \nabla(\rho\vec{v}) = S_m \tag{12}$$

For the inertial reference frame, the momentum conservation equation is:

$$\frac{\partial}{\partial t}(\rho\vec{v}) + \nabla(\rho\vec{v}\vec{v}) = -\nabla p + \nabla\tilde{\tau} + \rho\vec{g} + \vec{F} \tag{13}$$

where the stress tensor is given by:

$$\tilde{r} = \mu\left[\left(\nabla\vec{v} + \nabla\vec{v}^T\right) - \frac{2}{3}\nabla\vec{v}I\right] \tag{14}$$

The turbulence was modeled by using the Standard *k-ε* model. This model is a semi-empirical one being based on the transport equations for the turbulence kinetic energy and the specific dissipation rate. The model for transport equation *k* is deduced from the exact equation whilst the transport equation for *ε* was deduced by empirical rationale. It is assumed that the flow is fully turbulent and the effects of molecular viscosity are small.

The above mentioned transport equations are:

$$\frac{\partial}{\partial t}(\rho k) + \frac{\partial}{\partial x_i}(\rho k u_i) = \frac{\partial}{\partial x_j}\left[\left(\mu + \frac{\mu_t}{\sigma_k}\right)\frac{\partial k}{\partial x_j}\right] + G_k + G_b - \rho\varepsilon - Y_M$$

$$\frac{\partial}{\partial t}(\rho\varepsilon) + \frac{\partial}{\partial x_i}(\rho k u_i) = \frac{\partial}{\partial x_j}\left[\left(\mu + \frac{\mu_t}{\sigma_\varepsilon}\right)\frac{\partial\varepsilon}{\partial x_j}\right] + C_{1\varepsilon}\left(G_k + C_{3\varepsilon}G\right)_b -$$

$$- C_{2\varepsilon}\rho\frac{\varepsilon^2}{k} \tag{15}$$

The turbulent viscosity in this approach should be:

$$\mu_t = \rho C_\mu \frac{k^2}{\varepsilon}$$

2. NUMERICAL INVESTIGATION

The numerical simulation has as departure point a real pump which has the impeller blades geometry as follows:

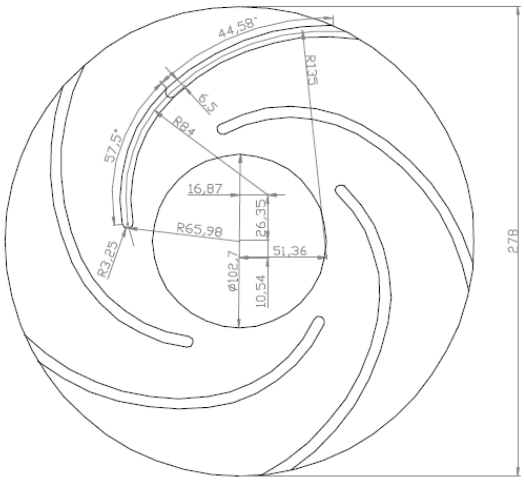

Figure 3 Impeller's blades geometry

The resulting Computer Aided Design (CAD) generated geometry is given in the Figure 4.

Nominal conditions are: rotational speed of 1500 rpm and the outlet pressure 0.4e6 Pa. The fluid considered was water with the density 998.2 kg/m^3 and constant viscosity 1.003e-3 kg/(m sec).

The inlet pressure was varied from 1500; 2000; 3585; 5000; 60000; 80000; 100000 and 300000 Pa in order to thoroughly investigate the cavitation phenomena inside the pump. The computational code used was Fluent 6.1. Only the results of the last two ranges of parameters are to be shown in this article due to space limits.

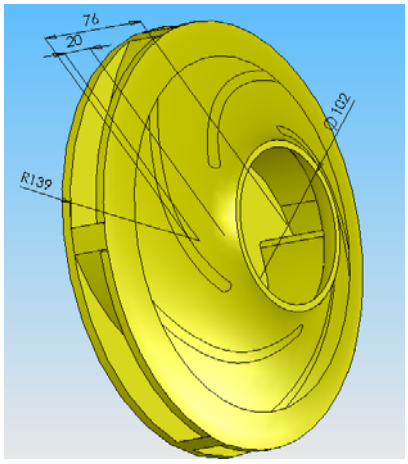

Figure 4 Impeller CAD geometry

The entire CAD model of the centrifugal pump considered in the numeric experiment is showed in the Figure below, only the impeller and the pump casing being considered:

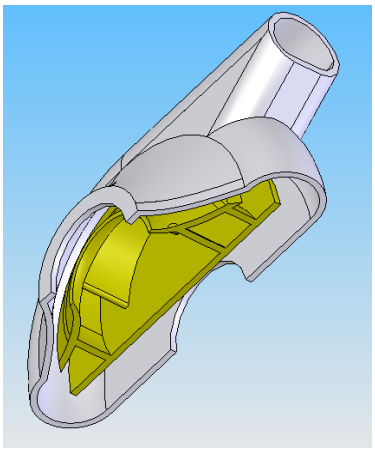

Figure 5. Centrifugal Pump CAD geometry- horizontal cutting plane

For numerical investigation of the fluid behavior inside the pump, then the fluid path is needed which, in fact, the "negative" of the pump assembly is showed above:

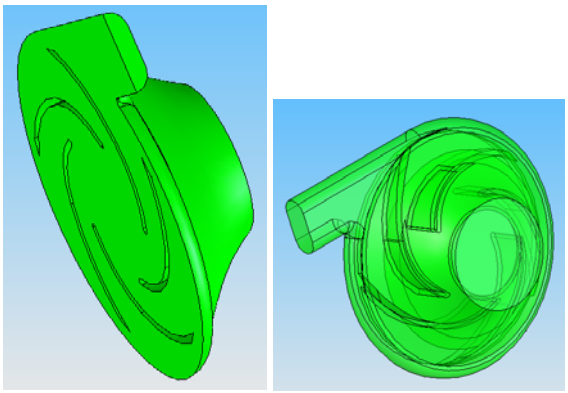

Figure 6. Centrifugal Pump "negative" fluid path CAD geometry

In order to investigate the fluid domain, 5 reference points were established as showed in the next Figure.

The first reference point is located at the suction flange of the pump, the second in the middle area of the pump, the third and fourth on the suction and pressure sides of one blade and the last to the outlet area of the pump.

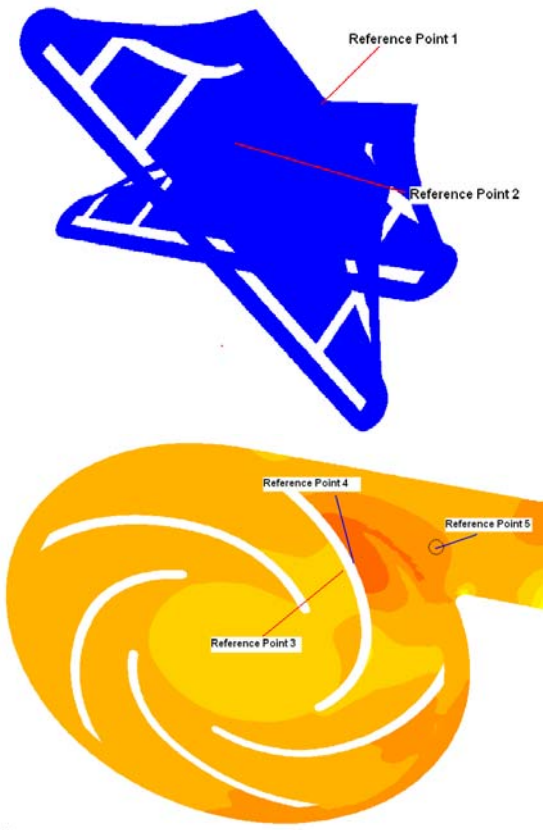

Figure 7. Reference points location

2.1 Numerical Simulation for Different Inlet Pressure

Numerical simulation for Inlet Pressure=100000 Pa.

The static pressure distribution calculated is showed in Figure 8:

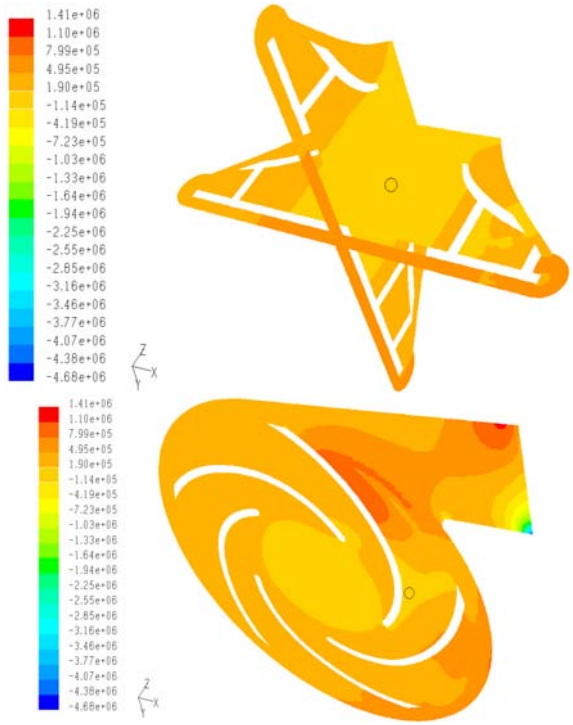

Figure 8.. Static Pressure Distribution (Pa)

In the suction area and in the central area of the pump the pressure was calculated: -79823 Pa (r) =21502 Pa (a)> 3585 Pa (a) which is the vaporization pressure. The overall functioning of the pump is improved by now but the negative relative static pressure is still a matter of concern.

The total pressure distribution calculated is showed in Figure 9:

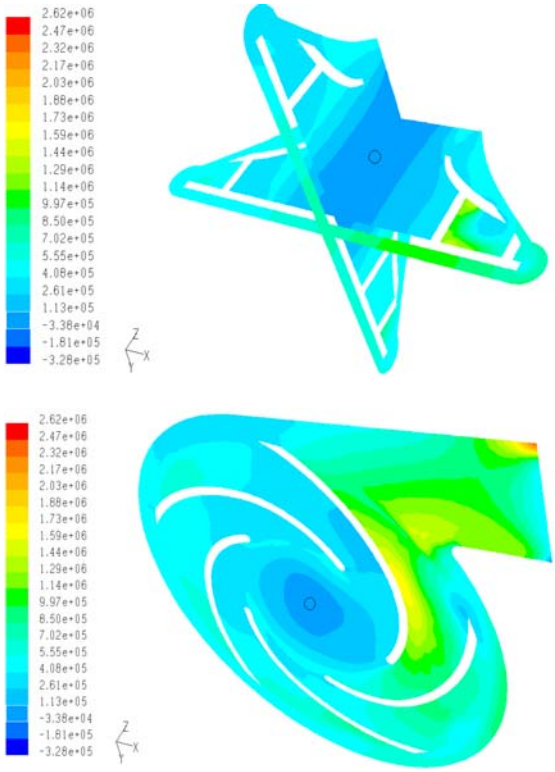

Figure 9. Total Pressure Distribution (Pa)

The minimum total pressure for this case, became negative (-33799 Pa (r)) at the inlet of the pump. Since the total pressure values in all the fluid domain is improving significantly, this is possible to occur on the expense of worsening of the inlet total pressure conditions.

The overall velocity distribution doesn't undergo massive changes, being pretty much the same to the previous studied case.

Numerical simulation for Inlet Pressure=300000 Pa.

The static pressure distribution calculated is showed in Figure 10:

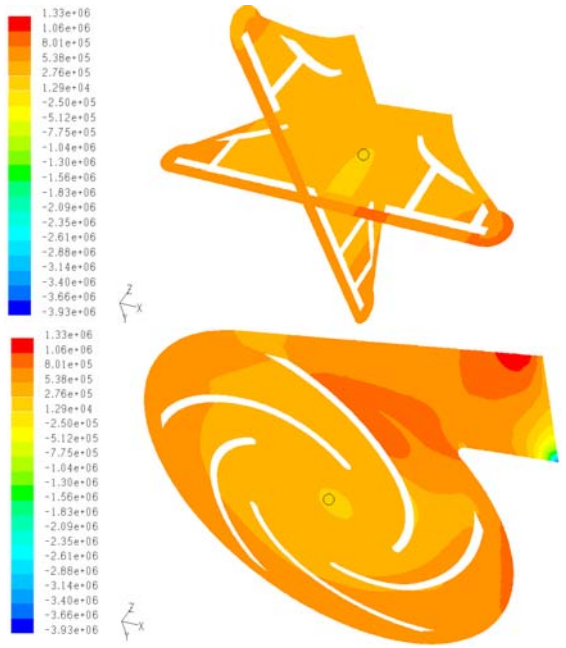

Figure 10 Static Pressure Distribution (Pa)

In the suction area and in the central area of the pump the pressure was calculated: 222814 Pa (r). The overall functioning of the pump is radically improved and the cavitation phenomena is no longer a matter of concern

The total pressure distribution calculated is showed in Figure 11:

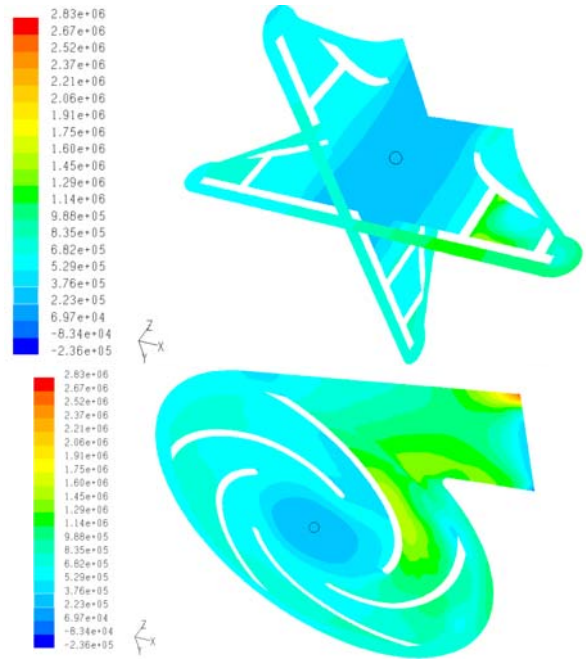

Figure 11. Total Pressure Distribution (Pa)

The minimum total pressure for this case is positive all over the domain, in the inlet area reaching values as 222814 Pa (r), which represents a certain improvement in comparison to the previous case.

The overall velocity distribution doesn't undergo massive changes, being pretty much the same to the previous studied case.

2.2 Analysis of Calculated Pressure Data on Reference Points

It is useful to draw some graphics regarding the calculated Static, Total Pressures for each of the defined reference points and for every Inlet Pressure, in order to pull some partial conclusions.

For the Reference Point 1 (Pump inlet)

The calculated pressure graphs are showed below:

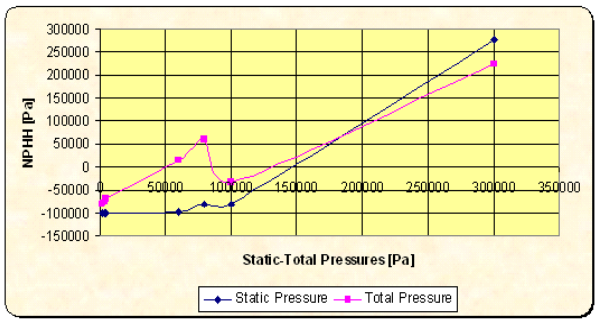

Figure 12. Static and Total Pressure Graphic-Reference Point 1

At the inlet location since at Inlet Pressure=100000…150000 Pa (r), the effect of increasing Inlet Pressure is lent and ambiguous for both pressures but after that their values start to rise steadily. The danger of cavitation in this region is present.

For the Reference Point 2 (Pump middle section)

The calculated pressure graphs are showed below:

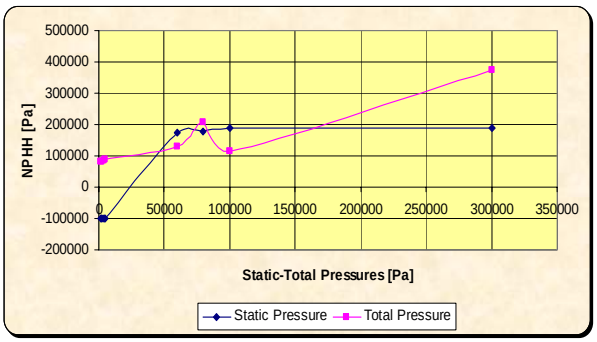

Figure 13. Static and Total Pressure Graphic-Reference Point 2

The static pressure in the middle section of the pump model is sharply rising in the Inlet Pressure range 1500….60000 Pa, and after that it will have an almost constant value. The total pressure will have the same ambiguous behavior in Inlet Pressure domain 60000…100000 Pa. The danger of cavitation in this region is present.

For the Reference Point 3 (Impeller back side of the most affected blade)

The calculated pressure graphs are showed below:

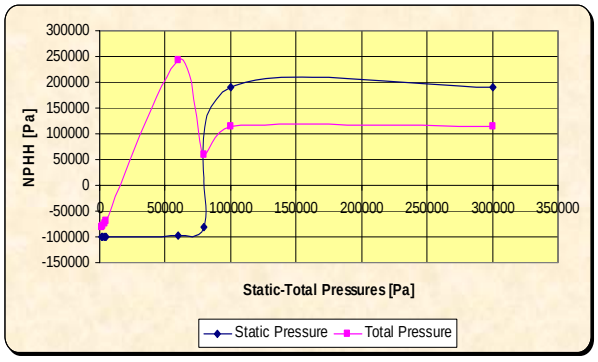

Figure 14. Static and Total Pressure Graphic- Reference Point 3

The total pressure is having a more accentuated ambiguous evolution in the Inlet Pressure domain 60000…100000 Pa; the static pressure sharply increasing in the same Inlet Pressure domain to positive values and remains constant. The danger of cavitation in this region is present.

For the Reference Point 4 (Impeller front side of the most affected blade)

The calculated pressure graphs are showed below:

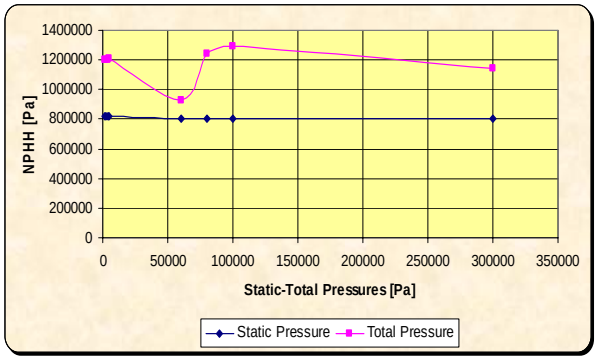

Figure 15 Static and Total Pressure Graphic- Reference Point 4

The total pressure is having an more accentuated ambiguous evolution in the Inlet Pressure domain 60000…100000 Pa; the static pressure remains constant all over Inlet Pressure domain to positive values, its shape being almost flat. The danger of cavitation in this region is not present

For the Reference Point 5 (Pump exit)

The calculated pressure graphs are showed below:

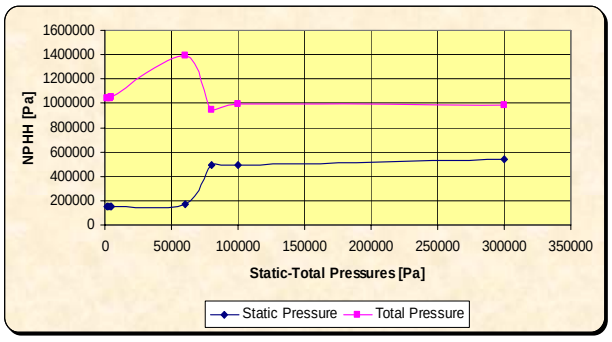

Figure 16. Static and Total Pressure Graphic- Reference Point 5

The total pressure is having a more accentuated ambiguous evolution in the Inlet Pressure domain 60000…100000 Pa; the static pressure remains constant all over Inlet Pressure domain to positive values. The danger of cavitation in this region is not present.

3. CONCLUSIONS

Numerical and experimental results were presented in this study, concerning a test impeller of a centrifugal pump. From the experimental point of view, the cavitation was visualized at different inlet pressure values. Image processing and statistical treatment of the photographs taken at given impeller position allowed to quantify the attached and cloud cavitation extent.

A numerical model of 3D cavitating flows, based on the CFD code Fluent 6.1, has been developed to predict the cavitation behavior in our model which is considering the entire pump, the impeller and also the casing of the pump, with all its complex geometry and flow parameters. Non-cavitating and cavitating conditions were investigated. Calculations were found to be in good agreement with experimental measurements and visualisations. Experimental and numerical results concerning the pump parameters were investigated. The results obtained show the ability of the model to simulate the main features of 3D cavitating flows in rotating machinery.

The overall conclusion is the obvious knowledge that the NPSH is indeed affecting the cavitation condition in the centrifugal pumps, having direct impact on the magnitude of static pressures in various locations inside the pump, but is not altering too much the velocities distributions of fluid.

The rich palette of results shown below is thoroughly investigating the flow parameters of the model.

4. REFERENCES

[1] ABBASS, H.A., *The Self-Adaptive Pareto Differential Evolution Algorithm.* In Congress on Evolutionary Computation (CEC'2002), volume 1, pages 831–836, Piscataway, New Jersey, May 2002. IEEE Service Center

[2] ARNOLD, D.V. and BEYER, H.G., *Noisy optimization with evolution strategies. Ci-report 117/01,* University of Dortmund, Germany, 2001

[3] ARNOLD, D.V. and BEYER, H.G., *A comparison of evolution strategies with other direct search methods in the presence of noise.* Computational Optimization and Applications, 24(1):135–159, 2003
[4] ARNOLD, D.V. and BEYER, H.G., *Investigation of the (μ, λ) -es in the presence of noise.* In Proceedings of the CEC'01 Conference, Piscataway, New York.
[5] BÄCK, T., FOGEL, D. B. and MICHALEWICZ, Z., *Handbook of Evolutionary Computation, Sec. C7.1: pp. 1-15*, 1997., pages 267–272, 1996.

NUMERICAL INVESTIGATION OF SWIRL INJECTOR LOX/GH_2 RATIO INFLUENCE OVER COMBUSTION CONDITIONS INTO A LIQUID ROCKET ENGINE

[1]CALIMANESCU IOAN, [2]GRIGORESCU LUCIAN

[1]Saipem SpA Italy,[2]Constanta Maritime University, Romania

ABSTRACT

Swirl injectors are widely used in liquid rocket engines, gas turbine engines, diesel engines, industrial furnaces and so forth. Even though design procedure of a swirl injector is more difficult than that of an impinging jet injector, swirl injectors have many advantages, such as atomization quality, wide operation range with stability and uniform mixing efficiency. Spraying mechanism of a swirl injector is that liquid sheet is injected with the tangential velocity due to tangential entries, so liquid sheet is discharged with specific spray angle which corresponds to the ratio of axial and tangential velocity and the air core is formed. The mixture ratio of Liquid O_2 and Fuel (H_2) for such type of injectors may be throttled from 2:1, which is the upper limit for functioning for current Liquid Rocket Engines (LRE) impinging jet axial injectors, up to 10:1. This paperwork intend to numerically investigate the impact of swirl injector LOX/GH_2 ratio over combustion conditions into a LRE using state of the art numeric simulation technologies. The outcome of this work is to completely define the relation between LOX/GH_2 ratio and the combustion conditions inside the rocket engine.

Keywords: *Numeric, Swirl Injector, Ratio, Rocket, Engine, Combustion.*

1. INTRODUCTION

A liquid rocket engine employs liquid propellants which are fed under pressure from tanks into a combustion chamber. The propellants usually consist of a liquid oxidizer and a liquid fuel. In the combustion chamber the propellants chemically react (burn) to form hot gases which are then accelerated and ejected at high velocity through a nozzle, thereby imparting momentum to the engine. Momentum is the product of mass and velocity. The thrust force of a rocket motor is the reaction experienced by the motor structure due to the ejection of the high velocity matter. A typical rocket motor consists of the combustion chamber, the nozzle, and the injector, as shown in Figure 1. The combustion chamber is where the burning of propellants takes place at high pressure. The chamber must be strong enough to contain the high pressure generated by, and the high temperature resulting from, the combustion process. Because of the high temperature and heat transfer, the chamber and nozzle are usually cooled. The chamber must also be of sufficient length to ensure complete combustion before the gases enter the nozzle. The function of the nozzle is to convert the chemical-thermal energy generated in the combustion chamber into kinetic energy. The nozzle converts the slow moving, high pressure, high temperature gas in the combustion chamber into high velocity gas of lower pressure and temperature. Since thrust is the product of mass (the amount of gas flowing through the nozzle) and velocity, a very high gas velocity is desirable.

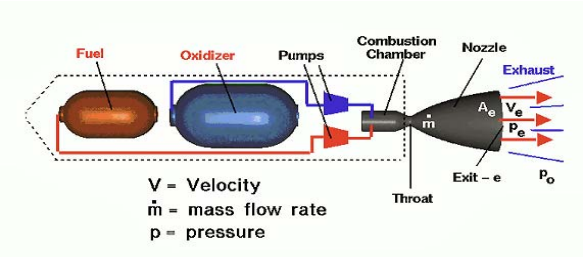

Figure 1 Liquid Rocket Engine

With the advent of oxygen (LOX)-hydrogen (GH2) as the bipropellant of choice, very high densities were achieved through high pressures and very low temperatures. Thanks to these low temperatures, usually around 10^0 K, the term cryogenic is often used to describe engine and the propellants, although they do not necessarily satisfy the National Institute Standards and Technology exact limit of 93.15^0 K for cryogenic regime. These high densities could mean a reduced storage volume for the propellants. Since LOX-GH2 systems mostly used in the Earth atmosphere, the drag reduction due to smaller tanks could been significant. However, basic analysis of the launch vehicle design reveals that it is beneficial to use low-pressure, lightweight but voluminous tanks for turbo-pump feed systems than high-pressure, heavy tanks.

A typical modern liquid rocket engine designed for space launch consists of tens of components, from the tanks to the feeding lines, from the turbo-pumps to the exhaust and pressurization systems, from the regenerative cooling system to the gas turbines, from the exhaust nozzle to the combustion chamber. In the case of a staged-combustion cycle, the propellants first go through a gas generator where the fuel-to-oxidizer ratio is far from stoichiometry. This usually leads to the injection of supercritical gaseous propellants in the chamber with very different mixing and combustion

characteristics compared to the other four main rocket cycles (gas generator, combustion tap-off, expander, coolant bleed). For the other engine cycles, the likeliest scenario is that the hydrogen enters the chamber in a supercritical gaseous state after having cooled the chamber walls while the oxygen is injected straight from the turbo-pump in a compressible liquid state. The most common solution to mix the two propellants is the shear coaxial injector because of its technological simplicity. A typical large liquid rocket engine will have an injector plate made of hundreds of single injection elements and thus the simplicity and reliability of each component is crucial. Also, shear coaxial injectors are naturally characterized by good chamber compatibility and good combustion stability. However, as the dynamics of the swirl coaxial injectors are better understood, such technology is gaining in popularity because of its potential higher performance.

In fact, they combine the benefits of two families of injectors, the pressure swirl atomizers and the air-blast atomizers. Thus, they are especially effective for liquid-liquid injection. For example, they are part of the original design of the Japanese engines H2-A and H2-B but are also in use in the current version of the RL-10 engine by Pratt & Whitney Rocketdyne as well as in several Russian engines.

After injection, the combustion chamber remains cylindrical for as long as it is necessary to get complete combustion and thus convert the maximum chemical energy of the reactants. Once this is achieved, a convergent-divergent nozzle accelerates the flow to achieve the best combination of specific impulse and thrust. The main constraints for the design of the nozzle are: Generate a uniform axial flow at the nozzle exit to prevent divergence losses; Prevent boundary layer separations; Remain as short as possible to reduce weight. These constraints are critical for the engine performance and represent unique fields of research.

2. NUMERICAL INVESTIGATION

2.1 CAD Geometry and the Numerical Scenario

The strategy for obtaining the Oxygen, Hydrogen and the Combustion Chamber flow-paths consisted in two CAD steps: the first was to obtain the CAD geometry of the Swirl injector assembly and further on, to obtain the “negative” of CAD geometry in order to have at the end the flow-paths inside the Injector corresponding to the Fluid/Combustion Computational domain.

The CAD geometry of the Injector along with the main dimensions is given in the Figure below:

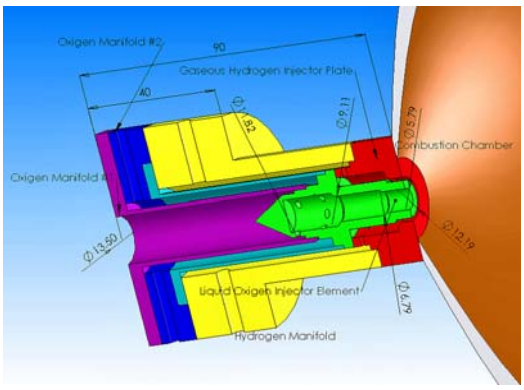

Figure 2 Section within the Swirl Injector Assembly

The main dimensions [mm] for the injections regions of Oxygen and Hydrogen are given in the figures below:

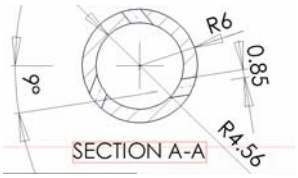

Figure 3 Section thru the Main Oxygen Injection Element

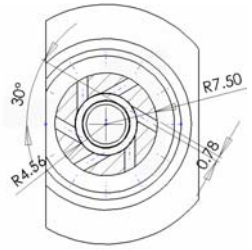

Figure 4 Section thru the Secondary Oxygen Injection Element

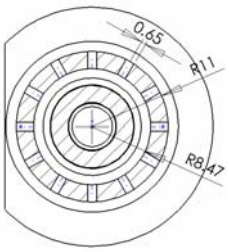

Figure 5 Section thru the Hydrogen Injection Plate

By manipulating the Injector Assembly CAD geometry, it was eventually possible to compose the “negative” flow paths of Oxygen, Hydrogen and a portion of Combustion Chamber, as seen below:

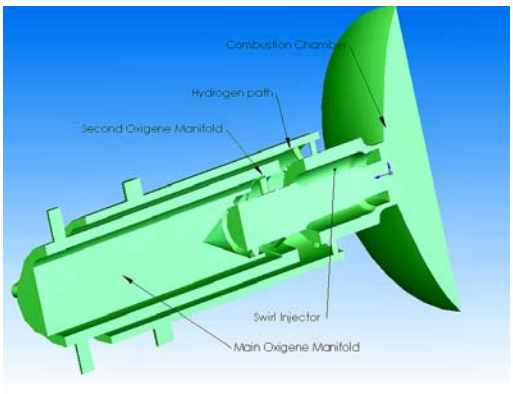

Figure 6 "Negative" Geometry of Flow Paths-Computational domain

The so obtained model was further submitted to the software Fluent for numerical simulation and post-processing. The materials used for simulation were, obviously, GH2 as fuel and LOX as oxidant, with all their known physical and chemical properties and following the reaction mechanisms also well known.
Since the main oxygen manifold has only one inlet hole and the secondary oxygen and hydrogen manifolds have 4 holes, the calculated inlet mass flows taking into account the holes areas, are given in Table 1. For every oxygen/fuel ratios, a separate numerical simulation was conceived.

Table 1 Mass Flows for Fuel and Oxidant for considered Ratios

Inlet Manifolds Mass Flows	LOX/GH2 Ratio				
	2:1	3:1	4:1	5:1	6:1
Inlet LOX Mass Flow [kg/sec]	Main Manifold (1 Inlet Hole)=0.254 Secondary Manifold (4 Inlet Holes)=4x0.11				
Inlet GH_2 Mass Flow [kg/sec]	4 Inlet Holes =4x 0.055	4 Inlet Holes =4x 0.0375	4 Inlet Holes =4x 0.02825	4 Inlet Holes =4x 0.0225	4 Inlet Holes =4x 0.01875

The proper boundary conditions were defined as to simulate as closely as possible the real functioning cases. The inlet boundary conditions were set as per the Table 1 and the outlet supposed the combustion chamber is open to the normal environment with 23% O_2 concentration and atmospheric pressure. The combustion chamber pressure may be increased to simulate the effect of nozzle and/or to model the nozzle itself, but such a model with multiple injectors and nozzle require a huge computational effort beyond our possibilities. The walls were simulated as adiabatic, with no exchange of heat and matter with the environment.

2.2 Fluid Pressure Evolution inside the Injector-Combustion Chamber Domain for Each Simulation Scenario

For each scenario defined in Table 1 a numeric simulation was conducted. One axial and four transversal sections were considered to be of interest in the injector domain, as seen in the figures. The transversal sections correspond to the O2 and H2 injection areas and the last at the border region between injector and combustion chamber (injector exit area). The fluid total pressure distribution [Pa] inside the domain for each case is shown below.

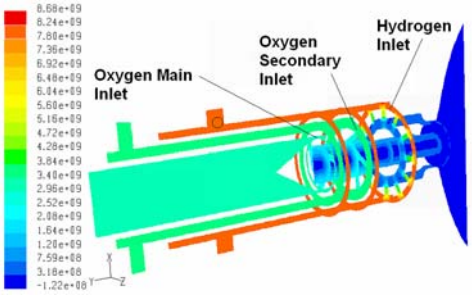

Figure 7 Pressure distribution for 2:1 Ratio

The pressure in 2:1 case will drop from the inlet regions toward the outlet of the combustion chamber. It may be seen that the pressure in the inlet H_2 flow path is higher that the pressure of O_2 inlet flow path.
Since the inlet H_2 flow is decreasing, the pressure in the H_2 flow path is decreasing as well for simulation with 3:1 ratio.

For ratio 4:1, the pressure in the H_2 inlet system continues to drop under the values registered in the O_2 system. The same fact is registered for the ratios 5:1 and 6:1 given in Figures 10 and 11.

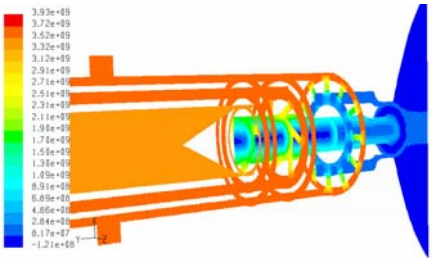

Figure 8 Pressure distribution for 3:1 Ratio

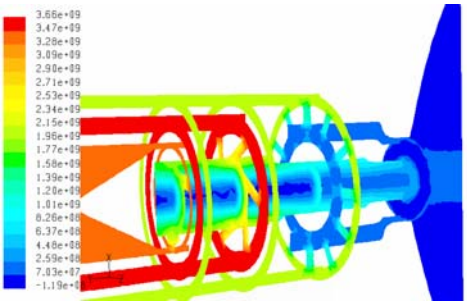

Figure 9 Pressure distribution for 4:1 Ratio

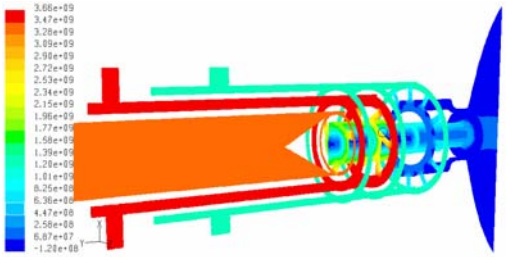

Figure 10 Pressure distribution for 5:1 Ratio

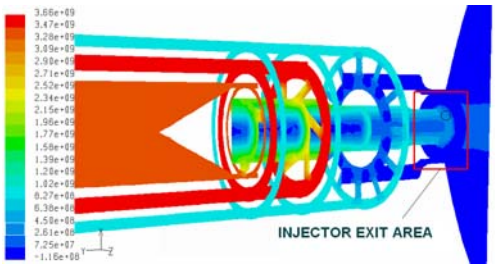

Figure 11 Pressure distribution for 6:1 Ratio

The most critical area in our point of view is the injector exit area which is placed at the border between the injector and combustion chamber, as shown in Figure 11 above. Here would be interesting to trace the maximum registered pressures evolution in time.

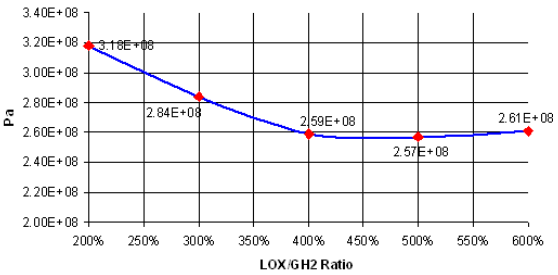

Figure 12 Pressure evolution in the injector exit area

The burned gases pressure is slowly decreasing from 3.18e8 Pa for the Ratio 2:1 to 2.61e8 Pa for Ratio 6:1, with a nearly constant value between Ratio 4:1 to 6:1. This behavior is due to the decreased quantity of fuel which reaches the reaction zone.

2.3 Fluid Velocity Evolution inside the Injector-Combustion Chamber Domain for Each Simulation Scenario

Since the overall efficiency of the Rocket Engine is highly dependant of the Velocity of burned gases ejected out of the combustion chamber, the variation of it versus oxidant/fuel ratio will be a good indicator and tool for the Designer to choose the best functioning parameters.

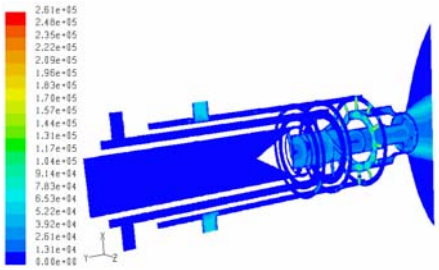

Figure 13 Velocity distribution for 2:1 Ratio

Due to the high pressure existing in the H_2 inlet system, the highest velocities are registered in this domain, for instance the velocity of fuel at the inlet manifold reaches values of 52,202 m/sec. and the top velocity will be registered in the H_2 injection plate holes with values near 247,962 m/sec. In the oxidizer system the top velocity is 39,151 m/sec calculated in the Secondary Oxygen Path Injection Element exit. In the combustion chamber the maximum velocities of burned gases reaches values of 52,202 m/sec in the reaction/flame cone and 13,050 m/sec in the core of it.

In order to have an idea over the velocity vector direction in oxygen injection elements, the figure below is given, the swirl effect induced by these elements holes position being obvious. Also the swirl effect is visible for the oxygen exiting the injector.

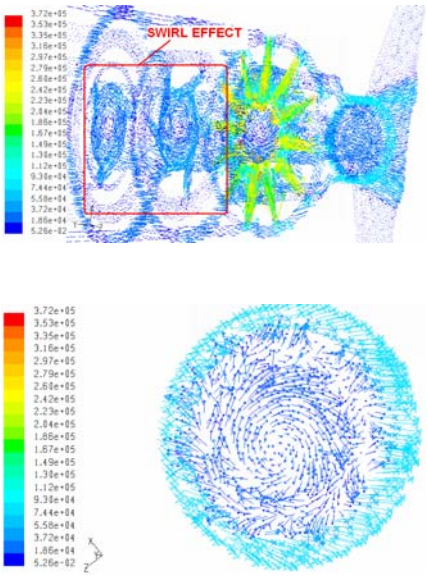

Figure 14 Velocity vector direction at O_2 inlet and detail for injector exit area (2:1 Ratio)-Swirl effect

For the rest of simulations the results are depicted in the figures below.

The maximum values of velocity inside the entire computational domain are slowly decreasing, the distribution remaining almost the same.

For the injector exit area, the graph of maximum velocity versus oxidizer/fuel ratio is given in Figure 19.

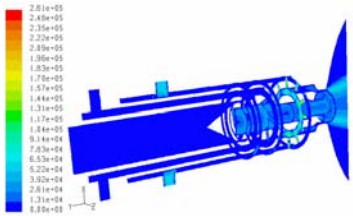

Figure 15 Velocity distribution for 3:1 Ratio

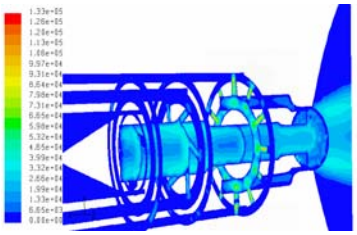

Figure 16 Velocity distribution for 4:1 Ratio

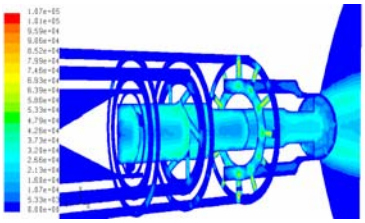

Figure 17 Velocity distribution for 5:1 Ratio

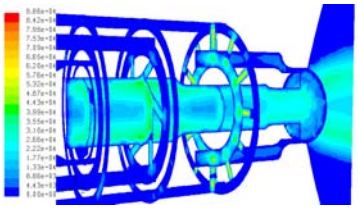

Figure18 Velocity distribution for 6:1 Ratio

By studying the graph given in Figure 19, the same conclusion is to be pulled, that between ratios 2:1 and 4:1 the efficiency of the LRE is more abruptly decreasing than between 4:1 and 6:1 ratios. The common sense conclusion seems to be true: Less fuel, less power.

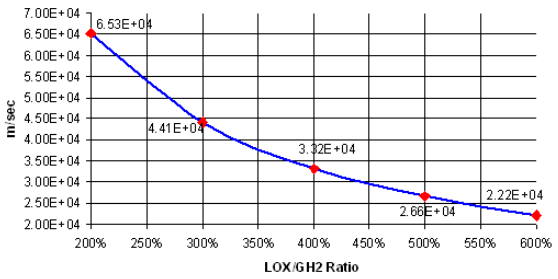

Figure 19 Maximum velocity evolution in the injector exit area

2.4 Fluid Temperature Evolution inside the Injector-Combustion Chamber Domain for Each Simulation Scenario

Temperature in the combustion process plays a key role in overall behavior of the injector in function. Since the main parameters as pressure and gas velocities are decreasing from 2:1 to 6:1 ratio, the same behavior is expected from temperatures calculated for each scenario. The combustion reaction taking place only into the combustion chamber, this region will be at interest in investigating the calculated data.

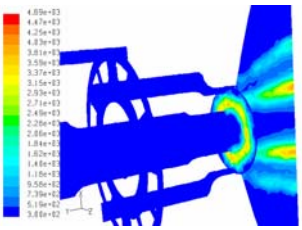

Figure 20 Temperatures distribution for 2:1 Ratio

It may be seen on the figure above that there are regions at the injector exit area and near the outlet area where a temperature of 3811^0 K is achievable. This temperature will decrease function of the decreased amount of fuel delivered into the system, as seen in the figures below.

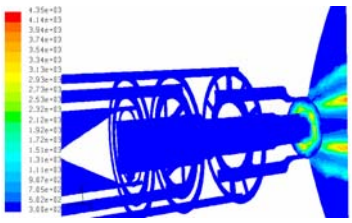

Figure 21 Temperatures distribution for 3:1 Ratio

By analyzing the graph given in Figure 25, once again begin obvious that the main parameters of combustion process in a swirl injector is heavily affected by the oxidizer/fuel ratio between 2:1 to 4:1, after that the ratio variation having a slight to no effect over these parameters.

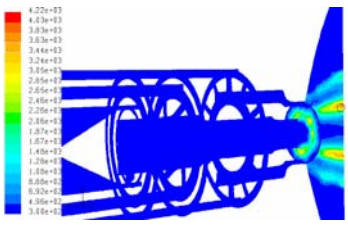

Figure 22 Temperatures distribution for 4:1 Ratio

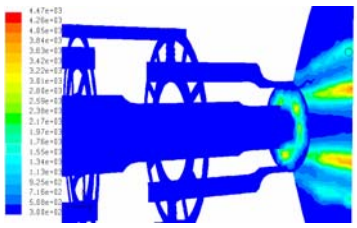

Figure 23 Temperatures distribution for 5:1 Ratio

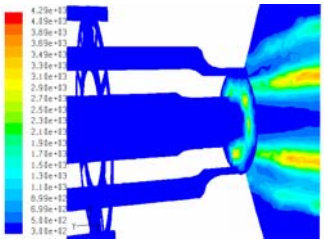

Figure24.Temperatures distribution for 6:1 Ratio

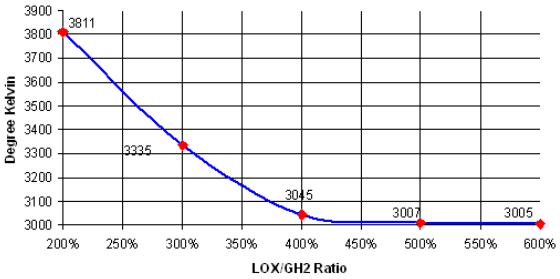

Figure 25 Maximum temperature evolution in the injector exit area

2.5 Fluid Turbulence Intensity Evolution inside the Injector-Combustion Chamber Domain for Some Simulation Scenarios

The Turbulence Intensity evolution in the injector exit area will give us a pretty clear idea on the combustion reaction rate in this zone.

The most turbulent zones for 2:1 ratio model, is in H2 injection element area reaching values of 4,751,395%. In the combustion zone its value reaches 1.5e6 %, at the injector exit area.

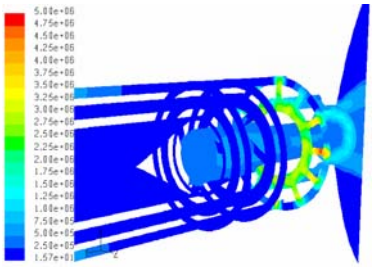

Figure 26 Turbulence Intensity distribution for 2:1 Ratio

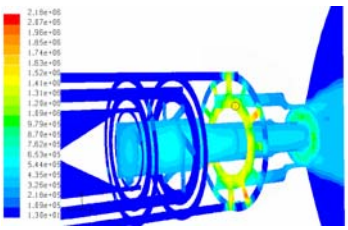

Figure 27 Turbulence Intensity distribution for 4:1 Ratio

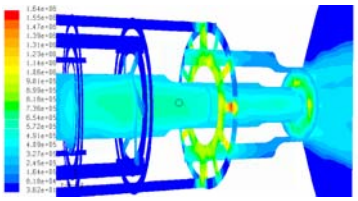

Figure 28 Turbulence Intensity distribution for 6:1 Ratio

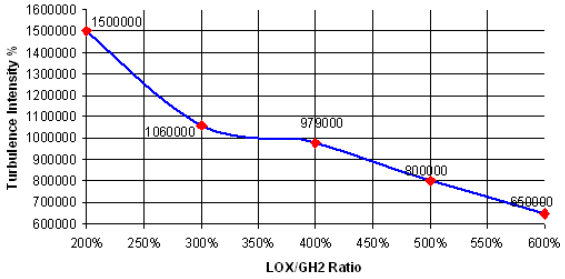

Figure 29 Maximum Turbulence Intensity evolution in the injector exit area

2.6 Reaction Rate Evolution inside the Combustion Chamber Domain for Each Simulation Scenario

Since in our models there is a close link between turbulence and the reaction rate, is to be expected that the reaction rate in the considered zone to follow the same evolution as turbulence does.

The reaction rate is specific to the combustion chamber and injector exit area where the reactants come in contact and start reacting. The reaction zone has a conical shape with a peak value of 30,720 kmol/(m^3sec), for ratio 2:1. The reaction rate then will decrease as peak value, but in the injector exit area, due to the diminishing values of reactants velocities and pressures, the reaction rate will be increased in relative terms (Figure 35).

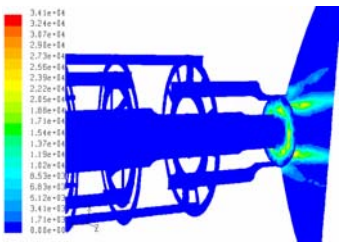

Figure 30 Reaction Rate distribution for 2:1 Ratio

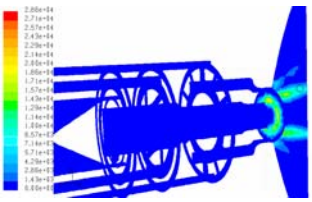

Figure 31 Reaction Rate distribution for 3:1 Ratio

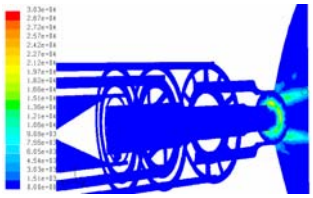

Figure 32 Reaction Rate distribution for 4:1 Ratio

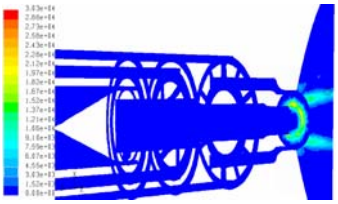

Figure 33 Reaction Rate distribution for 5:1 Ratio

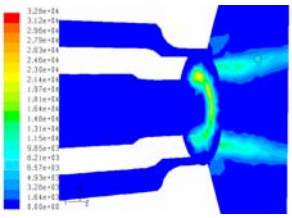

Figure 34 Reaction Rate distribution for 6:1 Ratio

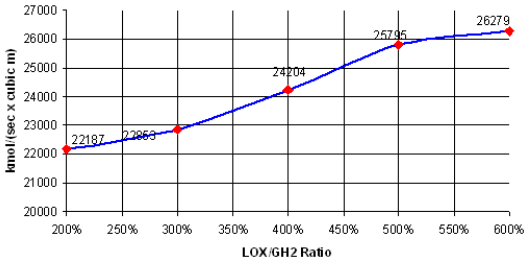

Figure 35 Reaction Rate evolution in the injector exit area

3. CONCLUSIONS

The numeric model provides consistent and reasonable results for swirl injector combustion process analysis. Its results are comparable with other approaches but the combustion process is complex and must be evaluated on a case-by-case basis.

Compared with other combustion models, Fluent provides much more information such as pressures, velocities, temperatures, enthalpies, entropies, discreet properties, reaction species distributions in the computational domain, which are very helpful for better understanding this kind of phenomena.

The results obtained from the finite element simulation, may be used for the assessment of swirl injectors for LRE behavior under several defined geometric/functional scenarios, for the relative comparison of dimensional arrangements, and for the validation of analytical/experimental techniques for modeling the combustion.

Based on the results obtained in the present work, the following main conclusions can be drawn:

• The first and the most obvious conclusion is that all the combustion parameters are worsening with oxidizer/fuel ratio increase. This is due to the decreasing of fuel quantity reaching the reaction zone which is leading to sensible decreasing in all combustion parameters as burned gasses pressures, velocities, ejected mass fractions. Finally these decreased parameters will worsen the rocket efficiency.

• The second conclusion is a little bit surprising. It was shown that between the ratios 4:1 and 6:1, almost ALL the combustion parameters showed a constant behavior. As a common sense further deduction, the combustion will be the same no matter the quantity of fuel injected into in combustion zone, meaning that with 4:1 ratio the efficiency of combustion process is the same to that of 6:1 ratio. In this functioning region the combustion parameters are almost the same even if the fuel injected in combustion zone is with 50% lesser.

In order demonstrate further the second conclusion, it was shown that the overall LRE efficiency depends heavily on the velocity of combustion gasses. By taking as reference the same injector exit area, and by considering all the values of all computational cells in this domain, the below graphs were obtained for velocities.

By studying the velocities distribution on the injector exit area, it is obvious that for the ratios 2:1 and 3:1 the average velocity is near 2e4 m/sec whereas for the ratios from 4:1 to 6:1, the average is 1.5e4 m/sec.

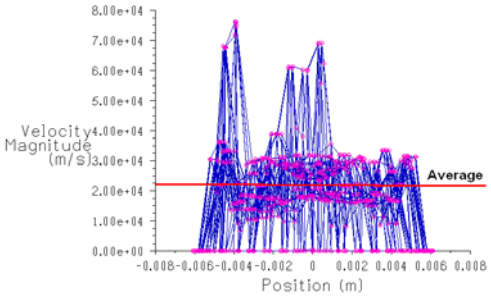

Figure 36 Fluid Velocities in the injector exit area for Ratio 2:1

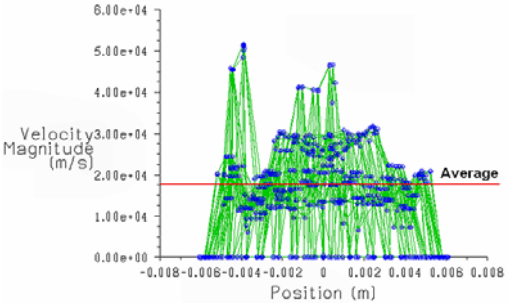

Figure 37 Fluid Velocities in the injector exit area for Ratio 3:1

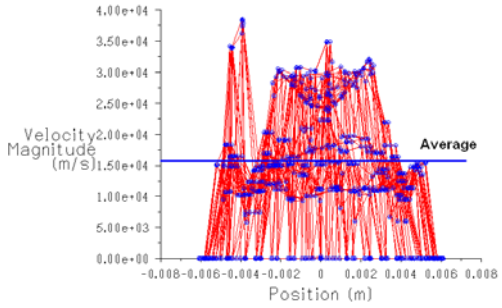

Figure 38 Fluid Velocities in the injector exit area for Ratio 4:1

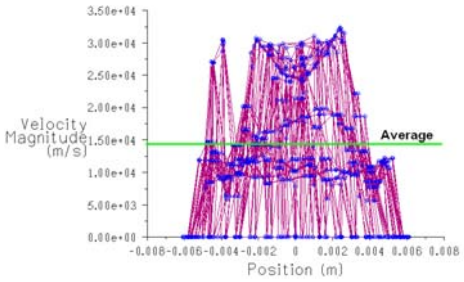

Figure 39 Fluid Velocities in the injector exit area for Ratio5:1

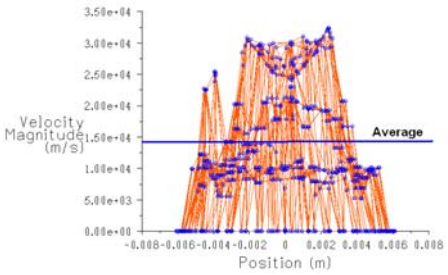

Figure 40 Fluid Velocities in the injector exit area for Ratio6:1

Dedication

This paperwork is dedicated to the memory of my late father, Engineer Ion Calimanescu.

4. REFERENCES

[1] SANTORO, R.J., *Demonstration of LOX/GH z Throttleable Injector Studies, Final Report, Propulsion Engineering Research Center*, The Pennsylvania State University, 2002

[2] DOUMAS, M. AND LASTER R., *Liquid-Film Properties for Centrifugal Spray Nozzles*, Chemical Enclineerinq Pro,qress, Vol. 49, No. 10, pp. 519-526, October 1953

[3] BAZAROV, V. G., *Hydraulics of Swirl Propellant Injectors*, Proceedings of the 9 th Annual PERC Symposium on Propulsion, Cleveland, OH, pp. 253-261, October 1-2, 1997

[4] KULAGIN, L. V. and OKHOTNIKOV, S. S., *Theory Of The Calculation of Single-Stage Centrifugal Atomizers*, Combustion of Heavy Liquid Fuels, Translated by Foreign Technology Division, Air Force Systems Command, FTD-HT-23-927-68, pp. 162-180, 1967

[5] BAZAROV V.G., *"Throttleable Liquid Propellant Engines Swirl Injectors for Deep Smooth Thrust Variations,"* AIAA 94-2978, AIAA/SAE/ASME/ASEE 30t" Joint Propulsion Conference, Indianapolis, IN, June 27-29, 1994

[6] LIMERICK, C. D., *Component Design Concerns For Deep Throttling H2/O2 Rocket Engines*, AIAA-91-2209-CP

[7] TAYLOR, G.I. , *The mechanics of swirl atomizers, 7th International Congress of Applied Mechanics*, vol. 2, 1948, pp. 280–285

[8] TAYLOR, G.I., *The boundary layer in the converging nozzle of a swirl injector*, Q.J. Mech. Appl. Math. 3 (1950) 129–139

[9]. REN, W.M, SHEN, J., NALLY J.F. JR., *Geometrical Effects Flow Characteristics of a Gasoline High Pressure Swirl Injector*, SAE 971641, 1997

[10] REN, W.M, NALLY J.F. JR., *Computations of Hollow-Cone Sprays from a Pressure-Swirl Injector*, SAE 982610, 1998

[11] J. COUSIN, W.M. REN, J.F. NALLY JR., *Transient Flows in High Pressure Swirl Injector*, SAE 980499, 1998

[12] Y. CHEN, S.D. HEISTER, *Modeling hydrodynamic non-equilibrium in bubbly and cavitating flows*, J. Fluids Eng. 118 (1995) 172–178

[13] D.P. SCHMIDT, C.J. RUTLAND, M.L. CORRADINI, *A fully compressible two-dimensional model of high speed cavitating nozzle, Atomiz.* Sprays 9 (3) (1999) 255–276

[14] R.F. KUNZ, D.A. BOGER, D.R. STINEBRING, T.S. CHYCZEWSKI, H.J. GIBELING, T.R. GOVINDAN, *Multi-phase CFD Analysis of Natural and Ventilated Cavitation About Submerged Bodies*, FEDSM99- 7364, 1999.

[15] R.F. KUNZ, D.A. BOGER, D.R. STINEBRING, T.S. CHYCZEWSKI, H.J. GIBELING, S. VENKATESWARAN, T.R. GOVINDAN, *A preconditioned Navier–Stokes method for two-phase flows with application to cavitation prediction, Comput. Fluids* 29 (8) (2000) 849–875.

[16] A. ALAJBEGOVIC, H.A. GROGGER, H. PHILIPP, *Calculation of Transient Cavitation in Nozzle Using the Two-Fluid Model*, ILASS-99 Conference Proceedings, 1999

[17] D.A. DREW, S.L. PASSMAN, *Theory of Multicomponent Fluids*, Springer, New York, 1998.

[18] R.T. LAHEY JR., D.A. DREW, *An Analysis of Two-Phase Flow and Heat Transfer Using a Multidimensional, Multi-Field, Two-Fluid Computational Fluid Dynamics (CFD) Model*, Japan/US Seminar on Two-Phase Flow Dynamics, Santa Barbara, California, 2000

[19] R.F. KUNZ, B.W. SIEBERT, W.K. COPE, N.F. FOSTER, S.P. ANTAL, S.M. ETTORE, *A coupled phasic exchange algorithm for multidimensional four-field analysis of heated flows with mass transfer*, Comput. Fluids 27 (7) (1998) 741–768.

EXPLICIT DYNAMIC SIMULATION OF A SHIP COLLISION WITH A JETTY WALL

[1]CALIMANESCU IOAN, [2]GRIGORESCU LUCIAN

[1]Saipem SpA Italy, [2]Constanta Maritime University, Romania

ABSTRACT

The International Maritime Organization (IMO) is responsible for regulating the design of oil tankers and other ships to provide for ship safety and environmental protection. Their ongoing transition to probabilistic performance-based standards requires the ability to predict the environmental performance and safety of specific ship designs. This is a difficult problem requiring the application of fundamental engineering principles and risk analysis. The serious consequence of ship collisions necessitates the development of regulations and requirements for the subdivision and structural design of ships so that damage and environmental pollution is reduced, and safety is improved. After a collision oil or other harmful substances may be spilled into the sea. It might even be possible for a ship to break apart and sink in a worst case scenario that includes failure of the structure of the ship. A numerical crash test was carried out in order to determine the aftermaths of a ship-jetty wall collision and to give hints to improve different ship structures. In combination with statistical data and determination of probabilities of the occurrence of different scenarios, safety assessment analysis can be carried out by certification agencies and administrative authorities. This paperwork develops a complete methodology for ship-to-jetty collision simulations using the explicit non-linear FE code ANSYS-LS-DYNA. The model was conceived in the explicit dynamics frame of work, the obtained results fully describing the complex phenomena associated with such catastrophic events.

Keywords: *FEA, Explicit Dynamics, Simulation, Ship, Collision, Jetty.*

1. INTRODUCTION

Ship and submarine structures have long been studied thanks to finite element methods. Their large dimension and complexity, the coupling with heavy fluid and the presence of a free surface rise many difficulties to the numerical problems on the field of dynamic analysis. This is particularly true for extreme or accidental situations such as collision and grounding, explosion and severe fluid impacts. This paper will present an application using the explicit ANSYS-LS-DYNA code, with emphasis on specific aspects and difficulties.

The continuous increase of maritime traffic makes the risk of collisions greater and several incidents have been reported during the last few years. Research work has been done for tanker , container and other ship types collisions; this paper describes numerical methods and tools developed in ANSYS-LS-DYNA and used in the simulation of ship-jetty collisions, with a focus on the outer collision dynamics, i.e. global motion of the impacted structure.

2. NUMERICAL INVESTIGATION

This section presents the development of collision simulations for bows striking a jetty rigid wall. The bow geometrical model is developed using Solid-Works software and then exported and analyzed using ANSYS-LSDYNA.

The 40K DWT Container Ship "collision" CAD model was also developed based on available 3-D information. Striking ship principal characteristics are provided:

40,000 DWT Container Ship Principal dimensions: LBP: 211.50 m; Breadth moulded: 32.20 m Depth mid to main deck: 21.00 m Depth to shelter deck 24.00m; Max. Draft 11.90m; Displacement (Loaded) 54,000 tons; Max. Service Speed 11.3 m/s (21.97 knots). It is assumed that the striking ship damage is restricted to the bow, and only the first sections in this bow are considered in the detailed bow model. The remainder of the ship is modeled using elements and mass densities such that the total mass and moments of inertia are the same as those of the real ship.

The conventional FEA model developed in this paperwork include side-shell, deck, longitudinal bulkhead and primary girder components in the bow of the ship, aft to the collision bulkhead. These components are modeled using meshed shell elements. The remainder of the ship is also modeled using elements and concentrated masses such that the model's mass and mass moment

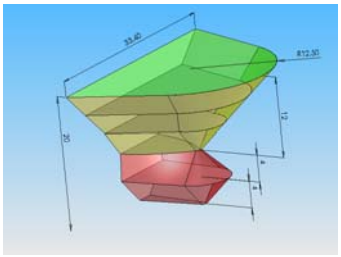

Figure 1 Solidworks bow CAD model (dimensions in meter)

of inertia are the same as in the real ship (including actual mass and added mass in the collision direction).

The material used for modeling the bow section of the ship is the Plastic Kinematic type which is isotropic, kinematic, or a combination of isotropic and kinematic hardening models with strain rate dependency and failure. Isotropic and kinematic contributions may be varied by adjusting the hardening parameter β between 0

(kinematic hardening only) and 1 (isotropic hardening only). Strain rate is accounted for using the Cowper-Symonds model which scales the yield stress by the strain rate dependent factor as shown below:

$$\sigma_Y = \left[1+\left(\frac{\dot{\varepsilon}}{C}\right)^{\frac{1}{P}}\right]\left(\sigma_0 + \beta E_p \varepsilon_p^{eff}\right) \quad (1)$$

where σ_0 is the initial yield stress, $\dot{\varepsilon}$ is the strain rate, C and P are the Cowper-Symonds strain rate parameters, ε_p^{eff} is the effective plastic strain, and E_p is the plastic hardening modulus.

The main characteristics are: Density 7865 kg/m^3; Young Modulus 2E+011 Pa; Poisson Coef. 0.27; Yield Stress 3.1E+008 Pa; Tangent Modulus 7.63E+008 Pa; Hardening Param. 0; Strain Rate (c) 40; Strain Rate (P) 5; Failure Strain 0.75.

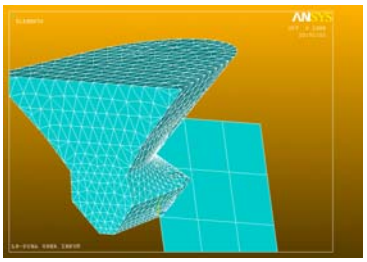

Figure 2 FEA Model

In the FEA model 3 Reference Points were established in order to pinpoint the variation in time of some characteristics, as we'll see below.

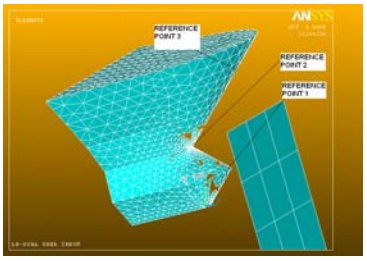

Figure 3 Reference Points

All nodes in the rigid jetty wall are fixed and it was made out of the Material Type Rigid. To model the real collision scenario, it would be ideal to free all nodes in the striking ship. This was tried, but it was found that the simple shell elements in the after part of the ship do not provide sufficient bending constraint at their connection with the bow. The bulb is much stronger than the upper bow so the upper bow has more deformation. This results in an unrealistic "nose-down" bending of the bow. By constraining nodes in the bulkhead of the bow in the one rotation (Rot X) and Y direction, a more reasonable bow constraint is obtained.

The velocity of the ship was assumed to be 5 m/sec, the collision angle being 90^0. No acceleration loading was imposed to the ship structure. The contact surfaces were defined automatically as surface to surface automatic contact definition option. The Adaptive Mesh option was set ON for the entire ship model.

The time range over the simulation was executed was 3 seconds but only at second 1.14 the ship structure is colliding the jetty wall.

After running the simulation the results obtained are presented in the followings.

At Impact Time (1.14 seconds from the start of simulation)

At impact time the ship structure enter in contact with jetty wall with its bowsprit.

The Velocity field in the structure starts to modify, in order that the front of the bowsprit is suddenly stopped and the rest of the structure still moves on:

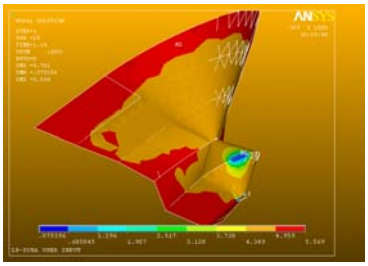

Figure 4 Velocity distribution at the impact time

Naturally, the variation of velocity changes the state of acceleration (deceleration) of points around the impact zone as per the figure below:

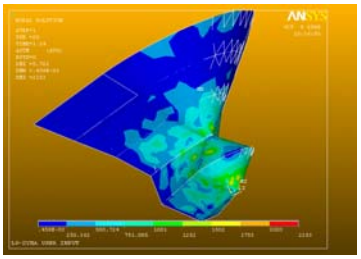

Figure 5 Deceleration distribution at the impact time

The deceleration is extremely sudden, in certain points of the structure reaching values of 2253 m/sec^2. The Von Misses equivalent stresses at this time are given below (Figure 6).

The stress state in and around the impact zone suffers a tremendous change in magnitude, locally being achieved maximums of 0.568e9 Pa, which is far beyond the ultimate strength of the material. Therefore a plastic regime will be induced in the area, the irreversible plastic deformation of the material starting at this point in time. As it is shown in the Figure 7, the Von Mises equivalent Strains are reaching values of 0.155 at the impact zone, which is far beyond the conventional plastic deformation limit of 0.2%.

In Figure 8, the calculated Plastic Strains witness the beginning of the plastic deformation of the structure.

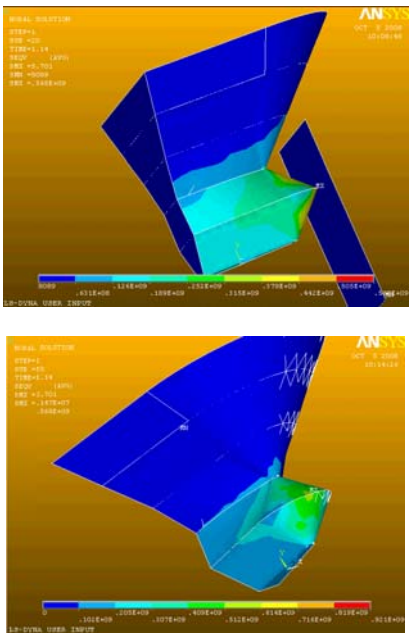

Figure 6 Von Mises Stresses distribution at the impact time

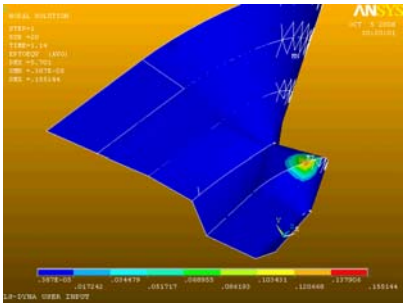

Figure 7 Von Mises Strain distribution at the impact time

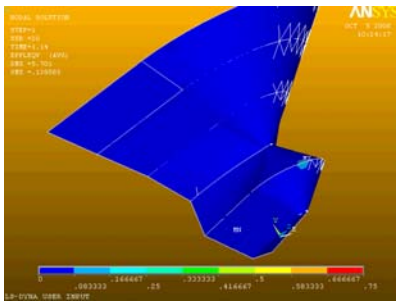

Figure 8 Plastic Strain distribution at the impact time

At this moment in time, the impact zone is getting bigger as the ship structure is advancing toward the jetty wall, the deformed zone spreading around the impact zone and also the stress state reaching maximums of 0.709e9 Pa.

At 0.36 sec after the Impact Time

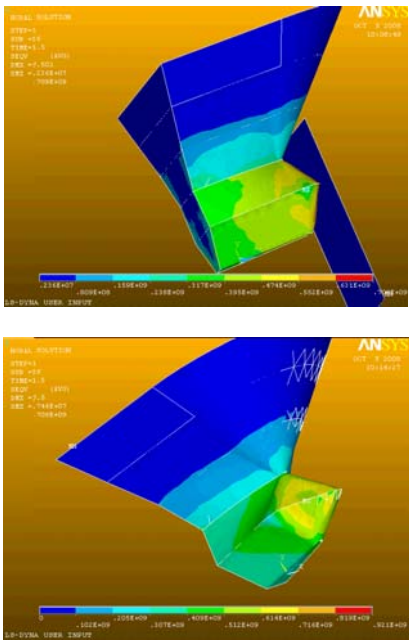

Figure 9 on Mises Stresses distribution at 0.36 sec after the Impact Time

At 0.9 sec after the Impact Time

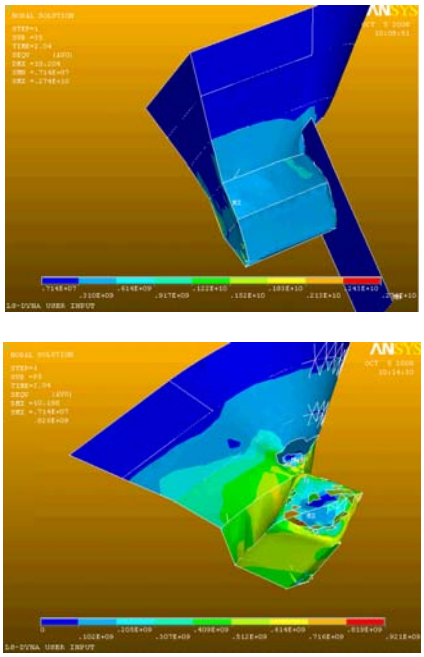

Figure 10 Von Mises Stresses distribution at 0.9 sec after the Impact Time

At this moment the structure around the impact point became so contorted that ruptures occurs in it and "pieces" of material are automatically removed from the structure by the adaptive re-mesh algorithm so that certain holes start to appear in the structure, following the failure criterion of the material.

At 1.38 sec after the Impact Time

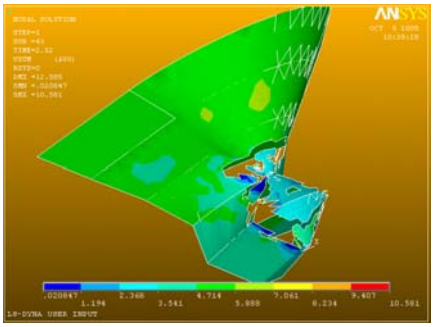

Figure 11 Velocity distribution at 1.38 sec after the Impact Time

At this time the entire ship structure starts to slow down, the kinetic energy being transformed into deformations and kinetic energy of ruptured structural pieces that are spreading all around. Also the average deceleration is 0.01 m/sec^2 for the bulk of the structure.

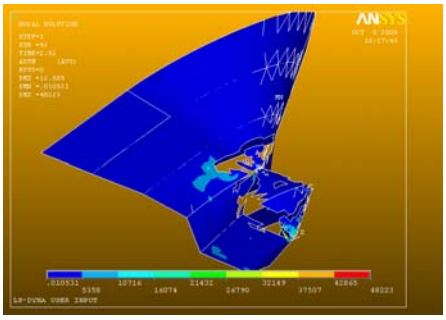

Figure 12 Deceleration distribution at 1.38 sec after the Impact Time

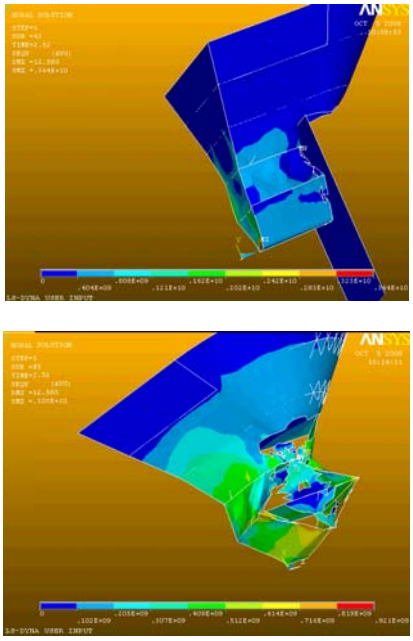

Figure 13 Von Mises Stresses distribution at 1.38 sec after the Impact Time

The rupture zone of the structure is further advancing in the material; the peak calculated stresses are reaching values of 0.1e10 Pa.

At 1.86 sec after the Impact Time

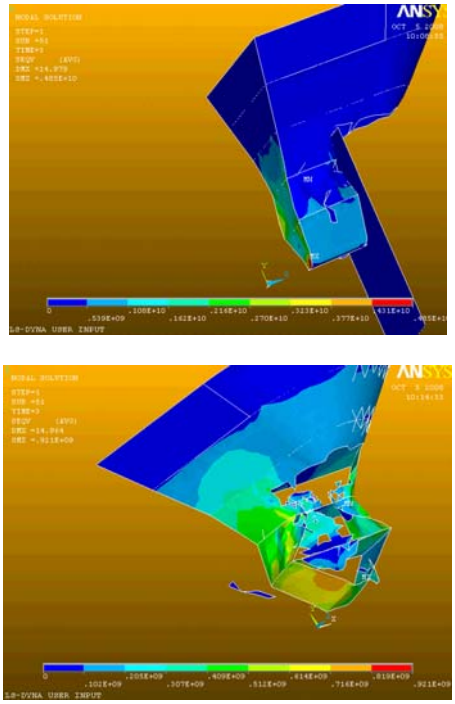

Figure 14 Von Mises Stresses distribution at 1.86 sec after the Impact Time

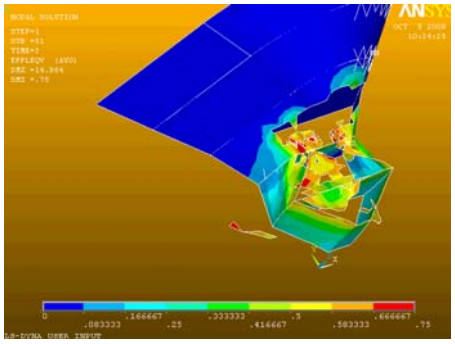

Figure 15 Plastic Strains distribution at 1.86 sec after the Impact Time

At this time the bow of the ship is completely demolished, the impact rupturing the entire structure of the ship.

Time History at Reference Points

Taking into account the Reference Points as defined in the Figure 5, it would be maybe interesting to see the evolution in time of some of the main simulation parameters.

For instance, at the *Reference Point 1* the main parameters graphs versus time are given below.

The velocity before impact is 5 m/sec. but at the impact time, the velocity is sharply decreasing to 0 m/sec. and after that getting reversed to a maximum negative value of -0.8 m/sec.

At the impact time the equivalent Von Mises Stress sharply increase to a maximum of 3e8 Pa, after that oscillating and decreasing until the end of the simulation.

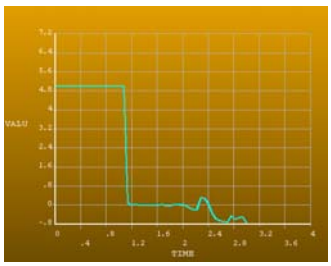

Figure 16 Velocity Time History for Reference Point 1

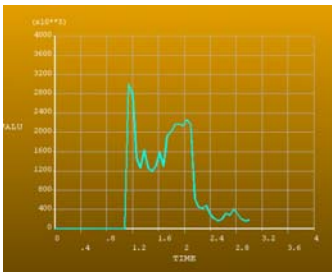

Figure 17 Von Mises Stress Time History for Reference Point 1

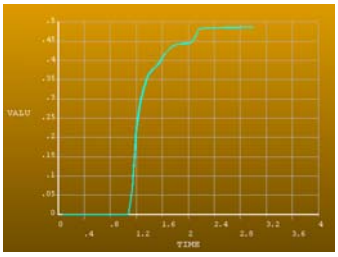

Figure 18 Plastic Strain Time History for Reference Point 1

The plastic strain is sharply increasing at the impact time and then stabilizing itself at a peak value of 0.5.

For the *Reference Point 2* the main parameters graphs versus time are given below.

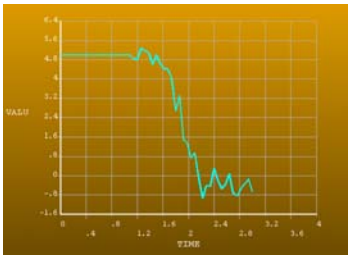

Figure 19 Velocity Time History for Reference Point 2

In this case the velocity declining is not as sharp as in previous case although the overall shape is almost the same, a negative velocity regime being installed at the end of the simulation.

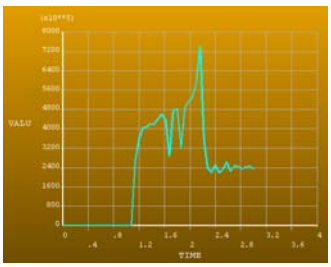

Figure 20 Von Mises Stress Time History for Reference Point 2

The peak Von Mises Stress is reached at 2.1 sec after the starting time of the simulation (0.96 sec after the impact) the top value being 7.4 e8 Pa.

For the *Reference Point 3* the main parameters graphs versus time are given below.

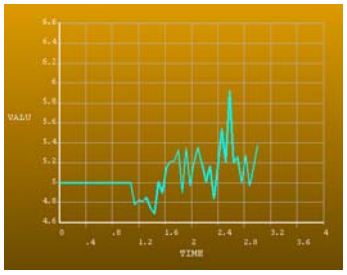

Figure 21 Velocity Time History for Reference Point 3

In this case the structure at this point is suddenly decreasing at the impact moment and then is oscillating reaching some peak values of 5.9 m/sec.

Figure 22 Von Mises Stress Time History for Reference Point 3

The Von Mises equivalent stresses are increasing to a value of 2.4 e7 Pa at the impact moment and afterward sharply increasing to 8e7Pa and starting to oscillate around this value.

The validation of the model is simple this time; we are just showing a real case incident in the photos below and acknowledge the resemblance of the numerical model and the real case.

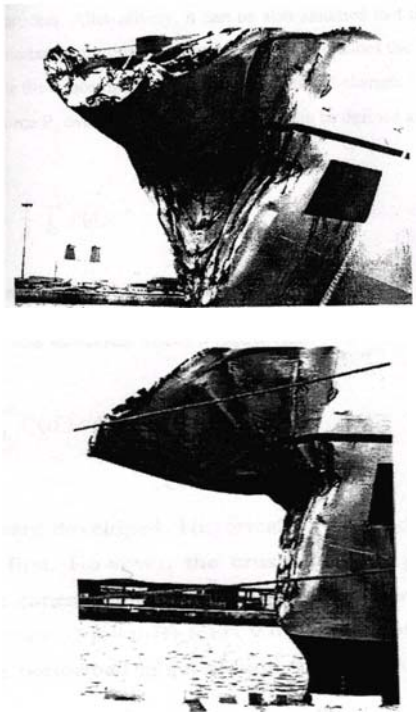

Figure 23 Real case frontal ship-jetty collision

3. CONCLUSIONS

Based on the analysis and results presented some conclusions are to be made.

The ANSYS-LS-DYNA model provides a consistent and reasonable result for ship collision analysis. Its results are comparable with other approaches. The collision process is complex and must be evaluated on a case-by-case basis. As shown, for this particular bow, the upper bow of the striking ship is very flexible and has a low "energy-folding" mode of deformation. The bulb is thoroughly affected by the collision, so most of the impact energy is absorbed the bulb and by the side structure of the struck ship contacted by the bulb.

Compared with other ship collision models, ANSYS-LS-DYNA provides much more information such as detailed time history curves, animation of the collision process, a series of damage pictures for any part of the ships, velocity and displacement histories. These are very helpful for better understanding of ship collisions.

The modeling extent of the struck ship should cover the plastic contact area and the elastically stressed areas in the compartments, which are adjacent the heavily deformed contact area. Further there are indications that an elastic stress field may be present over the whole breadth of the model, and therefore it is considered appropriate to model the whole structure in between two cross-sections. Equivalent orthotropic panel formulation should be investigated in order to determine whether such panels can be used in areas away from the struck region. The failure criterion, which has been used, is based on the plastic strain of an element. The value of the maximum plastic strain, which has been selected, is 75%. Such a value seems to result in realistic failure modes and in results, which are close to experimentally obtained values of penetration. More effort is needed in order to select a failure criterion, which would be used with more confidence in the collision simulation.

The results obtained from the finite element simulation, may be used for the assessment of the of collision behavior of a ship under the defined collision scenario, for the relative comparison of structural arrangements, and for the validation of analytical techniques for collision analysis.

4. REFERENCES

[1] SIRKAR, J. et al., *A Framework for Assessing the Environmental Performance of Tankers in Accidental Groundings and Collisions*, presented at the SNAME Annual Meeting, October 1997

[2] RAWSON, C., CRAKE, K. and BROWN, A.J., *Assessing the Environmental Performance of Tankers in Accidental Grounding and Collision* presented at the SNAME Annual Meeting, November 1998

[3] A.J. Brown and M. Amrozowicz, *Tanker Environmental Risk-Putting the Pieces Together",* SNAME/SNAJ International Conference on Designs and Methodologies for Collision and Grounding Protection of Ships, August 1996

[4] IMO, *Interim Guidelines for Approval of Alternative Methods of Design and Construction of Oil Tankers under Regulation 13F(5) of Annex I of MARPOL 73/78*, Resolution MEPC.66 (37), Adopted September 14, 1995

[5] MINORSKY, V.U. (1959), *An Analysis of Ship Collisions with Reference to Protection of Nuclear Power Plants*, Journal of Ship Research, Vol. 3, No. 1, 1959

[6] REARDON, P., and SPRUNG, J.L. (1996), *Validation of Minorsky's Ship Collision Model and Use of the Model to Estimate the Probability of Damaging a Radioactive Material Transportation Cask During a Ship Collision*, Proceedings of the Intl. Conference on Design and Methodologies for Collision and Grounding Protection of Ships, San Francisco, August 1996

[7] DONGHUI, CHEN, (Jan. 2000), *Simplified Collision Model (SIMCOL),* Dept. of Ocean Engineering, Virginia Tech Thesis, Jan. 2000

[8] PAIK, J.K. (1995), *The Idealized Structural Unit Method: Theory and Application,* Dept. of Naval Architecture and Ocean Engineering, Pusan National University, Pusan, Korea, August 1995

[9] HALLQUIST, J.O (1998), *LS-DYNA Examples Manual,* Livermore Software Technology Corporation (LSTC), March 1998

[10] HALLQUIST, J.O (1998), *"LS-DYNA Examples Manual",* Livermore Software Technology Corporation (LSTC), March 1998

[11] HALLQUIST, J.O (1998), *"LS -DYNA Theoretical Manual"*, Livermore Software Technology Corporation (LSTC), May 1998

STUDIES REGARDING THE EXPLOTATION CONDITIONS INFLUENCE UPON THE ACTIVE ZONE OF THE ROAD COMPLEX FOUNDATION GROUND

[1]COSTESCU CIPRIAN, [2]CIOPEC ALEXANDRA, [3]VOICU CRISTINA, [4]MIREA MONICA

[1,2,3,4]Politehnica" University of Timisoara, Civil Engineering Faculty, Department of Land Communication Ways, Foundations and Survey, Romania

ABSTRACT

Road structures, indifferently of their type and composition, are strongly influenced by the quality of the embankments on which they are realized. The practice confirmed that generally between the aggravation process of the defects and improper behaviour of the foundation ground exist a mutual potential relationship, each of the two processes influencing negative the other one. It is evident that there exist a series of defects and degradations of the roads whose causes cannot include the initial influence of the natural foundation ground influence or of the filling material from which it's made of. For this reason, the depth knowledge of the embankments active zone is extremely important and useful for preventing and avoiding undesired situations generated by the foundation ground in roads exploitation and also it offers the possibility of taking some measures for quality foundation ground improvement on a depth corresponding to the active zone. This paper presents results referring to the embankments active zone depth obtained on the basis of some studies based on the analytic calculus and numeric modelling of different road structures.

Keywords: *embankment, foundation ground, active zone, road complex.*

1. INTRODUCTION

Road complexes can be defined as being constructions composed by a road structure and a foundation (embankment and natural ground) with the purpose of serving in some conditions also in the safety of traffic. In consequence, when designing the whole road complex must be paid a major attention to each layer of the road structure and also to road structure, embankment and natural ground working together.

Unlike other constructions with a reduced area, on a road route the probability of the geological and geotechnical elements diversity is much wider.

The embankments are permanently exposed to the action of the exterior agents that have a major influence upon their behaviour. The variation of the moisture content and of the temperature during one year determines the enlargement or reduction of the embankments bearing capacity. Water in different forms may exert a decisive influence upon the embankments behaviour, resulting from infiltration of the rainfalls or by underground waters ascending.

By embankments is understood the total of the digging and filling works performed generally in soils, with shapes and dimensions given by the project, necessary to construction and reconstruction of the roads or railways. The ground on which are realized the embankments is considered foundation ground and the soils used for their realization are called materials for embankments.

2. DETERMINATION OF THE ACTIVE DEPTH BY AN ANALYTICAL CALCULUS

For modelling the foundation soil and for determining the depth to which traffic loads cause stresses and deformations in the embankment material, was studied the stress distribution in the foundation soil, assuming a semi-space with uniform distributed load of the contact surface between tire and clothing.

The standard axle 115 kN (OS 115) used in calculations for sizing of road pavements in Romania has the following characteristics: dual wheel load-57.5 kN, contact pressure-0.625 MPa and equivalent circular radius of the contact surface area of tire-track-0.171 m.

We may consider the situation presented in Figure 1, when the load is uniform distributed (6.25 daN/cm^2), on a circular surface with a 17.1 cm radius. The load distribution on the road structure is applied with an inclination of 45 ^{0}, so that at the superior level of the foundation ground (road bed foundation) were computed the uniform distributed loads and equivalent surfaces.

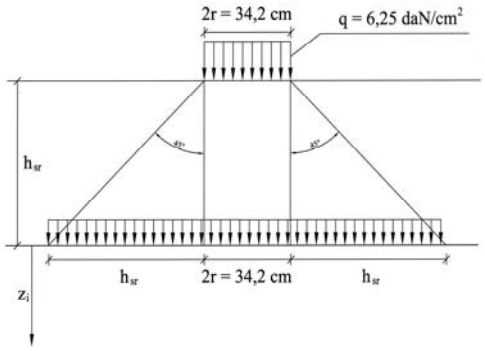

Figure 1. Uniform distributed load at the level of the foundation ground

The load at the level of the foundation ground may be expressed by the relationship:

$$p_k = \frac{q \times \pi \times r^2}{\pi \times (r + h_{sr})} \text{ [daN/cm}^2\text{]} \qquad (1)$$

where:

p_h - the uniform distributed load at the level of the foundation ground;

q - the uniform distributed load from traffic at the level of road surfacing (6.25 daN/cm^2);

r – the radius of the equivalent circular contact surface tire-road surfacing (17.1 cm);

h_{sr} –road structure width.

The calculus relationship for the vertical stress σ_z can be simplified as:

$$\sigma_z = k_c \cdot x \cdot p_h \qquad (2)$$

where:

k_c - dimensionless coefficient(function of the z/R_0 and R/R_0);

p_h – uniform distributed load on the surface with R_0 radius, (Figure 2).

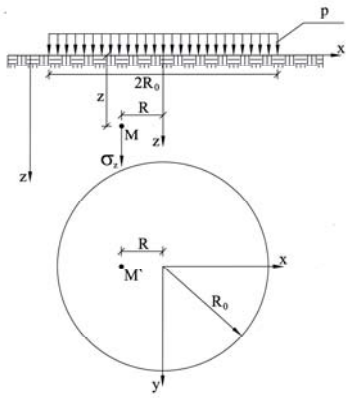

Figure 2. Circular surface loaded with a uniform distributed load

It is known that the vertical stresses from the foundation ground, determined on the basis of Boussinesq model, decreases with the depth increasing.

Based on this can be performed a calculus taken into account in the mathematical modelling of the road structures, especially of their foundation ground:

- for the road structures with a width of 30...50 cm, the vertical stresses σ_z reach values under 0.10 daN/cm^2 at a depth of 1.50...1.80 m, measured under the level of road bed foundation;

- for the road structures with a width of 50...75 cm, the vertical stresses σ_z reach values under 0.10 daN/cm^2 at a depth of 1.30...1.60 m, measured under the level of road bed foundation;

- for the road structures with a width of 75...91 cm, the vertical stresses σ_z reach values under 0.10 daN/cm^2 at a depth of 1.00...1.35 m, also measured under the level of road bed foundation.

The values of the depths z, for which the values of σ_z vertical stress decreases under the value of 0.10 daN/cm^2 is considered to correspond to the active depth of the foundation ground.

If we try to define the road complex zone (road structure + embankment active zone), zone that can be influenced by the traffic loads, it can extend till depths of approximately 1.80...2.30 m measured from the level of the runway.

3. DETERMINATION OF THE ACTIVE DEPTH BY MATHEMATICAL MODELLING

One of the possibilities of numerical modelling widely used in road pavements field is based on the Finite Element Method (F.E.M.). This is a general method for approaching the partial derivative differential equations describing various physical phenomena. F. E. M. has become lately one of the most "powerful" tools for solving engineering problems.

For modelling the infinite semi-plane are available infinite elements used for defining the boundary conditions in horizontal and vertical direction in the foundation ground. The tri-dimensional response of the finite element mesh was simulated using "axi-symmetric deformable" CAXA type finite elements, which are part of the ABAQUS program. ABAQUS is a commercial modelling program based on F.E.M. and has been widely applied to the analysis of road pavements. The simplified numerical model is defined using a revolution axis, the Y-Y axis and introducing the appropriate symmetry conditions (i.e. U1 = UR2 = UR3 = 0).

The used elements were in connection with the standard finite elements that modelled the road complex area of interest and for the foundation grounds modelling as a semi-infinite space were used infinite elements (CINAX5R).

Factors that influence the behaviour of the two studied road structures (flexible road structure and mixed road structure) refer to the road traffic, to the hypotheses of the link between the road layers, to the climate conditions and to the foundation ground. It was studied the behaviour in normal exploitation conditions of these two road structures and the variations of the considered parameters, observing the depth in the foundation ground at which is experienced their influence.

The flexible road pavement was modelled using the following initial characteristics:

- clothing bituminous: thickness 7 cm, E = 3000 MPa, μ = 0.35;

- ballast foundation layer: thickness 15 cm, E = 667 MPa, μ = 0.27;

- foundation layer obtained from initial pavement: thickness 10 cm, E = 350 MPa, μ = 0.27;

- foundation ground: semi-finite thickness, E = 65 MPa, μ = 0.30.

Figures 3 and 4 present the deformations of this road structure in normal exploitation conditions in two hypotheses: perfectly connected road layers and unconnected road layers.

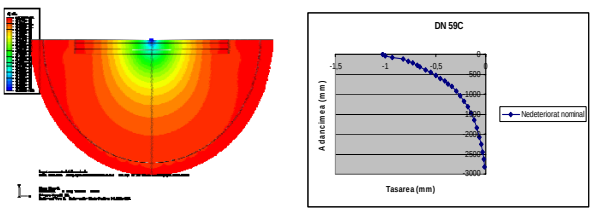

Figure 3. Perfectly connected road layers hypothesis (flexible road pavement)

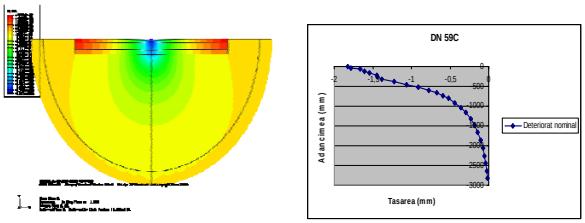

Figure 4. Unconnected road layers hypothesis (flexible road pavement)

The mixed road pavement was modelled using the following initial characteristics:

- bituminous layer: thickness 18 cm, E = 3800 MPa, μ = 0.35;
- crushed stone layer: thickness 20 cm, E = 400 MPa, μ = 0.27;
- stabilized ballast layer: thickness of 20 cm, E = 600 MPa, μ = 0.27;
- ballast foundation layer: thickness 15 cm, E = 114 MPa, μ = 0.27;
- foundation ground: semi-finite thickness, E = 60 MPa, μ = 0.30.

Figures 5 and 6 present the deformations of the mixed road structure modelled in the same two hypotheses as those used for the flexible road structure.

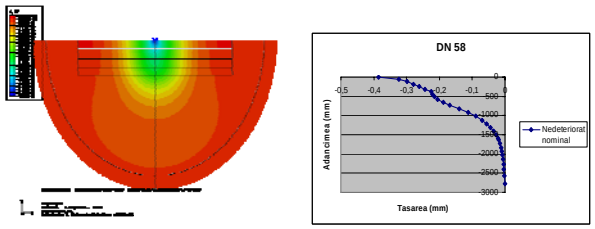

Figure 5. Perfectly connected road layers hypothesis (mixed road pavement)

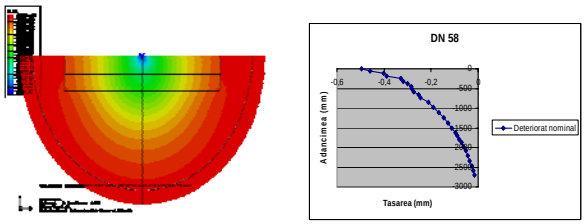

Figure 6. Unconnected road layers hypothesis (mixed road pavement)

In the case of flexible road structures the value of the foundation ground vertical deformations are relatively close beginning with the depth of 2.00 m and they differ for depths greater than 2.50 m. This fact can be explained by the presence of the stabilized material layer that assures a better protection of the foundation ground against the loads that may exceed allowable values, while flexible road structures have an elastic behaviour and a reduced stiffness.

Mathematical modelling continued in the two hypotheses, varying the axle load (axle load increase to 130 kN, respectively to 150 kN), deformability characteristics of the bituminous layers considering the value of the dynamic elasticity modulus half or double of the value of the rated modulus, foundation ground quality considering severe situations regarding the foundation ground soil type, the climate and the hydrological conditions.

Regarding the influence of the foundation ground quality upon the exploitation behaviour of the mixed road structures was observed that its influence is felt in depth in the hypothesis of unconnected layers and is as inexistent in the hypothesis of connected interfaces beginning with depths of over 1.00 m, while it is felt on greater depths of the embankments active zone in the case of flexible road structures where the foundation ground quality influences the road complex behaviour till depths of approximately 2.00 m.

The deformability characteristics variation in the hydrocarbon pavement mixture due to temperature variations, moisture content, fatigue phenomena and so on, does not modify the behaviour of the embankments active zone till depths of approximately 0.75 m in hypothesis of free interfaces and 1.25 m in hypothesis of perfectly connected layers of a flexible road structure and in the case of a mixed road structure the effects are felt till depths of approximately 1.50 m in hypothesis of perfectly connected layers and approximately 2.00 m in hypothesis of free interfaces.

Once with the road complex depth increasing, its deformability state is significantly different for the case of flexible and mixed road structures. For flexible road structures it begins with depths of approximately 1.00 m and this influence is almost inexistent, while in the case of mixed road structure this influence is felt till depths of approximately 2.00 m.

The increase of the axle load gives an evident increase of the road complex deformations and in the case of flexible structures this is felt in the embankments active zone till depths of approximately 2.50 m.

In the case of the mixed road structures the increase of the road complex deformations due to axle load increase is felt in the embankments active zone till depths of approximately 2.00 m in hypothesis of perfectly connected layers and over 2.50 m in hypothesis of free interfaces.

Figure 7 presents the obtained results by mathematical modelling for the analyzed flexible road structure. Can be observed that the effects of the considered factors are felt in the road complex till depths of approximately 2.50 m from where these do not influence the deformations of the foundation ground. The main effects are felt at the level of the road bed foundation and not at its superior levels (in the road structure), so that at this level exists a greater probability of road complex failure, fact that underlines the importance of the foundation ground quality upon the exploitation behaviour of the road complexes.

It is recommended that since the designing phase must be taken supplementary measures for foundation ground quality improvement, giving a supplementary stability of the road complex for the period of its exploitation.

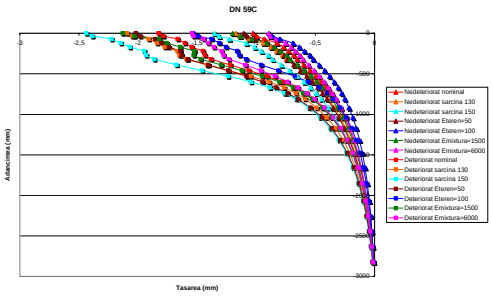

Figure 7. Superposition of all considered factors (comparative situation – flexible road structure)

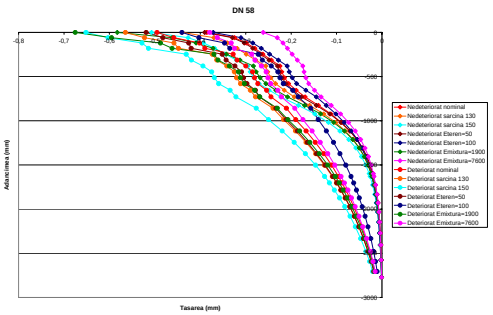

Figura 8. Superposition of all considered factors (comparative situation – mixed road structure)

Figure 8 presents the same results as Figure 7 obtained as a result of the mathematical modelling of the analyzed mixed road structure. From the obtained results analysis was noticed that in the case of considered factors variation, in hypothesis of free interfaces, their influence is felt till depths greater than 2.50 m, while in the case of the hypothesis of perfectly connected road layers, the influence depth does not exceed 1.50 m.

Simultaneously, the influence of the considered factors is much greater at the level of the road bed foundation than that at the base of the bituminous layers, in the hypothesis of the unconnected layers.

4. CONCLUSIONS

Referring to the analytical calculus of the foundation ground active zone and to the studies performed for mathematical modelling of two road structures, are presented in the following some final conclusions.

Starting from the researches carried out in France regarding the two hypotheses of the interface connection, on the basis of ALIZE elastic model showed that function of the working together of the road layers, the life span of one road structure may vary in very large limits, from 6 months till 15 years, the obtained results by mathematical modelling confirming that the state of stress and deformation in road complexes is influenced by the hypothesis of layers and foundation ground working together. So, can be observed that the relative deformations in the flexible road structure are approximately two times greater in the case of free interfaces hypothesis than those given in the hypothesis of perfectly connected layers and in depth, around a depth of 2.00...2.50 m the deformations are almost equal in both considered hypotheses.

In the case of the mixed road structure the effects of the hypotheses referring to the layers working together are felt till great depths in the foundation ground and are very important in the active zone of the embankment. Great differences in these deformations (values till three times greater) are found in the embankments active zone, in the depth of the foundation ground, with a maximum value at a depth of approximately 1.50...2.00 m.

Foundation ground quality influences vertical deformations of the road complex for flexible structures in a lesser extend at the inferior level of bituminous layers and in a greater extend at the level of the road bed foundation. From a foundation ground depth of approximately 2.00 m the influence of its quality is not felt. Regarding the foundation ground quality upon the exploitation behaviour of the mixed road structures, it is felt in depth in the hypothesis of unconnected layers and is as inexistent in the hypothesis of connected interfaces beginning with depths of over 1.00 m.

The variations in the deformability characteristics of the hydrocarbon pavement mixtures in flexible road structures bring modifications in the behaviour of road structures in their structure and a small depth under the level of the road bed foundation. So, can be observed that the variations of the dynamic modulus of elasticity of the hydrocarbon pavement mixtures does not modify the behaviour of the embankments active zone unless depths of approximately 0.75 m in the hypothesis of free interfaces and 1.25 m in the hypothesis of perfectly connected road layers.

The variations of the deformability characteristics of the bituminous layers during the exploitation period of road complexes with mixed structures do not bring modifications in the behaviour of the embankments active zone till depths of approximately 1.50 m in the hypothesis of perfectly connected road layers and of approximately 2.00 m in the hypothesis of free interfaces.

5. REFERENCES

[1] COSTESCU, C., BELC, F. *Comments on the Calculation of Flexibile and Semirigid Road Pavements in Romania*. Susteinability in Science Engineering. Proceedings of the 11th WSEAS International Conference on S.S.E., pp. 201-206, Timişoara, mayi, 2009

[2] LUCACI, G., BELC, F., BANCEA, C., COSTESCU, C. *Roads. Design Elements*. Politehnica Publishing House, Timişoara, 2010

[3] HAIDA, V., MARIN, M., MIREA, M. *Soil Mechanics*. Orizonturi Universitare Publishing House, Timişoara, 2004

[4] FODOR, G., POPESCU, N. *Technical Guide – Semirigid and Flexible Road Pavements. Dimensioning and Composition*. Compania Inedit Publishing House, Bucharest, 2000.

DETERMINATION OF THE INDUCED STRESSES AT THE LEVEL OF A FLOOR USING THE FINITE ELEMENT METHOD

CRISTEA ANISOARA-GABRIELA

„Dunarea de Jos" University of Galati, Faculty of Naval Architecture, Romania

ABSTRACT

The purpose of this paper is to verify the induced stresses of a framework element from central area of the chemical tanker ship type.

This static calculation was performed by the finite element method with Femap software as modeler and NX Nastran as solver.

Keywords: *mechanical structural, stress calculation, hogging, sagging.*

1. INTRODUCTION

The main concern regarding the development with finite element is to generate a model providing the best possible results of the structural strength.

Sizing of the model was made in accordance with the rules of the classification company Germanischer Lloyd.

For modelling and analysis of the stresses around the relief cut-outs of a frame element, in this case of a floor, we used finite element software system FEMAP version 9.3.1.

The ship considered is a chemical tank type ship being designed for transporting chemicals.

1.1 Main dimensions and characteristics

Length between perpendiculars	L_{pp} = 110,596 m
Length of water line at T	L_{wl} = 110,596 m
Breadth	B = 18,5 m
Depth	H = 10 m
Scantling draught	T = 7,4 m
Block coefficient	C_b = 0.730
Max. speed in calm water	v = 14 kn
Frame spacing in cargo holds area	a = 0.8 m
Web frame spacing	4a = 3.2 m
Displacement	Δ = 8000 dwt

1.2 Modeling the Structure:

The hull structure considered in the 3-D hold model includes three cargo tanks of the parallel mid-body, as shown in Figure 1.

The global coordinate system of the finite element model is defined as follows:

X-axis: Longitudinal, positive from aft to fore;

Y-axis: Transverse (athwart ships), positive toward portside;

Z-axis: Vertical, positive upwards;

Origin: Base-line.

The following units are used for analysis

- Length: millimeters (mm)
- Pressure: Megapascals (N/mm^2)
- Mass: kilogramme (kg)
- Stress: N/mm^2 (MPa)

2. DESCRIPTION OF THE MODEL

Register conditions recommend, for the analysis with the finite element method of a ship structure, to consider two or three merchandise store rooms (cargo tanks) in order to reduce the influence of the edge conditions, throughout pressure distribution in the master section.

For this calculation we used a model extended on the length of three store rooms from the central area of the ship, so as to avoid the end effect and more precisely we have studied the central store room.

The idealized model contains the bottom floors, deck, plating, double plating and embossed walls.

The following types of items are used in the structural model:

- The elements of plate and membrane for shell and the main elements of support. Most elements are QUAD type; some triangular elements are also used where needed.
- Two rigid elements placed at the ends of the model used in order to simplify application of marginal loads (on the contour– bending moments).

The size of total mesh is 1/2 of the longitudinal distance (400 mm). In the area of interest 1/8 (Figure 2) of the longitudinal distance (100 mm) was finely modeled.

The elements of the plate were used for ground, double bottom, supports, and rod elements were used for simple framework.

In order to highlight as fairly as possible the distribution of the stresses on the floor made of fine mesh both the simple framework on the floor and the logitudinals were made with finite elements, plate type 4 bends.

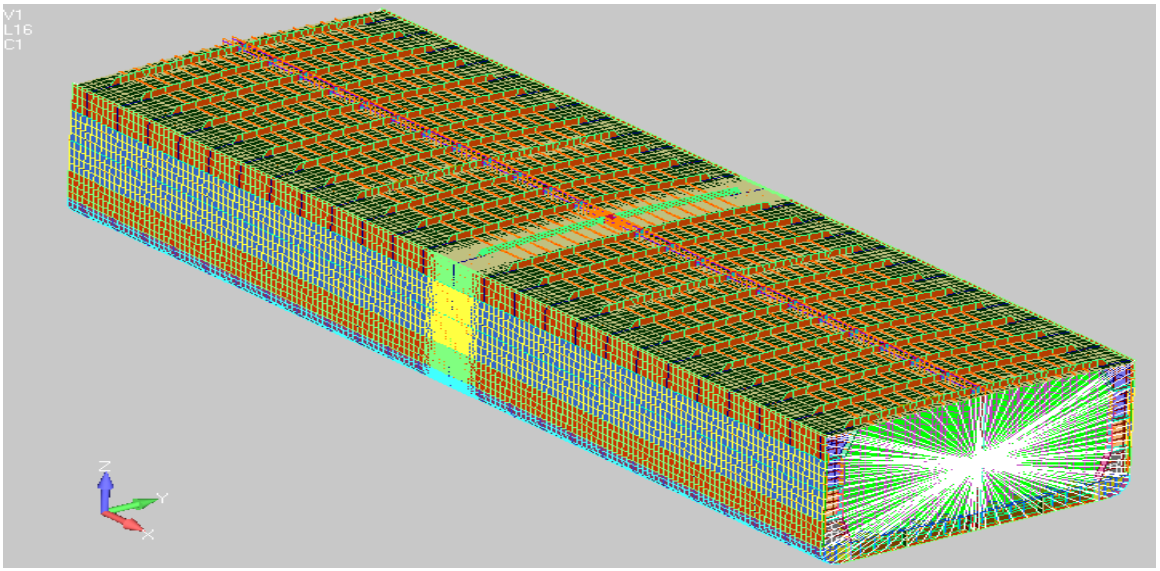

Figure 1 Global model

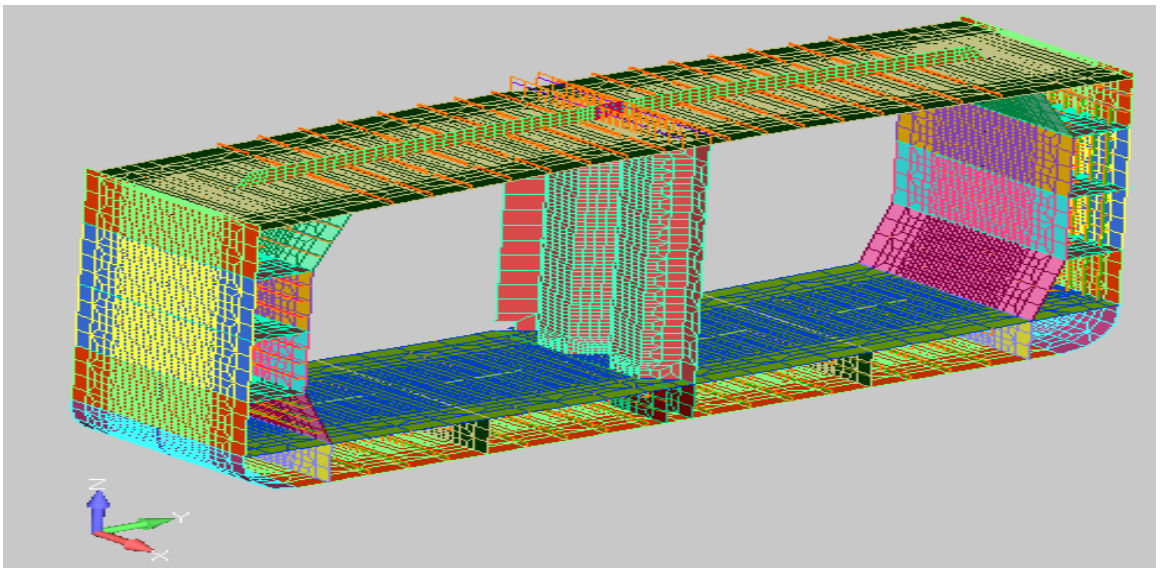

Figure 2 Detailed 3D model

Table 2 presents the characteristics of the model CAD-FEM and material characteristics of the ship.

Table 2 CAD-FEM characteristics of the model

The number of the elements of plate and membrane PLATE (QUAD)	158499
The number of bends	118421
Young's modulus	2,1E+5 N/mm2
Poisson's coefficient	0,3
Steel density, ρ	7,7E-6kg/mm3
Steel flow limit, R_{eH}	315 N/mm2

3. EDGE CONDITIONS

The end conditions of this model are: blocking movements in x, y and z directions, as well as spins around the x axis in the master node of the rigid from the stern and blocking movements in x, y and z directions, as well as spins around the x axis in the master node of the rigid from the bow.

The moments were applied at both ends of the structure in order to obtain the maximum moment of bending. According to Germanischer Lloyd rules, the maximum moment of bending (obtained from Poseidon v. 9.0) is M = 2.1 E+11 [Nmm].

These marginal loads were applied so that the model remains in balance.

To this end we used a solid type element that will transmit a rotation movement due to the bending moments; these moments are applied in the master nodes of the rigid situated in the neutral axis of the model.

The Figure 3(a, b) - highlights the edge conditions on this model.

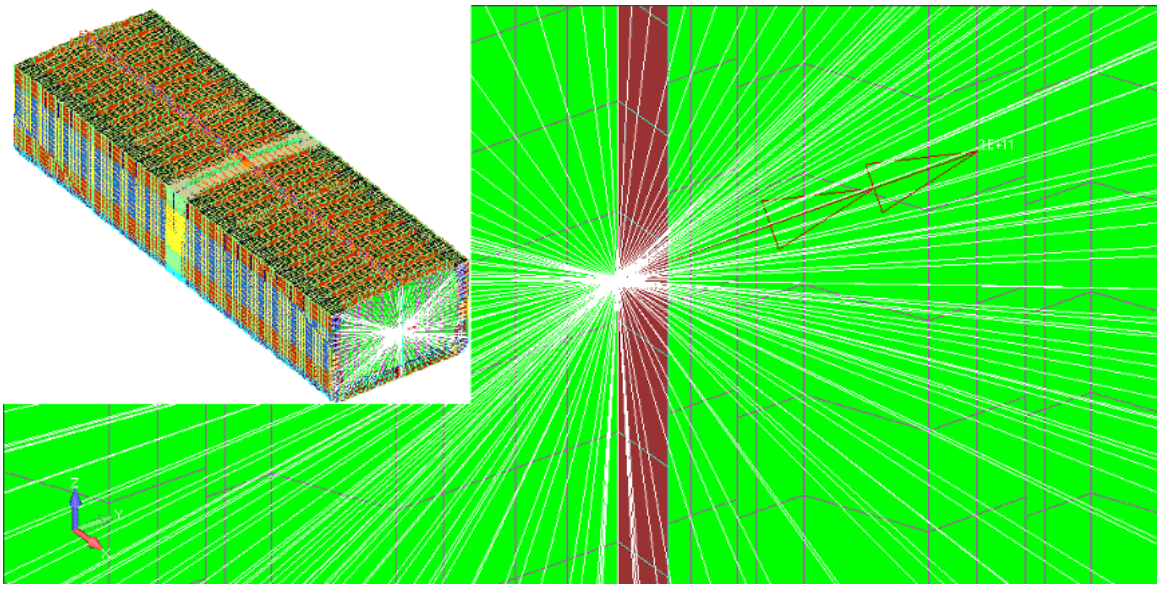

Figure 3a Edge conditions

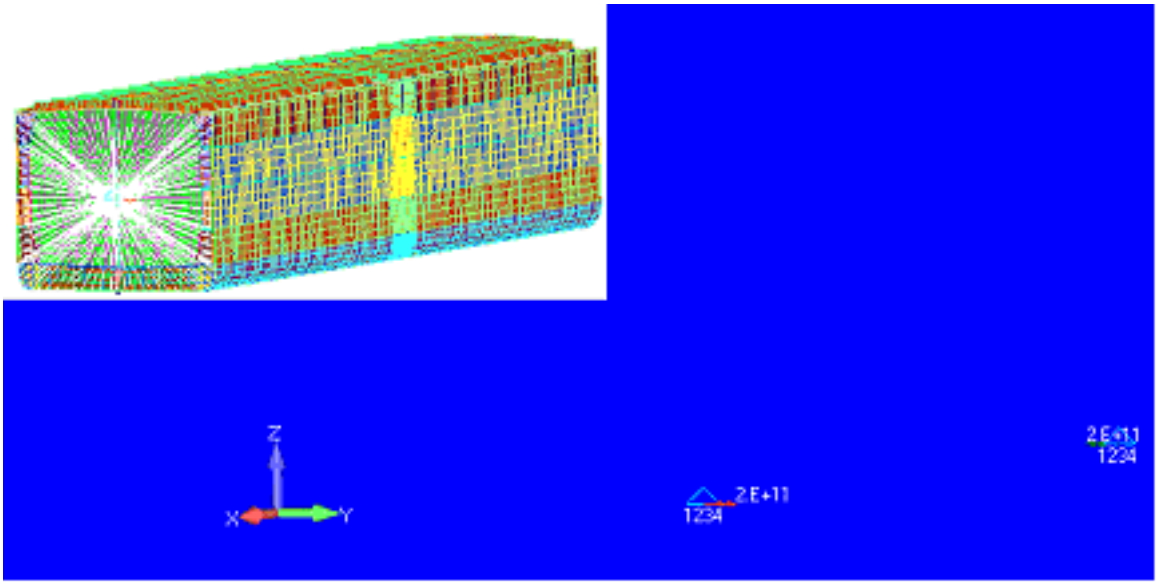

Figure 3b Edge conditions

4. LOADING THE STRUCTURE

The loading cases include:

- external pressures (still water and wave);
- internal pressures (hydrostatic, dynamic effect, safety pressure valve, sloshing, heeling);
- self gravity of the model;
- specific balanced boundary loads.

The section was modelled both with the pressure from the merchandise and the pressure on plating due to sea water.

- The static pressure of the merchandise (Figure 4)

The static pressure of the merchandise, P_{hys} is:

$$P_{hys} = \rho_{sw} g\left(T_{LC} - z\right), \text{ kN/m2} \quad (1)$$

where:

z - the vertical coordinate of loading point in [m] and it should not be higher than T_{LC} ;

$\rho_{sw} = 1{,}025 t/m^3$ - density of sea water;

T_{LC} - draft in m;

$g = 9{,}81 m/s^2$ - gravitational acceleration.

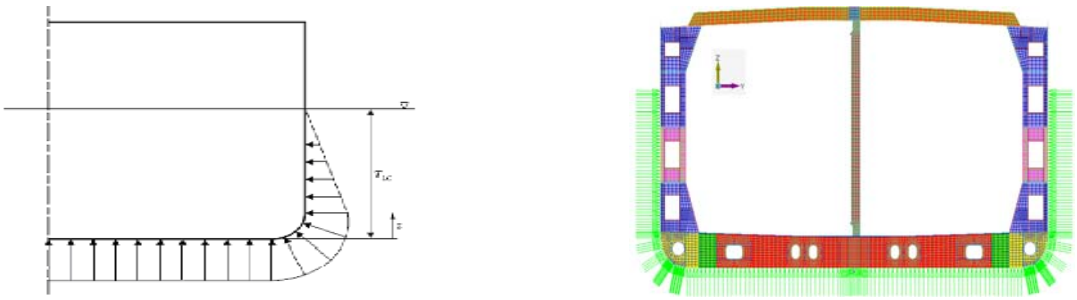

Figure 4 Hydrostatic watter pressure distribution

- The static pressure from the tank (Figure 5)

The static pressure of the merchandise, P_{in-tk}, is:

$$P_{in-tk} = \rho g z_{tk}, \text{ kN/m}^2 \quad (2)$$

where:

ρ - density of the merchandise in the tank, [t/m^3];

$g = 9{,}81 m/s^2$ - gravitational acceleration.

z_{tk} - vertical distance the highest point of the merchandise in the tank, [m];

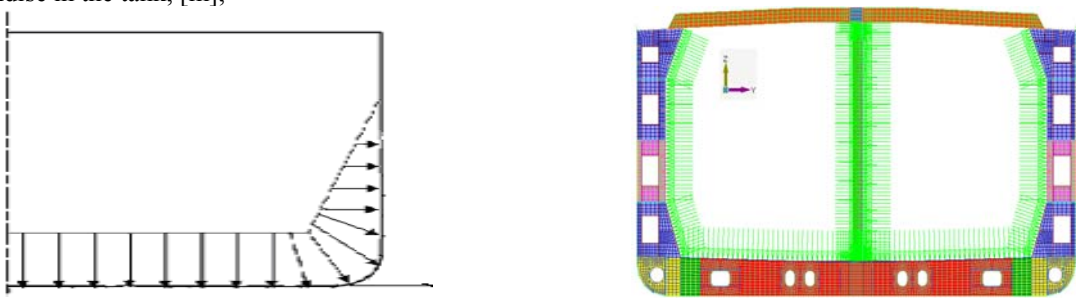

Figure 5 Hydrostatic cargo pressure distribution

4.1 L.C.1 – Alternate loading of cargo in holds

Ship on wave crest, maximum hogging bending moment (wave + static) obtained at middle of the structure.

The loading conditions for this loading case are:

- external hydrostatic pressures corresponding to Tmax (imported from Poseidon);
- external pressures due to wave crest (imported from Poseidon);
- internal pressures in the holds according to: GL Rules I-1-1, Sec.4, D1 (Figure 6);
- moments were applied at both ends of the structure in order to obtain the maximum bending moment (hogging - wave + static) at the middle of the structure.

For this loading case, significant results are expected for the shell plating, transverse bulkheads and stools, transverse rings, longitudinal girders.

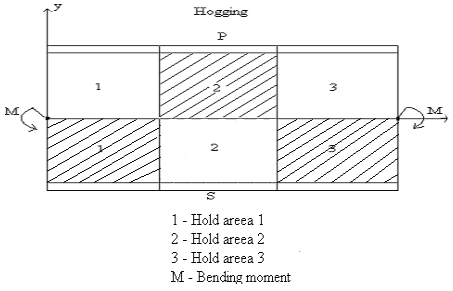

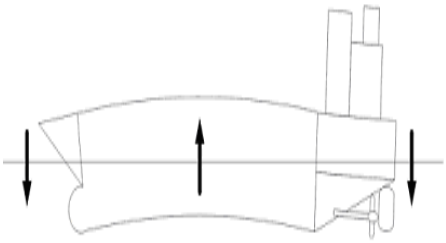

Figure 6 Hogging

4.2 L.C.2 - Homogeneous cargo in holds

Ship on wave trough, maximum sagging bending moment (wave + static) obtained at middle of the structure from all homogeneous cases.

The pressure calculation for this loading case is similar to loading case 1.

- external hydrostatic pressures corresponding to Tmin;
- internal pressures in the holds according to: GL Rules I-1-1, Sec.4, D1 (Figure 7);
- moments were aplied at both ends of the structure in order to obtain the maximum bending moment (wave + static - hogging) at the middle of the structure;
- the boundary loads were applied so that the model remains in equilibrium.

For this loading case, significant results are expected for the shell plating, transverse rings, longitudinal girders.

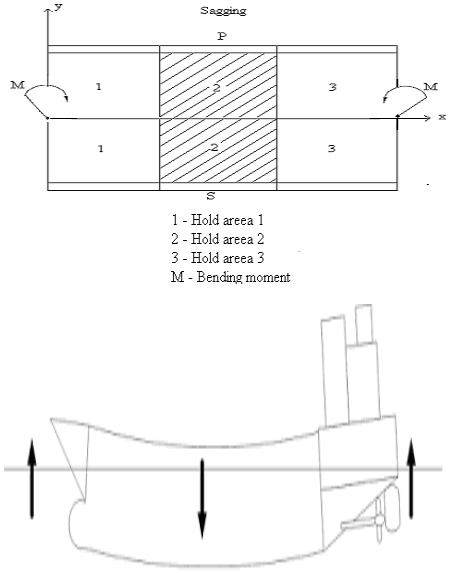

Figure 7 Sagging

5. CALCULATION AND EVALUATION OF THE RESULTS

The purpose of the 3D static analysis is to determine the overall structural response of the hull girder, and also to obtain appropriate boundary conditions for use in the 3D fine-mesh analysis of local structures.

Below we present the results obtained following the linear static analysis carried out for the ship loaded with merchandise and with the pressure of calm water.

These results are mainly charts with distribution of Von Mises stresses.

There is a color scale in the right of each figure, corresponding to stress levels plotted on each element of the structure represented. Stresses obtained correspond to the elements with the highest values of stresses.

Generally, one can say that, the edge conditions were chosen properly, reason for which there are no visible effects on the stress field.

The Figure (8-15) presents the distributions of Von Mises stresses for wave crest case and wave hole case.

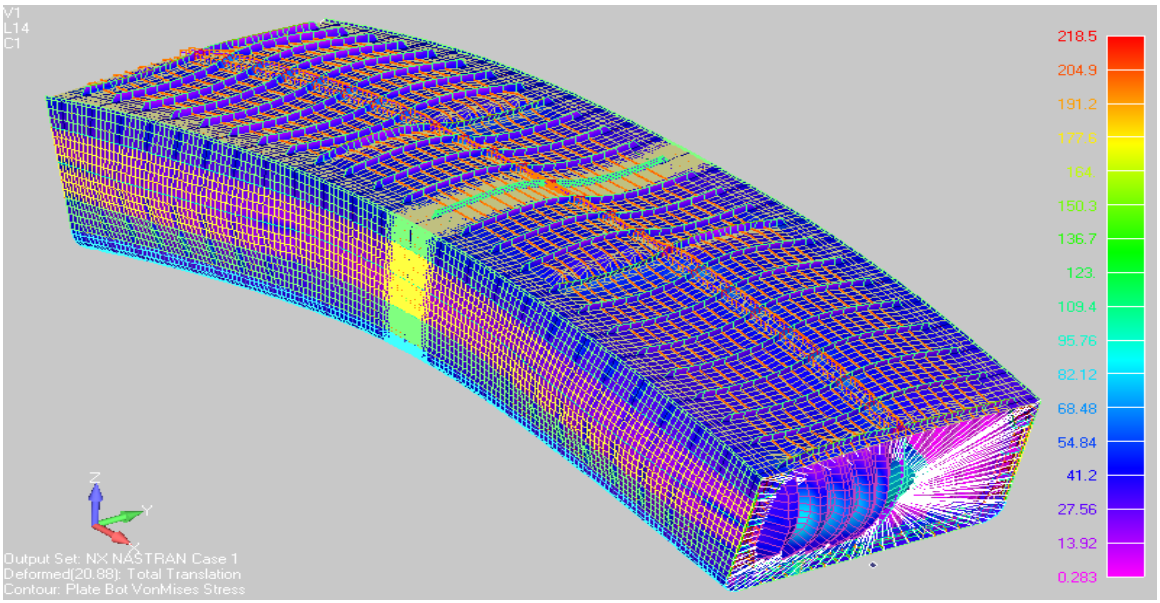

Figure 8 LC1 – Von Misses Stress – ½ + 1 + ½ model

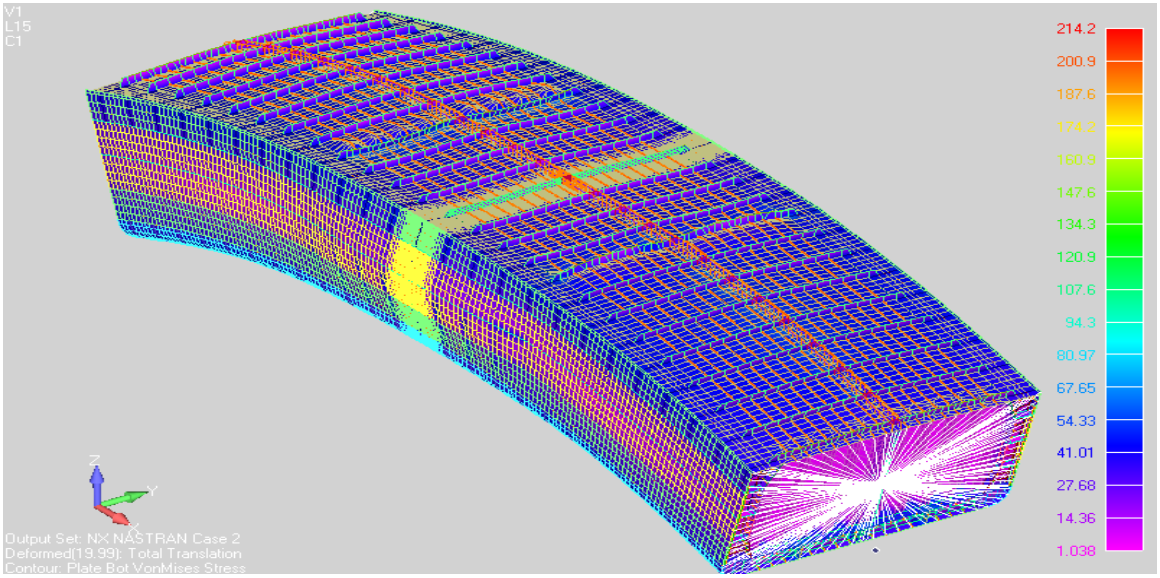

Figure 9 L.C.1 – Von Misses Stress – ½ + 1 + ½ model

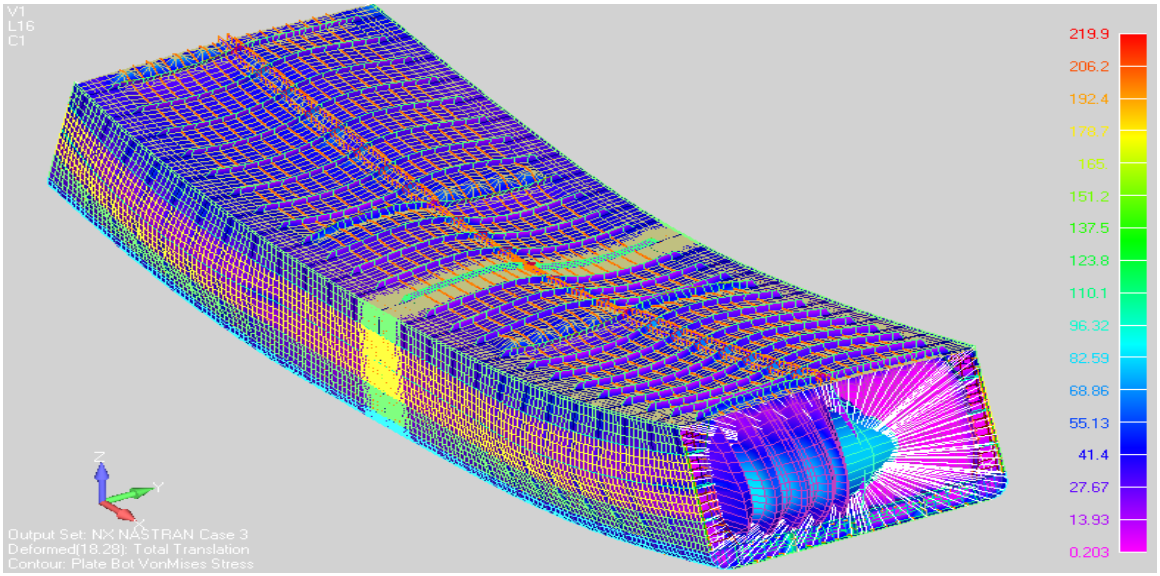

Figure 10 LC2 – Von Misses Stress – ½ + 1 + ½ model

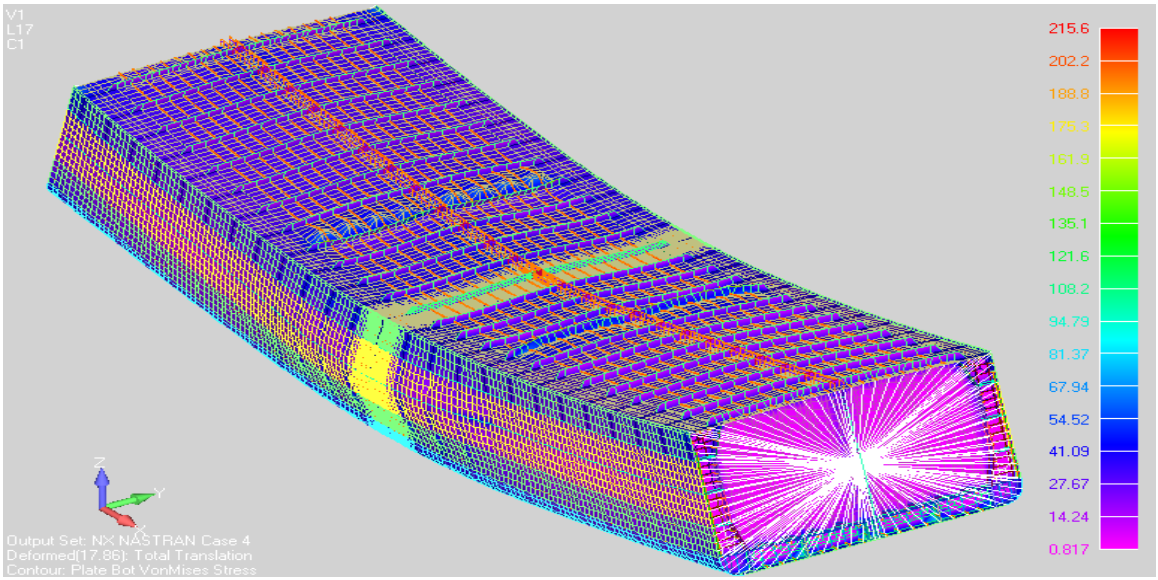

Figure 11 L.C.2 – Von Misses Stress – ½ + 1 + ½ model

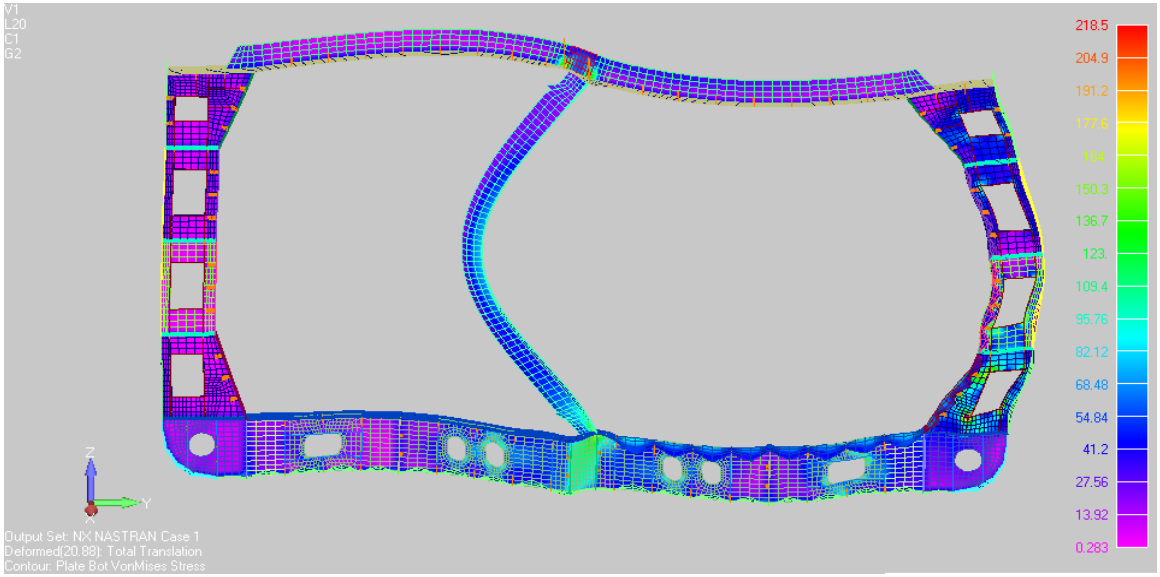

Figure 12 L.C.1 - Empty hold Tmax (wave crest) – Von Mises Stress [N/mm2]

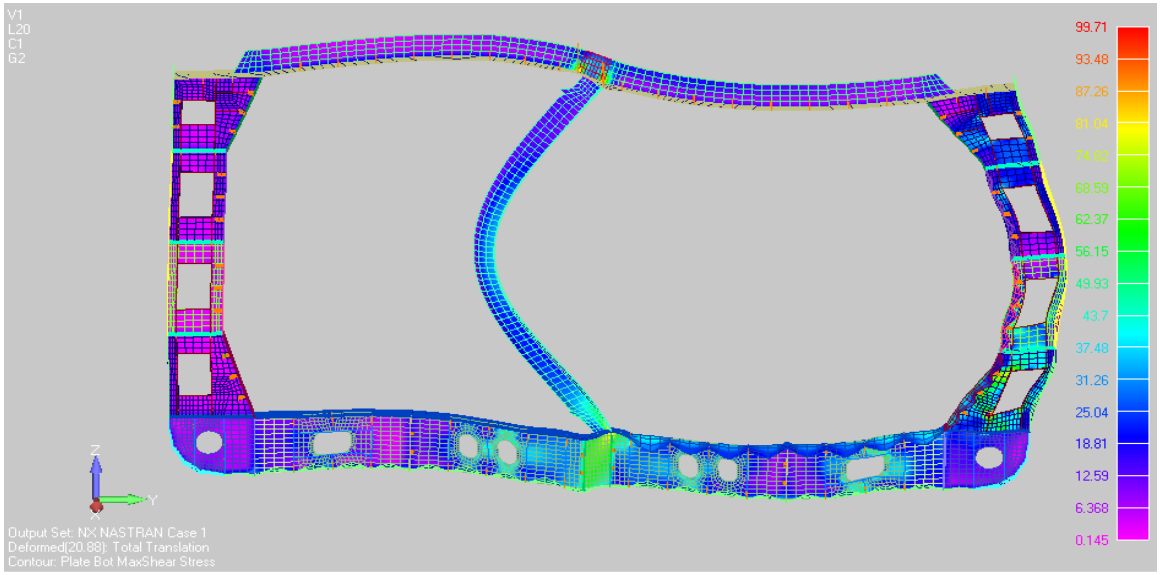

Figure 13 L.C.1 - Empty hold Tmax (wave crest) – Shear Stress [N/mm^2]

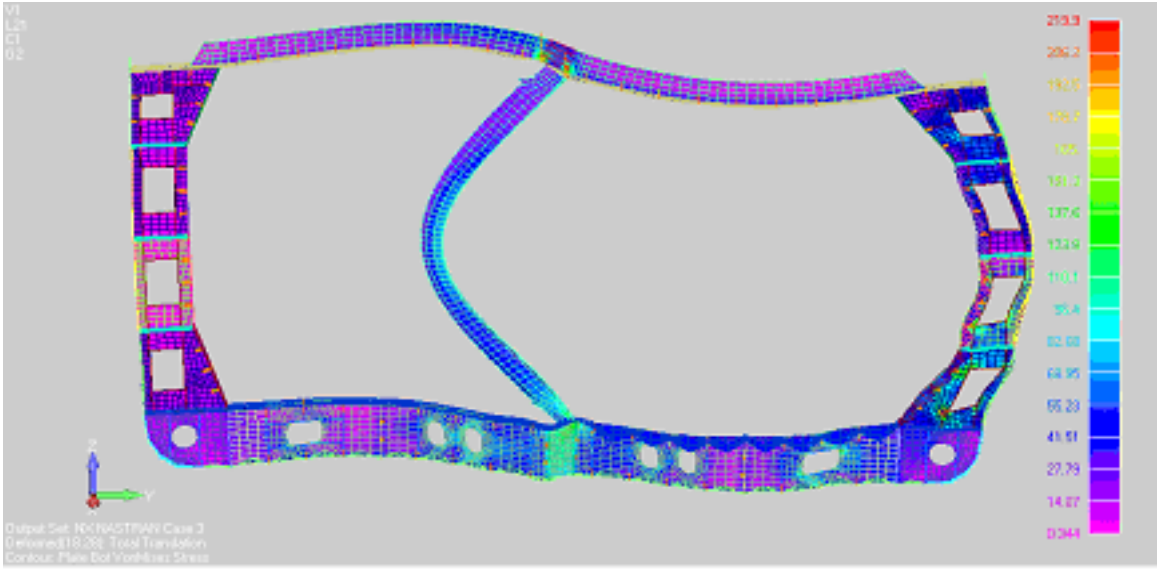

Figure 14 L.C.2 – Full hold ρ=1.025t/m^3; Tmin (wave trough) –Von Mises Stress [N/mm^2]

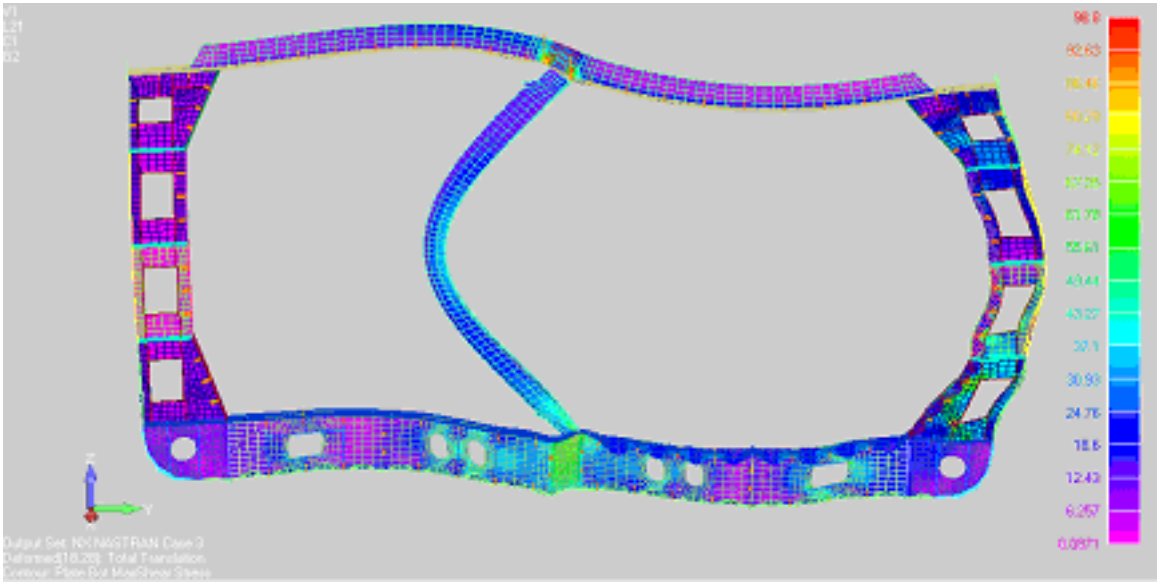

Figure 15 LC2 – Full hold ρ=1.025t/m^3; Tmin (wave trough) – Shear Stress [N/mm^2]

The Table also presents the total movements in the two cases studied.

Table 2 CAD-FEM characteristics of the model

Loading case	σvonMises_model	σvonM_model/σ_{adm}
1 – wave crest	94,29 N/mm^2	0,357
2 – wave hole	94,79 N/mm^2	0,359

As one can notice in the table, stresses are situated around the value of 95 N/mm2, and this shows that these values do not exceed the value recommended registry rules (264 N/mm2).

6. REFERENCES

[1] Domnişoru L., *Metoda elementului finit în construcţii navale. Aplicaţii*, Editura Editura Evrika, Brăila, 2003

[2] Domnişoru L., Găvan E., Popovici O., *Analiza structurilor navale prin metoda elementului finit,* Editura Didactică şi Pedagogică, Bucureşti, 2005

[3] **x x x** – FEMAP 9.3.1 / NX NASTRAN 5.0 User's Guide, UGS Corporation / Siemens PLM Software Inc., 2007

[4] Domnişoru L., *Analiza structurilor navale prin metoda elementului finit . Aplicatii numerice*, Editura Fundaţiei Universitare "Dunărea de Jos", Galaţi, 2009

GAMA RAY INTERACTION IN GERMANIUM WITH GEANT4

IONICA ROMEO

University "Politehnica" Bucharest, Romania

ABSTRACT

The aim of this work is as using AIDA implementation in Geant4 to analyze some characteristics of Compton interaction of gamma ray in germanium for incident energy of photons of 1-2MeV. So we verify starting points of algorithms for tracking reconstruction, both back-tracking and forward-tracking algorithms. We have generated a set constructed with interaction points and we found that this set scale with Hurst exponent 0.48.

Keywords: *Geant4, gamma tracking, Compton scattering.*

1. INTRODUCTION

In this work are reported results obtained simulating interaction of gamma photons in germanium (Ge), for incident energy in the interval 1-2MeV. The starting point was AIDA [1] implementation in Geant4 as a tool to obtain various physics analysis objects, as histograms, ntuples, etc. Using these objects we verify our previous simulation [2], and basic assumptions of some algorithms for tracking reconstruction of gamma trajectories. In the last decade a new generation of 4π photon spectrometers was developed [3-5], based on highly segmented Ge detectors, where the scattering path of each γ ray is identified and the full energy of the incident photon is recovered. Among high segmentation and pulse shape techniques, high-purity of Ge detectors, digital processing electronics, also tracking algorithms represent important pieces for these methods of reconstruction of gamma trajectories. Algorithms to reconstruct the trajectories of gamma rays can be classified as back-tracking algorithms and forward-tracking algorithms based on clusterisation [6-8]. Such algorithms use particular characteristics of gamma photon interactions, which will be analyzed in this work.

2. SIMULATION

The geometry used in simulation is a Ge cylinder, with the Z axis is oriented along of the height of the cylinder (used previously in another simulation [2]).The dimensions are: height = 150 mm, radius of the cylinder = 35mm. The gamma photons are emitted uniformly from the center of the cylinder in random directions.

For simulation was used Geant4.9.1 and Low Energy variant of electromagnetic processes. In the range of incident energy of 1-2MeV, the main physics processes of gamma interaction in Ge are Compton scattering, Rayleigh scattering (coherent scattering on atom), conversion of gamma in pair electron-positron and photoelectric interaction, but the dominant process is represented by Compton scattering.

In Figure 1 are plotted contributions of various interactions for 1MeV, and 2MeV incident energy. Rayleigh scattering is significant only at low energies, but contributes for all incident energies because the energy of the track is low at the end of the trajectories.

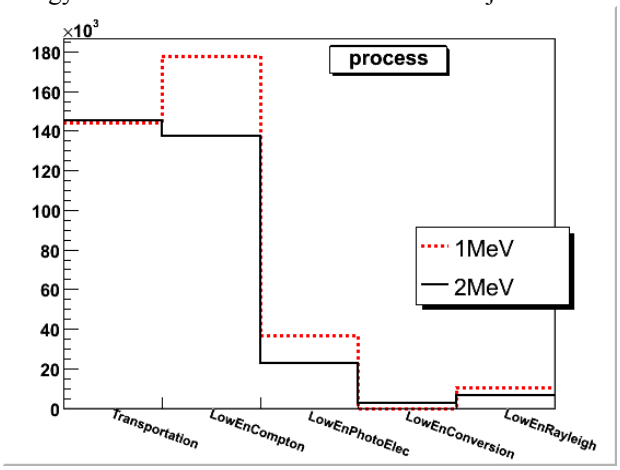

Figure 1. Interaction processes of gamma rays for 100000 events generated.

Transportation interaction is realised when gamma ray trajectories passes from one volume into another one volume (so it is a non physical interaction process).

Now we try to highlight the particular properties of the interaction of photons which underlie various tracking algorithms. Back-tracking algorithms start from the last point of the chain of interaction points, the point of photoelectric absorption. The guess of this point is based on the hypothesis that the photoelectric absorption in the chain is realized with incident photon energy between 100-250keV. Figure 2 presents energy then 10% of cases there are outside of the interval $[0,\alpha_0]$.

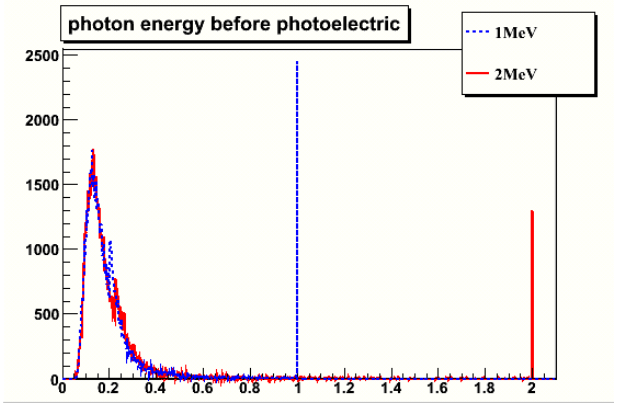

Figure 2. Photon energy before photoelectric interaction for gamma incident energy of 1MeV and 2MeV, normalized such that the bins integral is 100000.

distribution for photons just before photoelectric interaction, incident γ energy of 1MeV and 2MeV. Apart from photons which give only photoelectric interaction in Ge, the photoelectric interaction which follows after Compton interactions is realized at low photon energy, independent of incident γ energy.

In forward-tracking algorithms starting point is represented by clusterisation of interaction points according to their relative angular distance. For two interaction points i and j with angular coordinates (θ_i, φ_i), and (θ_j, φ_j), their relative angular distance is

$$\cos\alpha_{ij} = \cos\theta_i \cos\theta_j + \sin\theta_i \sin\theta_j \cos(\varphi_i - \varphi_j) \quad (1)$$

Because Compton interaction cross section is forward peaked and the mean path of photon is decreasing with energy, two interaction points are assigned to the same cluster if $|\alpha_{ij}| \le \alpha_0$ ($\alpha_0 = 0.15 - 1.0 rad$). Figure 3 presents relative angular distance distribution for points which belong to the same Compton chain, for various incident energies. Here, the origin of coordinate system is placed in the point where is placed the source (first point of the Compton chain). The width of the distribution is almost the same for both incident energies.

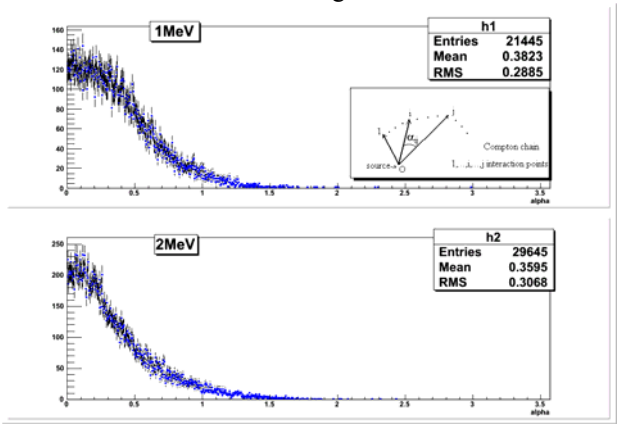

Figure 3. The distribution of angular distances of the same Compton chain is forward peaked, for 1MeV and 2MeV incident energy.

Table 1 presents percentage of cases with angular distances bigger then α_0 value. For $\alpha_0 \ge 0.8 rad$, less then 10% of cases there are outside of the interval $[0, \alpha_0]$.

Table 1. Percentage of angular distances in Compton chain with $\alpha_{ij} \ge \alpha_0$.

α_0 / E_{inc}	0.3	0.5	0.8	1.0	1.2
1MeV	53.8±0.6	28.6±0.4	9.3±0.2	4±0.1	1.3±0.1
2MeV	46.4±0.5	25.3±0.3	9.9±0.2	4.8±0.1	2.1±0.1

To see how this distribution is affected by errors in measuring position of interaction points, each interaction point was displaced in all directions (x, y and z) with quantities distributed after Gaussian distributions with mean=0, and standard deviation σ between 0.5mm and 5mm. Figure 4 presents distribution of angular distances of Compton chains for standard deviation σ=0.5mm and 5mm, for incident energy of 2MeV. The angular distances distribution depends of σ, so that the position of maximum and r.m.s. of the distribution rise with σ. The distributions for various σ were fitted with a Landau curve convoluted with a Gaussian. The Landau curve is the function *TMath::Landau(x, p0, p1)* from ROOT program's library, where *p0* parameter determines the most probable location of Landau distribution, and *p1* gives the width of the function.

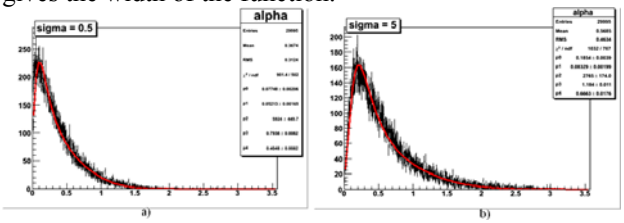

Figure 4. Distribution of angular distances for errors in position of interaction points distributed after a Gaussian with $\sigma = 0.5mm$ (part a) of the figure), and $\sigma = 5mm$ (part *b*) of the figure).

So, the 5 parameters fit function is

$$TMath::Landau(x, p0, p1) * p2 * \exp\frac{(x - p3)^2}{2 * p4}. \quad (2)$$

p2 is a scale parameter, *p3* is the mean of convoluted Gaussian function, and *p4* is sigma of this Gaussian.

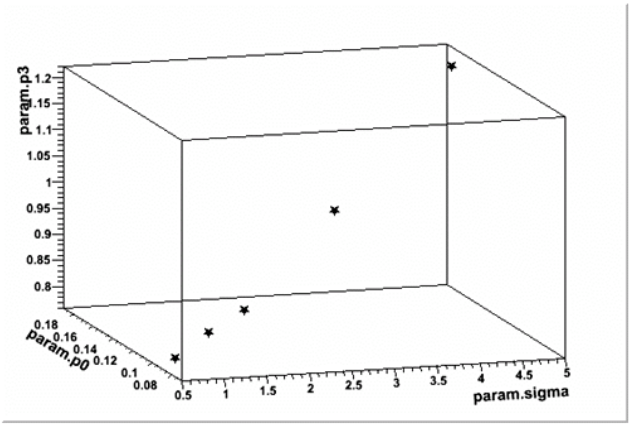

Figure 5. 3D representation of dependences of some fit parameters on standard deviation of interaction points errors.

Dependence between sigma width of errors distribution of positions for interaction points, *p0* and *par3* of the fit function is presented in Figure 5.

3. STEPPING SET

It was generated a set of points adding at the final point of the chain generated by the path of a gamma photon which undergoes Compton interaction in Ge (the last point is the last Compton interaction of photon in Ge cylinder) the chain generated in the next event: if $(X^f_{n-1}, Y^f_{n-1}, Z^f_{n-1})$ are the coordinates of the last point of the set generated previously, the points added in the set at the n-th event generated are $(X^1_n = X^f_{n-1} + x^1_n,\ Y^1_n = Y^f_{n-1} + y^1_n,\ Z^1_n = Z^f_{n-1} + z^1_n)$, …, $(X^i_n = X^f_{n-1} + x^i_n,\ Y^i_n = Y^f_{n-1} + y^i_n,\ Z^1_n = Z^f_{n-1} + z^i_n)$, where $(x^k_n, y^k_n, z^k_n), k = 1,...,i$ represent the coordinates of interaction points in Compton chain of this event. This set of points seams to be like the set obtained by fractional Brownian motion (the temporal step Δt corresponds now to interaction step in Geant4). Figure 6 presents evolution of this set when the number of events in the run is augmented (numerical values of distances are in mm, but this is not important now).

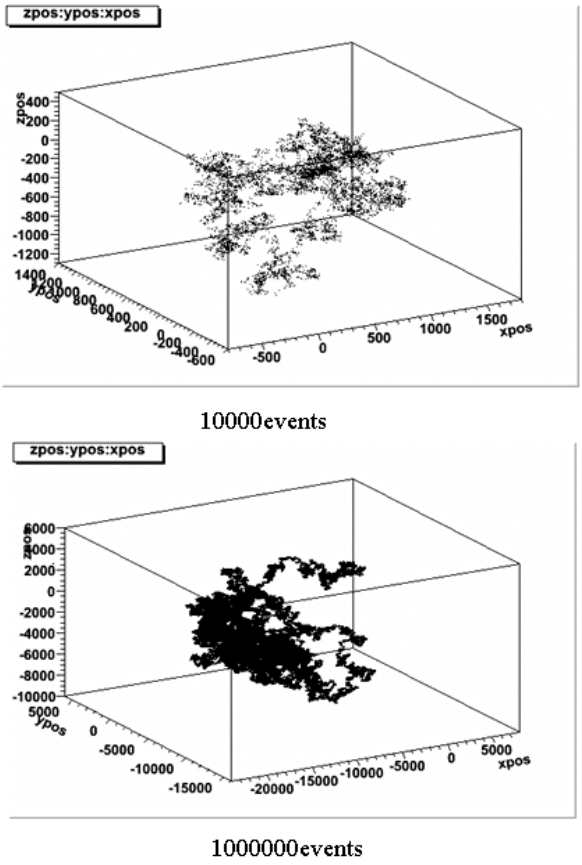

Figure 6. Stepping set for 10000events (up) and for 1000000events (bottom) generated.

A particular instance of the stepping set depends of the seed of the starting point of the simulation; however, statistical properties of this set depend only of the interaction (Compton process). To study statistical characteristics of this set it will applies methods used in the study of fractional Brownian motion [9].

Representing one coordinate of the ordered set of points of stepping set versus number n of the position in the set, we obtain a 'jerky' curve, analogouse of that obtained if we record position of a fractional Brownian motion at discrete time intervals, $\Delta t, 2\Delta t, \cdots, n\Delta t, \cdots$ and connect the observed points with straight line segments. In this last case, if take a pairs of points separated by the time interval T, the mean value of the absolute difference between the coordinates of the points, $< |\Delta X(T)| > = < |X(t+T) - X(t)| >$, depends of T as

$$< |\Delta X(T)| > \sim T^{\alpha} \qquad (3)$$

The exponent α is known as the Hurst exponent. It has a value between 0 and 1, with the value of 0.5 for the case of Brownian motion (also in the case of normal diffusion). The value of α of 0.5 separates qualitative difference between various motions. Values $\alpha \geq 0.5$ correspond to motions for which X(t) has the tendency to go outside of the initial region (this characteristic is known as persistence – the curve persists in its progression). For values $\alpha \leq 0.5$ the curve has tendency to turn back in the initial region (this characteristics is known as antipersistence).

In our case, the steps in time $\Delta t, 2\Delta t, \cdots, n\Delta t, \cdots$ correspond to steps in propagation of photon track in Geant4, $1, \cdots, n, \cdots$. Figure 7 presents X coordinates of points versus number of steps.

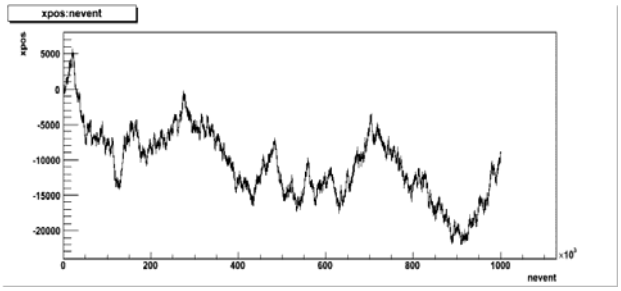

Figure 7. X trace: representation of X versus number of steps n, for 1000000events simulated.

If T represents a number of steps, we have tried to see how depends the mean absolute separation $<|\Delta X(T)|>=<|X(n)-X(n+T)|>$ depends of T as T^{α}, where α is Hurst exponent. As an example, Figure 8a presents $|X(n)-X(n+T)|$ for T= 80000. If we represent $\ln<|\Delta X(T)|>$ versus $\ln T$, the slope of the fit line is Hurst exponent α.

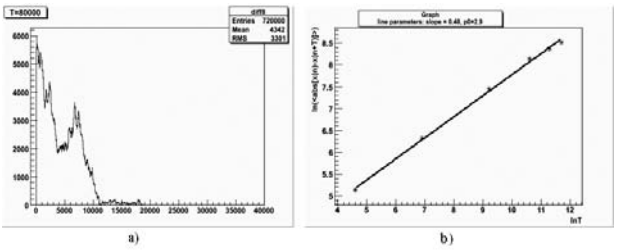

Figure 8. a) $|X(n)-X(n+T)|$ for T= 80000; b) log-log plot for Hurst exponent.

Figure 8b presents log-log plot to obtain Hurst exponent. We found $\alpha = 0.483 \pm 0.024$, like an antipersistent character, but 0.5 value of the limit persistent-antipersistent motion is still in the range of errors.

4. CONCLUSIONS

Simulation reproduces various characteristics of gamma interaction in Ge. Photoelectric interaction in Ge is realized at the end of Compton chain in a narrow interval, which permits that starting point in back-tracking algorithms to be selected with respect to interaction energy. The angular distances for points of a Compton chain are forward picked. Distributions depend of measuring errors of interaction points.

5. REFERENCES

[1] http://aida.freehep.org
[2] R. IONICA, Ghe. CATA-DANIL, "*Efficiency evaluation of a high resolution gamma spectrometer with Geant4*", UPB Sci. Bull., Series **A** vol **70,** Iss. 4, 2008,75-82.
[3] http://grfs1.lbl.gov/
http://www-win.gsi.de/agata/overview.htm
[4] M.A. DELEPLANQUE et al, ., *"GRETA:Utilizing new concepts in γ-ray detection",* Nucl.Instr.Meth. **A430**, 1999, 292-310.
[5] D. BAZZACCO, *"The Advanced Gamma Ray Tracking Array AGATA",* Nucl. Phys., **A746**, 2004, 248c-254c.
[6] A. LOPEZ-MARTENS, et al., *"γ-ray tracking algorithms: a comparison",* Nucl. Instr. Meth., **A533**, 2004, 454-466.
[7] J. van der MAREL, B. CEDERWALL, *"Backtracking as a way to reconstruct Compton scattered γ-rays",* Nucl.Instr. Meth., **A437**, 1999, 538-551.
[8] G. J. SCHMID et al., *"A γ-ray tracking algorithm for the GRETA spectrometer",* Nucl. Instr. Meth. **A430**, 1999,69-83.
[9] P. ADDISON, "*Fractals and Chaos"*, IOP Pubblishing, 1997.

NUMERICAL ANALYSIS OF THE AERODYNAMIC FORCES ACTING UPON A KITE USED AS AUXILIARY PROPULSION SYSTEM

[1]SCUPI ANDREI-ALEXANDRU, [2]DINU DUMITRU

[1,2]Constanta Maritime University, Romania

ABSTRACT

Air pollution caused by marine engines has increased during the last decades due to the rapid growth of shipping and to the improper operation of both ships and port equipment.

The unconventional naval propulsion system would solve some of the pollution problems posed by marine engines operation. This system also offers substantial fuel savings.

In the paper we simulate a kite used as auxiliary propulsion system. This simulation, performed with CFD (Computer Fluid Dynamics), was made for different working conditions by varying the incidence angle and the velocity at infinity. We also calculated total aerodynamic force, which projected on the water surface, gives us the force by which the ship is being towed (the component of the ship direction movement).

Kite simulation under different working parameters and calculation of forces acting upon the ship were achieved using a fluid flow computer modeling program (Ansys 12).

This unconventional propulsion system can be applied to commercial vessels and can also be used in various water sports such as kite-surfing.

Keywords: *kite, non-conventional propulsion.*

1. INTRODUCTION

Through his ability to discover, invent and create, man was found fit to make extensive and rapid changes to nature, to transform the environment in his favor and its fellow men. Lack of information led him to persist in actions that cause environmental damage, realizing that he himself had had a negative contribution in this respect.

He managed to bring environment to the stage in which pollution has become universal, reaching unlimited proportions and becoming one of the fundamental problems of mankind.

Although he attempted decades ago to fight against pollution, it has continued to expand. Some regulations should be taken so as to be able to meet the new environmental protection issues, which require a very good knowledge of the phenomenon, its development, and the factors that lead to its formation.

After having been thoroughly ignored for a long period of time, unconventional propulsion systems, that use Aeolian energy or electricity for propulsion, have become a present issue. One of the methods that have been already tested and is utilizing Aeolian energy, more precisely using the traction force of the wind in a kite rose to a certain height. The tests performed have presented us with a series of advantages compared with the classic sail cloths. [2]

We will consider an unconventional propulsion system – a kite. It will function as an auxiliary propulsion system contributing to saving the ship main engine fuel.

The calculation of aerodynamic forces that act upon a kite will help us weigh a solution to reduce pollution.

Kites are aerodynamic surfaces that raised to a certain altitude absorb a part of the wind power turning it into thrust.

Conditions to be satisfied by these kites to best propel the ship are:

- to be light and resistant to wind;
- to be dense, not to allow airflow to pass through it;
- to be impermeable;
- to have an aerodynamic profile.

Wind power acting upon kite produces a maximum effect when:

- kite's optimum position is oriented to the direction of the wind;
- the kite is giving maximum yield curve;

The drag and the lift force can easily be calculated using the following formulas [1]:

$$L = \frac{\rho}{2} C_z S v^2 \quad (1)$$

$$D = \frac{\rho}{2} C_x S v^2 \quad (2)$$

where:

L = lift force, perpendicular to the direction of airflow;

D = drag force, acting in the direction of airflow

S = body surface projected onto the plane that is tilted at an angle φ, against the wind;

v = velocity of airflow;

C_z, C_x = coefficient depending on the shape profile and the angle of inclination of the surface S to the direction of airflow (φ);

ρ = air density (at 1 atmospheric pressure and temperature 15^0C);

φ = angle of inclination of the surface S to the direction of airflow.

2. KITE SIMULATION

2.1 Kite characteristics

Main characteristics of the kite:

- Length 26.1 m;
- Width 7.0 m;
- Area 182.7 m^2;
- Thickness 0.7 m;
- Radius of curvature 15.0 m;
- Curvature 100^0.

The kite is represented in Fig. 1.

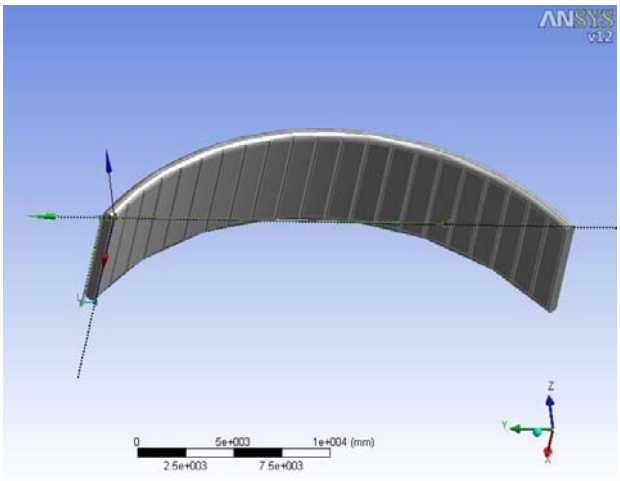

Fig. 1 Geometric representation of the kite

2.2 Kite discretization

After the geometric representation of the kite, we went to its discretization, shown in Fig. 2

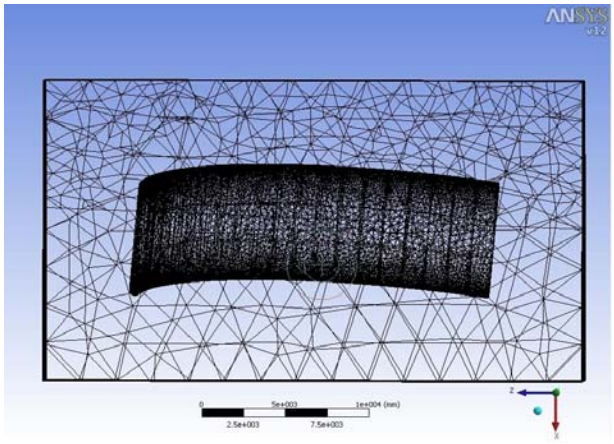

Fig. 2 Kite discretization

a) Scenario No.1

We first discretized the kite in approximately 200.000 cells, of which 180.000 are tetrahedrons and the rest are quadrilateral cells. There are also 35.000 triangular cells and the mesh has approximately 45.000 knots.

b) Scenario No.2

The second time we discretized kite in more than 3.7 million cells, of which 3.2 millions are tetrahedrons and the rest are quadrilateral cells. There are also 755.000 triangular cells and the mesh has approximately 900.000 knots.

2.3 Calculation of the aerodynamic forces for wind velocity 10 m/s.

Using Fluent program version 13.0, we put boundary conditions as follows:

- kite is attacked with a velocity of 10 m/s, under different angles, namely 0^0, 30^0, 60^0, 90^0,
- Behind the kite, atmospheric pressure is equal to 101325 Pa.
- The fluid motion is turbulent with a Prandtl number equal to 0.667.
- The air density is considered constant and it is equal to 1.225 $\frac{kg}{m^3}$;
- The air dynamic and cinematic viscosity are also considered constant and are equal to 1.7894 10^{-5} $\frac{kg}{ms}$, 0.0001460735 $\frac{m^2}{s}$, respectively;
- The turbulence viscosity ratio is set to 10.

a) For the Scenario No.1

Process has stabilized after 104 iterations allowing us to visualize the values of drag and lift forces that are presented in table 1.

Table 1 Results of drag and lift force for Scenario No.1

φ Incidence angle [^{0}]	D Drag force [N]	L Lift force [N]
0^0	35334.602	175.74034
30^0	25771.742	80.70095
60^0	12945.394	47.731575
90^0	5684.0103	11.345189

Velocity distribution from two different planes that intersects the kite is given in Fig. 3 and in Fig. 4.

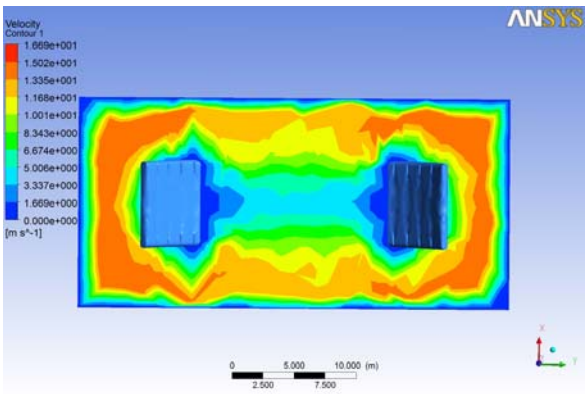

Fig. 3 Velocity distribution – longitudinal plan (Scenario No.1)

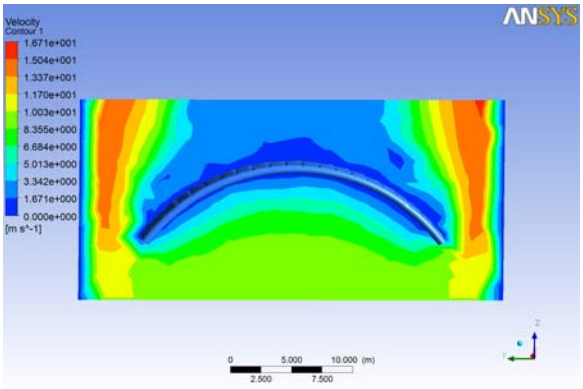

Fig. 4 Velocity distribution – transversal plan (Scenario No.1)

As shown in Fig. 3 and 4, for the Scenario No.1 velocity varies between 0 m/s and 16.6 m/s.

b) For the Scenario No.2

Process has stabilized after 575 iterations allowing us to visualize the values of drag and lift forces that are presented in table 2.

Table 2 Results of drag and lift force for Scenario No.2

φ Incidence angle [^{0}]	D Drag force [N]	L Lift force [N]
0^0	27398.592	46.10791
30^0	19294.783	25.33467
60^0	8770.355	13.85246
90^0	3579.736	8.43421

Velocity distribution from two different planes that intersects the kite is given in Fig. 5 and in Fig. 6.

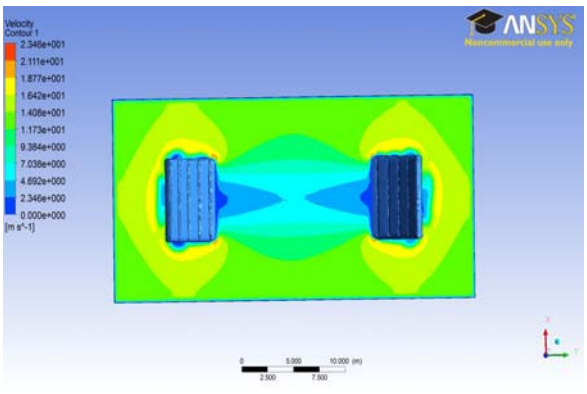

Fig. 5 Velocity distribution – longitudinal plan (Scenario No.2)

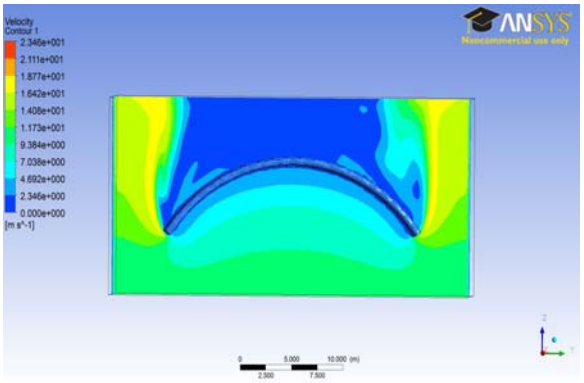

Fig. 6 Velocities distribution – transversal plan (Scenario No.2)

As shown in Fig. 5 and 6, for the Scenario No.2 velocity varies between 0 m/s and 23.46 m/s.

2.4 Calculation of the aerodynamic forces for wind velocity 20 m/s.

For the Scenario No.1 we also calculated the drag and the lift force when the kite is attacked with a velocity of 20 m/s.

The results are presented in table 3.

Table 3 Results of drag and lift force for Scenario No.1 (velocity is set to 20 m/s)

φ Incidence angle [^{0}]	D Drag force [N]	L Lift force [N]
0^0	141125.17	604.49036
30^0	103386.95	513.85455
60^0	52001.926	158.20213
90^0	22502.57	20.95566

Velocity distribution from two different planes that intersects the kite is given in Fig. 7 and in Fig. 8.

Velocity distribution from two different planes that intersects the kite is given in Fig. 7 and in Fig. 8.

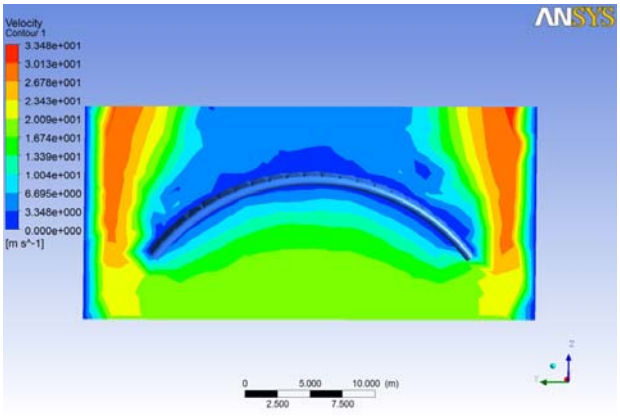

Fig. 7 Velocity distribution – longitudinal plan (Scenario No.1, velocity equals to 20 m/s)

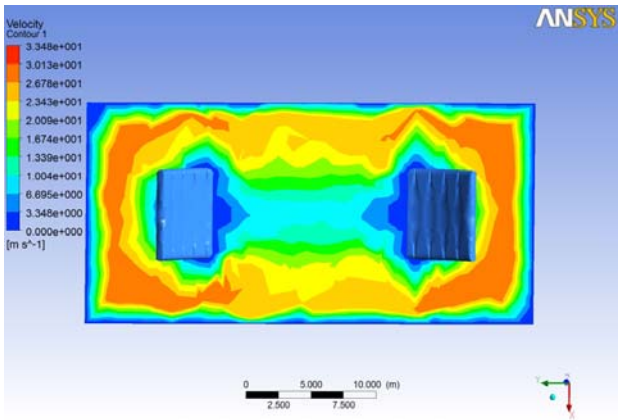

Fig. 8 Velocity distribution – transversal plan (Scenario No.1, velocity equals to 20 m/s)

As shown in Fig. 5 and 6, for the Scenario No.2 velocity varies between 0 m/s and 33.34 m/s.

3. CONCLUSIONS

Finite Element Analysis is a method to solve the mathematical model and to simulate the complex phenomena of Fluid Mechanics.

Therefore the person who uses a simulation program of a real physical phenomenon by finite element method using computer must well understand the physical processes that take place and to be able to correctly interpret the data that the computer has to offer. As seen from the data in Tables 1 and 2 that give us the result of drag force, when the kite is attacked with a speed of 10 m / s at an incidence angle of 0 degrees, the drag force decreases from approximately 35,000 N to 27,000 N, because in Scenario No. 2 the discretization kite is more detailed. A graphical representation of the variation of drag force is given in Fig 9.

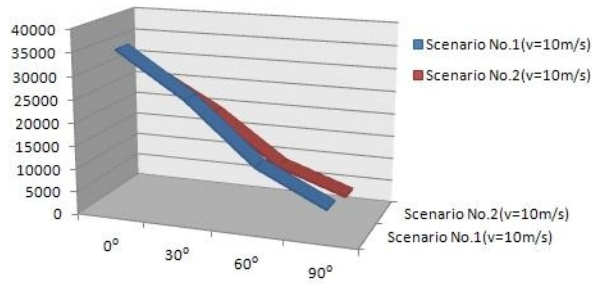

Fig. 9 Variation of drag force

Also, comparing the results of Scenario No. 1 when kite is attacked with different velocities (10 m/s and 20 m/s), we notice that the drag force increases with the velocity square, according to relation (2).

We conclude that that kite propulsion has good results and its use together with the main engine propulsion means a new opportunity considered unconventional up to now.

A representative graph is given in Fig 10.

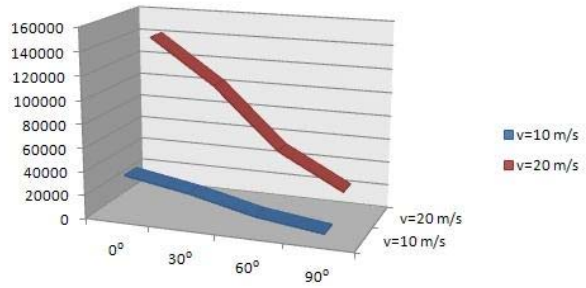

Fig.10. Variation of drag force

4. REFERENCES

[1] DINU, D., *"Mecanica fluidelor pentru navalisti"*, Ed. Nautica, 2010.

[2] GROŞAN, N., DINU, D *"Considerations regarding Kite Towed Ship's Maneuvering"*, The 3rd International Conference on Maritime and Naval Science and Engineering (MN 10), Constanta, 3-5 September 2010.

THE NUMBER OF LAYERS INFLUENCE FOR COMPOSITE MATERIALS SUBJECTED TO FATIGUE AT THE REQUEST OF FORCE BREAKING TO AXIAL LOAD

[1]TOCU FLORENTINA, [2]MOCANU COSTEL-IULIAN, [3]LEFTER SILVIU-VIOREL

[1,2] University "Dunarea de Jos", Faculty of Naval Architecture, Galati, [3]SC Metchim SA Galati, Romania

ABSTRACT

Fiberglass reinforced polyester (GRP) is the most used composite material in ship building industry and required a careful study when we talk about the mechanical characteristics and theie resistance to fatigue. The main objective of this work was to study the number of layers influence for composite materials subjected to fatigue at the request of force breaking to axial load. It was observed that the tests made to fatigue and then to traction have an real influence at the mechanical characteristics. The force break on traction is much larger of unsolicited specimens than those specimens tested to fatigue.

Keywords: *Composite Materials, Fatigue, Mechanical Characteristics, Fatigue - Variable Load*

1. INTRODUCTION

By definition, composite materials are made of two or more components. Their mechanical properties complete each other, this leading to a material that has superior mechanical properties comparing to its components. Composite materials are the first ones of which structure is conceived entirely by the human hand, not only in their molecular structure but in every way that their destination requires.

These materials have programmable properties and this way they have replaced traditional materials and have penetrated in many top industrial branches such as: aerospacial engineering, automobile manufacturing industry and electronics industry.

A common field of their application between others is the ship building industry. The use of composite materials in this branch is justified by the ship owners' desire to replace steel or other metallic materials used so far. Therefore, the most used composite material in ship building industry is the fiberglass reinforced polyester known as GRP.

Glass fibbers currently used in composites production have relatively high-strength and high modulus. Some types of glass fibbers have high heat resistance or particular dielectric characteristics.

The damage evolution mechanism is one of the important focuses of fatigue behaviour investigation of composite materials and also is the foundation to predict fatigue life of composite structures for engineering applications. As known, the fatigue damage and failure mechanism of composites is more complex than that of metals and four basic failure types will occur in composites under cyclic loading, which are matrix cracking, delaminating and fibber breakage.

As we know the fatigue phenomenon consist in changed the characteristics and properties of one material who is liable to repetitive load.

The variable load shall be classified in the following categories in: random load, and periodic load.

For asymmetry coefficient size should be classified in: symmetric cycles (where $\sigma_{maz} = -\sigma_{\min}, \sigma_m = 0,$ $\sigma_A = \sigma_{maz}$) *and* $\rho = -1$ and asymmetric cycles $(\rho \neq -1)$.

For stress algebraic signs should be classified in: alternating cycles (the stress change sign), and oscillatory cycles (stress keep the sign).

The mechanical properties reveal how the material respond to the mechanical stress.

The most important mechanical characteristics, used in the engineering calculations are: resistance to breaking, yield, hardness, tenacity, elongation and breaking bottleneck (all this is defining the material ductility). Sometimes, in specific cases, is necessary to determine the impact resistance, fatigue, wear resistance.

The determination of mechanical characteristics allow to estimate the products exploitation, by quantifying the resistance to testing.

2. MATERIAL DESCRIPTION

This study involved two unidirectional hand lay-up composites manufactured in Spat company from Galati.

As we know the fibbers orientation of composite materials can be: one-way, two-ways or three-ways.

We used two way fibbers orientation, figure 1.a, and the percentage of glass fibber in mass composite was 62%.

As we know if the percentage of glass fiber increases automatically increases the material characteristics.

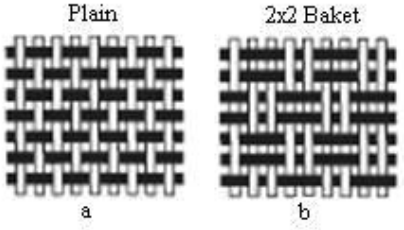

Figure 1. Fibbers Orientation

Composite materials reinforced with fiberglass for shipping industry are divided in two categories called "E" and "S" and is depending on which is made the fiber. Material type „E" are the most commonly used in construction plates, especially because of good water resistance properties.

Table 1. The characteristics of fibers

Name	Fibber diameter (μm-10^{-6} m)
C	4.57
D	5.84
DE	6.35
E	7.11
G	9.65
H	10.57

The „E" type material are the most commonly used in construction plates, especially because of good water resistance properties.

In the following studies resulted the mechanical characteristics of fiber reinforcement, see table 2.

Table 2. Mechanical characteristics

Type	Density (gr/cm^3)	Tensile stress (MPa)	Elasticity Module (MPa)
E	2.60	3450	7240
S	2.49	4500	8687

3. EXPERIMENT DESCRIPTION

The main objective of this work was to study the number of layers influence for composite materials subjected to fatigue at the request of force breaking to axial load.

Firs of all it was made four types of specimens with different thicknesses, figure 2 and table 3.

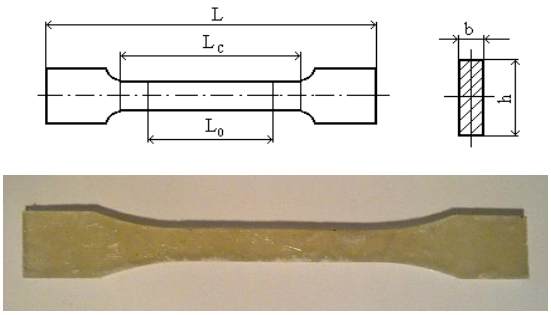

Figure 2. Specimens dimension

Table 3. Specimens dimension [mm]

Type	b	L	L_c	h
T1	1.34	150	115	9.96
T2	2.16	150	115	9.83
T3	2.98	150	115	9.99
T4	5.13	150	115	10.08

Before being subjected to traction these samples were tested to fatigue, this experiment was performed on a test machine, specially built for testing composite materials, figure 4.

The stress used with fatigue machine a pulsating with an symmetrical alternating cycle.

The machine is composed by the following constructive elements:

Figure 3. Fatigue machine

Engine, mechanical counter, probe support, amplitude measurement and control instrument, figure 3.

The first set of tests was composed of four samples that were subjected to fatigue to a certain number of cycles, table 4.

Table 4. Number of cycle

Type	Thickness [mm]	Number of cycle [N_b]
T_1	1.2	$6 \cdot 10^7$
T_2	2.2	$7 \cdot 10^9$
T_3	3.6	$3 \cdot 10^8$
T_4	5.15	$2 \cdot 10^6$

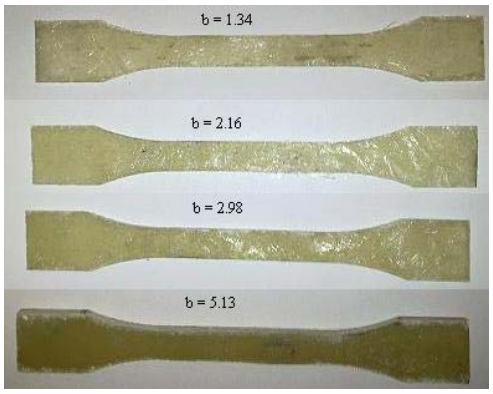

Figure 4. Specimens tested

Along way the experiment were also made some observations, the behaves of specimen made of GRP at the fatigue test.

The first specimen tested in fatigue after a number of 6 x 10^7, did not have any cracks or damage, this has led to testing the specimen number two, but it was intervened by attaching some metal plates for fixing the specimen in probe support.

For the second specimen, T_2, it was noted the first cracks appeared in the resin, at a total of 10^6 cycles.

Test specimens T_3 and T_4 was performed in the same way as for specimen two, the difference was the

thickness of the specimens. During the time it was observed that at 5 x 10^4 cycles the cracks was appeared in the structures, much earlier than the test with piece two, figure 5, figure 6.

Figure 5. The thickness of specimens.

Table 7. Longitudinal modulus E (Young) for samples tested to fatigue

Samples tested to fatigue	Longitudinal elastic modulus E (Young) [Pa]
T_1	5.3725e+09
T_2	6.1384e+09
T_3	4.3472e+09
T_4	3.5470e+09

Figure 6. The first cracks specimen two.

For test two of specimen T_{11} - T_{41} was considered the same test but with 10^{-1} number of cycles smaller then first, table 5.

Table 5. Number of cycle for test two

Type	Thickness [mm]	Number of cycle [N_b]
T11	1.27	$6 \cdot 10^6$
T21	1.95	$7 \cdot 10^8$
T31	2.99	$3 \cdot 10^7$
T41	4.72	$2 \cdot 10^5$

In order to compare the mechanical characteristics of fiberglass reinforced polyester who was tested to fatigue and the same mechanical characteristics of material not tested to fatigue it was made a series of mechanical measurements: longitudinal modulus E (Young)

The longitudinal modulus E (Young) mechanical properties are shown in table 6.

Table 6. Longitudinal modulus E (Young) for unsolicited samples

Unsolicited samples	Longitudinal elastic modulus E (Young) [Pa]
T_1	5.9414e+09
T_2	5.7382e+09
T_3	5.2411e+09
T_4	4.2332^e+09

4. RESULTS

After application of two sets of specimens one fatigue has worked in the laboratory and we tried this specimens to traction. The breaking speed was 0.1 m/s.

The test machine is a universal TESTOMETRIC M 350 - 5AT de 5KN, with electric drive, and mechanical clamping jaws. Data processing was done with V.3.5.5 Wintest Analysis, figure 5.

Tensile test were performed in the LCMP.

First time were tested specimens unsolicited to fatigue. Was observed the breaking strength was different depending on the thickness of each specimen, figure 6.a, 7.b.

Figure 5. Test machine

Figure 6.a. Breaked specimen

Figure 7.b. Breaked specimen

As can be seen breaking strength for the three cases are different, for fatigue specimens tested at the breaking strength up to 10^9 breaking strength is less than the amount, and for unsolicited specimens the breaking strength are much higher.

Table 8. Unsolicited samples 10^0 cycles

Number of layers	Thickness	Force - Breaking
[layers]	[mm]	[N]
1	1.34	1035.30
2	2.16	1520.29
3	2.98	2418.60
4	5.13	4600.38

Table 9. Samples tested to fatigue until 10^8 cycles

Number of layers	Thickness	Force - Breaking
[layers]	[mm]	[N]
1	1.27	673.50
2	1.95	1421.60
3	2.99	2127.40
4	4.72	4200.61

Table 10. Samples tested to fatigue until 10^9 cycles

Number of layers	Thickness	Force - Breaking
[layers]	[mm]	[N]
1	1.2	405.98
2	2.2	659.41
3	3.6	1130.56
4	5.15	2308020

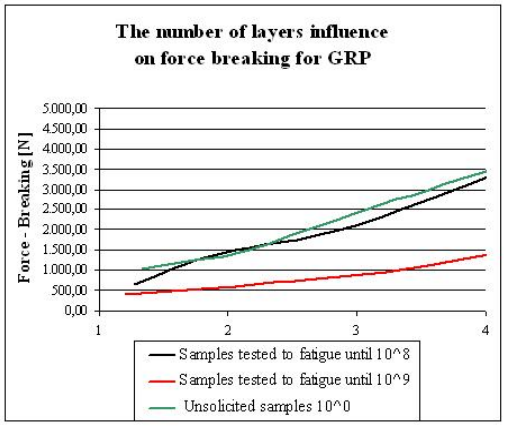

Figure 8. The number of layers influence on force - breking diagram

Table 11. Force – Break for all specimens

Set	Force - Breaking [N]		
	Unsolicited samples 10^0	Samples tested to fatigue until 10^8	Samples tested to fatigue until 10^9
1	1035.30	673.50	405.98
2	1520.29	1421.60	659.41
3	2418.60	2127.40	1130.56
4	4600.38	4200.61	2308.20

5. CONCLUSIONS

As can be seen from table 11 and figure 8 the number of cycles of fatigue loads increase is resulted their lower-breaking strength.

This was expected, interesting considering is that we would expected that the variation of breaking force to be linear. As seen in figure 7 it is not linear.

Experimental results suggested that the difference in the damage development mechanisms were caused by the different elastic response to the loading resulting in the localized or delocalized damage accumulation depending on the loading mode and interval time. The different damage development mechanisms, in turn, affect the absorption of loading energy resulting in the different fatigue life.

6. ACKNOWLEDGEMENTS

The present study has been performed in the frame of the PhD program POSDRU 88/15/S ID-61445– EFICIENT grant of the „Maritime" University of Constanta, 2010.

7. REFERENCES

[1] L. TONG, A.P. MOURITZ and M.K BANNISTER., *„3D Fibber Reinforced Polymer Composites"*, Elsevier Science Ltd, London, 2002

[2] C.I. MOCANU., *„Strength of materials"*, Zigotto Publisher, 2007

[3] BROUTMAN LJ, SAHU S., *„A new theory to predict cumulative fatigue damage in fiberglass reinforced plastics"*, Composite materials: testing and design (second conference). ASTM 497; 1972

[4] JORIS D, PAEPEGAM WV., *„Fatigue damage modeling of fiber reinforced composite materials"*, Appl Mech Rev, 2001

[5] TSAI SW., *„Composite design"*, 4th ed. Think Composites, 1988.

[6] LEE J, HARRIS B, ALMOND DP, HAMMETT F., *„Fiber composite fatigue life determination"*, Composite A, 1997

[7] WIRSCHING PH, YAO JTP. *"Statistical methods in structural fatigue"*, J Struct Div Proc ASCE 1970:1201–19.

CONSIDERATIONS REGARDING THE USE OF THE PENETRATION METHOD IN THE GEOTECHNICAL RESEARCH OF OVERLAND COMMUNICATING WAYS

[1]VOICU CRISTINA, [2]MIREA MONICA, [3]CIOPEC ALEXANDRA, [4]COSTESCU CIPRIAN

[1,2,3,4]„Politehnica" University of Timisoara, Civil Engineering Faculty, Department of Land Communication Ways, Foundations and Survey, Romania

ABSTRACT

In the beginning, the authors synthetically present some particularities of the geotechnical research for overland communicating ways. Next, the article presents some geotechnical investigation works conducted on two major road objectives in the Banat area (the Nădlac-Arad-Timişoara highway and the Timişoara bypass road), for which the penetration method has been successfully applied. Also contained in the article is an example of use of the penetration method for a landslide on DN57. The use of this method helped establish the sliding surface. In its conclusion, the article presents the main technical and economical advantages of the use of the penetration method in the geotechnical research of overland communicating ways.

Keywords: *geotechnical investigations, penetration method, landslide analysis, foundation ground.*

1. INTRODUCTION

Unlike other engineering works with smaller extent, on the layout of an overland communicating way the probability of a geological and geotechnical diversity is much higher; several areas with difficult terrains can appear (compressible, prone to moistening, with high swelling and contraction values, with high frost sensitivity, sliding etc.) Although the total land required is relatively small in size, the functionality and viability of the roadway can be heavily negatively influenced by the behaviour of the ground in adjacent areas (e.g. the case of adjacent potentially unstable slopes, of areas liable to flooding etc.) In such situations, the geotechnical engineering aspects must be thoroughly elaborated, as they have a crucial role in the adopted technical solutions and in the appreciation of the behaviour mode of the communicating way.

However, in the design and execution of overland communicating ways, including some modernization and rehabilitation works, in most of the cases, the type of soil on the route is of interest not only as a foundation ground, but also as a construction material for embankments. This underlines the need of a vast knowledge of the soil from the geotechnical point of view.

Practice has proven that neglecting the geotechnical aspects (by not conducting or conducting an insufficient study or by a superficial geotechnical design) leads to degradations of the communicating ways or of the respective engineering structures. The reparation of these degradations usually costs more than it would have cost to conduct complete geotechnical investigations, before the design process.

The geological-technical and geotechnical investigation program, comprising of the volume and nature of the research, as well as their placement along the communicating way, is established by the designer together with specialists in engineering geology and geotechnics, depending on the designing phase for which the investigations are conducted, on the existing knowledge regarding the prior behaviour of the soils in the area and on the particularities of the engineering work.

For the road, highway and railway routes, geological-technical and geotechnical research are programmed and executed before the following design stages:

- the feasibility study, when the conducted investigations target the collection of necessary geological-technical and geotechnical data for the establishing of possible routes and their economic evaluation
- the technical project, in which the geological-technical and geotechnical conducted investigations need to provide all the necessary data in order to establish the final technical solutions
- execution details, in which the investigations are realized in depth in order to obtain additional data for the adopted technical solutions, especially on more difficult road sectors or for engineering structures of the communicating ways

The stages of geological-technical and geotechnical studies and research for the overland communicating ways are the same as for other construction types. They comprise of soil identification, surface and in depth exploring of the ground, "in situ" and laboratory geotechnical determinations.

For overland communicating ways, as they are of important lengths, the way in which the identification of the soil is realized is very important. If professionally conducted, it can provide a lot of useful information which can aid in choosing the variants and elaborating the investigation program for the following stages.

2. GEOTECHNICAL INVESTIGATIONS CONDUCTED THROUGH PENETRATION ON THE ROUTES OF OVERLAND COMMUNICATION WAYS IN BANAT AREA

Through the Department of Overland Communication Ways, Foundations and Surveying at the "Politehnica" University in Timişoara, the authors have conducted geotechnical investigations and studies for some important objectives in Banat like the highway sector Nădlac-Arad-Timişoara and the Timişoara bypass road.

The conducted geotechnical investigations were based on a program, which was elaborated with regard to effectual geotechnical guidelines, regarding the nature of the soil, the destination of the investigated area (for the route of the communicating way or for respective engineering structures), as well as the designing phase for which the geotechnical study was elaborated.

The geotechnical in-depth investigations were conducted both through geotechnical borings and dynamic cone penetration surveys, placed according to the investigation program, realized after the identification of the routes.

On the sectors dedicated exclusively to the communicating way, the team conducted borings with Φ 2", which provided undisturbed samples, in order to establish the nature of the soil and its classification into one of the categories P1...P5 (according to granularity and plasticity indexes).

On the sites dedicated exclusively to engineering structures (bridges, passageways etc.), the team also conducted borings with Φ 7" and depth of 10...13 m for the exhaustion of the active area, which also provided clean samples. These were necessary in order to establish in the laboratory some geotechnical characteristics to aid in the evaluation of the foundation conditions of these buildings.

Dynamic penetration surveys were conducted with regard to effectual technical legislation [5], using both the light dynamic penetrometer (LDP) and the middle dynamic penetrometer (MDP).

Table 1 presents the geotechnical investigations conducted on the two aforementioned sites.

Aligment		**Borings**				**Penetrations**			
Project name		Φ 2"		Φ 7"		LDP		MDP	
	Length [km]	No.	Depth [m]	No.	Depth [m]	No.	Depth [m]	No.	Depth [m]
Highway sector Timisoara - Nadlac	89.05	95	3.5-6.0	-	-	136	3.0-5.7	-	-
By – pass Timisoara	12.70	24	3.0-5.0	6	10.0 - 13.0	24	2.8-5.5	13	10-12

For the reduction of the number of geotechnical borings, which are expensive and difficult to conduct, their placement was made on a distance of 500...1000 m, while dynamic cone penetration surveys (easier, quicker and less expensive to execute) were realized in between.

Near the geotechnical borings the team conducted penetration surveys; the resulting variation diagrams of the ground resistance are considered of reference. Additionally, guidance values for some geotechnical characteristics (which could not be determined in the laboratory on unclean samples) were established.

The processing of the primary data obtained through penetration surveys (namely the number of penetrometer hits for a penetration on an equidistance of 10 cm) has been conducted with regard to two aspects:

- the verification of the ground homogeneity between the geotechnical borings
- obtaining of guidance values for geotechnical parameters, necessary for the characterization of soils present in the ground stratification

The verification of the soil homogeneity between geotechnical borings was realized by comparing the penetration diagrams of the surveys executed between the geotechnical borings to the reference diagrams of surveys in line with adjacent borings. Thus, a penetration diagram allure close to the reference diagram certifies a stratigrafic column similar to the one in the boring, the soils in the penetration survey also have the geotechnical parameters with values similar to reference values, determined by laboratory investigations on probes from the respective survey.

In the areas where the penetration diagram allure was different from the two adjacent reference diagrams, supplementary geotechnical borings were executed in order to establish the stratigrafic column and some geotechnical characteristics on the obtained samples.

Because the borings with Φ 2" only provided unclean samples, part of the geotechnical parameters (which need to be determined on clean samples) were determined based on penetration resistance values, by using certain empirically obtained formulae [2][5]. As these formulae were obtained through statistic processing of experimental data, their viability is relative; they have been used by extrapolation, thus the obtained geotechnical parameters are to be taken as guidelines and are useful for characterizing soils.

The interpretation of dynamic cone penetration data is more difficult compared to the static penetration because of more complex phenomena appearing during their execution.

Consequently, dynamic cone penetration are recommended for unbinding soils and only with a guideline character for binding soils, which are more complex; thus, there are few formulae for evaluating geotechnical parameters obtained by dynamic cone penetration results.

By converting the dynamic penetration resistance Rd into static resistance Rp, it was possible to determine geotechnical parameters by using formulae used for the static penetration.

For the conducted geotechnical studies for the aforementioned communicating ways, certain geotechnical parameters like porosity (n), pore index (e), consistence index of binding soils, tamping degree of unbinding soils, edometric deformation module (M_{2-3}), linear deformation module (E) were determined based on the penetration resistance, as a middle value on 50 cm equidistance. Also, the bearing capacity of the soil was

roughly determined. The tamping degree and the edometric deformation module are very important geotechnical parameters for the characterization of soils; these can only be determined on unspoiled samples from the borings.

In appendixes 1 and 2, the geotechnical sheets of borings F_1 and F_2 for the investigation works conducted on the route of the Timişoara bypass road, as well as the processed data (penetration diagram, evaluated values of some geotechnical characteristics), which were obtained from the penetration surveys conducted near these borings (PDU_1 near F_1 and PDM I_a near F_I.

From the analysis of the data contained in Appendix 1, the foundation ground consists of clayish layers with close penetration resistances down to a depth of about 3.0 m; after this level a small increase proportional to the depth can be observed.

The consistency index was determined both on samples from borings and based on the penetration resistance. The aberrations of the values, corresponding to the same depth, can be considered acceptable if situated between 2% and 20%. The values determined in the laboratory as well as the values determined through penetration place the clayish soils in boring F1 in the same domain:

As boring F1 (Appendix 2) was placed in the area of an engineering structure, it was executed down to a depth of 13,0 m and the penetration survey near it (PDM I_a was realized with the middle dynamic penetrometer down to a depth of 11,00 m.

The clay packet found in boring P_I was depleted at a depth of 10.90 m from the surface of the terrain; after this level, a dusty sand saturated level begins.

The variation diagram of the penetration resistance presents a good uniformity of the clay packet to a depth of about 7,0 m, confirmed also by the values of the determined geotechnical parameters. Under this depth an increase of the penetration resistance can be observed; it continues also in the dusty sand layer, but this increase is partly artificial because of the adherence of the clayish soils to the rod column of the penetrometer.

The aberrations of the values of the consistence index and of the edometric deformation module are maximum 15% for the consistence index and 18% for the module. The value sets determined in the laboratory and based on the penetration resistance place the dusty clays in the plastic hard state domain down to 7.0 m and with middle compressibility beyond this level.

In the dusty sand layer, intercepted at a depth of - 10.90 m, the tamping degree and the edometric deformation module, necessary for the characterization of the respective layer, were evaluated solely based on the penetration resistance, as it was impossible to tap unspoiled samples for laboratory investigations.

3. USE OF THE PENETRATION METHOD FOR THE GEOTECHNICAL INVESTIGATION OF SOME GROUND INSTABILITY PHENOMENA

On the routes of overland communicating ways, especially those in areas with difficult relief, ground local instability phenomena occur frequently (especially landslides), which can affect both the embankment and the adjacent slopes and banks.

Near in-depth prospection of the ground through geotechnical borings and other field methods, the use of penetration as an additional correlative investigation method is efficient in these situations, mostly for the determination of the position and shape of the sliding surface.

The synthetic analysis of a landslide occurred on DN57 (fig.1) underlines the efficiency of the penetration method in determining the sliding surface [3].

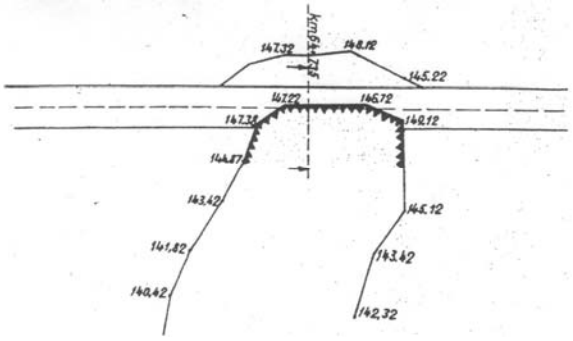

Fig. 1 Plan view of the landslide.

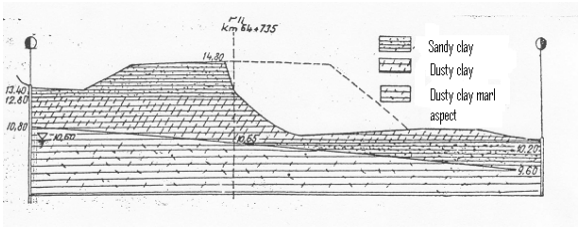

Fig. 2 Characteristic cross profile through landslide.

In the area of the landslide, the road route overpasses a small subsidence; thus the transversal alignment is in a mound on a distance of about 50 m.

The lithological profile of the ground in the sliding axis (fig. 2), determined based on geotechnical borings, underlines the presence on the surface of the terrain of a cover consisting of sandy and dusty clay, with a thickness of about 3.50 m underpinned on a dusty clay layer. The geotechnical characteristics, obtained through laboratory determinations on samples from the borings, indicated a higher consistency and a better tightness of the dusty clay layer, compared to the clayish layers above.

For the confirmation of the hypothesis that the land slide had occurred on the clay layer, both dynamic and static penetrations were conducted.

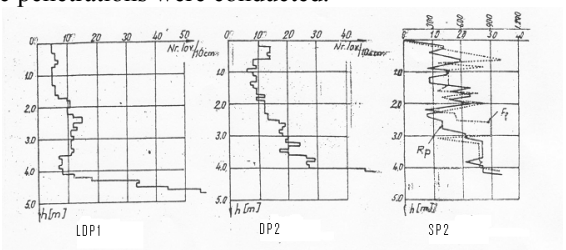

Fig. 3 Dynamic and static penetration diagrams

As it can be observed on the penetration diagrams shown in fig. 3, the results of the penetration surveys are in full correspondence with the ground stratification resulting from the borings; they indicate a sudden

increase of the resistance around the depth of 4,0 m. This fact confirmed the formation of the sliding surface around the depth of 4,0 m on the dusty clay layer and augmenting the confidence in the results of the conducted geotechnical investigations.

4. CONCLUSIONS

The aspects mentioned in the paper, sustained by the presented and analyzed examples, underline the technical and economical advantages of the "in situ" ground investigation through dynamic penetration surveys for overland communication ways; from these advantages, the following are mentioned:

- the possibility to verify the homogeneity of the field in depth, on the investigated road sectors, through execution of the penetration surveys near the borings as reference surveys and between them, as current investigation surveys
- the obtaining of supplementary in-depth continuous geotechnical data as opposed to the punctual information offered by the laboratory investigations on samples from specific levels
- the possibility to evaluate values of physical-mechanical ground characteristics also when from the borings no unspoiled samples can be provided
- the possibility to determine, rather easily but exactly, the position of the sliding surface in the case of landslides
- the high volume of geotechnical investigations conducted on the routes of some overland communicating ways through the two methods and the comparison of the geotechnical parameters
- obtained through laboratory investigations to those evaluated based on penetration resistance confirmed the possibility to use the latter with a high level of confidence ; the aberration was about 15-20% from the values determined through laboratory investigations
- the reduction of the time necessary for the in-depth ground investigation phase by about 30-40% through the combined use of geotechnical borings and penetration surveys
- the reduction of the geotechnical investigations costs by minimum 25-30%, depending on the conditions of the route of the overland communicating way

5. REFERENCES

[1] GRUIA, A., HAIDA, V. *Some aspects of the foundation ground researches with penetration method*. 7 – th National Conference for Geotechnical Engineering and Foundations, Timisoara

[2] HAIDA, V. *Some considerations regarding the stability of the versant and slopes* . 7 – th National Conference for Geotechnical Engineering and Foundations, Timisoara

[3] VOICU C., O., *Contributions to the study of the influence of the foundation ground on the viability of roads in Banat area,* . Phd thesis, 2003, Politechnica University of Timisoara.

[4] **** Technical instructions for the research of the foundation ground through static penetration method, dynamic penetration, vibro penetration.*. ID C 159 – 89.

ANEXA 1

UNIVERSITATEA "POLITEHNICA" TIMIŞOARA
FACULTATEA DE CONSTRUCŢII ŞI ARHITECTURĂ
DEPARTAMENTUL DE INGINERIE GEOTEHNICĂ ŞI
CĂI DE COMUNICAŢII TERESTRE

Proiect: STUDIU GEOTEHNIC PE TRASEUL CENTURII DE OCOLIRE A MUNICIPIULUI TIMIŞOARA
Faza: Proiect tehnic
Beneficiar: SEARCH CORPORATION BUCUREŞTI

FIŞA GEOTEHNICĂ a forajului **F 1** km 0+000

Cota terenului natural 92.00 NMB

Cotă strat față de ±0,00 foraj	Grosimea stratului, m	Cota apei subterane	Simbol stratificație	Denumirea stratului	Categoria de pământ	Tipul și cota probei	Granulozitate: Pietriș 2...20mm, %	Nisip 0,05...2mm, %	Praf 0,005...0,05mm%	Argilă <0,005mm, %	Umiditatea naturală w, %	Limita superioară de plasticitate, w_L, %	Limita inferioară de plasticitate, w_P, %	Indice de plasticitate I_P, %	Indice de consistență I_C
-0,50m	0,50	Nu s-a interceptat apă subterană		Strat vegetal	-	-	-	-	-	-	-	-	-	-	
-2,40m	1,90			Argilă prăfoasă cafenie, spre bază cu incluziuni calcaroase, plastic vârtoasă spre tare.	P_5	-1m -2m	- -	7 9	55 51	38 40	21 22	53 53	19 23	34 30	0,94 1,03
-4,20m	1,80			Argilă albăstruie cu incluziuni calcaroase plastic vârtoasă	P_5	-3m -4m	- -	5 10	53 47	42 43	23 23	65 60	23 20	42 40	1,00 0,93
-5,30m				Argilă prăfoasă verzuie plastic vârtoasă Stratul continuă	P_5	-5m	-	9	55	36	22	53	20	33	0,94

REZULTATUL INCERCARILOR DE TEREN PRIN PENETRARE DINAMICA CU CON

PDU 1 km 0+000
Cota absoluta teren natural: 92,00 m

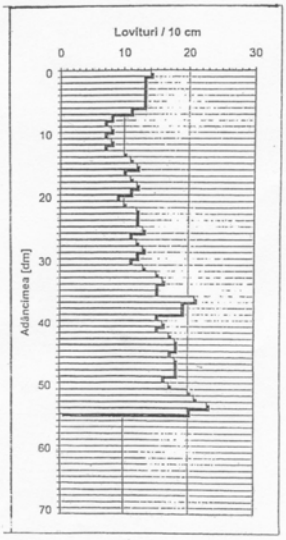

H	N10	Rd	Rp	n	e	Ic	I_D	M2-3	E	Pa *
m	lov/10cm	daN/cmp	daN/cmp	%	-	-	-	daN/cmp	daN/cmp	daN/cmp
0,0-0,5	13.2	41.04	32.01	0.45	0.81	0.87		92.51	157.27	2.05
0,5-1,0	9.4	29.22	22.80	0.46	0.86	0.78		82.03	106.64	1.46
1,0-1,5	8.6	23.78	18.55	0.47	0.90	0.77		79.28	87.21	1.19
1,5-2,0	11.2	30.97	24.16	0.46	0.85	0.82		87.44	131.16	1.55
2,0-2,5	11.0	27.39	21.36	0.47	0.87	0.82		86.88	130.32	1.37
2,5-3,0	12.2	30.38	23.69	0.46	0.86	0.85		90.08	153.13	1.52
3,0-3,5	14.0	31.37	24.47	0.46	0.85	0.89		94.33	160.36	1.57
3,5-4,0	17.8	39.89	31.11	0.45	0.81	0.97		101.74	172.96	1.99
4,0-4,5	16.8	33.87	26.42	0.46	0.84	0.95		99.96	169.93	1.69
4,5-5,0	17.4	36.64	28.58	0.45	0.83	0.96		101.04	171.77	1.83
5,0-5,5	20.2	36.62	28.57	0.45	0.83	1.03		105.65	179.60	1.83
5,5-6,0										
6,0-6,5										
6,5-7,0										

* - Valori orientative ale capacitatii portante a terenului

ANEXA 2

UNIVERSITATEA "POLITEHNICA" TIMIŞOARA
FACULTATEA DE CONSTRUCŢII ŞI ARHITECTURĂ
DEPARTAMENTUL DE INGINERIE GEOTEHNICĂ ŞI CĂI DE COMUNICAŢII TERESTRE

Proiect: STUDIU GEOTEHNIC PE TRASEUL CENTURII DE OCOLIRE A MUNICIPIULUI TIMIŞOARA
Faza: Proiect tehnic
Beneficiar: SEARCH CORPORATION BUCUREŞTI

FIŞA GEOTEHNICĂ a forajului **F I** km 0+120

Cota terenului natural 92,00m NMB

Cotă strat față de ±0,00 foraj	Grosimea stratului, m	Cotă apă subterană	Simboli stratificare	Denumirea stratului	Categoria de pământ	Cota și tipul probei	Granulozitate: Nisip 0,05...2mm, %	Granulozitate: Praf 0,005...0,05mm, %	Granulozitate: Argilă <0,005mm, %	Umiditatea naturală w, %	Limita sup. de plast. W_L, %	Limita inf. de plast. W_P, %	Indice de plasticitate I_P, %	Indice de consistență I_C	Ind. porilor, e	Densitatea ρ, t/m³	Modul edom. M, kPa	Unghiul de frecare Φ, °	Coeziunea c, kPa
-0,80	0,80			Strat vegetal															
		-2,25				-1,00	14	43	43	19	50	17	33	0,94	0,58	1,99	15341	22	55
						-2,00	19	39	42	21	51	16	35	0,86	-	-	-	-	-
						-3,00	16	49	35	24	48	16	32	0,75	0,61	2,01	9392	20	39
						-4,00	18	42	40	25	56	19	37	0,84	-	-	-	-	-
		-2,95		Argilă prăfoasă cafenie cu intercalații cenușii, cu concrețiuni calcaroase de la – 1,60m, plastic vârtoasă.	P_3	-5,00	22	38	40	24	53	17	36	0,81	0,70	1,96	7809	19	12,5
						-6,00	17	44	39	25	48	24	24	0,96	-	-	-	-	-
						-7,00	17	45	38	27	51	17	34	0,71	0,72	1,96	8478	23	26
						-8,00	19	39	42	24	53	16	37	0,78	-	-	-	-	-
						-9,00	24	40	36	25	61	17	44	0,82	0,66	1,99	10154	22	19
-10,90	10,10					-10,8	26	39	35	26	56	18	38	0,79	0,55	2,06	16129	23	55
						-11,0	86	14	-	20	-	-	-	-	-	-	-	-	-
				Nisip prăfos saturat, îndesat	P_3	-11,5	74	22	4	15	-	-	-	-	-	-	-	-	-
-13,00						-13,0	82	18	-	16	-	-	-	-	-	-	-	-	-
				Stratul continuă															

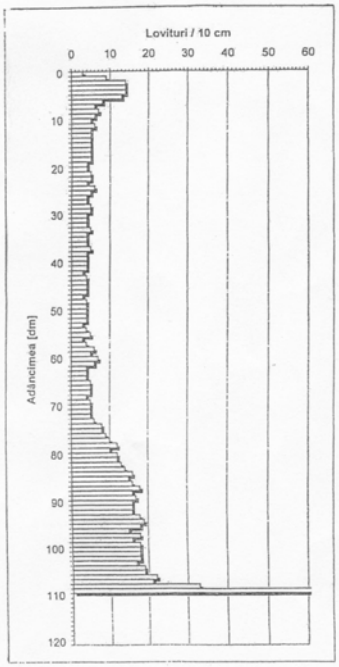

REZULTATUL INCERCARILOR DE TEREN PRIN PENETRARE DINAMICA CU CON

PDM la km 0+120
Cota absoluta teren natural: 92,00 m

H	N10 PDM	N10 PDU	Rd	Rp	n	e	Ic	I_D	M2-3	E	Pa *
m	lov/10cm	lov/10cm	daN/cm	daN/cm	%	-	-	-	daN/cmp	daN/cmp	daN/cmp
0,0-0,5	10.8	26,75	83.16	64.86	0.41	0.70	1.17		114.32	194.34	4.16
0,5-1,0	8	19.81	61.60	48.05	0.43	0.75	1.02		105.05	178.59	3.08
1,0-1,5	5.2	13.45	37.18	29.00	0.45	0.83	0.87		93.08	158.24	1.86
1,5-2,0	4.8	12.41	34.32	26.77	0.46	0.84	0.85		90.61	154.04	1.72
2,0-2,5	4.8	12.88	32.06	25.01	0.46	0.85	0.86		91.75	155.97	1.60
2,5-3,0	4.6	12.34	30.73	23.97	0.46	0.85	0.85		90.43	153.74	1.54
3,0-3,5	4.2	11.76	26.36	20.56	0.47	0.88	0.84		88.96	133.43	1.32
3,5-4,0	4.2	11.76	26.36	20.56	0.47	0.88	0.84		88.96	133.43	1.32
4,0-4,5	3.8	11.15	22.47	17.53	0.47	0.90	0.82		87.29	130.93	1.12
4,5-5,0	3.8	11.15	22.47	17.53	0.47	0.90	0.82		87.29	130.93	1.12
5,0-5,5	3.8	11.71	21.24	16.57	0.48	0.91	0.84		88.83	133.24	1.06
5,5-6,0	4.6	14.18	25.71	20.05	0.47	0.88	0.89		94.72	161.03	1.29
6,0-6,5	5	16.98	26.50	20.67	0.47	0.88	0.95		100.29	170.50	1.32
6,5-7,0	4.8	16.30	25.44	19.84	0.47	0.88	0.94		99.03	168.36	1.27
7,0-7,5	5.8	21.53	29.21	22.79	0.46	0.86	1.06		107.61	182.94	1.46
7,5-8,0	9.8	36.38	49.36	38.50	0.44	0.78			123.81	210.47	2.47
8,0-8,5	13.4	55.74	64.32	50.17	0.43	0.74			136.98	232.87	3.22
8,5-9,0	16.4	68.21	78.72	61.40	0.41	0.71			143.22	243.47	3.94
9,0-9,5	17	70.71	81.60	63.65	0.41	0.70			144.33	245.36	4.08
9,5-10,0	17	70.71	81.60	63.65	0.41	0.70			144.33	245.36	4.08
10,0-10,5	18	74.87	86.40	67.39	0.41	0.69			146.09	248.36	4.32
10,5-11,0	34.4	143.08	165.12	128.79	0.37	0.59		0.99	166.09	282.35	8.26
11,0-11,5											
11,5-12,0											

* - Valori orientative ale capacitatii portante a terenului

SECTION III

ELECTRONICAL ENGINEERING AND COMPUTER SCIENCE

THE STABILITY AND THE OFFSET OF HALL MICROSENSORS

[1]CARUNTU GEORGE, [2]DUMITRASCU ANA, [3]DRAGOMIRESCU OVIDIU

[1,2,]Constanta Maritime University, [3] "Politehnica" University Bucharest, Romania

ABSTRACT

In this paperwork is analysed the structure, the operating conditions and the main features of some magnetic microsensors structures realised in the MOS integrated circuits technology. By assimilating the MOSFET channel of almost constant depth with a Hall plate, the results obtained for the conventional Hall plates have been extended to MOS-Hall plates. In the paper is defined the stability and the offset equivalent magnetic induction for the MOS Hall plates. By using numerical simulation, the values of the sensor stability and the offset magnetic induction for the analysed structures are compared and it is also emphasized the way in which choosing the geometry and the material features allows getting high-performance sensors.

Keywords: *supply-current-related sensitivity, magnetic sensor, surface charge density, sheet resistance, oxide layer, offset voltage, offset equivalent magnetic induction.*

1. GENERAL CHARACTERIZATION OF THE MOS-HALL PLATES

In the MOSFET structure a Hall plate can be realised if the channel is the active region of the plate, and the source (S) and the drain (D) are the biasing contacts [1]. For the sensing contacts of the Hall voltage SH_1 and SH_2 are manufactured, two strongly doped regions n^+ type. The channel length is L, and the width is W.

The bias in the linear region ensures a continuous channel having a thickness almost constant δ, which could be assimilated with a Hall plate. Considering the Hall voltage mode of operation, the MOS-Hall plate is equivalent in the linear region with a conventional Hall plate differing by the fact that the charge carriers are due to the surface field effect.

The surface charge density in the channel is approximately constant and it has the following expression [1]:

$$Q_{Ch} = C_{ox}(V_G - V_P) \tag{1}$$

where C_{ox} is the gate oxide capacitance per unit area, V_G the gate to source voltage, and V_p the threshold voltage.

The very low value of the surface charge density in the channel of a MOSFET ensures a high magnetic sensitivity of the MOS–Hall plate. There is also the possibility to modify the channel depth by the drain-source potential difference.

In the case of a conventional Hall plate, the generated voltage generated by a magnetic field $B_\perp$ perpendicular to the plate surface is given by [2]:

$$V_H = G(r_H / qn\delta)I \cdot B_\perp \tag{2}$$

where G is the geometrical correction factor, r_H the Hall factor and δ the thickness of the plate.

By replacing in (2) the product $qn\delta$ by the surface charge density in the channel Q_{Ch}, and the current I by I_D it results:

$$V_H = G(r_H / Q_{Ch})I_D \cdot B_\perp \tag{3}$$

Using the drain current expression:

$$\begin{aligned} I_D &= (W/L)\mu_{Ch} \cdot C_{ox}(V_G - V_P)V_D = \\ &= (W/L)\mu_{Ch}Q_{Ch}V_D \end{aligned} \tag{4}$$

from (3) it results:

$$V_H = \mu_{H_{Ch}}(W/L)GV_D \cdot B_\perp \tag{5}$$

where $\mu_{H_{Ch}} = \mu_{Ch} \cdot r_H$ represents the Hall mobility of the charge carriers in the channel.

The absolute sensitivity for a Hall device used as a magnetic sensor is:

$$S_A = \left|\frac{V_H}{B_\perp}\right| = \left|\mu_{H_{Ch}}\right| \cdot \left(\frac{W}{L}G\right) \cdot V_D \tag{6}$$

and the supply-current-related sensitivity is defined by:

$$S_I = \frac{S_A}{I_D} = G(r_H / Q_{Ch}) \tag{7}$$

2. THE OFFSET OF THE MOS- HALL PLATES

The main causes of the offset in the case of Hall plates realized in the MOS integrated technology are due to the misalignment of contacts, to non-uniformity resistivity and channel thickness. Also a mechanical stress, and to the fluctuations in the oxide layer, or to the variation in the oxide-semiconductor interface may produce offset.

The asymmetries produced by the above causes can be represented by using for the Hall plate the simple Wheatstone bridge circuit model.

Ideally all the resistors should be equal. Any of the causes above mentioned can bring about bridge resistance variation ΔR, consequently between the sense contacts appears the offset voltage:

$$V_{off} = \frac{R+\Delta R}{2R}V_D - \frac{R-\Delta R}{2R}V_D = \frac{\Delta R}{R}V_D \quad (8)$$

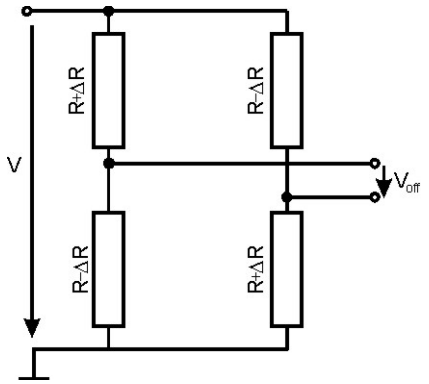

Figure 1. The bridge circuit for the Hall-plate

The value of the magnetic induction corresponding to a Hall voltage equal with V_{off} represent offset equivalent magnetic inductions and is got by replacing (8) into (6):

$$B_{off} = \frac{V_{off}}{S_A} = \frac{1}{\mu_{H_{Ch}}} \cdot \left(\frac{W}{L}G\right)^{-1} \frac{\Delta R}{R} \quad (9)$$

It is noticed that at given technological misalignment, B_{off} decreases if $\mu_{H_{Ch}}$ is of a high value. In the case of the MOS-Hall plates this is an inconvenience because the carrier mobility in the channel is half of its value in then volume of the equivalent conventional device.

3. THE SURFACE INSTABILITY OF THE HALL DEVICES

As sensitivity S_I depends on the surface density of charge carriers in the channel, any variation in the carrier density may disturb its stability. A source of instability particular to metal-SiO_2-Si structures is the oxygen vacancy and ions in excess at the SiO_2-Si interface. To this is added the ionic contamination and charges induced by radiations (X rays, γ rays electrons of low or high energy).If in the oxide layer or at the oxide–semiconductor layer interface of a Hall sensors, a variation ΔQ_S of the charge density occurs, it will cause a variation $-\Delta Q_S$ in the surface charge density in the MOS-Hall plate. Assuming that at the *n*-channel surface the inversion phenomenon does not occur, the corresponding variation of ΔQ_S will be ΔS_I. From (7) it results that:

$$\Delta S_I = \frac{\partial S_I}{\partial Q_{Ch}}\Delta Q_{Ch} = -\frac{Gr_H}{Q_{Ch}^2}\Delta Q_{Ch} = \\ = \frac{Gr_H}{Q_{Ch}} \cdot \frac{\Delta Q_S}{Q_{Ch}} = S_I \frac{\Delta Q_S}{Q_{Ch}} \quad (10)$$

or

$$\frac{\Delta S_I}{S_I} = \frac{\Delta Q_S}{Q_{Ch}} = \frac{S_I}{Gr_H}\Delta Q_S \quad (11)$$

Assuming that $G \cdot r_H = 1$, which is true in many practical situations:

$$\frac{\Delta S_I}{S_I} \cong S_I \cdot \Delta Q_S \quad (12)$$

Therefore, the surface instability influence on the device sensitivity is proportional to the sensitivity itself.

4. THE OFFSET EQUIVALENT MAGNETIC INDUCTION

Uncorrelated variations in interface charge may also bring about asymmetry in a MOS-Hall plate resistivity. Consequently, there is an offset. At low magnetic fields, if the biased voltage of device is constant, the channel sheet resistance can be expressed by:

$$R_S = \frac{\rho}{\delta} = \frac{1}{\mu q n \delta} = \frac{1}{\mu Q_{Ch}} \quad (13)$$

The absolute charge in the layer resistance is then:

$$\Delta R_S = \frac{\delta R_S}{\delta Q_{Ch}} \cdot \Delta Q_{Ch} = -\frac{\Delta Q_{Ch}}{\mu Q_{Ch}^2} = \frac{R_S}{Q_{Ch}}\Delta Q_S \quad (14)$$

From (15) it results:

$$\frac{\Delta R_S}{R_S} = \frac{\Delta Q_S}{Q_{Ch}} \quad (15)$$

By substituting (15) into (9) it is obtained the offset equivalent magnetic induction due to the fluctuation in surface charge[3]:

$$B_{off} = \frac{L}{\mu_{H_{Ch}} WG} \cdot \frac{\Delta Q_S}{Q_{Ch}} = \\ = S_I \frac{1}{\mu_{H_{Ch}}} \left(G\frac{W}{L}\right)^{-1} \cdot \frac{\Delta Q_{Ch}}{Gr_H} \quad (16)$$

For the practical situations when $Gr_H \cong 1$, relation (16) becomes:

$$B_{off} \cong S_I \frac{\Delta Q_{Ch}}{\mu_{H_{Ch}}} \left(G\frac{W}{L}\right)^{-1} \quad (17)$$

The product $G(W/L)$ is maximum for $(L/W)<0.5$, namely: $[G(W/L)]_{\max}=0.74$ [4].

Therefore:

$$(B_{off})_{\max}\cong S_1\frac{\Delta Q_S}{\mu_{H_{Ch}}}\cdot\frac{1}{0.74}=1.35\frac{\Delta Q_S}{\mu_{H_{Ch}}}S_1$$

For a high sensitivity Hall device the influence of the surface effects on its offset increases.

For a silicon MOS Hall device having $\varepsilon_{ox}=4\,(SiO_2), d_{ox}=50nm$, $\frac{W}{L}=2$,and being biased at $V_G=5V$ $V_p=1V$ it is in turn calculated:

$$C_{ox}=\varepsilon_{ox}\frac{\varepsilon_0}{d_{ox}}=7\cdot10^{-4}\,Fm^{-2}$$

$$Q_{Ch}=C_{ox}(V_G-V_P)\cong2.8\cdot10^{-3}\,Cm^{-2}$$

$$S_1=\frac{G\cdot r_H}{Q_{Ch}}\cong\frac{1}{2.8\cdot10^{-3}}\frac{m^3}{As}=357VA^{-1}T^{-1}$$

Considering a fluctuation in the surface charge density $\Delta Q_S=1.6\cdot10^{-5}\,Cm^{-2}$ one can calculate

$$B_{off}=\frac{S_1}{0.7}\cdot\frac{\Delta Q_{Ch}}{\mu_{H_{Ch}}}=0.116T$$

In figure 2 it can be seen the geometry influence on the MOS Hail plate stability for three devices structures realized on silicon $\mu_{H_{Ch}}=0.07m^2V^{-1}s^{-1}$ with the sensitivity $S_I=350VA^{-1}T^{-1}$, and having different ratios W/L $(W=50\mu m)$[4].

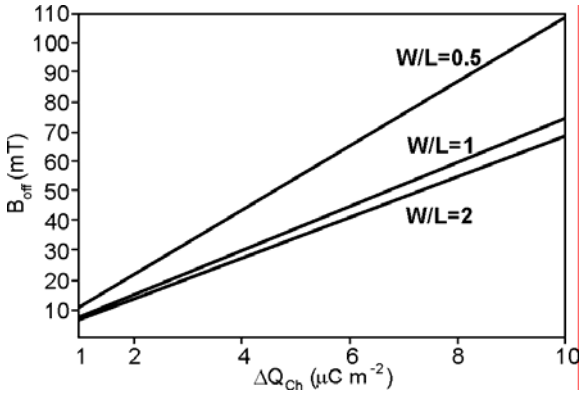

Figure 2. The B_{off} depending on ΔQ_{Ch} for three devices of different geometry.

MHP1: $\frac{W}{L}=0.5$; $G(W/L)=0.73$

MHP2: $\frac{W}{L}=1$; $G(W/L)=0.67$

MHP3: $\frac{W}{L}=2$; $G(W/L)=0.46$

The minimum values for B_{off} induction are obtained for the structures of $W/L\le0.5$ (*MPH1*). Once the channel length increases, the B_{off} caused by the surface charge instability, also increases.

This at the same variation ΔQ_{Ch} ,doubling the channel length brings about an increase of 46% of the B_{off} value as compared to the square structure value.

To emphasize the material influence on the B_{off} induction there were simulated three Hall devices, made of different materials:

MHP1: GaSb, $\mu_{H_{Ch}}=0.25m^2V^{-1}s^{-1}$

MHP2: GaAs, $\mu_{H_{Ch}}=0.42m^2V^{-1}s^{-1}$

MHP3: InAs, $\mu_{H_{Ch}}=1.65m^2V^{-1}s^{-1}$

Figure 3 shows the B_{off} dependence on the variation in the surface charge density for Mos-Hall plates made of materials having different mobility of the charge carriers.

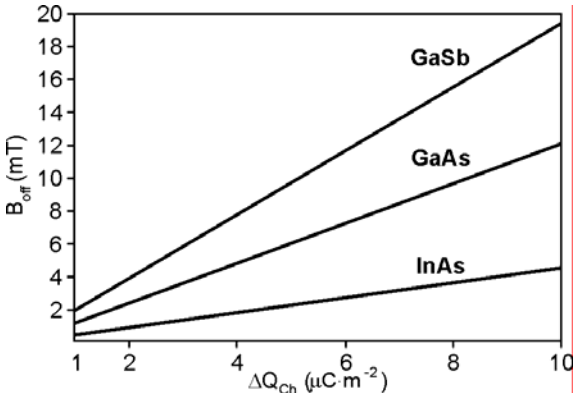

Figure 3. The B_{off} depending on ΔQ_{Ch} for three devices of different materials.

These have: $L=2W$, $(W=50\mu m)$, and sensitivity $S_I=350VA^{-1}T^{-1}$.

We can see that the sensors made from high mobility materials have a superior stability, the offset magnetic induction being inversely proportional to the mobility for the same fluctuation of the surface charge density.

At the InAs device, B_{off} decreases 4.25 times compared to the value for the GaAs, but due to the compatibility with the main microelectronics technologies, the latter is preferred.

5. THE OFFSET VOLTAGE AND THE OFFSET EQUIVALENT MAGNETIC INDUCTION

The main causes of the offset in the case of Hall plates realised in the MOS integrated circuits technology are due to the misalignment of contacts, to integral non-uniformity, the existence of mechanical stress, and to the fluctuations in the oxide layer charge, or to the variation in the oxide semiconductor interface.

The asymmetries produced by the above causes can be represented by using for the Hall plate the simple Wheatstone bridge circuit model.

In the case of the misalignment of the sensing contacts, for a tolerance ΔL the asymmetrical output voltage or the offset voltage is expressed by [5]:

$$V_{off} = \frac{\Delta L}{W} \cdot \frac{1}{\mu_{Ch} Q_{Ch}} \cdot I_D \qquad (18)$$

The value of the magnetic induction corresponding to a Hall voltage equal with V_{off} represents offset equivalent magnetic induction.

In the case of the geometrical offset of the sensing contacts, the expression of the offset equivalent magnetic induction is got by replacing (18) into (6):

$$B_{off} = \frac{V_{off}}{S_A} = \frac{\Delta L}{W} \cdot \frac{I_D}{\mu_{Ch} \cdot Q_{Ch}} \cdot \frac{Q_{Ch}}{r_H \cdot G} \cdot \frac{1}{I_D} = \\ = \frac{1}{\mu_{H_{Ch}}} \cdot \left(\frac{W}{L} G \right)^{-1} \frac{\Delta L}{L} \qquad (19)$$

It is noticed that at given technological misalignment, B_{off} decreases if $\mu_{H_{Ch}}$ is of a high value. In the case of the MOS-Hall plates this is an inconvenience because the carrier mobility in the channel is half of its value in the volume of the equivalent conventional device.

Assuming that the condition of a low magnetic field is fulfilled, minimal values for B_{off} are obtained if $\frac{L}{W} \le 0.5$ when the product $\left(\frac{W}{L} G \right)$ takes the maximal value 0.74 [4]:

$$(B_{off})_{\min} \cong \frac{1}{0{,}74 \cdot \mu_{H_{Ch}}} \cdot \frac{\Delta L}{L} \qquad (20)$$

In the figure 4 are represented the values B_{off} for three structures with an optimal geometry of the channel $(L = 2W)$ realised from different materials.

For values of the geometric offset within the range $[10^{-4}, 10^{-3}]$, in the *Si* device, $(B_{off})_{\min}$ varies between 2.2 mT and 22 mT and in GaAs device $(B_{off})_{\min}$ covers the range $[0.39;3.9]mT$, the increase of the offset equivalent induction slope being of 5.67 times smaller in GaAs.

MHP1: *Si* with $\mu_{H_{Ch}} = 0.07 m^2 V^{-1} s^{-1}$;

MHP2: *GaAs* with $\mu_{H_{Ch}} = 0.42 m^2 V^{-1} s^{-1}$;

MHP3: *InAs* with $\mu_{H_{Ch}} = 1.65 m^2 V^{-1} s^{-1}$

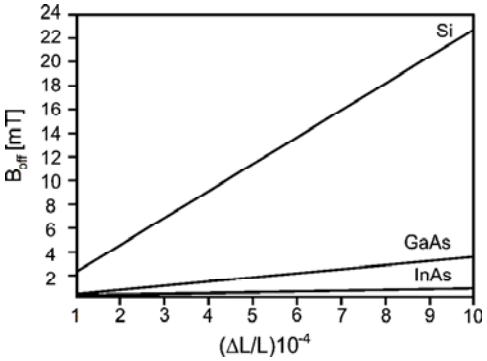

Figure 4. The B_{off} depending on the geometrical offset ΔL/L for three devices of different materials

6. CONCLUSIONS

The analysis of the characteristics of the MOS Hall plates shows that the $W/L = 0.5$ structure is theoretically favorable to high performance regarding the offset-equivalent magnetic induction due to the fluctuation in surface charge.

Also, substituting the silicon technology by using other materials such as GaAs or InSb with high carrier mobility values, assure higher characteristics of the sensors.

The B_{off} lowers with the increase of carriers mobility. So for the same variation in the interface charge density $\Delta Q_S = 8 \cdot 10^{-6} Cm^{-2}$, the B_{off} value of the GaAs devices decreases by 77% as compared to that of the silicon device.

Also the increase of the channel length brings about higher values for B_{off}.

7. REFERENCES

[1] STERE R., BODEA M., "Tranzistoare cu efect de camp", pp. 117, *Editura Tehnică*, Bucureşti, 1972

[2] KIREEV P.S., "Fizica semiconductorilor" *Editura Ştiinţifică şi Enciclopedică*, Bucureşti, 1977.

[3] CĂRUNTU G., PANAIT C., "The Stability of the Hall Semiconductors Plates", *in the Proceedings of the 9th International Conference on Applied and Theoretical Electricity,* vol. I, pp. 27-30,Craiva, 1998

[4] MIDDELHOEK S., AUDET S.A., "Physiscs of Silicon Sensors", pp. 5.20, 5.21, *Academic Press*, London, 1989

[5] CĂRUNTU G., *Caracterizarea plăcilor Hall pe siliciu utilizate ca senzori magnetici.* Referat doctorat, Universitatea "Politehnica" Bucureşti, 1994

THE SHOT NOISE OF HALL MICROSENSORS

[1]CARUNTU GEORGE, [2]PANAIT CORNEL, [3]CARUNTU IRINA

[1,2,3]*Constanta Maritime University, Romania*

ABSTRACT

In this paperwork is analysed the structure, the operating condition, and the main characteristics for the Hall microsensors realised in the MOS and bipolar integrated circuits technolog. By using the numerical simulation the values of the signal-to-noise ratio for different structure devices are compared and it is also emphasized the way in which choosing the geometry and the material features allows getting high-performance sensors.

Keywords: *double – drain MOS device, shot noise, signal-to-noise ratio, lateral bipolar magnetotransistor, double-collector magnetotransistor*

1. THE CHARACTERISATION OF THE DOUBLE-DRAIN MAGNETOTRANSISTOR

The double – drain MOS device (figure 1) is obtained from a MOSFET structure where its conventional drain region is replaced by two adjacent drain regions. Consequently, the total channel current shared between this two drain regions [1].

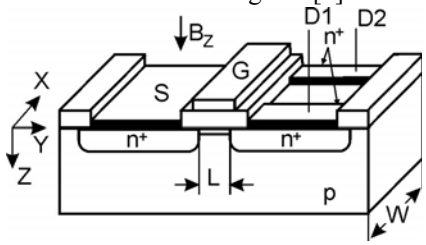

Figure 1 Double-drain magnetic – sensitive MOSFET structure

The result of the bias is the linear region is the obtained of a continuous channel of approximately constant thickness, which can be assimilated with a Hall plate.

The deflection of current lines appears under the action of a magnetic field $B_{\perp}$, perpendicular to the device surface. The carrier deflection causes a discrepancy between two drain currents:

$$\Delta I_D = \left| I_{D1}\left(\bar{B}\right) - I_{D1}\left(0\right)\right| = \left| I_{D2}\left(\bar{B}\right) - I_{D2}\left(0\right)\right| \quad (1)$$

Since the output signal of the double-drain MOS magnetotransistors consists of the current variation between its terminals, this device operates in the Hall current mode. Using the features of dual Hall devices, and the Hall current expression it results [2]:

$$\Delta I_D = \frac{I_H}{2} = \frac{1}{2}\mu_{H_{Ch}} \cdot \frac{L}{W} \cdot G \cdot I_D \cdot B_{\perp} \quad (2)$$

where $\mu_{H_{Ch}}$ is the carriers Hall mobility in the channel, and *G* denotes the geometrical correction factor.

The magnetic sensitivity related to the devices current is defined as follows:

$$S_I = \frac{1}{I_D} \cdot \left| \frac{\Delta I_D}{B_{\perp}} \right| = \frac{1}{2}\mu_{H_{Ch}} \cdot \frac{L}{W} G \quad (3)$$

For a given induction $\left(B = 0{,}4T\right)$ and at given drain current $I_D = 1mA$, the sensitivity depends of the device geometry and the material properties. In table 1are presented the obtained values for five magnetotransistors structures.

Table 1. The numerical values of the supply-current-related sensitivity

	W/L	$\mu_{H_{Ch}}[m^2V^{-1}s^{-1}$	$S_I[T^{-1}]$
MGT1	2	0,07 Si	0,018
MGT2	1	0,07 Si	0,025
MGT3	0,5	0,07 Si	0,028
MGT4	0,5	0,23 InP	0,084
MGT5	0,5	0,42 GaAs	0,146

2. SIGNAL – TO – NOISE RATIO

The noise affecting the drain current of a MOSFET magnetotransistors is shot noise and $1/f$ noise. Signal-to-noise ratio is defined by :

$$SNR(f) = \Delta I_D \cdot \left[S_{NI}(f) \cdot \Delta f\right]^{-1/2} \quad (4)$$

where Δf denotes a narrow frequency band around the frequency *f*, and $S_{NI}(f)$ is the noise current spectral density. In case of shot noise, the noise current spectral density at frequencies over 100 Hz is given by [3]:

$$S_{NI} = 2qI \quad (5)$$

where *I* is the device current. By substituting (2) and (5) into (4) it results:

$$SNR(f) = \frac{1}{2\sqrt{2}}\mu_{H_{Ch}}\left(\frac{L}{W}G\right)\frac{I_D}{\left(q \cdot I \cdot \Delta f\right)^{1/2}} B_{\perp} \geq$$

$$\geq \frac{1}{2\sqrt{2}}\mu_{H_{Ch}}\left(\frac{L}{W}G\right)\frac{I_0^{1/2}}{\left(q\Delta f\right)^{1/2}} \cdot B_L \quad (6)$$

In figure 2 is shown the *SNR(f)* dependence on magnetic induction of three MOS magnetotransistors

structures of different materials ($W/L = 0.5$, $\Delta f = 1Hz$, $I_D = 1mA$)

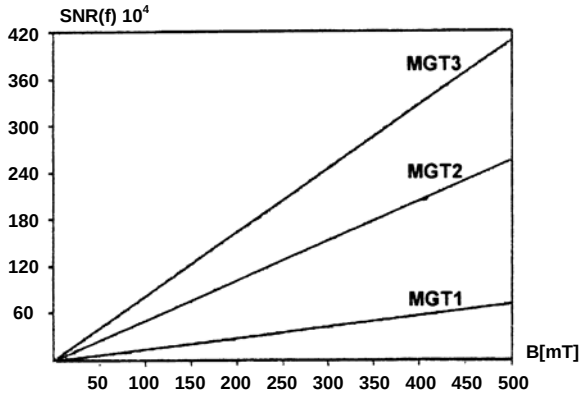

Figure 2. SNR(f) depending on B for three devices of different materials

MGT1:*Si*, $\mu_{H_{Ch}} = 0.07m^2V^{-1}s^{-1}$

MGT2:*GaS*, $\mu_{H_{Ch}} = 0.25m^2V^{-1}s^{-1}$

MGT3:*GaAs*, $\mu_{H_{Ch}} = 0.04m^2V^{-1}s^{-1}$

A high value of carrier mobility causes the increasing of *SNR(f)*. So for $B = 0{,}5T$, *SNR(f)* increase with 60% for GaAs comparative with GaSb.

To emphasize the dependence *SNR(f)* on device geometry there were simulated (figure 3) three MOS magnetotransistors structures realised on silicon $\mu_{H_{Ch}} = 0.07m^2V^{-1}s^{-1}$ and having different ratios L/W. ($W = 50\mu m$ $\Delta f = 1Hz$, $B = 0.2T$, $I_D = 1mA$).

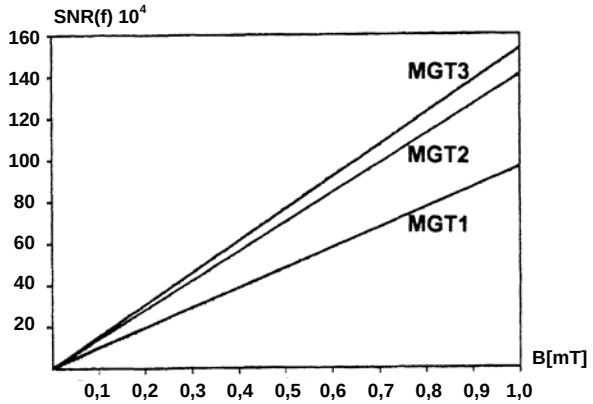

Figure 3. SNR(f) depending on B for three devices of different geometry

MGT1: $\frac{W}{L} = 2$ and $\left(\frac{L}{W}G\right) = 0.212$

MGT2: $\frac{W}{L} = 1$ and $\left(\frac{L}{W}G\right) = 0.409$

MGT3: $\frac{W}{L} = 0.5$ and $\left(\frac{L}{W}G\right) = 0.576$

It is noticed that the *SNR(f)* is maximum for $W/L = 0.5$, and for smaller values of this ratio. For the same *B* magnetic induction, increasing the channel wide, *SNR(f)* decreases with 44% for *W=2L* comparative with the $W/L = 0.5$ structure.

3. GENERAL CARACTERISATION OF THE LATERAL BIPOLAR MAGNETOTRANSISTORS

Figure 4 illustrates the cross section of a mangnetotransistors operating on the current deflection principle [4].

This device has the structure of a long channel

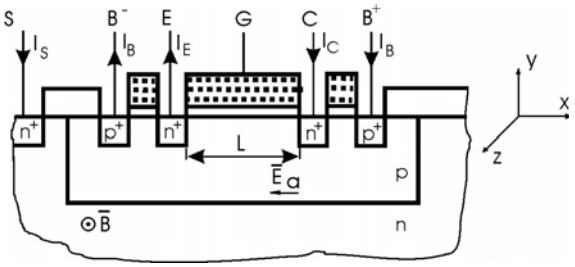

Figure 4. Cross section through a lateral magnetotransistor in CMOS technology

MOS transistor, but operates as a lateral bipolar transistor with a drift-aided field in base region.

The device is situated in a *p*-well, serving as the base region of the transistor. The two base contacts B^+ and B^-, allow the application of an accelerating voltage the minority carriers injected into the base region. The two n^+ regions laterally separated by the length of base along the distance L, serve as the emitter E and primary collector C. The substrate S works as the secondary collector.

In order to describe the qualitative operation of the device, let us assume that it is adequately biased for the forward active operation.

Owing to the acceleration field $\overline{E}_a$ in the base region, the most part of electrons injected into the base region drift mainly along the base length and are collected by collector C, producing collector current I_C. However, some of the which diffuse downwards, are collected by the secondary collector S, producing the substrate current I_S. The rising of ratio between the useful current I_C and the parasite current I_S is determined by the accelerating field. A magnetic induction $\overline{B}$ perpendicular to the figure plane, modulates the distribution of the emitter current I_E among I_C and I_S. The modulation in the collector current I_C is used as the sensor signal.

If the acceleration field $\overline{E}_a$ in the base region is very small the electrons moving essentially by diffusion, the transverse Hall current will be [2]:

$$I_H = I_\gamma = \frac{L}{Y} I_C \mu_{Hn} B_\perp = \Delta I_C \qquad (7)$$

where μ_{Hn} is the Hall mobility of electrons in the *p*-well, and *Y* is a geometrical parameter given approximately by $y_{jn} < Y < y_{jp}$. Here y_{jn} and y_{jp}

denote the junction depths of the collector region and the *p*-well respectively.

4. SIGNAL-TO-NOISE RATIO

The noise affecting the collector current of a lateral bipolar magnetotransistors is shot noise and $1/f$ noise. In case of shot noise, by substituting (7) and (5) into (4) it results:

$$SNR(f)=\frac{1}{\sqrt{2}}\mu_{Hn}\frac{L}{Y}\cdot\frac{I_C}{(q\cdot I\cdot\Delta f)^{\frac{1}{2}}}\cdot B_{\perp}\le$$

$$\ge 0.707\mu_{Hn}\frac{L}{Y}\left(\frac{I_C}{q\Delta f}\right)^{1/2}\cdot B_{\perp} \qquad (8)$$

In figure 5 is shown the $SNR(f)$ dependence on the collector current of three magnetotransistor structures of different materials: $L/Y=5,\Delta f=1Hz,B=0.2T$

MGT1: Si with $\mu_{Hn}=0.15m^2V^{-1}s^{-1}$,

MGT2: Ga Sb with $\mu_{Hn}=0.50m^2V^{-1}s^{-1}$

MGT3: Ga As with $\mu_{Hn}=0.80m^2V^{-1}s^{-1}$

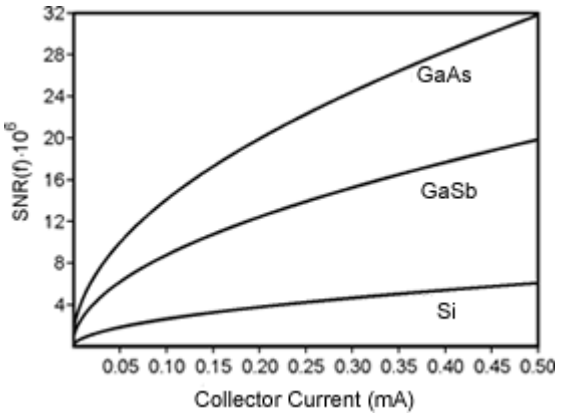

Figure 5. SNR(f) depending on collector current for three devices of different materials

A high value of carrier mobility causes the increasing of $SNR(f)$. So for $I_C=0.2mA$ $SNR(f)$ increases with 60% for Ga As comparative with Ga Sb.

To emphasise the dependence of $SNF(f)$ on device geometry there were simulated (figure 6) three magnetotransistor structures realised on silicon ($\mu_{Hn}=0.15m^2V^{-1}s^{-1}$) and having different ratios L/Y $(L=50\,\mu m;B=0.2T;\Delta f=1Hz)$.

$$MGT_1: L/Y=5;\ MGT_2: L/Y=3;$$
$$MGT_3: L/Y=2.$$

5. THE STRUCTURE AND THE PRINCIPLE OF OPERATION

Figure 7 shows the cross section of a double collector *npn* vertical magnetotransistor

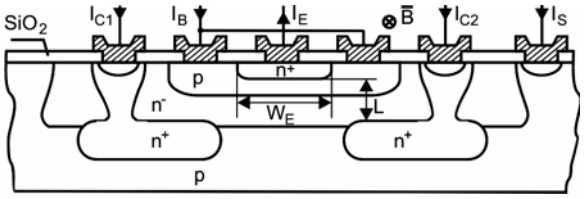

Figure 7. The structure of a double-collector magnetotransistor

This structure is compatible with the bipolar integrated circuit technology. The most of the *n* type low-doped epitaxial layer serves as the collector region and is depleted of the charge carriers upon reverse biasing of the collector-base junction.

The two collector contacts are realised by splitting the buried layer (n^+). L is the collector-emitter distance, and W_E is the width of the emitter. In the absence of the magnetic field the electron flow injected into the emitter, which crosses the base is symmetrical and the two collector currents are equal: $I_{C_1}=I_{C_2}$. In the presence of a magnetic field having the induction $\overline{B}$ parallel with the device surface, the distribution of the emitter electron current becomes asymmetrical and causes an imbalance of the collector currents: $\Delta I_C=I_{C_1}-I_{C_2}$.

The analysed magnetotransistor operates in the Hall current mode and ΔI_C depends on the Hall transverse current.

Assimilating the low-dopped emitaxial layer of the collector region with a short Hall plate, and based on the properties of dual Hall devices it results [2]:

$$\Delta I_C=\frac{I_H}{2}=\frac{1}{2}\mu_{Hn}\cdot\frac{L}{W_E}\cdot G\cdot I_C\cdot B \qquad (9)$$

where $I_C=I_{C_1}(0)+I_{C_2}(0)$.

The noise affecting the collector current of a double-collector magnetotransistor is shot noise and 1/f noise.

Signal-to-noise ratio is defined by (4):

$$SNR(f)=\frac{\Delta I_C}{[S_{NI}(f)\cdot\Delta f]^{1/2}} \qquad (10)$$

where Δf denotes a narrow frequency band around the frequency f, and $S_{NI}(f)$ denotes the noise current spectral density in the collector current.

In case of shot noise, in a narrow range f of frequency values, by subtituting (9) and (5) into (10) it results:

$$SNR(f)=\frac{\mu_{Hn}}{2\sqrt{2}}\left(\frac{L}{W_E}G\right)\frac{I_C}{(q\cdot I\cdot\Delta f)^{1/2}}B_{\perp}\geq$$
$$\geq\frac{1}{2\sqrt{2}}\mu_{Hn}\left(\frac{L}{W_E}G\right)\frac{I_C^{1/2}}{(q\Delta f)^{1/2}}B_{\perp} \quad (11)$$

To emphasise the dependence of $SNR(f)$ on device geometry there were simulated (figure 8) three magnetotrasistor structure realised on silicon ($\mu_{H_n}=0.15m^2V^{-1}s^{-1}$) and having different rations W_E/L ($W_E=40\mu m;\ \Delta f=1;\ I_C=1mA$).

MGT1: $W_E/L=2$;

MGT2: $W_E/L=1$;

MGT3: $W_E/L=0.5$;

The device were biased in the linear region at the collector current $I_C=1mA$, the magnetic field has a low level ($\mu_H^2B^2<<1$).

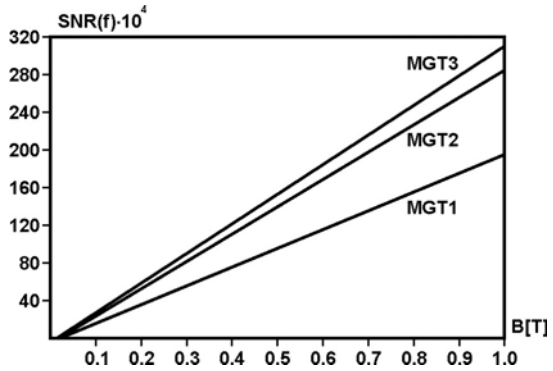

Figure 8. *SNR(f)* depending on *B* for three devices of different geometry

It is noticed that the $SNR(f)$ is maximum for $W_E/L=0.5$ and for smaller values of this ratio. For the same *B* magnetic induction, increasing the emitter width, $SNR(f)$ decreases with 37.2% for $W_E=2L$ comparative with the maximum value.

In figure 9 there are shown $SNR(f)$ values for three magnetotransistors structures made of different materials ($W_E/L=0,5$; $I_C=1$mA, $\Delta f=1Hz$).

MGT1(Si): $\mu_{Hn}=0,15m^2V^{-1}s^{-1}$;

MGT2(GaSb): $\mu_{Hn}=0,5m^2V^{-1}s^{-1}$;

MGT3(GaAs): $\mu_{Hn}=0,85m^2V^{-1}s^{-1}$.

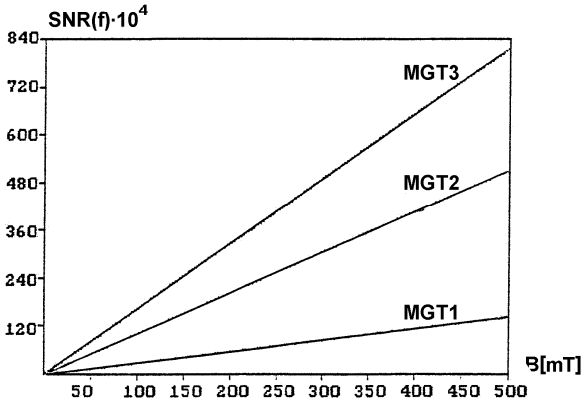

Figure 9. SNR(f) depending on collector current for three devices of different materials

6. CONCLUSIONS

The analisys of the characteristics of magnetotreansistor structures shows that the $W/L=0.5$ ratio is theoretically favourable to high performance regarding signal-to-noise ratio, as well as the offset equivalent magnetic induction.

Also substituting the silicon technology by using other materials such as GaAs or InSb with high carriers mobility values assure higher characteristics of the sensors. A high value of carrier mobility causes the increasing of *SNR(f)*. So for $B=0,5T$, *SNR(f)* increase with 60% for GaAs comparative with GaSb.

7. REFERENCES

[1] NATHAN A., HUISER, M. J.; BALTES, H. P., *Two Dimensional Numerical Moddeling of Magnetic Field Sensors in CMOS Technology*, IEEE Trans. Electron Device **ED**-32 1212-19, 1985.

[2] CĂRUNTU G., PANAIT C., *The Optimization of Magnetic Senzitive MOSFET Structures,* in the Proceedings of SPIE-Volume 6635, 2007

[3] GRAY R.P., MEYER G.R., *Circuite integrate analogice. Analize şi proiectare*. Editura Tehnică, Bucureşti, 1993.

[4] POPOVIC R.S., WIDMER R., *Magnetotransistor in CMOS Technology*, IEEE Trans. Electron Devices, **ED-33** 1334-40, 1986

THE MAIN NOISE CHARACTERISTICS FOR MOS MAGNETIC SENSORS

[1]CARUNTU GEORGE, [2]TAMAS RAZVAN

[1,2]*Constanta Maritime University, Romania*

ABSTRACT

The paper presents the results of research work regarding the analysis and optimization of magnetic microsensors realized in MOS integrated circuits technology.

On the basis of adequate models these have been established the noise main characteristics for MOS-Hall plates and for double-drain MOSFET magnetotransistors.

By using the numerical simulation the values of the signal-to-noise ratio and the detection limits for the two analysed structured are compared and it is also emphasized the way in which choosing the geometry and the material features allows getting high-performance sensors.

Keywords: *signal-to-noise ratio, detection limit, the transverse Hall current, supply-current-related sensitivity, noise equivalent magnetic induction, shot noise, carriers Hall mobility,*

1. INTRODUCTION

The possibility of modelling the channel depth by means of the external supply voltage and low value of area carrier density suggests the possibility of using the MOSFET channel as the active region of a Hall plate.

At the same time, it is outlined the advantage of integrating on the same chip of a magnetic sensor and the signal processing circuit.

The Hall devices in MOS structure have some drawbacks: the carrier mobility in the channel is half of its value in the volume of the device; the increasing of *1/f* noise, and the instability of device surface.

The analysis made in this paper outlines the way in which the possibility of choosing the adequate choice of device material and dimensions allows the improvement of the performances of magnetic sensors.

2. THE GENERAL CHARACTERIZATION OF THE MOS HALL PLATES

In the MOSFET structure (figure 1) a Hall plate can be realised if the channel is the active region of the plate, and the source (S) and the drain (D) are the biasing contacts. For the sensing contacts of the Hall voltage SH_1 and SH_2 are manufactured, two strongly doped regions n^+ type. The channel length is L, and the width is W [1].

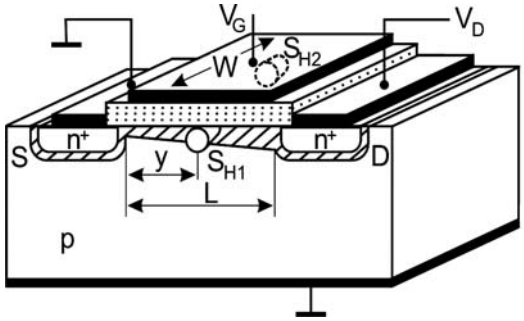

Figure 1 MOS-Hall plate

The bias in the linear region ensures a continuous channel having a thickness almost constant δ, which could be assimilated with a Hall plate.

Considering the Hall voltage mode of operation, the MOS-Hall plate is equivalent in the linear region with a conventional Hall plate differing by the fact that the charge carriers are due to the surface field effect. The surface charge density in the channel is approximately constant and it has the following expression [2]:

$$Q_{Ch} = C_{ox}(V_G - V_P) \tag{1}$$

where C_{ox} is the gate oxide capacitance per unit area, V_G the gate to source voltage, and V_p the threshold voltage.

The very low value of the surface charge density in the channel of a MOSFET ensures a high magnetic sensitivity of the MOS–Hall plate. There is also the possibility to modify the channel depth by the drain-source potential difference.

In the case of a conventional Hall plate, the generated voltage is [3]:

$$V_H = G(r_H / qn\delta)I \cdot B_\perp \tag{2}$$

where G is the geometrical correction factor, r_H the Hall factor and δ the thickness of the plate.

By replacing in (2) the product $qn\delta$ by the surface charge density in the channel Q_{Ch}, and the current I by I_D it results:

$$V_H = G(r_H / Q_{Ch})I_D \cdot B_\perp \tag{3}$$

Using the drain current expression:

$$I_D = \frac{W}{L}\mu_{Ch} \cdot C_{ox}(V_G - V_P)V_D = \\ = \frac{W}{L}\mu_{Ch}Q_{Ch}V_D \tag{4}$$

from (3) it results:

$$V_H = \mu_{H_{Ch}} \left(\frac{W}{L} G \cdot \right) V_D \cdot B_\perp \qquad (5)$$

where $\mu_{H_{Ch}} = \mu_{Ch} \cdot r_H$ represents the Hall mobility of the charge carriers in the channel.

The absolute sensitivity for a Hall device used as a magnetic sensor is:

$$S_A = \left| \frac{V_H}{B_\perp} \right| \qquad (6)$$

and the supply-voltage-related sensitivity is defined by:

$$S_V = \frac{S_A}{V_D} = \mu_{H_{Ch}} \left(\frac{W}{L} G \right) \qquad (7)$$

3. GENERAL CARACTERISATION OF THE DOUBLE-DRAIN MAGNETOTRANSISTOR

The double – drain MOS device (figure 2) is obtained from a MOSFET structure where its conventional drain region is replaced by two adjacent drain regions. Consequently, the total channel current

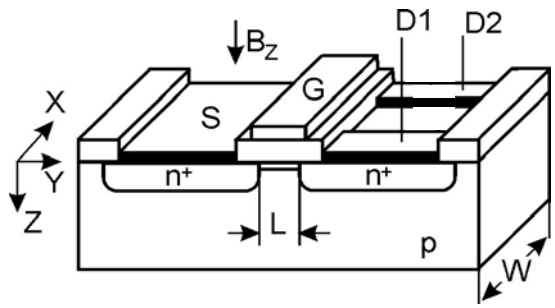

Figure 2 Double-drain MOSFET magnetotransistor

shared between this two drain regions[4].

The result of the bias in the linear region is the obtained of a continuous channel of approximately constant thickness, which can be assimilated with a hall plate.

The deflection of current lines appears under the action of a magnetic field $B_\perp$, perpendicular to the device surface. The carrier deflection causes a discrepancy between two drain currents:

$$\Delta I_D = \left| I_{D1}(\overline{B}) - I_{D1}(0) \right| = \left| I_{D2}(\overline{B}) - I_{D2}(0) \right| \qquad (8)$$

Since the output signal of the double-drain MOS magnetotransistors consists of the current variation between its terminals, this device operates in the Hall current mode. Using the features of dual Hall devices, and the Hall current expression it results [5]:

$$\Delta I_D = \frac{I_H}{2} = \frac{1}{2} \mu_{H_{Ch}} \cdot \frac{L}{W} \cdot G \cdot I_D \cdot B_\perp \qquad (9)$$

The supply-current-related sensitivity of the devices is defined by:

$$S_I = \frac{1}{I_D} \cdot \left| \frac{\Delta I_D}{B_\perp} \right| = \frac{1}{2} \mu_{H_{Ch}} \cdot \frac{L}{W} G \qquad (10)$$

where G denotes the geometrical correction factor and $\mu_{H_{Ch}}$ is the Hall mobility of the carriers in the channel.

4. SIGNAL-TO-NOISE RATIO FOR MOS HALL PLATES

In case of a MOS-Hall plate, at high frequencies, thermal noise dominates.

The voltage spectral density of thermal noise is given by [6]:

$$S_{NV} = 4kTR_{out} \qquad (11)$$

where $k = 1{,}38054 \cdot 10^{-23} JK^{-1}$ is the Boltzmann constant, and R_{out} is the output resistance of device.

The output resistance of a rectangular MOS-Hall plate with very small sense contacts is given by [7]:

$$R_{out} \cong 2 \frac{\rho_b}{\pi \delta} \ln \left(\frac{W}{s} \right) \qquad (12)$$

on condition that: $s << W << L$.

The coefficient ρ_b denotes the effective material resistivity, and s is the small sense contacts diameter.

If the biased voltage of device is constant, ρ_b practical not depends of magnetic field.

By substituting (12) into (11) it results the spectral density:

$$S_{NV} = \frac{8kT}{\pi n q \mu_{Ch} \delta} \ln \left(\frac{W}{s} \right) \qquad (13)$$

For a narrow bandwidth Δf around a frequency f, the signal-to-noise ratio, can be expressed as:

$$SNR(f) = \frac{V_H}{\left[S_{NV}(f) \cdot \Delta f \right]^{1/2}} \qquad (14)$$

where Δf denotes a narrow frequency band around the frequency f, ($f > 100kHz$,) and $S_{NV}(f)$ is the noise spectral density at the device output.

By substituting (2) and (13) into (14) it results[8]:

$$SNR(f) = \left(\frac{\pi \mu_{Ch}}{8hTqn\delta \Delta f \ln(W/s)} \right)^{1/2} r_H G I_D B_\perp \qquad (15)$$

Since the signal-to-noise ratio increases with the drain current I_D, the maximal *SNR(f)* is limited only by maximal acceptable device power dissipation P_{max}.

From (3) and (5), we also obtain the Hall voltage as a function of the power $P = V_D I_D$ dissipated in the device.

Multiplying (3) and (5) member-by-member it results:

$$V_H = G\left(\frac{W}{L}\right)^{1/2} r_H \left(\frac{\mu_{Ch}}{Q_{Ch}}\right)^{1/2} P^{1/2} \cdot B_\perp \qquad (16)$$

where $P = V_D I_D$ in the power dissipated in the device.

By substituting into (14) the expressions for the Hall voltage (16), and the noise voltage spectral density (13) it results:

$$SNR(f) = 1.11\mu_{H_{Ch}}\left[\frac{G^2(W/L)P}{kT\Delta f \ln(W/s)}\right]^{1/2} B_\perp =$$

$$= 9{,}7 \cdot 10^9 \mu_{H_{Ch}}\left[\frac{G^2(W/L)P}{\Delta f \ln(W/s)}\right]^{1/2} B \qquad (17)$$

where *T=300 K* and $k = 1{,}38054 \cdot 10^{-23} JK^{-1}$.

The *SNR(f)* dependence on magnetic induction for a given power dissipation ($P = 200mW$) and different L/W ratio values are shown in figure 3.

PHM1: $L/W = 0.5$ *;* PHM2: $L/W = 1$

PHM3: $L/W = 2$

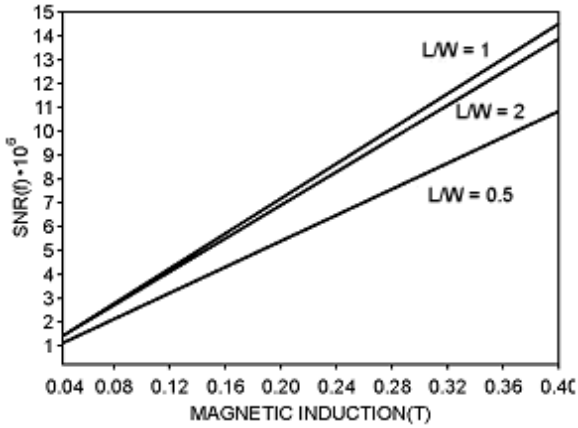

Figure 3 The SNR(f) depending on $B_\perp$ for three devices of different geometry

The frequency bandwidth is reduced, $\Delta f = 1Hz$, and the condition of low induction magnetic field is fulfilled. $\left(\mu_H^2 B^2 << 1\right)$.

It is noticed the *SNR(f)* values in maximum for the square device($L/W = 1$).

These values decrease with 25% when the length is half reduced (*PHM1*), also with 4.5% if the length doubles (*PHM3*).

5. SIGNAL TO NOISE RATION FOR DOUBLE-DRAIN MOSFET MAGNETOTRANSISTORS

The noise affecting the drain current of a MOSFET magnetotransistors is shot noise and $1/f$ noise. Signal-to-noise is defined by:

$$SNR(f) = \frac{\Delta I_D}{\left[S_{NI}(f) \cdot \Delta f\right]^{1/2}} \qquad (18)$$

where $S_{NI}(f)$ denotes the noise current spectral density in the drain current.

In case of shot noise, the current spectral density at frequencies more than *100 Hz* is given by [6]:

$$S_{NI} = 2qI \qquad (19)$$

where *I* is the device current.

In a small frequency range Δf at a frequency *f*, by substituting (9) and (19) into (18) it results[9]:

$$SNR(f) \geq \frac{1}{2\sqrt{2}} \mu_{H_{Ch}} \left(\frac{L}{W}\right) G \frac{I_D^{1/2}}{(q \cdot \Delta f)^{1/2}} B_\perp \qquad (20)$$

6. THE DETECTION LIMIT OF SENSORS IN MOS TECHNOLOGY

The value of the measurand corresponding to a signal-to-noise ration of one, constitute the detection limit of Hall device used as magnetic sensors.

In case of shot noise, for double-drain magnetotransistors using (20) it results for the detection limit:

$$B_{DL} \leq \frac{2\sqrt{2}(q\Delta f)^{1/2}}{\mu_{H_{Ch}}(L/W)G} I_D^{-1/2} \qquad (21)$$

To illustrate the B_{DL} dependence on device geometry there were simulated (figure 4) three double-drain magnetotransistors structures on silicon ($\mu_{H_{Ch}} = 0.07 m^2 V^{-1} s^{-1}$) and having different ratios $(W = 100\mu m)$.

MGT1: $W/L = 0.5$; MGT2: $W/L = 1$;

MGT2: $W/L = 2$

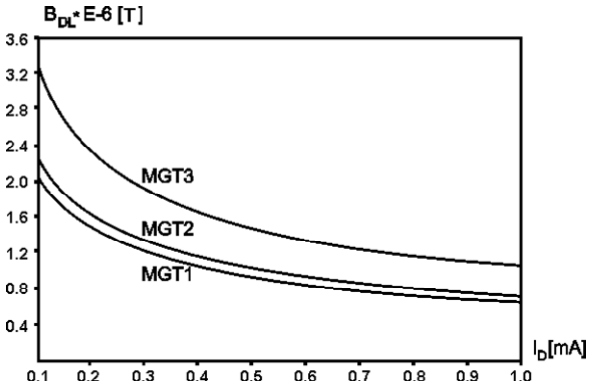

Figure 4 B_{DL} depending on the drain-current for three devices of different geometry.

It is noticed that the B_{DL} is minimum for $W/L = 0.5$ structure.For optimal structure B_{DL} decreases at materials of high carriers mobility.

In figure 5 it can be seen the material influence on B_{DL} values for three double-drain magnetotransistor structures realised from *Si*, *GaSb* and *GaAs* and having the same size: $L = 200\mu m$, $W = 100\mu m$.

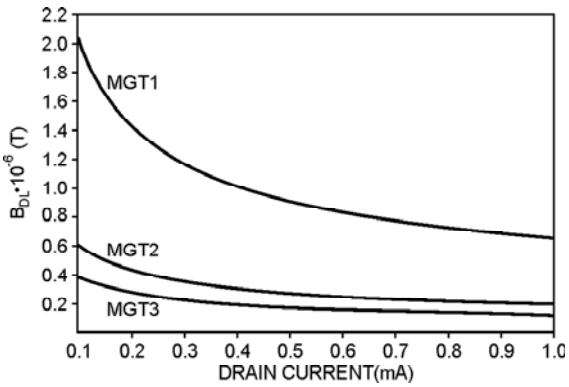

Figure 5 B_{DL} depending on the drain current for three devices of different materials

MGT1: *Si* with $\mu_{H_{Ch}} = 0.07 m^2 V^{-1} s^{-1}$;

MGT2: *GaSb* with $\mu_{H_{Ch}} = 0.25 m^2 V^{-1} s^{-1}$;

MGT3: *GaAs* with $\mu_{H_{Ch}} = 0.42 m^2 V^{-1} s^{-1}$.

A high value of carrier mobility causes the increasing of *SNR(f)*. So for $B = 0{,}5T$, *SNR(f)* increase with 60% for GaAs comparative with GaSb.

7. NOISE-EQUIVALENT MAGNETIC INDUCTION

The noise voltage at the output of a real Hall magnetic microsensor may be considered as an effect of an equivalent magnetic induction, acting on an ideal noiseless Hall device. The mean square noise – equivalent magnetic induction in a frequency range (f_1, f_2) , is obtained by substituting in the absolute sensitivity expression (6), the Hall voltage by the mean square noise voltage:

$$< B_N^2 >= \left(\int_{f_1}^{f_2} S_{NV}(f) df \right) \cdot S_A^{-2} \qquad (22)$$

At high frequencies, thermal noise dominates. For a narrow bandwidth Δf around a frequency f by substituting (6) and (13) into (22) it results :

$$< B_N^2 >= \frac{8kT\Delta f \rho_b \ln(W/s)}{\pi \delta \mu_{H_{Ch}}^2} \left(G\frac{W}{L} \right)^{-2} \cdot V_D^{-2} \quad (23)$$

To emphasize the geometry influence on *NEMI* there were simulated (figure 6) three MOS-Hall structures realised on silicon, $\mu_{H_{Ch}} = 0{,}07 m^2 V^{-1} s^{-1}$, $\Delta_f = 1Hz, \mu_{H_{Ch}}^2 \cdot B^2 << 1$, $W = 100\mu m$ and having different ratios L/W .

$MHP1 : L/W = 2; MHP2 : L/W = 1;$

$MHP3 : L/W = 0{,}5.$

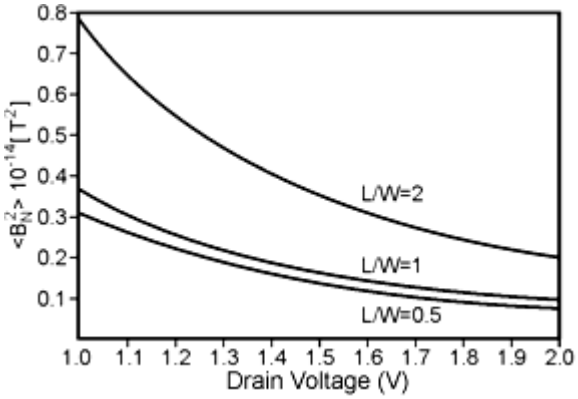

Figure 6 The NEMI depending on drain voltage, V_D for three devices of different geometry

The increasing of the channel length causes the decreasing of device performances.

If the length increases twice, the noise-equivalent magnetic induction spectral density increases with 18% and if the same distance increases four times (MHP1), *NEMI* increases with 148%.

In figure 7 it can be seen the material influence on *NEMI* values for three devices realised from GaSb, GaAs and PbTe and having the same sizes: $L = 50\mu m$, $W = 100\mu m$, $\delta = 10^{-7}\mu m$, $W/s = 50$

MHP1 (GaSb):

$\mu_{H_{Ch}} = 0.25 m^2 V^{-2} s^{-1}$; $\rho_b = 0.56 \Omega m$;

MHP 2 (GaAs):

$\mu_{H_{Ch}} = 0.42 m^2 V^{-2} s^{-1}$; $\rho_b = 0.32 \Omega m$;

MHP 3 (PbTe):

$\mu_{H_{Ch}} = 0.3 m^2 V^{-2} s^{-1}$; $\rho_b = 0.46 \Omega m$.

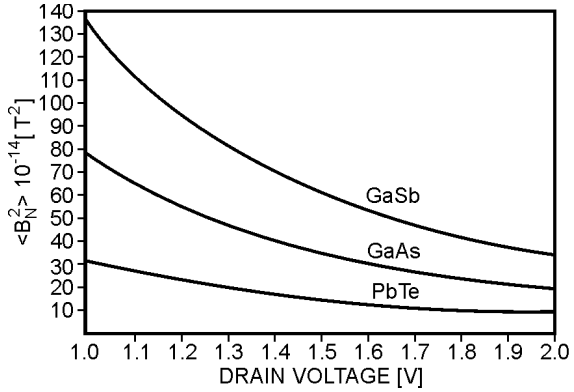

Figure 7 NEMI as a function of drain voltage, for three devices from different materials

At low frequencies,1/f noise dominates. By substituting (6) and (13) into (22) it is obtained:

$$< B_N^2 >= \frac{\alpha}{2\pi} \cdot \frac{\Delta f}{f} \cdot \frac{\ln(W/s)}{n\delta L^2 \mu_{H_{Ch}}^2} \cdot \left(G\frac{W}{L} \right)^{-2} \quad (24)$$

The numerical values of the *NEMI* for MOS- Hall devices made of different materials and having different channel size are listed in table 1.

($\alpha = 10^{-7}$, $f = 4Hz$, $\Delta f = 1Hz$, $\delta = 5 \cdot 10^{-7}\,\mu m$, $W/s = 50$, $n = 4{,}5 \cdot 10^{21} m^{-3}$, $W = 100\,\mu m$)

Table 1. The *NEMI* numerical values for different devices

Device	**Material**	μ_H $\left[m^2V^{-1}s^{-1}\right]$	W/L	$< B_N^2 >$ $\left[10^{-16}T^2\right]$
MHP1	Si	0.07	2	2320
MHP2	Si	0.07	1	2720
MHP3	Si	0.07	0.5	5840
MHP4	GaAs	0.42	2	8.16
MHP5	GaSb	0.25	2	20.8
MHP6	InAs	1.65	2	0.47

As the carrier mobility in the channel amounts to only half its value in equivalent conventional devices, and the depth of the channel is very small the values to noise-equivalent magnetic induction in Hall-MOS plates are higher than in conventional Hall plates.

The noise current at the output of a magnetotransistors can be interpreted as a result of an equivalent magnetic induction.The mean square value of noise magnetic induction (*NEMI*) is defined by:

$$\left\langle B_N^2 \right\rangle = \frac{\int_{f_1}^{f_2} S_{NI}(f) \cdot df}{(S_I \cdot I_D)^2} \tag{25}$$

Here S_{NI} is the noise current spectral density in the drain current, and (f_1, f_2) is the frequency range.

In case of shot noise, in a narrow frequency band around the frequency f by substituting (10) and (19) into (25) it results :

$$\left\langle B_N^2 \right\rangle = 2Iq\Delta f \cdot 4 \cdot \left(\frac{W}{L}\right)^2 \frac{1}{G^2 \mu_{H_{Ch}}^2} \cdot \frac{1}{I_D^2} \leq$$

$$\leq 8q\left(\frac{W}{L}\right)^2 \cdot \frac{\Delta f}{G^2} \cdot \frac{1}{\mu_{H_{Ch}}^2} \cdot \frac{1}{I_D} \tag{26}$$

Considering the condition of low value magnetic field fulfilled $\left(\mu_H^2 B^2 << 1\right)$, it is obtained a maximum value for $\frac{L}{W} G = 0{,}74$, if $\frac{W}{L} < 0{,}5$ [3]. In this case:

$$\left\langle B_N^2 \right\rangle_{\min} \leq 14{,}6q(\Delta f / I_D)\mu_{H_{Ch}}^{-2} \tag{27}$$

To emphasize the dependence of *NEMI* on device geometry there were simulated (figure 8) three double-drain magnetotransistors structures realised on silicon, $\mu_{H_{Ch}} = 0{,}07 m^2V^{-1}s^{-1}$, and having different ratios W/L ($W = 50\,\mu m$). The devices were based in the linear region and magnetic field has a low level $\left(\mu_H^2 B^2 << 1\right)$.

MGT1: $W/L = 0.5$ and $(L/W)G = 0.56$

MGT2: $W/L = 1$ and $(L/W)G = 0.409$

MGT2: $W/L = 2$ and $(L/W)G = 0.212$

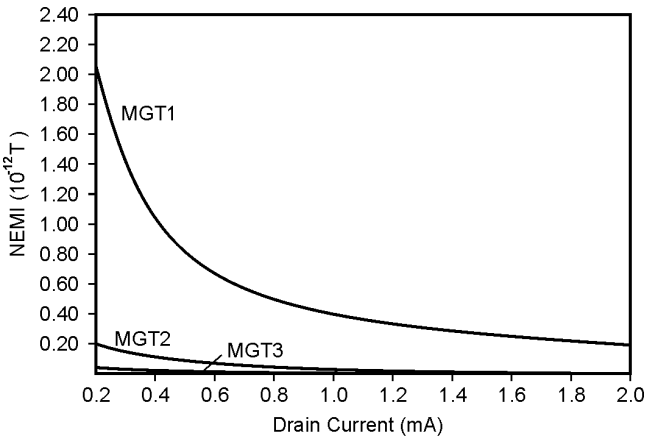

Figure 8 The NEMI depending on the drain current for three devices of different geometry

It is noticed that the *NEMI* is minimum for $W/L = 0.5$, and for smaller values of this ratio. The decreasing of the channel length causes the increasing of $NEMI(f)$ with 40,8% for a square structure $W = L$, and with 173% for $W = 2L$.

In figure 9 there are shown NEMI values obtained by simulation of three double-drain MOS magnetotransistors structures from different materials.

MGT1: *Si*, $\mu_{H_{Ch}} = 0.07 m^2V^{-1}s^{-1}$

MGT2: *InP*, $\mu_{H_{Ch}} = 0.23 m^2V^{-1}s^{-1}$

MGT3:*GaAs*, $\mu_{H_{Ch}} = 0.04 m^2V^{-1}s^{-1}$

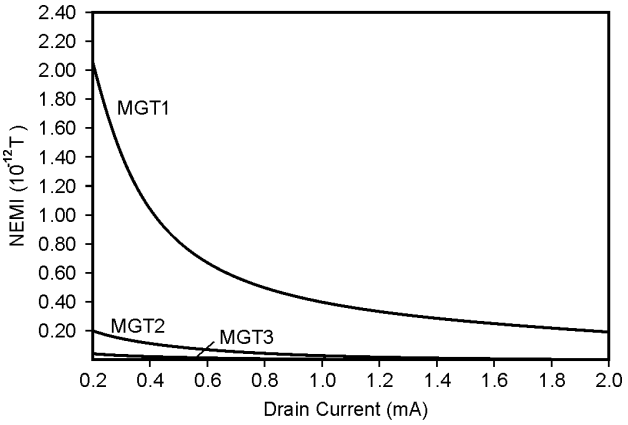

Figure 9 The NEMI depending on drain current, for three devices of different materials.

8. CONCLUSIONS

The analysis of the main noise characteristics of the MOS-Hall plates shows that in case of thermal noise, the square structure (*W=L*) is theoretically favourable to obtain magnetic sensors of performance. From double-drain MOSFET magnetotransistors, in case of shot noise,

the $W/L = 0.5$ structure provides superior *SNR* values, and smaller detection limit values. Also substituting the silicon technology by using other materials such as *GaAs* or *InSb* with high carriers mobility allows the made of higher characteristics devices.

It is noticed that the B_{DL} is minimum for $W/L = 0.5$ structure. For optimal structure B_{DL} decreases at materials of high carriers mobility.

Consequently, in spite of the low magnetic sensitivity of the magnetotransistors, very large signal-to-noise ratios are obtaining, resulting a high magnetic induction resolution.

A detection limit of about $0{,}2 \cdot 10^{-6} T$ at a total drain-current of *0,5 mA* has been obtained at double-drain MOSFET magnetotransistor in case *GaAs*.

By comparing the results for the two types of Hall devices used as magnetic sensors it is recorded a lower detection limit of almost 2-order in double-drain magnetotransistors.

The optimal processing of sensors – provided signal imposes their integration on the same chip with the amplifier circuit.

Figure 10 shows the electrical diagram of a transducer based on double-drain magnetotransistors

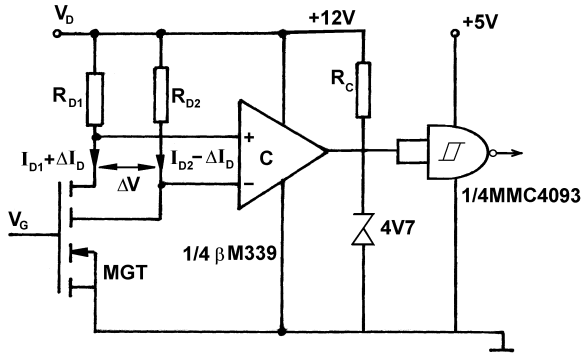

Figure 10 The electric diagram of transducers

In the double-drain MOSFET works in saturation the differential output voltage is:

$$\Delta V_D = \mu_{H_{Ch}} \frac{L}{W} G V_R B_\perp \qquad (28)$$

This equation has the same form as equation (5), pertinent to a conventional MOS-Hall plate, therefore the two devices are equivalent to magnetic sensitivity.

9. REFERENCES

[1] CĂRUNTU G., PANAIT C., The Noise-Equivalent Magnetic Induction Spectral Density of Magnetic Microsensors, in The Proceedings of the 2004 international Semiconductor Conference, CAS 2004, pp 259-262, October 4-6, 2004, Sinaia, Romania

[2] STERE R., BODEA M., *Tranzistoare cu efect de câmp.* Editura Tehnică, Bucureşti, 1972

[3] MIDDELHOEK S., AUDET S.A., *Physiscs of Silicon Sensors*, Academic Press, London, 1989

[4] PANAIT C. ,CĂRUNTU G., The Optimization of Magnetic Senzitive MOSFET Structures in the Proceedings of the 3rd edition of the International Conference Advanced Topics in Optoelectronics, Microelectronics and Nanotechnologies, 24-26 November 2006, Bucharest, Romania, ISBN 973-7622-34-0 [4] GRAY R.P., MEYER G.R., *Circuite integrate analogice. Analize şi proiectare.* Editura Tehnică, Bucureşti, 1993.

[5] CĂRUNTU G., PANAIT C., *The Optimization of Magnetic Senzitive MOSFET Structures* in the Proceedings of SPIE-Volume 6635, Advanced Topics in Optoelectronics, Microelectronics and Nanotechnologies III, May, 8, 2007

[6] PANAIT C. ,CĂRUNTU G., *The Noise of Hall Semiconductor Plates,* in The Proceedings of ISTET'05, pp.26-29, July 4-7,2005,Lviv,Ukraine

[7] PANAIT C. ,CĂRUNTU G., *The Noise of Hall Semiconductor Plates*, in The Proceedings of the XIII International Symposium on Theoretical Electrical Engineering ISTET'05, pp.26-29, July 4-7,2005, Lviv, Ukraine; ISBN 966-553-470-X.

[8] CĂRUNTU G., Raportul semnal-zgomot în câmp static pentru plăci Hall-MOS, în Buletinul Universităţii Petrol-Gaze din Ploieşti, Volum LVII, pp. 85-90, 11-13 mai 2005, Ploieşti, ISSN 1221-9371

[9] CĂRUNTU G., PANAIT C., The Detection Limit of MOS Structures Magnetic Microsensors in the Proceedings of Progress in Electromagnetics Research Symposium, PIERS 2004, pp 505-508, 28-31 March, 2004, Pisa, Italy

HALL DEVICES REALISED IN THE MOS TECHNOLOGY

CARUNTU GEORGE

Constanta Maritime University, Romania

ABSTRACT

This paperwork presents the structure, the operating conditions and the main features of some microsensors realised in the MOS integrated circuits technology. By using numerical simulation, the values of the sensor response for the two analysed devices are compared and it is also emphasized the way in which choosing the geometry and the material features allows getting high-performance sensors.

Keywords: *Hall current, noise equivalent magnetic induction, signal-to- noise ratio, sensor response*

1. THE LATERAL MAGNETOTRANSISTORS

Figure 1 illustrates the cross section of a lateral bipolar magnetotransistor structure, operating on the current deflection principle, realized in MOS integrated circuits technology[1].

The n^+ regions of emitter E and primary collector C, are laterally separated on an L distance from base type *p* region. The two p^+ base contacts, allow the application of the drift-aided field $\overline{E}_a$. On its action the most part of the minority carriers injected into the base drift to primary collector, producing collector current I_C. However some of electrons diffuse downwards to the *n* type substrate (the secondary collector) and thus produce the substrate parasitic current I_S

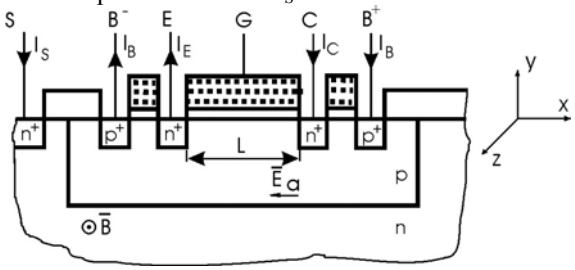

Figure 1. Cross section of the lateral magnetotransistor

In the presence a magnetic induction $B_\perp$, perpendicular to the plane of the section the ratio between I_C and I_S, change because of the current deflection.

In order to describe the qualitative operation of the device, let us assume that it is adequately biased for the forward active operation.If the very small magnetic field $\overline{E}_a$,is oriented as shown in figure 6, the electrons are deviated to substrate junction. Only a few electrons will contribute to collector current.

The area from base region, between the emitter contact and collector contact, operates as a short Hall plate, and an induction field $\overline{B}$ causes the deflection of current lines. The transverse will be:

$$I_Y = J_Y(LW) \tag{1}$$

where *W* is the dimension along the axis Z.

In the absence of a induction $\overline{B}$, the current density along the axis *X* has the following expression:

$$J_X = \frac{I_C}{WY} \tag{2}$$

The *Y* parameter takes values in (y_{jn}, y_{jp}). Here y_{jn} and y_{jp} denote the junction depths of the collector region and the *p*-well respectively.

If it is considered the Hall angle expression $tg\theta_{Hn} = \mu_{Hn} \cdot B$ [1] then it is obtained:

$$J_Y = J_X \cdot tg\theta_{Hn} = \frac{(\mu_{Hn} B) I_C}{WY} \tag{3}$$

By substituting (3) into (1) it results:

$$I_H = I_Y = (L/Y) I_C \mu_{Hn} B_\perp = \Delta I_C \tag{4}$$

where μ_{Hn} is the Hall mobility of electrons in the base region.

2. SENSITIVITY AND SENSOR RESPONSE

The absolute sensitivity of the devices is defined by:

$$S_A = |\Delta I_C / B| = (L/Y) I_C \mu_{Hn} \tag{5}$$

A magnetotransistor may be regarded as a modulation transducer that converts the magnetic induction signal into an electric current signal. This current signal or output signal is the variation of collector current, caused by induction $B_\perp$.

The sensor response is expressed by:

$$h(B) = \frac{\Delta I_C}{I_C} = \frac{L}{Y} \mu_{Hn} \cdot B \tag{9}$$

and it is linear for induction values which satisfy the condition: $\mu_H^2 \cdot B_\perp^2 << 1$. In figure 4 it can be seen the geometry influence on $h(\overline{B})$ values for three magnetotransistor structures, realized on silicon ($\mu_{Hn} = 0.15 m^2 V^{-1} s^{-1}$) and having different ratios L/Y $(L = 50 \mu m)$.

.MGT$_1$: $\frac{L}{Y}=0{,}5$; MGT$_2$: $\frac{L}{Y}=1$; MGT$_3$: $\frac{L}{Y}=2$;

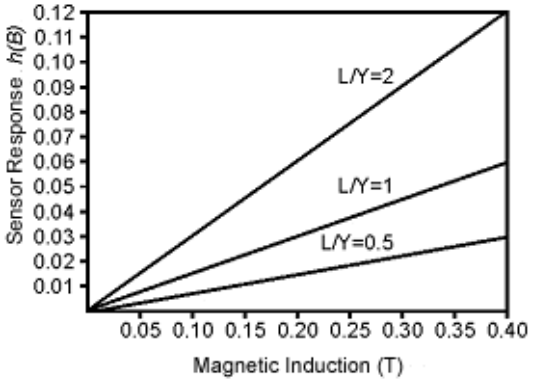

Figure 2. The *h(B)* depending on *B* for three devices of different geometry

For the same geometry ($L/Y=0.5$) the sensor response depends on material features.

In figure 3 there are shown $h(\overline{B})$ values for two sensor structures realized on Si ($\mu_{Hn}=0.15m^2V^{-1}s^{-1}$) and GaAs ($\mu_{Hn}=0.80m^2V^{-1}s^{-1}$).

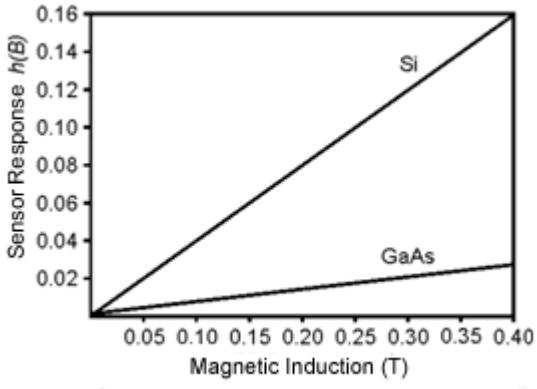

Figure. 3 The *h(B)* depending on *B* for three devices of different materials

3. THE NOISE-EQUIVALENT MAGNETIC INDUCTION SPECTRAL DENSITY

The mean square value of noise magnetic induction (NEMI) is defined by :

$$\left\langle B_N^2\right\rangle=\frac{\int_{f_1}^{f_2}S_{NI}(f)\cdot df}{(S_I\cdot I_C)^2} \tag{10}$$

Here S_{NI} is the noise current spectral density in the collector current, and (f_1,f_2) is the frequency range. In case of shot noise, the noise current spectral density at frequencies over 100 Hz is given by [2]:

$$S_{NI}=2qI \tag{11}$$

where *I* is the device current.

From (4) it is obtained the noise-equivalent magnetic induction spectral density:

$$S_{NB}(f)=\frac{\partial<B_N^2>}{\partial f}=\frac{S_{NI}(f)}{S_A^2} \tag{12}$$

In a narrow frequency band around the frequency *f*, by substituting (5) and (11) into (12) it results:

$$S_{NB}(f)\le 2q\left(\frac{Y}{L}\right)^2\frac{1}{\mu_{Hn}^2 I_C} \tag{13}$$

In figure 4 there are shown $S_{NB}(f)$ values for three magnetotransistor structures made of different materials ($Y/L=0.5;\Delta f=1Hz$)

MGT$_1$: Si,with $\mu_{Hn}=0.15m^2V^{-1}s^{-1}$

MGT$_2$: Ga Sb, with $\mu_{Hn}=0.50m^2V^{-1}s^{-1}$

MGT$_3$: Ga As, with $\mu_{Hn}=0.80m^2V^{-1}s^{-1}$

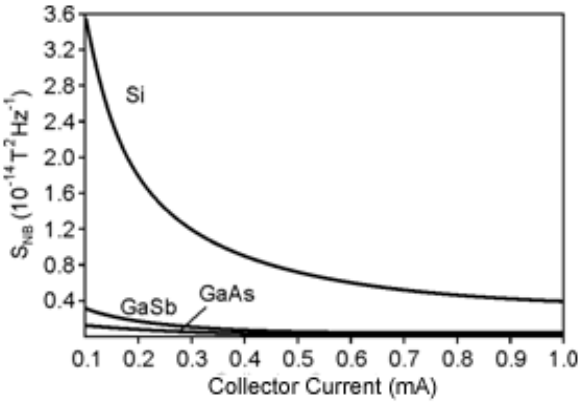

Figure 4. The S_{NB} (f) depending on the I_C for three devices of different materials

The noise-equivalent magnetic induction spectral density lowers with the increase of carriers mobility, this increase being significant for collector currents of relatively low values. So for the collector current $I_C=0.1mA$, the offset equivalent magnetic induction value of the GaSb device decreases by 91.5% as compared to that of the silicon device.

4 THE DOUBLE-DRAIN MOS DEVICE

The double-drain MOS device (figure 5) is a MOSFET with two adjacent drain regions replacing the conventional single drain region, the total channel current being shared between these regions[3].

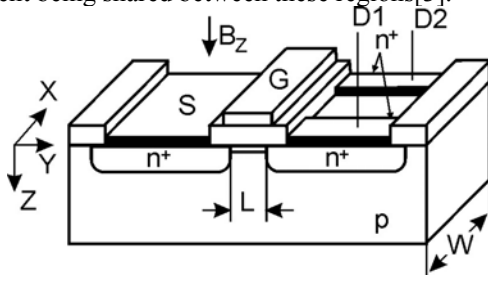

Figure 5. Double-drain MOSFET magnetotransistor

The result of the bias is the linear region is the obtained of a continuous channel of approximately constant thickness, which can be assimilated with a short Hall plate.The deflection of current lines appears under

the action of a magnetic field $B_\perp$, perpendicular to the device surface. The current deflection causes an imbalance between two drain currents:

$$\Delta I_D = I_{D1}\left(\overline{B}\right) - I_{D1}(0) = I_{D2}\left(\overline{B}\right) - I_{D2}(0) \quad (14)$$

Since the output signal of the double-drain MOS magnetotransistors consists of the current variation between its terminals, this device operates in the Hall current mode. Using the features of dual Hall devices, and the Hall current expression it results [4]:

$$\Delta I_D = \frac{I_H}{2} = \frac{1}{2}\mu_{H_{Ch}} \cdot \frac{L}{W} \cdot G \cdot I_D \cdot B_\perp \quad (15)$$

where $\mu_{H_{Ch}}$ is the carriers Hall mobility in the channel.

The supply-current-related sensitivity of the devices is defined by:

$$S_1 = \frac{1}{I_D} \cdot \left|\frac{\Delta I_D}{B_\perp}\right| = \frac{1}{2}\mu_{H_{Ch}} \cdot \frac{L}{W} G \quad (16)$$

and depends on the channel geometry.

5. THE SENSOR RESPONSE

The sensor response is expressed by:

$$h(B) = \frac{\Delta I_D}{(I_{d1} + I_{D2})_{B=0}} = \frac{1}{2}\mu_{H_{Ch}} \cdot \frac{L}{W} \cdot G \cdot B_\perp \quad (17)$$

and it is linear for induction values which satisfy the condition: $\mu_H^2 \cdot B_\perp^2 << 1$. In figure 6 it can be seen the geometry influence on $h(B)$ values for three magnetotransistor structures, realised on silicon ($\mu_{H_{Ch}} = 0.07 m^2 V^{-1} s^{-1}$) and having different ratios W/L $(W = 50\mu m)$.

MGT1: $W/L = 0.5$, $(L/W)G = 0.72$;

MGT2: $W/L = 1$, $(L/W)G = 0.68$;

MGT3: $W/L = 2$, $(L/W)G = 0.46$;

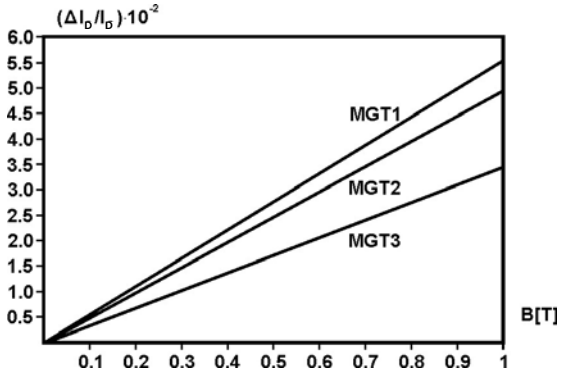

Figure 6. The *h(B)* depending on *B* for three devices of different geometry.

It is noticed that the response $h(B)$ is maximum for $W/L = 0.5$ structure. Decreasing the emitter-collector distance, $h(B)$ decreases with 37.5% for $W = 2L$, comparative with the maximum value.

The sensor response decreases with 10.7%, comparative with $W/L = 0.5$ structure if the distance between emitter and collector doubles.

For the same geometry $W/L = 0.5$, the response is depending on material features.

In figure 7 there are shown $h(B)$ values of three sensors MGT1, MGT2, MGT3 realised on:

Si ($\mu_{H_n} = 0.07 m^2 V^{-1} s^{-1}$);

InP($\mu_{H_n} = 0.23 m^2 V^{-1} s^{-1}$);

GaAs ($\mu_{H_n} = 0.40 m^2 V^{-1} s^{-1}$).

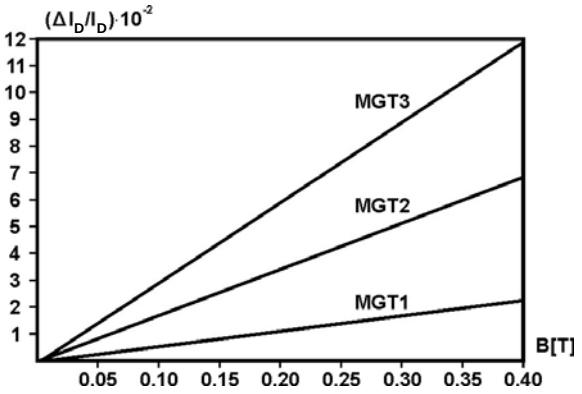

Figure 7. The *h(B)* depending on *B* for three devices on different materials.

6. THE NOISE-EQUIVALENT MAGNETIC INDUCTION SPECTRAL DENSITY

The noise current at the output of a magnetotransistors can be interpreted as a result of an equivalent magnetic induction. The mean square value of noise magnetic induction (*NEMI*) is defined by:

$$\left\langle B_N^2 \right\rangle = \frac{\int_{f_1}^{f_2} S_{NI}(f) \cdot df}{(S_I \cdot I_D)^2} \quad (18)$$

Here S_{NI} is the noise current spectral density in the drain current, and (f_1, f_2) is the frequency range.

From (18) it is obtained the noise-equivalent magnetic induction spectral density:

$$S_{NB}(f) = \frac{\partial < B_N^2 >}{\partial f} = \frac{S_{NI}(f)}{S_A^2} \quad (19)$$

In case of shot noise, by analogy with (13) it results:

$$S_{NB}(f) = 2qI \cdot 4\left(\frac{W}{L}\right)^2 \cdot \frac{1}{G^2 \mu_{H_{Ch}}^2} \cdot \frac{1}{I_D^2} \leq$$

$$\leq 8q\left(\frac{W}{L}\right)^2 \cdot \frac{1}{G^2} \cdot \frac{1}{\mu_{H_{Ch}}^2} \cdot \frac{1}{I_D} \quad (20)$$

Considering the condition of low value magnetic field fulfilled ($\mu_H^2 B^2 << 1$), it is obtained a maximum value for $(L/W)G = 0.74$, if $W/L < 0.5$ [5].

In this case:

$$(S_{NB}(f))_{\min} \le 14.6q\frac{1}{I_D\mu_{H_{Ch}}^2} \qquad (21)$$

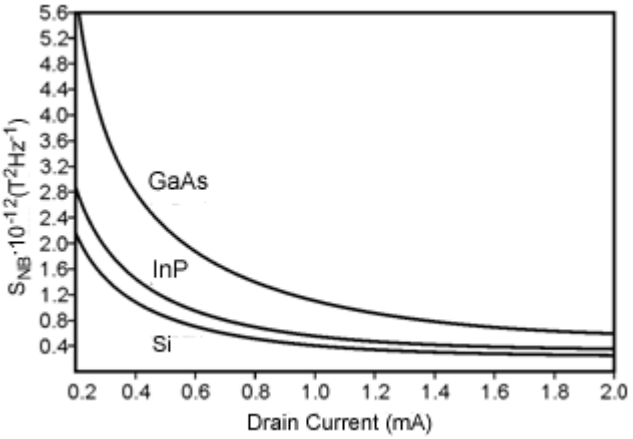

Figure 8. The S_{NB} depending on drain current, for three devices of different materials

In figure 8 there are shown $S_{NB}(f)$ values obtained by simulation of three double-drain MOS magnetotransistors structures from different materials.

MGT1: *Si*, $\mu_{H_{Ch}} = 0.07m^2V^{-1}s^{-1}$

MGT2: *InP*, $\mu_{H_{Ch}} = 0.23m^2V^{-1}s^{-1}$

MGT3:*GaAs*, $\mu_{H_{Ch}} = 0.04m^2V^{-1}s^{-1}$

To emphasize the dependence of $S_{NB}(f)$ on device geometry there were simulated (figure 9) three double-drain magnetotransistors structures realised on silicon, $\mu_{H_{Ch}} = 0{,}07m^2V^{-1}s^{-1}$, and having different ratios W/L ($W = 50\mu m$). The devices were based in the linear region and magnetic field has a low level $\left(\mu_H^2 B^2 << 1\right)$.

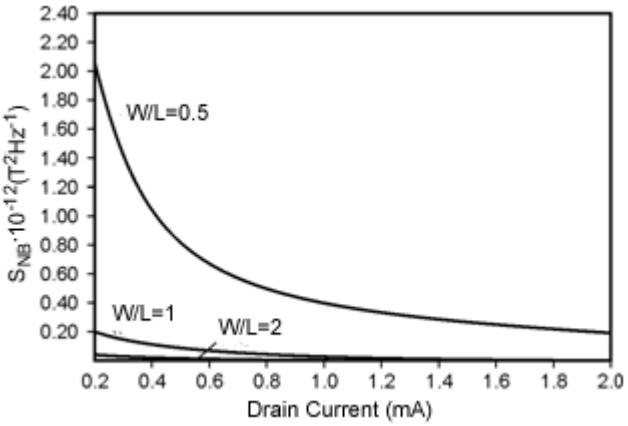

Figure 9. The S_{NB} depending on the drain current for three devices of different geometry

MGT1: $\frac{W}{L} = 0.5$ and $\left(\frac{L}{W}G\right) = 0.56$

MGT2: $\frac{W}{L} = 1$ and $\left(\frac{L}{W}G\right) = 0.409$

MGT3: $\frac{W}{L} = 2$ and $\left(\frac{L}{W}G\right) = 0.212$

It is noticed that the $S_{NB}(f)$ is minimum for $W/L = 0.5$, and for smaller values of this ratio. The decreasing of the channel length causes the increasing of $S_{NB}(f)$ with 40,8% for a square structure $W = L$, and with 173% for $W = 2L$.

6. CONCLUSIONS

From double-drain MOSFET magnetotransistors, in case of shot noise, the $W/L = 0.5$ structure provides smaller $S_{NB}(f)$ values. Also substituting the silicon technology by using other materials such as *GaAs* or *InSb* with high carriers mobility allows the made of higher characteristics devices.

The noise equivalent magnetic induction lowers with the increase of carriers mobility, this increase being significant for drain currents of relatively low values.

Although the magnetotransistors have a low magnetic sensitivity, very large signal-to-noise ratios are obtained, hence, a high magnetic induction resolution is resulting.

7. REFERENCES

[1] POPOVIĆ R.S., WIDMER R. *Magnetotransistor in CMOS technology,* IEEE Trans. Electron Devices, 1986, ED-33 1334-40

[2] GRAY R.P., MEYER G. R, *Circuite integrate analogice. Analize şi proiectare,* pp. 579, 583 Editura Tehnică, Bucureşti, 1993.

[3] CĂRUNTU G., *Măsurări galvanomagnetice în dispozitive semiconductoare.* SECOMAR '99, Academia Navală „Mircea cel Bătrân, vol. II, pp. 69-74, Constanţa, iunie, 1999.

[5] MIDDELHOEK S., AUDET S.A., *Physiscs of Silicon Sensors,* pp. 5.20, 5.21, Academic Press, London, 1989.

[4] NATHAN A., HUISER A. M. J., BALTES H. P., *Two Dimensional Numerical Moddeling of Magnetic Field Sensors in CMOS Technology,* IEEE Trans. Electron Device **ED**-32 1212-19, 1985.

THEORETICAL CONSIDERATIONS ON SUPERCONDUCTORS ELECTROMAGNETISM

CARUNTU GEORGE

Constanta Maritime University, Romania

ABSTRACT

The paper contains theoretical considerations regarding the behaviour of superconductors in a magnetic field. In the first part, based on the superconducting, two-fluid model, an original method is presented, in order to establish the dispersion relation, which indicates the connection between the wave vector $\overline{k}$ and the frequency ω in electromagnetic waves. At the same time, the paper contains some considerations on the contribution to conduction in the frequency function of normal and super fluid electrons.

In the second part of the paper, based on the Meissner effect, using elements of quantic physics, we establish the expression of the magnetic flux generated by the surface currents in a superconducting ring. We stress the fact that it can only assume such values as to quantify the total flux, which also depends on the contribution of external sources.

Keywords: *Meissner effect, coherence length, penetration depth, Cooper electronic pairs, potential magnetic vector, wave function, magnetic potential vector, dispersion relation, wave vector* $\overline{k}$*, second London equation, plasma frequency*

1. SUPERCONDUCTIVITY AND ACTION OF MAGNETIC FIELDS

Superconductivity is a property of some materials to present null electric resistance in direct current when the temperature is lower then a critical value T, and the magnetic field does not exceed the critical value H. Between the critical field and critical value of temperature a relation of the following type is established:

$$H_C = H_0[1-\left(\frac{T_C}{T_0}\right)^2] \qquad (1)$$

As shown in image 1 the surface limited by the

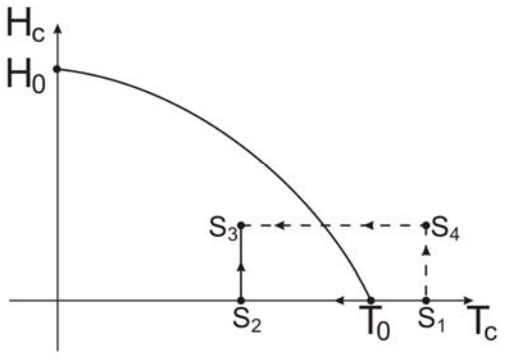

Figure 1 The dependence of H_C on T_C

curve and by the two axes corresponds to the superconductivity condition. If a sample of material successively passes from condition S_1 to S_2 and to S_3, there can be found turbines currents at its surface whose effect is the cancelling of the field inside the sample. If the same sample passes from S_1 to S_4 and then to S_3, it follows that in the moment of the transition in the superconductivity spontaneously surface induced currents develop that through the created field lead to cancelation the magnetic induction inside the sample. This is the Meissner effect whose manifestation is not identical for all the superconductive materials.

As for the superconductors of type I the field lines are completely expelled as long as the field applied is inferior to the value H_c. As for those of type II the Meissner effect disappears progressively as the field varies between the inferior critical value H_{c1} and the superior critical value H_{c2}.The essential difference between the two types of superconductor consists in the fact that the value of medium free way of the conduction electrons in the normal condition at low temperatures which determines the relationship between coherence length and penetration depth. A semiconductor is type I if the surface energy is always positive, and type II if the surface energy becomes negative when increasing the field. The Meissner effect points out the fact that the superconductor condition quality implies much more than a simple cancelling of the electrical resistance. According to the two fluids model, London establishes for the magnetic field along perpendicular direction z on the superconductor's surface the following relationship:

$$\overline{B}(z) = \overline{B}(0)\exp(-z/\lambda) \qquad (2)$$

This relation shows that $\overline{B}$ can get inside the superconductor on a very small depth, which explains the Meissner effect.

In the case of the action of high frequency, there is a change in steps of the resistance of the superconductor material from the zero value to that corresponding to the conductor condition. Between the current density of

normal electrons J_n and the density of the superconductor electrons J_s there is the relationship:

$$J_n = J_s(\lambda / d)^2 \quad (3)$$

Where d represents the penetration depth of the turbines currents:

$$d = (2\pi\omega\sigma)^{-1/2}$$

So for low frequency $d >> \lambda$ and $J_s >> J_n$ and for high frequencies $\lambda >> d$ and $J_n >> J_s$ that is characteristic of the normal conductor condition.

2. QUANTIFICATION OF THE MAGNETIC FIELD

The fundamental condition of the superconductor is given by the existence of the electronic pairs, poorly linked, characterized by a total null impulse. A Cooper pair, having the thorn equal to zero will subdue to Bose-Einstein, according to which the number of the particles that can be found in a quantic condition is unlimited. Accordingly all pairs of electrons are condensed in the same quantic condition described by the wave function:

$$\Psi(\bar{r},t) = \sqrt{\rho(\bar{r},t)}, \exp(i\gamma(\bar{r},t))$$

For the system of Cooper pair which appears in the described function, the temporal equation Shrödinger is:

$$i\hbar\frac{\partial\Psi}{\partial t} = -\frac{\hbar^2}{2m}\nabla^2\Psi + v\Psi \Leftrightarrow i\hbar\frac{\partial\Psi}{\partial t} = H \quad (4)$$

Where H represents the differential operator associated to the variable energy. The impulse in the field is a sum of two terms: mechanic impulse $P_m = mv$ and the impulse of the field $P_{imp} = \frac{q}{c} + A$; A is the potential magnetic vector.

The total impulse will be

$\bar{p} = \bar{p}m + \bar{p}_{cimp} = m\bar{v} + \frac{q}{c} + A$, and the kinetic energy of the particle :

$$\frac{1}{2}m\bar{v}^2 = \frac{1}{2m}(m\bar{v})^2 = \frac{1}{2m}(\bar{p} - \frac{q}{c}A)^2$$

The total energy of the particle is described by an operator H which is the sum of the operator that describes the kinetic energies and potential energies:

$$H = \frac{p^2 m}{2m} + v(x) = \frac{1}{2m}(p - \frac{q}{c}A)^2 + q\varphi \quad (5)$$

Where $v(x)$ is the potential energy and φ is the electrostatic potential. In the Schrödinger theory the impulse variable is represented by a differential operator which acts upon the wave function that is situated at its right, as follows:

$$P = -i\hbar\frac{\partial}{\partial x} \text{ and } P^2 = -i\hbar^2\frac{\partial^2}{\partial x^2}$$

So (5) becomes:

$$H = \frac{1}{2m}(-\hbar^2\frac{\delta^2}{\delta x^2} + 2i\hbar\frac{2A}{c}\frac{\partial}{\partial x} + \frac{q^2}{c^2}A^2) + q\varphi \quad (6)$$

By replacing (6) in equation (4) it is obtained:

$$i\hbar\frac{\partial\Psi}{\partial t} = \frac{1}{2m}(-\hbar^2\nabla^2\Psi + 2i\hbar\frac{qA}{c}\nabla\Psi) + \frac{1}{2m}\frac{q^2A^2}{c^2}\Psi + 2\varphi\Psi \quad (7)$$

We write the complex conjugated to t (7):

$$i\hbar\frac{\partial\varphi^*}{\partial t} = \frac{1}{2m}(-\hbar^2\nabla^2\Psi^* + 2i\hbar\frac{qA}{c}\nabla\Psi^*) + \frac{1}{2m}\frac{q^2A^2}{c^2}\Psi^* + 2\varphi\Psi^* \quad (8)$$

We multiply equation (7) by Ψ^* and equation (8) by Ψ and than we subtract following this order:

$$i\hbar(\Psi^*\frac{\partial\Psi}{\partial t} + \Psi\frac{\partial\Psi^*}{\partial t}) = \frac{1}{2m}(\hbar^2\Psi\Delta\Psi^* - \hbar^2\Psi\Delta\Psi^*) + \frac{1}{2m}(2i\hbar\frac{qA}{c}\Psi^*\nabla\Psi + 2i\hbar\frac{qA}{c}\Psi^*\nabla\Psi)$$

or

$$i\hbar\frac{\partial}{\partial t}(\Psi\Psi^*) = \frac{1}{2m}\psi(\hbar^2\Delta\Psi^* + 2i\hbar\frac{qA}{c}\nabla\Psi^*) - \frac{1}{2m}\Psi^*(\hbar^2\Delta\Psi - 2i\hbar\frac{qA}{c}\nabla\Psi) \quad (9)$$

The probability $dW(r,t)$ to find a particle described by the cave function Ψ in point r in the volume element $dr = dxdvdz$ is :

$$dW(\bar{r},t) = |\Psi|^2 d\bar{r} = \Psi\Psi^* d\bar{r}$$

Then the probability density is: $P = \frac{dW(\bar{r},t)}{d\bar{r}} = \Psi\Psi^*$

If in a system of particles a big number of the latter can be found in the same quantic condition described in the wave function as in the case of the pairs of electrons in superconductor, then the density of probability represents the density of particles: $P = \Psi\Psi^* = \rho_v$. By replacing in (9) it can be written:

$$\frac{\partial\rho_v}{\partial t} = \frac{q}{2m}\nabla[\Psi(\hbar grad\Psi^* + 2i\frac{qA}{c}\Psi^*)] - \frac{q}{2m}\nabla[\Psi^*(\hbar grad\Psi - 2i\frac{qA}{c}\Psi)]$$

Or

$$\frac{\partial\rho_v}{\partial t} + \frac{q}{2m}\nabla[\Psi^*(\frac{\hbar}{i}grad\Psi + 2\frac{qA}{c}\Psi)] -$$

$$-\frac{q}{2m}\nabla[\Psi(\frac{\hbar}{i}grad\Psi^* + 2\frac{qA}{c}\Psi^*)] = 0 \qquad (10)$$

By comparing the last relationship to the continuity equation $\frac{\partial \rho_v}{\partial t} + \nabla\bar{\Im} = 0$ results :

$$\bar{\Im} = \frac{q}{2m}\Psi^*(\frac{\hbar}{i}grad\Psi - 2\frac{qA}{c}\Psi) -$$

$$-\frac{q}{2m}\Psi(\frac{\hbar}{i}grad\Psi^* + 2\frac{qA}{c}\Psi^*) = 0$$

By replacing in the expression of the current density the wave function becomes

$\Psi(\bar{r},t) = \sqrt{\Psi\Psi^*}\exp(i\gamma(\bar{r},t))$ it is obtained:

$$\bar{\Im} = \frac{q}{2m}\Psi^*(\frac{\hbar}{i}igrad\Psi - 2\frac{qA}{c}\Psi) -$$

$$-\frac{q}{2m}\Psi(\frac{\hbar}{i}(-i)\Psi^* grad\gamma + 2\frac{qA}{c}\Psi^*) =$$

$$= \frac{q}{2m}[2\hbar\Psi\Psi^* grad\gamma - 4\frac{qA}{c}\Psi\Psi^* =$$

$$= \frac{q\hbar}{2m}(2grad\gamma - 4\frac{qA}{c\hbar})\rho_v =$$

$$= \frac{\hbar}{m}(grad\gamma(\bar{r}) - 2\frac{qA}{c\hbar})\rho_v \qquad (11)$$

Because of the Meissner effect we have inside the superconductor in any situated point it is obtained:

$\bar{\Im} = rot\bar{H} = \frac{1}{\mu}rot\bar{B} = 0$, it results :

$$\hbar c grad\gamma(\bar{r},t) = 2q\bar{A} \qquad (12)$$

Relationship that expresses the dependence between the phase of the wave function and the magnetic potential vector. If the superconductor is ring shaped, upon integration it results:

$$\hbar c\oint grad\gamma(\bar{r})d\bar{r} = 2q\oint\bar{A}d\bar{r} \qquad (13)$$

In the left member we keep in mind that it represents the phase change in a circuit round the ring, and in the right member we apply the Stokes theory. It follows:

$$(\gamma_2 - \gamma_1)\hbar c = 2q\iint_s rot\bar{A}d\bar{s} =$$

$$= 2q\iint_s\bar{B}d\bar{s} = 2q\Phi \qquad (14)$$

According to the condition that the wave function must be continuous in a complete circuit around the ring: $\gamma_2 - \gamma_1 = 2\pi l,\ l \in Z$, relation (14) becomes:

$$\Phi = \frac{\hbar c}{2q}(2\pi l), l \in Z \qquad (15)$$

The relationship (15) shows that in the case of superconductor ring, the magnetic flux produced by the surface currents must take such values so that the total flux, which also depends on the contribution of the flux produced by external sources, is quantified, the quantum of the flux being:

$$\frac{\hbar c}{2e} \cong \frac{1{,}035}{\pi}\cdot 10^{-15}Tm^2,\ \ e = q \qquad (16)$$

3. CONSIDERATIONS CONCERNING THE DISPERSION RELATIONSHIP FOR ELECTROMAGNETIC WAVES IN A SUPRACONDUCTOR

A convenient way to characterize the wave behavior of a system is to establish the dispersion relation expressing the connection between the wave vector $\bar{k}$ and the frequency ω.

Next, this relationship will be deducted for electromagnetic waves in a superconductor based on the bi-fluid model of superconductivity . Under this model, for temperatures below the transition value T_c, a part of the conduction electrons behave as normal being scattered and showing resistance to passing through metal, and another part, super electrons can pass through metal without resistance, without suffering any spill. Corresponding to current density we have:

$$\bar{J} = \bar{J}_n + \bar{J}_s$$

4. DEDUCTION OF THE DISPERSION RELATIONSHIP

Taking into account sinusoidal permanent regime, a complex representation can be used and the local form of magnetic circuit law for immovable objects becomes:

$$\nabla\times\bar{H} = \bar{J} + j\omega\varepsilon\underline{E} = \underline{J}_s + \underline{J}_n + j\omega\varepsilon\underline{E} \qquad (17)$$

where $\underline{J}_s$ represents the super fluid electrons contribution and is given by the second London equation:

$$\nabla + \underline{J}_s = -\frac{n_s l^2}{m}\underline{B} = -\frac{1}{\lambda^2}\underline{H}$$

λ is the London penetration depth, $\underline{J}_n = \sigma\underline{E}$ is the normal electron contribution, being the normal conductivity. The final component of the right member of the equation (17) is the current journey. By applying rotor operation to relation (17) it results:

$$\nabla\times(\nabla\times\underline{H}) = \nabla\times\underline{J}_s + \nabla\times\underline{J}_n + j\omega\varepsilon\nabla\times\underline{E} \qquad (18)$$

Left member turns as follows:

$$\nabla\times(\nabla\times\underline{H}) = \nabla(\nabla\underline{H}) - (\nabla\nabla)\underline{H} = -\Delta\underline{H}$$

Because $\nabla\underline{H} = 0$, magnetic field vector is solenoid.

In the right side of relation (18) the second Maxwell's equation gives us:

$\nabla\times\underline{J}_s = \sigma\nabla\times\underline{E} = -\sigma\frac{\sigma B}{\sigma t} = -j\omega\sigma\mu\underline{H}$, and in the second London equation:

$$\nabla \times \underline{J}_s = -(1/\lambda^2)\underline{H}$$

Upon the replacement, the equation (18) becomes:

$$\Delta \underline{H} = (\frac{1}{\lambda^2} + j\omega\sigma\mu - \omega^2\varepsilon\mu)\underline{H} \quad (19)$$

For a plane wave which propagates along a specific direction z normal to the superconductor surface equation (19) has the form:

$$\frac{\sigma^2 H}{\sigma z^2} = (\frac{1}{\lambda^2} + j\omega\sigma\mu - \omega^2\varepsilon\mu)\underline{H} \quad (20)$$

And admits a solution:

$$\underline{H}(z,t) = \underline{H}(0)\exp(-Kz) \quad (21)$$

From the condition that solution (21) verifies relation (20) it results:

$$K^2\underline{H}(z,t) = (\frac{1}{\lambda^2} + j\omega\sigma\mu - \omega^2\varepsilon\mu)\underline{H}(z,t)$$

And after simplifying:

$$K^2 = \frac{1}{\lambda^2} + j\omega\sigma\mu - \omega^2\varepsilon\mu \quad (22)$$

This is the dispersion relation connecting the wave vector $\overline{k}$ with the eave frequency ω. It is not accurate for fields with rapid variation in space. The calculations didn't take into account the environmental path of electrons and have neglected their restrictions on location imposed by the uncertainty principle.

5. OBSERVATIONS

In a superconducting phase the only field allowed is exponentially damped as it enters the inner from the outer surface. From the expression of dielectric function:

$\varepsilon(\omega) = 1 - \frac{\omega^2{}_p}{\omega^2}$ in which ω_p is the plasma frequency, we see that this corresponds to $\varepsilon(\omega) < 0$ therefore only the frequency domain of $\omega << \omega_p$ on interest.

At frequency $\omega = 1/\tau$, τ being the relaxation time of normal electrons , considering that $\sigma = n_n l^2 \tau / m$. It can be shown that in the dispersion relation the normal electron contribution is small, over current is short-circuiting normal electrons, so that current density is given by the second London equation:

$$rot\underline{J}_s = -\frac{\overline{B}}{\lambda^2} \quad (23)$$

At high frequency the applied electromagnetic field photons have an energy $\hbar\omega$ enough to produce transition to unoccupied "normal" energy levels, above the forbidden band. So excited, the super-electrons cross to superior energy states behaving like normal electrons. At $f = 0$ the field expression becomes:

$$\underline{H} = \underline{H}(z) = H_0 \exp(-2/\lambda) \quad (24)$$

In this case superconducting electrons bypass normal electrons which were not thermally excited above the forbidden band.

6. REFERENCES

[1] FRANK S. GRAWFORD I.R., *Cursul de fizică Barkeley. Unde*. Editura Didactică şi Pedagogică, 1983.
[2] TIMOTIN AL. *Lecţii de bazele electrotehnicii.* Editura Didactică şi Pedagogică, 1970.
[3] CONSTANTIN C., *Supracontuctibilitatea şi aplicaţiile ei.* Editura Ştiinţifică şi Enciclopedică, Bucureşti 1985.
[4] CHARLES K., *Introducere în fizică corpului solid.* Editura Tehnică Bucureşti, 1971.
[5] EMIL L.,Editura "Junimea", Iaşi, 1976.

CONTRIBUTIONS TO THE IMPLEMENTATION OF REDUNDANCY IN ELECTRONIC SYSTEMS

[1]CIUCUR VIOLETA, [2]DRAGOMIRESCU OVIDIU, [3]DUMITRASCU ANA

[1,3]Constanta Maritime University, [2]"Politehnica" University Bucharest, Romania

ABSTRACT

The paper presents a universal solution, simple and efficient to implement redundancy in electronic systems that process external signals.

Is presented the structural schematic diagram of a redundant system in which notification of any defect and correct interpretation of the break signal is carried by comparing the output signal from the base unit to the signal provided by a standard or control block, which in principle is identical to the base.

Keywords: *redundant stabilizer, redundant amplifier, basic unit/block, control block, backup block*

1. A UNIVERSAL SOLUTION, SIMPLE AND EFFICIENT TO IMPLEMENT REDUNDANCY IN ELECTRONIC SYSTEMS THAT PROCESS EXTERNAL SIGNALS

A redundant system consists of a basic block-BB, one or more backup blocks -BR and a switch to pass to pass to backup-CR, which is intended to refer to the basic block failure and order entry of the reserves into system. A good C.R. switch must satisfy following conditions:

-To notify any malfunction in the basic block and ensure passage on the reserve at the appearance of any malfunction (for example, in the case of linear amplifier must not notify only the defects that cause signal loss or strong attenuation of the output signal but other possible defects such as ,defects which changes the frequency characteristic, increasing gain or distortion, causing the system to oscillate);

-Not interpret the signal breaks or low-level signals, as defects of the basic block and thus not command passing to backup in these cases;

-To ensure switching to backup at any defect that appears at the CR switch ;

-To signalize optical, acoustic or otherwise, the damage of the basic block and passing to backup to allow use of the system under the SRS conditions;

-To ensure a good separation between the basic block and backup blocks , both during normal operation or in case of occurrence of any defects (particularly at fault type defects on entry or exit of a block).

Satisfy these requirements and especially the first two conditions seem generally very difficult. Thus, in practice there are known examples of redundant electronic systems in which for detecting defects is used a output signal detector. But these systems do not notify the appearance of distortion, the spurious oscillations, the changes in characteristic of frequency, (for example, low gain at low or high frequencies) and the signal breaks are interpreted as defects in the basic block. Are also known redundant systems in which the flaw notify is made through direct current, by notifying changes produced by defects on the static operating points, which ensures a correct interpretation of signal pauses. In these systems, however, was not brought before the a.c. power faults, such as pausing a coupling or decoupling capacitor.

In reality notification of any defect and interpret the signal breaks in the case of electronic systems (linear, nonlinear or digital) which processing external signal, can be done simply and effectively using the principle of comparison, meaning constantly comparing the output signal of the basic block $s_B(t)$ with the signal of a control block or reference block $s_M(t)$, which in principle is the same as the basic block.

The block diagram of a redundancy system built on this idea is shown in Figure 1. BM control block provides at its output a signal $s_M(t)$ identical to the output signal of the basic unit in good working order.

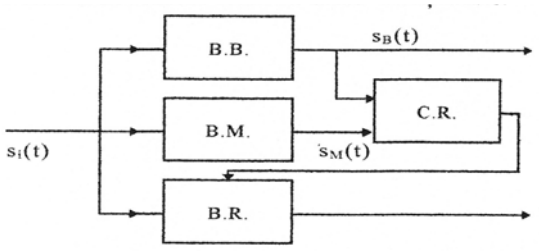

Figure 1 The block diagram of a redundant system

B.B. –basic unit/block
B.M. – control block
B.R. – backup block
C.R.- switching to backup circuit

The C.R. circuit makes the operation of subtraction between signals $s_B(t)$ and $s_M(t)$ and when the result is not zero and exceeds a certain level required, it commands passage to the backup block. In the case of broadband linear systems, control block may be missing, as it can make a direct comparison between input signal $s_i(t)$ and output signal $s_B(t)$, if it is adequately mitigated by a passive network. However for reasons of noise or frequency characteristic may require the use of a control block. In case of selective linear systems

(selective amplifiers) or the nonlinear systems and the digital systems the control block may not be missing because in these cases is not possible a direct comparison between the signals $s_i(t)$ and $s_B(t)$ because these signals have different waveforms and frequency spectrums.

In general it is preferable but not mandatory that the control unit to be more reliable than the basic block and the backup block.

Thus, for example if the basic block and the backup block are power amplifiers, control unit can be a simple voltage amplifier which should have just the same characteristic frequency as the basic unit and so by default will have a better reliability. If BB and BR are voltage amplifiers, or generally low power blocks then BM will be identical and will have the same reliability as well. CR circuit is basically a simple structure.

For analog systems it is reduced to a simple differential circuit $s_B(t) - s_M(t)$ that can be achieved with operational amplifier, or a simple resistive adder if control unit is designed to provide an output signal $-s_B(t) = s_M(t)$.

For digital systems it is reduced to an exclusive-OR circuit or more generally to an N-bit comparator, where N is the number of outputs that need to be compared. Should be noted that for digital systems, where BB and BM have independent clocks then may occur synchronism differences between signals $s_B(t)$ and $s_M(t)$ which could be misinterpreted as a defect in the BB.. To avoid this it is necessary that both BB and BM to use the same clock.

Even in this case is likely due to different propagation times through the BB and BM output signals of these blocks do not occur simultaneously which could generate false signals to the N bits comparator output if they are too fast.

To avoid this it is useful that the comparator output to be controlled by a clock pulse, conveniently made so that this output should be validated only after the transition and stabilization of the signals on the outputs of the two blocks.

The solution for achieving redundancy proposed here has the following advantages:

-can be applied to any electronic system for processing external signals;

-automatically satisfies the three conditions mentioned at the beginning of this paragraph, and allow notification of defects which allows even very small modification of the output signal;

-in some cases may lack control block;

-in principle the number of spare blocks may be increased and may make a ring reservation.

Equivalent circuit in terms of reliability are shown in figure 2. Intrinsic reliability function of the reserved system is:

$$R_r = R_{BR} + R_{BB}R_{BM} - R_{B\mathbf{B}}R_{BR}R_{BM} \qquad (1)$$

where $R_{B\mathbf{B}}, R_{BM}, R_{BR}$ are reliability functions corresponding to the three blocks.

If the blocks are identical, $R_{B\mathbf{B}} = R_{BR} = R_{BM} = R$ results:

$$R_r = R + R^2 - R^3 \qquad (2)$$

and the efficiency of reservation is: $\gamma = \frac{1}{1-R^2} > 1$, for any given time t.

If $R(t) = e^{-\lambda t}$, for medium functioning time without restore it results :

$$m_r \mid \underset{inc}{rez} = 1{,}16m; \qquad m_r \mid \underset{neinc}{rez} = 1{,}5m;$$

where $m = 1/\lambda$.

If $R_{BM} > R_{BB} = R_{BR} = e^{-\lambda t}$, it is obtained:

$$R_r \cong 2R - R^2 \qquad (3)$$

$$m_r \mid \underset{inc}{rez} = 1{,}5m;$$

$$m_r \mid \underset{neinc}{rez} = 2m;$$

If the system is restoring, and if we assume for its blocks constant restore constant intensity μ, then the average time between failures of its operation, under SRS and charged back will be:

$$m_r^* = 1{,}5m\left(\frac{2}{3} + \frac{\mu}{3\lambda}\right) \qquad (4)$$

meaning $m_r = 6m$ if $\frac{\mu}{\lambda} = 10$ or $m_r = 51m$ if $\frac{\mu}{\lambda} = 100$. It is noted that under the SRS condition even use a single loaded reserve brings a substantial amount extrinsic reliability if $\frac{\mu}{\lambda}$ is high enough. Clearly if the reserve will be unloaded the reliability gain will be even greater.

2. REDUNDANT AMPLIFIERS

A fair solution to achieve a redundancy amplifier after the original scheme proposed above is given in figure 2.

The solution has the following advantages:

- reserve is unloaded and therefore blocking efficiency is maximum;
- replacing an RS flip-flop with a T flip-flop we can get an ring reservation;
- by replacing the flip-flop with a shift register can increase the number of reservations and ensure a reservation in the ring

Based on this scheme, were conducted several laboratory models for studying redundancy amplifiers.

.

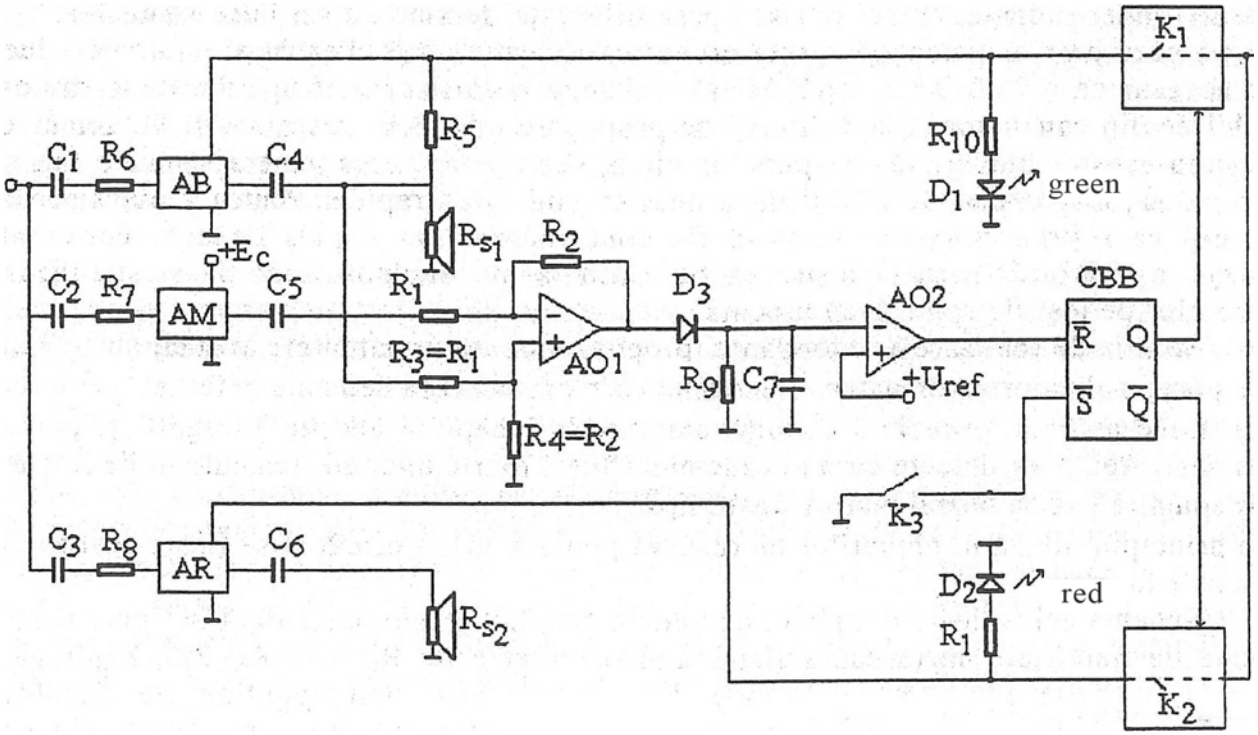

Figure 2 Redundant amplifier

3. REDUNDANT STABILIZERS

At voltage stabilizers, defects occur either by increasing or by decreasing the output voltage comparing to normal level.

Notification of defects is simplified if the stabilizer is equipped with a reliable circuit for output over-voltage protection, since in this case, any defect is manifested by decreasing the output voltage below normal.

Given this and taking into account the need to separate stabilizers in case of failure for a constant voltage redundant stabilizer, results the following block diagram:

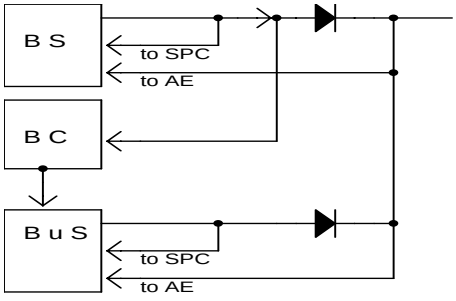

Figure 3 The block diagram of redundant stabilizer

SB base stabilizer

SR reserve stabilizer

D1, D2 separation diodes

CR circuit for passing to backup (you can refer only to the output voltage decreases)

AE error amplifier

CPS overvoltage protection circuit on the output

A practical solution to implement this scheme is given in figure 4. It has the following advantages:

-it has a simple scheme with a few additional elements to the case of two independent stabilizers;

-reservation is practically load and so the reliability is maximum;

-CR switch can be omitted but in this case the scheme may be used only under the SRN.

The redundant stabilizer described above has the following advantages:

- high reliability because of the small number of components on the one hand and because of the fact that the back-up stabilizer waits in an idle mode, on the other hand (unloaded back-up);
- practically null time of entering the back-up mode, which insures continuous functioning, without loading lock-out of the loaded equipment;
- automatic disconnection from the system of the malfunctioning stabilizers;
- optical signals for any malfunctioning within the system and, therefore, it allows its use in SRS conditions;

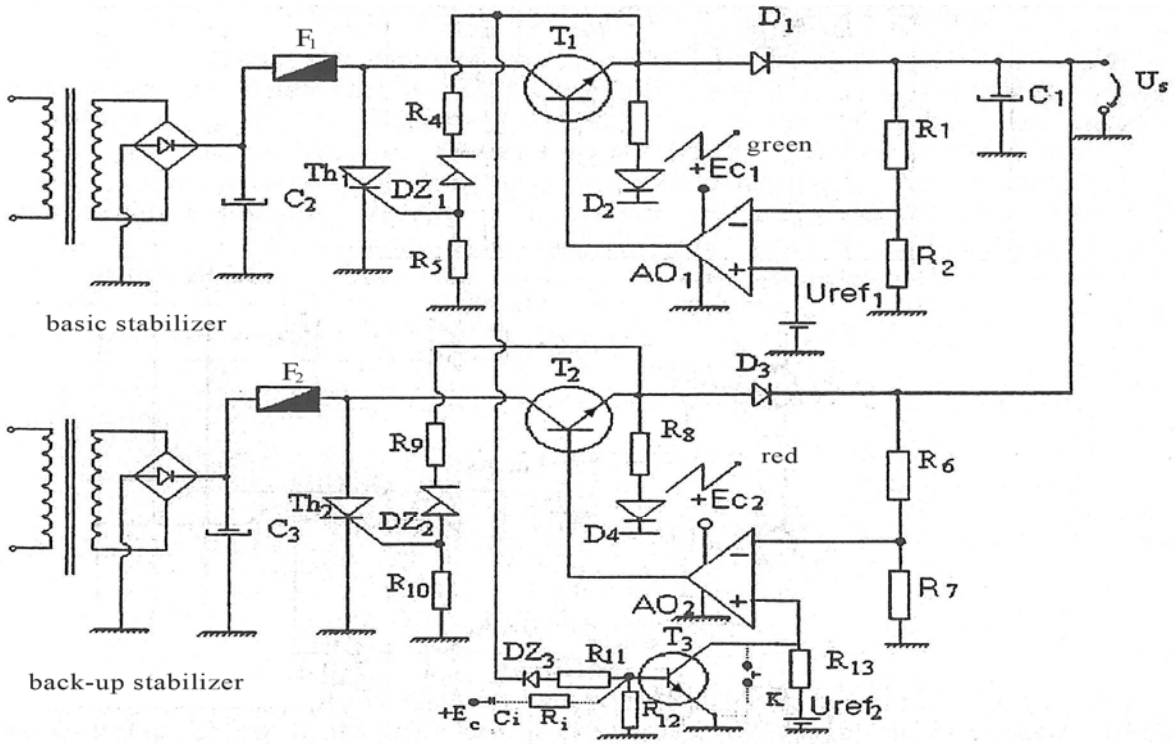

Figure 4 Redundancy stabilizer

4. CONCLUSIONS

It is clear that for any electronic system can be defined outside the principle diagram, and a topological scheme of principle that reveal details of topological components and in particular the connections between them. This scheme aims at minimizing the parasitic coupling of the system, getting performances, ensuring electromagnetic compatibility.

The redundant amplifiers, set up according to the original solution previously presented, have the following essential advantages:

- they notice and perform the switch to back-up amplifier any malfunctioning type within the main amplifier (the amplifier which insures the functioning of the system);
- can notice even the slightest deviation in the functioning of the main amplifier;
- can be used in all practical cases, irrespective of the signal structure - with or without spaces, with or without level variations-;

when a malfunctioning occurs within the main amplifier, it is automatically removed from the system and there is an automatic switch to the back-up

- amplifier, which makes the external intervention of a human operator unnecessary;
- the circuit which acknowledges the malfunctioning of the main amplifier and performs the switch to the back-up amplifier is a simple and very reliable circuit, made of uncomplicated components, which usually have a high reliability;
- the back-up amplifier (amplifiers) remains unloaded until it enters the system (without loading tension), which gives the redundant system a high reliability;
- they can be easily adapted so as to realize a ring back-up and / or to increase the number of back-ups.

5. REFERENCES

1. MANOLESCU A., "Circuite integrate liniare", Editura Didactică şi Pedagogică, Bucureşti 1983;
2. GRAY P., MAYER R., „Circuite integrale liniare. Analiză şi Proiectare", Editura Tehnică, Bucureşti, 1996;
3. DRAGOMIRESCU OV., „Căi de creştere a fiabilităţii sistemelor electronice", Teză de Doctorat, Editura „Politehnica" Bucureşi, 1999.

IMPLEMENTING OF PROGRAMMING LOGICS USING DIGITAL SEQUENTIAL ELECTRONIC EQUIPMENTS BASED ON LOGICAL FEEDBACK FROM THE MICROPROCESSOR AND MICROCONTROLLER SYSTEMS

COROESCU TIBERIU

Department of Automation, Applied Informatics and Computers, University of Petrosani, Romania

ABSTRACT

The paper presents the possibilities to realize and implement of programming logics based on logical feedback concept using digital sequential electronic equipments from the hardware structure of microprocessor and microcontroller systems. After the analysis of the realising principle used in logical feedback, were obtained the logical functions based on state transition, truth table and Y-maps for the flip-flop circuits. Then was realised the synthesis for an application of programmable logics in implementing the logical feedback. The application implements a driver for a matrix optical indicator from a computerized system with microprocessor.

Keywords: *Programming Logics, Sequential Equipments, Logical Feedback, Microprocessor and Microcontroller Hardware*

1. INTRODUCTION

A lot of digital applications need to realise a sequential progressive transformer which goes through a certain number of states. The basic blocks of such digital electronic equipment need to have a certain quantity of memory in order to use the sequencies from the past, which were memorized.

A simple example results making a compare between a push-button for a buzzer and a switch for an electric lamp. The push-button has no memory of the past events, because immediately after we take the finger from the button, this one comute and come back to its initial state. The switch has, instead, two stable states: "on" and "off". Acting on the switch, this one comutes in its "on" state, realising the lighting of the lamp and remaining in this state after we take the finger from the switch. So, in this way, it remembers the last command received.

Using a reverse logical connection, that is a logical feedback for combinational circuits, these ones can obtain the memorising quality so can realise a sequential action. On this propriety it's based the building of bistable circuits flip-flop type.

Going beyond this propriety, in the future applications, will be possible using JK flip-flops and gates to design synchronous sequential machines which will detect the movement direction of vehicles along a constricted roadway.

$$Y_1 = \overline{X_1 + y_2} \;\; ; \; Y_2 = \overline{X_2 + y_1} \qquad (1)$$

2. THE SYNTHESIS OF SEQUENTIAL LOGICAL FUNCTIONS IN CASE OF NETWORK USING LOGICAL FEEDBACK

To ilustrate the logical feedback principle, in Figure 1.a it's presented a network of two logical NOR circuits, connected in closed circuit or into a loop shape. The output of this network depends not only on the inputs X_1, X_2 , but on its own outputs Y_1, Y_2 , which are connected on the feedback through two crossing ways.

Establishing the answer for this simple network puts some problems because the outputs state applied to the input must be known apriori, in order to obtain the real state at the output. Solving of this problem it's possible through the analysis of the network's logical gates NOR in open circuit, presented in Figure 1.b. At this network, the inputs which came from the outputs are disconnected and are used as separate inputs, being marked with small letters y_1, y_2, known as inputs of feedback type or as secondary inputs. The original inputs marked with capital letters X_1, X_2 , are known as programmable inputs or as primary inputs.

The resulted network it's a simple combinational network with four inputs and two outputs, having the following logical functions:

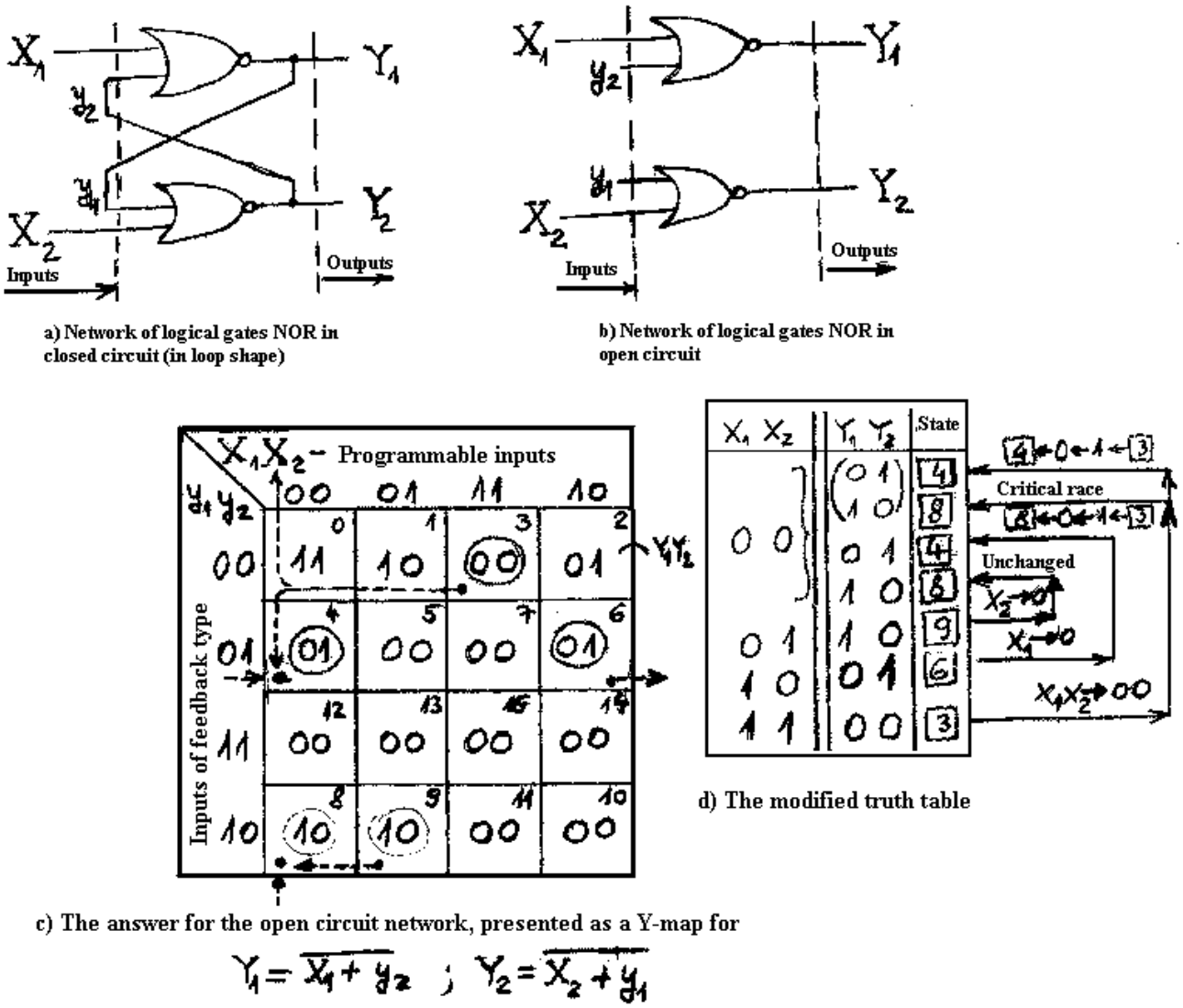

Figure 1. The realising principle for logical feedback using logical gates NOR

In this way, was obtained a truth table which indicates the output state for each input combination. This truth table has the form of a map containing all the output information inserted into each cell. This map has the name of Y-map and realizes in fact the global transfer characteristic for the open circuit.

We will apply then the restrictive conditions onto the Y-map according with the feedback connections. In the case of Figure 1.a, the restriction consists in the fact that into the stable state of the network, exist the relations $y_1 = Y_1$ and $y_2 = Y_2$ because of direct connection.

In the Figure 1.d this fact is indicated on the Y-map through the framing of the values from the cells which fulfil this criterion.

For instance, for the cell 6 we have $y_1\ y_2 = 01$ and $X_1\ X_2 = 10$, which cause $Y_1\ Y_2 = 01$ and this one is a stable state. After marking with framing of all stable states we obtain the annotated Y-map representing in fact the answer of the network in loop shape.

Taking into consideration all the programmable inputs X_1, X_2 and all the transitions it's possible to determine the way in which will react the network in loop shape. Thus, if $X_1\ X_2 = 01$, then will obtain $Y_1\ Y_2 = 10$, that is the state 9 which is the single stable state for this input. In the same way, the input $X_1\ X_2 = 11$ will generate the output $Y_1\ Y_2 = 00$ (state 3 stable and single), and the input $X_1\ X_2 = 10$ will generate the state $Y_1\ Y_2 = 01$ (state 6 stable and single).

For all that a problem appears when the programmable input is $X_1\ X_2 = 00$, in which case appear two stable states (4 and 8). In such cases it's necessary to analyse the transition towards $X_1\ X_2 = 00$ for each of others input combinations.

Thus if the input transition is $X_1\ X_2 = 01 \rightarrow 00$ then $Y_1\ Y_2 = 10$ (state 9, stable) $\rightarrow$ 10 (state 8 stable) that is a horizontal transition $9 \rightarrow 8$ without the changing of the output value 10. In the similar way, the input transition $X_1\ X_2 = 10 \rightarrow 00$ will produce the output transition $Y_1\ Y_2 = 01$ (state 6, stable) $\rightarrow$ 01 (state 4, stable) that is a horizontal transition $6 \rightarrow 4$ and without the changing of the output value 01, too.

But the input transition $X_1\ X_2 = 11 \rightarrow 00$ is much more complicated. The output realizes initially the transition $Y_1\ Y_2 = 00$ (state 3) $\rightarrow$ 10 (state 1) $\rightarrow$ 11 (state 0) that is a transition till the cell 0 which is but instable and leads to changing the state of output in 11. Therefore $Y_1\ Y_2 = 11$ because $X_1\ X_2\ y_1\ y_2 = 00$. For all that it's too unlikely that at the application of the inputs y_1 and y_2 the delays to be equal. So that, even both y_1 and y_2 are

changing from 0 → 1, only one of the inputs of feedback type will win the race, having a smaller delay.

If y_2 will win, that is $y_1\ y_2 = 01$, then appears a vertical transition downward from the state 0 into the state 4 for which $y_1\ y_2 = Y_1\ Y_2 = 01$, so into a stable finale state (0 → 4). But if y_1 will win, that is $y_1\ y_2 = 10$, then appears a vertical transition upward from the state 0 into the state 8 for which $y_1\ y_2 = Y_1\ Y_2 = 10$, so into a new stable finale state (0 → 8). A such situation, in which the result of a change for input depends of relative delays has the name of "critical race".

The two possibilities generated by the critical race of transition $X_1\ X_2 = 11 \rightarrow 01 \rightarrow 00$ are therefore: 3 → 1 → 0 → 4 and 3 → 1 → 0 → 8 , respectively, and the modified truth table for network in loop shape which centralised the results appears in Figure 1.d.

3. APPLICATION OF LOGICAL FEEDBACK FOR A MATRIX OPTICAL INDICATOR FROM A COMPUTERIZED SYSTEM WITH MICROPROCESSOR

A computerized automatic system with microprocessor has three computers which randomise access a single printer.

In order to assure an effective supervision of the printing process it's used a matrix optical indicator having a square vdimension 3 x 3. On the three rows A, B, C and on the three columns 1, 2, 3 it's displayed the sequence of arriving for the signals representing the access requests to the printer from the three computers.

Thus, if at the matrix optical indicator presented in Figure 2.a, there are lighting the lamps B_1, C_2, A_3 , then the order in which the computers initiated the access requests to the printer was B, C, A.

In this application will be conceived and implemented an electronic digital sequential equipment for this matrix optical indicator. This equipment will be in fact the driver for the indicator and will be realised using some networks of NOR gates with logical feedback.

The analyses of a network of NOR gates with logical feedback indicates the two programmable primary inputs X_1 and X_2 and the two secondary inputs y_1 and y_2 .

After the opening of the network was established the answer as the Y-map for the outputs Y_1 and Y_2. The results are presented in Figure 2.b.

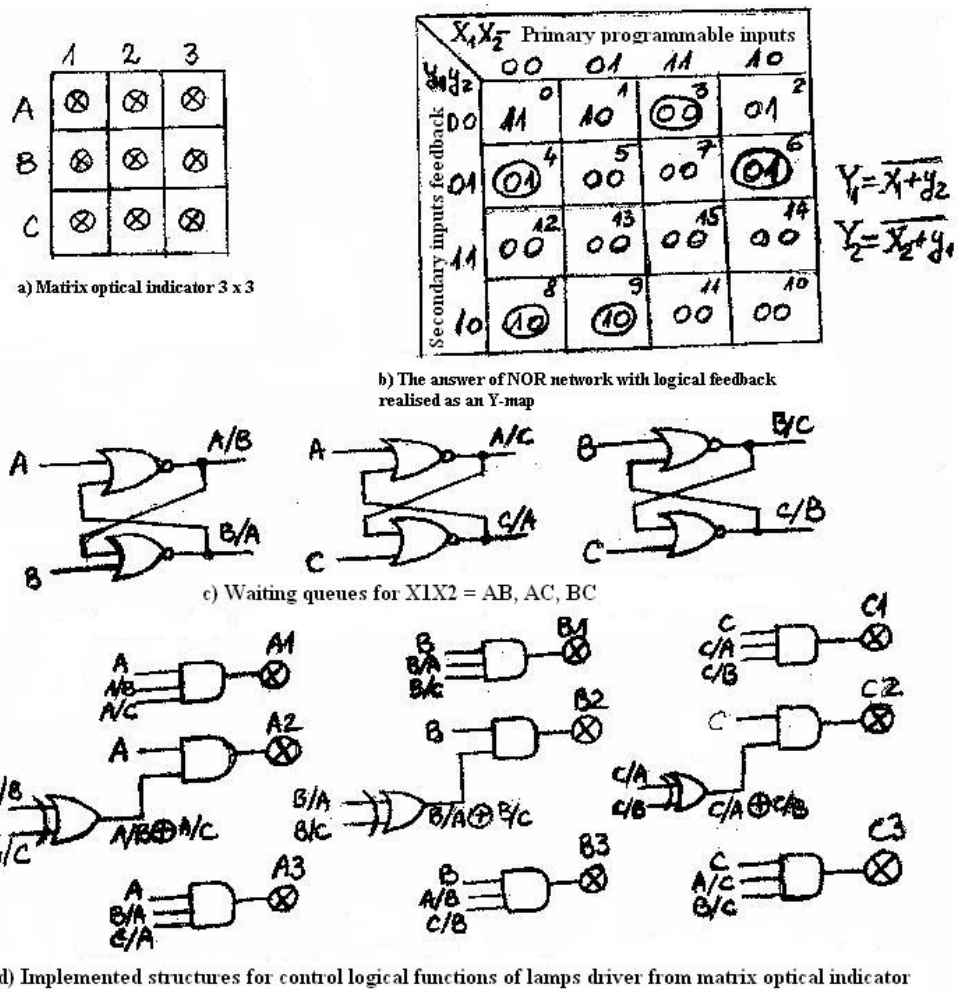

a) Matrix optical indicator 3 x 3

b) The answer of NOR network with logical feedback realised as an Y-map

c) Waiting queues for X1X2 = AB, AC, BC

d) Implemented structures for control logical functions of lamps driver from matrix optical indicator

Figure 2. Implementing the driver for the matrix optical indicator 3 x 3 to supervise the access requests to the printer

Such a NOR network with logical feedback can detect which one of the two principal inputs X_1 X_2 drops in logic 0, which is equivalent with the indication of an access request.

There will be necessary three such of networks, having the primary inputs X_1 X_2 = AB, AC, BC and obtaining the materialisation of threee waiting queues, as in Figure 2.c.

From the Y-map results that the missing of the access request (X_1 X_2 = 11) will generate the outputs Y_1 Y_2 = 00. If X_1 passes the first one through logic 0, followed then by the X_2 (X_1 X_2 = 11 → 01 → 00), then Y_1 will pass in logic 1 (Y_1 Y_2 = 00 → 10 → 10 through the stable states 3 → 9 → 8).

In the same way, the first passing of X_2 into logic 0 and followed then by X_1 (X_1X_2 = 11 → 10 → 00) will generate the passing of Y_2 into logic 1 (Y_1 Y_2 = 00 → 01 → 01 through the stable states 3 → 6 → 4). Therefore, in this context, the output Y_1 can be labeled as $Y_1 = X_1 / X_2$ (X_1 before X_2) and Y_2 as $Y_2 = X_2 / X_1$ (X_2 before X_1).

Using these notations for the networks of type NOR with logical feedback will be obtained information for the waiting queues from Figure 2.c as follows:

The 9 control logical functions for the lamps of the matrix will be obtained using a logical judgement based on the results obtained. So, for the lamps in row A we find:

- the lamp A_1 lights if the access request A exists, and A arrives before B **and** A arrives before C, that is A = A•(A/B) •(A/C);
- the lamp A_2 lights if the access request A exists, and A arrives before B **or** A arrives before C but no both (so it's imposed the function Exclusive OR – XOR), that is A = A•(A/B ⊕ A/C);
- the lamp A_3 lights if the access request exists, and A arrives after B and A arrives after C, too, that is A = A•(B/A) •(C/A).

Using the same type of judgement for rows B and C we have obtained the following final relations:

$$A_1 = A\cdot(A/B)\cdot(A/C);\quad A_2 = A\cdot(A/B\oplus A/C);\quad A_3 = A\cdot(B/A)\cdot(C/A)$$
$$B_1 = B\cdot(B/A)\cdot(B/C);\quad B_2 = B\cdot(B/A\oplus B/C);\quad B_3 = B\cdot(A/B)\cdot(C/B) \qquad (3)$$
$$C_1 = C\cdot(C/A)\cdot(C/B);\quad C_2 = C\cdot(C/A\oplus C/B);\quad C_3 = C\cdot(A/C)\cdot(B/C)$$

The implemented structures for these logical functions are presented in Figure 2.d

6. CONCLUSIONS

The present paper emphasizes the implementing possibilities of programmable logics based on logic

al feedback from systems with microprocessors and microcontrollers. In the hardware structure of these systems appears digital sequential electronic circuits, which implement the logical feedback concept. The optimal use of such circuits to realise the application modules in programmable logics needs to obtain the logical functions in a modern way. This implies torealise the synthesis using state transition, truth table and Y-map methods. This methodical approach in implementing the hardware structures, from the very simple ones to the very complex VLSI equipments, allows to eliminate the instable states and finally to increase the general stability of the resulted application.

7. REFERENCES

[1]. CAHILL, S.J., *Digital and Microprocessor Engineering*. Second Edition. Ellis Horwood Limited, Chichester, UK, 1993

[2]. COROESCU, T., *Control of Mining Hoisting Installations with Microproccessors*. PhD Thesis, University of Petrosani, 1989.

[3]. COROESCU, T., *Comunicarea interactivă om-calculator*. Ed. Lumina Lex, Bucureşti, 2001.

[4]. COROESCU, T., SÂRB, V., *Introducere în ştiinţa sistemelor şi a calculatoarelor*. Ed. Didactică şi Padagogică R.A., Bucureşti, 2003.

[5]. FINK, D., WAYNE BEATY, H. , *Standard Handbook for Electrical Engineering*. 15th Edition, McGraw Hill, 2006.

[6].LOXTON, R., *Problems and Solutions in Electronics*. Chapman & Hall, London, UK, 1994.

[7]. REAGAN, P., *IT Essentials: PC Hardware and Software. Labs and Study Guide*. Third Edition Instructor's Edition. Cisco Systems Inc, Indianopolis, USA, 2008

DEVELOPMENT SYSTEM BASED ON PROGRAMMABLE LOGIC CONTROLLER PLC-OMRON TO SAFETY DOORS STATE CONTROL OF THE SHAFT-SINKING PROCESS

COROESCU TIBERIU

Department of Automation, Applied Informatics and Computers, University of Petrosani, Romania

ABSTRACT

The paper analyses the real-time software structure of a development system based on OMRON Programmable Logic Controller PLC drawed to control the safety doors of the dynamic shaft-sinking process. The rock excavation and loading process into the front, directly depends on the good functionality of the shaft platform safety doors. A digital equipment for shaft platform doors position control allows automatic and safe control in real-time of the hoist for the shaft-sinking process. The very difficult tasks of real-time control can be achieved only with a computerised automatic equipment based on microprocessors and microcontrollers. This new equipment was conceived by logical identification and synthesis of command functions using KARNAUGH diagram method. The materialisation of logical functions is realised in programmable logic through a development system based on OMRON-PLC, type CPM2A, equiped with the adapter type MAD 11. Using the programming tool CX-Programmer of Omron Company, destinated for the creation, testing and maintenance of software for PLCs, were created the real-time ladder programs for the safety doors state control. This software was tested in laboratory conditions and will be implemented on a pilot installation.

Keywords: *Programmable Logic Controller PLC, Development System, State Control, Shaft-Sinking Dynamic Process*

1. MATHEMATICAL MODEL IDENTIFICATION FOR SHAFT-SINKING PROCESS

The optimal progress of work in safety conditions at the shaft-sinking front is in direct connection with the platform safety doors. Working examples indicate that, either through an oversight of the workers manipulating the plastform safety doors, or through other technological causes, happend grievous accidents in the shaft sinking process. To avoid such sort of accidentsit is necessary to accomplish the restrictions imposed by the norms, both in normal conditions and in extreme damages conditions.

To fulfil this desideratum, it is necessary to be conceived a new safety device to control the doors closing and opening, working in real-time and in an automatic mode, in order to eliminate the human operator who could make mistakes.

The safety and control device has to interlock the door closing and opening with the movement of the hoisting vessel, working both in manual working conditions and in automatic working conditions. But the command must be received directly from the hoisting vessel. The analyse of existing hoisting installations indicate as inadequate the actual drive of doors at the shaft platforms, which is realised with rotative electric motors and with devices to transfer and transform the rotative movement into the linear one. The same conclusion emerged concerning the actual command system, realised in dinamic commutation using start-stop push buttons and relay switches installed on the shaft platform nearby the safety doors.

The critical analyse of actual shaft-sinking installations emphasized their limits and imposed the replacement of the present electrical drive system with a new one, to direct transmission of the movement from the electrical motor to the door, without intermediate transmission systems which decrease the efficiency and increase the probability of deficiencies. The most indicate solution in this case is the driving system with asynchronous linear electric motor which transfers the linear movement of its mobile induce plate, direct to the shaft platform door [1].

The mathematical model of shaft-sinking process can be established using the bloc diagram of its structure, presented in Figure 1, which emphasized the component parts and the input, output and state parameters.

The laying modality of magnetic transducers into the shaft is indicated in Figure 2.

The security and control device DSC receives the information from outside environment (from the human operator) through the vector u_1, the state information concerning the position of the hoisting vessel through the vector u_2 generated by magnetic transducers TM from the shaft, the information concerning extreme positions of the vessels and doors through the vector u_3 generated by motion limit switches LC, and information about faults emerged into the electrical driving system through the vector u_4 generated by protection relais RP.

The components of the vector u_1 are the following: PS – push buton starting upward, PJ – push buton starting downward, O – push buton to stop, IMU1 – manual closing door at platform 1, IMU2 - manual closing door at platform 2, DMU1 – manual opening door at platform 1, DMU2 - manual opening door at platform 2.

The components of the vector u_2 are the following: TM1, TM1', TM3, TM3' – magnetic transducers for platform 1 and hoisting vessel movement upward, TM2, TM2', TM4, TM4' - magnetic transducers for platform 1 and hoisting vessel movement downward, TM5, TM5', TM7, TM7' – magnetic transducers for platform 2 and hoisting vessel movement upward, TM6, TM6', TM8,

TM8' - magnetic transducers for platform 2 and hoisting vessel movement downward.

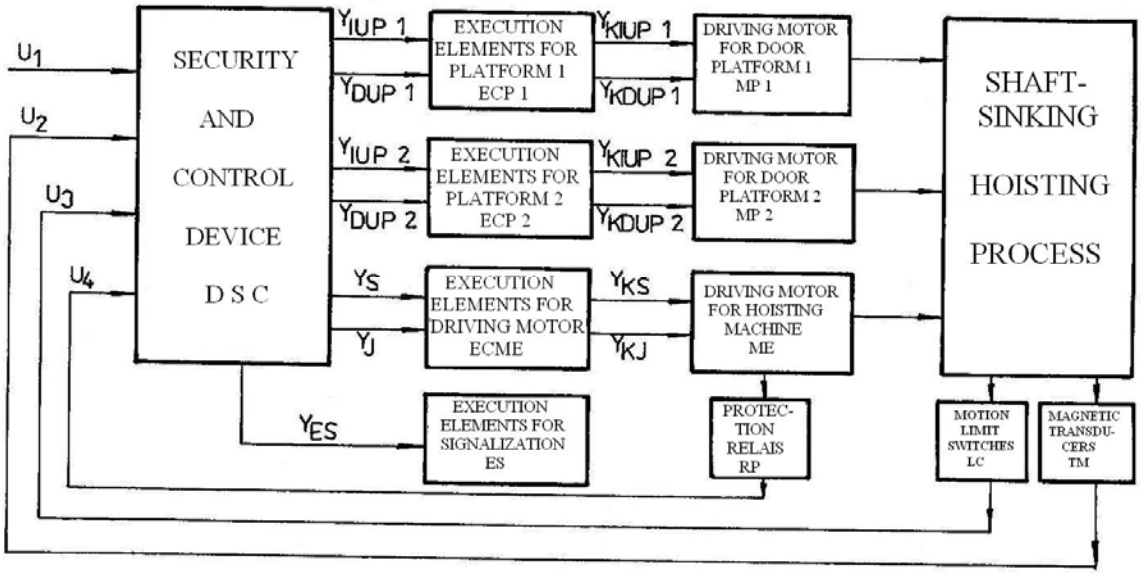

Fig.1. Bloc diagram of control system for shaft-sinking process

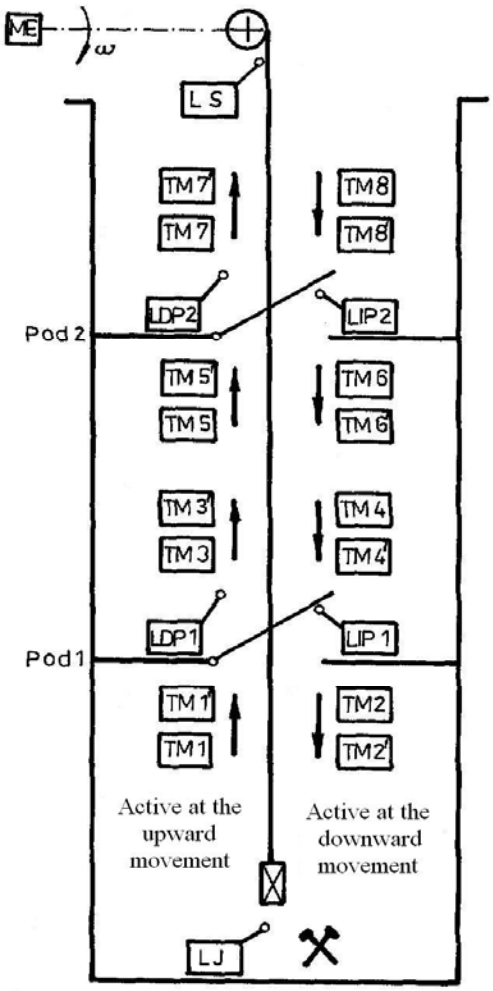

Fig. 2. The laying modality of magnetic transducers into the shaft at sinking process

The components of the vector u_3 are the following: LS – motion limit switch for extreme position up, LJ – motion limit switch for extreme position down, LIP1 – closing limit switch for door platform 1, LDP1 - opening limit switch for door platform 1, LIP2 - closing limit switch for door platform 2, LDP2 - opening limit switch for door platform 2.

The components of the vector u_4 are the following: RM – maximal current relais, RT – overload thermic relais, Z – general electric protection relais.

Input vectors [1[, [2], [6] have the following expression:

$$\begin{aligned} u_1 &= [PS, PJ, O, IMU1, IMU2, DMU1, DMU2]^T \\ u_2 &= [TM1, TM2, ..., TM8, TM1', TM2', ..., TM8']^T \\ u_3 &= [LS, LJ, LIP1, LDP1, LIP2, LDP2]^T \\ u_4 &= [RM, RT, Z]^T \end{aligned} \quad (1)$$

From the security and control device DSC it transmit, through the output vectors for the execution elements, the following commands: movement of the hoisting vessel upward through y_S and downward through y_J, respectvely, closing the door for platform 1 through y_{IUP1} and for platform 2 through y_{IUP2}, respectively, opening the door for platform 1 through y_{DUP1} and for platform 2 through y_{DUP2}, respectively, and signalization of hoisting vessel movement or faults through y_{ES}. These vectors activate the execution elements for driving the door from platform 1, through ECP1, and from platform 2 through ECP2, respectively, and for hoisting machine through ECME and for signalization through ES.

The execution elements generate specific vectors y_K and command the electrical motor of hoisting machine ME and of doors driving motors MP1 for platform 1 and MP2 for platform 2, respectively.

2. THE SYNTHESIS OF CONTROL LOGICAL FUNCTIONS FOR HOISTING VESSEL MOVEMENT

The identification of shaft-sinking process using hoisting vessels to transport the excavation rocks allows the synthesis of logical functions for the safety and control device which controls the hoisting vessel movement. The synthesis will be realised using Karnaugh diagrams method [3],[5].

For this, was attached a logical variable for each of magnetic transducers TM1, TM1', TM3, TM3', TM5, TM5', TM7, TM7' corresponding to movement upward of hoisting vessel, for each of magnetic transducers TM2, TM2', TM4, TM4', TM6, TM6', TM8, TM8' corresponding to movement downward of hoisting vessel, for closing limit switches of doors from both platforms LIP1 and LIP2, for opening limit switches of doors from platforms LDP1 şi LDP2, for motion limit switces of extreme position up LS and extreme position down LJ, respectively, for push buttons starting upward PS and starting downward PJ, respectively, for push button to stop O, for electrical protection against shortcuts and overload Z, for push button to manual opening doors of the platforms IMU1, IMU2, and for push buttons to manual closing doors of the platforms DMU1, DMU2.

The conceived Karnaugh diagram for synthesis of the control logical functions in case of hoisting vessel movement in upward direction appears in Figure 3a and in downward direction in Figure 3b.

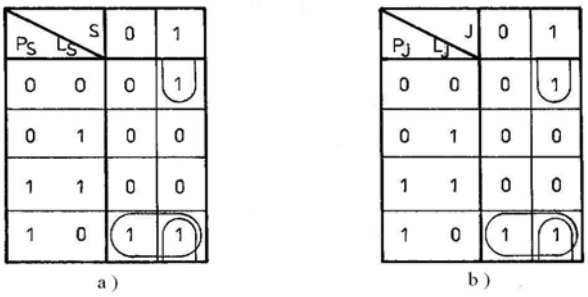

Figure 3. The Karnaugh diagram for synthesis of control logical function at the hoisting vessel movement a) upward movement; b) downward movement

The mathematical model it's represented by logical functions at hoisting vessel movement into upward direction y_S and into downward direction y_J, respectively, having the following expressions:

$$\begin{aligned} y_S &= \bar{O}\cdot\bar{Z}\cdot\overline{VDU1}\cdot\overline{VDU2}\cdot\overline{VIU1}\cdot\overline{VIU2}\cdot\bar{J}\cdot(PS+S)\cdot\overline{LS} \\ y_J &= \bar{O}\cdot\bar{Z}\cdot\overline{VDU1}\cdot\overline{VDU2}\cdot\overline{VIU1}\cdot\overline{VIU2}\cdot\bar{S}\cdot(PJ+J)\cdot\overline{LJ} \end{aligned} \quad (2)$$

3. THE SYNTHESIS OF CONTROL LOGICAL FUNCTIONS FOR CLOSING AND OPENING THE DOORS ON THE PLATFORMS

The conceived Karnaugh diagrams for synthesis of the control logical functions in case of closing doors at the platform 1 and platform 2, respectively, appear in Figure 4.

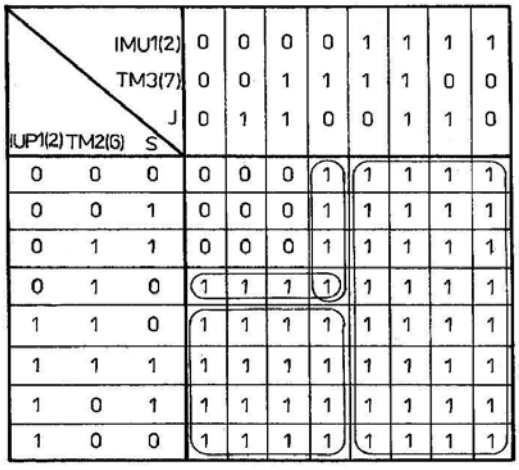

Figure 4. The Karnaugh diagram for synthesis of control logical function in case of platforms

The mathematical model obtained after the synthesis it's represented by logical function y_{IUP1} in

case of closing door at platform 1, and by logical function y_{IUP2} in case of closing door at platform 2, respectively. These functions have the following expressions:

$$\begin{aligned} y_{IUP1} &= \overline{LIP1} \cdot \overline{DUP1} \cdot (IMU1 + IUP1 + \bar{S} \cdot TM2 + \bar{J} \cdot TM3) \\ y_{IUP2} &= \overline{LIP2} \cdot \overline{DUP2} \cdot (IMU2 + IUP2 + \bar{S} \cdot TM6 + \bar{J} \cdot TM7) \end{aligned} \quad (3)$$

The conceived Karnaugh diagram for synthesis of the control logical functions in case of opening doors at the platform 1 and platform 2, respectively, appears in Figure 5.

DUP1(2)	TM1(5)	J \ DMU1(2)	TM4(8)	S							
			0	0	0	0	1	1	1	1
			0	0	1	1	1	1	0	0
			0	1	1	0	0	1	1	0
0	0	0	0	0	0	1	1	1	1	1
0	0	1	0	0	0	1	1	1	1	1
0	1	1	0	0	0	1	1	1	1	1
0	1	0	1	1	1	1	1	1	1	1
1	1	0	1	1	1	1	1	1	1	1
1	1	1	1	1	1	1	1	1	1	1
1	0	1	1	1	1	1	1	1	1	1
1	0	0	1	1	1	1	1	1	1	1

Figure 5. The Karnaugh diagram for synthesis of control logical functions in case of platforms 1 and 2 doors opening

The mathematical model obtained after the synthesis it's represented by logical function y_{DUP1} in case of opening doors at platform 1, and by logical function y_{DUP2} in case of opening doors at platform 2, respectively. These functions have the following expressions:

$$\begin{aligned} y_{DUP1} &= \overline{LDP1} \cdot \overline{IUP1} \cdot (DMU1 + DUP1 + \\ &\quad + \bar{J} \cdot TM1 + \bar{S} \cdot TM4) \\ y_{DUP2} &= \overline{LDP2} \cdot \overline{IUP2} \cdot (DMU2 + DUP2 + \\ &\quad + \bar{J} \cdot TM5 + \bar{S} \cdot TM8) \end{aligned} \quad (4)$$

4. THE SYNTHESIS OF CONTROL LOGICAL FUNCTIONS FOR CHECKING OF DOORS CLOSING AND DOORS OPENING

The conceived Karnaugh diagram for synthesis of checking logical functions in case of doors closing at the platform 1 and 2, respectively, appears in Figure 6.

S	TM2(6)	J \ TM3(7)			
		0	0	1	1
		0	1	1	0
0	0	0	1	0	0
0	1	1	1	1	1
1	1	0	1	0	0
1	0	0	1	0	0

Figure 6. The Karnaugh diagram for synthesis of checking logical functions in case of platforms 1 and 2 doors closing

The mathematical model obtained after the synthesis it's represented by logical function y_{VIU1} for checking the doors closing at platform 1, and by logical function y_{VIU2} for checking the door closing at platform 2, respectively. These functions have the following expressions:

$$\begin{aligned} y_{VIU1} &= \overline{LIP1} \cdot \overline{DUP1} \cdot (\bar{S} \cdot TM2' + \bar{J} \cdot TM3') \\ y_{VIU2} &= \overline{LIP2} \cdot \overline{DUP2} \cdot (\bar{S} \cdot TM6' + \bar{J} \cdot TM7') \end{aligned} \quad (5)$$

The conceived Karnaugh diagram for synthesis of checking logical functions in case of doors opening at the platform 1 and 2, respectively, appears in Figure 7.

J	TM1(5)	S \ TM4(8)			
		0	0	1	1
		0	1	1	0
0	0	0	1	0	0
0	1	1	1	1	1
1	1	0	1	0	0
1	0	0	1	0	0

Figure 7. The Karnaugh diagram for synthesis of checking logical functions in case of platforms 1 and 2 doors opening

The mathematical model obtained after the synthesis it's represented by logical function y_{VDU1} for checking the doors opening at the platform 1, and by logical function y_{VDU2} for checking the door opening at platform 2, respectively. These functions have the following expressions:

$$\begin{aligned} y_{VDU1} &= \overline{LDP1} \cdot \overline{IUP1} \cdot (\bar{J} \cdot TM1' + \bar{S} \cdot TM4') \\ y_{VDU2} &= \overline{LDP2} \cdot \overline{IUP2} \cdot (\bar{J} \cdot TM5' + \bar{S} \cdot TM8') \end{aligned} \quad (6)$$

5. PLC LADDER PROGRAM FOR REAL-TIME CONTROL OF SHAFT-SINKING PROCESS

The real-time software structure in the form of ladder program for shaft-sinking process it's based on implementation of Programmable Logic Controller PLC from Omron Japanese Company, into a development system.

The ladder program is converted in machine code, so it is presented in the form of the mnemonic code [4]. In the first step it was necessary to create the complete set of symbols presented in Table 1.

Table 1. The complete set of symbols created for the ladder program

Name	*Address*	*Description*	*Name*	**Address**	*Description*
stop_O	0.00	Stop Push-Button	trad_TM5	HR0.04	Magnetic Transducer before Platform 2 and movement upward
prot_Z	0.02	Electrical Protections	trad_TM8	HR0.05	Magnetic Transducer before Platform 2 and movement downward
init_AUT	10.00	Initiating Automatic Regime	exec_DUP1	10.10	Executes Opening the Door for Platform 1
but_PS	0.03	Push-Button Starting Upward	exec_DUP2	10.05	Executes Opening the Door for Platform 2
but_PJ	0.04	Push-Button Starting Downward	trad_TM1bis	HR0.06	Magnetic Verifying Transducer before Platform 1 and movement upward
lim_LS	0.05	Motion Limit Switch for Extreme Position Up	trad_TM2bis	HR0.07	Magnetic Verifying Transducer after Platform 1 and movement downward
lim_LJ	0.06	Motion Limit Switch for Extreme Position Down	trad_TM3bis	HR0.08	Magnetic Verifying Transducer after Platform 1 and movement upward
mers_YS	10.01	Movement Hoisting Vessel Upward	trad_TM4bis	HR0.09	Magnetic Verifying Transducer before Platform 1 and movement downward
mers_YJ	10.02	Movement Hoisting Vessel Downward	trad_TM5bis	HR0.10	Magnetic Verifying Transducer before Platform 2 and movement upward
lim_LIP1	0.07	Closing Limit Switch for Door Platform 1	trad_TM6bis	HR0.11	Magnetic Verifying Transducer after Platform 2 and movement downward
lim_LIP2	0.08	Closing Limit Switch for Door Platform 2	trad_TM7bis	HR0.12	Magnetic Verifying Transducer after Platform 2 and movement upward
but_IMU1	0.09	Push-Button for Manual Closing Door at Platform 1	trad_TM8bis	HR0.13	Magnetic Verifying Transducer before Platform 2 and movement downward
but_IMU2	0.10	Push-Button for Manual Closing Door at Platform 2	ver_VIU1	10.06	Verifying the Door Closing at the Platform 1
trad_TM2	0.11	Magnetic Transducer after Platform 1 and movement downward	ver_VIU2	10.07	Verifying the Door Closing at the Platform 2
trad_TM3	0.12	Magnetic Transducer after Platform 1 and movement upward	ver_VDU1	10.08	Verifying the Door Opening at the Platform 1
trad_TM6	0.13	Magnetic Transducer after Platform 2 and movement downward	ver_VDU2	10.09	Verifying the Door Opening at the Platform 2

trad_TM7	0.14	Magnetic Transducer after Platform 2 and movement upward	viz_LDU1	20.00	Vizualisation of the Door Opening at the Platform 1
exec_IUP1	10.03	Execute Closing the Door for Platform 1	viz_LIU1	20.01	Vizualisation of the Door Closing at the Platform 1
exec_IUP2	10.04	Execute Closing the Door for Platform 2	viz_LDU2	20.02	Vizualisation of the Door Opening at the Platform 2
lim_LDP1	0.15	Opening Limit Switch for Door Platform 1	viz_LIU2	20.03	Vizualisation of the Door Closing at the Platform 2
lim_LDP2	0.01	Opening Limit Switch for Door Platform 2	viz_LDS	20.04	Vizualisation the Movement Upward of the Hoisting Vessel
but_DMU1	HR0.00	Push-Button for Manual Opening Door at Platform 1	viz_LDJ	20.05	Vizualisation the Movement Downward of the Hoisting Vessel
but_DMU2	HR0.01	Push-Button for Manual Opening Door at Platform 2	viz_LAI1	20.06	Vizualisation the Closing Door Damage at the Platform 1
trad_TM1	HR0.02	Magnetic Transducer before Platform 1 and movement upward	viz_LAD1	20.07	Vizualisation the Opening Door Damage at the Platform 1
trad_TM4	HR0.03	Magnetic Transducer before Platform 1 and movement downward	viz_LAI2	20.08	Vizualisation the Closing Door Damage at the Platform 2
			viz_LAD2	20.09	Vizualisation the Opening Door Damage at the Platform 2

Then was conceived the ladder diagram in order to implement the equations (2), (3), (4), (5), (6) using the symbols from Table 1 and the facilities offered by the programming tool CX-Programmer developped into the Omron Company for PLC implementation. The resulted original software structure having the form of ladder diagram contains 7 mnemonic code sequencies with 137 specific instructions and it's presented in Table 2.

Table 2. The structure of specialised software in the form of ladder program for real-time control of shaft-sinking process using OMRON – PLC

REAL-TIME LADDER SOFTWARE INSTRUCTIONS					
Address	Mnemonic Code	Address	Mnemonic Code	Address	Mnemonic Code
'Initiating sequence for automatic cycle		'Working sequence for logical function YIUP2 of closing the door at platform 2 with verifying this door closing using YVIU2		'Working sequence for logical function YDUP2 of opening the door at platform 2 with verifying this door opening using YVDU2	
000000	LDNOT stop_O ANDNOT prot_Z ANDNOT ver_VDU1 ANDNOT ver_VDU2 ANDNOT ver_VIU1 ANDNOT ver_VIU2 OUT init_AUT	000052	LDNOT lim_LIP2 OUT TR0 ANDNOT exec_DUP2 OUT TR1 LDNOT mers_YS AND trad_TM6 LDNOT mers_YJ AND trad_TM7 ORLD OR exec_IUP2 OR but_IMU2 ANDLD OUT exec_IUP2	000100	LDNOT lim_LDP2 OUT TR0 ANDNOT exec_IUP2 OUT TR1 LDNOT mers_YJ AND trad_TM5 LDNOT mers_YS AND trad_TM8 ORLD OR exec_DUP2 OR but_DMU2 ANDLD OUT exec_DUP2
'Starting sequence with implementing the logical functions YS and YJ, for movement the hoisting vessel upward and downward, respectively					

000007	LD init_AUT OUT TR0 LD but_PS OR mers_YS ANDNOT mers_YJ ANDNOT lim_LS ANDLD OUT mers_YS LD TR0 AND mers_YS OUT viz_LDS LD TR0 LD but_PJ OR mers_YJ ANDNOT mers_YS ANDNOT lim_LJ ANDLD OUT mers_YJ LD TR0 AND mers_YJ OUT viz_LDJ		LD TR1 LDNOT mers_YS AND trad_TM6bis LDNOT mers_YJ AND trad_TM7bis ORLD ANDLD OUT ver_VIU2 LD TR0 AND exec_IUP2 OUT viz_LIU2		LD TR1 LDNOT mers_YJ AND trad_TM5bis LDNOT mers_YS AND trad_TM8bis ORLD ANDLD OUT ver_VDU2 LD TR0 AND exec_DUP2 OUT viz_LDU2
‘Working sequence for logical function YIUP1 of closing the door at platform 1 with verifying this door closing using YVIU1		‘Working sequence for logical function YDUP1 of opening the door at platform 1 with verifying this door opening using YVDU1		‘Final sequence with vizualisation the damage states at doors’ closing and opening	
000028	LDNOT lim_LIP1 OUT TR0 ANDNOT exec_DUP1 OUT TR1 LDNOT mers_YS AND trad_TM2 LDNOT mers_YJ AND trad_TM3 ORLD OR exec_IUP1 OR but_IMU1 ANDLD OUT exec_IUP1 LD TR1 LDNOT mers_YS AND trad_TM2bis LDNOT mers_YJ AND trad_TM3bis ORLD ANDLD OUT ver_VIU1 LD TR0 AND exec_IUP1 OUT viz_LIU1	000076	LDNOT lim_LDP1 OUT TR0 ANDNOT exec_IUP1 OUT TR1 LDNOT mers_YJ AND trad_TM1 LDNOT mers_YS AND trad_TM4 ORLD OR exec_DUP1 OR but_DMU1 ANDLD OUT exec_DUP1 LD TR1 LDNOT mers_YJ AND trad_TM1bis LDNOT mers_YS AND trad_TM4bis ORLD ANDLD OUT ver_VDU1 LD TR0 AND exec_DUP1 OUT viz_LDU1	000124	LD init_AUT OUT TR0 AND ver_VIU1 OUT viz_LAI1 LD TR0 AND ver_VIU2 OUT viz_LAI2 LD TR0 AND ver_VDU1 OUT viz_LAD1 LD TR0 AND ver_VDU2 OUT viz_LAD2

6. CONCLUSIONS

The present paper emphasizes one of priority directions for scientific research of the Automation, Applied Informatics and Computers Department from the University of Petrosani: conceiving, testing and implementation of modern software structures for real-time applications in industry and other domainsof activity, even non-conventional. In this matter, the realised development system based on PLC and tested in laboratory conditions, with perspectives to be implemented on a pilot installation, proves the doubtless application perspectives of PLCs in majority aspects of human activities.

7. REFERENCES

[1] COROESCU, T., *Control of Mining Hoisting Installations with Microproccessors.* PhD Thesis,

University of Petrosani, 1989.
2] COROESCU, T., *Computer Simulation and Optimal Control of Mining Hoisting Process.* Proceedings of the "Third International Symposium on Mine Mechanisation and Automation", Golden-Colorado (USA), June 1995, vol. II, section 20, pp. 25 - 34.
[3]. COROESCU, T., *Comunicarea interactivă om-calculator*. Ed. Lumina Lex, Bucureşti, 2001.
[4]. COROESCU, T., ş.a., *Automatizarea instalaţiilor de epurare a apelor reziduale la uzinele de preparare din Valea Jiului – faza: Documentaţia de execuţie pentru statia pilot echipată cu controler logic programabil PLC*. Contract de cercetare ştiinţifică cu ICPM-SA Petroşani, 2002
[5]. COROESCU, T., SÂRB, V., *Introducere în ştiinţa sistemelor şi a calculatoarelor*. Ed. Didactică şi Padagogică R.A., Bucureşti, 2003.
[6]. GIANNASI , F., LOW, R., *Maths for computing and information technology*. Longmain Harlow, Essex (UK), 1999.
[7]. * * * *A Beginner's Guide to PLC*. OMRON, Japan, 2001.
[8]. * * * *Programmable Controllers, Programming Manual*. OMRON, Japan, 2001

APPLICATION OF PROGRAMMABLE LOGIC CONTROLLER PLC FOR AUTOMATED WEIGHING CONTROL SYSTEM

COROESCU TIBERIU

Department of Automation, Applied Informatics and Computers, University of Petrosani, Romania

ABSTRACT

The paper analyses the large application possibilities offered by Programmable Logic Controller PLC for control dynamic systems in mining industry. In general, a Control System is a collection of electronic devices and equipment which are computerized controled in place to ensure the stability, accuracy and smooth transition of a process or a manufacturing activity. It takes any form and varies in scale of implementation, from a power plant to a semi-conductor machine. In underground mining, the electromechanical mining systems are quite nonlinear and dynamic being often too complicated and too fast to be accurately controled by an usual control system. As a result of rapid advancement of technology, complicated control tasks can be accomplished with a highly automated control system, which may be in the computerized form of Programmable Logic Controller PLC. As a special and concrete application of the programmable logic implemented in the form of ladder program is for the automatic weighing control for a coal mining hoisting installation with two skips.

Keywords: *Programmable Logic Controller PLC, Automated Weighing, Control System, Ladder Program.*

1. INTRODUCTION

The mining hoisting process is one of the most dynamic and complex technological processes. A quite important and critical part of the hoisting process is the continue weighing control system. The automatic optimal control of this process required the determination of the unsimplified mathematical model as the state mathematical model. Using the system theory it was possible to verify the structure proprieties: controllability and observability on the model and then to determine the restrictive conditions in which it was possible either to automatic control or the automatic supervision of this complex process [1].

The materialisation of the optimum command in positive conditions was achieved by a specific microsystem with microprocessor and intrinsically safety. In order to provide compatibility with available present hoisting engines, the design of some original electronic equipments, based on numerical technique has been imposed and realised [1], [2].

In this respect, for the weighing control system of the hoisting installations either with skips or with cages, in case of drive with d.c. electrical motors or a.c. electrical motors it is necessary to use a modern equipment based on microprocessor or microcontroller, the only capable to assure the necessary mobility and security in the automatic optimal control of the hoisting process. These aspects impose the use of the Programmable Logic Controller PLC to automate in programmable logic the Weighing Control System.

2. THE STRUCTURE ANALYSIS OF PROGRAMMABLE LOGIC CONTROLLER PLC

In an automated system, the Programmable Logic Controller PLC is commonly regarded as the heart of the control system. The PLC consists of a Central Processing Unit CPU containing an application program, a memory unit and the Input and Output Interface modules, which are directly connected to the field Input/Output I/O devices. The program controls the PLC so that when an input signal from an input device turns ON, the appropriate response is made. The response normally involves turning ON an output signal to some sort of output devices. The CPU is a microprocessor that co-ordinates the activity of the PLC system. It executes the program processing the I/O signals and communicating with external devices.

With a control application program in execution, program stored within the PLC memory, the PLC constantly monitors the state of the system through the field input devices' feedback signal. It will then based on the program logic to determine the course of action to be carried out at the field output devices. Besides signal interfacing to the field devices (such as operator panel, motors, sensors, switches, solenoid valves, etc.), capabilities in the network communication enable a big scale implementation and process co-ordination besides providing greater flexibility in realizing distributed control systems. A PLC would not know the happenings around it without any sensing device, so every single component in a control system plays an important role regardless of size. Depending of the complexity of the process, an area host computer can be in place for very complex systems, to co-ordinate the activity of some PLCs in a specific area, which is supervized by a central process computer for the whole process.

In a typical application of a PLC, the whole process sequence is controlled by that PLC. The various input devices such as selector switches, push buttons, toggle switches, sensors are connected to the input of the PLC via the input terminal block. The output devices such as the revolving light, indicators, relays, contactors and solenoid valves are connected to the output terminals of the PLC. A ladder program loaded into the Central Processing Unit CPU memory of the PLC controls the

whole process. The program will execute a sequence automatically according to the pre-defined sequence of operations. Manual operations are also provided to allow operator to activate the installation manually by switches like emergency push-button for the purpose of safety in case it needs to stop the operation abruptly.

The PLC may be used to control a simple and repetitive task, or a few of them may be interconnected together with other host controllers or host computers through a sort of communication network, in order to integrate the control of a complex process. Intelligence of an automated system is greatly depending on the ability of a PLC to read in the signal from various types of automatic sensing and manual input field devices. Push buttons, keypad and toggle switches, which form the basic man-machine interface, are types of manual input devices. On the other hand, for detection of workplace, monitoring of moving mechanism, checking on pressure and on liquid level and many other functions, the PLC will have to tap the signal from the specific automatic sensing devices like proximity switch, limit switch, photoelectric sensor, level sensor and so on. Types of input signal to the PLC would be of digital ON/OFF logic or of analogue logic. These input signals are interfaced to PLC through various types of PLC input module.

An automatic system is incomplete and the PLC system is virtually paralysed without means of interface to the field output devices. Some of the most commonly controlled devices are motors, solenoids, relays indicators, buzzers, etc. Through activation of motors and solenoids the PLC can control from a simple pick and place system to a much complex one, like a servo positioning system. These types of output devices affect directly the PLC system performances. The other output devices such as the pilot lamps, buzzers and alarms are merely meant for notifying purpose. Like input signal interfacing, signal from output devices are interfaced to the PLC through a wide range of PLC output modules.

The process of reading the inputs, executing the program and updating the outputs is known as the scan process. The scan time is normally a continuous and sequential process of reading the status of inputs, evaluating the control logic and updating outputs. Scan time specification indicates how fast the controller can react to the field inputs and correctly solve the control logic. The time required to make a single scan is named the scan time and varies from 0.1 ms to tens of ms depending on its CPU processing speed and the length of the user program. The use of remote I/O subsystems increases the scan time as a result of having to transmit the I/O updates to remote subsystem. Monitoring of the control program also adds overhead time to the scan, as the controller's CPU has to send the status of coils and contacts to the monitoring devices.

2. IMPLEMENTING OF OMRON PLC USING CX-PROGRAMMER

The more significant and useful series of PLC is issued by the OMRON Corporation from Kyoto - Japan and includes CS1-series, CV-series and C-series including the following well known PLC types: CPM1, CPM1A, CPM2A and CPM2C. The OMRON Corporation was set up in 1933 by Kazuma Tateisi and is now one of the biggest in the world, having more than 25,000 employees all over the world and a production of more than 10,000 types of products. This company is the leader in human-computer interfaces, advanced communication systems, PLCs, micro-components, and equipments based on fuzzy logic. The OMRON products are famous especially based on their quality and fiability being recognised and used by NASA for the spatial ships.

CX-Programmer is the OMRON's PLC programming tool for the creation, testing and maintenance of programs associated with OMRON's CS1-series, CV-series and C-series of PLC's.It provides facilities for the support of PLC devices and address information and for communications with OMRON's PLCs and their supported network types.

The actual more used PLC types CPM1A or CPM2A can be connected to the Personal Computer PC via an RS-232C cable. One end of the RS-232C cable is connected to the PC serial port (either 9 pin or 25 pin adapter), while the other end of the cable is to be connected to the RS-232C adapter type MAD11attached to the CPM1A OR CPM2A. The DIP switch of the adapter must be set to HOST in order to link to the PC. The CPM2A training kit comes with one CX-Programmer 's CD-ROM. The CX-Programmer works under the operating systems Windows 95, Windows 98, or Windows NT4.0. Using the CX-Programmer can be created a real-time ladder program for the PLC.

Writing a ladder program consists of following seven steps: (1) creating symbols, (2) creating the ladder program, (3) compiling or automatically checking the program, (4) transferring the program to and from the PLC, (5) comparing the program with the PLC program, (6) monitoring the program during execution, and (7) performing an on-line edit.

3. PLC LADDER PROGRAM FOR AUTOMATIC WEIGHING CONTROL OF A COAL MINING HOISTING INSTALLATION WITH TWO SKIPS

The application in underground mining industry of a real-time software for the OMRON PLC is materialised into a coal mining hoisting installation with two skips which works under an automatic cycle. The PLC ladder program controls the automatic weighing of each skip which loads and unloads periodically, in line with the extraction cycle. The weighing process is realised with two weighing conveyor belts marked with 1 and 2, respectively.

The ladder program is converted in machine code so it is presented in the form of the mnemonic code for this current application. First of all it was necessary to create the complete set of the symbols presented into the Table 1. Then were initiated the start addresses for the two weighing conveyor belts, which are presented into Table 2.

The ladder program in the form of mnemonic code for real-time control of the weighing conveyor belts 1 and 2 is presented into Table 3 and Table 4, respectively.

The ladder program instructions in the form of mnemonic code for alarm and end of the complete program are presented into Table 5.

The part of the ladder diagram for initiating start addresses appears in Figure 1 and for alarm is presented in Figure 2.

Table 1. Created symbols for the ladder program

NR. CRT.	NAME	TYPE	ADDRESS /VALUE	USE	COMMENT
1.	vas_inc_2	Bool	HR0.08	Work	The skip 2 was loaded from weighing conveyor belt 2
2.	vas_inc_1	Bool	HR0.04	Work	The skip 1 was loaded from weighing conveyor belt 1
3.	vas_gol_2	Bool	0.05	Work	Input from weighing conveyor belt 2 indicating the skip 2 is empty
4.	vas_gol_1	Bool	0.04	Work	Input from weighing conveyor belt 1 indicating the skip 1 is empty
5.	vas_desc_2	Bool	HR0.07	Work	The skip 2 was unloaded on weighing conveyor belt 2
6.	vas_desc_1	Bool	HR0.03	Work	The skip 1 was unloaded on weighing conveyor belt 1
7.	v4_desc	Bool	10.03	Work	The unloading valve of weighing conveyor belt 2
8.	v3_inc	Bool	10.02	Work	The loading valve of weighing conveyor belt 2
9.	v2_desc	Bool	10.01	Work	The unloading valve of weighing conveyor belt 1
10.	v1_inc	Bool	10.00	Work	The loading valve of weighing conveyor belt 1
11.	tara_c2	Bool	21.03	Work	Bit to activate weighing tare TARA2 of weighing conveyor belt 2
12.	tara_c1	Bool	20.03	Work	Bit to activate weighing tare TARA1 of weighing conveyor belt 1
13.	TARA_2	Bool	10.05	Work	The weighing tare of weighing conveyor belt 2
14.	TARA_1	Bool	10.04	Work	The weighing tare of weighing conveyor belt 1
15.	start_dif_up_2	Bool	21.02	Work	Start differentiation of weighing conveyor belt 2 on the increasing front
16.	start_dif_up_1	Bool	20.02	Work	Start differentiation of weighing conveyor belt 1 on the increasing front
17.	start_2	Bool	21.01	Work	Start automatic cycle of weighing conveyor belt 2
18.	start_1	Bool	20.01	Work	Start automatic cycle of weighing conveyor belt 1
19.	salvare_date_2	Bool	21.12	Work	Bit to data saving for weighing conveyor belt 2
20.	salvare_date_1	Bool	20.12	Work	Bit to data saving for weighing conveyor belt 1
21.	salv_imposibila	Bool	20.13	Work	Saving was impossible
22.	primul_ciclu_2	Bool	HR0.05	Work	Active only the first cycle 2 after start
23.	primul_ciclu_1	Bool	HR0.01	Work	Active only the first cycle 1 after start
24.	prima_rulare	Bool	HR0.00	Work	Initiating at the first run
25.	lampa_avarie	Bool	10.06	Work	Alarm lamp
26.	intarziere_2_ inc	Bool	21.06	Work	Delay between loading and growing empty for weighing conveyor belt 2
27.	intarziere_2_desc	Bool	21.11	Work	Delay between unloading and loading for weighing conveyor belt 2
28.	intarziere_1_ inc	Bool	20.06	Work	Delay between loading and growing empty for weighing conveyor belt 1
29.	intarziere_1_desc	Bool	20.11	Work	Delay between unloading and loading for weighing conveyor belt 1

30.	int2	Bool	24.02	Work	Delay for the signal of empty weighing conveyor belt 2
31.	int1	Bool	24.00	Work	Delay for the signal of empty skip
32.	inc_difd_2	Bool	21.05	Work	Closing the differentiated loading valve 2 on the decreasing front
33.	inc_difd_1	Bool	20.05	Work	Closing the differentiated loading valve 1 on the decreasing front
34.	greutate_1	UINT	DM200	Work	The reading weight on the weighing conveyor belt 1
35.	desc_difd_2	Bool	21.10	Work	Opening the differentiated unloading valve 2 on the decreasing front
36.	desc_difd_1	Bool	20.10	Work	Opening the differentiated unloading valve 1 on the decreasing front
37.	com2_err	Bool	23.01	Work	Communication error at the weighing conveyor belt 2
38.	com1_err	Bool	23.00	Work	Communication error at the weighing conveyor belt 1
39.	ch_st_2	Bool	0.01	Work	Start key of the weighing conveyor belt 2
40.	ch_st_1	Bool	0.00	Work	Start key of the weighing conveyor belt 1
41.	cant_2_term	Bool	0.03	Work	Weighing over for the weighing conveyor belt 2
42.	cant_1_term	Bool	0.02	Work	Stop weighing for the weighing conveyor belt 1 (setted value is reached)
43.	av_com_2	Bool	21.04	Work	Communication alarm for weighing conveyor belt 2
44.	av_com_1	Bool	20.04	Work	Communication alarm for weighing conveyor belt 1
45.	a_fost_salvare_2	Bool	HR0.06	Work	Bit indicating data saving at the weighing conveyor belt 2
46.	a_fost_salvare_1	Bool	HR0.02	Work	Bit indicating data saving at the weighing conveyor belt 1

Table 2. Initiating start addresses for the two weighing conveyor belts

RUNG ADDRESSES (INSTRUCTION ADDRESSES)	LADDER PROGRAM INSTRUCTIONS
000000 (000000)	‘initiating start addresses for the two weighing conveyor belts LD P_First_Cycle ANDNOT prima_rulare MOV(21) #0261 DM0 MOV(21) #5000 DM3 MOV(21) #2101 DM7 MOV(21) #150 DM8 MOV(21) #0000 DM9 MOV(21) #2101 DM10 MOV(21) #200 DM11 MOV(21) #0000 DM12 OUT prima_rulare

Table 3. Real-time control of the weighing conveyor belt 1

RUNG ADDRESSES (INSTRUCTION ADDRESSES)	LADDER PROGRAM INSTRUCTIONS	RUNG ADDRESSES (INSTRUCTION ADDRESSES)	LADDER PROGRAM INSTRUCTIONS
000000 (000012)	LD ch_st_1 ANDNOT com1_err SET start_1	000008 (000049)	LD inc_difd_1 OR intarziere_1_inc ANDNOT TIM001 OUT intarziere_1_inc TIM 001 #50
000001 (000015)	LD start_1 DIFU(13) start_dif_up_1	000009 (000054)	LD cant_1_term SET vas_inc_1

000002 (000017)	LD start_dif_up_1 SET primul_ciclu_1	000010 (000056)	LDNOT a_fost_salvare_1 AND start_1 ANDNOT intarziere_1_inc ANDNOT v1_inc AND vas_inc_1 OR salvare_date_1 LDNOT TIM003 ORNOT salv_imposibila ANDLD OUT salvare_date_1 TIM 003 #10 SET a_fost_salvare_1
000003 (000019)	LD start_1 AND vas_desc_1 ANDNOT intarziere_1_desc OR primul_ciclu_1 OR tara_c1 ANDNOT TIM000 OUT tara_c1 TIM 000 #5		
000004 (000027)	LD P_First_Cycle OR int1 ANDNOT vas_gol_1 OUT int1	000011 (000068)	LDNOT salvare_date_1 ANDNOT intarziere_1_inc ANDNOT v1_inc AND vas_inc_1 OR v2_desc ANDNOT vas_gol_1 OUT v2_desc RSET vas_inc_1 RSET a_fost_salvare_1
000005 (000031)	LD int1 AND P_1s LD v1_inc OR P_First_Cycle CNT 020 #2	000012 (000077)	LD v2_desc DIFD(14) desc_difd_1
000006 (000036)	LD CNT020 LD primul_ciclu_1 OR vas_desc_1 AND start1 AND tara_c1 ORLD OR v1_inc ANDNOT cant_1_term OUT v1_inc RSET vas_desc_1 RSET primul_ciclu_1	000013 (000079)	LD desc_difd_1 SET vas_desc_1 RSET start_1
		000014 (000082)	LD desc_difd_1 OR intarziere_1_desc ANDNOT TIM002 OUT intarziere_1_desc TIM 002 #50
000007 (000047)	LD v1_inc DIFD(14) inc_difd_1	000015 (000087)	LD tara_c1 OUT TARA_1

Table 4. Real-time control of the weighing conveyor belt 2

RUNG ADDRESSES (INSTRUCTION ADDRESSES)	LADDER PROGRAM INSTRUCTIONS	RUNG ADDRESSES (INSTRUCTION ADDRESSES)	LADDER PROGRAM INSTRUCTIONS
000000 (000090)	LD ch_st_2 ANDNOT com2_err SET start_2	000008 (000127)	LD inc_difd_2 OR intarziere_2_inc ANDNOT TIM005 OUT intarziere_2_inc TIM 005 #50
000001 (000093)	LD start_2 DIFU(13) start_dif_up_2	000009 (000132)	LD cant_2_term SET vas_inc_2

000002 (000095)	LD start_dif_up_2 SET primul_ciclu_2	000010 (000134)	LDNOT a_fost_salvare_2 AND start_2 ANDNOT intarziere_2_inc ANDNOT v3_inc AND vas_inc_2 OR salvare_date_2 LDNOT TIM006 ORNOT salv_imposibila ANDLD OUT salvare_date_2 TIM 006 #10 SET a_fost_salvare_2
000003 (000097)	LD start_2 AND vas_desc_2 ANDNOT intarziere_2_desc OR primul_ciclu_2 OR tara_c2 ANDNOT TIM004 OUT tara_c2 TIM 004 #5		
000004 (000105)	LD P_First_Cycle OR int2 ANDNOT vas_gol_2 OUT int2	000011 (000146)	LDNOT salvare_date_2 ANDNOT intarziere_2_inc ANDNOT v3_inc AND vas_inc_2 OR v4_desc ANDNOT vas_gol_2 OUT v4_desc RSET vas_inc_2 RSET a_fost_salvare_2
000005 (000109)	LD int2 AND P_1s LD v3_inc OR P_First_Cycle CNT 021 #2	000012 (000155)	LD v4_desc DIFD(14) desc_difd_2
000006 (000114)	LD CNT021 LD primul_ciclu_2 OR vas_desc_2 AND start2 AND tara_c2 ORLD OR v3_inc ANDNOT cant_2_term OUT v3_inc RSET vas_desc_2 RSET primul_ciclu_2	000013 (000157)	LD desc_difd_2 SET vas_desc_2 RSET start_2
		000014 (000082)	LD desc_difd_2 OR intarziere_2_desc ANDNOT TIM007 OUT intarziere_2_desc TIM 007 #50
000007 (000125)	LD v3_inc DIFD(14) inc_difd_2	000015 (000165)	LD tara_c2 OUT TARA_2

Table 5. Alarms and end of the ladder program

RUNG ADDRESSES (INSTRUCTION ADDRESSES)	LADDER PROGRAM INSTRUCTIONS
000000 (000168)	LD P_On OUT TRO CMP(20) DM150 #E999 AND P_EQ OUT com1_err LD TRO CMP(20) greutate_1 #E999 AND P_EQ OUT com2_err
000001 (000177)	LD com1_err AND com2_err

	LD com2_err AND P_1s ANDNOT com1_err ORLD LD com1.err AND P_1s ANDNOT com2_err ORLD OUT lampa_avarie
000002 (000188)	END(01)

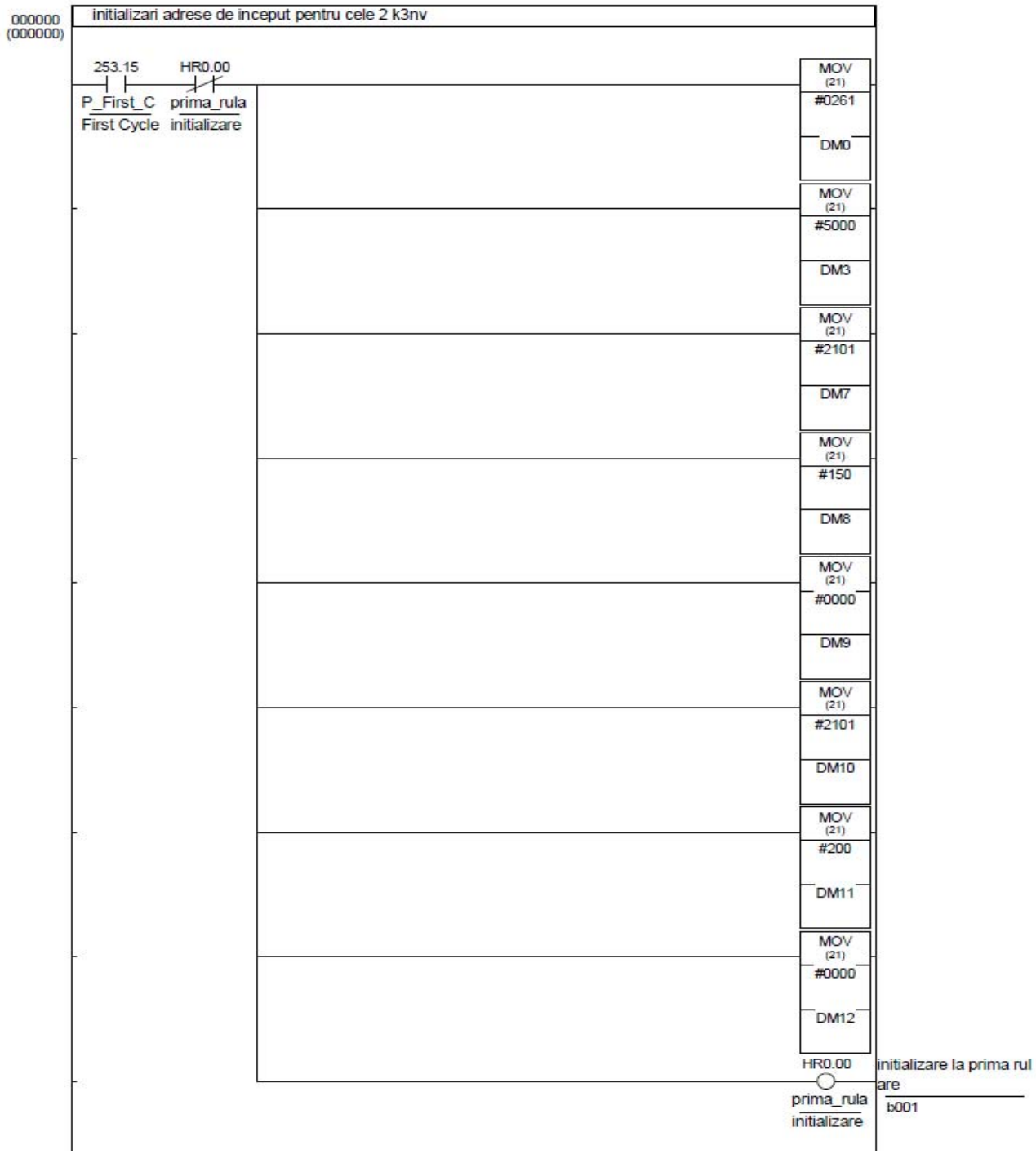

Figure 1 Ladder diagram for initiating start addresses

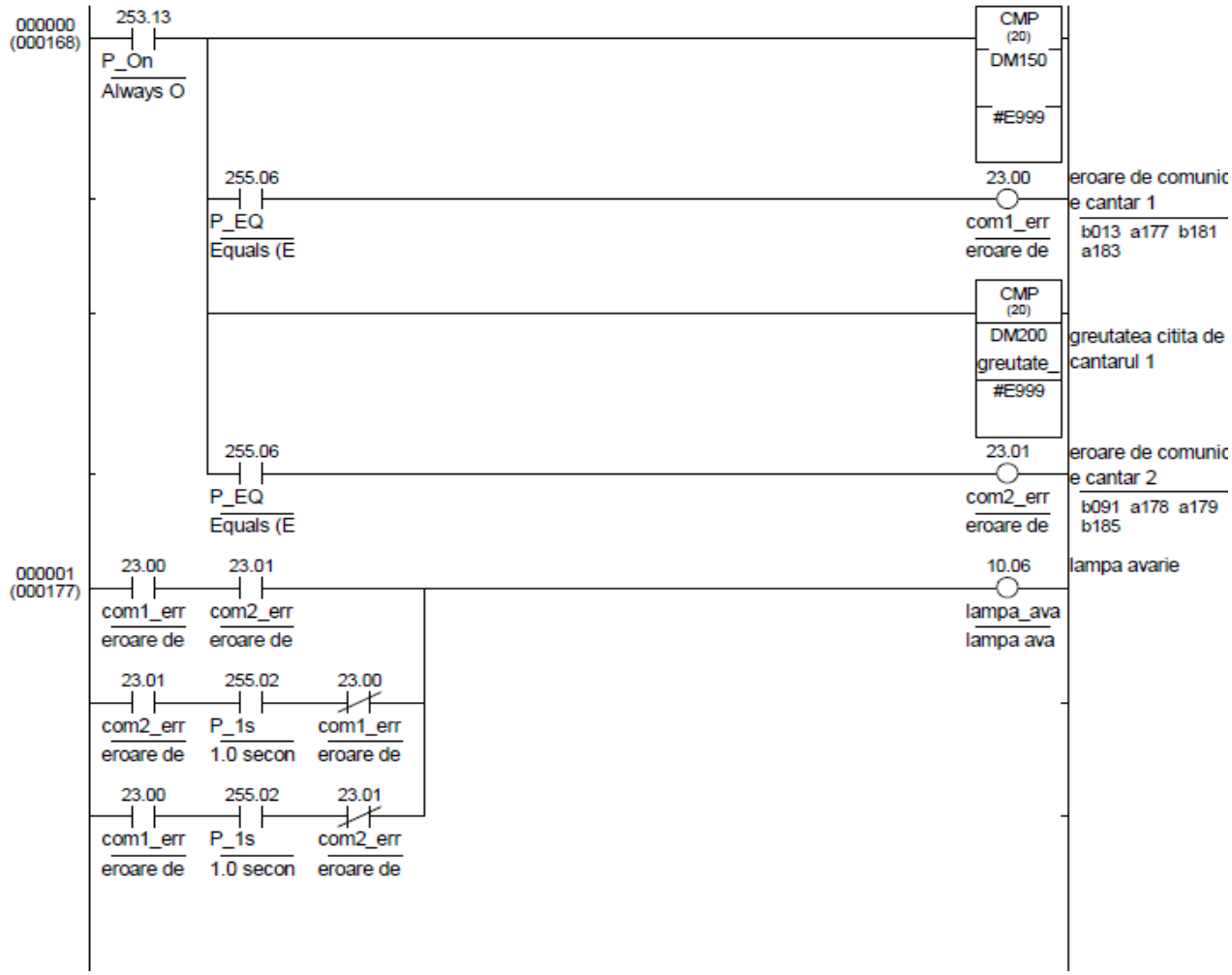

Figure 2 Ladder diagram for alarm

5. CONCLUSIONS

The paper emphasizes the doubtless application perspectives of Programmable Logic Controllers PLC for the electromechanical underground mining systems which are to be supervised with a real-time software in the form of ladder diagram program, realised in the mnemonic form with the useful software tool CX-Programmer. It is possible to extend this automated weighting control system for extraction with skips to extraction with cages, using either OMRON PLC or SIEMENS PLC in order to realise an adaptive system for mine vertical transport, as a part of the future intelligent mine.

6. REFERENCES

[1] Coroescu, T., *Control of Mining Hoisting Installations with Microproccessors.* PhD Thesis, University of Petrosani, 1989.

[2] Coroescu, T.,*Computer Simulation and Optimal Control of Mining Hoisting Process.* Proceedings of the "Third International Symposium on Mine Mechanisation and Automation", Golden-Colorado (USA), June 1995, vol. II, section 20, pp. 25 - 34.

[3] Coroescu, T., Sarb, V., *Sisteme automate speciale.* Universitatea din Petrosani, 1999.

[4] Coroescu, T., *Comunicarea interactiva om-calculator.* Ed. Lumina Lex, Bucuresti, 2001.

[5] Giannasi. F., Low, R., *Maths for computing and information technology.* Longmain Harlow, Essex (UK), 1999.

[6] Coroescu, T., Sarb, V., *Introducere in stiinta sistemelor si a calculatoarelor.* Ed. Didactica si Pedagogica R.A., Bucuresti, 2003.

[7] * * * *A Beginner's Guide to PLC.* OMRON, Japan, 2001.

[8] * * * *Programmable Controllers, Programming Manual.* OMRON, Japan, 2001.

PREDICTION ANALYSIS OF BANKRUPTCY RISK USING BAYESIAN NETWORKS

[1]CRACIUN MIHAELA-DACIANA, [2]BUCERZAN DOMINIC, [3]RATIU CRINA

[1,2]"Aurel Vlaicu" University of Arad, [3]Daramec srl Arad, Romania

ABSTRACT

The Bayesian probability, is widely misunderstood by the general public, as well as some economists. On the other hand, bankruptcy risk can be estimated in the static and dynamic analysis of the financial balance that outlines the former performance of the enterprise. A global evaluation of the enterprises future becomes interesting for the management of the enterprise and especially for its business partners: banks, clients, capital investors. Therefore, in this paper we mould the Anghel Prediction Model for bankruptcy risk using the Bayesian probability. To this purpose, we use Bayesian Networks (BN) and the AgenaRisk Tool. The result of this mould is a solution of bankruptcy risk prediction using BN.

Keywords: *Bayesian probability, Bayesian Network (BN), bankruptcy risk prediction, AgenaRisk Tool, Anghel Prediction Model*

1. INTRODUCTION

A Bayesian Network (BN) is a way of describing the relationships between causes and effects, and is made up of nodes and arcs. The collection of nodes and arcs is referred to as the *graph* or *topology* of the BN. In addition, in a BN each node has an associated probability table, called the Node Probability Table (NPT). The nodes represent variables. The arcs in a BN represent causal or influential relationships between variables. The key feature of BN is that they enable us to model and reason about uncertainty. The NPT for any node gives the *conditional probability* of each possible outcome given each combination of outcomes for its parent nodes. Usually, there are several ways of determining the probabilities in any of the tables. Alternatively, if no such statistical data is available we may have to rely on subjective probabilities entered by experts. A key feature of BN is that we are able to accommodate both subjective probabilities and probabilities based on objective data, as specified in [1].

Having entered the probabilities we can now use Bayesian probability to do various types of analysis. Bayesian probability is all about revising probabilities in the light of actual observations of events.

When we enter evidence and use it to update the probabilities in this way, we call it *propagation*. In theory we can enter any number of observations anywhere in the BN and use propagation to update the marginal probabilities of all the unobserved variables. This can yield some exceptionally powerful analyses that are simply not possible using other types of reasoning and classical statistical analysis methods, as you see in [5].

BN offer the following benefits, subject founded in [2]:

- *Explicitly model causal factors:* this key benefit is in stark contrast to classical statistics whereby prediction models are normally developed by purely data-driven approaches.
- *Reason from effect to cause and vice versa:* A BN will update the probability distributions for every unknown variable whenever an observation is entered into any node. So entering an observation in an "effect" node will result in back propagation, i.e. revised probability distributions for the "cause" nodes and vice versa. Such backward reasoning of uncertainty is not possible in other approaches.
- *Overturn previous beliefs in the light of new evidence:* The notion of explaining away evidence is one example of this.
- *Make predictions with incomplete data:* There is no need to enter observations about all the "inputs", as is expected in most traditional modelling techniques. The model produces revised probability distributions for all the unknown variables when any new observations (as few or as many as you have) are entered. If no observation is entered then the model simply assumes the prior distribution.
- *Combine diverse types of evidence including both subjective beliefs and objective data.* A BN is "agnostic" about the type of data in any variable and about the way the NPTs are defined.
- *Arrive at decisions based on visible auditable reasoning:* Unlike blackbox modelling techniques (including classical regression models and neural networks) there are no "hidden" variables and the inference mechanism is based on a long-established theorem (Bayes).

This range of benefits, together with the explicit quantification of uncertainty and ability to communicate arguments easily and effectively, makes BN a powerful solution for all types of risk assessment.

The first working applications of BN (during the period 1988-1995) tended to focus on classical diagnostic problems, primarily in medicine and fault diagnosis. Intelligence Group at Aalborg University produces the MUNIN system. Companies such as Microsoft and Hewlett-Packard have used the early BN for fault diagnosis, and in particular printer fault diagnosis. There have also been numerous uses of BN in military applications, for example the TRACS system for predicting reliability of land vehicles. Another high-stakes application domain where BN have been used

extensively by commercial organizations is fault prediction; subject is founded in [4].

Because of historical limitation even Bayesian statisticians have shunned BN for problems that involve continuous variables and complex stochastic models. Instead they have used tools like the WinBUGS software package, which are based on intensive sampling algorithms collectively known as *Markov Chain Monte Carlo* (MCMC) methods. Fortunately, there have been some recent breakthroughs in algorithms for hybrid BN. Building on the work of Koslov and Koller, Neil have developed and implemented a dynamic discretisation algorithm which works efficiently for a large class of continuous distributions.

Users of AgenaRisk Tool, which implements this algorithm, can simply define continuous nodes by their range and distribution. Without any of the complexities associated with the MCMC approach, they can achieve results of matching or greater accuracy for many classes of models, especially for models that include discrete variables, as specified in [6]. On a wider scale, there is considerable research into how to model extremely large problems involving hundreds of data points, with many variables, over long periods of time, or involving complex sequences of variables and data. A number of extensions to BN beyond the classical inference algorithms are being used for this purpose, including: Relational BN, Statistical parameter learning, Sensitivity analysis, Safety and reliability modelling, Operational risk in finance, Recommendation engines and information retrieval.

2. THE I. ANGHEL MODEL IN BANKCRUPTCY RISK PREDICTION

Anghel has developed a model based on discriminatory analysis, starting from a sample of 276 enterprises, grouped into non-bankrupt (60%) and bankrupt (40%), and belonging to a number of 12 industries of the national economy. The analysis covered the period 1994 -1998 and has initially used a number of 20 economic -financial indices.

After the selection stage, four financial rates have been established for the development of the score function:

- X_1 - earning after taxes / incomes;
- X_2 - Cash Flow / total assets;
- X_3 - liability / total assets;
- X_4 - liability/ sales * 360

All the above rates have been aggregated in the following score function: $A = 5.667 + 6.3718 * X_1 + 5.3932 * X_2 - 5.1427 * X_3 - 0.0105 * X_4$, subject is founded in [3].

Varying within the values established for this function, enterprises are included in one of the following three situations:

- When $\boldsymbol{A < 0}$, bankruptcy/failure situation;
- When $\boldsymbol{0 \leq A \leq 2.05}$, uncertainty situation demanding prudence;
- When $\boldsymbol{A > 2.05}$, a good financial situation.

The analysis of the previously presented models has revealed a certain facility in detecting bankruptcy in time.

Subject to bankruptcy risk prediction was been treated with interest over the years. The use of BN for BP was study, as you see in [7], by Lili Sun and Prakash P. Shenoy.

3. THE ANGHEL PREDICTION MODEL (PM) FOR BANKRUPTCY RISK (BR) EXPLAINED USING A BAYESIAN NETWORK

Accepting the Bayes' Theorem and the accuracy of the AgenaRisk software it is possible to explain the Anghel PM for BR without exposing the mathematical details. The vehicle for doing this is a visual model called Bayesian Network (BN) as shown in the Figure 1.

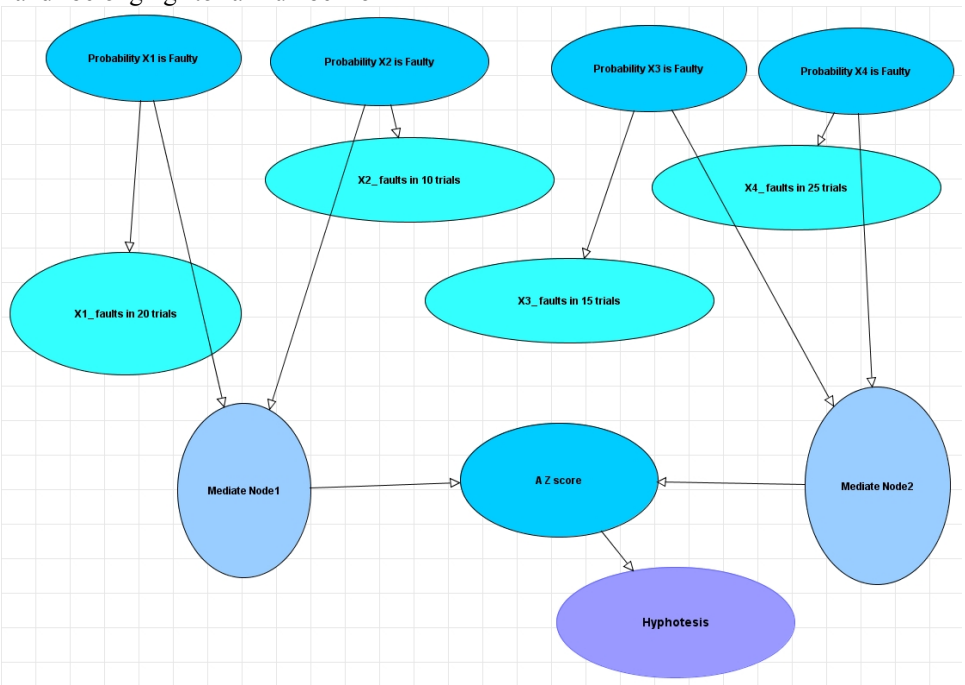

Figure 1 – BN showing causal structure

In this structure we have four types of nodes: *sample, probability, result* and *assumption nodes*. The *sample nodes* represent the probability that X_i is faulty (i = 1, 2, 3, 4). The *probability nodes* are X_i faults in *number* of trials, where *number*=20, 10, 15, 25. The *result nodes* are the following: Mediate Node1, Mediate Node2 and A Z score. The Hypothesis node is the *assumption node*. As mentioned in the previous section, the Anghel PM for BR is based on the function score A = $5.667+6.3718*X_1+5.3932*X_2-5.1427*X_3-0.0105*X_4$. In this case we are handling nodes with multiple parents. The initially model we built, was that all four sample nodes were parents for the result node. In this case the calculation was very slowly and difficult. So we introduce the two Mediate Nodes and so we reduce the number of parents' node and of the calculation time, too.

Next we explain how we built the nodes.

The sample nodes are simulation nodes, with continuous interval type. The lower bound is 0.0 and the upper bound is 1.0. The NPT is a Uniform Expression with lower bound 0 and upper bound 1. The graph types associated to this node are Histogram.

The probability nodes are simulation nodes, with integer interval type. The lower bound is 1 and the upper bound is 9. The NPT is a Binomial Expression with 20, 10, 15 and 25 trials and the probability of success given by the parents' node probability p_X_i_faulty. The graph types associated to this node are Histogram.

The result nodes are simulation nodes, too. They divide in two categories. The Mediate Nodes and the A Z score node. The types of Mediate Nodes are continuous interval with values between -10 and 50. The NPT is an arithmetic expression *6.3718*p_ X1_faulty +5.3932* p_ X2_faulty*. The graph types associated to this node are Histogram. The type of A Z score node is continuous interval with values between -20 and 100. The NPT is an arithmetical expression MN1+MN2. The graph type associated to this node is Histogram.

The assumption node Hypothesis is a simulation node, with Boolean type. The state options are customised, with positive Outcome "Good financial situation" and the Negative Outcome "Bankruptcy / failure situation". The NPT is a comparison expression: ***if(zscore<2.05,"Bankruptcy / failure situation", "Good financial situation")***. The graph type associated to this node is Histogram.

The statistic attached to the main risk graph is shown in Figure 2. In this case there is no observation.

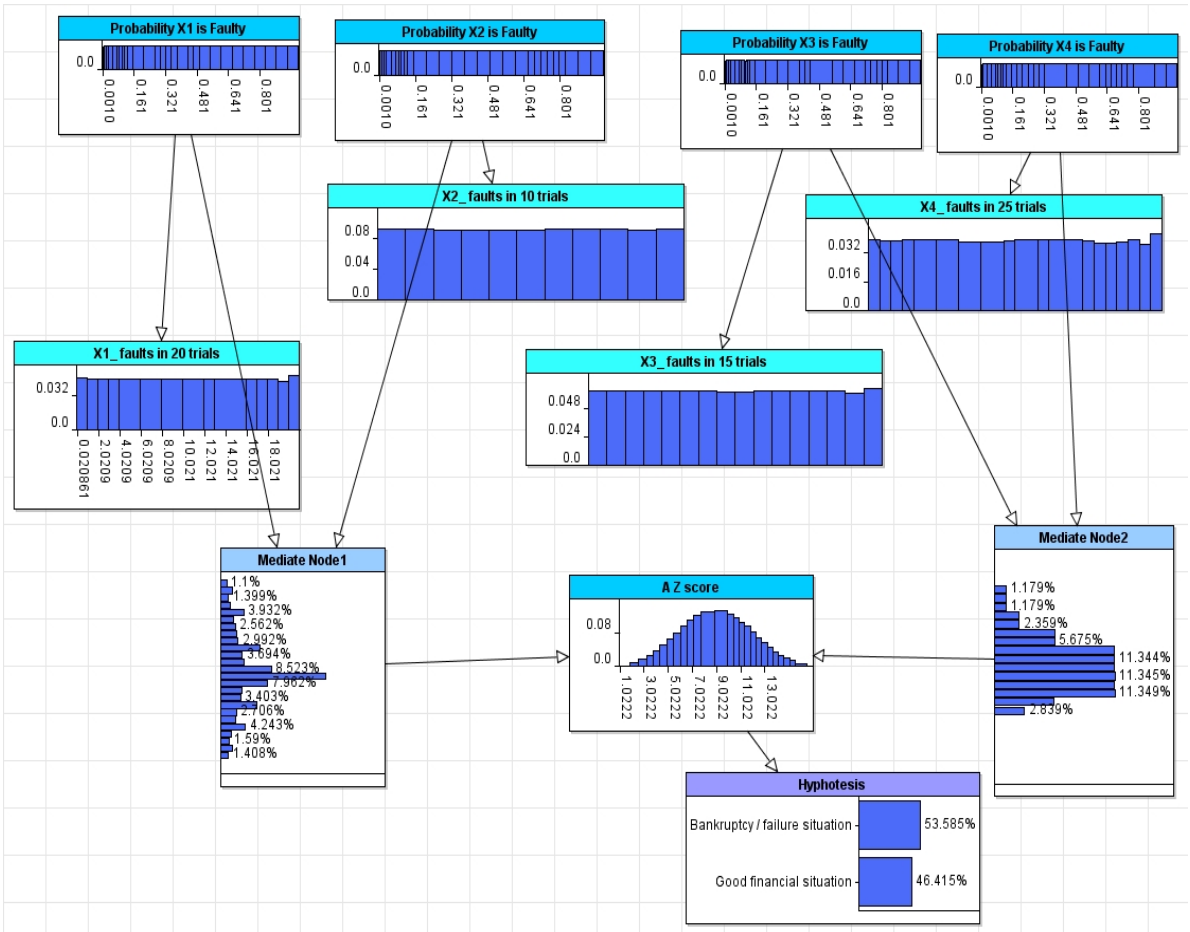

Figure 2 - Complete *Hypothesis Testing* model

In case that observations appear we can attached to each probability node a certain number of trials. Let`s consider the following observation: X_1 decrease the trials from 20 to 2, X_2 decrease the trials from 10 to 1, X_3 decrease the trials from 15 to 1, X_4 decrease the trials from 25 to 2. The result is shown in Figure 3.

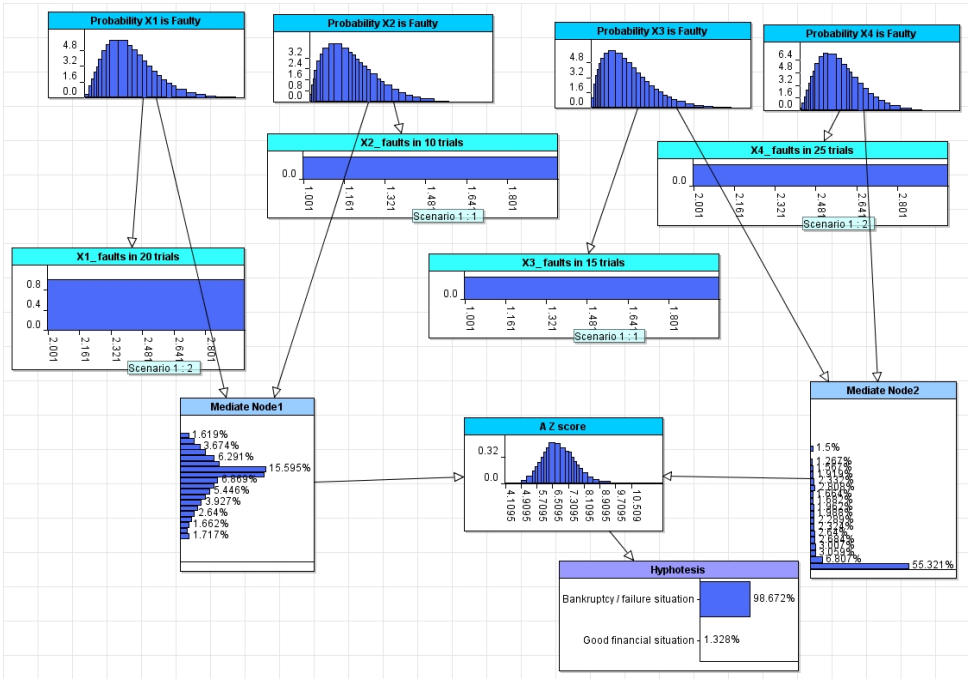

Figure 3 - Risk graph of *Hypothesis* after evidence has been entered

The risk map for this model has attached the following risk table, as shown in Figure 4.

Figure 4 – Risk table of *Hypothesis* generated after evidence has been entered

4. THE ANGHEL PREDICTION MODEL (PM) FOR BANKRUPTCY RISK (BR) USING HYPOTHESIS TESTING WITH EXPERT JUDGMENT

The structure of the risk map described at the previously section, will be changed. We add a new node at the top of the risk map named Prior Type. This node is a labelled type with Uniform and Beta label value. The NPT is a comparison expression with value 0. The graph type associated to this node is Histogram. (see Figure 5).

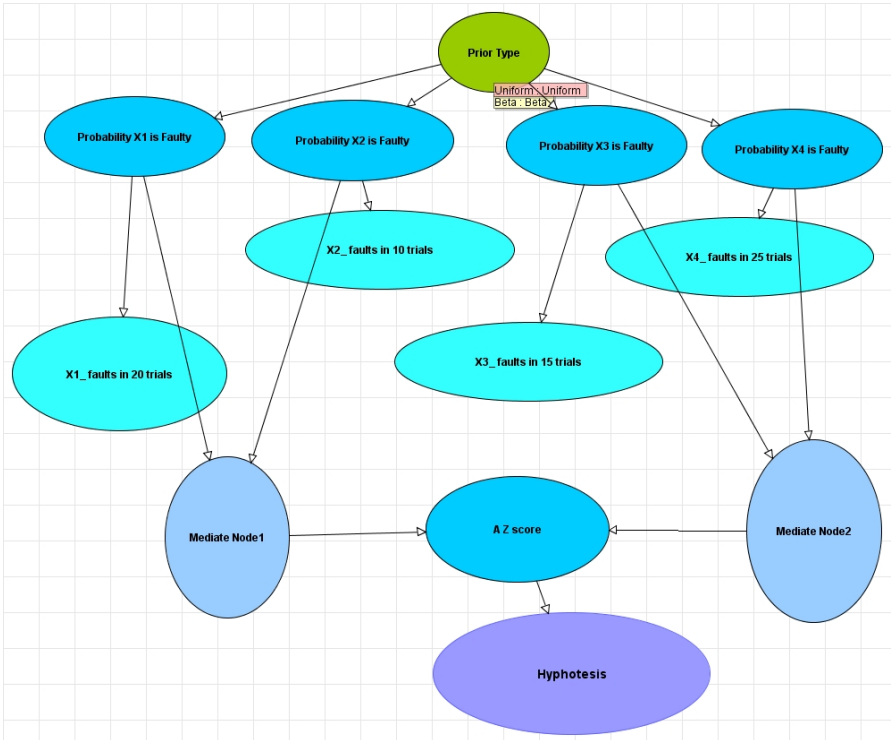

Figure 5 - Hypothesis Testing with Expert Judgment

In this case the sample nodes are modified only by the NPT. The NPT Editing Mode changes into Partitioned Expression. We specify the distribution as follows: for nodes X_1 and X_4 the uniform distribution is given by the function Uniform(0,1) and the beta distribution is given by the function Beta(1,9,0.0,1.0). So we obtain the chance of failure of 1 to 10. For nodes X_2 and X_3 the uniform distribution is given by the function Uniform(0,1) and the beta distribution is given by the function Beta(2,8,0.0,1.0). So we obtain the chance of failure of 1 to 5.

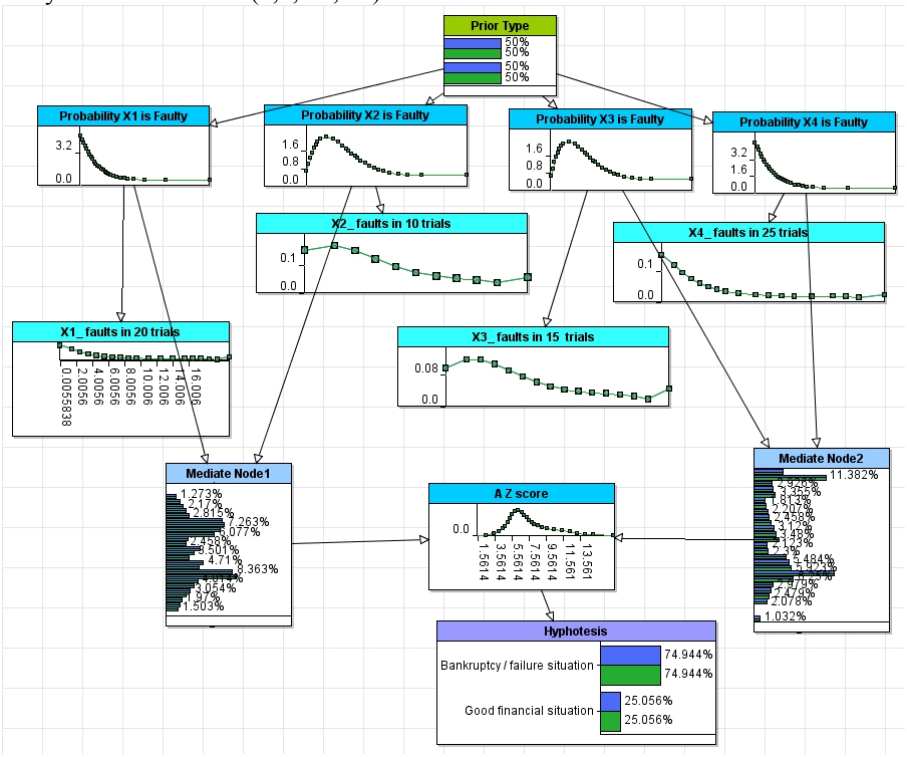

Figure 6 - Complete *Hypothesis Testing* model with Expert Judgment

Next, we define two scenarios one type *Uniform* and the second type *Beta*. The two scenarios will be correlated with the risk map entering the observation that the Prior Type is Uniform in the scenario that we have named Uniform and Beta in the scenario that we have named Beta (see Figure 7).

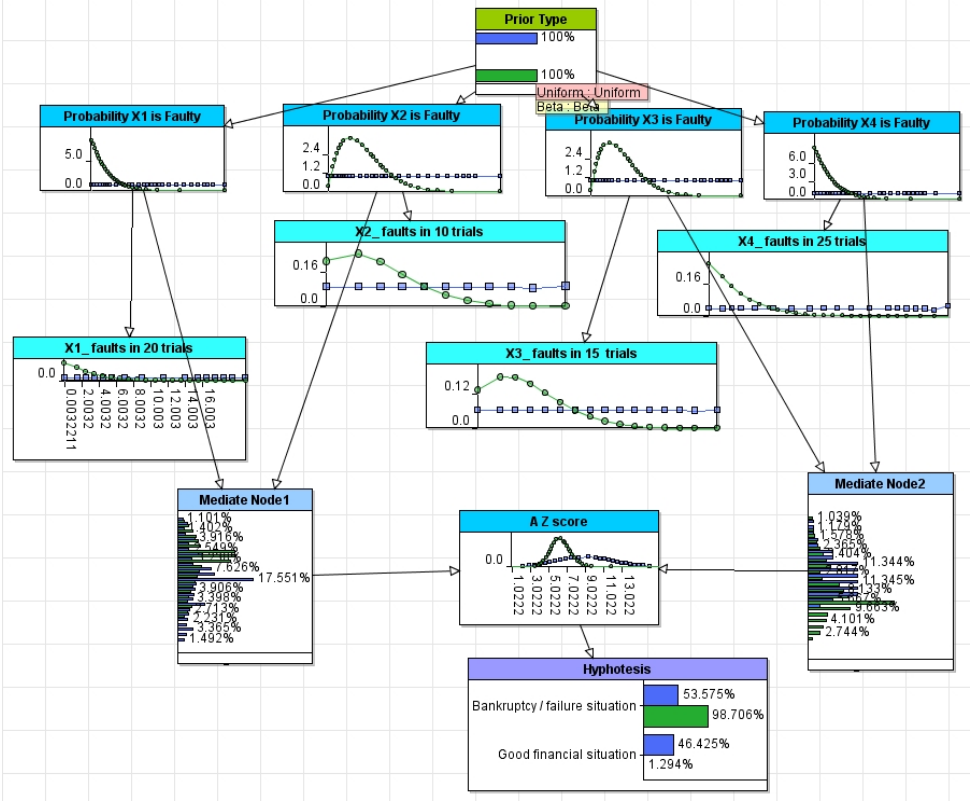

Figure 7 - Results of hypothesis test with two different prior assumptions

Comparing the last two figures we observe the difference of the results.

Combining Data and Prior Assumptions

We change the probability nodes so that we decrease 1/5 the trials: from 20 to 4, from 10 to 2, from 15 to 3 and from 25 to 5.

For the both scenarios, Uniform and Beta, we will introduce values as follow: for the probability nodes X_1 and X_4 Uniform and Beta receive the value 1, respectively the nodes X2 and X3 receive the value 0 for Uniform and Beta. The results are shown in Figure 8.

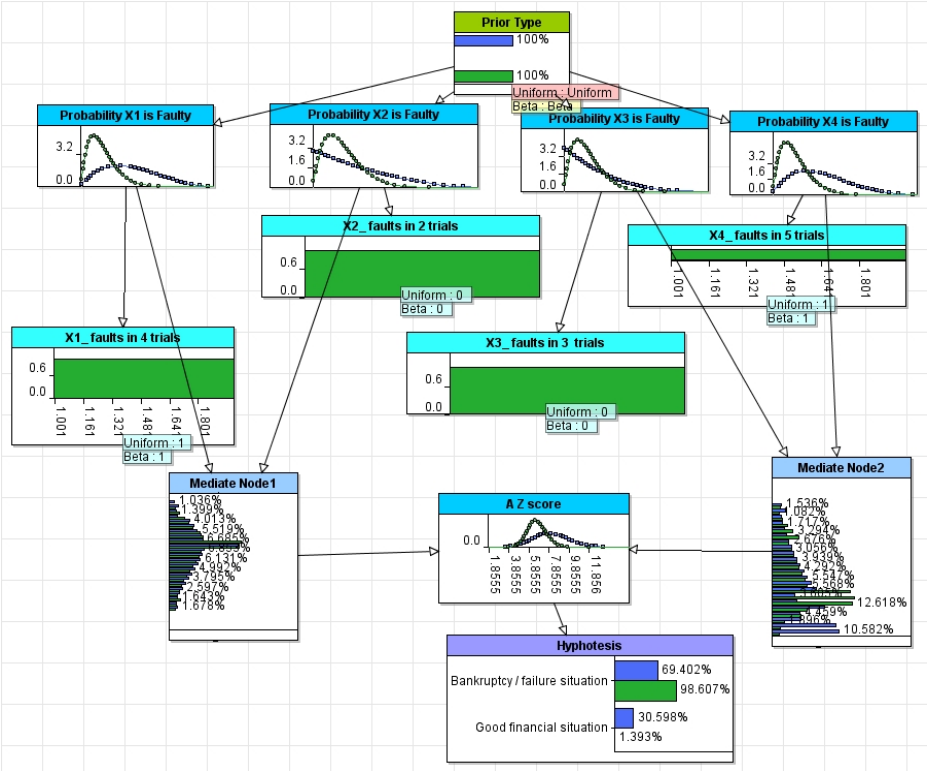

Figure 8 - Results of hypothesis test after entering sparse sample data

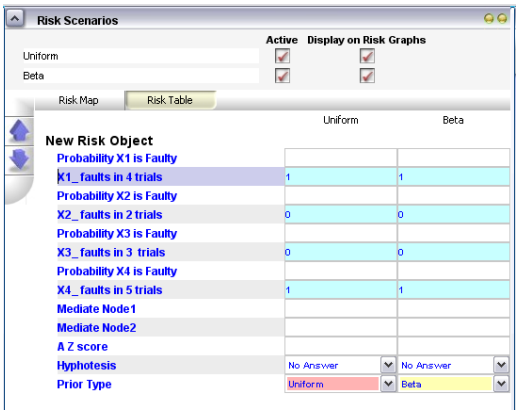

Figure 9 – Risk table of Hypothesis Testing with Expert Judgment after entering sparse sample data

Changing the Simulation Settings

We delete the Uniform scenario and we remove from the probability nodes X_1 and X_4 the value 1 for Beta. After we calculate we obtain the mean 0.40 for X_1 and 0.50 for X_4 and the variance value 0.46 for X_1 and 0.62 for X_4.

Next, we modify the properties for the defined model. The maxim number of iteration defined in the simulation settings are 25. We work with 5 iterations. Running the calculation we will obtain different values for both probability nodes.

5. CONCLUSIONS

We have shown that, using BN and AgenaRisk Tool, it is possible to show all of the implication and results of a complex Bayesian argument without requiring and understanding of the underlying theory of mathematics. Economists can use the obtained analysis to predict the bankruptcy risk using Bayesian probability.

6. REFERENCES

[1] JENSEN FINN V, GRAVEN-NIELSEN THOMAS - *Bayesian Networks and Decision Graphs*, Springer 2002

[2] POURRET OLIVIER, NAIMS PATRICK, MARCOT BRUCE – *Bayesian Networks - A Practical Guide to Applications*, John Wily & Sons Ltd, 2008

[3] ANGHEL ION – *Falimentul – radiografie şi predicţie,* Ed. Economică, Bucureşti, 2002

[4] NEAPOLITAN RICHARD E. – *Learning Bayesian Networks,* Prentice Hall Series in Artificial Intelligence

[5] HECKERMANN DAVID – *A Tutorial on Learning with Bayesian Network*, March 1995

[6] Agena 2007, Press Release, http://www.agenarisk.com/agenarisk/case_13.shtml

[7] SUN LILI, SHENOY PRAKASH P. – *Using Bayesian Networks for Bankruptcy Prediction – Some Methodological Issues*, European Journal of Operational Research, 2007

HIERARCHICAL OPTIMIZATION-BASED APPROACH FOR DYNAMIC FLEET MANAGEMENT

[1]DINU SIMONA, [2]BORDEA GHEORGHE

[1,2]*Department of Electrics, Electronics and Informatics, Constanta Maritime University, Romania*

ABSTRACT

A mathematical programming model suitable for addressing decision-making process within the supply chain of an organization is the multi-level (hierarchical) model. This is a useful approach for problems with conflicting objectives within a hierarchical structure. These problems occur in a variety of circumstances which involve vehicle fleet management.

This study deals with a challenging issue of vehicle fleet management, the allocation of vehicles, by taking into consideration the dynamic aspect of the problem and proposes an approach based on the hierarchical optimization.

Keywords: *Vehicle Fleet, Supply Chain Management, Multi-level programming, Dynamic Vehicle Allocation*

1. INTRODUCTION

Recent business environment has increased the demand for transportation services. Decisions about supplying goods and services to the final customers through the chain of activities of production, sales and distribution are becoming more important as customers demands increase. The efficient and effective movement of goods from raw material sites to processing facilities, component fabrication plants, finished goods assembly plants, distribution centers, retailers and customers is critical in today's competitive environment. Supply Chain M anagement (SCM) entails not only the movement of goods but also decisions about where to locate plants and distribution centers [12].

A distinctive feature of the management concept referring to the modern SCM is an integrated view that extends beyond the company, including suppliers, customers and carriers. Within the supply chain, decision-making in an organization influences the decision-making process from the others, but each tries to optimize their own objectives. Since each partner involved in the SCM has its own objective and constraints, these partners are playing Stackelberg game in a SC problem [13].

A mathematical programming model suitable for addressing this type of decentralized planning problem is the multilevel programming model.

Multi-level programming techniques are developed to solve decentralized planning problems with multiple decision makers in a hierarchal organization [6]. These decentralized planning problems are important issues in supply chain management (SCM) where many producers and carriers work together to design, produce and deliver the final product.

2. DESCRIPTION OF BI-LEVEL OPTIMIZATION PROBLEM

Bi-level optimization is a useful approach for problems with conflicting objectives within a hierarchical structure.

Originated from the fields of game theory and decision making, also describes a number of problems in transportation planning and modeling (road network design, space localization, traffic control, optimal congestion pricing), engineering design (optimal structure and shape), economic planning, etc.

A detailed list of references and various proposed methods for solving bi-level programming applications is found in [14].

Its sequential framework involves two optimization problems at different levels, where the feasible set of the first problem, called the upper-level (leader) problem, is determined by the other optimization problem, called the lower-level (follower) problem. (Fig.1). By extending this concept, one can define multi-level programs with any number of levels.

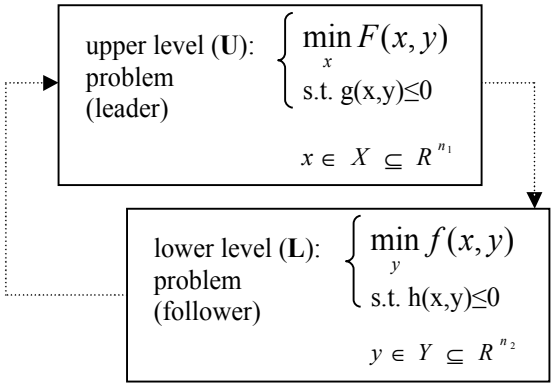

Figure 1: Bi-level model.

where:

x and y are the decision variable vectors of the upper level and lower level, respectively;

F(x,y) and f(x,y) are the leader's and the follower's objective functions, respectively;

g(x,y) and h(x,y) are the leader's and the follower's constraints, respectively;

X and Y represent upper and lower bounds on elements of the vectors x and y:

$$X = \{(x_1,...,x_{n_1})^T \in R^{n_1} \mid l_{s_i} \le x_i \le l_{d_i}, i = 1,...,n_1\} \quad (1)$$

$$Y = \{(y_1,...,y_{n2})^T \in R^{n_2} \mid \bar{l}_{s_j} \le x_j \le \bar{l}_{dj}, j = 1,..,n_2\} \quad (2)$$

For some particular cases of bi-level problems, the search spaces X and Y may introduce additional complicated requirements.

In Fig. 1 both the leader and the follower try to optimize their own objective function without considering the objective of the other one. The leader has complete information about the follower's optimization problem and its choice affects the lower level.

First, the leader makes a decision by selecting a vector $x \in X$ that optimizes its objective function. Then, for the given vector x, the follower reacts by selecting a vector $y \in Y$ that optimizes its own objective function. According to this, the leader integrates within its optimization process the feedback from the follower.

3. DYNAMIC FLEET MANAGEMENT

Fleet management is that part of Supply Chain Management (SCM) combining all aspects relating to a company's vehicle, from vehicle acquisition to vehicle dispatch and maintenance. A well organized delivery fleet ensures the reducing of transportation costs and provides high levels of customer service while maintaining route productivity and efficiency. The efficient and economical operation of the base vehicle fleet involves interdependent decision processes and implies complex problems of resource allocation and scheduling. These problems may take diverse forms, especially when taking into consideration the time dimension.

Fleet may represent many types of resources and consequently there has been a rich history of research in these fleet management problems. Dejax and Crainic[3], Powell[11], Powell and Topaloglu[10], Bienstock et al [1], Bramel and Simchi-Levi[2] provide in their survey papers a review of the operations research literature on the topic of fleet management models regarding: homogeneous/multiple vehicle types, weight, loading and capacity restrictions, fixed/variable fleet size, fleet based at single /multiple depots, etc.

The dynamic (time-dependent) aspect incorporates "explicitly the interaction of activities over time"[11]. White[16] describes one of the first dynamic models in fleet management for container allocation regarding the "repositioning" of the empty containers. Later extensions of his approach took the form of the dynamic transhipment network optimization problem[16, 7, 5, 9, 15, etc].

These dynamic models of fleet management occur in a variety of circumstances which involve the management of fleets of vehicles over time and have been extensively studied in recent years due to the high standards imposed by a competitive transportation market.

An intrinsic challenging issue of vehicle fleet management is minimizing "empty" miles: minimizing the number of empty vehicles movements for supply chain and environmental profit. This operation, known as repositioning is an essential, integral part of the vehicle routing model and one of the current challenges in transport optimization. Moving empty vehicles is caused by the unbalanced directional flows between pickup and delivery locations. It generates additionally logistic costs, but has a great impact on transportation system performance and continuity of operations.

The dynamic aspect of demands (transportation requests are randomly distributed through the time and can be foreseen with some uncertainty) makes minimizing repositioning even more challenging.

This problem is treated in the more generally Dynamic Vehicle Allocation (DVA) framework, where a fleet of vehicles is assigned to locations with dynamically occurring demands. DVA problems try to find the most efficient way to manage the empty repositioning flows from regions with unused vehicles to regions that require them. If the empty (available) are not located in the demand points at the requested time, the vehicles must be moved empty to another region to satisfy known future request (or which is more promising) or must be held in that region until a load is find (a demand arise). These decisions have future consequences and influence the fleet management.

The major assumptions that were made in the development of the model [11] are:

- a vehicle is dedicated to a single load at a time; the vehicle cannot take another demand until the current demand is completed and no vehicle can be shared by loads. More, there is no compatibility problem between loads and vehicles.
- each load fills an entire vehicle (there are no consolidations).
- each load must be delivered to a specified location within a specific time window.
- travel time between all regions are equal to one time period for both loaded or empty moves.

Dynamic transportation problems are usually represented by a space-time network (Fig. 2), where each node i represents a region at a specific time, t.

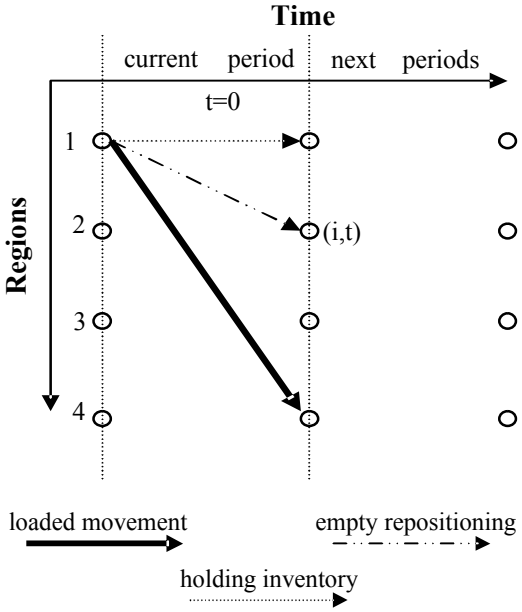

Figure 2: decisions in a dynamic network

The set of all possible movements (decisions) is represented in figure 2:

- loaded movement: arc representing loaded movement between two regions;
- empty repositioning: arc representing empty movement between two regions (vehicle repositioning);
- holding inventory: arc representing holding capacity in the same region from one time period to the next one.

4. DYNAMIC VEHICLE ALLOCATION: STATEMENT OF THE PROBLEM

The basic DVA problem seeks to optimize total profits obtained with the carried loads and minimize the cost of empty runs over a given planning horizon, T.

Starting from Powell [11] formulation, we propose an ADV bi-level model by taking into consideration the delays in service charge. In this model, the shipper (the producer of goods or an intermediary) is the leader, trying to optimize (minimize) the delays in shipment. He generates the demands (loads) and controls the periods in which the charges are being made. These are the decision variables for the upper level.

The carrier, located in the lower level, answer these demands by supplying transportation services and distributing the demands to the transportation network. He is trying to optimize (maximize) its total profit over the planning horizon. The corresponding decision variables are the loaded, the empty and the inventory movement variables. In order to formulate this model, we use the following notations:

Network variables:

T is the planning horizon, divided into discrete sets: T={0,1,2,…, T}.

C is the set of regions (points) in the network.

$\tau_{i,j}$ is the travel time between region i and region j.

N is the set of nodes (i,t); $i \in C$, $t \leq T$ in the dynamic network.

Activity variables:

D is the market demand, giving the set of demands (loads) l available within the planning horizon, T.

Γ_l is the set of feasible departure times for satisfying load $l \in D$, otherwise known as the departure time window.

$D_{i,j,t}$ is the set of loads l with origin i and destination j, which are available to move at time t and have not been moved at a time prior to time t at a given solution.

$R_{i,t}$ is the net inflow ($R_{i,t} > 0$) or outflow ($R_{i,t} < 0$) of vehicles at region i at time t. We assume that $R_{i,t} = 0$ for t= 0.

$r_{i,j,t}^{l}$ is the net contribution (revenue minus direct operating costs) derived from moving load l from i to j in period t.

$c_{i,j}$ is the cost of repositioning one vehicle over link (i,j,t); $c_{i,i}$ is the marginal cost of holding vehicles in inventory at region i.

Decision variables:

$x_{l,t} = 1$ if load l is served at time t.

$z_{l,t} = 1$ if load l is never served (within the time window).

$w_{i,j,t}$ is the total flow of vehicles on the link (i,j,t).

$y_{i,j,t}$ is the number of vehicles being repositioned empty along link (i,j,t), i.e. the number of vehicles moving empty from (i,t) to ($j,t+\tau_{ij}$).

If i = j, $y_{i,i,t}$ represents the number of vehicles in inventory at terminal i from time t to time t + 1.

The bi-level formulation of the problem can be stated as:

$$\min_{z} F(z) = \sum_{t=0}^{T} \sum_{i,j \in C} \sum_{l \in D_{i,j,t}} z_{l,t} \quad (3)$$

$$\max_{x,y} f(x,y) = \sum_{t=0}^{T} \sum_{i,j \in C} \left(\sum_{l \in D_{i,j,t}} r_{i,j,t}^{l} x_{l,t} - c_{i,j} y_{i,j,t} \right) \quad (4)$$

subject to:

$$\sum_{t \in \Gamma_l} x_{l,t} + z_l = 1, \forall l \in D \quad (5)$$

$$\sum_{l \in D_{ijt}} x_{l,t} + y_{i,j,t} - w_{i,j,t} = 0, \forall i,j \in C, t \leq T \quad (6)$$

$$\sum_{j \in C} w_{i,j,t} - \sum_{j \in C} w_{j,i,t-\tau_{j,i}} \forall (i,t) \in N \quad (7)$$

$$y_{i,j,t},\ w_{i,j,t} \geq 0 \quad (8)$$

$$x_{l,t} \in \{0,1\} \quad (9)$$

where constraints (5) restrict the maximum number of vehicles to be assigned to each load to one and constraints (6) and (7) enforce flow conservation [11]. This is an integrated approach which states the relationship between the shipper and the carrier and permits a trade-off between objectives in order to find a convergent result.

To illustrate the efficiency of the optimization model, we propose a computational experiment for a cost-benefit analysis between minimizing delays and maximizing profit. The main purpose of the computational experiment is to compare these results for different vehicle fleet size: 10, 15, 18, 25, 30 vehicles. The loads, the values for cost of moving empty and for the profit per loaded mile were randomly generated over a set of 20 regions. Also, the origin and the destination of each load is given, as well as the date of departure of each load. The computational results for a planning horizon of 10 periods (T = 10) and a travel time between region set to one period of time, are presented in table 1 for the different fleet sizes. The results in table 1 indicate that for the bi-level formulation a small diminution in total profit can lead to a substantial reduction in delays.

If the number of vehicles in the network increases, this reduction is even more evident.

5. CONCLUSIONS

In this paper we have proposed a new approach to solve DVA problem. WE have applied the bi-level optimization, considering the integration between carrier and shipper. Based on the results obtained for a network with 20 regions and 10 time periods, one can conclude that this approach is a starting point for testing large, realistic problems.

Table 1: Computational results for the proposed approach

Data set	Fleet size	Model	Total profit	Delays	Difference in profitability	Improvement in delays
1	10	one level	473	35		
		bi-level	459	23	-2.96%	-34.29%
			430	20	-9.10%	-42.86%
			416	19	-12.06%	-45.72%
			410	19	-13.32%	-45.72%
2	15	one level	520	32		
		bi-level	505	19	-2.89%	-41.63%
			490	17	-5.77%	-46.88%
			480	17	-7.70%	-46.88%
			465	15	-10.58%	-53.13%
3	18	one level	567	30		
		bi-level	545	15	-3.89%	-50.00%
			540	15	-4.77%	-50.00%
			525	13	-7.41%	-56.66%
			520	12	-8.29%	-60.00%
4	25	one level	709	26		
		bi-level	690	9	-2.68%	-65.39%
			680	7	-4.10%	-73.08%
			670	6	-5.51%	-76.93%
			665	6	-6.21%	-76.93%
5	30	one level	912	22		
		bi-level	885	4	-2.97%	-81.82%
			860	2	-5.71%	-90.91%
			855	2	-6.25%	-90.91%
			820	0	-10.09%	-100.00%

6. REFERENCES

[1]BIENSTOCK, D., BRAMEL, J. and SIMCHI-LEVI, D., *A probabilistic analysis of tour partitioning heuristics for the capacitated vehicle routing problem with unsplit demands,* Math. Oper. Res. 18, 786–802, 1993.

[2]BRAMEL, J., SIMCHI-LEVI, D., *Probabilistic analyses and practical algorithms for the vehicle routing problem with time windows*, Oper. Res. 44, 505–509, 1996.

[3]DEJAX, P.J., AND CRAINIC, T.G., *A review of empty flows and fleet management models in freight transportation*, Transportation Science, 21, 227-247, 1987.

[4]DEMPE, S., STAROSTINA, T., *On the solution of fuzzy bilevel programming problems*, Optimization Online, 2007

[5]FISCHER, T., GEHRING, H. *Planning Vehicle Transhipment in a Seaport Automobile Terminal using a Multi Agent System,* European Journal of Operational Research, 166, 726-740, 2005.

[6]HEJAZI,S.R., MEMARIANI,A., JAHANSHALOO, G., *Linear Bi-level Programming Solution by Genetic Algorithm*, Computers & Operations Research, Vol. 29, 1913-1925, 2002.

[7]HERREN, H., *The distribution of empty wagons by means of computer: An analytical model for the Swiss Federal Railways (SSB),* Rail International 4(1), 1005-1010 , 1973.

[8]LANGHAM, A.E. AND GRANT,P.W., *A Multilevel K-way Portioning Algorithm for Finite Element Meshes using Competing Ant Colonies,* Proceedings of the Genetic and Evolutionary Computation Conference, (2) 1602-1608, 1999.

[9]MCGAUGHEY, K., GOHRING, W. MCBRAYER, R.N., *Planning Locomotive and Caboose Distribution,* Rail International, 3,151—158, 1973.

[10]POWELL, W. AND H. TOPALOGLU, H., *Fleet management*, *Applications of Stochastic Programming*, MPS-SIAM Series on Optimization, 185-215, 2005.

[11]POWELL, W.B., PAPADAKI, K., *An adaptive dynamic programming algorithm for a stochastic multiproduct batch dispatch problem,* Naval Research Logistics 50 (7), 742–769, 2003.

[12]SIMCHI-LEVI, D., KAMINSKY, P. and SIMCHI-LEVI, E., *Designing and Managing The Supply Chain*, Irwin McGraw-Hill, 2000.

[13]TRASKALIK, T., MICHNIK, J., *Multiple Objective and Goal Programming. Recent Developments*, Physica-Verlag, Heidelberg, 297-309, 2002.

[14]VICENTE, L., CALAMAI, P., *Bilevel and multilevel programming: A bibliography review*, Journal of Global Optimization, 5, 291-306, 1994.

[15]VIS, I. F. A. and de KOSTER, R., *Transhipment of containers at a container terminal: An overview*, European Journal of Operational Research, Vol. 147, 1-16, 2003.

[16]WHITE, W., *Dynamic transhipment networks: An algorithm and its application to the distribution of empty containers*, Networks 2, 211-236, 1972.

ACTIVE STEERING-ELECTRIC THRUSTERS

[1]DORDEA STEFAN, [2]ZBURLEA ELENA

[1,2]*Constanta Maritime University, Romania*

ABSTRACT

The PWM electric drives permit a smooth ajustment of the thrusters operational parameters: voltage amplitude, voltage frequencies, sequences of three generated AC voltages. All these electric parameters can be independly controled for each electro-thruster, in order to increase the ship's maneuvrability.

Keywords: *electro-thruster, E-motor, PWM electric drives*

1. INTRODUCTION

Having this permanent target of Ship's increasing maneuverability, the modern steering systems include thrusters and azimuth propellers (azimuth spinning motion propellers).

Thrusters have become an essential addition for maneuvering today's maritime vessels.

2. TUNNEL THRUSTERS

Tunnel thrusters electrically driven using a *Pulse Width Modulation* (PWM) technique solve the ship's maneuvering problem within inside waters.

Fore and stern mounted thrusters that have been welded in transverse direction of the hull are used within inside waters for harbor maneuvers (fig.1).

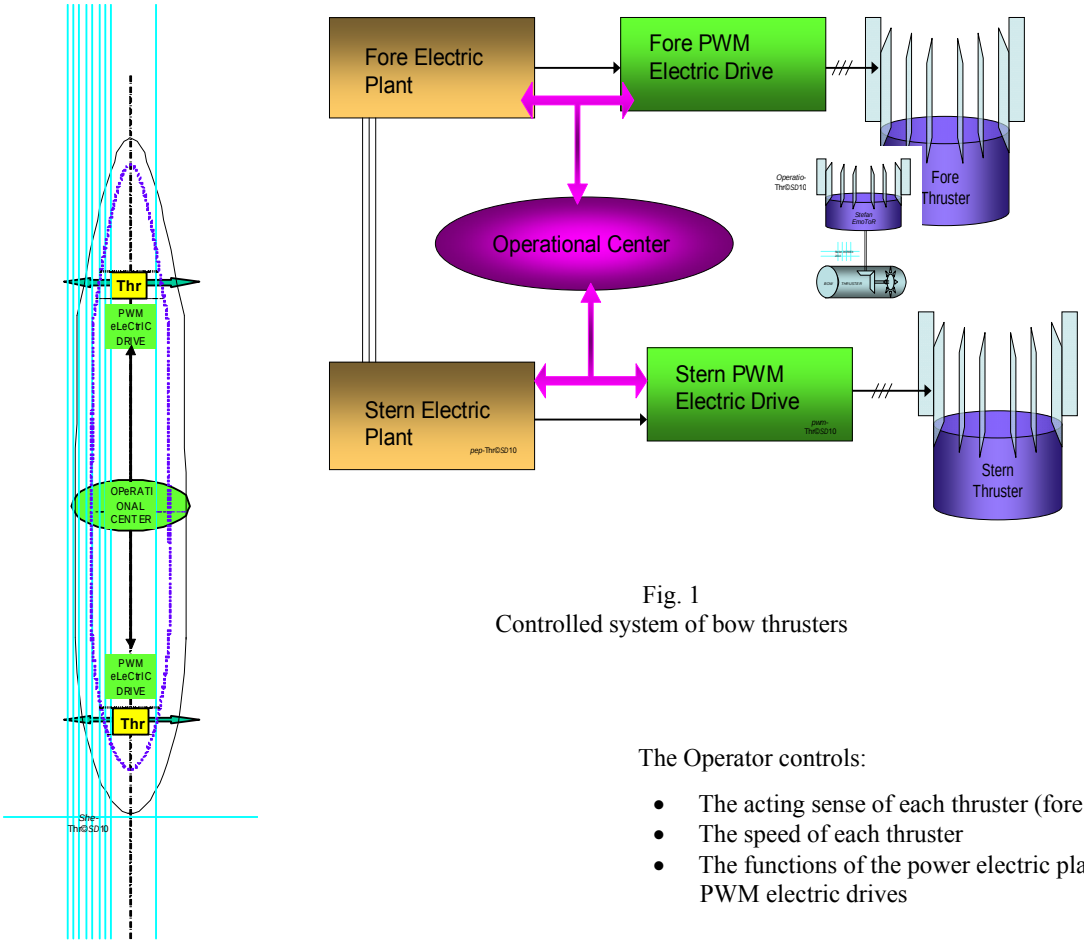

Fig. 1
Controlled system of bow thrusters

The Operator controls:

- The acting sense of each thruster (fore and stern)
- The speed of each thruster
- The functions of the power electric plants and the PWM electric drives

The electric motor (*E-motor*) driving the thruster is mechanically linked by means of a speed reducing gear to the bow propeller. The goal is to obtain a higher torque of the propeller at a lower speed of the E-motor.

Eluding the losses, the mechanical transfer of power is given by the following relations:

$$P_{EM} \cong P_{PROP} \quad ()$$

$$M_{EM} \cdot \omega_{EM} \cong M_{PROP} \cdot \omega_{PROP} \quad ()$$

where:

P_{EM} is the electromagnetic power,
P_{PROP} is the propeller power,
M_{EM} is the electromagnetic torque,
M_{PROP} is the propeller torque
ω_{EM} is the angular speed of the *E-motor*,
ω_{PROP} is the angular speed of Propeller

Since the diameter D_1 of input toothed wheel of the reducing gear is smaller than the output one (D_2), is obviously that

$$Z_1 < Z_2 \text{ because } \frac{D_1}{D_2} \cong \frac{Z_1}{Z_2}$$

where:

Z_1 is the teethes number of primary wheel
Z_2 is the teethes number of secondary wheel

and because

$$\frac{\omega_{EM}}{\omega_{PROP}} = \frac{M_{PROP}}{M_{EM}} \quad ()$$

results that

$$\omega_{PROP} < \omega_{EM} \text{ or, otherwise saying that } M_{PROP} > M_{EM}$$

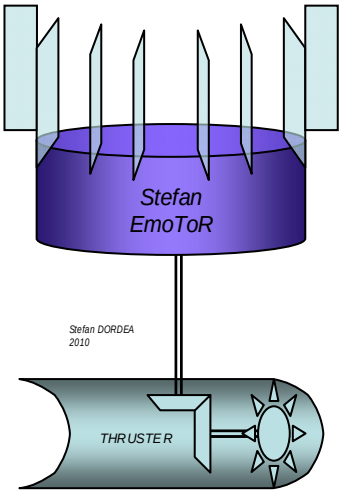

Fig.2
Assembly of *E-motor*. Transmission and Propeller

The vertical position of the motor (working outside of tunnel on a *fixed pod*) permits the interventions on the motor, as shown in fig.2.

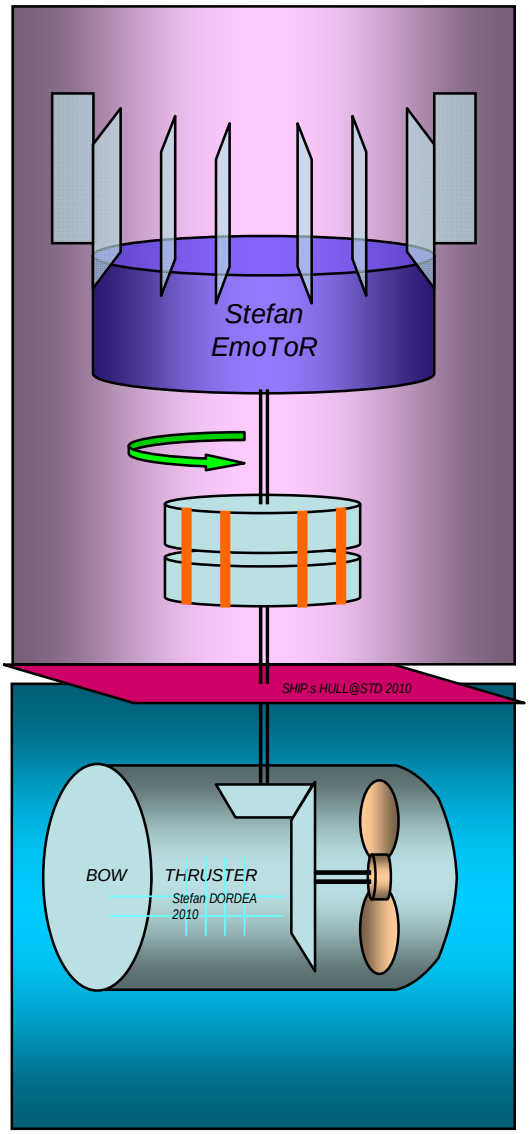

Fig.3
Demandable assembly
E-motor. Transmission and Propeller

Since the electro-motor is mounted above the ship's hull it is accessible and therefore dismountable and removable in order to be repaired.

The advantage of such architecture consists in facile measurements stator windings and the electric resistance of the E-motor in a dry environment .

The underwater overhauls and eventually repairs on reducing gear and propeller are to be made by specialized sea workers or by putting the ship into a dry shipyard.

3. THE POWER ELECTRIC PLANT AND THE PWM ELECTRIC DRIVE (FIG.3)

3.1. The power electric plant (PEP)

The mechanical energy of two Diesel engines is converted into electric energy by means of the corresponding three-phased synchronous generators coupled to a distribution switchboard.

There are two reasons for equipping the PEP with two Diesel – Generator groups:

- the maneuver safety
- the capability of supplying other minor consumers.

The Operator controls:

- The start and stop of each Diesel generator
- The induction fields of both generators
- The PWM voltages
- The PWM frequencies

The coupling and parallel operating of the generators is made automatically when a higher electric power is demanded by the system.

The main consumer of the power electric plant is obviously the thruster E-motor controlled by the electric adjustable drive.

The sum of the installed power of the two Diesel – Generators must be higher than the peak power asked by the thruster; it refers to the maneuver safety.

$$\sum P_{GEN} > \max P_{THRUSTER}$$

A single Diesel generator must cover the power consumption of the thruster.

$$P_{GEN} > P_{THRUSTER}$$

3.2. The PWM electric drive

Most of thrusters include asynchronous E-motors driven in Pulse Width Modulation (PWM) technique .

The supply of a thruster E-motor is made by means of a controlled PWM electric drive (fig.7).

The three-phased voltage U_{PEP} coming from the distribution of the power electric plant is first rectified within the **POWER RECTIFIER BRIDGE** (fig.4) and than the DC voltage U_{DC} is used to supply the **POWER STATIC SWITCHES BRIDGE** of the drive.

The minor **RECTIFIER** ensures the low voltage (U_{rect}) needed to be stabilized before supplying the ***PWM* CONTROL**.

This control unit delivers adequate voltages to the corresponding gate circuits of the PWM power switches block. ***PWM* CONTROL** ensures also the galvanic separation between its electronics and the circuitry of **POWER STATIC SWITCHES BRIDGE**.

The variable speed drive of induction motors requires generating three voltage sine waves and control of their amplitude, phase and frequency.

The first step is to digitize the three phase system in order to create all the necessary data to be stored into the ROM of the ST9 microcontroller.

4. THE SYNTHETIC VOLTAGES DELIVERED BY THE PWM ELECTRIC DRIVE

The tree-phased set of voltages delivered by the PWM electric drive has the wave shapes shown in fig.5.

The fundamental period of motor voltage is divided into 24 segments (each segment equals 15° of arc). This gives a good sine wave accuracy in many applications. During each "segment" the voltage is a percentage of the DC line voltage, given by duty cycle.

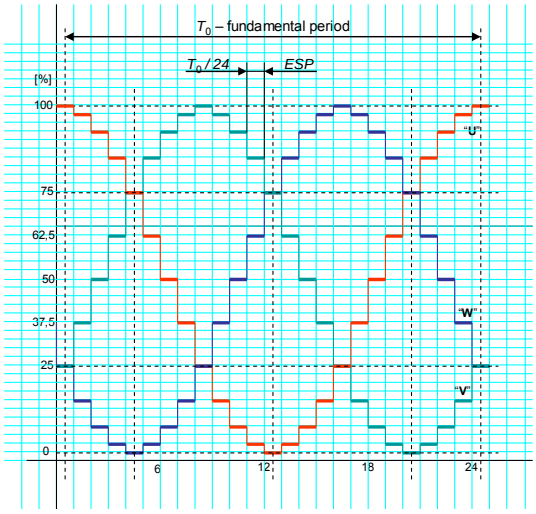

Fig.4
The wave shape of the voltages delivered by the PWM electric drive

The elementary switching period is subdivided into elementary time slots during which all 6 switches of the inverter are in a given state ("on" or "off"). The state of the switches can be represented with 6 bits stored in a byte: 1 = "on", 0 = "off".

Hence, a switching period can be represented with a pattern, i.e. a sequence of bytes corresponding to the different time slots (42 time slots in our example).

Each segment of the 3-phase sine waves can be represented with a defined average voltage during this segment on each of the 3 phases, and therefore with a given pattern. There must be as many different patterns as period segments (24 segments in our example).

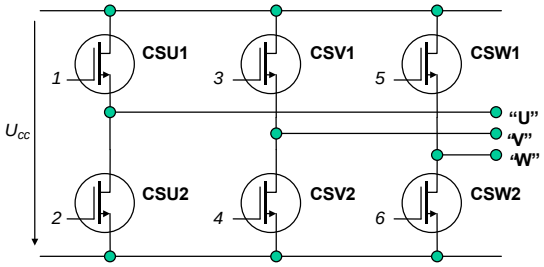

Fig.5
The 6 Connecting Switch of the Power Bridge

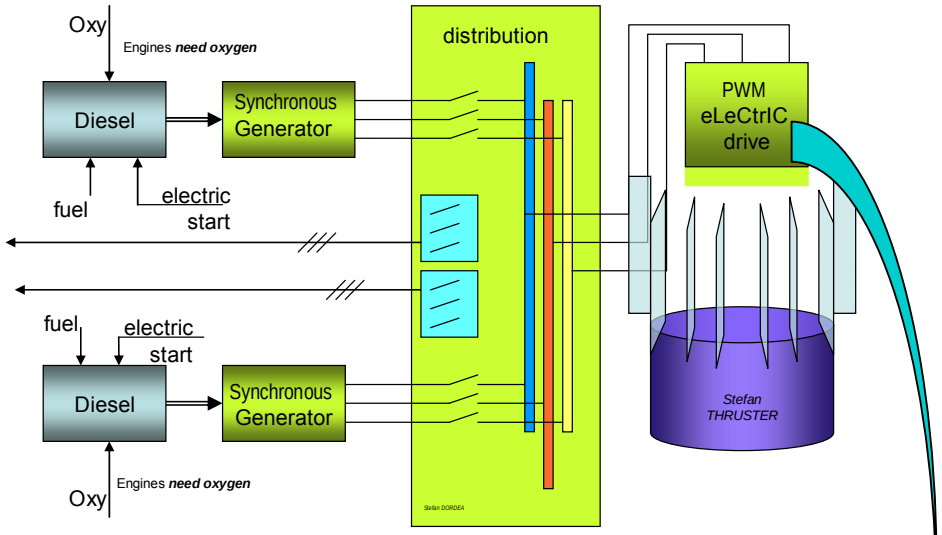

Fig.6
One of the two Power Electric Plants
Supplying the Thrusters by means of PWM electric drives

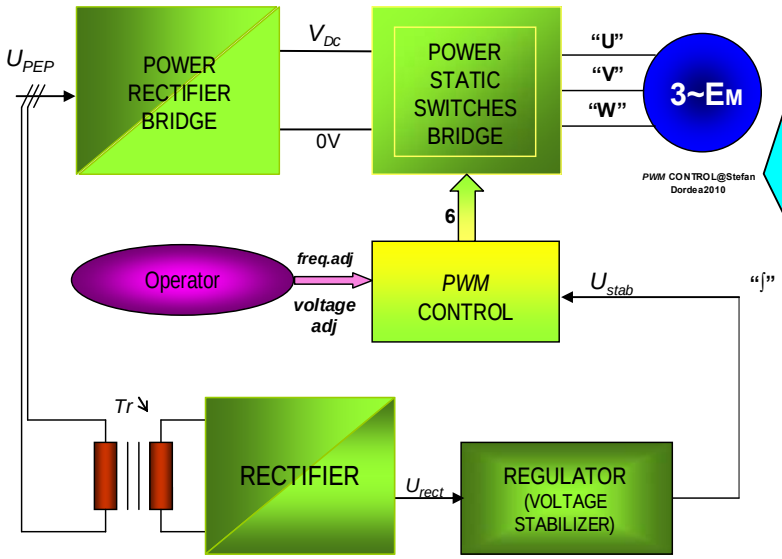

Fig.7a
The PWM electric drive

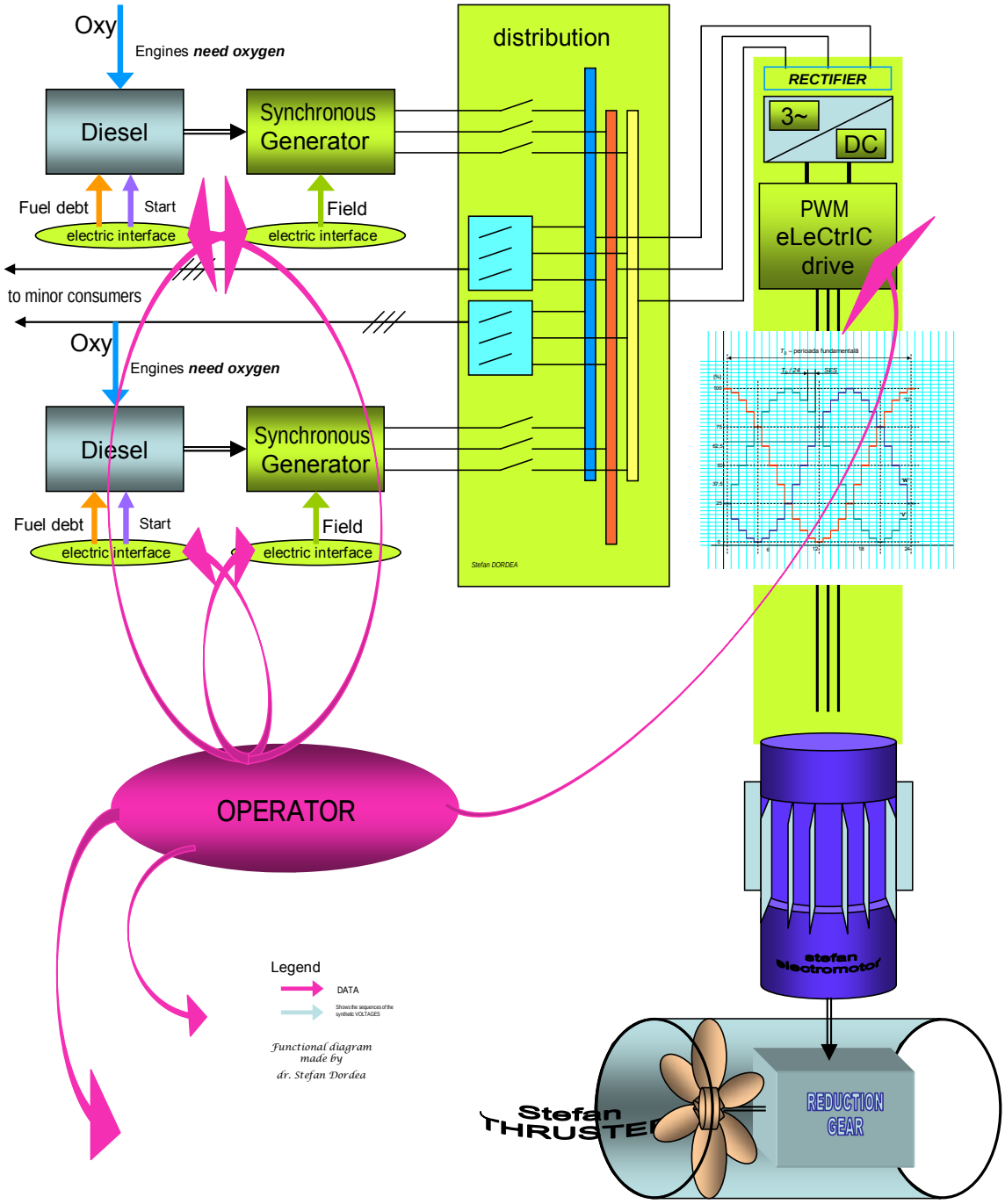

Fig.7b
The electric chain containing the fore section of thrusters driving

5. MANEUVERING

5.1. Coming along side

This maneuver suppose to get closer the ship by the shore until she touches the key or to release the shore (fig.10). Along side means in this case a parallel translating motion to or of the key.

In order to do this both propellers of the two thrusters (fore and stern) must have the same sense of rotating motion. It can be done by activating the two corresponding electric drives with the same sequence of the phases (fig.8 and fig.9).

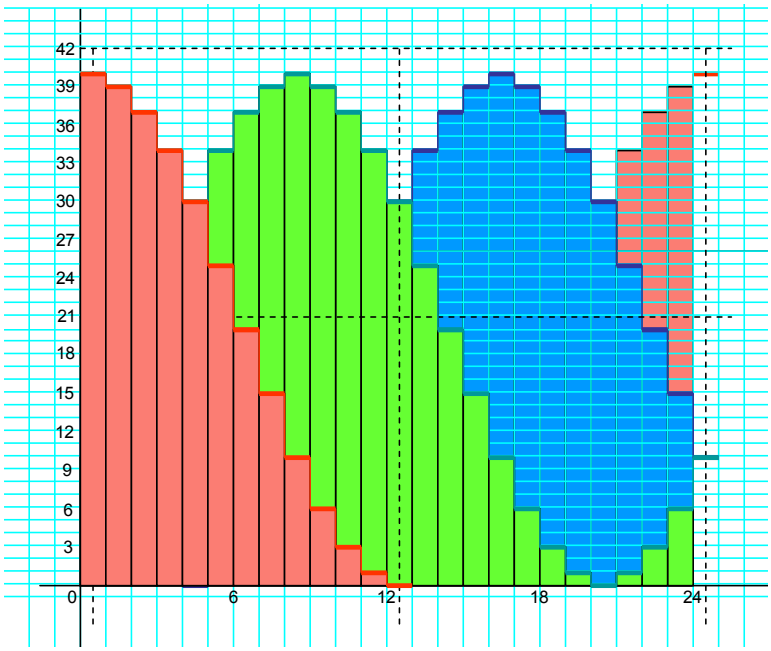

Fig.8
Sequence of voltages provided by the **fore** PWM electric drive

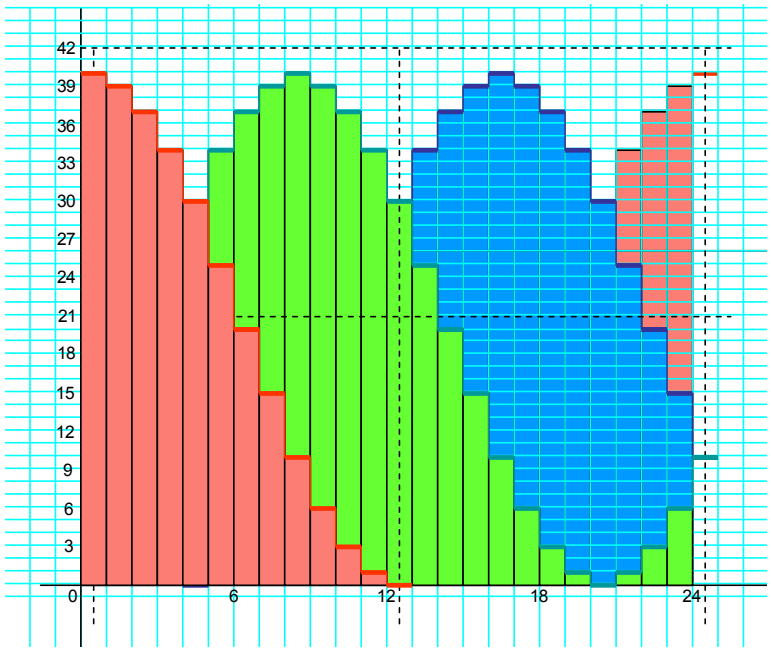

Fig.9
Sequence of voltages provided by the **stern** PWM electric drive

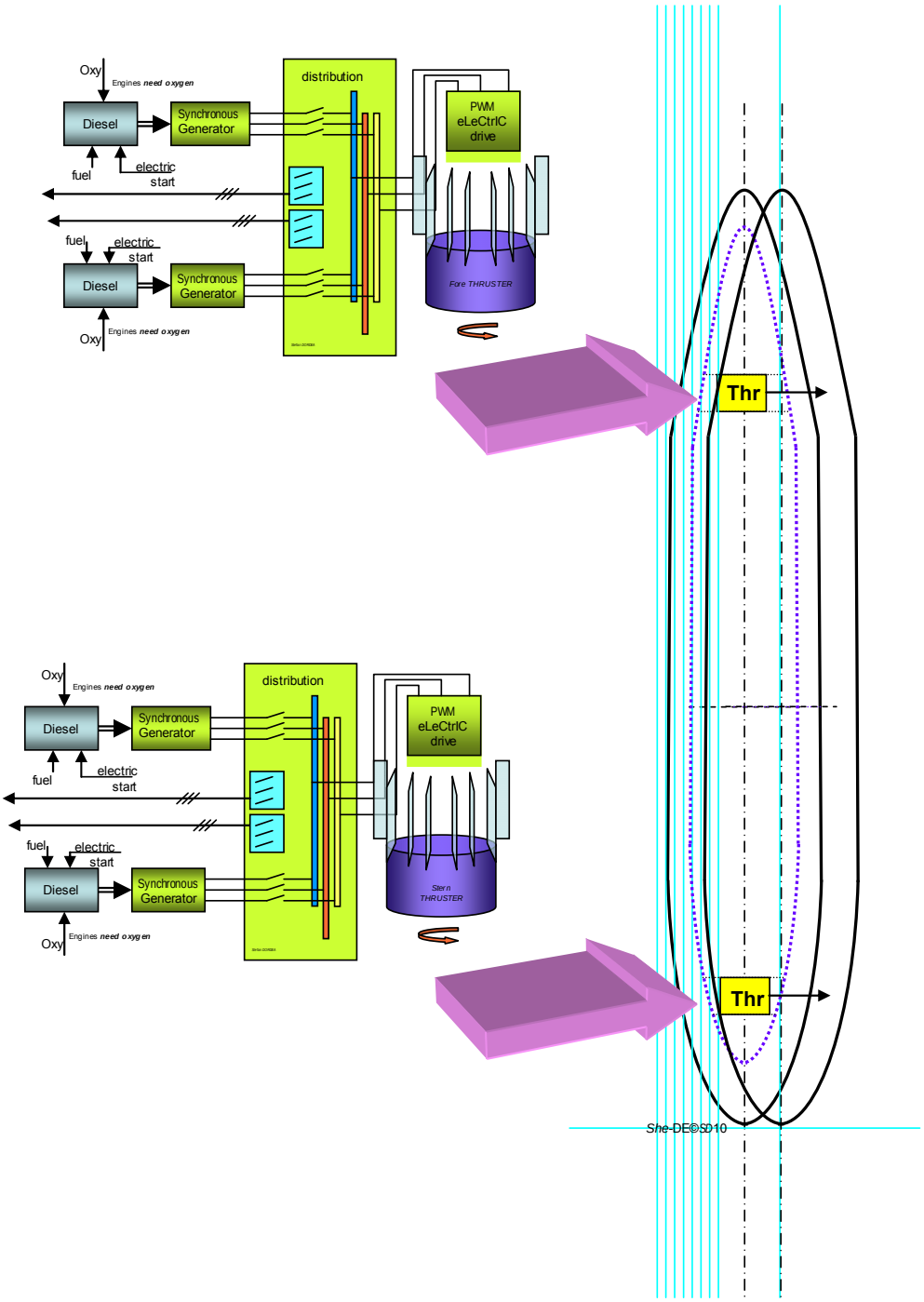

Fig.10

Electric motor of the fore thruster has the rotating sense as fig.8 is showing
Electric motor of the stern thruster has the same rotating sense

So, both thrusters are driven in the same sense in order to come alongside or to depart.

5.2. Relocation within harbor area

This maneuver suppose to get a ship rotating motion around she's vertical axis within an aquatorium area.

In order to do so the rotating sense of one electric motor (fore or stern) has to be reversed.
It can be done by changing the phase sequences of the fore electric drive (e.g. in fig.11, fig.12 and fig.13).

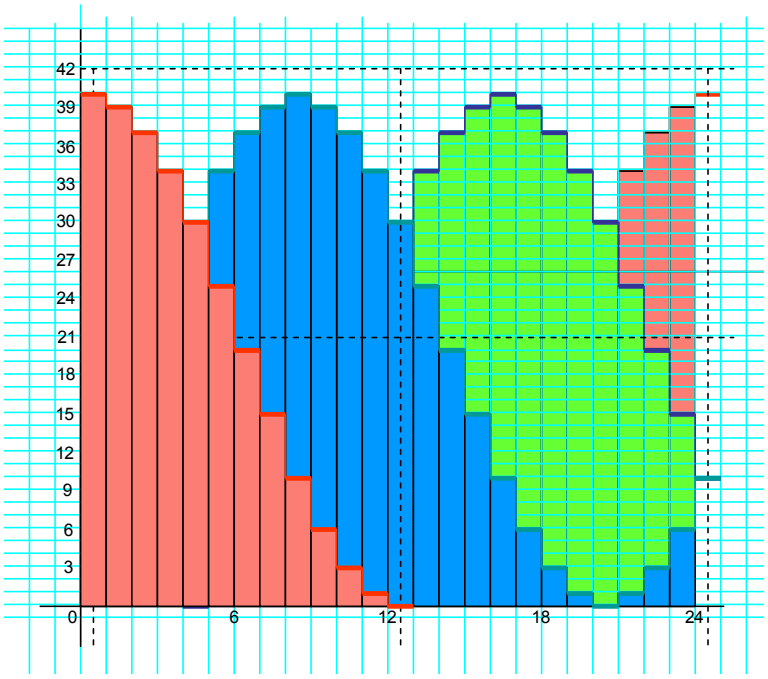

Fig.11
Sequence of voltages provided by the **fore** PWM electric drive

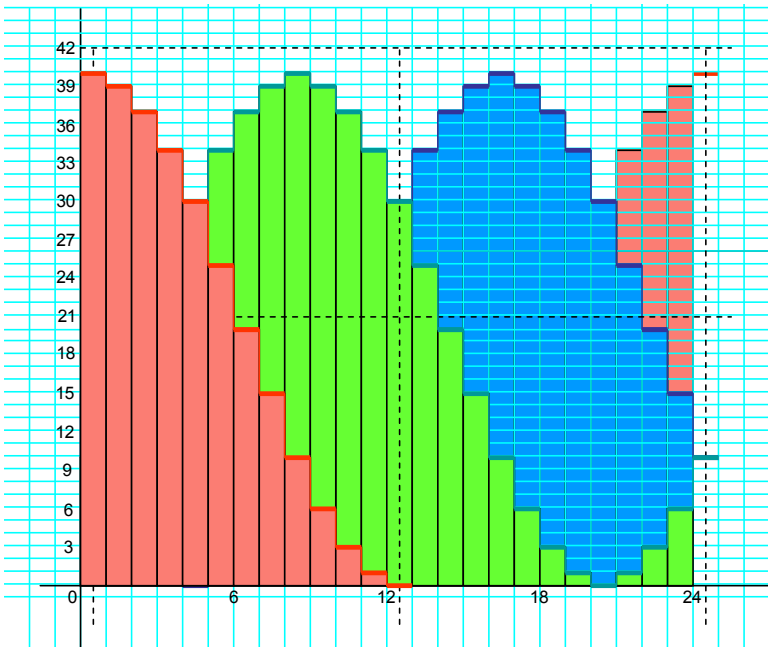

Fig.12
The Sequence of voltages provided by the **stern** PWM electric drive

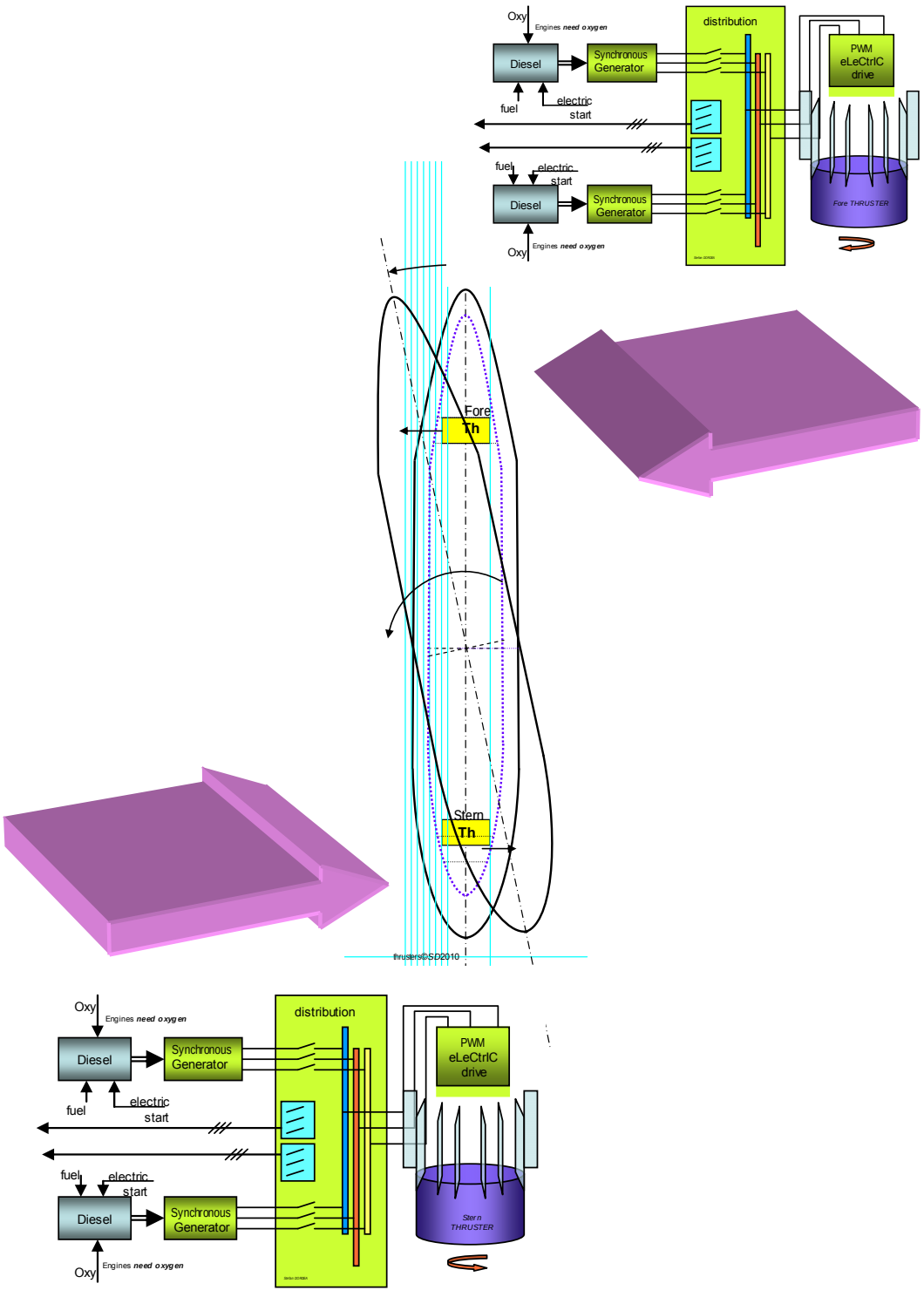

Fig.13

Electric motor of the fore thruster has a reversed rotating sense as fig.11 is showing
Electric motor of the stern thruster has the same rotating sense as the one of fig.12

Fore electric plant is supplying the corresponding thruster as the Ship has to spin to the Port as shown in fig.13.

6. CONCLUSIONS

The PWM electric drives permit a smooth ajustment of the thrusters operational parameters:

- Voltage amplitude
- Voltage frequencies
- Sequences of three generated AC voltages

All these electric parameters can be independly controled for each electro-thruster, in order to increase the ship's maneuvrability.

7. REFERENCES

[1] DORDEA, ŞT., *Proportional Steering System*, Analele Universităţii Maritime Constanţa, ISSN 1582-3601, pp. 165-173, 9 pg, 2010 (cotat B+ în sistemul CNCSIS)

[2] DORDEA, ŞT., ZBURLEA, E., *Anti-Hunt Control System*, Analele Universităţii Maritime Constanţa, ISSN 1582-3601, pp. 173-179, 8 pg, 2010 (cotat B+ în sistemul CNCSIS)

[3] DORDEA, ŞT., CIUCUR, V., *3-Phase Asynchronous Motors Pulse Width Modulation (PWN) Drive*, Analele Universităţii Maritime Constanţa, ISSN 1582-3601, pp. 301-309, 8 pg, 2009 (cotat B+ în sistemul CNCSIS)

[4] DORDEA, ŞT., ZBURLEA, E., BADEA, M., *Optoelectronic Hydraulic Device*, Analele Universităţii Maritime Constanţa, ISSN 1582-3601, pp. 309-317, 8 pg, 2009 (cotat B+ în sistemul CNCSIS)

[5] DORDEA, ŞT., ZBURLEA, E., BADEA, M., *Naval Steering Control By Means Of Optic Tracks*, Analele Universităţii Maritime Constanţa, ISSN 1582-3601, pp. 317-323, 6 pg, 2009 (cotat B+ în sistemul CNCSIS)

[6] DORDEA, ŞT., *Monitoring the steering failures*, Ovidius University Annals of Mechanical, Industrial and Maritime Engineering, Volume X, Tom I, 2008, cod CNCSIS 603, Editura Ovidius University Press, ISSN 1223-7221 (cotat B+ în sistemul CNCSIS)

[7] DORDEA, ŞT., *Double Track Steering Failure Monitoring System*, Annals of the „Dunarea de Jos" University of Galati, Fascicle III – Electrotechnics, Electronics, Automatic Control, Informatics, cod CNCSIS 482 ISSN 1221-454X, 2007 (cotat B+ în sistemul CNCSIS)

[8] DORDEA, ŞT., *A Ship's Rate of Turn Steeering Control*, A XXXII-a Sesiune de comunicări ştiinţifice cu participare internaţională „TEHNOLOGII MODERNE ÎN SECOLUL XXI, Academia Tehnică Militară, Bucureşti, 1 – 2 noiembrie 2007

[9] DORDEA, ŞT., *Aparate electrice de navigatie*, autor unic, Ed. Muntenia, ISBN (10) 973-692-154-9, ISBN (13) 978-973-692-154-4, 105 pag, Constanta, 2006

[10] DORDEA, ŞT., *Acţionări electrice cu undă sintetică*, autor unic, Ed. Muntenia, ISBN (10) 973-692-153-0, ISBN (13) 978-973-692-153-7, 155 pag, Constanta, 2006

[11] DORDEA, ŞT., *Maritime automatic steering system with off-course monitor*, Analele Universităţii Maritime Constanţa, ISSN 1582-3601, pp. 227-230, 4 pg, 2006

[12] DORDEA, ŞT*., Versatile automatic steering system with off-course monitor*, Analele Universităţii Maritime Constanţa, ISSN 1582-3601, pp. 231-234, 4 pg, 2006

[13] DORDEA, ŞT., *Digitaly activated electro hydraulic distributor*, A XXX-a Sesiune de comunicări ştiinţifice cu participare internaţională „Tehnologii moderne în secolul XXI", Academia Tehnică Militară, Bucureşti, 3-4 noiembrie 2005, pp.13.34-13.37, 4pg, ISBN 973-640-074-3

[14] DORDEA, ŞT., *Repartiţia secvenţială a sarcinii în acţionarea electronică a motoarelor asincrone trifazate*, A IX-a Sesiune de comunicări ştiinţifice cu participare internaţională „Ştiinţa şi învăţământul, fundamente ale secolului al XXI-lea", Ştiinţe tehnice, vol.I, ISBN 973 – 7809 – 04 – 1, ISBN 973 – 7809 – 03 – 3, Academia Forţelor Terestre „Nicolae Bălcescu", pp. 49 – 53, 5 pg, Sibiu, 2004

[15] DORDEA, ŞT., *Ship's rate-of-turn steering control*, Analele Universităţii Maritime Constanţa, ISSN 1582-3601, pp. 197-202, 6 pg, 2004

[16] DORDEA, ŞT., *Transferul de energie în sistemele electrohidraulice de guvernare navale*, Teză de doctorat, Universitatea „Dunărea de Jos" din Galaţi, 2002.

ELECTRIC DRIVES FOR AZIMUTH PROPULSORS

[1]DORDEA STEFAN, [2]ZBURLEA ELENA

[1,2]Constanta Maritime University, Romania

ABSTRACT

Azimuth thrusters allow ships to be more maneuverable and enable them to travel backward nearly as efficiently as they can travel forward.Now days cruisers are equipped with twin azimuthal systems. The operator controls the principal regime parameters (frequencies, magnitudes and sequences of voltages) and also the angular position of the propulsor.

Keywords: *Azimuth thrusters, steerable pod, Propulsor, Pulse Width Modulation (PWM), pod's propeller*

1. PREAMBLE

Azimuth thrusters[1]

Azimuth thrusters are marine propulsion and steering systems consisting of electrically driven propellers mounted on a *steerable pod* electrically driven also. Any of these systems contains two *E-motors* (fig.1):

- a main EM driving the propeller (by means of a reduction gear)
- a steering EM driving the pod.

Each of them is controllably supplied by its own *Pulse Width Modulation* electric drive giving to the operator two possibilities:

- to adjust the propeller speed
- to adjust the angular position of the pod

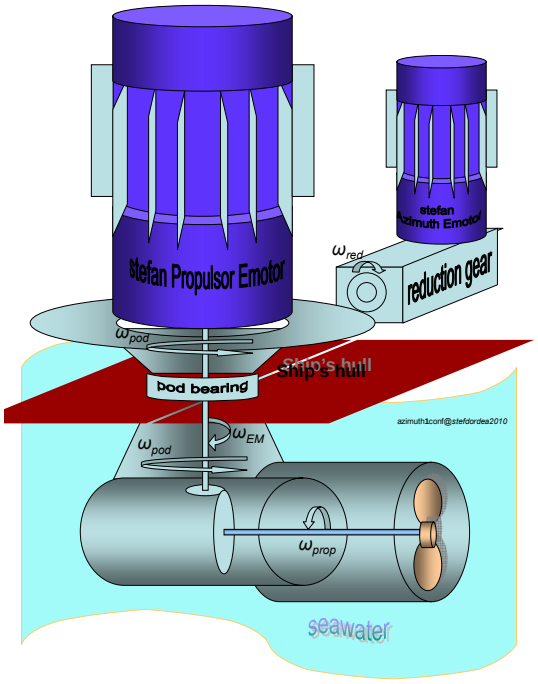

Fig.1
Azimuth thruster

2. FIRST GENERATION

First generation of propulsion and steering systems has located the PROPULSOR E-motor inside the ship's hull and rotation is transferred to the propeller through shafts and gearboxes (fig.2).

The azimuthal motion of the pod is provided through a reduction gear by the E-motor in charge.

Both E-motors are powered using a *Pulse Width Modulation* (PWM) technique by means of two electric drives that are controlled by the operational center and fed by the Power Electric Plant (PEP).

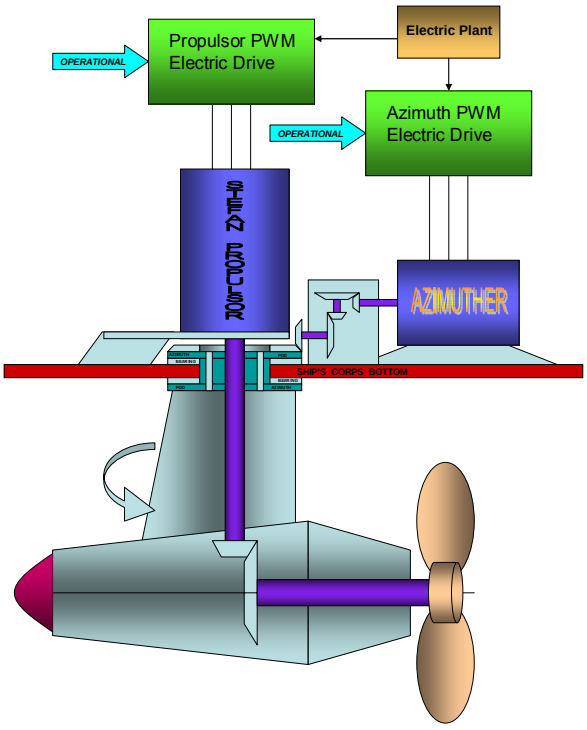

Fig.2
Both E-motors are located inside the ship's hull

[1] 360 degrees rotatable thrusters that are used for main propulsion

The *pod's propeller* usually faces forward because in this puller (or tractor) configuration the propeller is more efficient. Because it can rotate around its mount axis, the pod can apply its thrust in any direction.

Azimuth thrusters allow ships to be more maneuverable and enable them to travel backward nearly as efficiently as they can travel forward.

Now days cruisers are equipped with twin azimuthal systems (fig.3). The operator controls the principal regime parameters (frequencies, magnitudes and sequences of voltages) and also the angular position of the propulsor.

Figure 4 shows a stern part of ship equipped with two azimuthal units of first generation.

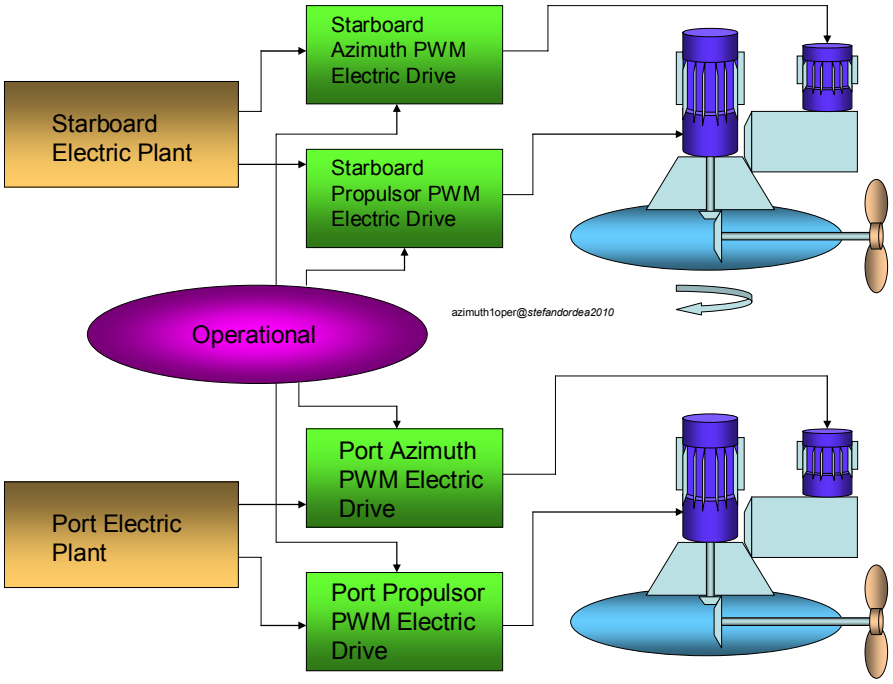

Fig.3
Twin azimuthal system of first generation

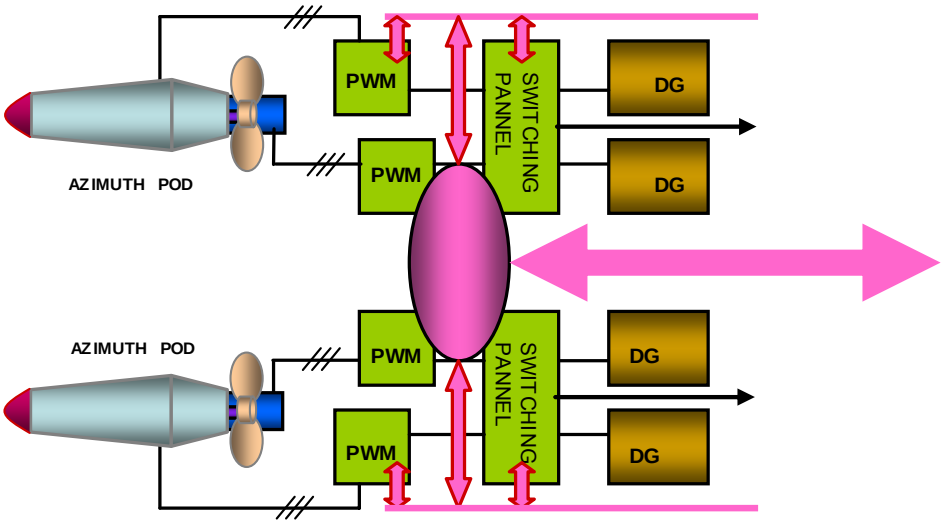

Fig.4
Stern part of a ship equipped with two azimuthal units of first generation

3. THE SECOND GENERATION

The second generation place the propulsion electric motor as installed inside the pod itself, and the propeller is connected directly to the motor shaft (fig.5).

By not using a traditional propeller shaft the propeller can be located farther below the stern of the ship in a clear flow of water providing greater hydrodynamic and mechanical efficiency.

Electric power for the propulsion E-motor is conducted through *slip rings* that allow the *PROPULSOR* to rotate azimuthally through 360 degrees.

Because fixed pitch propellers are used, power for the implied EM is fed through a variable frequency *PWM* electric drive that allows speed control of the propulsion motor.

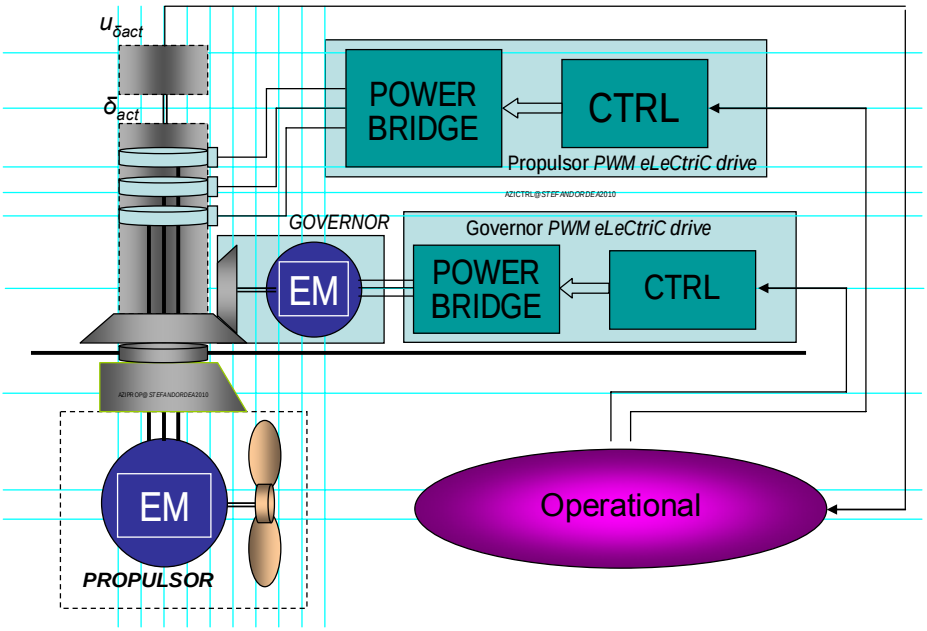

Fig.5
Azimuthal system of second generation

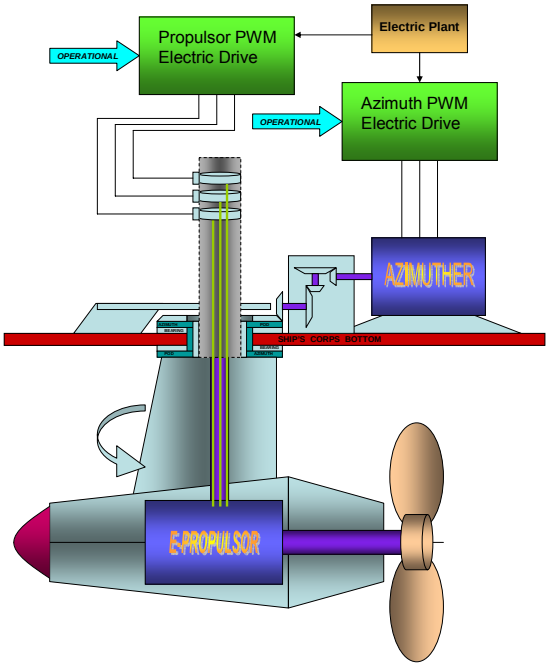

Fig. 6

The azimuthal unit is fixed outside the ship in a pod, or casing, which combines the functions of a propulsion motor, main propeller, rudder and stern thruster.

These traditionally separately installed units are no longer needed, vacating space on board for other purposes.

4. STATOR FREQUENCY CONTROL

The E-motor frequency is controlled via duration of the fundamental period T_0 (fig.8).

The shortest duration of the period (the highest frequency) is reached when each segment of this period corresponds to only one reading of the corresponding pattern.

In our example (fig.8) the pattern reading duration is 200μs, having 24 segments (T_0 = 4800μs, f_o = 208Hz).

When each segment corresponds with two readings of pattern, the fundamental period is twice as long. Thus the frequency (motor speed) can be controlled step by step whether the pattern is read once or several times. Consequently when starting from the highest frequency, it is possible to have discrete submultiples of frequency.

$$f = f_o/N$$

where N = number of times of patterns being read.

The speed resolution is low for high motor speed, but high for low motor speed. So, to perform the speed control by software, it is sufficient to give the number of times the pattern is to be read.

For example (fig.9), when repeating 2 times the same pattern the following results are obtained:

5μs = time unit

40 = number of time units per pattern

2 = number of patterns (or switching cycle) reading per segment

24 = number of segments per fundamental period

This gives:

- a period of 9600μs
- a frequency of 104Hz

When repeating 4 times the same pattern (fig.10) the results are T= 200x4x24=19200μs, $f = f_o/2$ =52Hz.

Another way to adjust the motor speed by software is to change the DMA timer period.

That is equivalent to modifying the "time unit" duration. The reduction of time unit duration is limited by the highest consumption of CPU time to be accepted and the shortest permissible dead time is according to power switches used.

By combining these two methods, pattern repetition and timer variation, it is possible to perform quasi-continuous variation of motor speed.

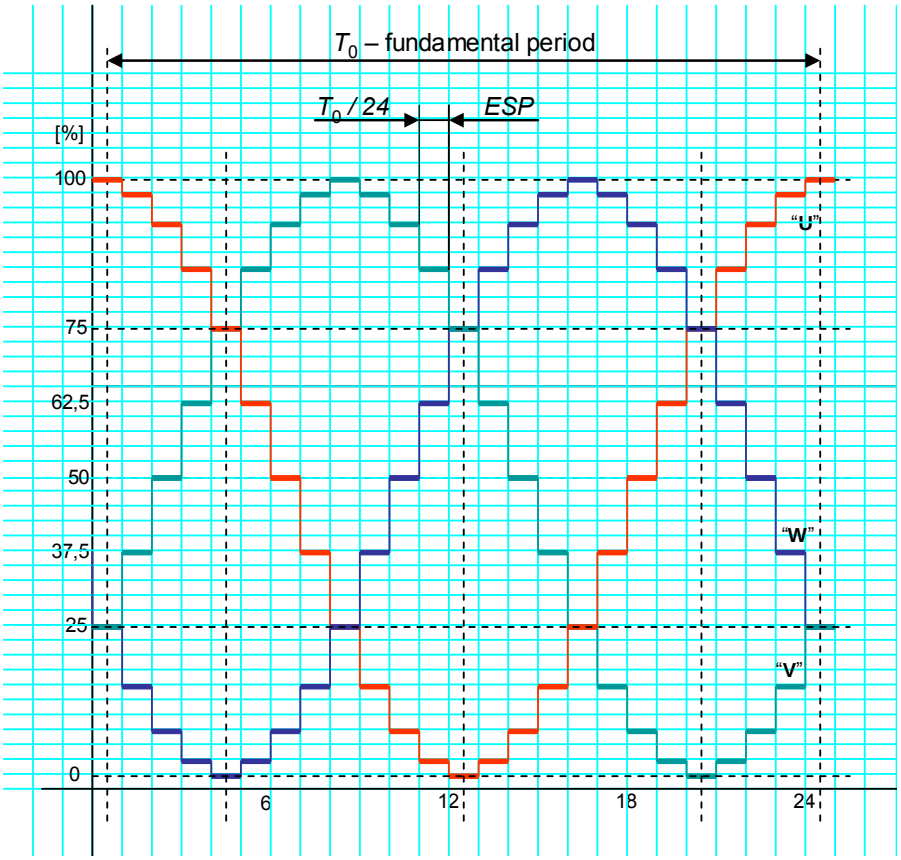

Fig.7
The fundamental period T_0

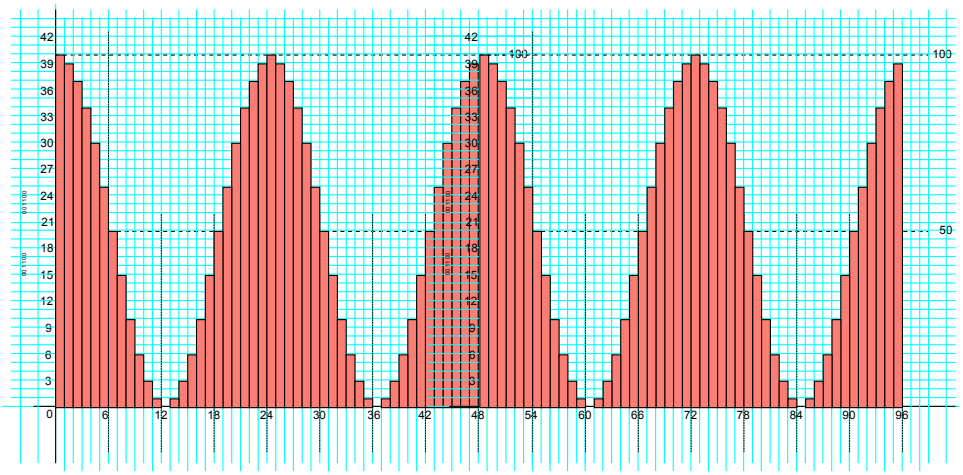

Fig.8
Fundamental Frequency
T_o = 210x24=4800μs f_o=208Hz

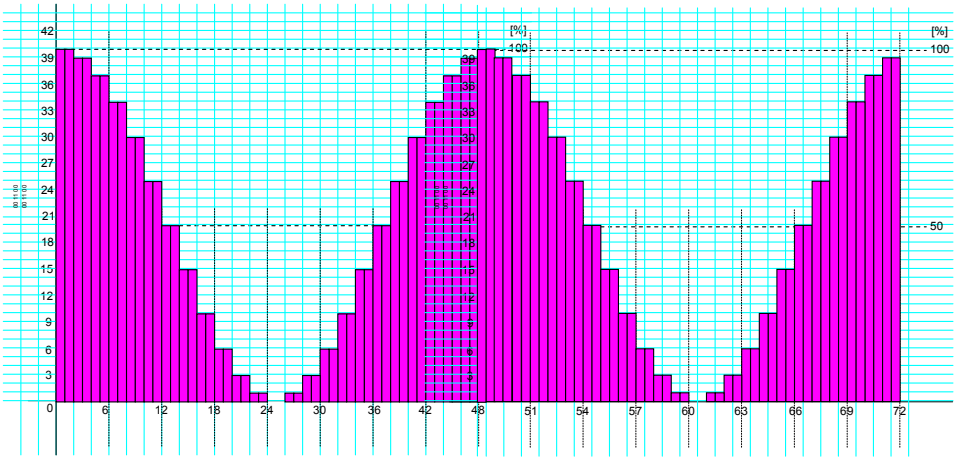

Fig.9
T =200x2x24=9600μs $f = f_o/2$ =104Hz

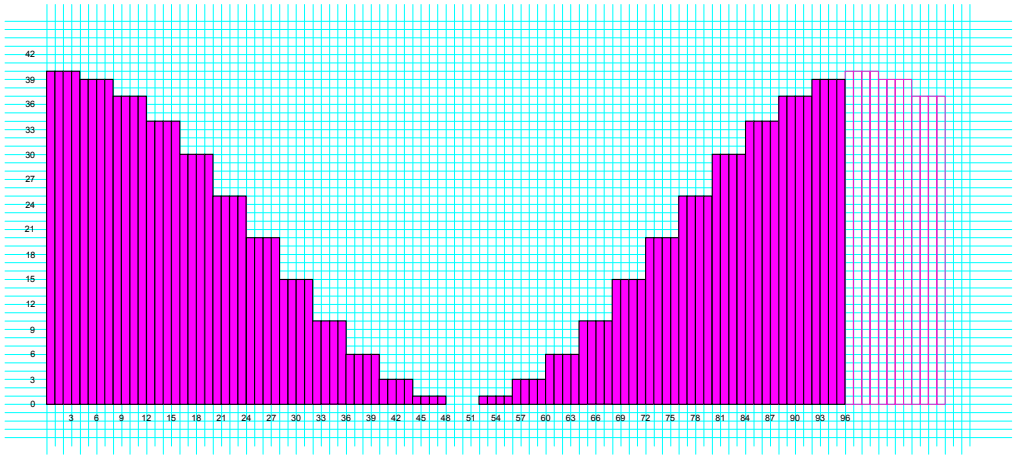

Fig.10
T= 200x4x24=19200μs $f = f_o/2$ =52Hz

5. E-MOTOR VOLTAGE CONTROL

One table of duty cycle defines the 24 stored patterns (set of patterns) containing information to one AC motor voltage. As an example, the peak value of phase voltage generated by the table given on Figure 13 is equal to 60% of VDC line. It is necessary to create a set of patterns for each of the needed motor voltage.

The motor voltage can be controlled independently of the frequency. This voltage depends on the set of pattern which the DMA is reading. By storing within ROM and reading different set of patterns, the voltage across the motor can be changed and shaped. In this example, a set of patterns includes 24 patterns of 40 bytes each = 960 bytes.

Figure 10 shows d1 duty cycle of the T1 switch for various values of motor voltage.

On the right side the chart gives the corresponding values of d3 and d5. Each line of these charts defines a pattern. These values respect the phase balance and avoid current in neutral line. The useful RMS voltage across motor phases is given by:

$$V_{RMS} = \frac{1}{2} k \sqrt{\frac{3}{2}} \cdot V_{DCline}$$

The k factor corresponds to modulation depth of the duty cycle as shown on examples a, b, c.

a: k = 1.0 when duty cycle varies from 0% to 100% (fig.11);

b: k = 0.8 when duty cycle varies from 10% to 90% (fig.12);

c: k = 0.6 when duty cycle varies from 20% to 80% (fig.13).

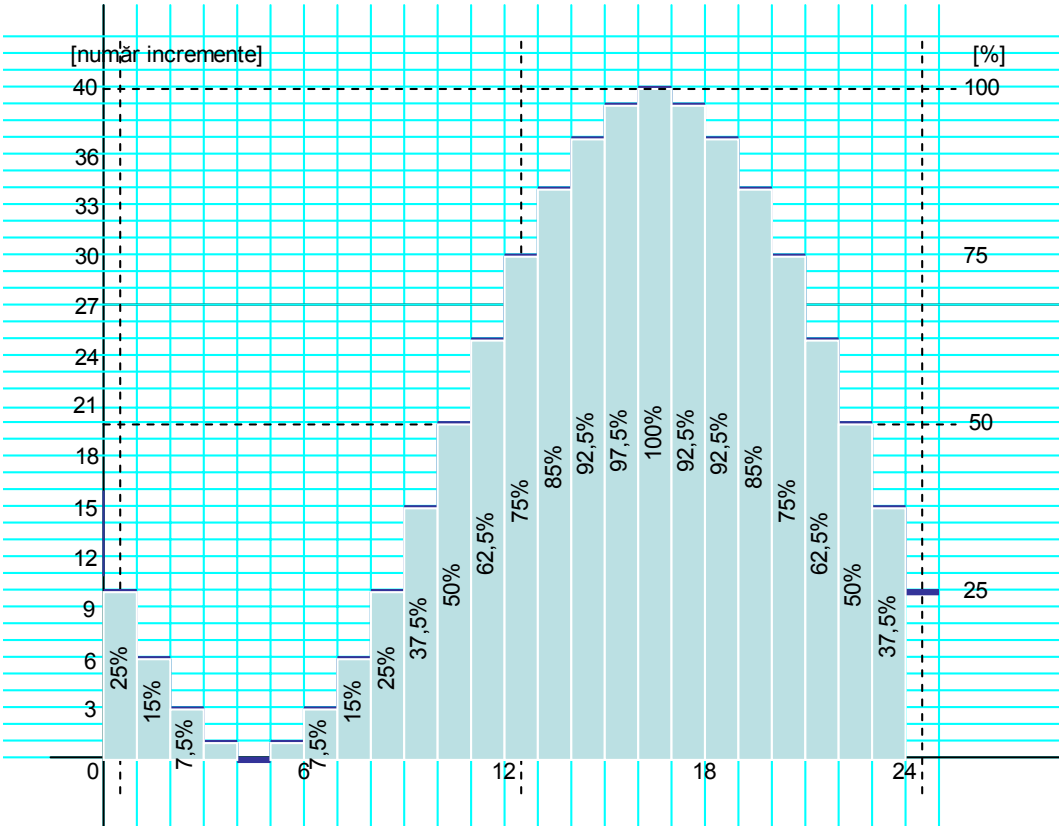

Fig.11
k = 1.0 when duty cycle varies from 0% to 100%

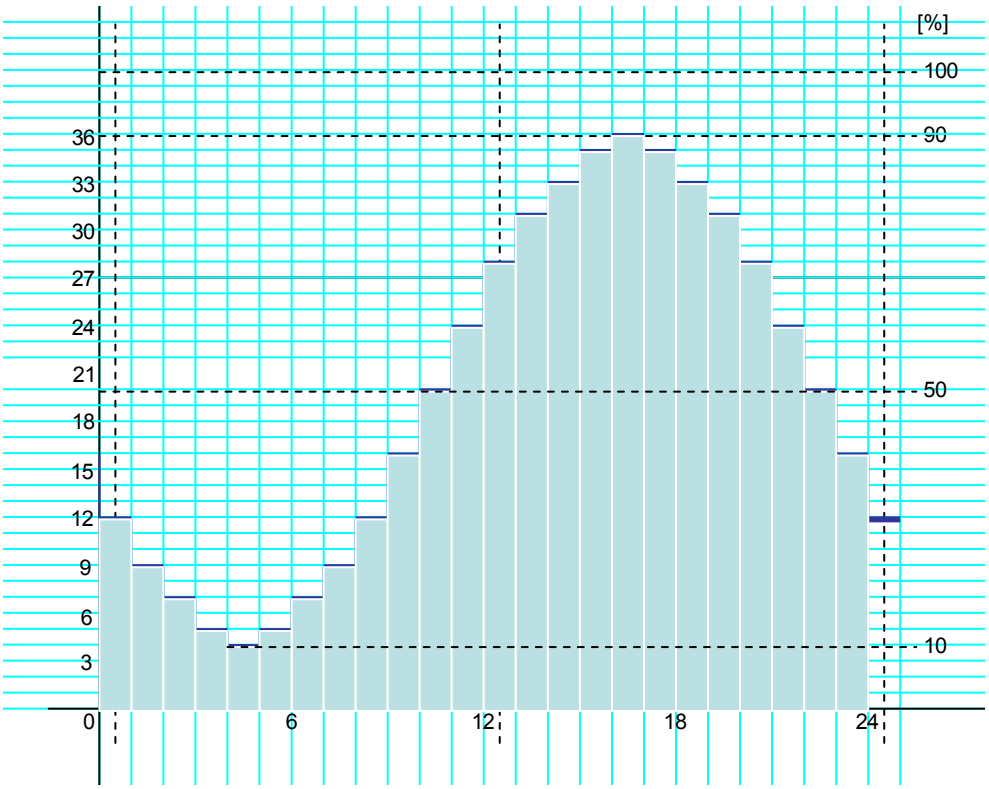

Fig.12
k = 0.8 when duty cycle varies from 10% to 90%

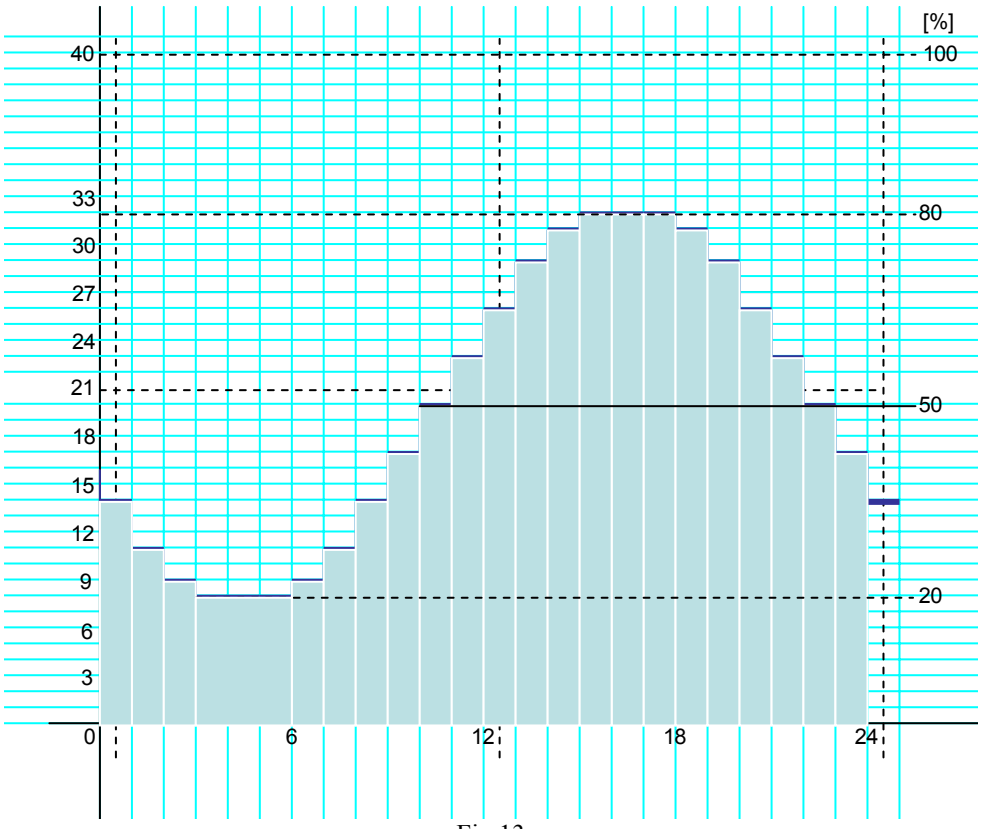

Fig.13
k = 0.6 when duty cycle varies from 20% to 80%

6. CONCLUSIONS

In this system, the electrical propeller motors, which are the largest consumers of electricity, are controlled by drives that provide stepless power and control the speed of the propellers. The electric propulsion system is therefore able to run the diesel engines at or close to their optimum efficiency point regardless of the vessel's speed. Using electric cables rather than a mechanical transmission system also reduces vibration on board.

Azipod propulsion is based on electric propulsion concept where generator sets can be freely located to the vessel. Further many systems inside the ship hull (propulsion motors, long shaftlines, stern thrusters and rudders) are not needed. This gives a lot of freedom to the ship design and construction. Space can be saved inside the vessel which can be used for extra payload or even may make it possible to build a smaller ship. From shipbuilding poit of view a lot of installation hours can be saved due to simpler construction.

Due to azimuthing thrusters the vessels have an excellent maneuverability characteristics. This improves the vessels safety but as well minimizes the harbour maneuvering time and can in some cases may eliminate the need of harbour tug assistance.

7. ACKNOWLEDGMENTS

Azipod® Propulsion

Azipod® is a podded electric propulsion unit where the variable speed electric motor driving the fixed pitch propeller is in a submerged pod outside the ship hull, and the pod can be rotated around its vertical axis to give the propulsion thrust freely to any direction. Thus the ship does not need rudders, stern transversal thrusters or long shaftlines inside the ship hull.

Azipod is the registered trademark of a family of electric propulsion systems for ships, the first of which was developed by ABB about two decades ago. The latest product in the range is the most energy-efficient electric propulsion system on the market.

8. REFERENCES

[1] DORDEA, ŞT., *Proportional Steering System*, Analele Universităţii Maritime Constanţa, ISSN 1582-3601, pp. 165-173, 9 pg, 2010 (cotat B+ în sistemul CNCSIS)

[2] DORDEA, ŞT., ZBURLEA, E., *Anti-Hunt Control System*, Analele Universităţii Maritime Constanţa, ISSN 1582-3601, pp. 173-179, 8 pg, 2010 (cotat B+ în sistemul CNCSIS)

[3] DORDEA, ŞT., CIUCUR, V., *3-Phase Asynchronous Motors Pulse Width Modulation (PWN) Drive*, Analele Universităţii Maritime Constanţa, ISSN 1582-3601, pp. 301-309, 8 pg, 2009 (cotat B+ în sistemul CNCSIS)

[4] DORDEA, ŞT., ZBURLEA, E., BADEA, M., *Optoelectronic Hydraulic Device*, Analele Universităţii Maritime Constanţa, ISSN 1582-3601, pp. 309-317, 8 pg, 2009 (cotat B+ în sistemul CNCSIS)

[5] DORDEA, ŞT., ZBURLEA, E., BADEA, M., *Naval Steering Control By Means Of Optic Tracks*, Analele Universităţii Maritime Constanţa, ISSN 1582-3601, pp. 317-323, 6 pg, 2009 (cotat B+ în sistemul CNCSIS)

[6] DORDEA, ŞT., *Monitoring the steering failures*, Ovidius University Annals of Mechanical, Industrial and Maritime Engineering, Volume X, Tom I, 2008, cod CNCSIS 603, Editura Ovidius University Press, ISSN 1223-7221 (cotat B+ în sistemul CNCSIS)

[7] DORDEA, ŞT., *Double Track Steering Failure Monitoring System*, Annals of the „Dunarea de Jos" University of Galati, Fascicle III – Electrotechnics, Electronics, Automatic Control, Informatics, cod CNCSIS 482 ISSN 1221-454X, 2007 (cotat B+ în sistemul CNCSIS)

[8] DORDEA, ŞT., *A Ship's Rate of Turn Steeering Control*, A XXXII-a Sesiune de comunicări ştiinţifice cu participare internaţională „TEHNOLOGII MODERNE ÎN SECOLUL XXI, Academia Tehnică Militară, Bucureşti, 1 – 2 noiembrie 2007

[9] DORDEA, ŞT., *Aparate electrice de navigatie*, autor unic, Ed. Muntenia, ISBN (10) 973-692-154-9, ISBN (13) 978-973-692-154-4, 105 pag, Constanta, 2006

[10] DORDEA, ŞT., *Acţionări electrice cu undă sintetică*, autor unic, Ed. Muntenia, ISBN (10) 973-692-153-0, ISBN (13) 978-973-692-153-7, 155 pag, Constanta, 2006

[11] DORDEA, ŞT., *Maritime automatic steering system with off-course monitor*, Analele Universităţii Maritime Constanţa, ISSN 1582-3601, pp. 227-230, 4 pg, 2006

[12] DORDEA, ŞT., *Versatile automatic steering system with off-course monitor*, Analele Universităţii Maritime Constanţa, ISSN 1582-3601, pp. 231-234, 4 pg, 2006

[13] DORDEA, ŞT., *Digitaly activated electro hydraulic distributor*, A XXX-a Sesiune de comunicări ştiinţifice cu participare internaţională „Tehnologii moderne în secolul XXI", Academia Tehnică Militară, Bucureşti, 3-4 noiembrie 2005, pp.13.34-13.37, 4pg, ISBN 973-640-074-3

[14] DORDEA, ŞT., *Repartiţia secvenţială a sarcinii în acţionarea electronică a motoarelor asincrone trifazate*, A IX-a Sesiune de comunicări ştiinţifice cu participare internaţională „Ştiinţa şi învăţământul, fundamente ale secolului al XXI-lea", Ştiinţe tehnice, vol.I, ISBN 973 – 7809 – 04 – 1, ISBN 973 – 7809 – 03 – 3, Academia Forţelor Terestre „Nicolae Bălcescu", pp. 49 – 53, 5 pg, Sibiu, 2004

[15] DORDEA, ŞT., *Ship's rate-of-turn steering control*, Analele Universităţii Maritime Constanţa, ISSN 1582-3601, pp. 197-202, 6 pg, 2004

[16] DORDEA, ŞT., *Transferul de energie în sistemele electrohidraulice de guvernare navale*, Teză de doctorat, Universitatea „Dunărea de Jos" din Galaţi, 2002.

UWB IMPULSE RADIO RECEIVER ARCHITECTURES PERFORMANCES ON AWGN CHANNEL FOR SENSOR NETWORK APPLICATIONS

[1]DRAGOMIRESCU DANIELA, [2]LECOINTRE AUBIN, [3]PLANA ROBERT, [4]DRAGOMIRESCU OVIDIU,

[1,2,3]CNRS; LAAS Toulouse, France,[1,2,3,]University of Toulouse ;Toulouse, France
[4]Politehnic University of Bucharest, Electronics, Telecommunication and Information Technology Faculty , Romania

ABSTRACT

This paper presents two major UWB impulse radio architectures and compare their performances in the case of AWGN channel propagation for sensors networks applications. We study the TH-PPM and the TH-OOK receiver architecture in order to establish their best performances. Our study shows that TH-PPM receiver can achieve very good performances when the emitted pulse is used as correlation template. We'll also show that the IR-UWB TH-PPM receiver on an AWGN channel has better performances in term of BER than classical narrow band techniques such as PSK, QAM, or FSK. TH-OOK is an interesting receiver technique because of its simplicity (no need of synchronization mechanism), low cost, and low power. The comparison between the two architectures TH-PPM and TH-OOK shows, however, that the TH-PPM is better with respect to BER criteria.

Keywords: *UWB impulse radio architecture, TH-PPM, TH-OOK*

1. INTRODUCTION

We lead our study in the context of wireless sensors networks (WSN). We define WSN as systems having a very large number of nodes on a small area. WSN is a WPAN-like concept (Wireless Personal Area Networks). There are a lot of kinds of applications for this variety of networks; such as: monitoring, military applications, house automation, civil safety applications, etc. By considering these applications, we could deduce easily that there are some intrinsic constraints for WSN, which are: low cost, low power, simplicity and tiny nodes. Indeed, without theses characteristics none networks could be a viable WSN.
Thus throughout this article we keep in mind this context in order to compare correctly the performances of the two major methods used in IR-UWB (Impulse Radio - Ultra Wide Band) systems: Time Hopping – Pulse Position Modulation (TH-PPM) and Time Hopping – On Off Keying (TH-OOK). We will compare these architectures regarding the BER (Bit Error Rate) versus SNR (Signal to Noise Ratio) criteria and regarding the four WSN constraints.
The Federal Communications Commission (FCC) defines a radio system to be an UWB system if the -10 dB bandwidth of the signal is at least 500 MHz or the fractional bandwidth is greater than 20% [1]. With:

$$B_f = 2 \times \frac{f_H - f_L}{f_H + f_L}$$

IR-UWB is a very promising technology for this kind of applications, i.e. short range wireless data applications. Indeed, IR-UWB has some properties which confer it a good capability to respond to our problematic. Let us quote these advantages: 7,5 GHz of free spectrum which could permit to reach high data rate, extremely low transmission energy, extremely difficult to intercept, multi-path immunity, low cost (mostly digital architecture), "Moore's Law Radio" (performances, size, data rate, cost follow Moore's Law), simple CMOS transmitter at very low power [2]. Among the various families within UWB, we find family IR-UWB, Impulse Radio UWB, which includes in particular TH-PPM and TH-OOK, and which can be appropriate for our context of application: wireless sensor network.
The paper is organised as follows: Section II presents the TH-PPM and the TH-OOK principle. Section III describes the AWGN channel. The TH-PPM and TH-OOK performances, obtained using Matlab simulation, are exposed in the section IV and V. A comparative analysis is carried out in the section VI, before conclusion in the section VII.

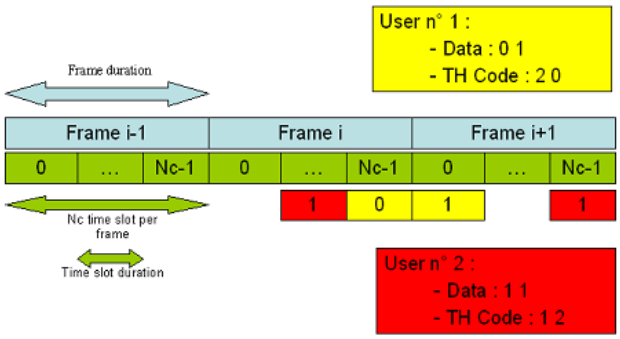

Figure 1 – Illustration of Time Hopping with two users

2. CONCEPT OF TH-PPM AND TH-OOK

In this part, we will specify the TH-PPM and TH-OOK characteristic.
At first, we mention the principle of Time Hopping. TH looks like a dynamic TDMA. Indeed, TH consists of the sharing of the medium in frame. Each frame is divided in time slots. The repartition of information depends of the time hopping code which is associated with each user. The figure 1 shows an example of Time Hopping with two users.

Once slots are defined, we could apply the modulation either PPM (Pulse Position Modulation) or OOK (On Off Keying).
For the PPM, bits are differ by a time shift in each time slot selected by the TH code, as we can see on the figure 2.
Concerning the OOK, we send a pulse in the slot for transmitting a binary one. The binary zero will correspond to an absence of impulsion (cf. fig 3).

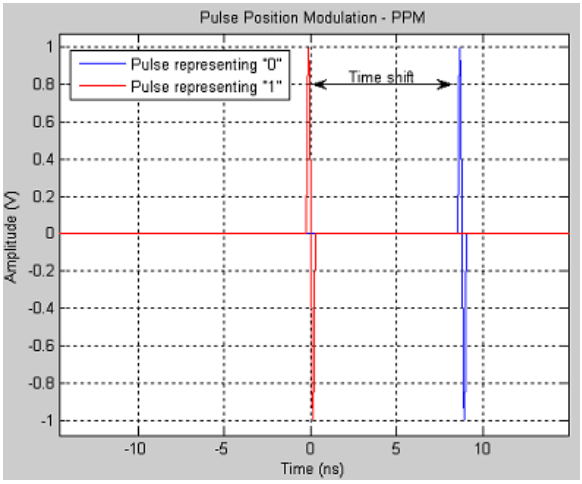

Figure 2 – Pulse Position Modulation

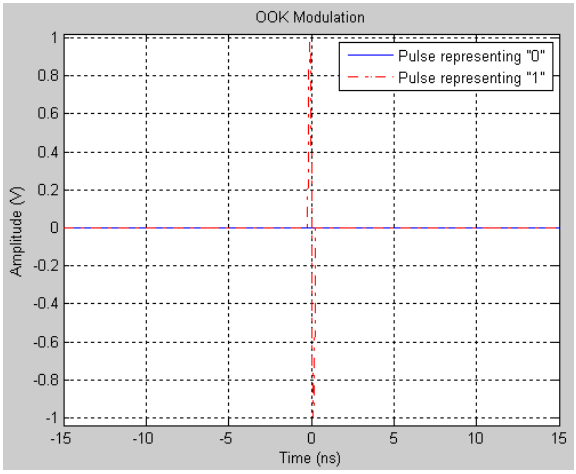

Figure 3 – On Off Keying Modulation

At the reception, we decide to use the schema represented figure 4 for TH-PPM and figure 5 for TH-OOK.
The TH-PPM coherent receiver is based on the correlation, with a template waveform, principle [1]. That is to say that the receiver generates a pulse whose form must be as far as possible like the received pulse. This should allow reaching better performances. The nearer the template waveform looks like the received pulse, the better the performances are. Once the template is achieved, the correlation between the template and the received pulse is carried out. The concept is to compare the received pulse with the expected pulse corresponding to a “one” or a “zero”. The higher the resemblance with a “one” template is, the probability that the received pulse is a one logic, is more important. At the output of the two correlation blocs (one and zero logic), it is enough to place a comparator with two inputs to distinguish, according to the amplitude, one logic from zero logic.

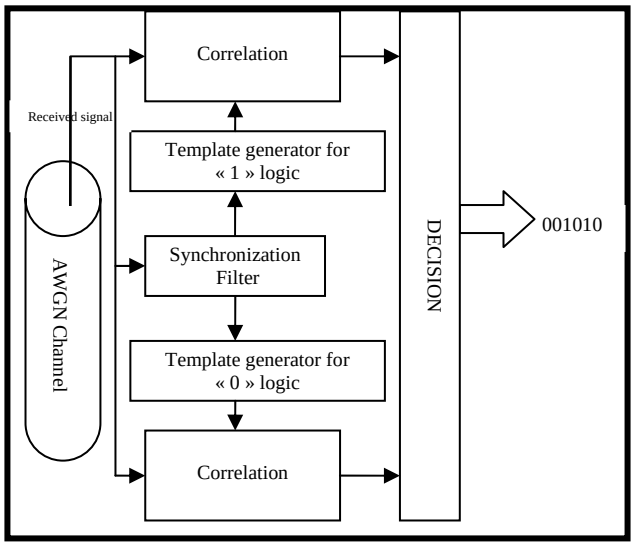

Figure 4 – TH-PPM coherent receiver

A synchronization bloc is also necessary, in order to provide a synchronous correlation between the received pulse and the template waveform [3]. This function is carried out by a matched filter defined on a sequence of pulse, which is known by the receiver and the transmitter. This sequence has a good autocorrelation property. This filter generates a peak in the presence of a synchronization trailer at its input. Thus, we detect the peak, thanks to a comparator, and we have the time arrival of the pulse. As the result we are able to synchronize the receiver. This synchronization is difficult, because of the pulse duration (< 1 ns) and should be the most precise otherwise the correlation output will be always at zero, and so the received bit will be also always at zero.

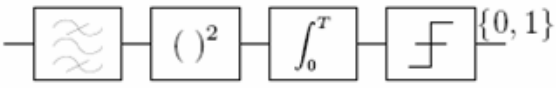

Figure 5 – Non coherent OOK receiver

The TH-OOK receiver is a non coherent architecture, as exposed on figure 5 [4]. This receiver is composed of four blocs: a filter on the considered band, a square bloc, an integrator bloc, and a decision bloc. The biggest advantage of this design is the absence of synchronization mechanism. Indeed, this schema is based on the energy detection. Thus, this receiver is less expensive, simpler, less greedy in power consumption, and it has smaller overall dimensions than the TH-PPM receiver.
We have just presented our two techniques IR-UWB, so it remains us to present the channel of propagation considered, before exposing the various performances.

3. THE AWGN CHANNEL

This part is dedicated to the channel considered in our simulations. We have decided to use the AWGN (Additive White Gaussian Noise).
It consists of a simple addition between the emitted signal and a Gaussian variable, which represents the noise of the channel.
The SNR (Signal to Noise Ratio) defines the importance of the noise in comparison of the power of the payload signal. SNR is expressed in dB. It will be the criteria of comparison with the BER (Bit Error Rate) in order to determine which technique is most adequate.
Moreover, we add a delay to this model in order to be capable of deal with the problems of synchronization. This delay should be modelled the time of propagation between the transmitter and the receiver. We could define the channel as followed:

$$y(t) = x(t-\tau) + n(t)$$

With x(t) the signal at the input of the channel; y(t) the signal at the output; τ the propagation delay; and n(t) the Gaussian noise. The value of n(t) is the key parameter for adjusting the SNR.

4. PERFORMANCES OF TH-PPM

Throughout this study, we will user our model of IR-UWB transmission developed with Matlab. This model is based on, the main equations defining IR-UWB techniques, different channel model and various receivers. Moreover thanks to the configurable aspect of this unit we are able to propose a platform of comparison of various IR-UWB methods.
Concerning the TH-PPM technique, we could highlight that there are three parameters which could affect the performances. The first is the choice of the template waveform used in the correlation. The second is the template used in the synchronization filter. And the third is the value of the time shift used in the PPM for distinguishing the one from the zero logic.
The table 1 exposes the BER according to the template of correlation and in function of SNR on an AWGN channel without delay. These values are obtained using our model of IR-UWB transmissions developed with Matlab. We compare, on the table 1, three templates of correlation:

- "emitted pulse": the receiver generates, as a template, exactly the same pulse that he would send if it was been the emitter
- "estimated pulse with known SNR" : the receiver generate, as a template, an emitted pulse and it adds on this pulse an Gaussian noise in order to reach the expected SNR.
- "perfect estimated pulse" : the receiver use as a template, the exact replica of the received pulse.

Behind the generation of template, there is the channel estimation notion. Indeed, here, for our three case of template, there are three levels of channel estimation. Theoretically, the better the estimate of the channel is, the better the performances are. With the first template, there is no estimation of the channel response, whereas, the two others templates implement a partially and a totally channel estimation. So the "perfect estimated template" template will be our configuration of reference because it corresponds to the perfect case.
The table 1 proves the importance of the channel estimation in order to achieve good performances. As we can see, the third template allow to reach perfect BER (BER = 0) for any value of SNR. This comes from the fact, that as we have a perfect estimate of the channel for any value of the SNR, thus we know all the time the impulse response of the channel even in the cases of a weak SNR.

	SNR (dB)					
Correlation template / SNR (dB)	-50	-44	-40	-34	-30	-28
emitted pulse	0,41	0,42	0,37	0,16	0,02	0
estimated pulse with known SNR	0,46	0,5	0,5	0,5	0,48	0,42
perfect estimated pulse	0	0	0	0	0	0
	SNR (dB)					
Correlation template / SNR (dB)	-24	-20	-18	-16	-14	-10
emitted pulse	0	0	0	0	0	0
estimated pulse with known SNR	0,5	0,27	0,14	0	0	0
perfect estimated pulse	0	0	0	0	0	0

Table 1 – BER/SNR performances for TH-PPM on AWGN channel without propagation delay

Besides, we could notice that the template "emitted pulse" offers better performances that the second template. Indeed, for the first, we reach a BER at zero starting from a SNR at -28 dB, whereas for the other template, it is necessary to await -16 dB. There is thus a gain of 12 dB between these two templates.
This is interesting within the framework of sensors networks where there are many constraints like in particular the size and the simplicity, the cost. However here, we could see that by selecting the template "emitted pulse", on the one hand we achieve win in performance, but moreover we also win in size and simplicity. Any kind of channel estimation, involves, inevitably, an increase of the complexity and additional circuits.
We iterate the complexity of the channel in order to approach a real channel gradually. With this intention, we add a propagation delay ($\tau \neq 0$). The fact of adding this delay, involves the birth of a need for synchronization between the transmitter and the receiver in order to ensure that multiplication between the template and the train of received pulses, is done well in a synchronous way, in the correlation. Synchronization is made by the use of a filter matched on a known sequence of impulses UWB. Let us visualize performances (BER) on such a channel and the precision of synchronization (table 2).

Synchronization template	-50	-45	-40	-35	-30	-25	-20	-15	5
perfect estimated pulse	0,43	0,4	0,43	0,23	0,16	0,06	0	0	0
emitted pulse	0,4	0,5	0,43	0,23	0,3	0,1	0	0	0
estimated pulse with known SNR	0,4	0,46	0,36	0,4	0,5	0,36	0,03	0	0
perfect estimated pulse	0	0	0	0	0	0	0	0	0
emitted pulse	0,43	0,43	0,5	0	0	0	0	0	0

Synchronization template	-50	-45	-40	-35	-30	-25	-20	-15	5
perfect estimated pulse	0	0	0	0	0	0	0	0	0
emitted pulse	41	-69	45	0	0	0	0	0	0
estimated pulse with known SNR	-43	50	11	-2009	-23	79,1	0	0	0
perfect estimated pulse	0	0	0	0	0	0	0	0	0
emitted pulse	142	93	31	0	0	0	0	0	0

Correlation template : emitted pulse

Correlation template: perfect estimated pulse

Table 2 – BER/SNR performances and synchronization error for TH-PPM receiver on AWGN channel with propagation delay.

This table 2 shows the BER in function of the template of correlation, the template of synchronization, and the SNR. The two different colors in the table represent two various correlation templates (yellow: “perfect estimated pulse” and purple: “emitted pulse”).

By analyzing this table we notice that except the perfect case of reference, perfect synchronization is reached for a SNR of -35 dB at best (case of the template: “emitted pulse”). Moreover, we note, which is reassuring, that we find the same results as in the preceding table (i.e work on channel AWGN without delay: table 1). We have seen that, from -35 dB of SNR, synchronization was perfect, i.e. we find a channel without delay in this case. Thus the channel with delay includes the channel without delay. Moreover we notice that the BER tends towards 0 starting from -20 dB of SNR, which corresponds almost to the results previously found.

We can also affirm that the stage of perfect synchronization is reached more quickly than the stage of the perfect reception (respectively to -35 dB and -20 dB).

On the table 2, by studying the two last lines, we note that it is the synchronization which prevails, compared to the template of correlation, on the performances of transmission (BER). As long as synchronization is not perfect, even if the estimate of the form of received impulse is perfect, reception will not be good (BER different from 0). It could be explained by the fact that the emitted and received pulses are very short. Thus to have perfect reception (BER=0), we must have a synchronous multiplication; i.e. the impulse template and the received impulse overlap .Otherwise, we will always have zero at exit. This is feasible only when perfect synchronization is reached (or at least that the error is lower than Tp, duration of the impulse).

With regards of the various results exposed here, we can say that for an AWGN channel the use of the template emitted pulse, is perfectly appropriate, since it offers the best performances constraints (simplicity, cost, size) ratio.

5. PERFORMANCES OF TH-OOK

In this part, we will keep the same procedure as for the TH-PPM. We will work at first, on an AWGN channel without delay first and then study BER on an AWGN channel with propagation delay.

Our model, developed under Matlab, lead us at the table 3, which expose the performance of TH-OOK on an AWGN channel without delay, according to the BER/SNR criteria.

	SNR (dB)								
BER vs SNR	-50	-45	-40	-35	-30	-25	-20	-15	5
TH-OOK	0,5	0,47	0,48	0,45	0,38	0,48	0,48	0	0

Table 3 – BER/SNR performance for TH-OOK on AWGN channel without propagation delay

We notice that the performances are less important than TH-PPM: we notice a loss of about 15 dB. We could make the same observation if we see the BER on an AWGN channel with delay (table 4). But this table 4 allows us to detect that the TH-OOK is very resistant to the implementation of the delay in the channel. Indeed, we could observe that the BER is the same for the two versions of the channel. This is due to the fact that the technique we study is a non-coherent and an energy detection technique.

	SNR (dB)								
BER vs SNR	-50	-45	-40	-35	-30	-25	-20	-15	5
TH-OOK	0,42	0,47	0,4	0,49	0,45	0,38	0,43	0	0

Table 4 – BER/SNR performances for TH-OOK on AWGN channel with propagation delay

The last part, before the conclusion, will be dedicated to the comparison of the performance of the two techniques.

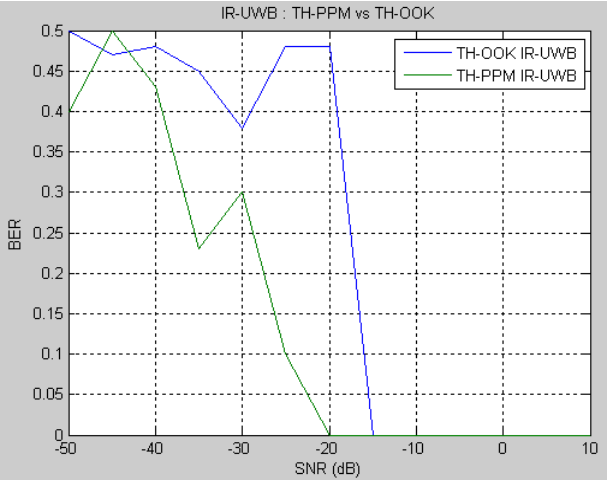

Figure 6 – Comparison between TH-PPM and TH-OOK, regarding BER/SNR criteria, on AWGN channel

6. COMPARISON TH-OOK VERSUS TH-PPM

This part is dedicated to the graphic comparison of the two techniques exposed during this paper: TH-OOK and TH-PPM. Next, we will compare IR-UWB performances with narrow band (PSK, QAM, …) performances.

Figure 6 illustrate the BER regarding the SNR for our two IR-UWB propositions.

We could observe that the TH-PPM propose better performances, a gain of about 5-10 dB, than the TH-OOK.

Nevertheless, in the framework considered here, i.e. sensors networks, it must be interesting, in function of the needs of the applications, to compare this loss of performance with the gain which is brought by the choice of TH-OOK. In other words, the designer must be choose between, either nodes with better properties such as low power, small size, low cost, simplicity, or better BER-performances but while sacrificing energy, size, and cost considerations. Indeed, as we said before, TH-OOK is less expensive, simpler, less voluminous, and less greedy in power consumption than TH-PPM.

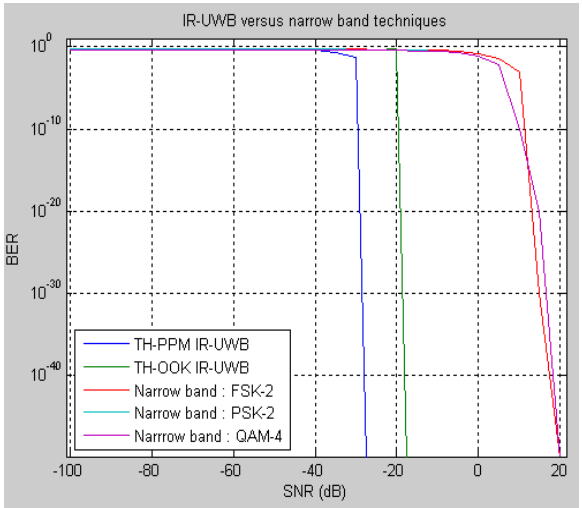

Figure 7 – IR-UWB versus narrow band, according to BER/SNR criteria, on AWGN channel without delay.

In order to show the interest of the IR-UWB versus narrow band technique, we present in Figure 7, a comparative between the two techniques according to the BER/SNR criteria, for a AWGN channel without delay.

This figure 7 illustrates the interest of TH-PPM because we can see a gain of 50 dB in order to reach an equivalent BER. So the TH-PPM technique with the "emitted pulse" template as correlation and synchronization is better than narrow band technique in the AWGN channel. TH-OOK reaches a gain of 40 dB in comparison with narrow band technique, i.e. 10 dB lesser than TH-PPM.

7. CONCLUSIONS

Two UWB impulse radio techniques for sensors networks are presented and simulated using Matlab. We compare their performances on an AWGN propagation channel while keeping in mind sensors networks constraints. Our study proves that TH-PPM used with the "emitted pulse" template for correlation and synchronization achieved very good BER performances. The TH-PPM performances are better than TH-OOK performances on an AWGN channel, and better than the classical narrow band techniques such as PSK, QAM, and FSK. We could see a gain of about 40 – 50 dB for IR-UWB techniques versus the narrow band techniques. Concerning the evaluation of the TH-OOK with the TH-PPM, our study has showed that TH-PPM has better BER-performances. Nevertheless, this gain is only about 10 dB, and we should keep in mind, especially in the sensors networks context, that TH-OOK proposes some very interesting properties, such as low power, low cost, and small size.

We will note, also, that we are leading a similar study on an UWB channel in order to determine, on a realistic channel, which IR-UWB technique is the most adequate for sensors networks [5][6].

8. REFERENCES

[1] I. Opperman et al., *UWB Theory and Applications*, WILEY 2004.

[2] D. Morche et al., *Vue d'ensemble des architecture RF pour l'UWB*, LETI, Summer School UWB, Valence 2006.

[3] Di Benedetto et al., *(UWB)²: Uncoordinated, Wireless, Baseborn Medium Access for UWB Communication Networks*, Mobile and Networks Applications, 2005 Springer Sciences.

[4] LM Aubert, PH.D. *Thesis : Mise en place d'une couche physique pour les futurs systèmes de radiocommunications hauts débits UWB*, INSA Rennes, 2005.

5] A.Lecointre, D. Dragomirescu, R.Plana *IR-UWB Channel Capacity for Analog and Mostly Digital Implementation*, Proceedings of 31 IEEE International Semiconductor Conference CAS 2008, 13-15 Octobre 2008, Sinaia, Roumanie, 4 pages, pp.403 -406

[6] Aubin Lecointre, Daniela Dragomirescu, Robert Plana *Channel capacity limitations versus hardware implementation for UWB impulse radio communication***s** Romjist, Romanian Journal of Information Science and Technology, Vol.12, N°3, pp. 339 -353, November 2009
[6] .

UWB RADIO LAYER MODELING PLATFORM FOR WIRELESS SENSOR NETWORK

[1]DRAGOMIRESCU DANIELA, [2]LECOINTRE AUBIN, [3]PLANA ROBERT, [4]DRAGOMIRESCU OVIDIU

[1,2,3]CNRS ; LAAS Toulouse, France, [1,2,3,]University of Toulouse, Toulouse, France,[4]Politehnic University of Bucharest, Electronics, Telecommunication and Information Technology Faculty, Romania

ABSTRACT

This paper deals with the Mobile Ad-hoc NETwork MANET problematic for using a viable and new wireless technique considerations in this particular context MANET. Our study exposes the weak points of actual solutions, especially, the weakness of new IR-UWB radio layer and channel modeling in classical network simulator. A full-parametric Matlab platform is proposed fill this lack. Our model deals with MAC and PHY layer based on reconfigurable IR-UWB radio. Capabilities, limitations and evolutions of our model are introduced here.
Index Terms – Channel, IR-UWB, MANET, modeling, co-simulator system and hardware level, transceiver, hardware in the loop.

1. INTRODUCTION

This paper proposes to study the design of a radio layer for Mobile Ad-hoc NETwork (MANET). Because of the particular constraints of this context, actual solution based on WPANs (Wireless Personal Area Network), such as BlueTooth, Zigbee, WiMedia, are not able to respond these MANET applications needs. Indeed, in order to be a viable radio interface for MANET, a radio layer must have three main characteristics: low power, low cost, small dimensions. The simplicity needs could be considered as the common factor. The first objective of the MANET radio layer must be the respect of these three constraints. Nevertheless, actual WPAN solutions are good solutions under certain conditions. For example Zigbee is adapted for short-range low data rate wireless sensor network. Zigbee is not fully optimized regarding the ultra low power and scalability constraints. Here we propose to study the design of a reconfigurable radio interface for MANET. Our proposition is to achieve a unique radio interface, whose properties are able to follow the application needs. The reconfigurability is inspired from the software defined radio concept [1].

In order to obtain a reconfigurable radio layer for MANET applications, we study the capability of Impulse Radio Ultra WideBand (IR-UWB) [2] for reconfigurability. Indeed, the IR-UWB state-of-art [2] has illustrated its good behavior regarding low power, low cost, small dimension and simplicity. In addition IR-UWB technique has the preponderant advantage of the mostly digital architecture [3] (cf. fig. 1) capability in comparison with classical continuous wave technique.

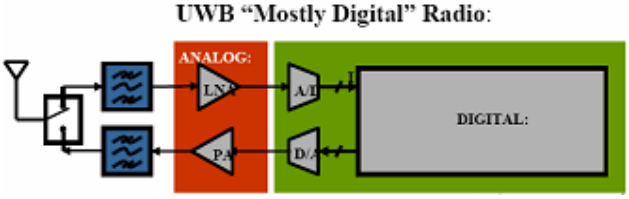

Fig. 1. UWB mostly digital radio architecture

This architecture confers two inherent advantages. The first one is that performances, such as data rate, circuitry size, power consumption, cost, will follow the Moore's Law. The facility of reconfigurability implementation in mostly digital architecture embodies the second one.

In other words we propose to examine a new wireless technique for MANET context. However it doesn't exist any simulator, network emulator or model for this kind of technique which could allow to test, develop, design, model, or evaluate IR-UWB reconfigurable radio interface.

For example present network simulator solutions for modeling and testing such as NS-2 (Network Simulator), GloMoSim, Qualnet, … have some limitations, especially regarding the PHY (PHYsical) layer and the channel modeling. Ussually the physical layer is based on classical narrow band technique such as QPSK (Quadrature Phase Shift Keying), QAM (Quadrature Amplitude Modulation). Thus, how could you test or evaluate the interest of IR-UWB reconfigurable layer for MANET if actual simulators don't consider it? How could you fairly compare different proposition?

That's why we present here our Matlab platform for modeling, designing, simulating, classifying, comparing and characterizing reconfigurable radio layer based on IR-UWB. In order to deal with reconfigurability problematic, we have proposed a full parametric platform. This platform allows studying all the possibility offered by the reconfigurability.

The paper is laid out as follow. In Section II we will introduce capabilities and the principle of the Matlab platform. Next, in Section III will expose the evaluation tools for radio layer, while Section IV will present future improvements, just before the conclusion.

2. A FULL PARAMETRIC IR-UWB RADIO LAYER MODEL ON MATLAB

2.1 The framework and the principle of the platform

The Matlab platform proposed here, aims to model a radio interface, including a fine PHY layer modeling and an outline of MAC (Medium Access Control) layer. Because of MANET context, the model is multi-users

oriented. The typical objectives of the platform are: model, validate, characterize and simulate multi-nodes MANET in realistic UWB channel.

The three main components of modeling are: emitter, realistic channel, and receiver.

The four main functionalities of the platform are: design, modeling, simulation, characterization.

Thanks to its parametric capability, the platform permits to deals with a large range of PHY layer based on IR-UWB. In addition, with the implementation of distinct evaluation tools, we are able to classify, compare, and characterize the solutions obtained thanks to parameter setting. Furthermore, the platform permits easily to simulate MANET application behavior, in order to dimension the radio layer, and for determining if IR-UWB could be a viable solution in such case. Finally, by proposing three approaches, i.e. digital signal processing modeling with Matlab classical development, system modeling with Simulink, and technology-dependent (for example constraints on FPGA development) modeling and implementation with Simulink and Synplicity (Synplify DSP).

2.2 Parameters at emission

In our IR-UWB platform there are several parameters to be determined for setting up a communication link at emission side:

- Emitted pulse properties: duration, amplitude, and waveform.
- Kind of pulse modulation.
- Time-Hopping (TH) parameters setting
- Synchronization parameters
- Generals emission parameters (number of emitter, frequency sampling, number of data, etc.)

Pulse properties are very important parameters in order to respect the regulation (FCC (Federal Communications Commission) in US, and CEPT (European Conference of Postal and Telecommunications Administrations) in Europe). The IR-UWB platform proposes different pulse waveform, such as first and fifth derivate of Gaussian pulse, sinus based pulse and wavelet based pulse.

The figure 2 describes the five pulse modulations proposed in the model.

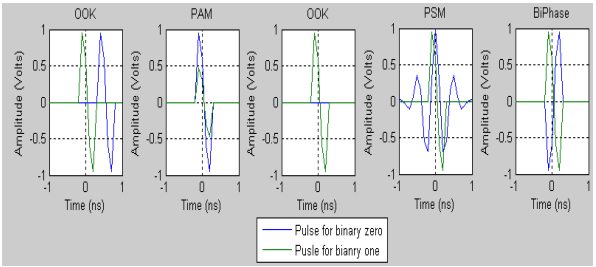

Fig. 2. Different pulse modulations: OOK, PAM, PSM, BiPhase.

For Time-Hopping (TH), we have to define four values. Three values will dimension the TH super-frame (frame duration: $T_{f,}$, chip duration: T_c, and N_c the number of chip per frame. TH-code is the last value. It allows associating one user with one chip in each frame. In order to achieve good performances in multi-user context, TH-code must be orthogonal.

Concerning synchronization, we propose to use a scheme based on a preamble before sending payload data (cf. fig. 3). This preamble is defined thanks to pseudo-random sequence based on Gold or MLLFSR (Maximum Length Linear Feedback Shift Register) codes. They have good statistic properties, which enabling to carry out synchronization at receiver side thanks to a filter matched on this kind of code sequence.

Fig. 3. MLLFSR based preamble for synchronization

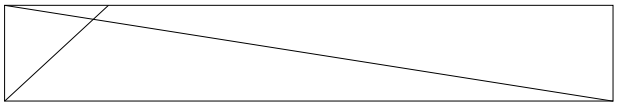

Generals parameters (number of emitters, frequency sampling, number of data, etc …) have to used for adapt the simulation to the MANET application simulated.

This set of parameters is important because it will dimension the performances of the link. Indeed, it will determine the spectrum occupation, the energy consumption, the data rate, etc. For example, the data rate depend on the pulse duration, the modulation valence and TH parameters ($T_{f,}$, T_c, and N_c).

2.3 Channel Modeling

The channel model is essential in this kind of platform. Indeed the more the channel model is realistic, the more the simulation results are near of the reality and confident. Here, in our Matlab platform, we propose to choose among four channels: a perfect channel (i.e. transparent) and three IEEE UWB channels at 1GHz, 3-10GHz and 60GHz (with directional antenna for this latter). We reuse the channel proposed in IEEE 802.15.4a [4] and IEEE 802.15.3c [5]. As described in figure 4, for each channel we have added the possibility to take into account the Additive White Gaussian Noise (AWGN). This latter is vital in order to obtain BER (Bit Error Rate) versus Eb/No (the ratio of Energy per Bit (Eb) to the Spectral Noise Density (No)) as performance criteria.

Fig. 4. Channel modeling and parameters.

In addition we have set up optional parameters in order to optimize the simulation in the MANET context. Thus the following parameters have been added:

-Mobility consideration: (coherence time).

-Delay and path loss due to the propagation.

Concerning mobility, in function of the movement speed of the emitter or receiver, the impulse response of the channel will be constant only during X send bits (with X depends on speed and data rate).

The delay and the path loss representing impact of propagation have been added them in order to model the impact of the distance between emitter and receiver. These two functionalities could be seen as follow (fig. 5)

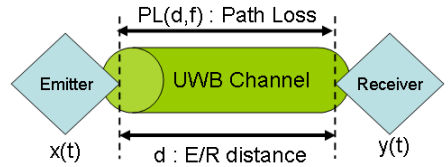

$$y(t) = PL(d,f) \times \left(h(t) \otimes x(t - \tau(d))\right) + n(t)$$

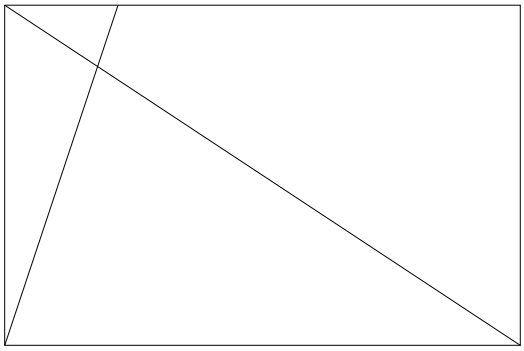

Fig. 5. Impact of Emitter Receiver distance for the channel modeling.

2.4 Parameters at reception

On this side we have also parameterize the receiver in order to obtain a large panel of possible architecture. They are designed on the following set of parameters:

- Operating frequency (1, 3-10 and 60 GHz)
- Coherent / non-coherent technique
- With or without synchronization
- Kind of decision bloc
- With or without integration bloc
- Correlation type

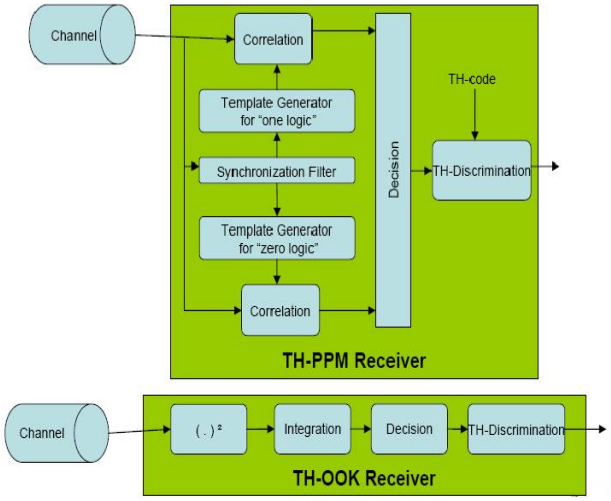

Figure 6 and 7 give example of operating architectures defined on these previous parameters.

- With or without channel estimation
- With or without Intermediate Frequency (IF) stage

Fig. 6. IR-UWB receiver architecture for TH-PPM and TH-OOK (Time-Hopping Pulse Position Modulation and On-Off Keying) at 3-10 GHz.

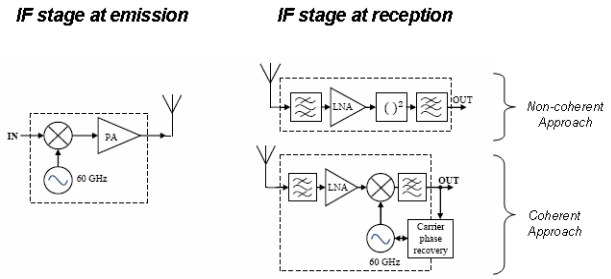

Fig. 7 Two distinct up and down conversion architectures for IR-UWB technique at 60 GHz [6].

This architecture modelling allow to verify, validate, compare and estimate the performances of a large range of available system for MANET.

There is also, at receiver side, a localization bloc, which could be added in the receiver. This latter is based on ToA (Time of Arrival) and allow a position estimation of the emitter by the receiver (cf. figure 8).

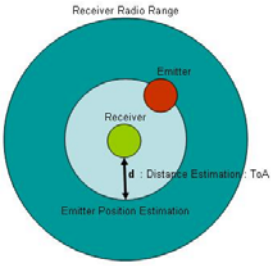

Fig. 8. Localization thanks to ToA

3. EVALUATION TOOLS FOR IR-UWB RADIO LAYER.

In order to achieve a fair comparison between the different possible architectures we have to use some criteria. In our IR-UWB platform, we propose to use the following criterion: synchronization error, BER versus E_b/N_0 ,budget link, achievable data rate, MANET constraints (low cost, low power, small dimension).

The MANET criteria are not completely implemented actually, because they depend of the hardware implementation. This approach will be treated further in the article (Section IV- Further Improvements).

The data rate, BER versus E_b/N_0 and budget link criteria are linked to each other. Indeed a proper budget link is obtained thanks to data rate and BER information. Remind that BER versus E_b/N_0 is the most common used criteria in wireless domain for performances estimation.

Besides, by using these kinds of criteria we could easily determine if IR-UWB is a good solution for one or another one application. The full parametric model permits to simulate quickly a valid model, while performances criteria give us information if the IR-UWB solution is viable in this case and eventually its cost.

For example [7] gives us the budget link and the BER versus E_b/N_0 for distinct configurations of an in-flight entertainment (IFE) network. BER results are exposed in fig. 9.

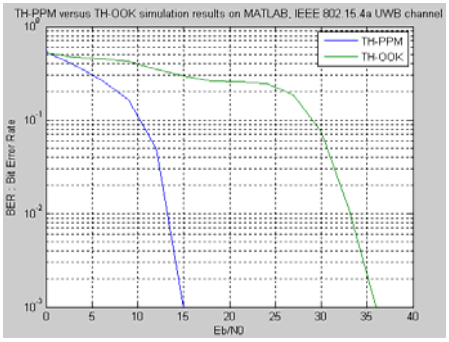

Fig. 9. BER performances for TH-OOK and TH-PPM.

4. FURTHER IMPROVEMENTS

The aim is to approach closer to reality in order to obtain better and more precise information from our platform. As a result, we have to develop the abilities to our model, and especially the range of parameters. For compensating its limitations we propose to develop the following set of parameters. Regarding the emission/reception techniques, we want to develop:

- Redundancy code, for upgrading the BER versus E_b/N_0 criteria.
- Pulse modulation with M > 1 bits/symbol, to improve data rate
- Set up more precisely directional antenna and determine theirs impacts in the access to the medium (MAC layer level)

Concerning distance estimation mechanism, we wish to deal with directional antenna more precisely, in order to profit from their advantages for localization. SSR (Signal Strength Ranging) technique will be also explored.

The most important developments are about system modelling and hardware implementation by using automatic VHDL code generation on FPGA and ASIC. This work will allowed to deal with the FPGA and ASIC implementation problematic such as power consumption and circuit size consideration, which is an essential criteria in MANET context [8]. The co-design system and hardware level permits to carry out very quickly FPGA prototyping [9]. Indeed the passage from the system level (Matlab & Simulink) to the hardware level (FPGA implementation) is automatic thanks to Synplify DSP. This functionality coupled with our IR-UWB parametric platform is very interesting for design rapidly on FPGA UWB impulse radio layer. Using this approach we also achieve a completely reconfigurable UWB impulse radio small size, low power ASIC [10].

5. CONCLUSIONS

In this article we have exposed the limitations of actual solutions concerning MANET radio layer modelling and simulation. The critical point is the lack of products for taking account of new techniques interest at PHY and MAC level, especially reconfigurable UWB impulse radio techniques. We proposed here a new platform based on the concept of hardware in the loop using Matlab and Xilinx tools and FPGAs for modelling, simulation, design and characterization of MANET layers. Principle, advantages, evolutions and limitations of our proposed solution are described in this paper.

6. REFERENCES

[1] J. Mitola III, “Software Radio Architecture”, Hardcover, October 2000.
[2] I. Oppermann, M. Hamalainen, J. Linatti, ”UWB Theory and Applications”, Wiley, 2004.
[3] Ian O’Donnell, et al., “An Integrated, Low-Power, Ultra-Wideband Transceiver Architecture for Low-Rate Indoor Wireless Systems”, Berkeley Wireless Research Center, Univ. of California, Berkeley, IEEE CAS Workshop on Wireless Communications and Networking, Pasadena, 2002.
[4] A. Molisch, K. Balakrishnan, C. Chong, S. Emani, A. Fort, J. Karedal, H. Schantz, U. Schuster, K. Siwiak, « IEEE 802.15.4a channel model – final report », IEEE 802.15.4a sub-group modelling.
[5] Su-Khiong Yong, « IEEE 802.15.3c Channel Modeling Sub-committee Report», IEEE 802.15.3c sub-group modelling, March 2007.
[6] M. Kraemer, A. Lecointre, D. Dragomirescu and R. Plana, «Architecture consideration for 60 GHz pulse transceiver front-ends”, IEEE CAS, october 2007.
[7] R.Albu, A.Lecointre, D. Dragomirescu, T.Gayraud, P. Berthou, “Evaluation of UWB communication for in-flight entertainment system in the aircraft cabin” Proceedings of 7th IFAC International Conference on Fieldbuses and nETworks in industrial and Embedded Systems, FET 2007, 7-9 Novembre 2007,Toulouse, France, 8 pages
[8] A.Lecointre, **Daniela Dragomirescu**, R.Plana “System architecture modeling of an UWB receiver for wireless sensor network” Proceedings of International Conference on Systems, Architectures, Modeling and Simulation (SAMOS VII), Samos (Grèce), 16-19 Juillet 2007, 12 pages.
[9] D. Dragomirescu, A. Lecointre, R. Plana “SOPC Co-Design Platform for UWB Systems in Wireless Sensor Network Context”. Proceedings of IEEE Third International Conference on Systems ICONS 2008 Avril 2008, Cancun, Mexique, 6 pages, ***Best Paper Award***
[10] A.Lecointre, D. Dragomirescu, R.Plana “A Largely Reconfigurable Impulse Radio UWB Transceiver”, IEE Electronics Letters, Vol.46, No.6, pp.453-455, Mars 2010

THE INDIRECT MEASURING METHODS OF GALVANOMAGNETIC EFFECTS

[1]DUMITRASCU ANA, [2]CIUCUR VIOLETA, [3]CARUNTU IRINA

[1,2,3]*Constanta Maritime University, Romania*

ABSTRACT

On the basis of physical models of field-substance interaction it can be quantitative described the dependence between material characteristics and certain physical measures like temperature, electric field intensity, magnetic induction, etc.

It is possible this way to use solid body transducers for experimental determining of these measures. The paper presents computing examples for errors in the case of indirect measuring methods.

Keywords: *logarithmic differential method, Hall constant, Hall field, Hall coefficient, average Hall mobility, galvanomagnetic measurements, sheet resistance, physical magnetoresistance*

1. PROBLEM PRESENTATION

The physical models of field-mater interaction give the possibility of establishing, by means of the matter characteristics, of some relations among parameters such as: temperature, frequency, electric field intensity, magnetic induction, etc. this opens up the possibility of using the transducers on solid body in order to establish this parameters in an experimental way.

In most cases the results are obtained by indirect methods. Therefore, besides the errors caused by the influence of perturbation factors there will also be indication errors of the gauges, errors that will have effects on the outcome of the measurement.

2. THE METHOD OF LOGARITHMIC DIFFERENTIATION

Do not change the styles included in this document We must begin with the logarithm of application of the above mentioned method for the parameter.

$$X = f(u, v, z, ...) \tag{1}$$

Where *u*,*v*,*z*, etc. are parameters whose values can be directly measured or are given by the manufacturer. If these parameters are affected by the absolute errors $\Delta u, \Delta v, \Delta z$, etc. then we have:

$$X + \Delta X = f(u + \Delta u, v + \Delta v + ...) \tag{2}$$

The absolute error of "*X*" can be found by making the difference between the two relations:

$$\Delta X = f(u + \Delta u, v + \Delta v + ...) - f(u, v, z, ...) = \frac{\partial f}{\partial u}\Delta u + \frac{\partial f}{\partial v}\Delta v + ... \tag{3}$$

Taylor's theory doesn't take into account the terms which contain absolute errors that have higher exponent than one. Both members are divided by "*X*":

$$\frac{\Delta X}{X} = \frac{f'u}{f}u\frac{\Delta u}{u} + \frac{f'v}{f}v\frac{\Delta v}{v} + ... \tag{4}$$

In the worst possible case, when the effect of the errors of *u*,*v*,*z*, etc. add up, we get maximum probable relative error:

$$(\frac{\Delta X}{X})_{\max.p} = \frac{|f'u|}{f}u\frac{|\Delta u_{\max}|}{u} + \frac{|f'v|}{f}v\frac{|\Delta v_{\max}|}{v} + ... = ...$$

$$= \frac{|f'u|}{f}u\varepsilon_{lu} + \frac{|f'v|}{f}v\varepsilon_{lv} + \tag{5}$$

where ε_{lu} is the limit relative percentage error at the measurement of parameter *u*. If this error is obtained from an analogical device with indicator needle, which is in the "c_u" precision class, then:

$$\varepsilon_{lu} = c_u\frac{u_{\max}}{u}$$

Relation (4) represents the logarithmic differential of function $X = f(u, v, z, ...)$, in which the differential of *u*,*v*,*z*, etc. have been replaced by absolute errors.

3. EXAMPLES OF CALCULATION IN CASE OF GALVANOMAGNETIC EFFECTS

If a conductor or parallelepiped shaped semiconductor (see figure 1) introduced in a magnetic field with induction $\overline{B}$, is covered by an electric current

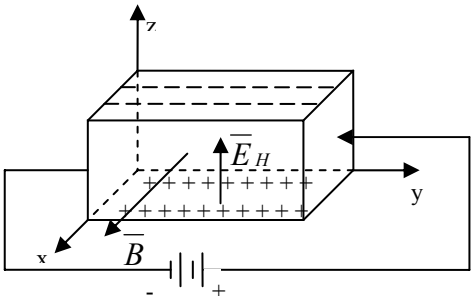

Figure 1 The rectangular sample

with density $\overline{J}$, then, on the elementary particles q will act Lorentz force:

$$\overline{F} = q(\overline{v_d} \times \overline{B}) \quad (6)$$

where $\overline{v}_d$ is the drift velocity.

$$\overline{J} = nq\overline{v}_d;\ \overline{F} = \frac{1}{n}(\overline{J} \times \overline{B}) \quad (7)$$

The opposite faces of the sample will be charged with elementary particles, with opposite signs. This pact will generate a transversal electrical field "$\overline{E}_H$" named Hall field. The effect of Hall field for the charge carriers is an effect against induction $\overline{B}$. An equilibrium is the moment when $\overline{E}_H$ will satisfy the equation:

$$q\overline{E}_H = \frac{1}{n}(\overline{J} \times \overline{B})$$

and then:

$$\overline{E}_H = R_H(\overline{J} \times \overline{B}) \quad (8)$$

$R_H = \frac{1}{nq}$, represents Hall constant. This constant is a reverse proportion with the concentration of charge carriers.

The sign of this constant will be the same as the sign of elementary particles.

In the case of a substance with two kind of electrical carriers, the formula of R_H becomes more complex, it's value will now depend on the temperature and concentration of these two types.

In constant Hall definition we use $\overline{E}_H$ field, but experimentally we determine the difference of Hall potential:

$V_H = b \cdot E_H$, and instead of current density we will measure the electrical intensity: $I = a \cdot bJ$, thus, R_H becomes[1]:

$$R_H = \frac{E_H}{JB} = \frac{V_H}{B} \cdot \frac{1}{\frac{I}{ba}B} = \frac{aV_H}{IB} \quad (9)$$

The Hall effect is used to measure different parameters like: mobility, charger, carriers concentration, electric field intensity.

We must notice that R_H depends on the magnetic field.

In weak fields $u^2B^2 << 1$, $R_H = A/qn$, where $A = \frac{R_0}{R_\infty}$, R_0 is the value of R_H in weak fields, and R_∞ is the value of R_H in intense fields.

In intense fields $\mu^2B^2 >> 1$, $R_H = 1/qn$ [2]. If the Hall constant in known, the Hall effect will permit to measure the magnetic field intensity.

It is preferable to use semiconductor materials in this application, because we have a large R_H value, which will produce a high E_H value, improving this way the sensibility of the measurement system.

If we determine R_H in datum constant field, and we measure U_H directly with an electronic analogical milivoltmeter, and *I* with a precise miliampermeter, the errors of these devices will influence the measurement result.

We use the logarithmic differentiation method:

$$\ln R_H = \ln(\frac{aU_H}{IB}) \quad (10)$$

By making the differentiation for every member and considering invariable parameters *a* and *B*, we obtain:

$$\frac{dR_H}{R_H} = \frac{IB}{aU_H}[\frac{a}{B}(\frac{dU_H}{I} - \frac{U_H dI}{I \sup 2})] = \frac{dU_H}{U_H} - \frac{dI}{I}$$

In maximum absolute errors, changing the sign of the negative term from the right member we obtain:

$$(\frac{\Delta R_H}{R_H})_{\max.p} = c_V \frac{U_{\max}}{U_H} + c_A \frac{I_{\max}}{I} \geq c_V + c_A \quad (11)$$

So, the probable maximum relative error, will exceed the lump sum of class indexes of the two gauges. If the value of R_H is known and we want to determine the field, we successively obtain:

$$B = \frac{R_H I}{aU_H};\ \ln B = \ln(\frac{R_H I}{aU_H})$$

$$(\frac{\Delta B}{B})_{\max.p} = \frac{|\Delta I|_{\max}}{I} + \frac{|\Delta U_H|_{\max}}{U_H} =$$

$$= c_A \frac{I_{\max}}{I} + c_v \frac{U_{\max}}{U_H}$$

3. THE GAUSS EFFECT

In the absence of magnetic field, a charger carrier has a rectilinear movement, and between two successive collisions it covers a space equal with the freely medium route. The presence of the field has as effect the covering, in the same time, of a short distance after $\overline{E}$ direction. This is a result of the trajectory which is curve. The simultaneous action of the electric and magnetic field will determine a diminution of drift velocity or the mobility of charger carriers. The resistivity will increase, so:

$$\frac{R - R_0}{R_0} = \frac{\mu^2 B^2}{2} \Rightarrow R_0(1 + \frac{\mu^2 B^2}{2}) \quad (12)$$

Where R_0 is the material resistance in absence of field induction $\overline{B}$. In the weak field domains, for a finite semiconductor, the magnetoresistant coefficient $C_H = \mu^2/2$ is constant, but in the intense field

$\mu^2/2 \approx B^{-2}$ the magneto resistivity will be saturated. As a result of the changing charger carriers density, the temperature will change the value of magnetoresistance.

If we consider a material sample in an invariable magnetic field with induction $\overline{B}$, at invariable temperature we can establish its value using a direct current compensator. With this device we will measure the electric voltage on the terminals of R_E, standard resistance.

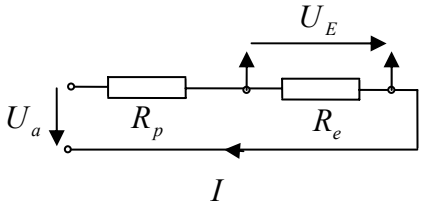

Figure 2 The direct current potentiometer

The standard resistance will be in a serial fitting with our sample in study. The power supply source shall offer invariable electric voltage:

$$U_e = \frac{R_e U_a}{R_e + R_p}, \text{ so } R_p = R_e(\eta - 1) \qquad (13)$$

Where $\eta = \frac{U_a}{U_e} = 1 + \frac{R_p}{R_e}$

Using again the logarithmic differential method we successively obtain:

$$\frac{dR_p}{R_p} = \frac{(n-1)dR_e + R_e d}{R_e(\eta - 1)} = \frac{R_e}{R_\eta} + \frac{\eta}{\eta - 1} \cdot \frac{dU_a}{U_a}$$

Because $R_e = ct$ during the experiment we obtain:

$$\frac{dR_p}{R_p} = \frac{\eta}{\eta - 1} \cdot \frac{dU_a}{U_a}$$

The maximum relative error will be:

$$\left(\frac{\Delta R_p}{R_p}\right)_{\max.p} = \frac{\eta}{\eta - 1} \frac{|\Delta U_a|_{\max}}{U_a} \qquad (14)$$

In case we use an electronic analogical milivoltmeter:

$$\left(\frac{\Delta R_p}{R_p}\right)_{\max.p} = \frac{\eta}{\eta - 1} e_V \frac{U_{\max}}{U_a} \qquad (15)$$

The factor $\frac{\eta}{\eta - 1}$ represents a function $f(\eta): (0,1) \to (-\infty, 0)$. Theoretically, if $\eta \to 1$, so $U_e \to U_a$, the error will tend to infinite. Actually, if $R_p << R_e$, the error shall increase to a high value. In order to obtain correct results we must respect the condition: $R_e << R_p$. We can express the increasing of magnetoresistance, in the absence of field, making a determination for the same sample:

$$\Delta R_p = R_p - R_{p0} = \left(\frac{U_a}{U_e} - 1\right) - \left(\frac{U_a}{U_{e0}} - 1\right) R_e =$$

$$= R_e \left(\frac{U_a}{U_e} - \frac{U_a}{U_{e0}}\right) \qquad (16)$$

Where U_{e0} is the measure of voltage when $B = 0$

4. MEASUREMENT OF RESISTIVITY

An adequate form for the galvanomagnetic measurements, which allows an easy extraction of the relevant material characteristics from experimental result, is represented by a long sample ($l >> w$, $l >> \delta$)[3] fitted with five small-area contacts (figure 3). Under these circumstances the geometrical correction factor approximately equals unity.

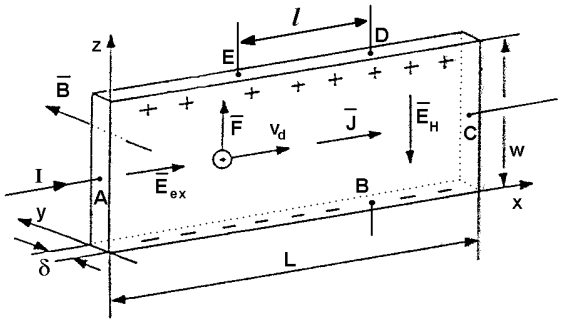

Figure 3 The long sample for galvanomagnetic measurements

The supply current *I* is forced along the sample between the contact *A* and *C*.

The longitudinal drop voltage is measured between the contacts *E* and *D*, and also Hall voltage, between the contacts *B* and *D*.

By the Hall experimental device already described it easy to find the quantities: ρ_b, R_s, $\frac{\Delta R_b}{R_b(0)}$, and V_H.

The resistance of the plate between the contacts *E* and *D*, can be expressed as a function of the effective material resistivity on the direction of the total current density ρ_b when the plate is exposed to a magnetic field action, perpendicular to this surface:

$$R_{ED} = \rho_b \, l / w\delta \qquad (17)$$

The drop voltage between the contacts *E* and *D* is $V_{ED} = R_{ED} \cdot I$, so:

$$\rho_b = \frac{w\delta}{l} R_{ED} = \frac{w\delta}{l} \cdot \frac{V_{ED}}{I} \qquad (18)$$

Knowing the sample dimensions it is determined ρ_b by measuring V_{ED} and I. If ρ_b is considered as a

function of variables V_{ED} and I, the error sent over the measurement result due to a possible variation ΔV_{ED}, ΔI, can be determined by the differential logarithmic method [4].

A logarithm is applied to the relation which expresses the measurement quantities and then it is transformed into a differential member by member:

$$\frac{d\rho_b}{\rho_b} = \frac{l}{\delta w}\left(\frac{dV_{ED}}{V_{ED}} - \frac{dI}{I}\right) \tag{19}$$

To obtain the probable maximum relative error when the errors of V_{ED} and I are the highest add to each other the sign of negative factor on the right member of relation (19) is changed and the differentials by maximum are substituted by absolute errors.

$$\left(\frac{\Delta\rho_b}{\rho_b}\right)_{\max.p} = \frac{l}{\delta w}\left[\frac{(\Delta V_{ED})_{\max}}{V_{ED}} + \frac{(\Delta I)_{\max}}{I}\right] \tag{20}$$

The obtained percentage is:

$$\left(\frac{\Delta\varphi_b}{\varphi_b}\right)_{\max.p}[\%] = \frac{l}{\delta w}\left[\frac{(\Delta V_{ED})_{\max}}{V_{ED}} + \frac{(\Delta I)_{\max}}{I}\right]\cdot 10^2 \tag{21}$$

If V_{ED} and I values are determined directly by analogue measurement instruments with the rated measurement ranges U_N and I_N, and also the accuracy closes c_V and c_A, the relation (20) becomes:

$$\left(\frac{\Delta\rho_b}{\rho_b}\right)_{\max.p}[\%] = \frac{l}{\delta w}\left(c_V\frac{U_N}{U} + c_A\frac{I_N}{I}\right) \tag{22}$$

To obtain a superior precision, the value of the electric current I can be measured by a potentiometer by the drop voltage that it produces on measurement standard resistance.

Knowing V_{ED} and I the sheet resistance of the materials can be expressed thus:

$$R_S = \frac{\rho_S}{\delta} = \frac{1}{\delta}\cdot R_{ED}\frac{\delta w}{l} = \frac{w}{l}R_{ED} = \frac{w}{l}\cdot\frac{V_{ED}}{I} \tag{23}$$

Doing the measurements in the absence of the magnetic field and also in the presence of a $\overline{B}_\perp$ value of the normal induction, on the device surface, the physical magnetoresistance can be determined:

$$\frac{\Delta R_b}{R_b(0)} = \frac{R_b(B_\perp) - R_b(0)}{R_b(0)} = \frac{\Delta\rho_b}{\rho_b(0)} \tag{24}$$

where

$$R_b(B_\perp) = \frac{w}{l}\cdot\frac{V_{ED}(B_\perp)}{I} \tag{25}$$

$$R_b(0) = \frac{w}{l}\cdot\frac{V_{ED}(0)}{I} \tag{26}$$

For a precise determination of V_{ED} values the measuring potentiometers can be used.

5. REFERENCES

[1] KIREEV, P.: *Fizica semiconductorilor*, Editura Ştiinţifică şi Enciclopedică, Bucureşti, 1977

[2] CĂRUNTU, G.: *Consideraţii privind structura, efectele fizice de bază, condiţiile de funcţionare şi caracteristicile dispozitivelor Hall neconvenţionale realizate pe siliciu.* Master Reference, „Politehnica" University, Bucharest, 1994

[3] CĂRUNTU, G.: *Despre eficienţa senzorilor magnetici Hall*. Sesiunea de Comunicări Ştiinţifice a Universităţii din Piteşti, pp. 52-56, Piteşti, noiembrie, 1997

[4] CĂRUNTU, G.; DRAGOMIRESCU, O.: *Errors Computing in the Case of Using, Solid Body Transducers*. Proceedings OPTIM'94, pp. 189-192, Braşov, Mai 1994

SPREADING CODE EFFECTS ON SYNCHRONOUS CONVENTIONAL AND MMSE MULTIUSER DETECTION ALGORITHMS

[1]HALUNGA SIMONA, [2]FRATU OCTAVIAN, [3]VIZIREANU DRAGOS, [4]CARUNTU GEORGE

[1,2,3]University Politehnica of Bucharest, Telecommunications Department, [4]Constanta Maritime University, Romania

ABSTRACT

Multiuser detection technique implies joint demodulation of different overlapping data streams sent by different users, improving their individual performances based on the knowledge of some key parameters of all users. Each user is identified by its own signature code, which should be, in the ideal case, orthogonal on all the others. This paper analyzes the performances synchronous of conventional and MMSE multiuser detectors algorithms when different type of spreading codes is used, namely. The results are compared in terms of Bit Error Rate (BER) as function of Signal to Noise Ratio (SNR) as well as in terms of the overall signal power spectra density characteristics. The results obtained lead to several interesting conclusions that are highlighted in the last section.

Keywords: *MMSE detector; conventional detector; Walsh codes; PN codes; Gold codes; Bit Error Rate.*

1. INTRODUCTION

The theory of multiuser detection technique has been developed during the 90s [1], but the interest on the domain increased in the last years with the development of modern mobile communications systems and especially with the usage of MIMO techniques [2, 3]. Also, the application of this technique was of large interest in mobile communications, especially at base station level, where all the signal have to be demodulated [4, 5].

The domain is still under research, since it hasn't been found yet an optimal solution that maximizes the performances, minimize the cost and takes into account the channel impairments and system imperfections. Several research studies have been made in order to determine less complex receiver algorithms and to determine their performances under different propagation conditions [6]. The high demand for mobile networks increased the interest on multiuser detection for receivers in the presence of severe fading [6, 7] or on a combined solution between multiuser detection and diversity techniques [8]. Iterative decoding algorithms based on turbo decoding principles have also been studied [9], as well as evaluation of performances in different fading channel conditions [10]. The dynamic environment and the capability to select the number of active users are also analysed [11, 12].

However, even with the classical multiuser detection algorithms, there are important issues when the users are not perfectly orthogonal and / or when they have un-equal amplitude [13]. Also coding techniques have been used to increase the system performances [14].

This paper aims to analyze the influence of spreading codes in conventional and MMSE multiuser detectors as well as the spreading codes effects on the channel signal power spectral density bandwidth and uniformity. First, 32 bits length Walsh codes are studied been used; since these codes are sensitive to synchronization miss-matches (i.e. they are perfectly orthogonal if perfectly aligned at the receiver, but the inter-correlation increase significantly when they are no longer synchronized) both the ideal and non-ideal (i.e. when the recived codes are not perfectly aligned) cases are studied. Next we determined the performances when other codes with good correlation properties are used, namely 31 bits length PN and Gold codes. Extended Monte Carlo simulations have been performed in order to obtain the bit error rate results presented in section III. Moreover, since in CDMA systems the amplitude and the bandwidth of the power spectral density of the overall channel signal is important, we determined this averaged power spectral density and compared the three cases analyzed in terms of the occupied bandwidth, amplitude and uniformity. Based on the results obtained, some interesting conclusions have been highlighted in the last chapter.

2. SYSTEM MODEL

The basic CDMA N user system model assumes that all users transmit binary data using antipodal synchronous signature waveforms. The channel is affected only by additive white Gaussian noise (AWGN). The received signal is therefore,

$$y(t) = \sum_{k=1}^{N} A_k b_k s_k(t) + \sigma n(t), \quad t \in [0, T] \tag{1}$$

where T is the bit period, b_k {-1, 1} is the information bit transmitted by user k during time interval T, A_k is the amplitude of data received from user k, $n(t)$ is the AWGN with unit power spectral density (which models the thermal noise and all other noise sources unrelated to the transmitted signals) and σ is the standard deviation of the noise. The code sequences are normalized such that

$$\int_0^T s_k^2(t)dt = 1, \ (\forall)k \tag{2}$$

and the cross-correlation between the i^{th} user sequence and the j^{th} one is defined by

$$\rho_{ij} = \int_0^T s_i(t)s_j(t)dt < 1 \tag{3}$$

The simplest strategy to demodulate CDMA signals is the use of a bank of matched filters that operates simultaneously, each of them matched to one user signature signal

$$h_k(t) = s_k^*(T-t),\ k=1,\quad N \tag{4}$$

This represents the simplest linear detection approach, that maximizes the signal to noise ratio for each individual matched filter output, assuming that the channel noise and interference from all other users are modelled as AWGN. The structure is known as ***conventional multiuser detector.***

Using this approach, the k^{th} user matched filter output, sampled at the end of the bit period is

$$y_k = A_k b_k + \sum_{j\neq k} A_j b_j \rho_{jk} + n_k,\quad k=\overline{1,N} \tag{5}$$

where

$$n_k = \sigma\int_0^T n(t)s_k(t)dt,\quad k=\overline{1,N} \tag{6}$$

is the noise component at the matched filter output, that can be modelled as a Gaussian random variable with zero mean and variance σ^2. Using a matrix representation, (5) may be expressed as

$$\mathbf{Y} = \mathbf{RAb} + \mathbf{N} \tag{7}$$

where $\mathbf{Y} = [y_1,\ y_2,\ ...\ ,y_N]^T$ is a column vector that includes the sampled outputs of the matched filters,

$$\mathbf{R} = \begin{pmatrix} \rho_{11} & \rho_{12} & .. & \rho_{1N} \\ \rho_{21} & \rho_{22} & .. & \rho_{2N} \\ .. & .. & .. & .. \\ \rho_{N1} & \rho_{N2} & .. & \rho_{NN} \end{pmatrix} \tag{8}$$

is the correlation matrix of the signature waveforms, $\mathbf{A} = diag\{A_1, A_2, ...\ A_N\}$ is a diagonal matrix of the amplitudes of the received bits, $\mathbf{b} = [b_1, b_2, ...\ b_N]^T$ is a column vector that contains the bits received from all users, and $\mathbf{N} = [n_1, n_2, ...\ n_N]^T$ is the sampled noise vector, such that

$$E[\mathbf{N}\cdot\mathbf{N}^T] = \sigma^2\mathbf{R} \tag{9}$$

The estimated bit, after the threshold comparison, is

$$\hat{b}_k = \text{sgn}(y_k) = \text{sgn}(A_k b_k + n_k) \tag{10}$$

The conventional receiver requires no knowledge beyond the signature waveforms patterns and the timing for all users in order to demodulate the received signal coherently. The results obtained by the conventional detectors are near optimum for a large number of equal power users, in accordance to central limit theorem. However, if the amplitudes of the users is not equal, or if the signature sequences are not perfectly correlated (i.e. the inter-correlation coefficients are not zero) the central limit theorem is no longer valid and the results deteriorates rapidly.

Another implementation is the one that uses a linear combination of the matched filter outputs that minimizes the mean square error between these outputs and the correspondent transmitted data, maximizing thus the bit error probability. The structure is known as ***Minimum Mean Square Error*** detector. For each user *k*, the detector has to determine a vector of N weighting coefficients m_k that maximize

$$E\left[\left(b_k - m_k^T y\right)^2\right] \tag{11}$$

Using the matrix representation from previous chapter and after algebraic manipulation the linear transformation matrix is

$$M^* = \mathbf{A}^{-1}\left[\mathbf{R} + \sigma^2\mathbf{A}^{-2}\right]^{-1} \tag{12}$$

where where $\mathbf{M}$ is a $N\times N$ matrix whose k column is equal to m_k., $\mathbf{R}$ is the correlation matrix (8) and $\sigma^2\mathbf{A}^{-2} = diag\left\{\frac{\sigma^2}{A_1^2},...,\frac{\sigma^2}{A_2^2}\right\}$ The decision on the estimated transmitted bit of *k* user can be determined as

$$\hat{b}_k = \text{sgn}\left(\frac{1}{A_k}\left(\left[\mathbf{R}+\sigma^2\mathbf{A}^{-2}\right]^{-1}\mathbf{y}\right)_k\right) = \text{sgn}\left(\left(\left[\mathbf{R}+\sigma^2\mathbf{A}^{-2}\right]^{-1}\mathbf{y}\right)_k\right) \tag{13}$$

3. SIMULATION RESULTS

Extensive Monte Carlo simulations have been performed for the two multiuser detection algorithms and for three types of spreading sequences frequently used in CDMA systems, namely 32 bits length Walsh-Hadamard codes, 31 bits length PN codes and Gold codes. The results are compared in terms of the Bit Error Rate (BER) achieved by the two structures as a function of Signal to Noise Ratio (SNR), but also in terms of the averaged Fast Fourier Transform (FFT) of the signal transmitted by all users over the common channel.

3.1 Walsh-Hadamard sequences of length 32

The first spreading sequences used are the Walsh-Hadamard ones, which have the property that are perfectly orthogonal when perfectly aligned. Each user transmits 1000 bits of data, and they have equal amplitudes. The spreading codes used are rows $\left[H_9^{32},\ H_{13}^{32},\ H_{22}^{32},\ H_{30}^{32}\right]$ from the 32x32Hadamard matrix, normalized as specified in (2). The correlation matrix is, therefore,

$$R = \begin{bmatrix} 1 & 0 & 0 & 0 \\ 0 & 1 & 0. & 0 \\ 0 & 0 & 1 & 0 \\ 0 & 0 & 0 & 1 \end{bmatrix} \tag{14}$$

It can be observed that, in this case, both receiver algorithms and all users have very close performances. The BER decrease with SNR, reaching a value of -16.73 dB at SNR=6dB, and -30dB at SNR=10dB. Some significant values are given in table 1

Table 1

RSZ (dB)	2	4	6	8	10
BER (dB)	-9.86	-12.34	-16.73	-22.43	-30.03

If the codes are not received synchronously (i.e. at the receiver they are cyclically shift in time with a number of bits) they are no longer orthogonal, and both receiver results in terms of BER. For a cyclic shift of 3, 4

and 5 bits of the above mentioned codes, we obtain the correlation matrix

$$R = \begin{bmatrix} 1 & 0 & 0 & 0.3750 \\ 0 & 1 & -0.25 & 0 \\ 0 & -0.25 & 1 & 0 \\ 0.375 & 0 & 0 & 1 \end{bmatrix} \quad (15)$$

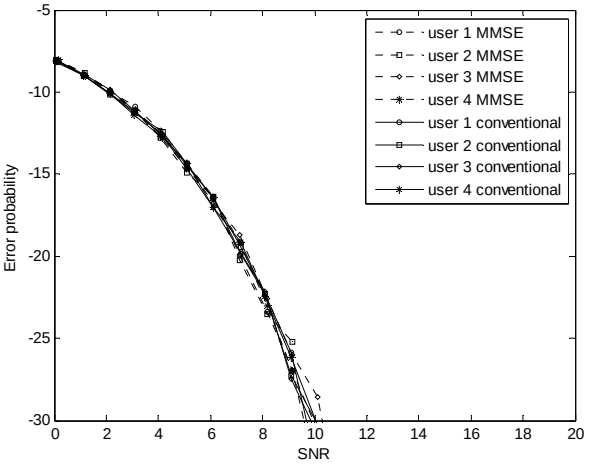

Fig.1. BER versus SNR for conventional and MMSE multiuser receivers using Walsh Hadamard codes of length 32, correlation matrix (15)

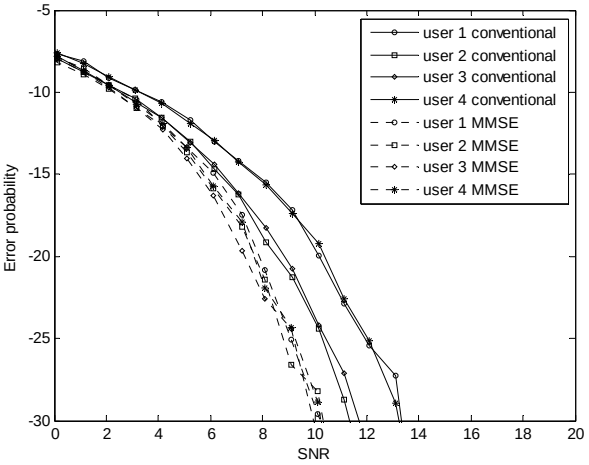

Fig.2. BER versus SNR for conventional and MMSE multiuser receivers using Walsh Hadamard codes of length 32, correlation matrix (16)

Some results are given in table 2a for Conventional detector, and 2b for MMSE detector

Table 2a. Conventional detector

RSZ (dB)	2	4	6	8	10
BER $u_{1\&2}$ (dB)	-9.02	-10.71	-12.8	-15.35	-19.13
BER $u_{3\&4}$ (dB)	-9.45	-11.35	-14.3	-17.98	-29.82

Table 2b. MMSE detector

RSZ (dB)	2	4	6	8	10
BER $u_{1\&2}$ (dB)	-9.50	-11.7	-14.86	-20.53	-28.3
BER $u_{3\&4}$ (dB)	-9.68	-12.14	-16.02	-22.42	-29.83

It can be easily observed that the BER increase for users 1 and 4 which are stronger correlated $\rho_{14} = \rho_{41} = 0.375$ more then for users 2 and 3 that are less correlated $\rho_{23} = \rho_{32} = -0.25$. Moreover, the increase more important for the conventional receiver (for users 1 and 4 between 0.84 dB at SNR=2dB and 10,87 dB at SNR=10dB) rather then for the MMSE one (between 0,34 dB at SNR=2dB and 2 dB at SNR=10dB)

For a cyclic shift of 10, 13 and 22 bits of the above mentioned codes, we obtain the correlation matrix

$$R = \begin{bmatrix} 1 & 0 & 0 & 0 \\ 0 & 1 & -0.6875 & 0 \\ 0 & -0.6875 & 1 & 0.0625 \\ 0 & 0 & 0.0625 & 1 \end{bmatrix} \quad (16)$$

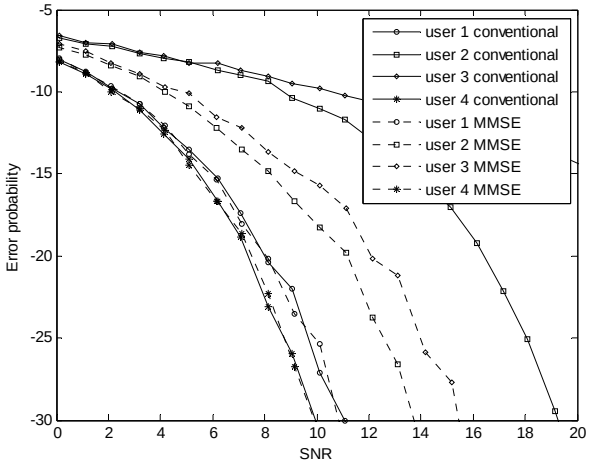

Fig.3. BER versus SNR for conventional and MMSE multiuser receiver, Walsh Hadamard codes of length 32, correlation matrix (16)

Some results are given in table 3a for Conventional detector, and 3b for MMSE detector.

Table 3a. Conventional detector

RSZ (dB)	2	4	6	8	10
BER u_1 (dB)	-7.08	-7.74	-8.23	-8.93	-9.72
BER u_2 (dB)	-7.175	-7.88	-8.62	-9.24	-10.95
BER u_3 (dB)	-9.6	-12.01	-14.95	-19.91	-26.63
BER u_4 (dB)	-9.63	-12.4	-16.2	-22.6	-29.98

Table 3b. MMSE detector

RSZ (dB)	2	4	6	8	10
BER u_1 (dB)	-8.09	-9.54	-11.35	-13.41	-15.52
BER u_2 (dB)	-8.31	-9.85	-12.01	-14.69	-17.98
BER u_3 (dB)	-9.63	-11.79	-15.08	-19.87	-25.49
BER u_4 (dB)	-9.85	-12.18	-16.27	-20.03	-29.98

In this case user 1, which is uncorrelated with other users achieve similar results with the ideal case presented in figure 1. User 2, which is loosely correlated with 3 $\rho_{13} = \rho_{31} = 0.0625$ have a small decrease in BER (obtaining a maximum increase of 3.4 dB at SNR=10dB). The results obtained with the conventional detector are very close with the ones obtained with

MMSE. For user 2, which is closely correlated with user 3 $\rho_{23} = \rho_{32} = -0.6875$ the decrease in performances is more significant (getting at a maximum of almost 20 dB at SNR=10dN for conventional detector and almost 12 dB for MMSE detector). Finally, for user 3, which is correlated with both users 2 and 4, the conventional detector is achieving very poor results (a loss of almost 20 dB at SNR=20dB); the MMSE detector has also a loss in performances (of about 12dB at SNR=20dB) but the loss is not as dramatic as in the conventional detector case.

In figure 4 is presented the averaged FFT of the data transmitted through the common channel, assuming that the bit period is 1μs. The average has been made on 1000 bits of data and 100 trails for each bit.

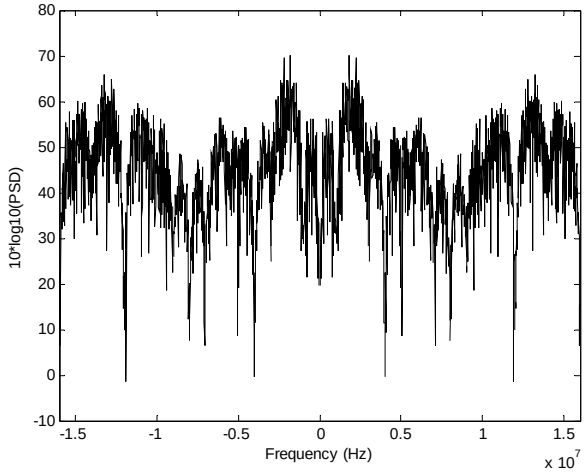

Fig.4. Averaged FFT for multiuser receiver using Walsh Hadamard codes of length 32

The calculated mean value of the averaged FFT, within all its frequency range, is 21.17 dB, but the spectral components are not uniformly distributed within its bandwidth, having peak values as high as 65 dB. Moreover, the spectral distribution depends on the codes chosen for data spreading.

3.2 Pseudonoise (PN) sequences of length 32

In the second case we used as signature waveform a 31 bits length PN code, generated with the polynomial

$$G(D) = 1 + D^3 + D^5 \qquad (17)$$

The four users are assigned different phases of the same PN sequence, which means different initial conditions of the generator. The associated cross-correlation matrix is

$$R = \begin{bmatrix} 1 & -0.0323 & -0.0323 & -0.0323 \\ -0.0323 & 1 & -0.0323 & -0.0323 \\ -0.0323 & -0.0323 & 1 & -0.0323 \\ -0.0323 & -0.0323 & -0.0323 & 1 \end{bmatrix} \qquad (18)$$

The results obtained using the PN codes are shown in figure 5. Some results are given in table 4a for Conventional detector, and 4b for MMSE detector.

Table 4a. Conventional detector

RSZ (dB)	2	4	6	8	10
BER (dB)	-9.82	-14.43	-16.39	-22.01	-29.05

Table 4b. MMSE detector

RSZ (dB)	2	4	6	8	10
BER (dB)	-9.95	-12.48	-16.28	-22.49	-30.01

Comparing with figure 1, it can be observed that the results are very close with the ones obtained in perfect correlation conditions (the difference being less 0.5 dB at all SNR's); moreover, there is no significant difference between the conventional and the MMSE multiuser detectors algorithms. This can be intuitively deduced from the correlation matrix, which shows that even if the codes are not perfectly orthogonal, the inter-correlation coefficient is relatively small $(\rho_{12} = \rho_{13} = \rho_{14} = -0.0323)$ and it doesn't affect significantly the performances of the MMSE multiuser system.

Figure 6 shows the average FFT of the signal transmitted through the common channel. The calculated mean value of the FFT, within all its frequency range, is 14.1 dB, which is 7 dB smaller then the one obtained by using Walsh-Hadamard codes. Moreover, the spectral components are more uniformly distributed within its bandwidth, the peak values being less then 30 dB.

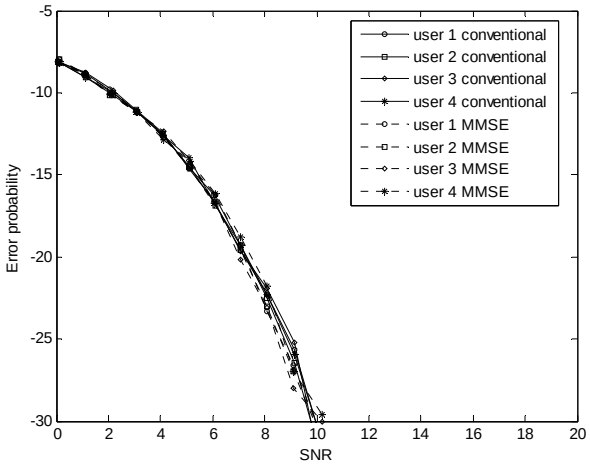

Fig.5. BER versus SNR for conventional and PN codes length 31, generator polynomial (17)

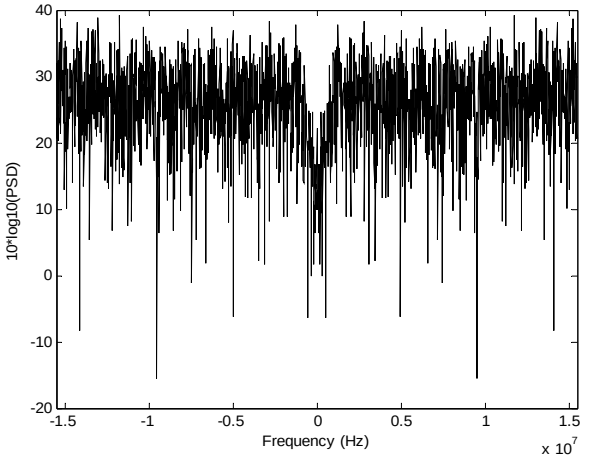

Fig.6. Averaged FFT for multiuser receiver using PN codes of length 31

3.2 Gold sequences of length 32

Finally, we will take into consideration the Gold codes that are derived from the PN ones by adding the PN code from C and the same code decimated with 3. Different phases of the same Gold code are used to separate the users. The cross-correlation matrix is

$$R = \begin{bmatrix} 1.0000 & 0.2258 & -0.0323 & -0.0323 \\ 0.2258 & 1.0000 & 0.2258 & -0.0323 \\ -0.0323 & 0.2258 & 1.0000 & 0.2258 \\ -0.0323 & -0.0323 & 0.2258 & 1.0000 \end{bmatrix} \quad (19)$$

The results obtained using the Gold codes are shown in figure 7. Some results are given in table 5a for Conventional detector, and 5b for MMSE detector.

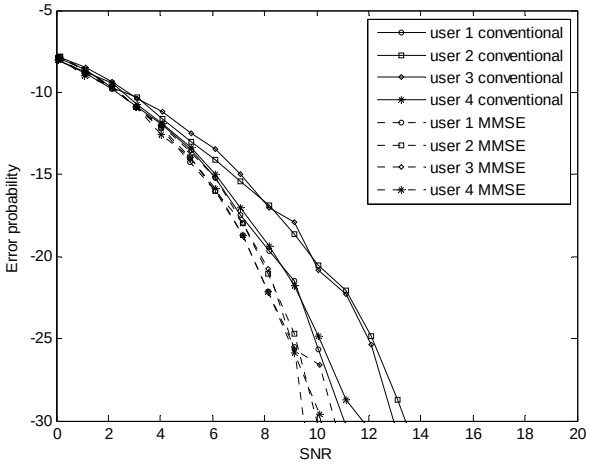

Fig.7. BER versus SNR for conventional and Gold codes length 31

Table 5a. Conventional detector

RSZ (dB)	2	4	6	8	10
BER $u_{2\&3}$ (dB)	-9.25	-11.29	-13.67	-16.63	-20.43
BER $u_{1\&4}$ (dB)	-9.6	-11.84	-14.92	-19.11	-24.71

Table 5b MMSE detector

RSZ (dB)	2	4	6	8	10
BER $u_{2\&3}$ (dB)	-9.53	-12.00	-15.31	-20.46	-27.72
BER $u_{1\&4}$ (dB)	-9.55	-12.3	-15.73	-21.63	-30.05

It can be seen that users 2 (closely correlated with user 1 and 3 and less correlated with user 1) and 3 (closely correlated with user 2 and 4 and less correlated with user 1) $\rho_{12} = \rho_{23} = 0.2258$ achieve higher BER then users 1 (closely correlated with 2 and less correlated with 3 and 4) and 4 (closely correlated with 3 and less correlated with 1 and 2) $\rho_{13} = \rho_{14} = \rho_{23} = -0.0323$. The conventional detector achieves a loss of almost 10 dB in SNR at RSZ=10dB in the most unfavorable case while the MMSE one has close results to the ones obtained in ideal correlation conditions.

Figure 8 shows the averaged FFT of the signal transmitted through the common channel. The calculated mean value of the FFT, within all its frequency range, is 16.87 dB, which only approximately 3dB larger then the one obtained by using PN codes, but the spectral components are less uniformly distributed within its bandwidth, reaching peak values being as high as 60 dB (double the values obtained by using PN codes).

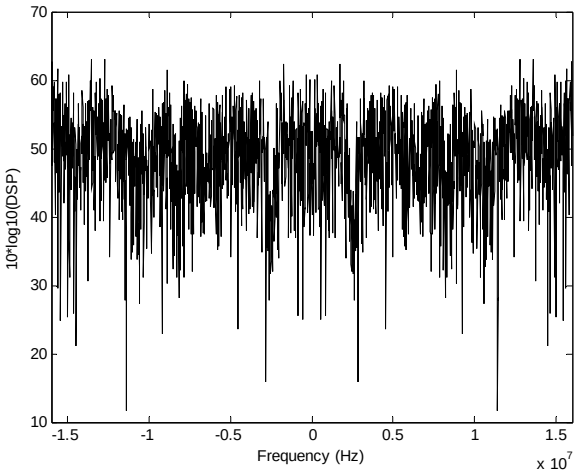

Fig.8. Averaged FFT for multiuser receiver using Gold codes of length 31

4. CONCLUSIONS

From the results presented above, several conclusions can be highlighted:

- both conventional and MMSE multiuser receiver using Walsh-Hadamard codes of length 32 achieve very good performances if the codes are perfectly orthogonal (i.e. perfectly aligned); a small missalignment between users may lead to large cross-correlation coefficients and a significant degradation of the results obtained with respect to the BER; the degradation due to inter-correlation between users increase as the SNR increases. The conventional receiver is more sensitive to cross-correlation between users the the MMSE one, since the degradation achieved for the same conditions is larger. From spectral point of view, the Walsh-Hadamard does not spread the signal uniformly within the whole bandwidth, the spectral distribution being also dependent on the particular codes chosen;
- the PN codes are a good candidate for spreading codes in MMSE multiuser receivers since they have small inter-correlation values, so the results obtained are close to the ones achieved in perfect correlation conditions, for both conventional and MMSE receiver. From spectral point of view the signal is uniformly distributed within its bandwidth, this distribution being independent of the codes chosen;
- the Gold codes have also a good behavior, but not as good as the PN ones. For MMSE receiver the results are close to the one achieved in optimal conditions, while for the conventional receiver the inter-correlation might lead to a degradation of less then 10 dB in BER. From spectral point of view the signal is more distributed then in the

case of Walsh-Hadamard codes, but less uniform the in the case of ON codes.

5. ACKNOWLEDGMENTS

The research activity for this paper was supported by UEFISCDI Romania under the grant PNCDI-II ID_1695 "Contribution to the development of the video signals processing and coding in multiuser wireless systems through the psycho-perceptual quality parameters optimization" between UEFISCDI and UPB No 635/15.01.2009 for the period 2009-2011 and under the grant PNCDI-II "Partnership" no. 12-126/2008 "Hybrid wireless access system with unique addressing (SAWHAU)".

6. REFERENCES

[1] VERDU, S., *Multiuser Detection,* Cambridge University Press, 1988.
[2] RASHID, M. M., HOSSAIN, E., BHARGAVA, V. K., "Cross-layer analysis of downlink V-BLAST MIMO transmission exploiting multiuser diversity", *IEEE Transactions on Wireless Communications*, Vol. 8, no. 9, September 2009 , pp. 4568-4579.
[3] TRIVELLATO, M., TOMASIN, S., BENVENUTO, N., "On channel quantization and feedback strategies for multiuser MIMO-OFDM downlink systems", *IEEE Transactions on Communications*, Vol. 57, no. 9, September 2009 , pp. 2645-2654.
[4] SAKRISON, D. J., "Stochastic approximation: A recursive method for solving regression problems," in *Advances in Communication Systems 2*, A. V. Balakrishnan, Ed. New York: Academic, 1966, pp. 51–106.
[5] LUPAS, R. and VERDU, S., "Linear multiuser detectors for synchronous code-division multiple-access channels," *IEEE Trans. Inform. Theory*, vol. 35, pp. 123–136, Jan. 1989.
[6] FAHMY, Y. A., MOURAD, H. M. and AL-HUSSAINI, E. K., "Multi-User MIMO Mobile CDMA Uplink System Employing Turbo Coding and Joint Detection Through a Multipath Rayleigh Fading Channel", *Wireless Personal Communications* (Springer), Volume 38, Number 3 / August, 2006, p. 325-341.
[7] TSENG, S.-M., "Vector Channel Estimation and Multiuser Detection for Multicarrier DS CDMA in Time and Frequency Selective Fading Channels", *Wireless Personal Communications* (Springer), Volume 43, Number 2 / October, 2007, p. 481–494.
[8] SAAIFAN, K. A., AL-HUSSAINI, E. K., "Diversity Reception of an Asynchronous Blind Adaptive Multiuser Detector Through Correlated Nakagami Fading Channel", *Wireless Personal Communications* (Springer), Volume 40, Number 4 / March, 2007, p. 539–555.
[9] LUO, J., *Improved Multiuser detection in Code Division Multiple Access Communications,* PhD Thesis, University of Connecticut, 2002.
[10] YANG, L., HANZO, L., "Adaptive Space-Time-Spreading-Assisted Wideband CDMA Systems Communicating over Dispersive Nakagami Fading Channels", *EURASIP Journal of Wireless Communications and Networking,* 2005 pp. 216-230.
[11] ANGELOSANTE, D., BIGLIERI, E., LOPS, M., "Multiuser detection in a Dynamic Environment – Part II: Joint User Identification and Parameter Estimation", *IEEE Transactions on Information Theory*, vol. 55, No. 5, May 2009, pp. 2365-2374
[12] CAMPO, A. T., GUILLEN I FABREGAS, A., BIGLIERI, E., "High-SNR Analysis of Optimum Multiuser Detection with an Unknown Number of Users", *Information Theory Workshop 2009*, ITW2009, pp. 283-287.
[13] HALUNGA, S., VIZIREANU, D.N., "Performance evaluation for conventional and MMSE multiuser detection algorithms in imperfect reception conditions", *Digital Signal Processing*, Elsevier, ISSN: 1051-2004, 2010, p 166-168
[14] HALUNGA, S., VIZIREANU, D.N., FRATU, O., „Imperfect cross-correlation and amplitude balance effects on conventional multiuser decoder with turbo encoding", *Digital Signal Processing*, Elsevier, ISSN: 1051-2004, 2010, p. 191-200

SIGNAL PROCESSING TECHNIQUES FOR SYNCHRONIZATION OF WIRELESS SENSOR NETWORKS

[1]JAEHAN LEE, [2]YIK-CHUNG WU, [3]QASIM CHAUDHARI, [4]KHALID QARAQE, [5]ERCHIN SERPEDIN

[14,5]Texas A&M University, Electrical and Computer Eng., College Station, TX 77843-3128, USA,[2]EEE Dept.,University of Hong Kong,Pokfulam Road, Hong Kong;[3]Iqra University, Islamabad, Pakistan

ABSTRACT

Clock synchronization is a critical component in wireless sensor networks, as it provides a common time frame to different nodes. It supports functions such as fusing voice and video data from different sensor nodes, time-based channel sharing, and sleep wake-up scheduling, etc. Early studies on clock synchronization for wireless sensor networks mainly focus on protocol design. However, clock synchronization problem is inherently related to parameter estimation, and recently, studies of clock synchronization from signal processing point-of-view begin to emerge.
In this article, a survey of latest advances on clock synchronization is provided by adopting a signal processing viewpoint. We demonstrate that many existing and intuitive clock synchronization protocols can be interpreted by common statistical signal processing methods. Furthermore, the use of advanced signal processing techniques for deriving optimal clock synchronization algorithms under challenging scenarios will be illustrated.

Keywords: *Clock Synchronization, Wireless Sensor Networks*

1. INTRODUCTION

The clock or time synchronization problem in Wireless Sensor Networks (WSNs) resumes to finding a procedure for providing a common notion of time across the nodes of WSNs. In general, clock synchronization is viewed as a very critical factor in maintaining the good functioning of wireless sensor networks due mainly to their decentralized organization and timing uncertainties caused by the imperfections in hardware oscillators and message delays at the physical and Medium Access Control (MAC) layers. In addition, synchronization of the nodes of wireless sensor networks is crucial for implementing fundamental operations such as power management, transmission scheduling, data fusion, localization and tracking, and security protocols to name only a few applications.
The clock synchronization issue has been studied thoroughly in the areas of Internet and local-area networks (LANs) for the last several decades. Many existing synchronization algorithms rely on the clock information from GPS (Global Positioning System). However, GPS-based clock acquisition schemes exhibit some weaknesses: GPS is not available ubiquitously (for example, underwater, indoors, under foliage) and requires a relatively high-power receiver, which is not feasible on tiny and cheap sensor nodes. This is the motivation for developing software-based approaches to achieve in-network time synchronization. Among many protocols that have been developed for maintaining synchronization in computer networks, NTP (Network Time Protocol) [1] is conspicuous due to its ubiquitous deployment, scalability, robustness related to failures, and self-configuration in large multi-hop networks. Furthermore, the combination of NTP and GPS has shown that it is capable of achieving high precision on the order of a few microseconds [2]. However, NTP is not proper for a wireless sensor environment, since wireless sensor networks pose a number of challenges of their own; to name a few, limited energy and bandwidth, limited hardware, latency, and unstable network conditions caused by mobility of sensors, dynamic topology, and multi-hopping. Therefore, clock synchronization protocols different from the conventional protocols are needed so as to cope with the challenges specific to WSNs.
One of the most popular clock synchronization protocols in wireless sensor networks is the Reference Broadcast Synchronization (RBS) [3], which is based on the post-facto receiver-receiver synchronization approach. In RBS, a reference broadcast message is sent by a node to two or more neighboring nodes which record their own local clocks at the reception of broadcasted message. After collecting a few readings, the nodes exchange their observations and a linear regression approach is used to estimate their relative clock offset and skew.
Timing Synch Protocol for Sensor Networks (TPSN) [4] is a conventional sender-receiver protocol which assumes two operational stages: the level discovery phase followed by the synchronization phase. During the level discovery phase, the wireless sensor network is organized in the form of a spanning tree, and the global synchronization is achieved by enabling each node to get synchronized with its parent (the node located in the adjacent upper level) by means of a two-way message exchange mechanism through adjusting only its clock offset.
Timing Synchronization protocol for High Latency acoustic networks (TSHL) [5] combines both of these approaches, namely the receiver-receiver (RBS) and sender-receiver (TPSN), in two stages. The Flooding Time Synchronization Protocol (FTSP) [6] also combines the two approaches in the sense that the beacon node sends its time stamps within the reference broadcast messages. The Time Diffusion Protocol (TDP) proposed by [7] achieves network-wide time equilibrium by using an iterative, weighted averaging technique based on a diffusion of messages involving all the nodes

in the synchronization process. Also, the Asynchronous Diffusion Protocol (ADP) [8] uses a diffusion strategy similar to TDP, but the network nodes execute the protocol and correct their clocks asynchronously with respect to each other.

The aim of this tutorial is to provide an introduction to the clock synchronization problem of wireless sensor networks from a statistical signal processing viewpoint. This tutorial might present interest to all practitioners who are looking for techniques to improve the performance of existing protocols such as NTP (Network Time Protocol), TPSN (Time Protocol for Synchronization of Sensor Networks), RBS (Reference Broadcast Synchronization), PBS (Pairwise Broadcast Synchronization), etc., and for developing new synchronization protocols through novel signal processing algorithms with improved performance. We believe that this tutorial will prove also very beneficial to the community of signal processing researchers because it will outline a number of important open research problems and advanced statistical signal processing approaches to solve these challenges.

This paper is organized as follows. Section 1 yields a short introduction into the time synchronization problem, its history and importance. Section 2 discusses three general packet-based synchronization approaches for wireless sensor networks, focuses on the most representative synchronization protocols for wireless sensor networks by outlining their main features, and proposes a variety of statistical signal processing algorithms for improved estimation of clock phase offset. We also address the problem of building clock offset estimators that are robust to the distribution of network delays. Finally, Section 3 concludes the paper with several open research problems and possible solutions to resolve these issues. A special emphasis in this tutorial will be put towards developing optimal signal processing schemes for estimation of clock phase offset in the recent protocols proposed for synchronization of wireless sensor networks.

2. CLOCK SYNCHRONIZATION TECHNIQUES FOR WSNS

In [9], the synchronization protocols can be classified according to a variety of issues and characteristics. However, this paper deals with the synchronization protocols in terms of three general packet-based synchronization approaches; namely, sender-receiver synchronization, receiver-receiver synchronization, and receiver only synchronization. Basically, time synchronization in wireless sensor networks can be obtained by transferring a group of timing messages to the target sensors. The timing messages contain the information about the time stamps measured by the transmitting sensors. There exist two well-known approaches for time synchronization in wireless sensor networks, which are classified as sender-receiver synchronization (SRS) and receiver-receiver synchronization (RRS). Sender-receiver synchronization is based on the conventional model of two-way message exchanges between a pair of nodes. For receiver-receiver synchronization, the nodes to be synchronized receive a beacon packet from a common sender at first, and then compare their receiving time readings of the beacon packet to compute the relative clock offset. Most of the existing clock synchronization protocols count on one of these two mechanisms. For example, the Network Time Protocol (NTP) [1] and the Timing-sync Protocol for Sensor Networks (TPSN) [4] use sender-receiver synchronization because they depend on a series of pairwise synchronization assuming two-way timing message exchange scheme, whereas the Reference Broadcast Synchronization (RBS) [3] adopt receiver-receiver synchronization since it requires pairs of message exchanges among children nodes (except the reference) to compensate their relative clock offsets.

Recently, a new scheme for time synchronization was proposed, which is called receiver-only synchronization (ROS) [10]. This approach aims at minimizing the number of required timing messages and energy consumption during synchronization while preserving a high level of precision. This method can be used to achieve network-wide synchronization with much lesser timing messages than other well-known existing protocols such as TPSN and RBS. In the following sections, we present and analyze each of three synchronization approaches mentioned above more specifically.

2.1. Sender-Receiver Synchronization (SRS)

As mentioned before, this approach is based on the traditional two-way timing message exchange mechanism between two adjacent nodes. The clock model for the two-way message exchange mechanism is shown in Fig. 1, where θ_A denotes the clock offset between Sensor A and Sensor B and timing messages are assumed to be exchanged multiple times. In this figure, the time stamps made during the i_{th} message exchange $T_{1,i}$ and $T_{4,i}$ are measured by the local clock of Sensor A, and $T_{2,i}$ and $T_{3,i}$ are measured by the local clock of Sensor B, respectively. Sensor A sends a synchronization packet, which includes the value of time stamp $T_{1,i}$ to Sensor B. Sensor B receives it at time $T_{2,i}$ and sends an acknowledgement packet to Sensor A at time $T_{3,i}$. This packet contains the value of time stamps $T_{1,i}$, $T_{2,i}$ and $T_{3,i}$. Finally, Sensor A receives the packet at time $T_{4,i}$.

F

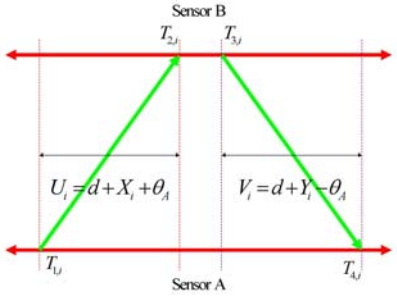

Fig. 1. Two-way message exchange model with clock offset (θ_A : clock offset, d : propagation delay, X_i, Y_i : random delays, $U_i = T_{2,i} - T_{1,i}$, $V_i = T_{4,i} - T_{3,i}$)

Packet delays can be decomposed into four distinct components: send time, access time, propagation time, and receive time [3]. First, *send time* is the time spent by the sender to construct the message, including kernel protocol processing and variable delays introduced by the operating system, e.g., context switches and system call overhead incurred by the synchronization application. Secondly, *access time* is the delay incurred while waiting for access to the transmission channel. Thirdly, *propagation time* is the time for the message to travel from the sender to the destination node through the channel since it left the sender. Lastly, *receive time* is the time for the network interface on the receiver side to get the message and notify the host of its arrival. These delay components can be divided into the fixed part d and the variable part X_i, Y_i. The variable delay portion depends on diverse network parameters such as network status and traffic, and setup. Therefore, any single delay model cannot satisfy every case.

So far, several probability density function (PDF) models have been proposed for modeling the random delays, and Gaussian, exponential, Gamma, and Weibull PDFs are the most widely deployed [11], [12]. Gaussian delay model is proper if the delays are assumed to be the addition of numerous independent random processes. [3] showed that the variable portion of delays can be modeled as Gaussian random variables with 99.8% confidence by the chi-squared test. On the other hand, a single-server M/M/1 queue can properly represent the cumulative link delay for point-to-point hypothetical reference connection, where the random delays are independently modeled as exponential random variables [13]. In this paper, we mainly deal with the situations where random delays are Gaussian or exponential.

TPSN is one of the representative examples of sender-receiver synchronization and uses the two-way message exchange scheme shown in Fig. 1 to acquire the synchronization between two sensors [4]. In [4], the authors argue that for sensor networks, the classical approach of implementing a handshake between a pair of nodes is better than synchronizing a set of receivers. This observation results from time stamping the packets at the time when they are sent, namely, at MAC layer, which is indeed feasible for sensor networks. [4] provided the comparison of the performance of TPSN with that of RBS based on the receiver-receiver synchronization approach, and illustrated that TPSN provides about two times better performance, in terms of accuracy, than RBS on the Berkeley motes platform. The TPSN protocol consists of two steps; namely, level discovery phase and synchronization phase. In level discovery phase, a hierarchical topology is created in the network. Each node is assigned a level in this hierarchical structure and a node belonging to level *i* can communicate with at least one node belonging to level *i* - 1. Only one node is assigned level 0, and it is referred to as the root node. Once the hierarchical tree structure is set up, the root node initiates the second step of the protocol, called the synchronization phase. In this second phase, a node with level *i* synchronize with a node with level *i* - 1. After all, every node is synchronized to the root node with level 0 and TPSN achieves network-wide time synchronization.

2.1.1 Clock Offset Estimation

Assuming that the clock frequencies of two sensors are equal during the synchronization period, and both X_i and Y_i are normal distributed random variables with mean μ and variance $\sigma^2/2$, U_i and V_i can be expressed as the following.

$$U_i = T_{2,i} - T_{1,i} = d + \theta_A + X_i, \quad V_i = T_{4,i} - T_{3,i} = d - \theta_A + Y_i \tag{1}$$

, where the variables θ_A, d, X_i and Y_i denote the clock offset between the two nodes, the propagation delay, and the variable portions of delays, respectively. By doing some mathematical manipulations, we can obtain the likelihood function based on the observations U_i and V_i, which is given by

$$L(\theta_A, \mu, \sigma^2) = (\pi\sigma^2)^{-\frac{N}{2}} e^{-\frac{1}{\sigma^2}\left[\sum_{i=1}^{N}(U_i - d - \theta_A - \mu)^2 + \sum_{i=1}^{N}(V_i - d + \theta_A - \mu)^2\right]} \tag{2}$$

where N represents the number of message exchanges. We can obtain the following equation by differentiating the log-likelihood function.

$$\frac{\partial \ln L(\theta_A)}{\partial \theta_A} = -\frac{2}{\sigma^2}\left[\sum_{i=1}^{N}(U_i - d - \theta_A - \mu) + \sum_{i=1}^{N}(V_i - d + \theta_A - \mu)\right] \tag{3}$$

Therefore, the maximum likelihood estimate (MLE) of clock offset is given by [15]

$$\hat{\theta}_A = \arg\max_{\theta_A}[\ln L(\theta_A)] = \frac{\sum_{i=1}^{N}(U_i - V_i)}{2N} = \frac{\overline{U} - \overline{V}}{2}. \tag{4}$$

Also, since the expected value of equation (4) is 0, the regularity condition [[14], p.30] holds for the above MLE. Hence, the Cramer-Rao lower bound (CRLB) for the MLE can be derived by differentiating (4) with regard to θ_A, which is given by

$$\mathrm{var}(\hat{\theta}_A) \geq -E\left[\frac{\partial^2 \ln L(\theta_A)}{\partial \theta_A^2}\right]^{-1} = \frac{\sigma^2}{4N}. \tag{5}$$

For exponential delay model, the likelihood function based on the observations $\{U_i\}_{i=1}^{N}$ and $\{V_i\}_{i=1}^{N}$ is

$$L(\theta_A, \lambda) = \lambda^{-2N} e^{-\frac{1}{\lambda}\sum_{i=1}^{N}[U_i + V_i - 2d]} \cdot \prod_{i=1}^{N} I\left[U_i - \theta_A - d \geq 0, V_i + \theta_A - d \geq 0\right] \tag{6}$$

where λ is the mean value of X_i and Y_i, and $I(\cdot)$ represents the indicator function; in other words, $I(\cdot)$ is 1 whenever its inner condition holds, otherwise it is 0. In [16], it was proven that the maximum likelihood estimate of θ_A exists when d is unknown and is given by

$$\hat{\theta}_A = \frac{\min_{1 \leq i \leq N} U_i - \min_{1 \leq i \leq N} V_i}{2} \tag{7}$$

,where N stands for the number of observations of delay measurements. We note that only one round of message

exchange is performed (N = 1), the MLEs of clock offset for both Gaussian and exponential delay models become $\hat{\theta}_A = (U_1 - V_1)/2$, which is the same as the clock estimator given in [4].

By letting $\{U_{(i)}\}_{i=1}^{N}$ and $\{V_{(i)}\}_{i=1}^{N}$ represent the order statistics of the sequences of delay observations $\{U_i\}_{i=1}^{N}$ and $\{V_i\}_{i=1}^{N}$, respectively, equation (7) can be expressed as

$$\hat{\theta}_A = \frac{U_{(1)} - V_{(1)}}{2} = \theta_A + \frac{X_{(1)} - Y_{(1)}}{2} \tag{8}$$

, where $X_{(1)}$ and $Y_{(1)}$ denote the order statistics corresponding to $\{X_i\}_{i=1}^{N}$ and $\{Y_i\}_{i=1}^{N}$, respectively. Let $Z \triangleq U_{(1)} - V_{(1)}$, then the probability density function of Z as a function of θ_A is expressed by

$$f_W(w;\theta_A) = \begin{cases} \dfrac{N}{(\lambda_1+\lambda_2)} e^{-\frac{N}{\lambda_1}(w-2\theta_A)}, & w > 2\theta_A \\ \dfrac{N}{(\lambda_1+\lambda_2)} e^{\frac{N}{\lambda_2}(w-2\theta_A)}, & w < 2\theta_A \end{cases} \tag{9}$$

where λ_1 and λ_2 are the mean values of X_i and Y_i, respectively. In case that the random delays are symmetric, $\lambda_1 = \lambda_2 = \lambda$, then the above equation becomes

$$f_W(w;\theta_A) = \frac{N}{2\lambda} e^{-\frac{N}{\lambda}|w-2\theta_A|} \tag{10}$$

Since this equation is finite and its expected value is 0, the regularity condition of the Cramer-Rao lower bound (CRLB) is satisfied. Applying some mathematical manipulations, we can obtain the CRLB of clock offset $\hat{\theta}_A$, which is given by

$$\mathrm{var}(\hat{\theta}_A) \geq -E\left[\left(\frac{\partial \ln f_W(w;\theta_A)}{\partial \theta_A}\right)^2\right]^{-1} = \frac{\lambda^2}{4N^2} \tag{11}$$

It is clear that the performance of the maximum likelihood estimate of the clock offset strongly depend on the type of random delay models. In other words, observing the facts that the distribution of network delays in general can not be predicted accurately, and the estimators reported in the literature are not robust with respect to the unknown possibly time-varying distribution of network delays, we have to be able to address the problem of building clock offset estimators that are robust to the distribution of network delays.

Now we are going to take a look at an estimator based on the Gaussian Mixture Kalman Particle Filter (GMKPF) [17] that is robust to the distribution of random delays. With the observation samples $\mathbf{z}_k = [U_k, V_k]^T$, the goal is to find the minimum variance estimator of the unknown clock offset θ_A, where $U_k = T_{2,k} - T_{1,k} = d + \theta_A + L_k$ and $V_k = T_{4,k} - T_{3,k} = d - \theta_A + M_k$. For convenience, the notation $x_k \triangleq \theta_A$ will be used henceforth. Therefore, it turns out to determine the estimator, $\hat{x}_k = E\{x_k \mid \mathbf{Z}^l\}$, where $\mathbf{Z}^l$ denotes the set of observed samples up to time l, $\mathbf{Z}^l = \{\mathbf{z}_0, \mathbf{z}_1, \ldots, \mathbf{z}_l\}$. Since the clock offset value is assumed to be a constant, the clock offset can be modeled as obeying a Gauss-Markov dynamic channel model of the following form, $x_k = Fx_{k-1} + v_{k-1}$, where F is the state transition matrix for clock offset. The additive noise component v_k can be modeled as Gaussian with zero mean and covariance $E\{v_k v_k^T\} = Q$. The vector observation model is given from the observed samples and it is expressed as

$$\mathbf{z}_k = \begin{bmatrix} d + \theta_A + L_k \\ d - \theta_A + M_k \end{bmatrix} = \begin{bmatrix} 1 \\ 1 \end{bmatrix} d + \begin{bmatrix} 1 \\ -1 \end{bmatrix} x_k + \mathbf{n}_k$$

where the observation noise vector $\mathbf{n}_k = [L_k, M_k]^T$ accounts for the random delays. We note that the equations related to x_k and $\mathbf{z}_k$ recast our initial clock offset estimation problem into a Gauss-Markov estimation problem with unknown states.

Particle filtering is a sequential Monte Carlo sampling method built within the Bayesian paradigm. From a Bayesian viewpoint, the posterior distribution is the main entity of interest. However, due to the non-Gaussianity of the above model, the analytical expression of the posterior distribution cannot be obtained in closed-form expression, except for some special cases like Gaussian or exponential probability density functions. Alternatively, particle filtering can be applied to approximate the posterior distribution by stochastic samples generated using a sequential importance sampling strategy.

Since the particle filtering with the prior importance function employs no information from observations in proposing new samples, its use is often ineffective and leads to poor filtering performance. Herein, we take a look at a slightly changed version of the Gaussian Mixture Sigma Point Particle Filter (GMSPPF) proposed in [18]. The GMSPPF is a family of methodologies that make use of hybrid sequential Monte Carlo simulation and a Gaussian sum filter to efficiently estimate posterior distributions of unknown states in a non-linear dynamic system. However, in our state space modeling, we do modify this method appropriately because of the linear model. Following [18], we will next describe briefly the general framework assumed by the GMKPF method, obtained by replacing the Sigma Point Kalman Filter (SPKF) with a Kalman Filter (KF). We next outline the main features of the approach. First, we remark that any probability density *p(x)* can be approximated as closely

as desired by a Gaussian mixture model (GMM) of the following form [19], $p(x) \approx p_g(x) = \sum_{g=1}^{G} \alpha^{(g)} N(x; \mu^{(g)}, P^{(g)})$, where G represents the number of mixing components, $\alpha^{(g)}$ denotes the mixing weights and $N(x; \mu^{(g)}, P^{(g)})$ is a normal distribution. Hence, the predicted and updated Gaussian components, i.e., the means and covariances of the involved probability densities (posterior, importance, and so on) are calculated using the Kalman filter (KF) instead of the Sigma Point Kalman Filter (SPKF) [18], [20]. Since the state and observation equations are linear, the KF was employed instead of the SPKF. Therefore, the resulting approach is called the Gaussian mixture Kalman particle filter (GMKPF). In order to avoid the particle depletion problem in cases where the observation (measurement) likelihood is very peaked, the GMKPF represents the posterior density by a GMM which is recovered from the re-sampled equally weighted particle set using the Expectation-Maximization (EM) algorithm.

A pseudo-code for a GMKPF algorithm that is fit for estimating clock offsets in non-Gaussian delay models are described below.

Algorithm

1) At time k-1, initialize the densities
- The posterior density is approximated by $p_g(x_{k-1} \mid \mathbf{z}_{k-1}) = \sum_{g=1}^{G} \alpha_{k-1}^{(g)} N(x_{k-1}; \mu_{k-1}^{(g)}, P_{k-1}^{(g)})$
- The process noise density is approximated by $p_g(v_{k-1}) = \sum_{i=1}^{I} \beta_{k-1}^{(i)} N(v_{k-1}; \mu_{v_{k-1}}^{(i)}, Q_{k-1}^{(i)})$
- The observation noise density is approximated by $p_g(\mathbf{n}_k) = \sum_{j=1}^{J} \gamma_k^{(j)} N(\mathbf{n}_k; \mu_{\mathbf{n}_k}^{(j)}, R_k^{(j)})$

2) Pre-prediction step
- Calculate the pre-predictive state density using KF, $\tilde{p}_g(x_k \mid \mathbf{z}_{k-1})$
- Calculate the pre-posterior state density using KF, $\tilde{p}_g(x_k \mid \mathbf{z}_k)$

3) Prediction step
- Calculate the predictive state density using GMM, $\hat{p}_g(x_k \mid \mathbf{z}_{k-1})$
- Calculate the posterior state density using GMM, $\hat{p}_g(x_k \mid \mathbf{z}_k)$

4) Observation Update step
- Draw N samples $\{\chi_k^{(l)}; l = 1, \cdots, N\}$ from the importance density function, $q(x_k \mid \mathbf{z}_k) = \hat{p}_g(x_k \mid \mathbf{z}_k)$
- Calculate their corresponding importance weights: $\tilde{w}_k^{(l)} = \dfrac{p(\mathbf{z}_k \mid \chi_k^{(l)}) \hat{p}_g(\chi_k^{(l)} \mid \mathbf{z}_{k-1})}{\hat{p}_g(\chi_k^{(l)} \mid \mathbf{z}_k)}$
- Normalize the weights: $w_k^{(l)} = \tilde{w}_k^{(l)} / \sum_{l=1}^{N} \tilde{w}_k^{(l)}$
- Approximate the state posterior distribution using the EM-algorithm, $p_g(x_k \mid \mathbf{z}_k)$

5) Infer the conditional mean and covariance:
- $\overline{x}_k = \sum_{l=1}^{N} \tilde{w}_k^{(l)} \chi_k^{(l)}$ and $\overline{P}_k = \sum_{l=1}^{N} \tilde{w}_k^{(l)} (\chi_k^{(l)} - \overline{x}_k)(\chi_k^{(l)} - \overline{x}_k)^T$

Fig. 2 and Fig. 3 show the MSE (Mean Square Error) of the estimators assuming that the random delay models are asymmetric Gaussian, exponential, Gamma, Weibull pdfs, respectively. The subscripts 1 and 2 are used to differentiate the parameters of delay distributions corresponding to uplink and downlink, respectively. Note that the GMKPF (G=3 and G=5) performs much better when compared to SGML or SEML. The GMKPF-estimator did adaptively fit the posterior probability function(likelihood function) using EM, so the performance of GMKPF depend on the ability of GMM fitting for the distribution such as process noise, measurement noise, posterior PDFs, and so on.

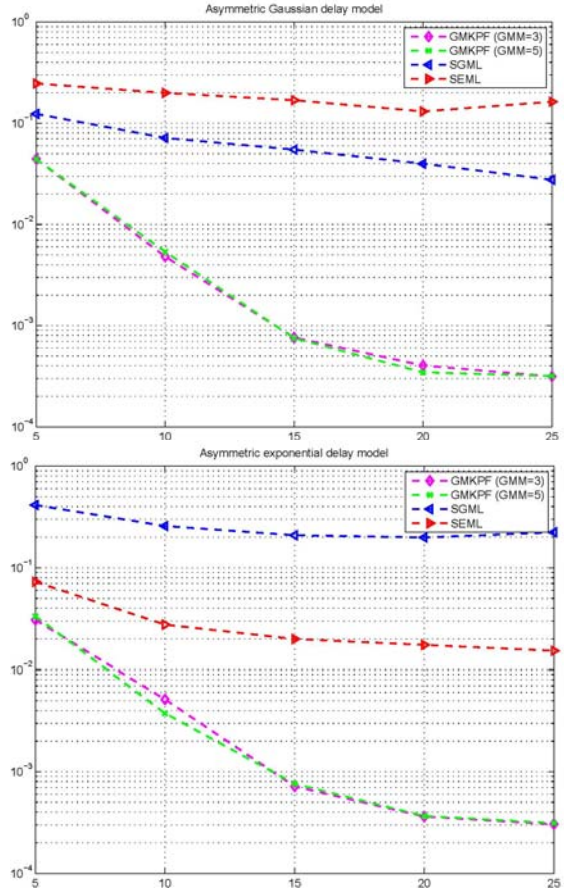

Fig. 2. MSEs of clock offset estimators for asymmetric Gaussian ($\sigma_1 = 1, \sigma_2 = 4$) and exponential random delays ($\lambda_1 = 1, \lambda_2 = 5$)

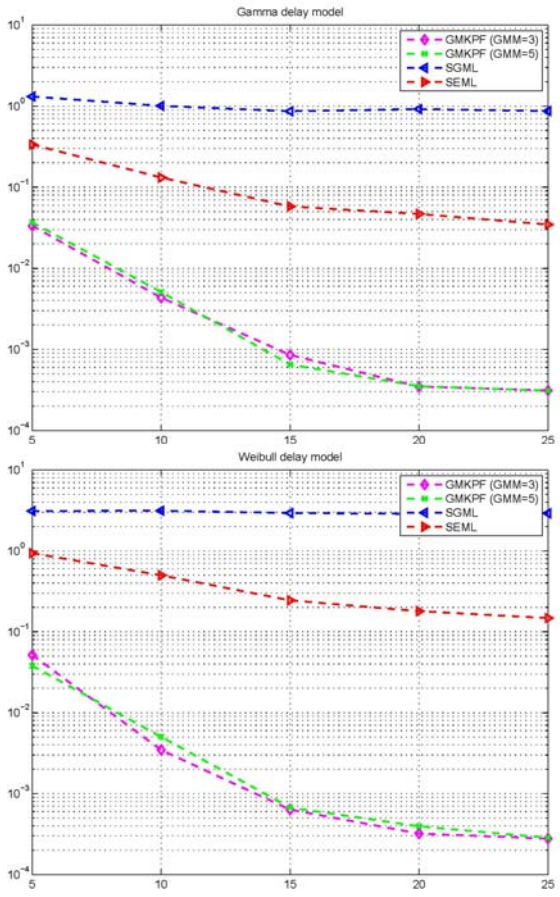

Fig. 3. MSEs of clock offset estimators for Gamma ($\alpha_1 = 2, \beta_1 = 1$) and Weibull random delays ($\alpha_1 = 2, \beta_1 = 2; \alpha_2 = 6, \beta_2 = 2$)

2.2. Receiver-Receiver Synchronization (RRS)

This method is an approach to synchronize a group of children nodes which receive the beacon messages from a parent node. RBS (Reference Broadcast Synchronization) protocol [3] is a representative example of receiver-receiver synchronization. The fundamental property of RBS is that a broadcast message is only used to synchronize a set of receivers with one another, in contrast with traditional protocols that synchronize the sender of a message with its receiver. By doing this, it eliminates the Send Time and Access Time from the critical path. This is a significant advantage for synchronization in a LAN, where the Send Time and Access Time are typically the main reasons for the non-determinism in the latency.

An RBS broadcast is always used as a relative time reference, and never to communicate an absolute time value. Indeed, this property removes the error caused by the Send Time and Access Time: each receiver synchronizes to a reference packet which was inserted into the physical channel at the same instant. The message itself does not include a timestamp generated by the sender, nor is it important exactly when it is sent. As a matter of fact, the broadcast does not even need to be a dedicated time synchronization packet. Almost any extant broadcast can be used to recover timing information - for example, ARP packets in Ethernet, or the broadcast control traffic in wireless networks (e.g., RTS/CTS exchanges or route discovery packets).

As mentioned above, RBS eliminates the effect of the error sources of Send Time and Access Time altogether; thus, the two remaining factors are Propagation Time and Receive Time. In [25], the Propagation Time is considered to be effectively 0. The propagation speed of electromagnetic signals through air is close to *c* (1nsec/foot), and through copper wire about 2*c*=3. In case of a LAN or ad-hoc network spanning tens of feet, propagation time is at most tens of nanoseconds, which does not contribute significantly to the sec-scale error budget. Moreover, RBS is only sensitive to the difference in propagation time between pair of receivers.

The simplest form of RBS is broadcasting a single message to two receiver nodes, making it possible for them to estimate their relative clock offsets. In other words, at first, a sender broadcasts a reference packet to two receivers (*i* and *j*) and then each receiver records the time when the reference packet arrived, according to its own local clock. Finally, the receivers exchange their observation data. Based on this single broadcast alone, the receivers have sufficient information to form a local or relative timescale. This basic RBS scheme can be extended by allowing synchronization between *n* receivers by a single packet, where n may be larger than two or increasing the number of reference packets to acquire higher precision. Numeric simulation results in [5] shows that in the simplest case of 2 receivers, 30 reference broadcasts can improve the precision from 11 sec to 1.6 sec, after which there is a point of diminishing return. This redundancy was also used for estimating clock skews. Instead of averaging the phase offsets from multiple observations, a least-squares linear regression method was applied. This presents a fast, closed-form method for finding the best fit line through the phase error observations over time. The clock offset and skew of the local node with respect to the remote node can be recovered from the intercept and slope of the line. Now let us take a look at one method of estimating clock offset and clock skew jointly in RBS protocol.

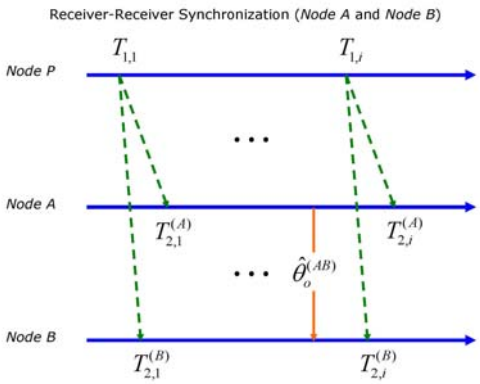

2.2.1 Joint Clock Offset and Clock Skew Estimation

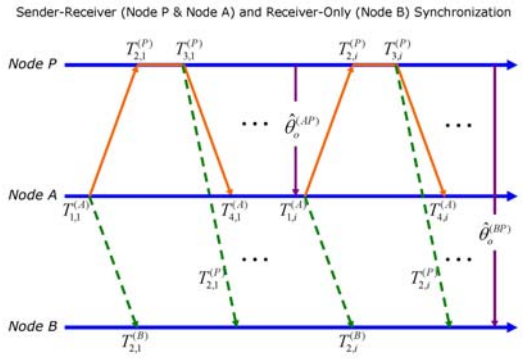

Fig. 4. Clock synchronization models in receiver-receiver and sender-receiver & receiver-only synchronizations

Consider a parent node *P* and arbitrary nodes *A* and *B*, which are located within the communication range of the parent node *P*. In Fig. 4, we assume that both *Node A* and *Node B* receive the i_{th} beacon from *Node P* at $T_{2,i}^{(A)}$ and $T_{2,i}^{(B)}$ of their own clocks, respectively. Nodes *A* and *B* record the arrival time of the broadcast packet according to their own timescales and then exchange their time stamps. Suppose that $X_i^{(PA)}$ denotes the nondeterministic delay components (random portion of delays) and $d^{(PA)}$ denotes the deterministic delay component (propagation delay) from *Node P* to *Node A*, then $T_{2,i}^{(A)}$ can be written as

$$T_{2,i}^{(A)} = T_{1,i} + d^{(PA)} + X_i^{(PA)} + \theta_o^{(PA)} + \theta_s^{(PA)} \cdot (T_{1,i} - T_{1,1}) \tag{12}$$

$T_{1,i}$ where is the transmission time at the reference node, $\theta_o^{(PA)}$ and $\theta_s^{(PA)}$ are the clock offset and skew of *Node A* with regard to the reference node, respectively. Likewise, the arrival time at *Node B* can be decomposed as

$$T_{2,i}^{(B)} = T_{1,i} + d^{(PB)} + X_i^{(PB)} + \theta_o^{(PB)} + \theta_s^{(PB)} \cdot (T_{1,i} - T_{1,1}) \tag{13}$$

where $d^{(PB)}$, $X_i^{(PB)}$, $\theta_o^{(PB)}$ and $\theta_s^{(PB)}$ represent the propagation delay, random delays, clock offset and skew of *Node B* with respect to the parent node, respectively. From these two equations above,

$$T_{2,i}^{(A)} - T_{2,i}^{(B)} = \theta_o^{(BA)} + \theta_s^{(BA)} \cdot (T_{1,i} - T_{1,1}) + d^{(PA)} - d^{(PB)} + X_i^{(PA)} - X_i^{(PB)} \tag{14}$$

where $\theta_o^{(BA)} \equiv \theta_o^{(PA)} - \theta_o^{(PB)}$ and $\theta_s^{(BA)} \equiv \theta_s^{(PA)} - \theta_s^{(PB)}$ are thee relative clock offset and skew between *Node A* and *Node B* at the instant the i_{th} broadcast message packet is received from the reference node, respectively. Random delays $X_i^{(PA)}$ and $X_i^{(PB)}$ are assumed to be Gaussian random variables with mean μ and variance $\sigma^2/2$.

In equation (14), we can define the noise component as $z[i] \equiv \mu' + X_i^{(PA)} - X_i^{(PB)}$, where $\mu' = d^{(PA)} - d^{(PB)}$ and $z[i] \equiv N(\mu', \sigma^2)$. Putting $x[i] \equiv T_{2,i}^{(A)} - T_{2,i}^{(B)} - \mu'$ and $w[i] \equiv z[i] - \mu'$ gives the following matrix notation and the linear regression technique can be applied to the equation.

$$\mathbf{x} = \mathbf{H}\boldsymbol{\theta} + \mathbf{w} \tag{15}$$

, where $\mathbf{x} = [x[1]\ x[2] \cdots x[N]]^T$, $\mathbf{w} = [w[1]\ w[2] \cdots w[N]]^T$, $\boldsymbol{\theta} = [\theta_o^{(BA)}\ \theta_s^{(BA)}]^T$, and

$$\mathbf{H} = \begin{bmatrix} 1 & 1 & \cdots & 1 \\ 0 & T_{1,2} - T_{1,1} & \cdots & T_{1,N} - T_{1,1} \end{bmatrix}^T$$

By using the theorem from [14], [Theorem 3.2, pp. 44], we can obtain the minimum variance unbiased estimator (MVUE) for the relative clock offset and skew, which is given by

$$\hat{\boldsymbol{\theta}} = (\mathbf{H}^T\mathbf{H})^{-1}\mathbf{H}^T\mathbf{x} \quad , \quad \mathbf{I}(\boldsymbol{\theta}) = \frac{\mathbf{H}^T\mathbf{H}}{\sigma^2}$$

where $\mathbf{I}(\boldsymbol{\theta})$ is the Fisher information matrix. By applying some mathematical operations, the joint clock offset and skew estimator can be written as [10]

$$\begin{bmatrix} \hat{\theta}_o^{(BA)} \\ \hat{\theta}_s^{(BA)} \end{bmatrix} = \frac{1}{N\sum_{i=1}^{N} D_i^2 - \left[\sum_{i=1}^{N} D_i\right]^2} \begin{bmatrix} \sum_{i=1}^{N} D_i^2 \sum_{i=1}^{N} x[i] - \sum_{i=1}^{N} D_i \sum_{i=1}^{N} D_i \cdot x[i] \\ N\sum_{i=1}^{N} D_i \cdot x[i] - \sum_{i=1}^{N} D_i \sum_{i=1}^{N} x[i] \end{bmatrix}$$

where $D_i \equiv T_{1,i} - T_{1,1}$. Inverting the Fisher information matrix $\mathbf{I}(\boldsymbol{\theta})$ gives the Cramer-Rao Lower Bound (CRLB). Therefore,

$$\mathrm{var}(\hat{\theta}_o^{(BA)}) \geq \frac{\sigma^2 \sum_{i=1}^{N} D_i^2}{N\sum_{i=1}^{N} D_i^2 - \left[\sum_{i=1}^{N} D_i\right]^2},$$

$$\mathrm{var}(\hat{\theta}_s^{(BA)}) \geq \frac{N\sigma^2}{N\sum_{i=1}^{N} D_i^2 - \left[\sum_{i=1}^{N} D_i\right]^2} \tag{17}$$

On the other hand, under the exponential random delay model for Reference Broadcast Synchronization (RBS), the joint maximum likelihood estimator (JMLE) and Gibbs Sampler can be used for estimating clock offset and skew, which are proposed in [21], where lower and upper bounds for the mean squared errors (MSEs) of JMLE and Gibbs Sampler are introduced in terms of the MSE of the Uniform Minimum Variance Unbiased

estimator (UMVUE) and the conventional Best Linear Unbiased Estimator (BLUE), respectively.

2.3. Receiver-Only Synchronization (ROS)

The communication range of a sensor is strictly limited to a circle whose radius is dependent on the transmission power owing to the energy constraint. In Fig. 3, *Node B* receives messages from both *Node P* and *Node A* under the assumption that *Node B* lie within the communication ranges of both *Node P* and *Node A*. Assuming that *Node P* is a reference node, and *Node P* and *Node A* perform a pairwise synchronization using two-way timing message exchanges [4], then all the nodes in the common coverage area of *Node P* and *Node A* can receive a series of synchronization messages containing the information related the time stamps of the pairwise synchronization. With this information, *Node B* can also be synchronized to the reference node without any extra timing message transmissions. This method is referred to as receiver-only synchronization (ROS). By using receiver-only synchronization, all the sensor nodes within the common coverage region of *Node P* and *Node A* can be synchronized by only receiving the timing messages.

2.3.1 Joint Clock Offset and Clock Skew Estimation

Let's assume that an arbitrary node, *Node B*, is located within the common coverage area of *Node P* and *Node A*. *Node B* can overhear the timing messages from the communication of *Node P* and *Node A*. In other words, *Node B* is able to observe a set of time stamps $\{T_{2,i}^{(B)}\}_{i=1}^{N}$ at its own local clock when it receives packets from Node A as shown in Fig. 3. Moreover, Node B can also obtain the information about a set of time stamps $\{T_{2,i}^{(P)}\}_{i=1}^{N}$ by receiving the packets transmitted by *Node P*. Considering the effects of both clock offset and skew, $T_{2,i}^{(P)}$ is represented by

$$T_{2,i}^{(P)} = T_{1,i}^{(A)} + d^{(AP)} + X_i^{(AP)} + \theta_o^{(AP)} + \theta_s^{(AP)} \cdot (T_{1,i}^{(A)} - T_{1,1}^{(A)}) \quad (18)$$

where $\theta_o^{(AP)}$ and $\theta_s^{(AP)}$ denote the relative clock offset and skew between *Node A* and *Node P*, respectively. Similarly, $T_{2,i}^{(B)}$ can be written as

$$T_{2,i}^{(B)} = T_{1,i}^{(A)} + d^{(AB)} + X_i^{(AB)} + \theta_o^{(AB)} + \theta_s^{(AB)} \cdot (T_{1,i}^{(A)} - T_{1,1}^{(A)}) \quad (19)$$

.

The random delay portions $X_i^{(AP)}$ and $X_i^{(AB)}$ are assumed to be Gaussian random variables with mean μ and variance σ^2. From (16) and (17), we obtain

$$T_{2,i}^{(P)} - T_{2,i}^{(B)} = \theta_o^{(BP)} + \theta_s^{(BP)} \cdot (T_{1,i}^{(A)} - T_{1,1}^{(A)}) + d^{(AP)} - d^{(AB)} + X_i^{(AP)} - X_i^{(AB)} \quad (20)$$

,where $\theta_o^{(BP)} \square \theta_o^{(AP)} - \theta_o^{(BP)}$ and $\theta_s^{(BP)} \square \theta_s^{(AP)} - \theta_s^{(BP)}$. (20) takes exactly the same form as (14). Therefore, the same mathematical operations can be applied to this equation so as to derive the joint clock offset and skew estimator for receiver-only synchronization scheme. Using similar steps as in RRS, we can obtain the minimum variance unbiased estimators (MVUEs) and the Cramer-Rao lower bounds (CRLBs) for the relative clock offset and skew in receiver-only synchronization, which is given by [10] and takes the same forms as (16) and (17), respectively. As a result, using these results, *Node B* can be synchronized to *Node A*. Similarly, all the other nodes in the common coverage area of *Node P* and *Node A* can be simultaneously synchronized to the reference node *Node P* without any extra timing messages, which enables a considerable amount of energy. Furthermore, there is no loss of synchronization precision in comparison with other approaches.

3. CONCLUSIONS

Recently, wireless sensor networks have attracted a tremendous attention in the literature due to a lot of possible applications. Clock synchronization plays a crucial role in a number of fundamental operations, such as power management, data fusion, and transmission scheduling. However, the conventional clock synchronization protocols are not proper for wireless sensor networks and so a number of synchronization protocols have been proposed to satisfy the specific requirements of wireless sensor networks applications. This paper has provided an introduction to the clock synchronization problem of wireless sensor networks from a viewpoint of statistical signal processing. Moreover, it has also presented a tutorial for building efficient clock offset or skew estimation algorithms for general synchronization schemes relying on sender-receiver, receiver-receiver, and receiver-only synchronization approaches. Synchronization of WSNs is currently quite a active research area that witnessed a large number of results and diverse contributions coming from an equally various body of researchers: computer scientists, electrical engineers, mathematicians, statisticians, etc. In spite of the deployed efforts, the general problem of developing efficient global synchronization protocols for large-scale wireless sensor networks is still open and there is a lot of possibility that interesting signal processing approaches are available in order to attack this challenging problem.

4. REFERENCES

[1] Mills, D. L., "Internet time synchronization: the network time protocol," IEEE Transactions on Communications, 10, 1482-1493(1991).

[2] Bulusu, N., Jha, S., [Wireless Sensor Networks: A Systems Perspective], Artech House, 2005.

[3] Elson, J., Girod, L., and Estrin, D., "Fine-grained network time synchronization using reference broadcasts," Proc. 5th Symposium on Operating System Design and Implementation, 147-163 (2002).

THE MAIN CHARACTERISTICS FOR HALL SEMICONDUCTOR PLATES

[1]PANAIT CORNEL, [2]CARUNTU GEORGE

[1,2]*Constanta Maritime University, Romania*

ABSTRACT

In this paperwork is analysed the structure, the operating condition, and the main characteristics for the Hall semiconductor plates realised in the bipolar integrated circuits technolog. By using the numerical simulation the values of the signal-to-noise ratio and the detection limits of noise equivalent magnetic induction and the noise-equivalent magnetic induction spectral density for different structure devices are compared and it is als o emphasized the way in which choosing the geometry and the material features allows getting high-performance sensors.

Keywords: *signal-to-noise ratio, detection limit, the transverse Hall current, supply-current-related sensitivity, noise equivalent magnetic induction, shot noise, carriers Hall mobility, the offset-equivalent magnetic induction*

1. INTRODUCTION

Hall device is a rectangular homogenous plate of length l, width w and thickness δ, having point contacts, the voltage generated by a magnetic field $B_\perp$, perpendicularly to the plate surface, is given by:

$$V_H = \frac{R_H}{\delta} \cdot I \cdot B_\perp \tag{1}$$

where R_H denotes the Hall coefficient, and I the total biasing current.

In the case of a Hall device with finite contacts V_H is [1]:

$$V_H = G\frac{R_H}{\delta} \cdot I \cdot B_\perp \tag{2}$$

G being the geometrical correction factor. For an extrinsic semiconductor:

$$V_H = G\frac{r_H}{qn\delta} \cdot I \cdot B_\perp \tag{3}$$

where r_H is the Hall factor.

At low magnetic inductions, $\overline{B} \cong 0$, for an extrinsic semiconductor, the Hall voltage can be expressed in terms of the bias voltage V, as follows:

$$V_H = \mu_H \frac{w}{l} \cdot GVB_\perp \tag{4}$$

where μ_H is the Hall mobility of the charge carriers.

From (3) and (4) we also obtain the Hall voltage as a function of the power $P = V \cdot I$ dissipated in the device:

$$V_H = Gr_H B_\perp \left(\frac{w}{l}\right)^{\frac{1}{2}} \cdot \left(\frac{\mu}{qn\delta}\right)^{\frac{1}{2}} \cdot P^{1/2} = \tag{5}$$

$$= \mu_H \left(\frac{\rho_b}{\delta}\right)^{\frac{1}{2}} \cdot G\left(\frac{w}{l}\right)^{\frac{1}{2}} \cdot P^{1/2} B_\perp$$

The absolute sensitivity of a Hall magnetic sensor is its transduction ratio for large signals:

$$S_A = \left(\frac{V_H}{B_\perp}\right)_c ; V_H = S_A B_\perp \tag{6}$$

where *c* denotes a set of operating conditions, such as temperature, frequency, biasing current. Supply current related sensitivity is defined by:

$$S_I = \frac{S_A}{I} = \left|\frac{1}{I} \cdot \frac{V_H}{B_\perp}\right| ; V_H = IS_I B_\perp \tag{7}$$

y of device surface.

The analysis made in this paper outlines the way in which the possibility of choosing the adequate choice of device material and dimensions allows the improvement of the performances of magnetic sensors.

2. THE NOISE OF THE HALL PLATES

At the output of a Hall device the noise voltage is due to the generation-recombination noise, thermal noise, and $1/f$ noise. Because the generation-recombination noise is negligible in comparison with the $1/f$ noise, the voltage noise spectral density at the sense contacts of the Hall device is given by:

$$S_{NV}(f) = S_{V\alpha}(f) + S_{VT} \tag{8}$$

Here $S_{V\alpha}(f)$ is the noise voltage spectral density of the noise of the $1/f$ noise and S_{VT} denotes the noise voltage spectral density due to thermal noise.

The noise voltage spectral density of thermal noise is given by [2]:

$$S_{NV} = 4kTR_{out} \tag{9}$$

where $k = 1{,}38054 \cdot 10^{-23} JK^{-1}$ is the Boltzmann constant, and R_{out} is the output resistance of device.

For a Hall plate, where the sense contacts are very small comparative to the other dimensions of the device, the resistance between them can be directly calculated.

Figure 1 shows a small sense contact placed along the isolated boundary of a long rectangular Hall

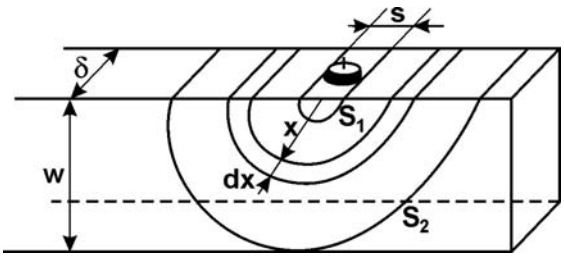

Figure 1. The contribution to the device resistance of a small dimension contact

plate.To simplify the calculation we may approximate the flat contact surface by the cylindrical surfaces S_1 and S_2. The elementary resistance calculated on the direction of the electric current that passes between the two contacts is:

$$dR = \rho \frac{dx}{S_x} \tag{10}$$

where S_x is half the lateral surface of a x-radius and δ generator cylinder. Therefore:

$$S_x = \frac{1}{2} \cdot 2 \cdot \pi \cdot x \cdot \delta = \pi x \delta \tag{11}$$

The contribution of the C_1 contact to the plate resistance between the two S_1 and S_2 surfaces is:

$$R = \int_s^w \rho \cdot \frac{1}{\pi\delta} \cdot \frac{dx}{x} = \frac{\rho}{\pi} \cdot \frac{1}{\delta} \ln\left(\frac{w}{s}\right) \tag{12}$$

where s is the C_1 contact diameter. Therefore, the output resistance of a rectangular Hall plate with very sense contacts is given by:

$$R_{out} \approx 2\frac{\rho_b}{\pi\delta} \ln\left(\frac{w}{s}\right) \tag{13}$$

on condition that: $s << w << l$.

The coefficient ρ_b denotes the effective material resistivity, and s is the small sense contacts diameter.

If the biased voltage of device is constant, ρ_b practical not depends of magnetic field.

By substituting (13) into (9) it results the spectral density:

$$S_{NV} \cong 8kT \frac{\rho_b}{\delta} \ln\left(\frac{w}{s}\right) \tag{14}$$

The current spectral density of $1/f$ noise can be described by expression [2]:

$$S_{NI} = I^2 \frac{\alpha}{N} \cdot \frac{1}{f^\beta} \tag{15}$$

where I is the device current, N is the total number of charge carriers in the device, α is a non-dimensional parameter called the Hooge parameter and β is a constant $(\beta \cong 1 \pm 0.1)$.For semiconductors, that α values of 10^{-9} to 10^{-7} were reported.The $S_{V\alpha}(f)$ for a conventional rectangular Hall plate is given by [3]:

$$S_{V\alpha}(f) \cong \alpha\left(\frac{V}{l}\right)^2 (2\pi \cdot n \cdot \delta \cdot f)^{-1} \cdot \ln\left(\frac{w}{s}\right) \tag{16}$$

3. SIGNAL TO-NOISE RATIO FOR HALL PLATES

In the application of a Hall device, one measures the output voltage in order to determine the Hall voltage. At a steady magnetic field, the signal-to-noise ratio (*SNR*) is given by:

$$SNR(f = 0) = V_H / V_{off} \tag{17}$$

where $V_{off} \neq 0$ is the offset voltage. The major causes of offset in real Hall devices are imperfections in the fabrication process such as misalignment of contacts and non - uniformity of material resistivity and thickness. For a narrow bandwidth Δf around a frequency f, the signal-to-noise ratio, can be expressed as:

$$SNR(f) = \frac{V_H(f)}{\left[S_{NV}(f) \cdot \Delta f\right]^{1/2}} \tag{18}$$

where $S_{NV}(f)$ denotes the noise spectral density at the device output.

At low frequencies, $1/f$ noise dominates.

By substituting (4) and (16) into (18) it is obtained

$$SNR(f) = \mu_H \left[\frac{2\pi n \delta l w f}{\alpha \ln(w/s)\Delta f}\right]^{\frac{1}{2}} G\left(\frac{w}{l}\right)^{\frac{1}{2}} B_\perp \tag{19}$$

This relation holds for $f << f_t$, f_t being the transition frequency defined by $S_{V\alpha}(f) = S_{VT}$.

The *SNR* at low frequencies does not depend on biasing conditions of the device but at high frequencies, the signal-to-noise ratio increases with the device current *I*. The maximal *SNR* is limited only by maximal acceptable device power dissipation $P_{\max}$.

At high frequencies, thermal noise dominates. By substituting into (18) the expressions for the Hall voltage (5), and the noise voltage spectral density (14) it results:

$$SNR(f)=\mu_H\left[\frac{\pi\Delta f^{-1}P}{8kT\ln(w/s)}\right]^{\frac{1}{2}}G\left(\frac{w}{l}\right)^{\frac{1}{2}}B_{\perp} \quad (20)$$

The *SNR(f)* dependence on magnetic induction for a given power dissipation ($P=200mW$) and different l/w ratio values $w=100\mu m$ are shown in figure 2. It is assumed that the sense contacts are points, the frequency bandwidth is reduced, $\Delta f=1Hz$ and the magnetic induction is low ($\mu_H^2B^2<<1$).

HP1: $l/w=0.5$; $G(w/l)^{1/2}=0.52$

HP 2: $l/w=1$; $G(w/l)^{1/2}=0.67$

HP 3: $l/w=2$; $G(w/l)^{1/2}=0.65$

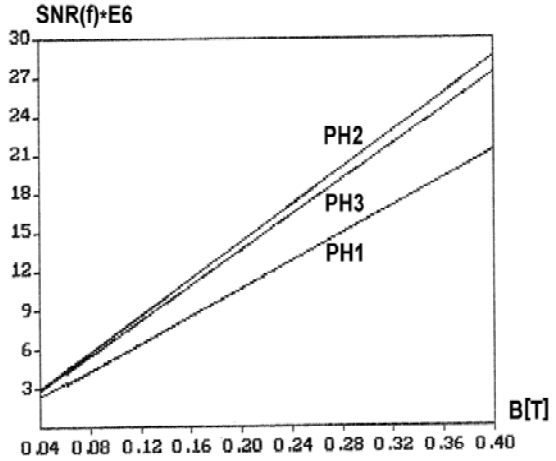

Figure 2. The *SNR* dependence on *B*⊥ for devices of different geometry

The maximum *SNR* values are obtained for the square device ($w/l=1$). These values decrease with 25% when length is half reduced HP1, also with 44% if the length doubles HP3. In figure 3 it can be seen the carriers mobility influence on *SNR* value for thermal noise. The three devices have a $l/w=1.35$ ratio, which represents the optimal value [4], and they are made of different materials:

PH1: *Si* ($\mu_H=0.15m^2V^{-1}s^{-1}$)

PH2: *GaSb* ($\mu_H=0.5m^2V^{-1}s^{-1}$)

PH3: *GaAs* ($\mu_H=0.85m^2V^{-1}s^{-1}$)

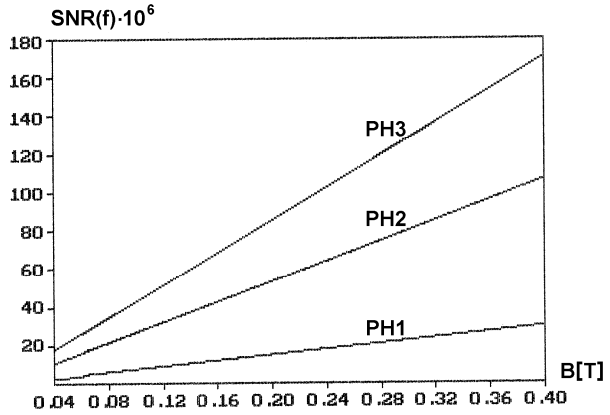

Figure 3. The *SNR* dependence on *B*⊥ for devices of different materials

The high carriers mobility provides superior the signal-to-noise ratio increase slopes for the *GaAs* and *GaSb* devices: 5.67 and 3.4 times higher than for the *Si* devices.

4. THE NOISE-EQUIVALENT MAGNETIC INDUCTION SPECTRAL DENSITY

The noise voltage at the output of a Hall magnetic sensor can be interpreted as a result of an equivalent magnetic induction, acting on a noiseless Hall device. Replacing the Hall voltage in (5) by the mean square noise voltage:

$$v_n=\left(\int_{f_1}^{f_2}S_{NV}(f)\right)^{1/2} \quad (21)$$

it is obtained:

$$\left\langle B_N^2\right\rangle=\left(\int_{f_1}^{f_2}S_{NV}(f)\right)\cdot S_A^{-2} \quad (22)$$

Here $\left\langle B_N^2\right\rangle$ is the mean square noise-equivalent magnetic induction in a frequency range (f_1,f_2), and $S_{NV}(f)$ is the noise voltage spectral density at the sensor output.

At high frequencies, thermal noise dominates. For a narrow bandwidth Δf around a frequency f by substituting (7) and (14) into (22) it results:

$$\left\langle B_N^2\right\rangle=\frac{8kT\Delta f}{\pi}\cdot\frac{\rho_bV^{-2}\ln(w/s)}{\delta\mu_H^2}\left(G\frac{w}{l}\right)^{-2} \quad (23)$$

From (22) it is obtained the noise-equivalent magnetic induction spectral density:

$$S_{NB}(f)=\frac{\partial<B_N^2>}{\partial f}=\frac{S_{NV}(f)}{S_A^2} \quad (24)$$

By analogy with (23) it is deduced:

$$S_{NB}(f)=\frac{8kT\rho_b\ln(W/s)}{\pi\delta\mu_{H_{Ch}}^2}\left(G\frac{W}{L}\right)^{-2}\cdot V_D^{-2} \quad (25)$$

At low frequencies,1/f noise dominates. By substituting (7) and (16) into (22) it is obtained:

$$\left\langle B_N^2\right\rangle=\frac{\alpha}{2\pi}\cdot\frac{1}{f}\cdot\frac{\ln(w/s)}{n\delta L^2\mu_{H_{Ch}}^2}\cdot\left(G\frac{w}{l}\right)^{-2} \quad (26)$$

The numerical values of the $\left\langle B_N^2\right\rangle$ for Hall semiconductor plates made of different materials and having different geometry are listed in table 1.

($\alpha=10^{-7}$, $f=4Hz$, $\Delta f=1Hz$, $\delta=5\cdot10^{-7}\mu m$, $w/s=50$, $n=4.5\cdot10^{21}m^{-3}$, $w=100\mu m$)

Table1. The $S_{NB}(f)$ numerical values for different devices

Device	Material	μ_H $\left[m^2V^{-1}s^{-1}\right]$	w/l	$S_{NB}(f)$ $\left[10^{-16}T^2\cdot Hz^{-1}\right]$
HP1	Si	0.15	2	2900
HP2	Si	0.15	1	3400
HP3	Si	0.15	0.5	7300
HP4	GaAs	0.85	2	10.2
HP5	GaSb	0.50	2	26
HP6	InAs	3.30	2	0.59

To emphasize the geometry influence on $S_{NB}(f)$ there simulated (figure 4) three Hall semiconductor plates structures realised on silicon :

$$\mu_H = 0.15m^2V^{-1}s^{-1}, \rho_b = 10^{-2}\Omega m$$

HP 1: $l/w = 2$; HP 2: $l/w = 1$; HP3: $l/w = 0.5$;

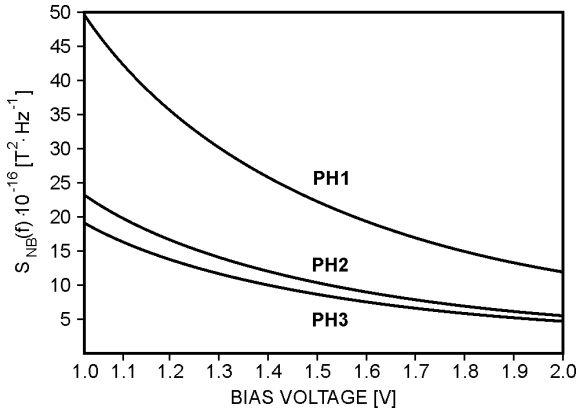

Fig. 4. The $S_{NB}(f)$ depending on bias voltage for three devices from different materials

The increasing of the device length causes the decreasing of device performances. If the length increases twice, the noise-equivalent magnetic induction spectral density increases with 18% and if the same distance increases four times (PH1), $S_{NB}(f)$ increases with 148%. In figure 5 it can be seen the material influence on $S_{NB}(f)$ values for three devices realised from GaSb, GaAs and PbTe and having the same sizes: $l = 50\mu m$, $w = 100\mu m$, $\delta = 10^{-7}\mu m$, $w/s = 50$.

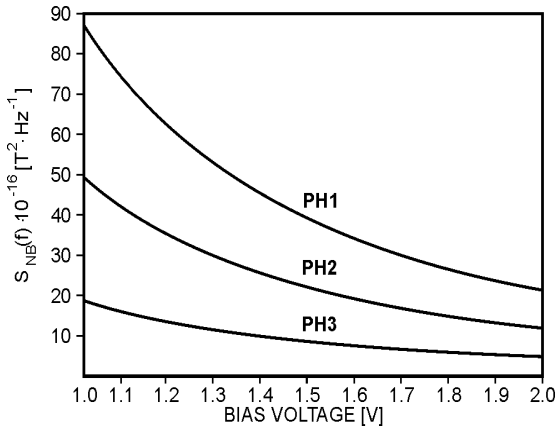

Fig. 5. The $S_{NB}(f)$ depending on bias voltage for three devices from different materials

PH1 (GaSb): $\mu_H = 0.5m^2V^{-2}s^{-1}$; $\rho_b = 0.27\Omega m$

PH2 (GaAs): $\mu_H = 0.85m^2V^{-2}s^{-1}$; $\rho_b = 0.16\Omega m$;

PH3 (PbTe): $\mu_H = 0.6m^2V^{-2}s^{-1}$; $\rho_b = 0.23\Omega m$.

5. CONCLUSIONS

The analysis of the noise-equivalent magnetic induction of the Hall plates shows that the $l/w = 0.5$ structure is theoretically favourable to obtain magnetic sensors of performance. At high frequencies in case of thermal noise, the square structure ($w = l$) provide superior signal-to-noise ratio values.

Also substituting the silicon technology other materials such as *GaAs* or *InSb* with high carriers mobility allows the made of higher characteristics devices.

A signal-to-noise ratio of about $18\cdot10^6$ at a magnetic induction of $40mT$ has been obtained at Hall semiconductor plates in case *GaAs*.

6. REFERENCES

[1]. KIREEV P.S., *Fizica semiconductorilor*, Editura Ştiinţifică şi Enciclopedică, Bucureşti 1977

[2] GRAY R.P., MEYER G.R., *Circuite integrate analogice. Analiză şi proiectare*, Editura Tehnică, Bucureşti, 1993.

[3] KLEIMPENNING T.G.M., VANDAME L.K.J., *Comment on Travers 1/f noise in InSb thin films and the SNR of related Hall elements*, J. Appl. Phys. **50** 5547, 1979

[4] CĂRUNTU G., DRĂGULINESACU M., *The Offset of Magnetic Microsensors*, Proceedings of The33 rd International Scientific Symposium of the Military Equipment and Technology Research Agency, pp 254-257,Bucharest,2002.

[5] MIDDELHOEK S., AUDET S.A., *Physiscs of Silicon Sensors,* pp. 5.20, 5.21, Academic Press, London, 1989.

MAGNETIC SENSITIVE MICROSTRUCTURES

[1]PANAIT CORNEL, [2]TAMAS RAZVAN, [3]CARUNTU GEORGE

[1,2,3]*Constanta Maritime University, Romania*

ABSTRACT

The optimal processing of sensors – provided signal, imposes their integration on the same chip with the amplifier circuit. In this paperwork is analysed the structure, the operating conditions and the main features of some microsensors realised in the MOS and bipolar integrated circuits technology. A convenient way of describing the noise properties of a sensors is in terms of detection limit, defined as the value of the measurand corresponding to a signal-to-noise ratio of one. By using numerical simulation the values of the detection limit for the two analysed devices are compared, and it is also emphasised the way in which choosing the geometry and the material features allows getting high performance sensors.

Keywords: *signal-to-noise ratio, detection limit, noise-equivalent magnetic induction spectral density offset equivalent magnetic induction,*

1. THE MOS HALL PLATES

In the MOSFET structure a Hall plate can be realised if the channel is the active region of the plate, and the source (S) and the drain (D) are the biasing contacts. For the sensing contacts of the Hall voltage SH_1 and SH_2 are manufactured, two strongly doped regions n^+ type. The channel length is L, and the width is W.

The bias in the linear region ensures a continuous channel having a thickness δ almost constant, which could be assimilated with a Hall plate.

Considering the Hall voltage mode of operation, the MOS-Hall plate is equivalent in the linear region with a conventional Hall plate differing by the fact that the charge carriers are due to the surface field effect.

The very low value of the surface charge density in the channel of a MOSFET ensures a high magnetic sensitivity of the MOS–Hall plate. In the case of a conventional Hall plate, the voltage generated by the magnetic field $B_\perp$, perpendicularly to the plate surface, is given by[1]:

$$V_H = G\left(r_H / qn\delta\right) I \cdot B_\perp \tag{1}$$

where G is the geometrical correction factor, r_H the Hall factor and δ the thickness of the plate.

By replacing in (1) the product $qn\delta$ by the surface charge density in the channel Q_{Ch}, and the current I by I_D it results for MOS-Hall plate:

$$V_H = G\left(r_H / Q_{Ch}\right) I_D \cdot B_\perp \tag{2}$$

Using the drain current expression [2]:

$$I_D = (W/L)\mu_{Ch} \cdot C_{ox}(V_G - V_P)V_D = \\ = (W/L)\mu_{Ch} Q_{Ch} V_D \tag{3}$$

from (2) it results:

$$V_H = \mu_{H_{Ch}} (W/L) G V_D \cdot B_\perp \tag{4}$$

where $\mu_{H_{Ch}} = \mu_{Ch} \cdot r_H$ represents the Hall mobility of the charge carriers in the channel, and V_D is the drain voltage.

2. SIGNAL-TO-NOISE RATION FOR MOS-HALL PLATES

The voltage noise spectral density at the sense contacts
of the Hall device is given by:

$$S_{NV}(f) = S_{V\alpha}(f) + S_{VT} \tag{5}$$

Here $S_{V\alpha}(f)$ is the noise voltage spectral density of the $1/f$ noise and S_{VT} denotes the noise voltage spectral density due to thermal noise.
The noise voltage spectral density of thermal noise is given by [3]:

$$S_{NV} = 4kTR_{out} \tag{6}$$

where $k = 1{,}38054 \cdot 10^{-23} JK^{-1}$ is the Boltzmann constant, and R_{out} is the output resistance of device.
For a rectangular MOS-Hall plate with very small sense contacts the output resistance is given by [4]:

$$R_{out} \cong 2\frac{\rho_b}{\pi\delta}\ln\left(\frac{W}{s}\right) \tag{7}$$

on condition that: $s << W << L$.

The coefficient ρ_b denotes the effective material resistivity, and s is the small sense contacts diameter.

If the biased voltage of device is constant, ρ_b practical not depends of magnetic field.
By substituting (7) into (6) it results the spectral density:

$$S_{NV} = \frac{8kT}{\pi nq\mu_{Ch}\delta}\ln\left(\frac{W}{s}\right) \tag{8}$$

In case of MOS-Hall plates, at high frequencies, thermal noise dominates.

For a narrow bandwidth Δf around a frequency f ($f > 100kHz$), the signal-to-noise ratio, can be expressed as:

$$SNR(f) = V_H / [S_{NV}(f) \cdot \Delta f]^{1/2} \quad (9)$$

By substituting (2) and (8) into (9) it results:

$$SNR(f) = \left(\frac{\pi \mu_{Ch}}{8kTqn\delta\Delta f \ln(W/s)} \right)^{1/2} r_H G I_D B_\perp \quad (10)$$

Since the signal-to-noise ratio increases with the drain current I_D, the maximal *SNR(f)* is limited only by maximal acceptable device power dissipation P_{max}.

From (1) and (4), we also obtain the Hall voltage as a function of the power $P = V_D I_D$ dissipated in the device.

Multiplying (1) and (4) member-by-member is obtained:

$$V_H = G \left(\frac{W}{L} \right)^{1/2} r_H \left(\frac{\mu_{Ch}}{Q_{Ch}} \right)^{1/2} P^{1/2} \cdot B_\perp \quad (11)$$

The expression of the $SNR(T = 300K)$ is got by replacing (8) and (11) into (9):

$$SNR(f) = \mu_{H_{Ch}} \left[\frac{\pi G^2 (W/L) P}{8kT\Delta f \ln(W/s)} \right]^{1/2} B_\perp =$$

$$= 9.7 \cdot 10^9 \mu_{H_{Ch}} \left[\frac{G^2 (W/L) P}{\Delta f \ln(W/s)} \right]^{1/2} B_\perp \quad (12)$$

3. THE DETECTION LIMIT OF MOS-HALL PLATES

The value of the measuring corresponding to a signal-to-noise ratio of one, constitute the detection limit of Hall device used as magnetic sensors.

In case of thermal noise for MOS-Hall plates itis obtained from expression (12):

$$B_{DL} = \frac{2}{\mu_{H_{Ch}}} \cdot \sqrt{\frac{2kT}{\pi}} \cdot \frac{[\Delta f \ln(W/s)]^{1/2}}{G(W/L)^{1/2}} \cdot P^{-1/2} \quad (13)$$

The detection limit of the sensor decreases when the power dissipated in the device increases, but for the same power the limit depends on the device dimensions and the material it is made of.

In figure 1 are shown B_{DL} values obtained by the simulation of three MOS-Hall plates structures realised on silicon ($\mu_{H_{Ch}} = 0.07 m^2 V^{-1} s^{-1}$) and having different ratios L/W ($W = 100\mu m$, $W/s = 50$, $\Delta f = 1Hz$).

It is assumed that the sense contacts are points and the magnetic induction is low ($\mu_{H_{Ch}}^2 B^2 << 1$).

MHP1 : $L/W = 0.5$; *M*HP2 : $L/W = 1$;
MHP3 : $L/W = 3$

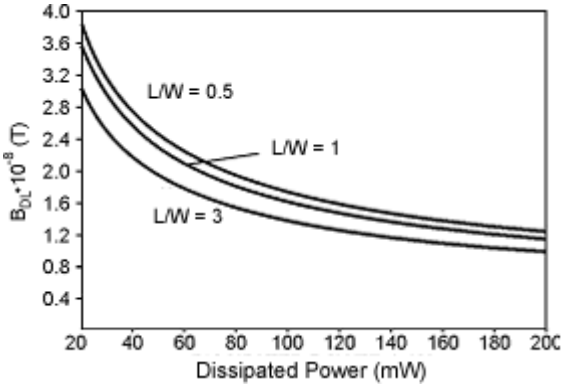

Figure 1 B_{DL} depending on the P for three devices of different geometry

For same dissipate power *P,* the detection limit is minimum in case of square structure (MHP2).

It is noticed that B_{DL} increases with 18,4% comparative with MHP2 device, if the distance between the current contacts increases three times.

In figure 2 are shown the detection limit dependence on dissipated power of three MOS Hall plates structures from different materials ($W = 200\mu m$, $L = 100\mu m$, $W/s = 50$, $\Delta f = 1Hz$).

MHP1: *Si* with $\mu_{H_{Ch}} = 0{,}07 m^2 V^{-1} s^{-1}$;

MHP2: *GaSb* with $\mu_{H_{Ch}} = 0{,}25 m^2 V^{-1} s^{-1}$;

MHP3: *GaAs* with $\mu_{H_{Ch}} = 0{,}42 m^2 V^{-1} s^{-1}$

Figure 2 BDL depending on P for three MOS-Hall plates of different materials

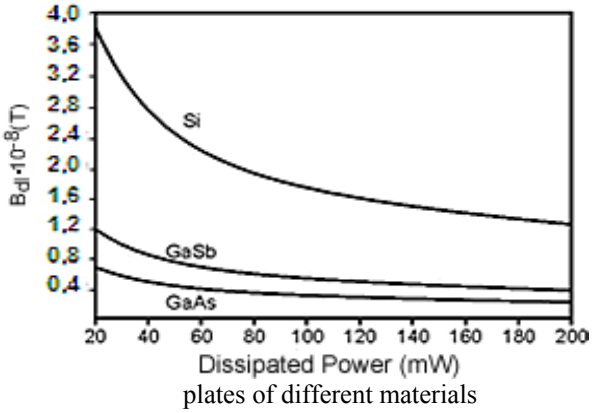

It is also assumed that the contacts are points and the magnetic induction is low ($\mu_H^2 B^2 << 1$)

A high value carrier's mobility causes the decreasing of detection limit so. B_{DL} decreases with 45% for *GaAs* comparative with *GaSb*.

4. THE DOUBLE-COLLECTOR BIPOLAR MAGNETOTRANSISTOR

Figure 3 shows the cross section of a double collector *npn* vertical magnetotransistor operating on the current deflection principle [5]. This structure is compatible with the bipolar integrated circuit technology. The most of the *n* type low-doped epitaxial layer serves as the collector region and is depleted of the charge carriers upon reverse biasing of the collector-base junction.

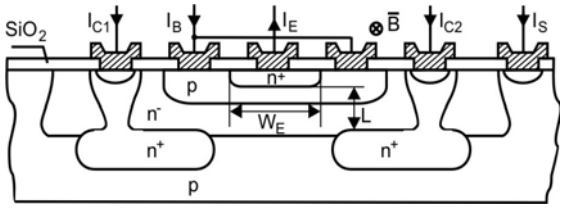

Figure 3 The structure of a double-collector

The two collector contacts are realised by splitting the buried layer (n^+). L is the collector-emitter distance, and W_E is the width of the emitter.

In the absence of the magnetic field the electron flow injected into the emitter, which crosses the base is symmetrical and the two collector currents are equal: $I_{C_1} = I_{C_2}$. In the presence of a magnetic field having the induction $\overline{B}$ parallel with the device surface, the distribution of the emitter electron current becomes asymmetrical and causes an imbalance of the collector currents: $\Delta I_C = I_{C_1} - I_{C_2}$.

The studied magnetotransistors work in the Hall current mode of operation and the deviation ΔI_C is given by the transverse Hall current.

Its expression is determined by equalizing the epitaxial layer of the collector region with a short Hall plate and applying the properties of the dual Hall devices.

Based upon the Hall current expression in the devices which are in the Hall current mode of operation it can be written [6]:

$$\Delta I_C = \frac{I_H}{2} = \frac{1}{2}\mu_{Hn} \cdot \frac{L}{W_E} \cdot G \cdot I_C \cdot B \qquad (14)$$

where $I_C = I_{C_1}(0) + I_{C_2}(0)$.

The sensor response is expressed by:

$$h(B) = \frac{\Delta I_C}{(I_{C1} + I_{C2})_{B=0}} = \frac{1}{2}\mu_{Hn}\frac{L}{W_E} \cdot G \cdot B_\perp \qquad (15)$$

The magnetic sensitivity related to the devices current is defined as follows:

$$S_I = \frac{1}{I_C}\left|\frac{\Delta I_C}{B_\perp}\right| = \frac{1}{2}\mu_{Hn}\frac{L}{W_E}G \qquad (16)$$

For a given induction $(B = 0{,}4T)$ and at given collector current $I_C = 1mA$, the sensitivity depends of the device geometry and the material proprieties. In table 1. are presented the obtained values for five magnetotransistors structures.

Table 1. The numerical values of the offset equivalent magnetic induction

	W_E / L	μ_{Hn} $[m^2V^{-1}s^{-1}]$	S_I $[T^{-1}]$
MGT1	2	0,15 Si	0,035
MGT2	1	0,15 Si	0,05
MGT3	0,5	0,15 Si	0,055
MGT4	0,5	0,46 InP	0,168
MGT5	0,5	0,85 GaAs	0,292

5. THE NOISE-EQUIVALENT MAGNETIC INDUCTION SPECTRAL DENSITY

A magnetotransistor may be regarded as a modulation transducer that converts the magnetic induction signal into an electric current signal.

This current signal or output signal is the variation of collector current, caused by induction $B_\perp$.

The absolute sensitivity of a magnetotransistor used as magnetic sensors is:

$$S_A = \left|\Delta I_C / B\right| = \frac{1}{2}\mu_{Hn} \cdot \frac{L}{W_E} G \cdot I_C \qquad (17)$$

and the supply-current-related sensitivity of the device is defined by:

$$S_I = \frac{1}{I_C}\left|\frac{\Delta I_C}{B_\perp}\right| = \frac{1}{2}\mu_{Hn}\frac{L}{W_E}G \qquad (18)$$

The noise current at the output of a magnetotransistor can be interpreted as a result of an noise equivalent magnetic induction.

The mean square value of noise equivalent magnetic induction (*NEMI*) is defined by:

$$\left\langle B_N^2 \right\rangle = \frac{\int_{f_1}^{f_2} S_{NI}(f) \cdot df}{(S_I \cdot I_C)^2} \qquad (19)$$

Here S_{NI} is the noise current spectral density in the collector current, and (f_1, f_2) is the frequency range. In case of shot noise, the noise current spectral density at frequencies over 100 Hz is given by [7]:

$$S_{NI} = 2qI \qquad (20)$$

where *I* is the device current.

From (19) it is obtained the noise-equivalent magnetic induction spectral density:

$$S_{NB}(f)=\frac{\partial < B_N^2 >}{\partial f}=\frac{S_{NI}(f)}{S_A^2} \qquad (21)$$

For a narrow bandwidth Δf around a frequency f by substituting (17) and (20) into (21) it results:

$$S_{NB}(f)=2qI\cdot 4\left(\frac{W_E}{L}\right)^2\cdot\frac{1}{G^2\mu_{Hn}^2}\cdot\frac{1}{I_C^2}\le \le 8q\left(\frac{W_E}{L}\right)^2\cdot\frac{1}{G^2}\cdot\frac{1}{\mu_{Hn}^2}\cdot\frac{1}{I_C} \qquad (22)$$

In figure 4 there are shown $S_{NB}(f)$ values obtained by simulation of three magnetotransistors structures from different materials.

MGT_1: Si with $\mu_{Hn}=0.15m^2V^{-1}s^{-1}$

MGT_2: InP with $\mu_{Hn}=0.46m^2V^{-1}s^{-1}$

MGT_3: GaAs with $\mu_{Hn}=0.85m^2V^{-1}s^{-1}$

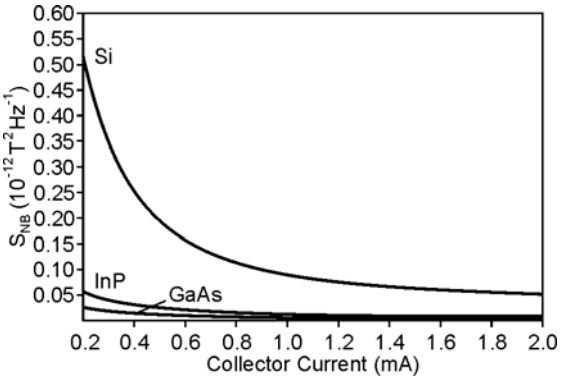

Figure 4 The S_{NB} (f) depending on the collector current for three devices of different materials

Considering the condition of low value magnetic field fulfilled ($\mu_H^2B^2 << 1$), it is obtained a maximum value for $(L/W_E)G=0.74$, if $W_E/L<0.5$. [8]

In this case:

$$(S_{NB}(f))_{\min}\le 14.6q\frac{1}{I_C\mu_{Hn}^2} \qquad (23)$$

To emphasize the dependence of $S_{NB}(f)$ on device geometry there were simulated (figure 5) three double-collector magnetotransistors structures realised on silicon, $\mu_{Hn}=0.15m^2V^{-1}s^{-1}$, and having different ratios W_E/L $(W_E=50\mu m)$. The devices were based in the linear region and the magnetic field a low level $(\mu_H^2B^2<<1)$.

$MGT1: W_E/L=0.5$ and $(LG/W_E)^2=0.576$

$MGT2: W_E/L=1.0$ and $(LG/W_E)^2=0.409$

$MGT3: W_E/L=2$ and $(LG/W_E)^2=0.212$

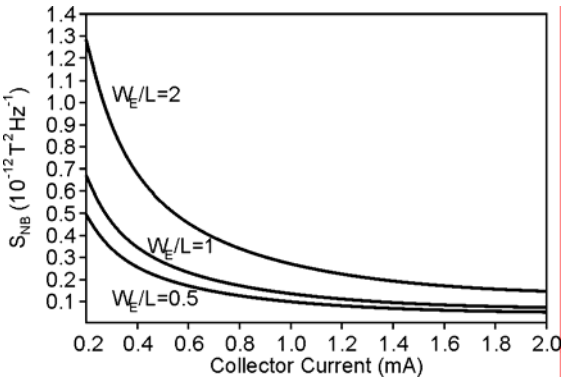

Figure 5 The S_{NB} (f) depending on the collector current for three devices of different geometry

It is noticed that the S_{NB} (f) is minimum for $W_E/L=0.5$, and for smaller values of this ratio. The decreasing of the channel length causes the increasing of S_{NB} (f) with 40.8 % for a square structure $W_E=L$ and with 173 % for $W_E=2L$.

6. GENERAL CHARACTERISATION OF THE LATERAL MAGNETOTRANSISTOR

Figure 6 illustrates the cross section of a split-collector magnetotransistor operating on the current deflection principle [9] This device has the structure of a long channel MOS transistor, but operates as a lateral bipolar transistor with a drift-aided field in the base region.

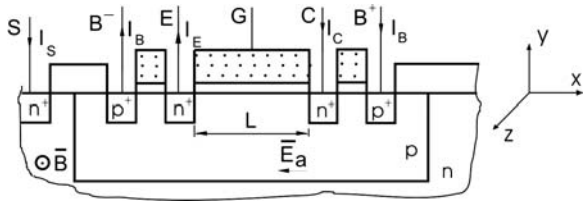

Figure 6 Cross section through a lateral magneto-transistor

The device is situated in a *p*-well, serving as the base region of the transistor.

The two base contacts B^+ and B^- , allow the application of an accelerating voltage for the minority carriers injected into the base region. The two N^+ regions laterally separated by the length of base along the distance L serve as the emitter E and the primary collector C.

The substrate S works as the secondary collector. If the acceleration field $\bar{E}_a$ in the base region is very small, the electrons moving essentially by diffusion the transverse Hall current will be [6]:

$$I_H=I_Y=\frac{L}{Y}I_C\mu_{Hn}B_\perp=\Delta I_C \qquad (24)$$

where μ_{Hn} is the Hall mobility of electrons in the *p*-well, and Y is a geometrical parameter given approximately by $y_{jn}<Y<y_{jp}$; y_{jn}, y_{jp} being the junction depths of the collector region , the *p*-well respectively.

7. HE OFFSET EQUIVALENT MAGNETIC INDUCTION

For bipolar lateral magnetotransistor presented in figure 8 the offset current consists in the flow of minority carriers which, injected into the base region in absence of magnetic field diffuse downwards and are collected by the secondary collector S.

The main causes of the offset are due to the misalignment of contacts to non-uniformity of the thickness and of the epitaxial layer doping.

Also a mechanical stress combined with the piezo-effect, may produce offset.

To describe the error due to the offset it is determined the magnetic induction, which produces the imbalance $\Delta I_C = \Delta I_{Coff}$.

The offset equivalent magnetic induction is expressed by considering the relation (24):

$$B_{off} = \frac{\Delta I_{C_{off}}}{S_I I_C} = \frac{1}{\mu_{Hn}} \cdot \frac{\Delta I_{C_{off}}}{I_C (L/Y)} \qquad (25)$$

Considering $\Delta I_{Coff} = 0.10 \mu A$ and assuming that the low magnetic field condition is achieved, in figure 7 is presented the dependence of B_{off} on I_C for three magnetotransistors with the same geometry $L/Y = 0.5$ realized from different materials:

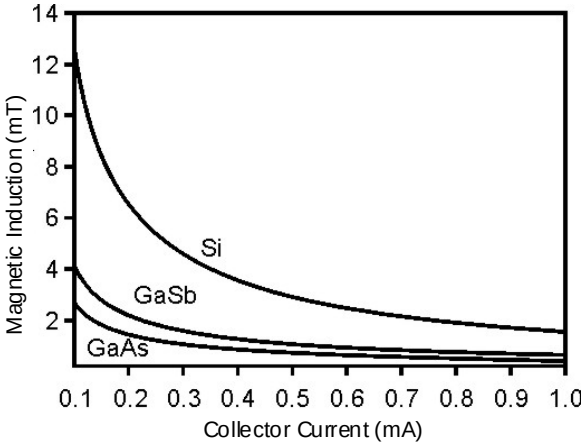

Figure 7 The B_{off} depending on the I_C for three devices of different materials

MGT1: Si with $\mu_{Hn} = 0.15 m^2 V^{-1} s^{-1}$;

MGT2: GaSb with $\mu_{Hn} = 0.50 m^2 V^{-1} s^{-1}$;

MGT3: GaAs with $\mu_{Hn} = 0.85 m^2 V^{-1} s^{-1}$;

The offset-equivalent magnetic induction lowers with the increase of carriers' mobility.

So for the same collector current $I_C = 0.1 mA$ the B_{off} value of the GaAs device decreases by 70% as compared to that of the silicon device.

8. HE DOUBLE-DRAIN MOS DEVICE

The double – drain MOS device (figure 8) is a

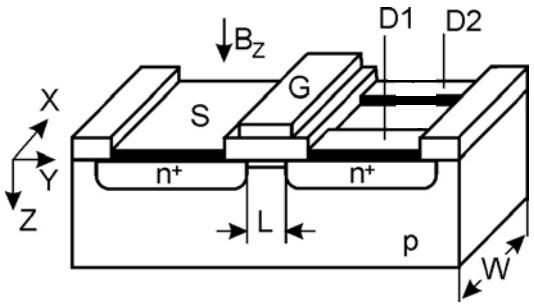

Figure 8 Double-drain MOSFET magnetotransistor

MOSFET with two adiacent drain regions replacing the conventional single drain region, the total channel current being shared between these regions [1].

The deflection of current lines appears under the action of a magnetic field $B_{\perp}$, perpendicular to the device surface.The difference between the two drain currents in the absence of the magnetic field is the offset collector current: $\Delta I_{D_{off}} = I_{D1}(0) - I_{D2}(0)$.

To describe the error due to the offset it is determined the magnetic induction, which produce the imbalance $\Delta I_D = \Delta I_{D_{off}}$.

9. HE OFFSET EQUIVALENT MAGNETIC INDUCTION

The offset equivalent magnetic induction is expressed by considering the relation:

$$B_{off} = \frac{\Delta I_{D_{off}}}{S_I I_D} = \frac{2}{\mu_{Hn}} \cdot \frac{\Delta I_{D_{off}}}{I_D} \cdot \left(G \frac{L}{W} \right)^{-1} \qquad (26)$$

where $\mu_{H_{Ch}}$ is the carriers Hall mobility in the channel, and *G* denotes the geometrical correction factor.

Considering $\Delta I_{D_{off}} = 0.10 \mu A$ and assuming that the low magnetic field condition is achieved in figure 9 is presented the dependence of B_{off} on I_D for three magnetotransistors with the same geometry $W/L = 0.5$ realised from different materials:

MDD1: Si with $\mu_{H_{Ch}} = 0.07 m^2 V^{-1} s^{-1}$;

MDD2: InP with $\mu_{H_{Ch}} = 0.23 m^2 V^{-1} s^{-1}$;

MDD3: GaAs with $\mu_{H_{Ch}} = 0.43 m^2 V^{-1} s^{-1}$.

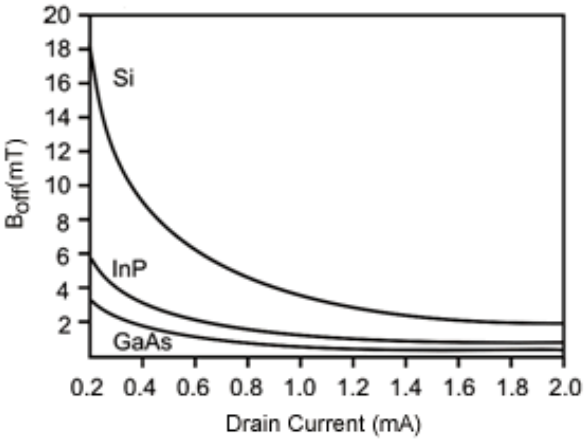

Figure 9. The B_{off} depending on the drain current for three devices of different materials

10. CONCLUSIONS

The magnetotransistors have a lower magnetic sensitivity than the conventional Hall devices but allow very large signal-to-noise ratios, resulting a high magnetic induction resolution. The analisys of the characteristics of three magnetotransistors structures shows that the $W/L = 0.5$ ratio is theoretically favourable to high performance regarding signal-to-noise ratio, noise equivalent magnetic induction as well as the offset equivalent magnetic induction.

Also substituting the silicon technology by using other materials such as GaAs or InSb with high carriers mobility values assure higher characteristics of the sensors

The offset equivalent magnetic induction lowers with the increase of carriers mobility, this increase being significant for collector currents of relatively low values. So for the collector current $I_C = 0.2mA$, the offset equivalent magnetic induction value of the GaAs device decreases by 81.8% as compared to that of the silicon device. For the same collector current I_C, B_{off} is maximum when $W_E = 2L$. It is noticed that by the increasing of the emitter-collector distance, causes the decreasing of B_{off} with 31% for a square structure ($W_E = L$) and with 38% for $W_E = 0.5L$. The further increase of *L* parameter does not change much the B_{off} value.

The uses of magnetotransistors as magnetic sensors allows the archieving of some current-voltage conversion circuits, more efficient that conventional circuits with Hall plates.

The transducers with integrated microsensors have a high effieciency and the possibilities of using them ca be extended to some measuring systems of thickness, short distance movement, level, pressure, linear and revolution speeds. In figure 7 shown the electrical diagram of a speed of rotation transducers based on a double-collector vertical magnetotransistors.

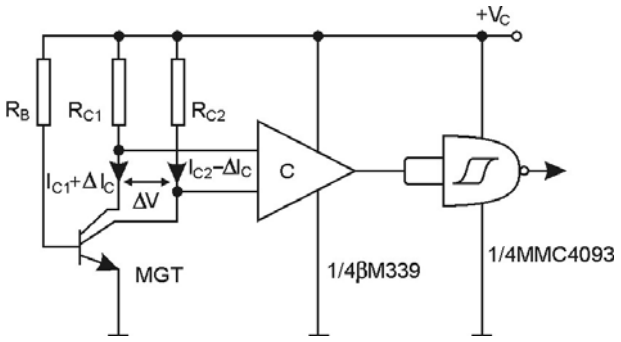

Figure 11 The electric diagram of transducer

When a magnetic field is present there takes place an imbalance of the collector currents and the effect is potential difference between the two collectors which is proportional to the induction value $B_\perp$.

$$\Delta V_C = \mu_{Hn}\left(\frac{L}{W_E}G\right)R_C I_C B_\perp \qquad (27)$$

This voltage is applied to a comparator with hysteresis, which acts as a comutator. The existence of the two travel thresholds ensure the immunity at noise to the circuit. The monostable made with *MMC 4093* ensures the same duration for the transducers generated pulses.

11. REFERENCES

[1] KIREEV P.S., *Fizica semiconductorilo*r Editura Ştiinţifică şi Enciclopedicã, Bucureşti, 1977.
[2] STERE R., BODEA M., *Tranzistoare cu efect de câmp, Editura Tehnică*, Bucureşti, pp. 117, 1972
[3] GRAY R.P., MEYER G. R. *Circuite integrate analogice. Analiză şi proiectare,* pp. 579, 583 *Editura Tehnică*, Bucureşti, 1993.
[4] PANAIT C. ,CĂRUNTU G. *The Noise of Hall Semiconductor Plates*, *in The Proceedings of ISTET'05*, pp.26-29, July 4-7,2005,Lviv,Ukraine
[7] MIDDELHOEK S., AUDET S.A., *Physiscs of Silicon Sensors*, pp. 5.20, 5.21, *Academic Press*, London, 1989.
[5] BODEA M. *Traductoare indegrate*, Microelectronica, Vol. 15, pp. 73-86, Bucureşti**,** 1987.
[6] CĂRUNTU G., PANAIT C., *The Optimization of Bipolar Magnetotransistor Structures,* in the Proceedings of SPIE-Volume 6635, Advanced Topics in Optoelectronics, Microelectronics and Nanotechnologies III, May, 8, 2007
[8] PANAIT C., CĂRUNTU G., M. JURIAN., The Optimization of Microsensors Structures, in Conference Proceedings XII, ISTET `03, volume I, pp 441-444, Julz 6-9, 2003, Warsaw, Poland

THE VERTICAL BIPOLAR MAGNETORANSISTOR AND THE MOS HALL PLATES

[1]PANAIT CORNEL, [2]CARUNTU GEORGE

[1,2]*Constanta Maritime University, Romania*

ABSTRACT

In this paperwork, based on the model of dual Hall devices, it is analysed the operating conditions, and are established the main characteristics for microsensor structures realised in the bipolar and MOS circuits technology. In the same time it is emphasized the way in which the adequate choise of its geometry and material features, allow the obtaining of high performance devices. There are also presented and described the electrical diagrams of the transducers which contain such sensors.

Keywords: *equivalent magnetic induction, signal-to- noise ratio, sensor response, the offset collector current, the offset equivalent magnetic induction point size 10, 10 points before, 10 points after.*

1. THE DOUBLE-COLLECTOR VERTICAL MAGNETOTRANSISTOR

1.1 General characterisation

In the absence of the magnetic field the electron flow injected into the emitter, which crosses the base is symmetrical and the two collector currents are equal: $I_{C_1} = I_{C_2}$. In the presence of a magnetic field having the induction $\overline{B}$ parallel with the device surface, the distribution of the emitter electron current becomes asymmetrical and causes an imbalance of the collector currents: $\Delta I_C = I_{C_1} - I_{C_2}$.

The analysed magnetotransistor operates in the Hall current mode and ΔI_C depends on the Hall transverse current.

Assimilating the low-dopped emitaxial layer of the collector region with a short Hall plate, and based on the properties of dual Hall devices it results [1]:

$$\Delta I_C = \frac{I_H}{2} = \frac{1}{2}\mu_{Hn} \cdot \frac{L}{W_E} \cdot G \cdot I_C \cdot B \qquad (1)$$

where $I_C = I_{C_1}(0) + I_{C_2}(0)$

1.2 The sensor response and the sensitivity related to the bias current

The sensor response is expressed by:

$$h(B) = \frac{\Delta I_C}{(I_{C1} + I_{C2})_{B=0}} = \frac{1}{2}\mu_{Hn}\frac{L}{W_E} \cdot G \cdot B_{\perp} \qquad (2)$$

and it is linear for induction values which satisfy the condition: $\mu_H^2 \cdot B_{\perp}^2 << 1$.

The magnetic sensitivity related to the devices current is defined as follows:

$$S_I = \frac{1}{I_C}\left|\frac{\Delta I_C}{B_{\perp}}\right| = \frac{1}{2}\mu_{Hn}\frac{L}{W_E}G \qquad (3)$$

For a given induction $(B = 0{,}4T)$ and at given collector current $I_C = 1mA$, the sensitivity depends of the device geometry and the material properties. In table 1 are presented the obtained values for five magnetotransistors structures.

Table 1. The numerical values of the supply-current-related sensitivity

	W_E / L	$\mu_{Hn}[m^2V^{-1}s^{-1}]$	$S_I[T^{-1}]$
MGT1	2	0,15 Si	0,035
MGT2	1	0,15 Si	0,05
MGT3	0,5	0,15 Si	0,055
MGT4	0,5	0,46 InP	0,168
MGT5	0,5	0,85 GaAs	0,292

1.3 The noise equivalent magnetic induction

A magnetotransistor may be regarded as a modulation transducer that converts the magnetic induction signal into an electric current signal. The noise current at the output of a magnetotransistor can be interpreted as a result of an equivalent magnetic induction.

The mean square value of noise equivalent magnetic induction (NEMI) is defined by:

$$\left\langle B_N^2 \right\rangle = \frac{\int_{f_1}^{f_2} S_{NI}(f) \cdot df}{(S_I \cdot I_C)^2} \qquad (4)$$

where S_{NI} is the noise current spectral density in the collector current, and (f_1, f_2) is the frequency range.

In case of shot noise, the noise current spectral density at frequencies over 100 Hz is given by [2]:

$$S_{NI} = 2qI \qquad (5)$$

where *I* is the device current.

In a narrow frequency band around the frequency *f*, by substituting (3) and (5) into (4) it results:

$$< B_N^2 >= 2qI \cdot \Delta f \cdot 4\left(\frac{W_E}{L}\right)^2 \cdot \frac{1}{G^2\mu_{Hn}^2} \cdot \frac{1}{I_C^2} \leq$$

$$\leq 8q\left(\frac{W_E}{L}\right)^2 \cdot \frac{\Delta f}{G^2} \cdot \frac{1}{\mu_{Hn}^2} \cdot \frac{1}{I_C} \quad (6)$$

Considering the condition of low value magnetic field fulfilled ($\mu_H^2 B^2 << 1$), it is obtained a maximum value for $(L/W_E)G = 0.74$, if $W_E / L < 0.5$ [3].

In this case:

$$< B_N^2 >_{\min} \leq 14.6q\frac{\Delta f}{I_C} \cdot \frac{1}{\mu_{Hn}^2} \quad (7)$$

1.4 The offset-equivalent magnetic induction

The difference between the two collector currents in the absence of the magnetic field is the offset collector current:

$$\Delta I_{C_{off}} = I_{C1}(0) - I_{C2}(0) \quad (8)$$

The causes consist of imperfections specific to the manufacturing process: the contact misalignment, the non-uniformity of the thickness and of the epitaxial layer doping, the presence of some mechanical stresses combined with the piezo-effects. To describe the error due to the offset it is determined the magnetic induction, which produces the imbalance $\Delta I_C = \Delta I_{C\,off}$. The offset equivalent magnetic induction is expressed by:

$$B_{off} = \frac{\Delta I_{C_{off}}}{S_I I_C} = \frac{2}{\mu_{Hn}} \cdot \frac{\Delta I_{C_{off}}}{I_C} \cdot \left(G\frac{L}{W_E}\right)^{-1} \quad (9)$$

If the width of the emitter is maintained constant, B_{off} increases as the emitter-collector distance decreases.

High values carrier's mobility causes the decreasing of the offset-equivalent magnetic induction.

1.5 Signal-to-noise ratio

The noise affecting the collector current of a magnetotransistor is shot noise and 1/f noise.

Signal-to-noise ratio is defined by:

$$SNR(f) = \frac{\Delta I_C}{[S_{NI}(f) \cdot \Delta f]^{1/2}} \quad (10)$$

where Δf denotes a narrow frequency band around the frequency f , and $S_{NI}(f)$ denotes the noise current spectral density in the collector current.

In case of shot noise, in a narrow range f of frequency values, by subtituting (1) and (5) into (10) it results:

$$SNR(f) = \frac{1}{2\sqrt{2}}\mu_{Hn}\left(\frac{L}{W_E}G\right)\frac{I_C}{(q \cdot I \cdot \Delta f)^{1/2}}B_\perp \geq$$

$$\geq \frac{1}{2\sqrt{2}}\mu_{Hn}\left(\frac{L}{W_E}G\right)\frac{I_C^{1/2}}{(q\Delta f)^{1/2}}B_\perp \quad (11)$$

In case of $1/f$ noise, the noise current spectral density at the device output is given by [4]:

$$S_{NI}(f) = I^2 \alpha N^{-1} f^{-\beta} \quad (12)$$

where I is the device current, $N = n\delta LW_E$ is the total number of charge carriers in the device, α is a parameter called the Hooge parameter and $\beta \cong 1 \pm 0.1$ (tipically). For semiconductors, it is reported that α values range from 10^{-9} to 10^{-7} . Subtituting (1) and (12) into (10) it is obtained:

$$SNR(f) \cong \frac{(ndLW_E)^{1/2}\mu_{H_n}}{2\alpha^{1/2}}\left(\frac{f}{\Delta f}\right)^{1/2}\left(\frac{L}{W_E}G\right)B_\perp \quad (13)$$

2. THE MOS-HALL PLATES

2.1 General characterization of the MOS-Hall plates

In a MOSFET structure, an extremely thin Hall plate can be realised if the channel constitutes the active region of plate, and the source (S), and drain (D) are the biasing contacts.

For the sensing contacts of the Hall voltage SH_1 and SH_2 are manufactured, two strongly doped regions n^+ type. The channel length is L, and the width is W.

The bias in the linear region ensures a continuous channel having a thickness almost constant δ , which could be assimilated with a Hall plate.

Considering the Hall voltage mode of operation, the MOS-Hall plate is equivalent in the linear region with a conventional Hall plate differing by the fact that the charge carriers are due to the surface field effect.

The surface charge density in the channel is approximately constant and it has the following expression [5]:

$$Q_{Ch} = C_{ox}(V_G - V_P) \quad (14)$$

where C_{ox} is the gate oxide capacitance per unit area, V_G the gate to source voltage, and V_p the threshold voltage.

The very low value of the surface charge density in the channel of a MOSFET ensures a high magnetic sensitivity of the MOS–Hall plate. There is also the possibility to modify the channel depth by the drain-source potential difference.

In the case of a conventional Hall plate, the generated voltage is [6]:

$$V_H = G(r_H / qn\delta)I \cdot B_\perp \quad (15)$$

where G is the geometrical correction factor, r_H the Hall factor and δ the thickness of the plate.

By replacing in (15) the product $qn\delta$ by the surface charge density in the channel Q_{Ch} , and the current I by I_D it results:

$$V_H = G(r_H / Q_{Ch})I_D \cdot B_\perp \quad (16)$$

Using the drain current expression:

$$I_D = (W/L)\mu_{Ch} \cdot C_{ox}(V_G - V_P)V_D = \\ = (W/L)\mu_{Ch}Q_{Ch}V_D \quad (17)$$

from (16) it results:

$$V_H = \mu_{H_{Ch}}(W/L)GV_D \cdot B_\perp \quad (18)$$

where $\mu_{H_{Ch}} = \mu_{Ch} \cdot r_H$ represents the Hall mobility of the charge carriers in the channel.

The absolute sensitivity for a Hall device used as a magnetic sensor is:

$$S_A = \left|\frac{V_H}{B_\perp}\right| = \frac{I_D G}{Q_{Ch}} \quad (19)$$

and the supply-voltage-related sensitivity is defined by:

$$S_V = \frac{S_A}{V_D} = \mu_{H_{Ch}}(W/L)G \quad (20)$$

The sensor response is given by:

$$h(B_\perp) = \frac{V_H}{V_D} = \mu_{H_{Ch}}\left(\frac{W}{L}G\right)B_\perp \quad (21)$$

and it is linear for magnetic induction values that satisfy the condition: $\mu_{H_{Ch}}^2 \cdot B_\perp^2 << 1$.

It is noticed that the response $h(B)$ is maximum for $L/W = 0.5$ structure.

For the same geometry $L/W = 0.5$, the response is depending on material features.

2.2 The offset equivalent magnetic induction

The main causes of the offset in the case of Hall plates realised in the MOS integrated circuits technology are due to the misalignment of contacts, to integral non-uniformity, the existence of mechanical stress, and to the fluctuations in the oxide layer charge, or to the variation in the oxide semiconductor interface.

The asymmetries produced by the above causes can be represented by using for the Hall plate the simple Wheatstone bridge circuit model.

In the case of the misalignment of the sensing contacts, for a tolerance ΔL the asymmetrical output voltage or the offset voltage is expressed by [7]:

$$V_{off} = \frac{\Delta L}{W} \cdot \frac{1}{\mu_{Ch}Q_{Ch}} \cdot I_D \quad (22)$$

The value of the magnetic induction corresponding to a Hall voltage equal with V_{off} represents offset equivalent magnetic induction.

In the case of the geometrical offset of the sensing contacts, the expression of the offset equivalent magnetic induction is got by replacing (22) into (19):

$$B_{off} = \frac{V_{off}}{S_A} = \frac{1}{\mu_{H_{Ch}}} \cdot \left(\frac{W}{L}G\right)^{-1}\frac{\Delta L}{L} \quad (23)$$

It is noticed that at given technological misalignment, B_{off} decreases if $\mu_{H_{Ch}}$ is of a high value. In the case of the MOS-Hall plates this is an inconvenience because the carrier mobility in the channel is half of its value in the volume of the equivalent conventional device.

Assuming that the condition of a low magnetic field is fulfilled, minimal values for B_{off} are obtained if $\frac{L}{W} \le 0.5$ when the product $(W/L)G$ takes the maximal value 0.74 [6]:

$$(B_{off})_{\min} \cong \frac{1}{0{,}74 \cdot \mu_{H_{Ch}}} \cdot \frac{\Delta L}{L} \quad (24)$$

For values of the geometric offset within the range $[10^{-4},10^{-3}]$, in the *Si* device, $(B_{off})_{\min}$ varies between 2.2 mT and 22 mT and in GaAs device $(B_{off})_{\min}$ covers the range $[0.39;3.9]mT$, the increase of the offset equivalent induction slope being of 5.67 times smaller in GaAs.

2.3 Signal-to-noise ration for MOS-Hall plates

At the output of a Hall device the noise voltage is due to the generation-recombination noise, thermal noise, and $1/f$ noise.

In case of a MOS-Hall Plates, at high frequencies, thermal noise dominates.The voltage spectral density of thermal noise is given by [2]:

$$S_{NV} = 4kTR_{out} \quad (25)$$

where $k = 1.38054 \cdot 10^{-23} JK^{-1}$ is the Boltzmann constant, and R_{out} is the output resistance of device.

The output resistance of a rectangular MOS-Hall plate with very small sense contacts is given by [8]:

$$R_{out} \cong 2\frac{\rho_b}{\pi\delta}\ln\left(\frac{W}{s}\right) \quad (26)$$

on condition that: $s << W << L$.

The coefficient ρ_b denotes the effective material resistivity, and *s* is the small sense contacts diameter.

If the biased voltage of device is constant, ρ_b practical not depends of magnetic field. By substituting (26) into (25) it results spectral density:

$$S_{NV} = \frac{8kT}{\pi nq\mu_{Ch}\delta}\ln\left(\frac{W}{s}\right) \quad (27)$$

For a narrow bandwidth Δf around a frequency *f*, the signal-to-noise ratio, can be expressed as:

$$SNR(f) = V_H\left[S_{NV}(f)\cdot\Delta f\right]^{-1/2} \quad (28)$$

where Δf denotes a narrow frequency band around the frequency f, ($f > 100kHz$, [9]) and $S_{NV}(f)$ is the noise spectral density at the device output.

By substituting (15) and (27) into (28) it results:

$$SNR(f) = \left(\frac{\pi}{8hT} \cdot \frac{\mu_{Ch}}{qn\delta\Delta f \ln(W/s)} \right)^{1/2} r_H G I_D B_\perp \quad (29)$$

Since the signal-to-noise ratio increases with the drain current I_D, the maximal *SNR(f)* is limited only by maximal acceptable device dissipated power P_{max}.

From (15) and (18), we also obtain the Hall voltage as a function of the power $P = V_D I_D$ dissipated in the device.

Multiplying (15) and (18) member-by-member it results:

$$V_r = G\left(\frac{W}{L}\right)^{1/2} r_H \left(\frac{\mu_{Ch}}{\theta_{Ch}}\right)^{1/2} P^{1/2} \cdot B_\perp \quad (30)$$

where $P = V_D I_D$ in the power dissipated in the device.

From (29) and (30) it results:

$$SNR(f) = 1.11G\left(\frac{W}{L}\right)^{\frac{1}{2}} \left[\frac{\mu_{H_{Ch}}^2 \cdot P}{kT\Delta f \ln(W/s)} \right]^{\frac{1}{2}} B_\perp =$$

$$= 9.7 \cdot 10^9 \mu_{H_{Ch}} \left(G\frac{W}{L} \right)^{\frac{1}{2}} \left[\frac{P}{\Delta f \cdot \ln(W/s)} \right]^{\frac{1}{2}} B_\perp \quad (31)$$

where $T=300\ K$ and $k = 1.38054 \cdot 10^{-23} JK^{-1}$.

2.4 The NEMI for MOS –Hall plates

The mean square noise – equivalent magnetic induction, *NEMI*, in a frequency range (f_1, f_2), is obtained by substituting in the absolute sensitivity expression (19), the Hall voltage by the mean square noise voltage:

$$< B_N^2 >= S_A^{-2} \cdot \int_{f_1}^{f_2} S_{NV}(f) df \quad (32)$$

At high frequencies, thermal noise dominates. For a narrow bandwidth Δf around a frequency f by substituting (20) and (27) into (32) it results:

$$< B_N^2 >= \frac{8kT}{\pi} \cdot \frac{\rho_b \ln(W/s)}{\delta \mu_{H_{Ch}}^2} \cdot \Delta f \left(G\frac{W}{L} \right)^{-2} V_D^{-2} \quad (33)$$

The increasing of the channel length causes the decreasing of device performances. If the length increases twice, the noise-equivalent magnetic induction spectral density increases with 18% and if the same distance increases four times, *NEMI* increases with 148%.

3. CONCLUSIONS

The analysis of the main noise characteristics of the MOS-Hall plates shows that in case of thermal noise, the square structure (*W=L*) is theoretically favourable to obtain magnetic sensors of performance. The B_{DL} analysis shows that the $l/w = 0.5$ structure istheoretically favorable to obtain magnetic sensors of performance. Also substituting the silicon technology by using other materials such as *GaAs* or *InSb* with high carriers mobility allows the made of higher characteristics devices.

The analisys of the main characteristics of the double-collector magnetotransistor shows that the $W_E / L = 0.5$ structure is theoretically favourable to high performance regarding signal-to-noise ratio, as well as the offset equivalent magnetic induction.

The uses of magnetotransistors as magnetic sensors allows the achieving of some current-voltage conversion circuits, more efficient that conventional circuits with Hall plates.

The transducers with integrated microsensors have a high effieciency and the possibilities of using them can be extended to some measuring systems of thickness, short distance movement, level, pressure, linear and revolution speeds.

4. REFERENCES

[1] CĂRUNTU G., *Măsurări galvanomagnetice în dispozitive semiconductoare*,SECOMAR'99, Academia Navală "Mircea Cel Bătrân", Constanța, vol. II, pp. 69-74, 1999

[2] GRAY R.P., SEARLE C.L., *Bazele electronicii moderne*, vol. 1, Editura Tehnică, Bucureşti, 1973

[3] MIDDELHOEK S., AUDET S.A. *Physics of Silicon Sensors,* Academic Press, London, 1989*,* pp. 5.20-5.24

[4] R.P. GRAY, G. R. MEYER, *Circuite integrate analogice. Analize şi proiectare,* Editura Tehnică, Bucureşti, 1993, pp. 579, 583

[5] STERE R., BODEA M., *Tranzistoare cu efect de câmp,* Editura Tehnică, Bucureşti, 1972, pp. 117

[6] CĂRUNTU G.,*Microsenzori magnetici. Aplicații* Editura Societatea Autonomă de Informatică, Bucureşti, 1998

[7] CĂRUNTU G., Consideration about Thermal Noise for Magnetic Sensors*, Proceedings of the 9th Intenational Conference on Applied and Theoretical Electricity*, vol. I, Craiova, June 4-6, 1998, pp. 21-26

[8] BALTES H., POPOVIĆ R.S., Integrated Semiconductor Magnetic Field Sensors, *Proc IEEE* **74** 1107-32, 1986

POTENTIAL OF THE DISCRETE WAVELET TRANSFORM IN OCEANOGRAPHY SIGNAL PROCESSING

[1]PRICOP CODRUTA, [2]PRICOP MIHAIL

[1]Department of Naval Electrotechnics, Electronics and Computer Science, Constanta Maritime University ,
[2]Department of Naval Architecture, Naval Academy Constanta, Romania

ABSTRACT

In this paper we present a time-frequency signal processing techniques used to extract the salient features of underwater signal. The Discrete Wavelet Transform (DWT) is a transformation that can be used to analyze the temporal and spectral properties of non-stationary signals like underwater signal. In this paper we describe some applications of the DWT to the problem of extracting information from underwater signals. We analize the potential of the Discrete Wavelet Transform (DWT) in oceanography signal processing. We use for these purposes real signals, recorded with a Bruel&Kjaer measurement system from Black Sea environment.

Keywords: *underwater signal, signal processing, discrete wavelet decomposition, approximations and details signal components.*

1. INTRODUCTION

The signals in oceanography are complex and contain a lot of information. The underwater signals can be considered to comprise sounds - acoustic events of interest superimposed on background underwater sound environment. For this kind of signals, the low-frequency content is the most important because gives the signal identity. On the other hand, the high- frequency components of the signal gives the flavour, the nuance.

For these reasons, a signal decomposition method to extract the low-frequency and high-frequency of the underwater signal can be very efficiently exploited to extract different features of the highly non-stationary underwater signal.

The time-frequency signal processing technique used for the above purposes is the wavelet technique – discrete wavelet decomposition.

Underwater signal decomposition through Discrete Wavelet Transform (DWT) provide a compact representation of the signal that shows the energy distribution of the signal in time and frequency.

The DWT coefficients can be used to extract the main characteristics of the underwater signal and to compress the signal.

The DWT signal processing method can be also used to extract or minimise the white or coloured noise from underwater signal.

These lead to accurately describe to underwater sea environment.

2. WAVELET DECOMPOSITION MULTIRESOLUTION ANALYSIS

Every signal that belong to $L^2(R)$, the vectorial space of square integrable function, becames [1]:

$$f = \sum_i \alpha_i \psi_i \qquad , i \in Z \tag{1}$$

where $\{\psi_i\}_{i \in Z}$ is an orthogonal or biorthogonal bases of $L^2(R)$.

The coefficient α_i is the inner product:

$$\langle \psi_i, f \rangle = \alpha_i \qquad , i \in Z \tag{2}$$

These functions are called *atoms.* Relates to atom ψ, was defined the following operators[524]:

- the dilatation operator:

$$\sigma^s \psi = \sigma_2^s \psi(t) = 2^{-s/2} \psi\left(2^{-s} t\right) \tag{3}$$

- the modulation operator:

$$\mu_f \psi = e^{2\pi i f t} \psi(t) \tag{4}$$

- the translated operator:

$$\tau_p \psi = \psi(t - p). \tag{5}$$

The wavelet bases are obtained from a prototip atom ψ by *shift, modulation and scaling operations,* such as every signal $f \in L^2(R)$ can be decomposed as follows [1]:

$$f = \sum c_{j,k} \psi_{j,k} \tag{6}$$

where:

$$\psi_{j,k}(t) = 2^{-j/2} \psi\left(\frac{t-k}{2^J}\right) \tag{7}$$

The coefficients $c_{j,k}$ are given by:

$$c_{j,k} = \left(W_\psi f\right)\left(\frac{k}{2^j}, \frac{1}{2^j}\right) \tag{8}$$

The wavelet ψ generates an o.n. basis $\{ \psi_{j,k} ; j,k \in Z\}$ of $L^2(R)$ such as for each $j \in Z$ the subfamily $\{ \psi_{j,k} ; k \in Z\}$is a an o.n. basis that span subspace Wj and $\psi_{j,k}$ is a time window for extracting local information (on both magnitudes and locations) within the j^{th} frequency band or j^{th} octave:

$$H_j = \left(2^{j+1}\Delta\psi, 2^{j+2}\Delta\psi\right) \quad (9)$$

Sometimes we must drawn proprieties like time-frequency localization of signal. A signal is concentrated or spread in a region of time frequency plane, defined in accordance with a suitable measure of spread in time and frequency (e. g. second moment in time and frequency of the function normalized to unit energy) [2]. In this case the signal decomposition must be made in accordance with this task.

Recently, the interes was focused by wavelet signal decomposition, based on an wavelet atom ψ. Each atom has in time frequency plane a specific localization. A wavelet based decompozition leads to a TF localization of a signal in tiles with adapted sizes, a dyadic tiles [1]. These tiles in TF plane is called information cells. Relates to this time-frequency tiles, was defined time and frequency uncertainties. Heisenberg's uncertainty principle in time frequency measurements implies that the area of an information cell of a continous wavelet can never be less than $1/4\pi$. The information that we can obtain from such information cells are scale, position, and amplitude information.

In mathematical sens, wavelet was defined as 2D function depending on two parameters [3]:

- *s - scale parameter*, that can be related to frequency, and
- *τ (position) - localization translation parameter.*

Small scales-s correspond to high frequency (coarse frequency resolution and fine time resolution) and large scales-s correspond to low frequency (fine frequency resolution and coarse time resolution).

The localization parameter τ gives give the time frequency to the scale s.

$$\psi(s,\tau) = s^{-1/2}\psi\left(\frac{t-\tau}{s}\right) \quad (10)$$

These wavelets by translation and scaling, form a basis for R^2 ,the n vectorial space of square integrabil functions. Besides, the term *wavelet* was defined in [PH] în physical sense. Physical wavelet are defined as acoustic or electromagnetic waves, resulting from the emission of a time signal by a localized acoustic or electromagnetic source moving along an arbitrary trajectory in space.

The wavelet decomposition is a succesive approximation method wich adds more and more projections onto spaces spanned by wavelets and their shifts at different scales.

Multiresolution means the approximation of signal at different levels of resolution.

The definition of multiresolution analysis is given in [1]:

The wavelet $\psi \in L^2(R)$ generates a family of subspaces of $L^2(R)$, W_j ,such as:

$$L^2(R) = \sum_{j\in Z} W_j := \ldots + W_{-1} + W_0 + W_1 + \ldots \quad (11)$$

where

$$W_j := clos_{L^2(R)}\left\langle \psi_{j,k}; k \in Z \right\rangle \quad (12)$$

Every $f \in L^2(R)$ has a unique decomposition

$$f(x) = \ldots + g_{-1}(x) + g_0(x) + g_1(x) + \ldots \text{ ,where } g_j \in W_j. \text{ for all } j \in Z. \quad (13)$$

The coefficient sequence of g_j (the unique wavelet series representation of f in W_j) gives localized spectral information of f in j-th octave in terms of the integral wavelet transform $W_{f,\psi}$.

The vectorial space $L^2(R)$, is also represented as [2]:

$$clos_{L^2(R)}\left(\bigcup_{j\in Z} V_j\right) = L^2(R). \quad (14)$$

The subspaces V_j, defined as $V_j := \ldots + W_{j-2} + W_{j-1}$ satisfy:

1. $\ldots \subset V_{-1} \subset V_0 \subset V_1 \ldots$;
2. $clos_{L^2(R)}\left(\bigcup_{j\in Z} V_j\right) = L^2(R)$;
3. $\bigcup_{j\in Z} V_j = \{0\}$ (15)
4. $V_{j+1} = V_j + W_j; j \in Z$
5. $f(x) \in V_j \Leftrightarrow f(2x) \in V_{j+1}; j \in Z$.

The function $\phi(x) \in V_0$, if exist and has the that $\{\phi(\bullet - k) : k \in Z\}$ is a Riesz basis of V_0 with bounds A ,B, and $\{\phi_{j,k} : k \in Z\}$ is a Riesz basis of Vj , is called "scaling function "or "father wavelet". This scaling function generates a multiresolution analysis $\{V_j\}$ of $L^2(R)$ [4].

3. DISCRETE WAVELET TRANSFORM

The wavelet signal analysis based by Discrete Wavelet Transform (DWT) is a *time / frequency* method that decompose signal in low frequency and high-frequency components.

Signal decomposition through Discrete Wavelet Transform can be efficiently realized by means of a pair of low-pass and high-pass wavelet filter (Mallat, 1989), denoted as *h(k)* and $g(k) = (-1)^k h(1-k)$, respectively.

These filters, also known as *Quadrature Mirror Filters (QMF),* are constructed from the selected mother wavelet $\psi(t)$ and its corresponding scaling function $\phi(t)$, expressed as:

$$\begin{cases} \phi(t) = \sqrt{2}\sum_k h(k)\phi(2t-k) \\ \psi(t) = \sqrt{2}\sum_k g(k)\psi(2t-k) \end{cases}. \quad (16)$$

Using the wavelet filters, the signal being analysed is decomposed into a set of low and high-frequency components (Mallat, 1999):

$$\begin{cases} a_{j,k} = \sum_m h(2k-m)a_{m,j-1} \\ d_{j,k} = \sum_m g(2k-m)a_{m,j-1} \end{cases} . \quad (17)$$

In equation (17), $a_{j,k}$ is the approximation coefficient, which represents the low-frequency component of the signal, and $d_{j,k}$ is the detail coefficient, which corresponds to the high-frequency component. The approximate and detail coefficients at wavelet scale 2^j (with j denoting the level) are obtained by convolving the approximate coefficients at the previous level (j-1) with the low-pass and high-pass filter coefficients, respectively.

4. UNDERWATER SIGNAL PROCESSING BY USING WAVELET - BASED TECHNIQUES

In underwater signal recognition the task is to extract relevant features in both time and frequency domain. For underwater signal the salient features are sharp peaks, that correspond to isolated sounds, and the discrete frequency events can be attributed to biological or another type of sound or vibration sources from ocean environment [7].
Fine resolution in time in processing of underwater signal leads to low frequency components extracting. That is essential in characterization of complex underwater signal because these components correspond to ocean environment.

Fine resolution in frequency in processing of underwater signal leads to extraction and localization of individual sounds from, that correspond of biological underwater sound sources.

The noise reduction is based on the selection of the most significant wavelet coefficients by using discriminant analysis betweeen the signal with noise and noise-only.

Local signal features are essential in interpreting of underwater information and is very important to extract these from multiresolution analyzing of this kind of signal.

Multiresolution processing, multiscale ridge detection, structure coherent/noncoherent discrimination, noise reduction based by wavelet techniques might be successfully used in underwater signal processing [5].

5. DISCRETE MEYER WAVELET TRANFORM FOR UNDERWATER SIGNAL DECOMPOSITION AND RECONSTRUCTION

In this paper we use The Discrete Meyer Wavelet for underwater signal analysis because this wavelet has a shape suited for this kind of signal.

The recorded signal was decomposed with Discrete Transform at 5 and 12 level of decomposition.

For Meyer Wavelet and scaling function are defined in frequency domain, starting with an auxiliary function ν [3].

The Meyer Wavelet and scaling function are defined as follows in [3]:

- Meyer Wavelet function:

$$\hat{\psi}(\omega) = \left(2\pi^{1/2}\right) e^{i\omega/2} \cos\left(\frac{\pi}{4}\nu\left(\frac{3}{4\pi}|\omega|-1\right)\right)$$

$$\text{if} \quad \frac{4\pi}{3} \le |\omega| \le \frac{8\pi}{3}$$

$$\hat{\psi}(\omega) = \left(2\pi^{1/2}\right) e^{i\omega/2} \sin\left(\frac{\pi}{2}\nu\left(\frac{3}{2\pi}|\omega|-1\right)\right)$$

$$\text{if} \quad \frac{2\pi}{3} \le |\omega| \le \frac{4\pi}{3}$$

$$\hat{\psi}(\omega) = 0 \qquad \text{if} \quad \omega \notin \left(\frac{2\pi}{3}, \frac{8\pi}{3}\right) \quad (18)$$

- Meyer scaling function:

$$\hat{\phi}(\omega) = \left(2\pi^{-1/2}\right) \qquad \text{if} \qquad |\omega| \le \frac{2\pi}{3}$$

$$\hat{\phi}(\omega) = \left(2\pi^{-1/2}\right) \cos\left(\frac{\pi}{2}\nu\left(\frac{3}{2\pi}|\omega|-1\right)\right)$$

$$\text{if} \quad \frac{2\pi}{3} \le |\omega| \le \frac{4\pi}{3}$$

$$\hat{\phi}(\omega) = 0 \qquad \text{if} \quad \omega > \frac{4\pi}{3} \quad (19)$$

The Meyer scaling function and the Meyer Wavelet are represented in Figure 1.

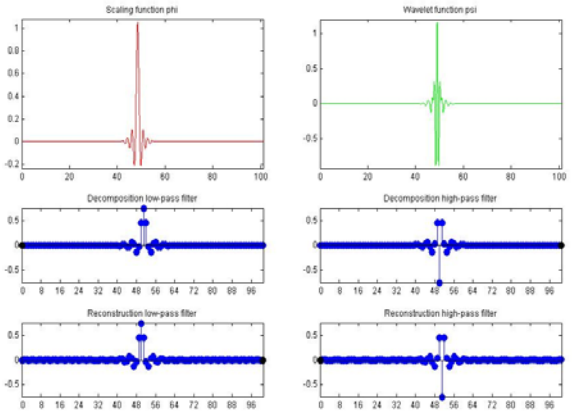

Figure 1 Scaling Meyer Function and and Meyer Wavelet. The Meyer wavelet: decomposition low-pass filter and decomposition low-pass filter

6. DWT SIGNAL PROCESSING OF THE UNDERWATER RECORDED DATA: OBJECTIVES AND RESULTS

Underwater signals were recorded in the Black Sea, in Constantza harbour.

The very long data recording were partitioned into 30 second time blocks. Each block was sampled at sampling period $T_S = 5.72 \cdot 10^{-6}$ s and sampling frequency F_s = 17.476 kHz. Each block contains 524288 measurements points.

The recorded signal blocks were decomposed with MATLAB - Wavelet toolbox [8] through Discrete Meyer Wavelet Transform at 5 level and at 12 level decomposition.

The Discrete Meyer Wavelet decompositions of the recorded underwater signal are represented in Figure 2, Figure 3, Figure 4.

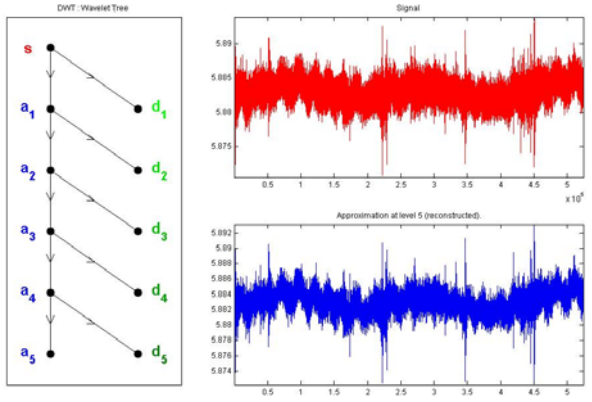

Figure 2 Discrete Meyer Wavelet Decomposition (5 Levels) applied to underwater signal: Wavelet Tree. Signal and Approximation at level 5 (reconstructed)

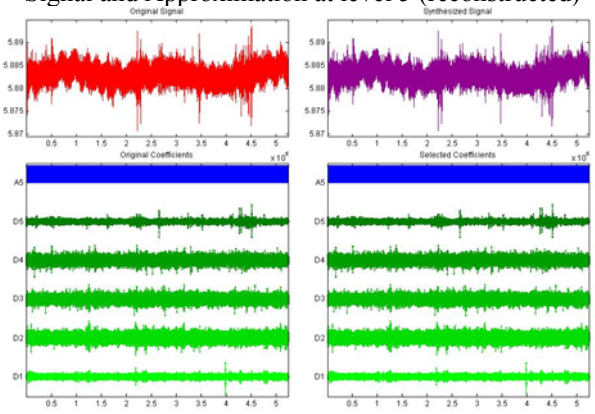

Figure 3 Discrete Meyer Wavelet Transform (5 Levels) applied to underwater signal: original signal and synthesized (reconstructed) signal

The Discrete Meyer Wavelet Transform (12 Levels) applied to underwater signal is represented in Figure 4. In this figure the recorded signal, the approximations and details components are displayed.

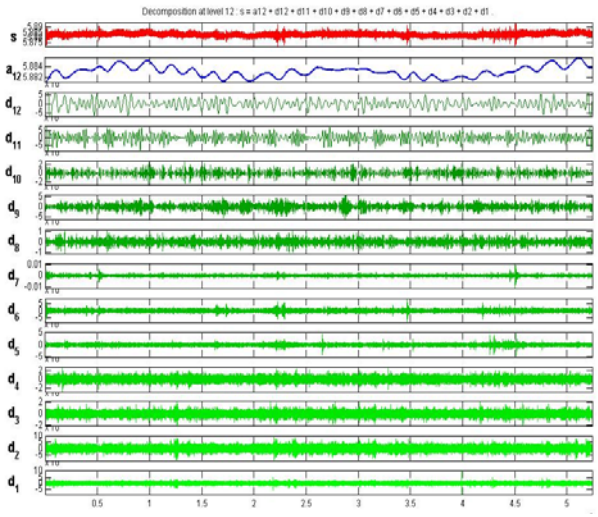

Figure 4 Discrete Meyer Wavelet Transform (12 Levels) applied to underwater signal: Signal, Approximations and Details

The Discrete Wavelet transform split the frequency band of the signal into disjunct frequency subbands as related in Table 1.

Table 1. Discrete Wavelet Transform (DWT) and splitting of the frequency band for the recorded signal

Signal	Band: [0 ; 25 600 Hz]	
1 level Discrete Wavelet Decomposition	Approximation A1: [0 ; 25 600 Hz]	Details D1: [0 ; 25 600 Hz]
2 level Discrete Wavelet Decomposition	Approximation A2: [0; 12800 Hz]	Details D2: [12800 Hz; 25 600 Hz]
3 level Discrete Wavelet Decomposition	Approximation A3: [0; 6400 Hz]	Details D3: [6400; 12 800 Hz]
4 level Discrete Wavelet Decomposition	Approximation A4: [0 ; 3200 Hz]	Details D4: [3200 ; 6400 Hz]
5 level Discrete Wavelet Decomposition	Approximation A5: [0 ; 1600 Hz]	Details D5: [1600; 3200 Hz]
n level Discrete Wavelet Decomposition	Approximation An: [0 ; $25600/2^n$ Hz]	Details Dn: [$25600/2^n$; $25600/2^{n-1}$ Hz]
12 level Discrete Wavelet Decomposition	Approximation An: [0 ; $25600/2^{12}$ Hz]	Details Dn: [$25600/2^{12}$; $25600/2^{11}$ Hz]

DWT underwater signal decomposition calculates the DWT coefficients. These DWT coefficients provide a compact representation that shows the energy distribution of the signal in time and frequency.

In order to compress the underwater signal (to reduce the dimensionality of the extracted feature vectors associated to DWT signal decomposition) statistics over the set of the discrete wavelet decomposition can be used.

For extracting features in order to characterise the underwater signal we can use:

- the mean of the absolute value of the coefficients in each subband. These features provide information about the frequency distribution of the audio signal;
- the standard deviation of the coefficients in each subband. These features provide information about the amount of change of the frequency distribution;
- ratios of the mean values between adjacent subbands. These features also provide information about the frequency distribution.

These statistical characteristics of the recorded underwater signal, of the reconstructed (synthesized) signal and detail coefficients for Discrete Meyer Wavelet Transform at 12 level decomposition approximation are represented in Figure 5 and Figure 6.

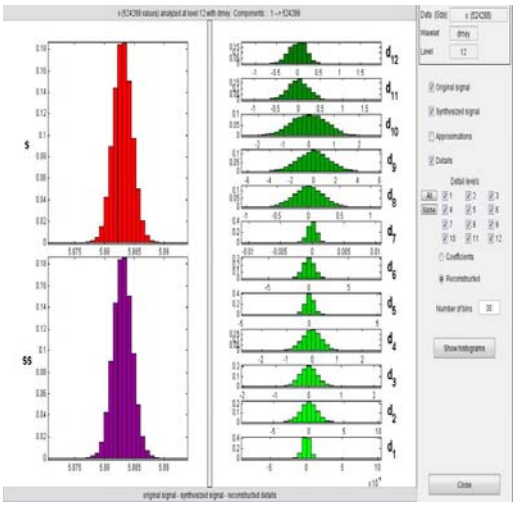

Figure 5 Discrete Meyer Wavelet Transform (12 Levels) applied to underwater signal: Signal, Approximations and Details - statistical characteristics

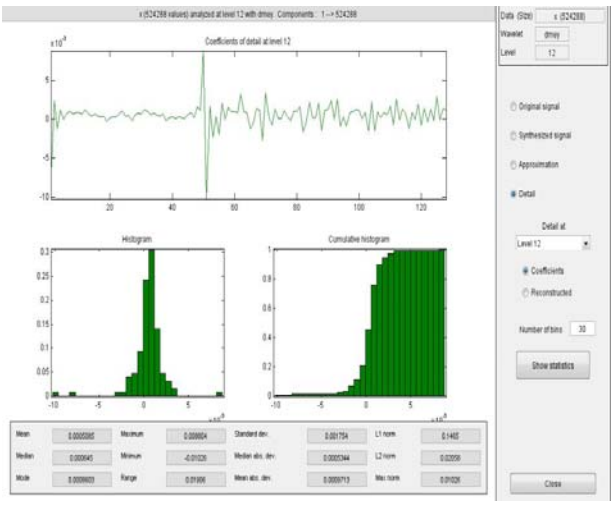

Figure 6 Discrete Meyer Wavelet Transform (12 Levels) applied to underwater signal: Details component at Level12 - statistical characteristics

7. CONCLUSIONS

The aim of this paper has been to provide an introduction to promising potential application of wavelets in underwater signal processing field.

In this paper we showed that many wavelet-based techniques developed for underwater signal processing applications should be successfully applied to analyze and characterize this kind of signal.

Since the backscattering in oceanography is a non-stationary process, the simultaneous time-frequency localization characteristics are considerably important. The two dimensional space described by time and frequency is called phase space .

Wavelet-based techniques used in underwater signal processing leads to an optimum time-frequency localization and characterization of salient signal features as transient or isolated components.

8. REFERENCES

[1] Charles K. Chui, *Wavelets: A Tutorial in Theory and Applications*, vol II *of Wavelet Analysis and its Applications*, Academic Press, USA, 1992.

[2] R.A. Gopinath, C.S. Burrus, *Wavelet Transforms and Filter Banks* printed in *Wavelets; A Tutorial in Theory and Applications*, vol II, Academic Press, USA, 1992.

[3] I. Daubechies, *The wavelet transform, time-frequency localization and signal analysis,* IEEE Transactiomns on Information Theory, 1990.

[4] N. Hess-Nielsen, M.V. Wickerhauser, *Wavelets and Time-Frequency Analysis,* Proc. of the IEEE, vol.84, No.4, 1996.

[5] Pricop Codruta: *Procesarea Wavelet A a Semnalelor Radar,* Editura MATRIX, Bucureşti, 1999.

[6] Marco Cagnozzo, *Wavelet Transform And Three Dimensional Data Compresssion,* Ph.D. Thesis, University of Napoly *Federico II*, 2004.

[7] David Havelock, Sonoko Kuwano, Michael Vorlander (editors): *Handbook of Signal Processing in Acoustics,* USA, 2008.

[8] Michel Misiti, yve misiti, Georges Oppenheim, Jean Michel Poggi, *Wavelet Toolbox- User's Guide*, The MathWorks, USA, 2006.

APPLICATIONS OF WAVELET ANALYSIS IN COMPRESSION OF QUASIPERIODIC SIGNALS

RADUCANU MIRCEA

University "Politehnica" Bucharest, Romania

ABSTRACT

In this paper we present an algorithm for quasi-periodic signal compression using wavelet analysis and linear prediction. We use this algorithm for ECG compression. The algorithm begins with the segmentation of quasi-periodic signal and then we perform a period and amplitude normalization of each period. In the case of ECG we detect the R wave for the signal segmentation. For these vectors we apply the wavelet analysis and we obtain the first level of compression by eliminating the lowest coefficients of the wavelet transform. The second level of compression is achieved by applying for the rest of the coefficients the linear prediction to reduce the number of bits for each coefficient. We have implemented the algorithm in Matlab and we tried to choose a wavelet family to obtain a better ratio of compression than those reported.

Keywords: *Data compression, wavelet analysis, linear prediction.*

1. INTRODUCTION

Data compression is a largely used procedure for data storage purposes. There exists a large variety of compression algorithms, many of them being standardized and each of them having its advantages and drawbacks. They offer speed, high compression rate and portability, but there is no single algorithm which best fits to all kind of applications. An overview of ECG compression research is presented in [4].

The compression of electrocardiogram (ECG) data is of great practical significance for transmission over telephone lines. In the techniques of compression we try to detect and remove the redundant information from signal.

The algorithm presented exploits the correlation between cycles. There is also some redundancy within each cycle (intrabeat correlation). Generally direct time domain techniques and transform domain techniques consider only the intrabeat correlation between successive samples. The algorithm presented is very flexible and exploits both the intercycle correlation and intracycle correlation.

2. ALGORITHM

The algorithm begins with the segmentation of signal.

2.1 Detection of R Wave

In order to make the segmentation of ECG signal we need first to find the positions of R peak waves. For detecting R waves we have used the technique reported in [5]. We consider a cycle as the signal from one R wave to the next.

The algorithm for detection of R waves use also the wavelet analysis. It begins with the selection of characteristic scale (the scale of multiresolution analysis where are concentrated the most energy of QRS complex). For this reason we select scales from 2^1 to 2^4.

Determination of modulus maximum lines of R waves is the next step of algorithm. A wave corresponds to two modulus maximum lines with opposite signs of $W_{2^j} f(n)$. The modulus maximum lines corresponding to R wave at characteristic scales is determined beginning with the scale 2^4. If several modulus maxima exist, we select the largest one. If no modulus maximum exists, then we set to zero.

Let $a_j(n_k) = |W_{2^j} f(n_k)|$. We can calculate the regularity exponent[5], [7]:

$$\alpha = log_2 a_{j+1}(n_k) - log_2 a_j(n_k) \quad (1)$$

and

$$\alpha = log_2 a_{j+1}\left(n_k^{j+1}\right) - log_2 a_j\left(n_k^{j}\right) \quad (1)$$

where $a_j\left(n_k^{j}\right)$ are the modulus maxima of wavelet transform in the point n_k at the scale j. For characteristic scales we calculate α_1, α_2 and α_3 for a singularity point. It is demonstrated that R wave corresponds to $\alpha_1 > 0$ and mostly $\alpha_2 > 0$. For most R wave we calculate $\alpha' = \frac{\alpha_1 + \alpha_2}{2}$ and it must $\alpha' > 0$ for the most R wave.

Next step in the algorithm is elimination of isolation and redundant modulus maximum lines. First we eliminate isolation modulus maximum lines. R wave corresponds to positive maximum-negative minimum and for the scale 2^1 the distance between these maximum is shorter than other scales. For these motif we serch all pairs that correspond to R waves and eliminate the isolated modulus maximum. For eliminate we use an interval around we search these pairs of maximum of wavelet transform. Next, we eliminate redundant modulus maximum lines. If we find more than two modulus maximum lines it must eliminate, because R wave correspond only for two modulus maximum lines.

In figure 1.a we show that the R peak detection is at the zero crossing point of a positive maximum-negative minimum pair at the scale 2^1 (figure 1.b).

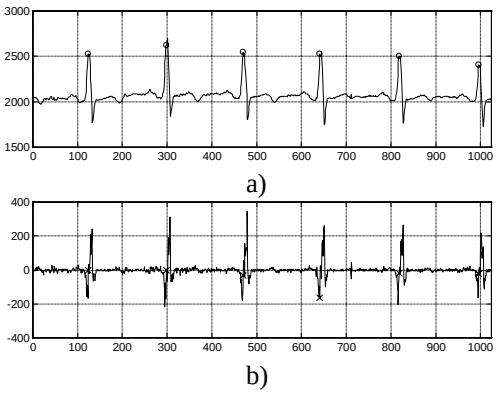

Figure 1 (a). The R peak detection; (b) Positions of zero crossing for positive-negative maximum for R wave at level 1.

2.2 Period and Amplitude Normalisation:

Generally, each cycle have a different length. It is necessary to normalise the length of each cycle and this is doing by the multirate technique [9]. So, we convert the beat of ECG signal into beats of a constant period eliminating the effect of heart rate variability.

The choice of the fixed length is not difficult: the new sampling rate must still satisfy the Nyquist criterion, it must be greater than the maximum possible period of any cycle and for the use of the fast wavelet transform it must be a power of 2. For the ECG signal used we select the fixed length to 256 samples. It is necessary to send to the decoder the original length for each beat in order to make the reconstruction.

For reduce de rate of transmission we calculate at the encoder a mean beat period (MBP) from some initial cycles and we transmit the MBP and the difference between the length of a beat and MBP.

The normalisation is made by interpolation of the variable length by the fixed length and then we made the downsampling with the variable length factor for each beat. The block for this operation is show in figure 2.

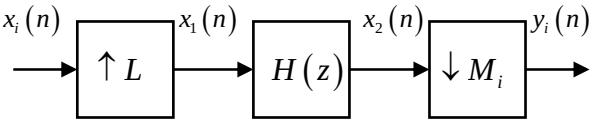

Figure 2. Period normalisation

The output of the system is given by:

$$y_i(n) = \sum_{k=0}^{P_i} x_i(k)\, h(nM_i - kL) \qquad (2)$$

where:

- $x_i(n)$, $y_i(n)$ are the n-th samples of the i-th input beat and output beat, respectively;
- $h(n)$ is the impulse response of the filter who remove the aliasing caused by the downsampling of the signal;
- P_i is the total number of samples in i-th original beat;
- L, M_i are the upsampling and respectively downsampling factors for the i-th beat vector.

We also make an amplitude normalisation foe each beat. Each sample of a beat is divided by magnitude of the largest sample of that beat. Similarly we calculate the average amplitude scale (AASF) from a few initial beats and send to the decoder the AASF and the difference between of maximum amplitude of a beat and AASF.

2.3 Wavelet Transform for Signal Decomposition

For each beat we apply the wavelet transform[1], [2], [3]. The general expression for this decomposition is

$$x(t) = \sum_j \sum_k \omega_{j,k} \Psi_{j,k}(t) \qquad (3)$$

where:

- $x(t)$ is the signal to be analysed;
- $\Psi_{j,k}(t)$ is the dilated and shifted version of mother wavelet $\Psi(t)$,
- j, $k \in \mathbb{Z}$ determine the dilation and shift factor, respectively;
- $\omega_{j,k}$ are the wavelet coefficients

and

$$\begin{aligned} \Psi_{j,k}(t) &= \Psi\left(2^j t - k\right), \\ \omega_{j,k} &= \left\langle x(t),\ \Psi_{j,k}(t) \right\rangle, \\ x(t) &= \sum_j \sum_k \omega_{j,k} \Psi\left(2^j t - k\right) \end{aligned} \qquad (4)$$

For each Period and Amplitude Normalisation (PAN) beat we calculate the wavelet coefficients using the Mallat's pyramidal algorithm (DWT) [6]:

$$X_i = \left[\omega_{01} \quad \omega_{11} \quad \omega_{21} \quad \omega_{22} \quad \ldots\right] \qquad (5)$$

The first level of compression is realised by retaining only a few coefficients, without loss of significant information,

2.4 Linear Prediction of Wavelet Coefficients

In the wavelet transform we have a correlation between the wavelet coefficients of different normalised beats. This we call the interbeat correlation. Instead to transmit the coefficient we transmit a residual coefficient. This residual coefficient is the difference between the coefficients and the estimate from a certain number of past coefficients. The magnitude of residual coefficient is less than the original and also we can reduce the number of bits. This is the idea of linear prediction (LP). A general theory is presented in [8].

The residual is defined by:

$$e_{jn}(i) = \omega_{jn}(i) - \hat{\omega}_{jn}(i) \qquad (6)$$

and the estimated coefficient is:

$$\hat{\omega}_{jn}(i) = a_{1,jn}\omega_{jn}(i-1) + \cdots + a_{p,jn}\omega_{jn}(i-p) \qquad (7)$$

where:

- p is the order of prediction;
- $a_{1,jn}$, ..., $a_{p,jn}$ are the LP coefficients.

We calculate the wavelet transform for each beat and the result are organised as follows:

$$V = \left[X_1 \quad X_2 \quad X_3 \quad \cdots \quad X_{N_{tot}} \right] \tag{8}$$

where N_{tot} is the total number of beats. We group the corresponding coefficients from all beats:

$$U_i = \left[V(i) \quad V(P+i) \quad \cdots \quad V\left((P-1)N_{tot}+i\right) \right] \tag{9}$$

Where $i = \overline{0, P-1}$; P is the length of wavelet transform.

Instead to transmit these vectors U_i we make linear prediction and also we reduce the rate of data. It is not necessary to transmit all these sets, because not all the coefficients are significant.

2.5 Choice of Significant Coefficients

Now, we must find an algorithm that selects only the important coefficients. One significant coefficient for one vector U_k is not compulsory significant for other vector U_m, and for the increasing rate of compression w must transmit only one list of the positions of coefficients for all vectors.

First we sort the coefficients of vectors of vectors X_i in the decreasing order and keep the position of coefficients in a vector Pos_i. The length of vector Pos_i is P and suppose that we wish that the list had L elements. First we select from each vector Pos_i, $i = \overline{1, N_{tot}}$ the first location and we put in the variable $List$ (only one times a location).

If the length of $List$ is little than L we go to the next location for all vectors Pos_i, $i = \overline{1, N_{tot}}$. We repeat this procedure until the length of variable $List$ is equal or greater than L.

If is greater than L we remove the last few position in order to obtain the length L. The length L is a parameter of the algorithm that must be selected for having a good reconstruction signal. We make linear prediction of vectors U_i only if $i \in List$.

2.6 Choice of Wavelet Transform

We observe that for different wavelet functions and for the same rate of compression we obtain a different error of reconstructed signal. We use the normalized root mean square error:

$$NRMSE = \sqrt{\frac{\sum_{i=0}^{N-1} \left[x_0(i) - x_r(i) \right]^2}{\sum_{i=o}^{N-1} x_0^{\,2}(i)}} \tag{10}$$

where:

- N is the total number of samples;
- $x_0(n)$ and $x_r(n)$ are the n-th samples of original and reconstructed ECG.

Also we mention that the formula for the rate of compression is:

$$CR = \frac{K \sum_{i1=}^{P} T_i}{P\left(N_{tot} b + \alpha_a + \alpha_p\right) + N_{tot}\left(p b_p + b_{nz}\right) + b_{ap} + b_{aa}} \tag{11}$$

where:

- K is the number of *bits*/*sample* in the original signal;
- T_i is the period of i-th beat;
- P is the total number of beats;
- N_{tot} is the number of coefficients whose residuals are transmitted for each cycle,
- b, α_a, α_p are the number of bits used for transmitting each residual, scale factor difference and period difference, respectively;
- p is the order of the LP filter;
- b_p, b_{nz}, b_{ap}, and b_{aa} are the number of bits used for transmitting each LP parameter, each element of $List$, the MBP and the AASF, respectively.

In figure 3 and figure 4 we present a zoom for one beat of the original signal, reconstructed signal and the error of reconstructed signal for the same parameters of compression: 53 beats, numbers of elements of $List = 31$, $p = 3$, $b_p = 12$, $b_{nz} = 12$, $b_{ap} = 8$, $b_{aa} = 8$. In these conditions we obtain a same $CR = 7{,}67:1$ using Haar wavelet filter (figure3) and Daubechies wavelet filter with $N = 20$ (figure4).

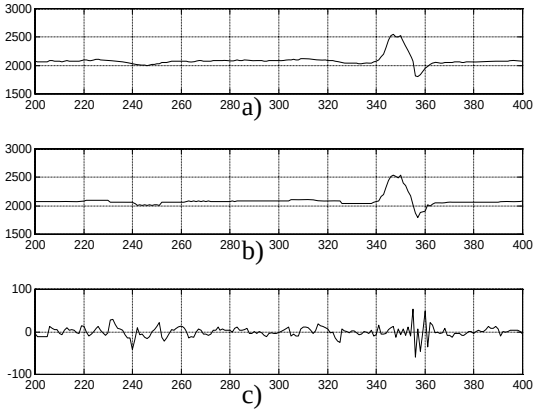

Figure 3 (a) The original ECG signal; (b) the reconstructed ECG signal after compression using Haar wavelet filter; (c) the error of reconstructed signal

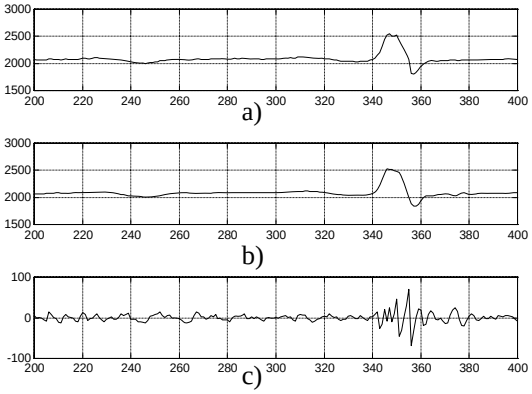

Figure 4 (a) The original ECG signal; (b) the reconstructed ECG signal after compression using Daubechie wavelet filter with length 20; (c) the error of reconstructed signal

In table 1 we present the normalized root men square error calculated for:

- 1500 samples using the prediction order 6;
- the *List* of wavelet coefficients 31;
- numbers of bits for coefficients of prediction filter 10;
- the numbers of bits for residual coefficients 7.

For these parameters we obtain a rate of compression 4.18:1

Table 1. Normalized root men square error (NRMSE) for different wavelet filter

Wavelet filter	NRMSE
Haar	0.82
Daubechies, $N = 4$	0.62
Daubechies, $N = 20$	0.86
Symmlet, $N = 4$	0.68
Symmlet, $N = 10$	0.63
Coiflet, $N = 1$	0.67
Coiflet, $N = 5$	0.59
Beylkin	0.88
Vaidyanathan	0.89

3. CONCLUSIONS

The presented algorithm exploits the intercycle correlation which was not used for the most of other algorithms. Although the algorithm is complicated (a high volume of computations) we obtain a good rate of compression (12:1) without loss of significant rhythm or morphological information.

We mention that the error is uniformly distribuited for all the samples of a beat. The QRS complexes are coded with an error equal to that in the other regions in each cardiac cycle.

4. REFERENCES

[1] DAUBECHIES, I., *Ten Lectures on Wavelet*, SIAM, Philadelphia, 1992

[2] DAUBECHIES, I., "The Wavelet Transform, Time-Frequency Localization and Signal Analysis", IEEE Transaction on Information Theory, vol. 36, no. 5, pp. 961-1005, September 1990

[3] DAUBECHIES, I., *Othonormal Bases of Compactly Supported Wavelets"*, Communication on Pure Applied Mathematics, no. 41, pp. 909 – 996, 1998

[4] JALALEDDINE, S.M.S., HUTCHENS, C.G., STARRAN, R.D., COBEERLY, W.A., "ECG Data Compression Techniques – A Unified Approach", IEEE Transaction on Biomedical Engineering, vol. 37, pp. 329-343, 1990

[5] LI, C., ZENG, C., TAI, C., "Detection of ECG Characteristic Points Using Wavelet Transforms, IEEE Transaction on Biomedical Engineering, vol.42, pp. 21-28, 1995

[6] MALLAT, S., " A Theory for Multiresolution Signal Decomposition: The Wavelet Representation", IEEE Transaction on Pattern Analysis Machine Intelligence, vol. 11, pp. 674-693, 1989

[7] MALLAT, S., HWANG, W.L., *"Singularity Detection and Processing with Wavelets"*, IEEE Transaction on Information Theory, vol. 38, pp. 617-643, 1992

[8] RAMAKRISHNAN, A.G., SAHA, S., " ECG Coding by wavelet Based Linear Prediction", IEEE Transaction on Biomedical Engineering, vol. 44, no. 12, pp. 1253-1261, 1997

[9] WALNUT, D.F., *An Introduction to Wavelet Analysis*, Birkhauser, 2002

STATISTICAL MODEL OF THE PEOPLE CONFIDENCE IN e-BUSINESS SERVICES

[1]RATIU CRINA, [2] CRACIUN MIHAELA-DACIANA, [3]BUCERZAN DOMINIC

[1]Daramec srl Arad Romania, [2,3] "Aurel Vlaicu" University of Arad, Romania

ABSTRACT

The e-Banking system is a new service in Romania for some banks; up to present the specialists reveal some flows concerning its security. In the near future it is expected to become to be as used as the credit card. The new terms of competition and the explosion of personal computers on the Romanian market brought new compartments at the bank level that support automated information processing service. Based on these considerations we have developed a statistical model to see the level of confidence granted by people to e-Banking services.

Keywords: *e-Business, e-Banking, statistical study, SPSS.*

1. INTRODUCTION

Digital economy has emerged as a consequence of changes caused by information technology, communications and economic globalization. The digital economy can be described as knowledge-based economy, as a economy based on information and on Information and Communication Technology (ICT). The digital economy is based on digital goods and services (intangible) and partly digital products (products sold through the Internet) for which ICT offers a support. The digital economy has not only emerged as a result of the ICT industry, but also because of the macroeconomic effects arising due to the new technology (increased productivity, lower inflation, changes in production structure, etc.).

In the business world, the concept of e-business, along with e-economy and e-commerce are familiar terms already famous. E-business represents a new way of leading business through electronic networking (Internet) in an effective way, by increasing speed, innovating and creating new values inside of organizations.

The market globalization, the technology and communication revolution, increasing competition between banks have resulted in unprecedented global changes in activities of this area.

Following the surveys conducted by the National Bank of Romania, it was concluded that the most important competitive advantages of a bank are: the management policy, the skilled personnel and technology - which grows continuously.

Information technology in banking has grown rapidly, because of the banking system evolution under the influence of the following factors: privatization, new competitors, co-branding (alliance between the two companies together to promote their products or services), mergers and acquisitions.

A significant change in the information processing method was waiving bank data processing system for the regional centers.

The new Competitive conditions, the massive penetration of the personal computers on the Romanian market have allowed the establishment of departments responsible for automatic data processing.

The main feature of a modern banking system is the level of connectivity maintained between the factors involved in banking activity.

A factor with an important role in the evolution of information technology in the banking system is the growing number of users of Internet. In Romania the rate of increase in the number of Internet users is one million per year according to PricewaterhouseCoopers.

The first attempts of the bank institutions to break the client - desk relationship can be found somewhere in prehistory of electronic services in the late '60s. In 1969, the Chemical Bank placed the first ATM in history in the New York Queens neighbourhood. The initiative was followed by an explosive expansion of electronic devices for money withdrawal and, therefore, bank cards, PIN codes and methods of protection against fraud.

Electronic banking services are the banking class of services that can be offered by a bank to individuals and companies through electronic means via a fixed or mobile telephone, and Internet. These services allow total or partial management of a bank account - a current account, a deposit or a credit card - by its owner, this being possible from any PC connected to Internet without being necessary the displacement to the bank.

Electronic banking offers the account holders access to information of the account and various financial and banking information in general. They may have access to these services if they register and after the bank accepts the registration, they will get a unique method of identification (name, password, PIN, control expressions, special device) to allow safe use of these kind of services.

Recently, In Romania, e-Banking services are developing rapidly. Under Ministerial Order No.16 of February 2003 and No.218/2004 on the approval of payment instruments with remote access, in 2004 the Ministry of Communications and Information Technology has freed opinions of electronic banking to 21 banks in Romania.

First there was the e-banking, Internet banking followed, and recently, in Romania was introduced mobile banking service. All three services offer bank customers about the same facilities. The difference between these facilities is given by the freedom of movement and the channel used to communicate with the bank.

Today we can say that all banks in Romania offer these kinds of services to clients. Despite this because of the risks of theft and electronic fraud, the majority of the Romanian population regards the new technologies with reluctance and mistrust. Taking this fact into consideration banking institutions must make significant efforts to familiarize the public with the new services and to highlight their advantages in terms of saving time, space and money.

2. CASE STUDY

In this paper we conducted a statistical study to analyze the level of trust granted by the population to e-banking services.

To achieve these goals we chose the working environment "Statistical Package for the Social Science " (SPSS) because it is a complex and powerful statistical program by any standards and it is able to perform essentially any type of statistical analysis ever used in the social sciences, in the business world, and other scientific disciplines.

The questionnaire applied batch of participants is as follows:

a) Gen : 1. Masculin_____ 2. Feminin_____

b) Varsta _____ (in ani)

c) Vechimea utilizarii serviciilor de e-banking_____ (in ani)

d) Tipurile de plati effectuate online 1. Plati utilitati/furnizori_____ 2. Plati catre trezoreria statului_____ 3. Plati in valuta_____ 4. Transfer intre conturi proprii_____

e) Domeniul de activitate 1. Prestari servicii_____ 2. Productie_____ 3. Bancar____

f) Mediul de rezidenta 1. Urban_____ 2. Rural_____

g) Urmatoarele afirmatii vizeaza opinia dumneavoastra privind increderea pe care o acordati serviciilor online oferite de banci. Va rugam sa le cititi cu atentie si a indicati masura in care sunteti de accord cu fiecare dintre aceste afirmatii, incercuind cifra corespunzatoare:

(1) Serviciile e-banking permit o mai buna dezvoltare a mediului economic

1 total dezacord 2 dezacord 3 relativ dezacord 4 relativ de accord 5 de accord 6 total de accord

(2) Serviciile e-banking conduc la o reducere semnificativa a cheltuielilor administrative

1 total dezacord 2 dezacord 3 relativ dezacord 4 relativ de accord 5 de accord 6 total de accord

(3) Serviciile e-banking nu vor determina o scadere a furtului electronic de bani

1 total dezacord 2 dezacord 3 relativ dezacord 4 relativ de accord 5 de accord 6 total de accord

(4) Serviciile e-banking vor conduce la o crestere a colaborarii intre institutiile financiare (banci) si clientii acestora

1 total dezacord 2 dezacord 3 relativ dezacord 4 relativ de accord 5 de accord 6 total de accord

(5) Serviciile e-bankingvor permite o mai buna promovare a imaginii institutiei financiare (bancii) care le furnizeaza

1 total dezacord 2 dezacord 3 relativ dezacord 4 relativ de accord 5 de accord 6 total de accord

Figure 1 Questionnaire applied in the study

The coding of the responses of subjects in the SPSS environment is:

- Subjects gender
  - variable names in SPSS : *Genul subiectilor*
  - Coding : 1 = masculin, 2 = feminin
- Subjects age
  - variable names in SPSS : *Varsta subiectilor*
  - Coding : Age in years
- Age using e-Banking
  - variable names in SPSS: *Vechimea utiliarii serviciilor de e-banking*
  - Coding: Age using e-Banking in years
- Payment tipes
  - variable names in SPSS: *Tipurile de plati effectuate online*
  - Coding: 1 = Paying utilities / suppliers; 2 = Payments to state treasury; 3 = Currency Payments, 4 = Transfer between own accounts
- The field of activity of the subjects
  - variable names in SPSS: *Domeniul de activitate al subiectilor*
  - Coding: 1 = services; 2 = Manufacturing, 3 = Banking
- Place of residence of subjects
  - variable names in SPSS: *Mediul de rezidenta al subiectilor*
  - Coding: 1 = Urban, 2 = Rural
- Item (1) - E-banking services allow better development to economic environment
  - variable names in SPSS : *Serviciile e-banking permit o mai buna dezvoltare a mediului economic*
  - Coding: 1 =" total dezacord"- totally disagree, 2 = "dezacosd" - disagree, 3 ="relativ dezacord"- rather disagree, 4 ="relativ de acord" - rather agree, 5 ="de acord" - agree, 6 = "total de acord" - totally agree
- Item (2) - E-banking service leads to a significant reduction in administrative expenses
  - variable names in SPSS: *Serviciile e-banking conduc la o reducere semnificativa a cheltuielilor administrative*

- Coding: 1 = ”total dezacord”- totally disagree, 2 = “dezacosd” - disagree, 3 =”relativ dezacord”- rather disagree, 4 =”relativ de acord” - rather agree, 5 =”de acord” - agree, 6 = “total de acord” - totally agree

➢ Item (3) - e-banking services will not decrease the electronic theft of money
- variable names in SPSS: *Serviciile e-banking nu vor determina o scadere a furtului electronic de bani*
- Coding: 1 = ”total dezacord”- totally disagree, 2 = “dezacosd” - disagree, 3 =”relativ dezacord”- rather disagree, 4 =”relativ de acord” - rather agree, 5 =”de acord” - agree, 6 = “total de acord” - totally agree

➢ Item (4) - e-banking services will lead to increased cooperation between financial institutions (banks) and their customers
- variable names in SPSS: *Serviciile e-banking vor conduce la o crestere a colaborarii intre institutiile financiare (banci) si clientii acestora*
- Coding: 1 = ”total dezacord”- totally disagree, 2 = “dezacosd” - disagree, 3 =”relativ dezacord”- rather disagree, 4 =”relativ de acord” - rather agree, 5 =”de acord” - agree, 6 = “total de acord” - totally agree

➢ Item (5) - e-banking services will help promote the financial institutions (banks) which provide them
- variable names in SPSS: *Serviciile e-bankingvor permite o mai buna promovare a imaginii institutiei financiare (banii) care le furnizeaza*
- Coding: 1 = ”total dezacord”- totally disagree, 2 = “dezacosd” - disagree, 3 =”relativ dezacord”- rather disagree, 4 =”relativ de acord” - rather agree, 5 =”de acord” - agree, 6 = “total de acord” - totally agree

The group of participants is formed of 21 subjects. After entering the data in SPSS environment it shows the following:

➢ The sample description is based on the following variables: subjects gender and field of activity. We may note that:
- 11 are men, representing 52% of the total and 9 are female, representing 42% of the total.
- 9 subjects working in the field of services, representing 43% of total, 7subjects working in the field of manufacturing and they represent 33% of the total and 4 subjects work in the banking environment, representing 19% of the total.
- from the total of 18 subjects from urban areas, nine (50%) have masculine gender and 9 (50%) have feminine gender, also the participants from rural areas 2 (100%) have masculine gender

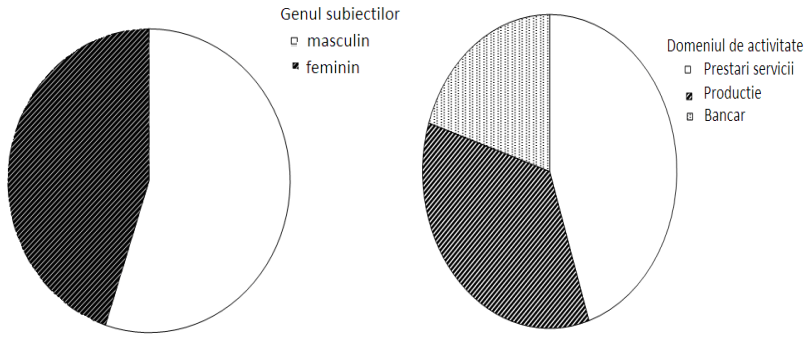

Figure 2 – Graphic illustration of a lot of subjects

We used the "T test" to assess whether respondents salary is significantly higher or lower than the average salary of 600 Ron. The table "One-Sample Statistics" shows information on the number of subjects (20), their average salary (1095), the standard deviation of the mean and the standard error of the mean. Comparing the average salary of respondents to the average wage (1095> 600) we conclude that the subjects surveyed have a higher salary than the average.

One-Sample Statistics

	N	Mean	Std. Deviation	Std. Error Mean
salariul	20	1095,0000	538,49205	120,41048

Table 1 One-Sample Statistics

The table "One-sample Test" shows t test results of comparing the average wages in question. We observe that t (19) = 4.11, the significance test is less than 0.05 which means that the difference between average wages of 495 is statistically significant.

The table shows the confidence interval with a probability of 95% in which the difference between mean is included. We observe that zero is not included in this range because the difference between average wages is significant. The conclusion is that the subjects interviewed have a salary significantly higher than the medium wage.

One-Sample Test

	Test Value = 600					
	t	df	Sig. (2-tailed)	Mean Difference	95% Confidence Interval of the Difference	
					Lower	Upper
salariul	4,111	19	,001	495,00000	242,9780	747,0220

Table 2 One-sample Test

The "Binomial Test" checks if the proportion of men and women in the sample differs significantly from 0.50.

The column N of the table "Binomial Test" shows the real frequencies which occurred in men and women from the sample surveyed.

We observe that 9 are women and 11 men. In Prop Observed column are presented the proportions by gender.

The 11 men represent 55% of the total 20 respondents. The proposed test column shows the proportion of reference with which to compare the proportion of men and women in the sample. How the threshold of significance is> 0.05 (0.824) it follows that men predominate insignificantly compared with women in the sample surveyed.

Table 3 Binomial Test

Binomial Test

	Category	N	Observed Prop.	Test Prop.	Exact Sig. (2-tailed)
genul subiectilor Group 1	feminin	9	,45	,50	,824
Group 2	masculin	11	,55		
Total		20	1,00		

"CHI - square" test check if there is a formed opinion in the sample regarding the 5 items included in the questionnaire. The first table compares observed frequencies with theoretical frequencies, the column "Residual" are presented the differences for each variable.

In the table "Test Statistics" we find the value of chi-square = 14.000. Because Sig (0.007) <0.05 leads to the fact that distribution is not uniform, the six categories of attitudes have not the same frequency.

Through the One-Way ANOVA method we check if there are differences depending on the field of activity regarding the trust in the statements from the questionnaire.

There are three areas of activity, so the null hypothesis H0 is that the averages of the three areas of activity are equal. Research hypothesis H1 is that the averages of the groups are different. Significant results are presented in Table Tests of Normality.

We observe that the results of the Shapiro - Wilk test, which is stronger than Kolmogorov - Smirnov are statistically insignificant, therefore the distribution is normal for each of the three fields, thus one can apply the ANOVA test.

The ANOVA table shows the sum of the squares, the degrees of freedom, the variances, F test result, the error. The probability of error when we reject the hypothesis is 0.068 > 0.05, thus null hypothesis is accepted, that the activity does not influence the degree of confidence statements in the questionnaire.

Using the regression test we can determine how the Place of residence of subjects influences the age of e-banking usage. We obtain the regression line equation:

$$Y = a + b\,X = 3{,}333 + 1{,}333\,X \qquad (1)$$

Following the analysis of the results we can say that the Place of residence of subjects influences the period of using e-Banking services.

3. CONCLUSIONS

Society changes at an increasing speed. Nowadays, progress and success can be achieved much faster than in the past.

The Internet is the communication tool and source of information that experienced the largest development in the whole history of civilization, and may be the fastest-spreading tool ever. Dissemination of economic knowledge through Information and Communication Technology (ICT), Internet and e-commerce becomes as important as changes brought by the industrial revolution. The global economic landscape continues to change and to reconfigure organizational structures. The new economy changes the conditions in which people live and work, makes it possible to leap over the existing barriers of traditional economic development.

Although grows rapidly and electronic financial services are used increasingly, considering the study that we conducted we may conclude that Romania has a large population that is not familiar with these notions. Although banks make a lot of investments to increase the degree of the use of electronic services, still there are a lot of clients that are reluctant and mistrustful in this kind of tranzactions.

Most subjects who participated in the study say that security of electronic transactions, how this services are implemented and their quality are the arguments for their final choice in the use or disuse of electronce banking services.

Yet banks have to endeavor to remove significant population reluctance and mistrust on online services.

Among the measures that credit institutions have adopted in this regard are included lowers transactions fees through Internet banking, going even to their gratuity.

Each bank has its peculiarities of internet banking operations, but most of them try to improve this service by implementing as many facilities as possible and by the improvement of the security of transactions.

Despite these issues raised by e-Banking services based on the results from the study that we conducted we may conclude that unlike e-commerce sites or entertainment ones, online banking is enjoying increased attention from a major part of the population from Romania, due to the impact that bank account has in the economic life of its user.

The Statistical Model that we developed in this case study will be implemented in a project that includes a large number of subjects relevant to determine the level of public confidence in online banking services. We need to corroborate it with the result of a marketing study and analysis of rapid change, risks and progress of the cyber world.

4. ACKNOWLEDGMENTS

This paper would not have been written without the help of several colleagues who offered their knowledge and unconditional support.

Also special thanks to the family and best friends who have always been there for us.

5. REFERENCES

[1] ADRIAN VICENTIU LABAR, *SPSS pentru stiintele educatiei* , Editura Polirom, 2008

[2] *** - http://www.ehow.com/about_5459472 _spss-software.html - vizitat 29.10.2010

[3] *** - http://www.google.ro/url?sa=t&source =web&cd=1&ved=0CBUQFjA%2Fspss%rad=rja-vizitat 29.10.2010

[4] *** - http://www.ghiseulbancar.ro/articole Studiu_privind_serviciile_de_e-banking.htm - vizitat 30.10.2010

[5] *** - http://www.google.ro/url?sa=t&source =web – Economia bazată pe cunoaştere – vizitat 30.10.2010

[6] DONATH LILIANA, ŞEULEAN VITORIA, CERNEA VERONICA, *Operaţiuni, instrumente şi riscuri în sistemele de plăţi,* Editura Mirton, 1999

[7] Legea nr. 455 din 18 iulie 2001 privind semnătura electronică, publicată în Monitorul Oficial, Partea I nr. 429 din 31 iulie 2001

[8] VASILACHE DAN , *Plăţi electronice*, Editura Rosetti Educational, 2004

SECTION IV

MATHEMATICAL SCIENCES AND PHYSICS

BORDERS CONDITIONS INFLUENCE ON THE HID LAMPS TEMPERATURE PROFILE

CRISTEA MIHAIL

„Politehnica" University of Bucharest, Faculty of Applied Science, Physics I Department, Romania

ABSTRACT

Type the abstract here using the Times New Roman font with point size 10. Leave a space of 10 points before and 10 points after it. The abstract should be brief, concise and have a maximum length of 10 lines. It should be informative giving the scope and emphasize the main conclusions, results and the significance of the work described.

Keywords: *HID lamps, positive column plasma, temperature profile index.*

1. INTRODUCTION

A high-pressure mercury arc lamp is a common HID lamp used in the lighting activity. The light emission in a mercury vapour electric discharge depends on the plasma discharge pressure. Mercury resonance line of $253.7nm$ has a natural spectral width due to the short lifetime of state level 6^3P_1 ($1.18\times10^{-7}s$). By increasing the pressure the resonance line will be prevented to leave the lamp (by self-absorption processes). The visible lines due to transitions from the upper levels $6D$ and $7S$ are enlarged enough so these are not suffer the phenomenon of "retention" in the plasma. Thus, the plasma radiation will be dominant in visible range.

The "retention" phenomenon is determined by the plasma mercury atoms distribution, which depends on the temperature distribution. Many works consider that the temperature profile is parabolic, with index up to 2 [1-3]. In most cases, the value of β is around 2.8 [4]. Exact knowledge of this index allows a better calculation of plasma parameters. The paper proposes a parametric analysis of the temperature profile exponent.

The first part of the paper presents the basic ideas of the model, while the second one is focused on the results of simulations. The final section contains conclusions and suggestions for further work needed for the improvement of the design of Hg lamps.

2. THEORY

2.1 Temperature distribution in the positive column plasma

In the case of HID lamps, the electron density is sufficiently high so that the number of collisions between electrons and heavy plasma species (neutral, positive ions) leads to a plasma micro equilibrium in every point. The distribution functions for each of plasma components are maxwelliane, the plasma being considered in the conditions of local thermodynamic equilibrium (LTE).

The high-pressure mercury lamps can be considered at LTE and the second moment of the Boltzmann's equation becomes important for knowing the temperature distribution. Once known the temperature, all other interest quantities can be calculated, such as: electrons distribution, heavy particles (neutral and ions) distributions, mobility of various species, convection movements and other.

Several approximations are considered in our model. All these approximations have practical justification. Thus, we assume that is not axial convection and cataphoresis in the positive column plasma. The first approximation is valid for vertical lamps which discharge tubes lengths around of $10\,cm$. The second assumption is justified by the changing of lamp power supply polarity.

We assume a constant pressure in any point of positive column plasma. The boundary effects are neglected, which means an infinite stretch supposition for the plasma column.

In the stationary regime the second momentum of Boltzmann equation became:

$$\frac{1}{r}\frac{\partial}{\partial r}\left(rk_{pl}\frac{\partial T}{\partial r}\right)+S=0 \qquad (1)$$

where k_{pl} is plasma thermal conductivity and S is the source term.

The plasma thermal conductivity is given by the formula [5]:

$$k_{pl}(T)=8.326\times10^{-2}\frac{\sqrt{T/m_{Hg}}}{r_m^2\Omega^{(2,2)}\left(T^*\right)} \qquad (2)$$

where $\Omega^{(2,2)}\left(T^*\right)$ is the plasma colission integrale at the reduced temperature $T^*=\frac{T}{(\varepsilon/k_B)}$, r_m and ε are respectively the distance and the interaction energy between the plasma constituents at equilibrium, k_B is the Boltzmann constant and m_{Hg} is the mercury atom mass.

For a Lenard-Jones interaction potential between mercury atoms, r_m and ε takes the values: $r_m=2.898$ Å and $\varepsilon/k_B=851K$.

The source term is $S(r,z)=U_J-U_{rad}$, where U_J is the Joule power contribution and U_{rad} is the radiant term.

The last term, related to the plasma net emission, raises many problems, in terms of correct estimation, but also from numerical convergence point of view after multiple iterations. This is the most affected term by the numerical diffusion. In this work, we preffere to use the aproximation given by Elenbaas [6]:

$$U_{rad} = 1.08\times10^{-10} n_{Hg}(T)\exp\left(-\frac{eV^*}{k_B T}\right) \quad (3)$$

where n_{Hg} is the mercury atoms density, e is the electron charge and $V^* = 7.8V$ is the average excited potential for the mercury atom.

Even in simple formula given by Elenbaas, the radiative term is very sensitive to the temperature distribution.

The term describing the heating through Joule effect is:

$$U_J = \sigma_{pl}\left|\vec{E}\right|^2 \quad (4)$$

where $\vec{E}$ is the electric field intensity inside the plasma and σ_{pl} is the plasma electrical conductivity.

The intensity of the electrical field $\left|\vec{E}\right|$ is calculated from the local Ohm's law for a given discharge intensity current I:

$$\left|\vec{E}\right| = \frac{I}{2\pi}\left(\int_0^R r\sigma_{pl}dr\right)^{-1} \quad (5)$$

where *R* is the discharge vessel radius.

The plasma electric conductivity is mainly due to the electrons, the ions having a much smaller mobility:

$$\sigma_{pl} = e\mu_e n_e \quad (6)$$

where n_e is the electron number density and μ_e is the electron mobility.

The electron number density is obtained from Saha's equation in the plasma neutrality condition $n_e = n_i$:

$$\frac{n_e n_i}{n_0} = \frac{2U_i}{U_0}\frac{(2\pi m_e k_B T)^{3/2}}{h^3}\exp\left(-\frac{E_i - \Delta E}{k_B T}\right) \quad (7)$$

where n_e, n_i and n_0 are the electronic, ionic and respectively neutrals species densities distributions.

In relation (7) factor 2 corresponds to statistical weight associated to the electron, U_i, U_0 are the ions and neutrals partitions functions, h is the Planck constant, E_i is the mercury ionisation energy, ΔE is the ionisation energy correction due to the electric charge distribution and m_e is the electron mass.

For the electron mobility we use the first approximation of the Shkarofsky formalism [7]:

$$\mu_e = \frac{3}{16}e\frac{\sqrt{2\pi/m_e k_B T}}{n_{Hg}\langle Q\rangle} \quad (8)$$

with $\langle Q\rangle = 120\times10^{-20} m^2$ taken from literature.

2.2 Boundaries conditions

Schafer shows that during current-off [8] only the temperature in the electrode regions is increased by probe current, whereas the temperature remains unchanged in the positive column plasma. Due to these reasons we investigate only the effect of wall temperature conditions, the central plasma temperature being less sensitive with power lamp input.

The heat transport equation (1) is solved within the Dirichlet boundary condition:

$$T(R) = T_w \quad (8)$$

where the wall temperature T_w is a variable parameter. The problem can be solved also with Neumann boundaries conditions.

3. RESULTS AND DISCUTIONS

To obtain the plasma temperature distribution the equation (1) with boundary conditions (8) was solved using the Galerkin's variant of the Finite Element Method, with triangular grid and variable step.

The numerical procedure was verified for errors induced by numerical diffusion effects. The steps of this code are:

- a) the triangular grid generation;
- b) establishment of a convergence criterion (temperature value in a random point do not differ by more than 0.001 from the value calculated in the previous iteration);
- c) an arbitrary choice for the temperature distribution inside the lamp;
- d) all functions are calculated for this temperature distribution;
- e) a new temperature distribution is obtained by using Eq. (1);
- f) in the zone where the variations of the temperature from one iteration to the next exceeds a certain value, the grid step is diminished correspondingly;
- g) the procedure is repeated from d) until b) is satisfied.

The calculation is made for different current rage intensity [1 - 5] A.

Stormberg [4] describes the radiative term as function of radial temperature distribution with a standard parabolic exponent $\beta^* = 2.8$. This exponent is determined by the plasma core temperature T_0 and by the wall temperature T_w.

In reality, the value of the exponent profile index differs from the standard value. The index β is commonly developed as series around standard value β^* in order to best fit of experimental data.

Considering a radial distribution of the parabolic temperature profile

$$T(r) = T_0 - (T_0 - T_w)\left(\frac{r}{R}\right)^{\beta(r/R)} \quad (9)$$

with β variable, we have calculated the temperature exponent profile distribution for given values of discharge current, the amount of mercury mass and discharge tube radius.

Some results are presented below.

In Fig. 1 the temperature distribution in the transversal positive column plasma cross-section is represented for a discharge radius tube equal with 10 *mm* and a discharge current equal at 3 A.

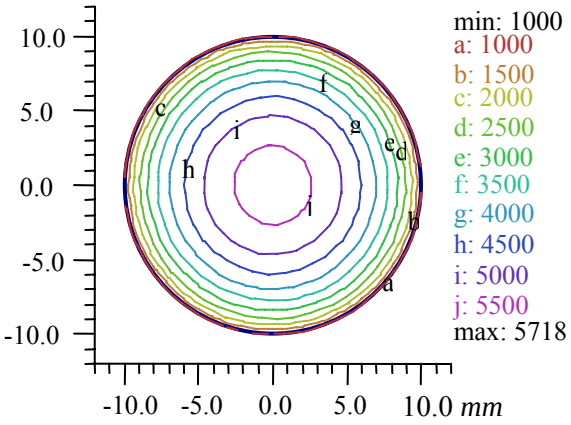

Fig. 1. Plasma column transversal cross-section temperature distribution

First, the result of mathematical model must be validated. For this, our temperature distribution results are compared with other results from the literature. The comparison was done with Charrada [9] and Elloumi [10] profiles.

The comparison of our radial temperature profile with both results mentioned before is presented in Fig. 2.

The calculations are carried out for similar parameters: 2.89 atmosphere pressure and 3A current intensity discharge.

The first profile [9] is obtained by solving Elenbaas-Heller equation. The second profile [10] is obtained starting from experimental determination of the luminance at $\lambda = 577\,nm$ and by using the Abel inversion technique for the calculation of the plasma emission coefficient. Supposing a Boltzmann distribution for excited mercury atoms and using an iterative algorithm the temperature profile is extracted.

Our results are in excellent agreement with the results of Charrada on the whole range. The agreement with the results of Elloumi in the central zone is consistent with the fact that at high discharge currents, the electron temperature and the heavy particle temperature are close one to another on the axis, while their difference increases towards the discharge tube wall.

Experimentally, the wall temperature was measured by using an optical pyrometer and was found to be around of $1000\,K$ with a variation $\Delta T_w = \pm 200\,K$. The simulations are made for 900, 1000 and $1100\,K$ respectively.

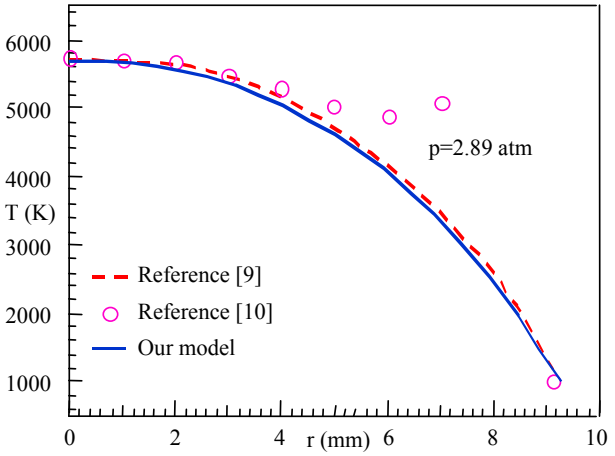

Fig. 2. Radial temperature distribution and comparison with other results

In Fig. 3 the index temperature profile dependence on reduced radius for different vessel temperature is presented.

Some differences in the index profile temperature distribution can be observed.

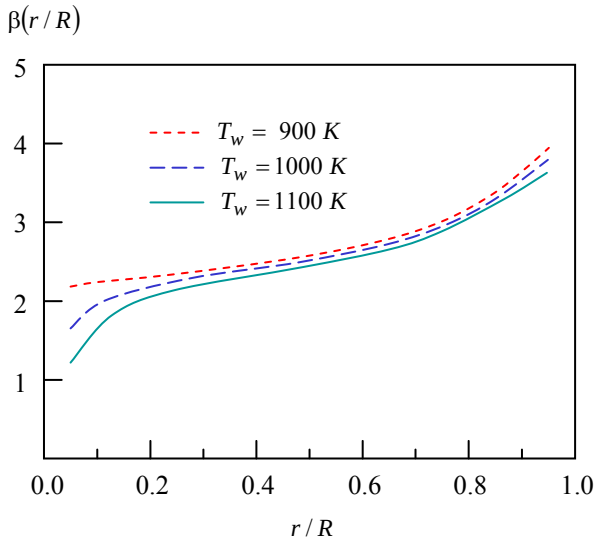

Fig. 3. Index temperature profile dependence on the reduced radius for different wall temperatures.

At the changing of the wall temperature the index profile remain cvasiconstant in the most part of the discharge tube. In the vessel vicinity the radial temperature profile index is less sensitive at the wall temperature change.

Not the same can be said regarding the temperature profile index changing in the neighbourhood of the lamp symmetry axe. Here, the temperature index profile is sensitive at the wall temperature changing. This means that the lamp can operate with different parameters at different external conditions.

Must be pointed out that even in stationary regime the radial index temperature profile value is found in a large range, but this range is smaller than the one in the transient regime. So, an index $\beta(0) = 3.6 \pm 0.1$ was found

[2] at the lamp ignition ($t = 0\ ms$). After $5\ ms$ the index value decrease at $\beta(5) = 3.1 \pm 0.1$.

When the tube radius R increase, the temperature profile of the discharge is changed. If the radius tube is less than $10\ mm$ the parabolic profile is correct. For the tube radius higher than $15\ mm$ the temperature profile hav two inflexion point so the relation (9) is not valid. The numerical result is in good agreement with [9] and [11]. Moreover, when the vessel discharges radius increase sufficiently, the arc discharge is not stabilised by the wall and the arc have a free burning character.

4. CONCLUSIONS

A mathematical model based of energy balance equation in the positive plasma column of HID lamp is made in order to study the influence of the boundaries conditions on the temperature distribution and on the radial index temperature profile.

The model allows also a parametric study regarding the tube radius and discharge core temperature.

The model can be improved by solving the heat transport equation in non stationary regime, but also by considering the electrodes effects. The wall temperature is not constant along the wall. The temperature is higher on the top of the lamp. To obtain the exact temperature distribution the energy balance equation near the tube wall must be solved in a 2D or 3D model.

Despite that the axial temperature distribution remains constant along of the lamp symmetry axe, the temperature transversal profile on the top of the lamp is different from the bottom one. Responsible for this difference is the wall temperature but also the convective movement. The convection leads to a channel discharge constriction in the bottom of the lamp and also of the enlargement of the discharge channel on the top. So, the model can be more advanced taking in to account the convective motions.

Also, in the future model, the Dirichlet boundary condition (8) must be replaced with Neumann condition of a normal derivative temperature on the wall surface. This condition assures the thermal flux continuity between the lamp and the external medium being more realistic in the lamp functioning real conditions simulation.

5. REFERENCES

[1] KARABOURNIOTIS, D., *Opt. Commun*., **61**, 38 (1987).
[2] ELLOUMI, H., AUBES, M., SIMONET, F., DAMELINCOURT, J.J., *J Phys D: Appl. Phys*. **30**, 1893 (1997)
[3] CRISTEA, M., IOVA, I., CRISTESCU, C.P., POPESCU I.M., DAMELINCOURT, J.J., *Contr. Plasma Phys.* **40,** 5-6, 545 (2000)
[4] STORMBERG, H. P., SCHAFER, R., *J. Appl. Phys*., **54**, 8, 4338 (1983)
[5] HIRSCHFELDER, J. O., CURTISS, C. F., BIRD, R. B., *"Molecular Theory of Gases and Liquids"*, John Wiley and Sons, New-York (1954).
[6] ELENBAAS, W., *The high pressure mercury vapour discharge*, North-Holland Publishing Company, Amsterdam (1951).
[7] SHKAROFSKY, I. P., JOHNSTON, T. W., BACHYNSKI, M. P., *"The Particle Kinetic of Plasmas"*, Addison-Wesley, Reading, Pennsylvania, (1966).
[8] SCHAFER, R., STORMBERG, H.P., *J. Appl. Phys.* **57,** 7, 2512 (1985).
[9] CHARRADA, K., ZISSIS, G., STAMBOULI, M., *ESCAMPING 94*, Noordwijkerhout, The Netherland, (1994).
[10] ELLOUMI, H., AUBES, M., DAMELINCOURT, J. J., *XII Int. Conf. Gas Discharges*, Greifswald, Germany, (1997).
[11] HASHIGUCHI, S., MORI, S., TACHIBANA, K., *Jpn. J. Appl. Phys.,* **36**, 10, 6533 (1997).

NUMERICAL SOLUTIONS FOR SOME BOUNDARY VALUE PROBLEMS ENCOUNTERED IN BEAM THEORY

DELEANU DUMITRU

Constanta Maritime University, Romania

ABSTRACT

In this research, some boundary value problems encountered in beam theory are considered. The shooting method is used for numerically solving the ODEs associated with these problems. The results of applying this procedure show the high accuracy and efficiency of the method. For computational and plots MATLAB has been used..

Keywords: *beam theory, boundary value problems, shooting method.*

1. INTRODUCTION

A boundary value problem (BVP) is a system of ordinary differential equations (ODE) with solution and derivative values specified at more than one point. Most commonly, the solution and derivatives are specified at just two points (the boundaries) defining a two-point boundary value problem.

There is no general theory regarding existence and uniqueness for BVP. Additionally, exact solution methods for general nonlinear BVPs are simply not available. In this paper, we are mainly interested in the solution of BVPs that occur in real engineering applications, more precisely in beam theory. The only general solution method for these problems relies on numerical schemes.

The shooting method is essentially an iterative application of the numerical integration techniques. It can be very successful on simple problems such as the projectile problem. It can be extended easily to suggest a method of solution for almost any BVPs and it has been automated in many pieces of mathematical software. However, its success depends on a number of factors the most important of which is the stability of the initial value problem (IVP) that must be solved at each integration. Unfortunately, it is the case that for many stable BVPs the corresponding IVPs are insufficiently stable for shooting to succeed. So, shooting method is not computationally suitable for the whole range of practical BVPs, particularly those on very long or infinite intervals.

The Finite Difference Method takes a completely different approach to the problem. It essentially converts the ordinary differential equations into a set of algebraic equations, with one balance equation for each finite volume or node in the system. The technique is very powerful, and it is easily extended to multidimensional and space-time situations.

2. SHOOTING METHOD. BASIC IDEAS

Let us consider the two-point boundary value problem

$$y'' = f(x, y, y') \quad , \quad y(a) = \alpha \, , \, y(b) = \beta \tag{1}$$

It can be turn into initial value problem

$$y'' = f(x, y, y') \quad , \quad y(a) = \alpha \, , \, y'(a) = u \tag{2}$$

where u is an unknown. The correct value of u could be found by trial and error: guess u and solve the initial value problem by marching from $x = a$ to $x = b$. If the solution agrees with the prescribed boundary condition $y(b) = \beta$, we are done; otherwise we have to adjust u and try again.

More systematic methods become available to us if we realize that the determination of u is a root-finding problem. Because the solution of the initial value problem depends on u, the computed boundary value $y(b)$ is a function of u, $y(b) = \theta(u)$. Hence, u is a root of

$$r(u) = \theta(u) - \beta = 0 \tag{3}$$

where *r(u)* is the boundary residual.

The procedure we'll use in solving the boundary value problems proposed in section 3 is:

a) Specify the starting values u_1 and u_2 which must bracket the root u of eq. (3);
b) Apply Brent's method to solve eq. (3) for u;
c) Having determined the value of u solves the differential equations with Runge-Kutta's method and records the results.

3. SAMPLE EXAMPLES

Example 1: The simply supported beam has a circular cross section. A couple of magnitude M_0 is applied to the left of the beam (see Figure 1). The differential equation for the displacement v is

$$\frac{d^2 v}{dx^2} = -\frac{M}{EI} = -\frac{M_0 (1 - x/L)}{E I_0 (d/d_0)^4} \tag{4}$$

where

$$v(0) = v(L) = 0 \tag{5}$$

$$d = d_0 \left[1 + \left(\frac{d_1}{d_0} - 1 \right) \frac{x}{L} \right] \quad , \quad I_0 = \frac{\pi d_0^4}{64} \tag{6}$$

Solve the problem using appropriate numerical methods and compare the solution with the exact one.

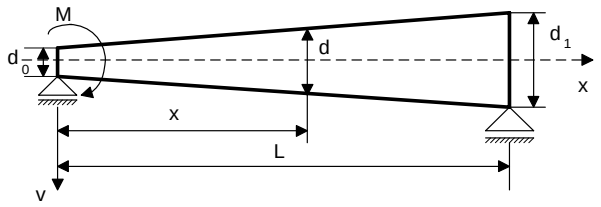

Figure 1. Simply supported beam carried by a couple of magnitude M_0

Solution: Substituting

$$\xi = \frac{x}{L} \quad , \quad y = \frac{E I_0}{M_0 L^2} \quad , \quad \delta = \frac{d_1}{d_0} \tag{7}$$

changes the differential equation (4) to

$$\frac{d^2 y}{d\xi^2} = \frac{\xi - 1}{\left[1 + (\delta - 1)\xi\right]^4} \quad , \quad \xi \in [0,1] \tag{8}$$

with the boundary conditions

$$y\big|_{\xi=0} = y\big|_{\xi=1} = 0 \tag{9}$$

The equivalent first-order problems is

$$\begin{cases} y_1' = y_2 \\ y_2' = \dfrac{\xi - 1}{\left[1 + (\delta - 1)\xi\right]^4} \\ y_1(0) = y_1(1) = 0 \end{cases} \tag{10}$$

A first task is to estimate the trial values of $y_1'(0) = u$, the unspecified initial condition. We start by making the reasonable assumption that y is smooth in interval [0, 1]. Because $\frac{d^2 y}{d\xi^2} \in (-1,0)$ we can conclude that y is concave on [0, 1] so y does to increase near $\xi = 0$ and than decrease near $\xi = 1$. It is clear now that $y_1'(0) > 0. u_1 = 0$ and $u_2 = 2$ appear to be reasonable values for the brackets of $y_1'(0)$. If they are not, Brent's method will display an error message (function *brent* in our program in MATLAB). We are chosen then the Runge-Kutta method of order four for integration (function *RK4*).

Apart from the function *difEq* that defines the differential equations, we also need the functions *initCond* to specify the initial conditions for integration and *rezid* that provides Brent's method with the boundary residual. For brevity, the program is omitted.

The numerical solution is compared in Table 1 and Figure 2 with the exact solution

$$y_{exact}(\xi) = -\frac{(3 + 2\delta\xi - 3\xi)\xi^2}{6\left[1 + (\delta - 1)\xi\right]^2} + \frac{\xi}{3\delta} \tag{11}$$

in particular case $\delta = 1.5$. The plot shows a very good accuracy of the numerical solution. Note that $y_1'(0) = 0.223$, so that our guesses of 0.0 and 2.0 for the brackets of $y_1'(0)$ were on the mark. The maximum deformation $y = 0.337$ is obtained at $\xi = 0.352$.

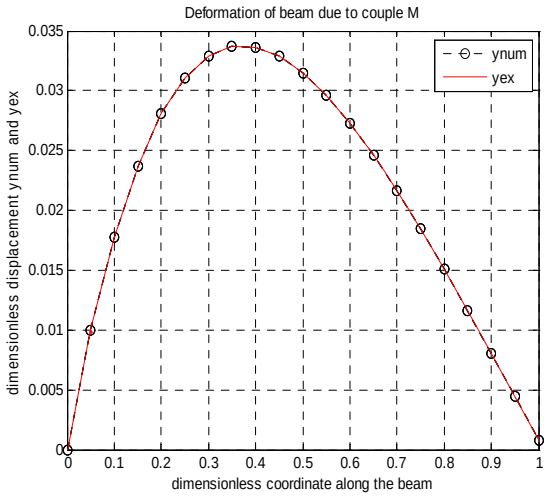

Figure 2. Deformations of a. simply supported beam carried by a couple of magnitude M_0

Example 2: The simply supported beam carries a uniform load of intensity w_0 and the tensile force N (Figure 3). The differential equation for the vertical displacement is

$$\frac{d^4 v}{dx^4} - \frac{N}{E I}\frac{d^2 v}{dx^2} = \frac{w_0}{E I} \tag{12}$$

where $E I$ is the bending rigidity. The boundary conditions are

$$v = \frac{d^2 v}{dx^2} = 0 \quad \text{at} \quad x = 0 \quad \text{and} \quad x = b \tag{13}$$

Determine the maximum displacement if

$$N = 1.65929\frac{E I}{L^2}.$$

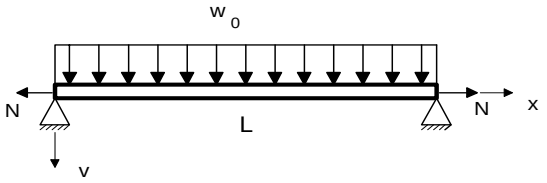

Figure 3. Simply supported beam carried by a uniform load of intensity w_0

Solution: Changing the variables to $\xi = \frac{x}{L}$ and $y = \frac{E I}{w_0 L^4} v$ transforms the problem to the dimensionless form

$$\frac{d^4y}{d\xi^4}-\gamma\frac{d^2y}{d\xi^2}=1,\quad \gamma=\frac{NL^2}{EI},\quad \xi\in[0,1] \tag{14}$$

$$y|_{\xi=0}=\left.\frac{d^2y}{d\xi^2}\right|_{\xi=0}=y|_{\xi=1}=\left.\frac{d^2y}{d\xi^2}\right|_{\xi=1}=0 \tag{15}$$

with exact solution

$$y_{exact}(\xi)=\frac{1}{\gamma^2}\left[-\frac{\gamma}{2}\xi^2+\frac{\gamma}{2}\xi-1+\frac{\exp\left(\sqrt{\gamma}\,\xi\right)+\exp\sqrt{\gamma}(1-\xi)}{1+\exp\left(\sqrt{\gamma}\right)}\right] \tag{16}$$

The equivalent first-order equations and the boundary conditions are

$$\begin{cases} y_1'=y_2 \\ y_2'=y_3 \\ y_3'=y_4 \\ y_4'=\gamma y_3+1 \end{cases},\quad y_1(0)=y_3(0)=y_1(1)=y_3(1)=0 \tag{17}$$

To solve this problem with the shooting method we turn it into the initial value problem

$$\begin{aligned} &\frac{d^4y}{d\xi^4}-\gamma\frac{d^2y}{d\xi^2}=1,\ y|_{\xi=0}=0, \\ &\left.\frac{dy}{d\xi}\right|_{\xi=0}=\alpha,\left.\frac{d^2y}{d\xi^2}\right|_{\xi=0}=0,\left.\frac{d^3y}{d\xi^3}\right|_{\xi=0}=\beta \end{aligned} \tag{18}$$

Again, determination of α and β is a root-finding problem. Because the solution of the initial value problem depends on α and β, the computed boundary values at $\xi=1$ depend on the choice of α and β. We express this dependence as

$$y(1)=f_1(\alpha,\beta)\quad,\quad y''(1)=f_2(\alpha,\beta) \tag{19}$$

The correct choice of α and β yields the given boundary conditions at $\xi=1$:

$$f_1(\alpha,\beta)=f_2(\alpha,\beta)=0 \tag{20}$$

These are simultaneous equations that can be solved by the Newton-Raphson method. The program used is similar to the one in first example. With appropriate changes in functions *difEq*, *initCond* and *rezid* the program can solve boundary value problems of any order greater than two.

The output for the numerical solution and the exact one is compared in Table 2 and Figure 4. The agreement between these two solutions is excellent. The maximum displacement $y_{\max}=0.011141$ is obtained at $\xi=0$. Other useful values are $\alpha=y_1'(0)=0.035747$ and $\beta=y_1'''(0)=-0.44069$

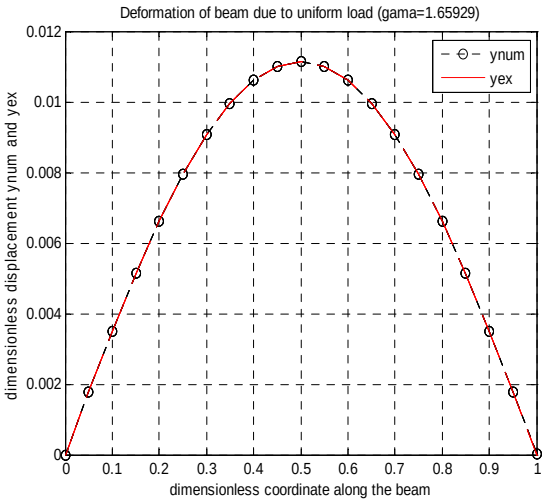

Figure 4. Deformations of a simply supported beam carried by a uniform load of intensity w_0

4. CONCLUSIONS

This article deals with the numerical solutions of some BVPs encountered in beam theory using the shooting method. This technique was tested on two examples and was seen to produce satisfactory results. The MATLAB program, which solves numerically these examples, can be simply extended to more complex BVPs. The basic difficulty with shooting method is that a well - posed BVPs can require the integration of IVPs that are unstable. One way to overcome difficulties due to instability of the IVPs is to
do a detective work, for estimating the unspecified initial conditions, if possible. If the estimation is not good, the program displays an error message and another estimation is necessary.

5. REFERENCES

[1] GHINEA, M., FIRETEANU, V., MATLAB, *Calcul numeric, grafica si aplicatii*, Ed. Teora, 2004.
[2] SCHARF, L.L., SCHRAUS, R.T., *A first Course in Electrical and Computer Engineering with MATLAB Programs and Experiments*, Addison-Wesley Publishing Company, Reading, Massachusetts, 1990.
[3] SOARE, M., TEODORESCU, P.P., TOMA, I., *Ecuatii diferentiale cu aokicatii in mecanica constructiilor*, Ed.Tehnica, Bucuresti, 1999.
[4] STEPHEN, N.G., *The second spectrum of Timoshenko beam theory*, Journal of Sound and Vibration, 292:372-389, 2006
[5] TIMOSHENKO, S., YOUNG, D.H., WEAVER, E.Jr., *Vibration Problems in Engineering*, Willey, New York, 1974
[6] VOINEA, R., STROE, I., PREDOI, M.V., *Technical Mechanics*, Geometry Balkan Press, Bucharest, Romania, 1996
[7] VOINEA, R., VOICULESCU, D., SIMION, F.P., *Introducere in mecanica solidului cu aplicatii in inginerie*, Ed. Academiei Romane, Bucuresti, 1989

[8] WILSON, H.B., TURCOTTE L.B., HALPERN, D., *Using MATLAB*, Chapman @Hall/CRC, London, 2003
Advanced Mathematics and Mechanics Applications

Table 1. Comparison between numerical and exact solutions
for a simply supported beam carried by a couple of magnitude M_0

ξ	$y_{num}(\xi)$	$\lvert y_{exact}(\xi) - y_{num}(\xi)\rvert \cdot 10^{-4}$	0.50	0.031500	0.2036
0.00	0.000000	0.0000	0.60	0.027291	0.1668
0.10	0.017765	0.1426	0.70	0.021669	0.1260
0.20	0.028071	0.2144	0.80	0.015134	0.0851
0.30	0.032873	0.2381	0.90	0.008071	0.0457
0.40	0.033644	0.2303	1.00	0.000077	0.0078

Table 2. Comparison between numerical and exact solutions
for a simply supported beam carried by a uniform load of intensity w_0

ξ	$y_{num}(\xi)$	$\lvert y_{exact}(\xi) - y_{num}(\xi)\rvert \cdot 10^{-4}$	0.50	0.0111413	0.2036
0.00	0.0000000	0.0000	0.60	0.0106129	0.1418
0.10	0.0035054	0.0478	0.70	0.0090653	0.1030
0.20	0.0066267	0.1194	0.80	0.0066267	0.0982
0.30	0.0090653	0.1783	0.90	0.0035054	0.0231
0.40	0.0106126	0.2501	1.00	0.0000392	0.0009

CONCERNING AN APPLICATION OF DIRECT INTEGRATION METHODS IN MECHANICS OF CONSTRUCTIONS

DELEANU DUMITRU

Constanta Maritime University, Romania

ABSTRACT

In this paper our attention is focused on the dynamics of a linear structure subjected to periodic forces. The structural dynamics equation can be solved using frequency analysis methods or step-wise integration methods. Although these approaches are easy to implement, the resulting analysis can be very time consuming for systems involving several hundred degrees of freedom. Variable step integrators make adjustements to control stability and accuracy which can require very small integration steps. Consequently, less sophisticated formulations employing fixed step-size are often employed. We investigate in our paper two such algorithms in particular case of a machine tool fitted out with a dynamic damper. A program to solve the above mentioned problem was developed and questions regarding computational efficiency and numerical accuracy of these algorithms are examined.

Keywords: *direct integration methods, efficiency of a dynamic damper.*

1. INTRODUCTION

The dynamics of a linear structure subjected to periodic forces obeys the matrix differential equation

$$M\,\ddot{X}+C\,\dot{X}+K\,X=P(t) \tag{1}$$

with initial conditions

$$X(0)=D_0\,,\ \dot{X}(0)=V_0 \tag{2}$$

The solution vector $X(t)$ has dimension n and M, C and K are real square matrices of order n. The mass matrix, M, the damping matrix, C, and the stiffness matrix, K, are all real. The forcing function, $P(t)$, assumed to be real and having period T, can be approximated by a finite trigonometric series

$$P(t)=\sum_{k=-n}^{n} C_k\,\exp(i\,\omega_k\,t)\quad,\quad \omega_k=\frac{2\pi k}{T} \tag{3}$$

The Fourier coefficients C_k are vectors that can be compute using the Fast Fourier Transform. The n degree-of-freedom system (1.1) can be expressed as a first order system in $2n$ unknowns for a vector $Z=[X\,;V]$, with $V=\dot{X}$:

$$\begin{cases}\dot{X}=V\\ M\,\dot{V}+C\,\dot{X}+K\,X=P\end{cases} \tag{4}$$

2. DIRECT INTEGRATION METHODS

In the following we'll investigate the solution of system (4) by means of two direct integration methods derived from trapezoidal integration rule:

$$\int_a^b f(t)\,dt=\frac{h}{2}\big(f(a)+f(b)\big)-\frac{h^3}{12}\,f''(\varepsilon_1) \tag{5}$$

$$\int_a^b f(t)\,dt=\frac{h}{2}\big(f(a)+f(b)\big)+\frac{h^2}{12}\big(f'(a)-f'(b)\big)+\frac{h^5}{720}\,f^{iv}(\varepsilon_2)$$

where $\varepsilon_i\in(a,b),\ i=1,2,$ and $h=b-a.$ The first formula gives a zero truncation error term when applied to a linear function, whereas the second formula has a zero final term for a cubic integrand.

We suppose next that M, C and K are constant matrices. By integrating system (4) from t to $t+h$ we get

$$\begin{cases}M\int_t^{t+h}\dot{V}\,dt+C\int_t^{t+h}V\,dt+K\int_t^{t+h}X\,dt=\int_t^{t+h}P\,dt\\ \int_t^{t+h}\dot{X}\,dt=\int_t^{t+h}V\,dt\end{cases} \tag{6}$$

For brevity we note

$$X(t)=X_0\quad,\quad X(t+h)=X_1\quad,\quad \tilde{X}=X_1-X_0 \tag{7}$$

Using the trapezoidal rule (5) leads to

$$\begin{cases}\left[M+\frac{h}{2}C+\frac{h^2}{4}K\right]\cdot\tilde{V}=\int_t^{t+h}P(t)\,dt-\\ -h\left[C\,V_0+K\,X_0+\frac{h}{2}K\,V_0\right]+O(h^3)\\ \tilde{X}=\frac{h}{2}(V_0+V_1)+O(h^3)\end{cases} \tag{8}$$

To integrate the forcing function we can use the midpoint rule:

$$\int_a^b f(t)\,dt=(b-a)\,f\left(\frac{a+b}{2}\right)+O\big((b-a)^3\big) \tag{9}$$

Solving (8) for $\tilde{V}$ yields

$$\tilde{V} = \left[M + \frac{h}{2} C + \frac{h^2}{4} K \right]^{-1} \cdot \cdot \left(P\left(t + \frac{h}{2} \right) - C V_0 - K X_0 - \frac{h}{2} K V_0 \right) h + O\left(h^3\right) \quad (10)$$

The velocity and position at $(t+h)$ are then computed as

$$V_1 = V_0 + \tilde{V} \quad , \quad X_1 = X_0 + \frac{h}{2}(V_0 + V_1) \quad (11)$$

A more accurate formula with truncation error of order h^5 can be developed from the extended trapezoidal rule (2.2). This leads to a matrix equation to be solved for $\tilde{X}$ and $\tilde{V}$:

$$\begin{bmatrix} -\left(\frac{h}{2} M + \frac{h^2}{12} C \right) & \left(M - \frac{h^2}{12} K \right) \\ \left(M - \frac{h^2}{12} K \right) & \left(C + \frac{h}{2} K \right) \end{bmatrix} \cdot \begin{pmatrix} \tilde{V} \\ \tilde{X} \end{pmatrix} = = \begin{pmatrix} h M V_0 + \frac{h^2}{12}(P_0 - P_1) \\ \int_t^{t+h} P(t)\,dt - h K X_0 \end{pmatrix} + O\left(h^5\right) \quad (12)$$

For $\int_t^{t+h} P(t)\,dt$ we can use the Gauss two-point formula:

$$\int_t^{t+h} P(t)\,dt = \frac{h}{2}\left(P(t+\alpha h) + P(t+\beta h)\right) + O\left(h^5\right) \quad (13)$$

where $\alpha = \frac{3-\sqrt{3}}{6}$ and $\beta = \frac{3+\sqrt{3}}{6}$.

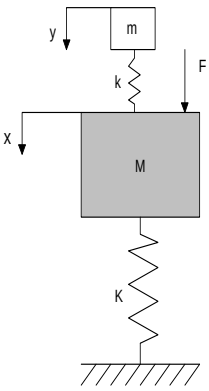

Figure.1. Machine tool equipped with a dynamic damper

3. CASE STUDY: DYNAMIC DAMPER

A machine tool having mass *M*, relied on floor with an elastic spring of constant *K*, is subject to an harmonic vertical force $F = F_0 \sin \omega t$. Because, in certain conditions, it is possible to appear the resonance (when the driven frequency is equal with the natural frequency of the machine tool), it is usual to fit out the equipment with a dynamic damper, which consist in a mass *m* attached to machine by means of a spring having elastic constant *k* (Figure1). Mechanical system so obtained has two degree of freedom and the differential equations of motion, in unknowns *x* and *y*, and initial conditions are:

$$\begin{cases} m \ddot{y} = -k(y - x) \\ M \ddot{x} = k(y - x) - K x + F_0 \sin \omega t \end{cases} \quad (14)$$

$$x(0) = y(0) = \dot{x}(0) = \dot{y}(0) = 0 \quad (15)$$

With notations

$$\frac{K}{M} = \alpha^2 \, , \frac{k}{m} = \beta^2 \, , \frac{k}{M} = \gamma^2 \, , \frac{F_0}{M} = f_0 \quad (16)$$

the system (14) is rewritten as

$$\begin{cases} \ddot{y} + \beta^2 y - \beta^2 x = 0 \\ \ddot{x} + \left(\alpha^2 + \gamma^2\right) x - \gamma^2 y = f_0 \sin \omega t \end{cases} \quad (17)$$

and has the particular solution:

$$x_p = \frac{1}{N} f_0 \left(\beta^2 - \omega^2 \right) \sin \omega t$$

$$y_p = \frac{1}{N} f_0 \beta^2 \sin \omega t \quad (18)$$

where $N = \omega^4 - \left(\alpha^2 + \beta^2 + \gamma^2\right)\omega^2 + \alpha^2 \beta^2$. The particular solution must be combined with the homogeneous (or transient) solution. Because the damping matrix C is zero, the eigenvalues associated with transient solution are purely imaginary, and the homogeneous solution does not die out. Indeed, the equation for eigenvalues $\lambda_i, i = \overline{1,4}$, is

$$\lambda^4 - \left(\alpha^2 + \beta^2 + \gamma^2\right)\lambda^2 + \alpha^2 \beta^2 = 0 \quad (19)$$

However, it is often customary in practical situations to ignore the homogeneous solution because it is usually small compared to the contribution of the particular solution.

For resonance conditions ($\alpha = \omega$), we get

$$x_p = -\frac{1}{\omega^2 \gamma^2} f_0 \left(\beta^2 - \omega^2 \right) \sin \omega t$$

$$y_p = -\frac{1}{\omega^2 \gamma^2} f_0 \beta^2 \sin \omega t \quad (20)$$

We can easy see that the amplitude of x_p, which in absence of dynamic damper it would be infinity, has the finite value of $\frac{1}{\omega^2 \gamma^2} f_0 \left| \beta^2 - \omega^2 \right|$. If, in addition, choose *m* and *k* so that $\alpha = \beta$, relations (20) become

$$x_p = 0 \quad , \quad y_p = -\frac{f_0}{\gamma^2}\sin \omega t \qquad (21)$$

In this case, the damper cancels entirely the vibrations of machine tool.

4. NUMERICAL RESULTS

To verify the above calculations and numerical accuracy of the two direct integration methods described in section 2, we are considered

$$M = 500\,kg,\ m = 5\,kg,\ K = 500\ N/m,$$
$$k = 10\ N/m,\ F_0 = 50\ N,\ \omega = 1\,rad/s$$

For these values we have

$$\alpha^2 = 1,\ \beta^2 = 2,\ \gamma^2 = 0.02,\ f_0 = 0.1$$

$$x(t) = 4.954497\sin(0.990331\,t) + 0.063626\sin(1.428021\,t) - \\ - 5\sin t \qquad (22)$$

In absence of dynamic damper, the machine tool's motion is governed by

$$x(t) = \frac{f_0}{2\omega^2}\left(\sin(\omega t) - \omega t\cos(\omega t)\right)$$

Its amplitude tends to infinity (see Figure 2).

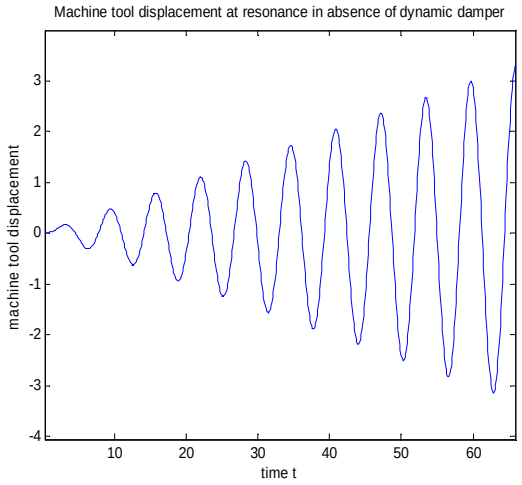

Figure 2. Machine tool displacement in absence of dynamic damper

Presence of dynamic damper has an immediate effect: the amplitudes become finite (Figure 3). The first and the third terms in (22) have, as result, the so-called phenomenon of beatings. The amplitude become very small when β is closed to ω.

Next, the computational efficiency and numerical accuracy of the direct integration methods are examined for two different step-sizes h. Figures 4, 5 and 6 present the differences between the exact solution and the approximate solution given by direct integration methods. The error measure is compared for different integrators and time steps in the figures. We can see that the fourth order integrator is more efficient then the second integrator because a larger integration step can be taken into account, without excessive loss in accuracy.

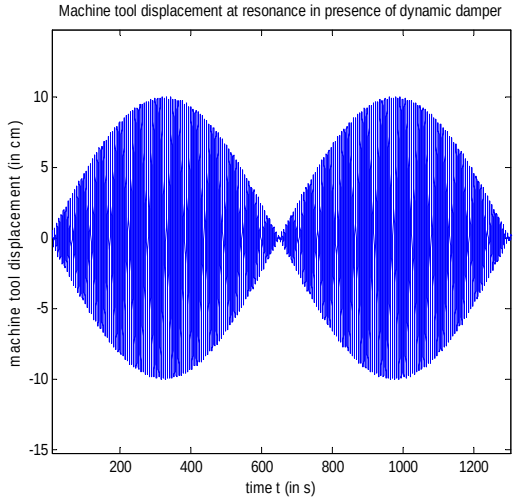

Figure 3. .Machine tool displacement in presence of dynamic damper

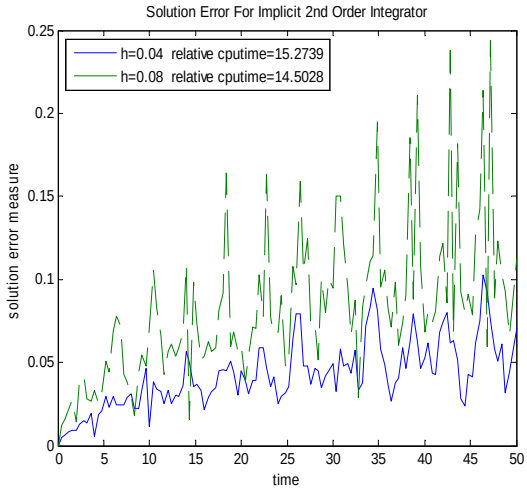

Figure 4

5. CONCLUSIONS

In this study, two-fixed step-size integrators derived from trapezoidal rule were used to finding approximate solutions for the motion of a machine tool equipped with a dynamic damper. This approach wants to be an alternative to step-wise integrators, which can be very time consuming for systems with a grat number of degrrs of motion. The error measure is displayed for both integrators and for different step of integration. The results show that above-mentioned integrators provides a good degree of, accuracy, even for a long period of time. MATLAB has been used for computational and plots.

6. REFERENCES

[1] GHINEA, M., FIRETEANU, V., MATLAB, *Calcul numeric, grafica si aplicatii*, Ed. Teora, 2004.
[2] SCHARF, L.L., SCHRAUS, R.T., *A first Course in Electrical and Computer Engineering with MATLAB*

Programs and Experiments, Addison-Wesley Publishing Company, Reading, Massachusetts, 1990.

[3] SOARE, M., TEODORESCU, P.P., TOMA, I., *Ecuatii diferentiale cu aplicatii in mecanica constructiilor*, Ed.Tehnica, Bucuresti, 1999.

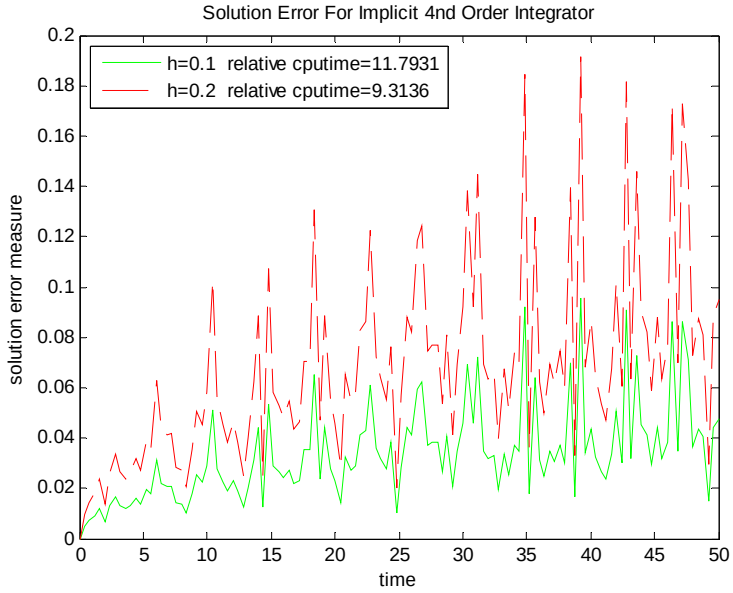

Figure 5

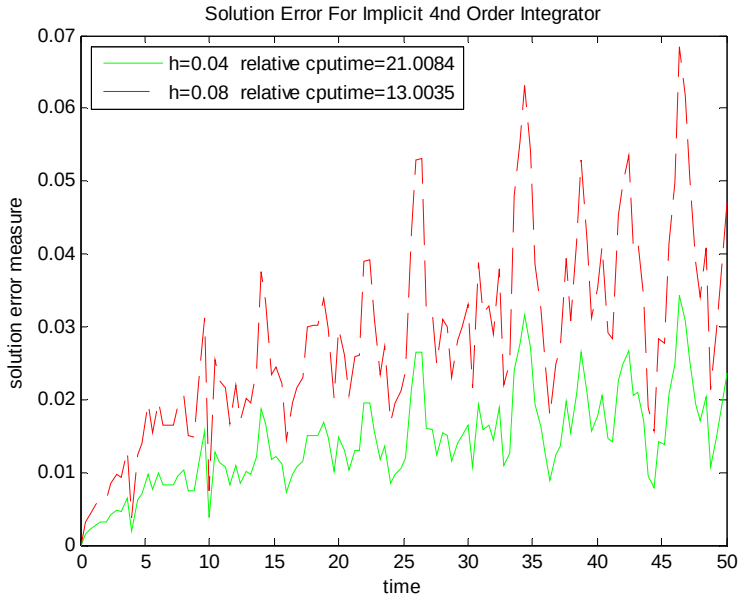

Figure 6

EXACT SOLUTIONS OF SEVERAL WAVE-LIKE EQUATIONS BY HOMOTOPY PERTURBATION METHOD

DELEANU DUMITRU

Constanta Maritime University, Romania

ABSTRACT

In this paper, we implement a relatively new analytical technique, the homotopy perturbation method for solving several wave-like equations. The solution is calculated in the form of a series with easily computable components. The advantage of this method is that it provides a direct scheme for solving the problem, without the need for linearization, massive computation and any transformation. Numerical results show that this method is a powerful tool for finding solutions for a large class of partial differential equation, in particular wave-like equations.

Keywords: *Homotopy perturbation method, wave-like equation, approximate and exact solution.*

1. INTRODUCTION

There are several basic models in the subject of partial differential equations (PDE), which describe very different physics and have very different mathematical properties. They are relative simple in form, yet realistic for many problems in science and engineering. In addition, they teach us what to expect when we encounter more complicated equations used to model complicated laboratory situations.

One of these equations is the wave equation

$$u_{tt} = c^2 u_{xx} \tag{1}$$

where *c* is a physical constant. The unknown function u may have a different interpretation (for example, the height of a taut membrane, a magnetic potential, deformation of a string, etc) but the mathematics remain the same.

We can solve today the classical wave equation in two entirely ways. Unfortunately, for the PDE's, not very different from (1), we couldn't find so easy an exact solution, especially in nonlinear case. In these cases, some new analytical methods like decomposition methods or perturbation methods, comes to give alternative techniques for finding approximate solutions.

In this paper, the homotopy perturbation method (hereafter, noted HPM) will be applied to solve several wave-like equations. In this method, proposed by J.H. He, which requires neither a small parameter nor a linear term in the differential equation, an artificial perturbation equation is constructed by embedding an artificial parameter $p \in [0,1]$, which is used as an expanding parameter. This technique yields a very rapid convergence of the solution series; in most cases only one or two iterations lead to high accuracy of the solution.

It has now been applied to a large class of linear and non-linear equations, involving algebraic differential, integro-differential, differential-delay, and partial differential equations and systems [1-7].

The rest of the paper is organized as follows. In section 2, we briefly describe the basic ideas of homotopy perturbation method. In section 3, we present five examples to demonstrate the efficiency of HPM. Section 4 consists of main conclusions.

2. HOMOTOPY PERTURBATION METHOD. BASIC IDEAS

Let us consider the following functional equation:

$$A(u) - f(r) = 0, \; r \in \Omega \tag{2}$$

with the boundary conditions:

$$B\left(u, \frac{\partial u}{\partial n}\right) = 0, \; r \in \Gamma \tag{3}$$

where $A, B, f(r)$ and Γ are a general differential operator, a known analytical function and the boundary of the domain Ω, respectively. By dividing the operator *A* into a linear part *L* and a nonlinear part *N* equation (2) is written as:

$$L(u) + N(u) - f(r) = 0 \tag{4}$$

By the homotopy technique, we construct a homotopy $v(r, p): \Omega \times [0,1] \to R$ which satisfies

$$\begin{aligned} H(v, p) &= (1-p)(L(v) - L(u_0)) + \\ p\,&[A(v) - f(r)] = 0, \; p \in [0,1], \; r \in \Omega \end{aligned} \tag{5}$$

where $p \in [0,1]$ is an embedding parameter and u_0 is an initial approximation of the solution , which satisfies the boundary conditions (3). The changing process of *p* from zero to unity is just that of $v(r, p)$ from u_0 to $u(r)$. In topology, this is called deformation, while $L(v) - L(u_0)$ and $A(v) - f(r)$ are called homotopy.

We can first use the embedding parameter *p* as a "small parameter ", and assume that the solutions of eqs. (2) ca be written as a power series in *p*:

$$v = v^{(0)} + p v^{(1)} + p^2 v^{(2)} + \ldots \tag{6}$$

Setting $p = 1$ yields the approximate solutions of (2) to:

$$u = \lim_{p \to 1} v = v^{(0)} + v^{(1)} + v^{(2)} + \ldots \tag{7}$$

The combination of the perturbation method and the homotopy method is called the homotopy perturbation

method (HPM). The series (7) is convergent for most cases. However, the convergent rate depends on the nonlinear operator $A(v)$ [4].

3. APPLICATIONS OF HPM. SOME EXAMPLES

Example 1: Let us consider first the classical wave equation

$$u_{tt} - u_{xx} = 0 \tag{8}$$

with initial conditions:

$$u(x,0) = \cos 4x,\ u_t(x,0) = x^2 - \frac{1}{3} \tag{9}$$

In view of the homotopy (5), we have

$$(1-p)v_{tt} + p\left(v_{tt} - v_{xx}\right) = 0 \tag{10}$$

Assume that the solution of (8) can be written as a power series in *p*:

$$v(x,t) = v^{(0)}(x,t) + p\,v^{(1)}(x,t) + p^2 v^{(2)}(x,t) + \ldots \tag{11}$$

Substituting (11) and initial conditions (9) into the homotopy (10) and equating the terms with identical powers of *p*, we obtain the following set of linear differential equations:

$$\begin{aligned} &p^0: v_{tt}^{(0)} = 0,\ v^{(0)}(x,0) = \cos 4x,\ v_t^{(0)}(x,0) = x^2 - \frac{1}{3} \\ &p^1: \quad v_{tt}^{(1)} - v_{xx}^{(0)} = 0,\ v^{(1)}(x,0) = 0,\ v_t^{(1)}(x,0) = 0 \\ &p^2: \quad v_{tt}^{(2)} - v_{xx}^{(1)} = 0,\ v^{(2)}(x,0) = 0,\ v_t^{(2)}(x,0) = 0 \end{aligned} \tag{12}$$

and so on.

Solving the above equations, we get

$$\begin{aligned} v^{(0)}(x,t) &= \cos 4x + t\left(x^2 - \frac{1}{3}\right) \\ v^{(1)}(x,t) &= -8t^2\cos 4x + \frac{t^3}{3} \\ v^{(2)}(x,t) &= \frac{32}{3}t^4\cos 4x \\ v^{(3)}(x,t) &= -\frac{256}{45}t^6\cos 4x \\ &\ldots\ldots\ldots\ldots\ldots\ldots\ldots\ldots \end{aligned} \tag{13}$$

Having $v^{(i)}, i = 0, 1, 2, 3, \ldots$ series solution is as follows

$$\begin{aligned} u(x,t) \cong \sum_{i=0}^{4} v^{(i)}(x,t) &= t\left(x^2 - \frac{1}{3} + \frac{t^2}{3}\right) + \\ &\left(1 - 8t^2 + \frac{32}{3}t^4 - \frac{256}{45}t^6\right)\cos 4x \end{aligned} \tag{14}$$

If we'll consider an infinite series solution we reach the exact solution

$$u_{exact}(x,t) = \frac{1}{3}\left(t^3 + 3t\,x^2 - t\right) + \cos 4x \cos 4t \tag{15}$$

Example 2: As a second example, on consider the homogeneous wave equation with variable coefficients:

$$u_{tt} - \frac{x^2}{2}u_{xx} = 0,\ u(x,0) = x,\ u_t(x,0) = x^2 \tag{16}$$

Using the HPM, we have

$$(1-p)v_{tt} + p\left(v_{tt} - \frac{x^2}{2}v_{xx}\right) = 0 \tag{17}$$

where

$$v = v^{(0)} + p\,v^{(1)} + p^2 v^{(2)} + \ldots \tag{18}$$

From (17) and (18), we get

$$v_{tt}^{(0)} + p\left(v_{tt}^{(1)} - \frac{x^2}{2}v_{xx}^{(0)}\right) + p^2\left(v_{tt}^{(2)} - \frac{x^2}{2}v_{xx}^{(1)}\right) + \ldots = 0$$

In order to obtain the unknowns $v^{(i)}, i = 0, 1, 2, \ldots$ we must solve the following equations:

$$\begin{aligned} &p^0: v_{tt}^{(0)}(x,t) = 0 \\ &p^1: v_{tt}^{(1)}(x,t) - \frac{x^2}{2}v_{xx}^{(0)}(x,t) = 0 \\ &p^2: v_{tt}^{(2)}(x,t) - \frac{x^2}{2}v_{xx}^{(1)}(x,t) = 0 \\ &\ldots\ldots\ldots\ldots\ldots\ldots\ldots\ldots\ldots\ldots \end{aligned} \tag{19}$$

with initial conditions:

$$\begin{aligned} &v^{(0)}(x,0) = x, \quad v_t^{(0)}(x,0) = x^2 \\ &v^{(i)}(x,0) = 0, \quad v_t^{(i)}(x,0) = 0, \quad i = 1,2,\ldots \end{aligned} \tag{20}$$

Therefore,

$$\begin{aligned} v^{(0)}(x,t) &= x + t\,x^2 \\ v^{(1)}(x,t) &= \frac{t^3 x^2}{6} \\ v^{(2)}(x,t) &= \frac{t^5 x^2}{120} \\ v^{(3)}(x,t) &= \frac{t^7 x^2}{5040}, \ldots \end{aligned} \tag{21}$$

From (7) results

$$\begin{aligned} u(x,t) &= \lim_{p\to 1}\left(v^{(0)} + p\,v^{(1)} + p^2 v^{(2)} + \ldots\right) = \\ &v^{(0)} + v^{(1)} + v^{(2)} + \ldots = x + x^2\left(t + \frac{t^3}{3!} + \frac{t^5}{5!} + \ldots + \frac{t^{2n+1}}{(2n+1)!} + \ldots\right) \end{aligned} \tag{22}$$

We can easy see that series (3.16) is equivalent with closed form $u(x,t) = x + x^2\sinh t$.

Example 3: The third example is that of a non-homogeneous wave-equation with a damping term:

$$u_{tt} + 4u_t - u_{xx} = 8t + 2$$

$$u(x,0)=\sin 2x,\ u_t(x,0)=-2\sin 2x \tag{23}$$

Applying HPM, we can write successively

$$(1-p)v_{tt}+p\left(v_{tt}+4v_t-v_{xx}-8t-2\right)=0 \tag{24}$$

$$v=v^{(0)}+p\,v^{(1)}+p^2v^{(2)}+\ldots \tag{25}$$

$$p^0: v_{tt}^{(0)}(x,t)=0,\quad v^{(0)}(x,0)=\sin 2x,\ v_t^{(0)}(x,0)=-2\sin 2x$$

$$p^1: v_{tt}^{(1)}+4v_t^{(0)}-v_{xx}^{(0)}-8t-2=0,\ v^{(1)}(x,0)=0,\ v_t^{(1)}(x,0)=0$$

$$p^2: v_{tt}^{(2)}+4v_t^{(1)}-v_{xx}^{(1)}=0,\ v^{(2)}(x,0)=0,\ v_t^{(2)}(x,0)=0$$

……

$$v^{(0)}(x,t)=(1-2t)\sin 2x \tag{26}$$

$$v^{(1)}(x,t)=\left(2t^2+\frac{4}{3}t^3\right)\sin 2x+t^2+\frac{4t^3}{3}$$

$$v^{(2)}(x,t)=\left(-\frac{8}{3}t^3-2t^4-\frac{4}{15}t^5\right)\sin 2x-\frac{4}{3}t^3-\frac{4}{3}t^4$$

$$v^{(3)}(x,t)=\left(\frac{8}{3}t^4+\frac{32}{15}t^5+\frac{4}{9}t^6+\frac{8}{315}t^7\right)\sin 2x+\frac{4}{3}t^4+\frac{16}{15}t^5$$

$$v^{(4)}(x,t)=\left(-\frac{32}{15}t^5-\frac{16}{9}t^6-\frac{48}{105}t^7-\frac{2}{45}t^8-\frac{4}{2835}t^9\right)\sin 2x-$$

$$-\frac{16}{15}t^5-\frac{32}{45}t^6$$

and

$$u(x,t)\cong\sum_{i=0}^{4}v_i(x,t)=\left(1-2t+2t^2-\frac{4}{3}t^3+\frac{2}{3}t^4\right)\sin 2x+$$

$$+\left(\frac{4}{15}t^5-\frac{4}{3}t^6-\frac{136}{315}t^7-\frac{2}{45}t^8-\frac{4}{2835}t^9\right)\sin 2x+$$

$$+t^2-\frac{32}{45}t^6 \tag{27}$$

The exact solution is

$$u_{exact}(x,t)=\sin 2x\cdot e^{-2t}\cong$$

$$=\left(1-2t+2t^2-\frac{4}{3}t^3+\frac{2}{3}t^4-\frac{4}{15}t^5\right)\sin 2x+t^2 \tag{28}$$

The same equation was solved by means of variational iteration method (VIM) in [??]. Using the multiplier identified optimally via the variational theory, the result (27) is obtained after only one iteration. That means VIM converges faster than HPM for this example.

Example 4: As a fourth example on considers the non homogeneous nonlinear wave-like equation

$$u_{xx}-u\,u_{tt}=-x^2e^{-2t},\ u(0,t)=0,\ u_x(0,t)=e^{-t} \tag{29}$$

with exact solution $u_{exact}(x,t)=x\cdot e^{-t}$.

In view of the homotopy (5), we have

$$(1-p)v_{xx}+p\left(v_{xx}-v\,v_{tt}+x^2e^{-2t}\right)=0$$

$$v=v^{(0)}+p\,v^{(1)}+p^2v^{(2)}+\ldots$$

$$p^0: v_{xx}^{(0)}=0,\quad v^{(0)}(0,t)=0,\ v_x^{(0)}(0,t)=e^{-t} \tag{30}$$

$$p^1: v_{xx}^{(1)}-v^{(0)}v_{tt}^{(0)}+x^2e^{-2t}=0,\quad v^{(1)}(0,t)=0,\ v_x^{(1)}(0,t)=0$$

$$p^2: v_{xx}^{(2)}-v^{(0)}v_{tt}^{(1)}-v^{(1)}v_{tt}^{(0)}=0,\quad v^{(2)}(0,t)=0,\ v_x^{(2)}(0,t)=0$$

……

$$v^{(0)}(x,t)=x\,e^{-t},$$

$$v^{(1)}(x,t)=0,\ v^{(2)}(x,t)=0,\ldots,v^{(n)}(x,t)=0,\ n\ge 1$$

Only one iteration is necessary to reach the exact solution.

Example 5: The last example is that of a two-dimensional nonlinear wave-like equation with variable coefficients

$$u_{tt}=\frac{\partial^2}{\partial x\,\partial y}\left(u_{xx}u_{yy}\right)-\frac{\partial^2}{\partial x\,\partial y}\left(xyu_xu_y\right)-u, \tag{31}$$

$$u(x,y,0)=e^{xy},\quad u_t(x,y,0)=e^{xy}$$

with exact solution

$$u_{exact}(x,y,t)=e^{xy}(\sin t+\cos t) \tag{32}$$

According to HPM, we can write successively

$$(1-p)v_{tt}+p\left(v_{tt}-\frac{\partial^2}{\partial x\,\partial y}\left(u_{xx}u_{yy}\right)+\frac{\partial^2}{\partial x\,\partial y}\left(xyu_xu_y\right)+u\right)=0$$

$$v=v^{(0)}+p\,v^{(1)}+p^2v^{(2)}+\ldots$$

$$p^0: v_{tt}^{(0)}=0,\ v^{(0)}(x,y,0)=e^{xy},\ v_t^{(0)}(x,y,0)=e^{xy}$$

$$p^1: v_{tt}^{(1)}-\frac{\partial^2}{\partial x\,\partial y}\left(v_{xx}^{(0)}v_{yy}^{(0)}\right)+\frac{\partial^2}{\partial x\,\partial y}\left(xyv_x^{(0)}v_y^{(0)}\right)+$$

$$+v^{(0)}=0,\ v^{(1)}(x,y,0)=0,\ v_t^{(1)}(x,y,0)=0$$

$$p^2: v_{tt}^{(2)}-\frac{\partial^2}{\partial x\,\partial y}\left(v_{xx}^{(1)}v_{yy}^{(1)}\right)+\frac{\partial^2}{\partial x\,\partial y}\left(xyv_x^{(1)}v_y^{(1)}\right)+$$

$$+v^{(1)}=0,\ v^{(2)}(x,y,0)=0,\ v_t^{(2)}(x,y,0)=0$$

……

$$v^{(0)}(x,y,t)=e^{xy}(1+t) \tag{33}$$

$$v^{(1)}(x,y,t)=-e^{xy}\left(\frac{t^2}{2!}+\frac{t^3}{3!}\right)$$

$$v^{(2)}(x,y,t)=e^{xy}\left(\frac{t^4}{4!}+\frac{t^5}{5!}\right)$$

$$v^{(3)}(x,y,t)=-e^{xy}\left(\frac{t^6}{6!}+\frac{t^7}{7!}\right)$$

$$v^{(4)}(x,y,t)=e^{xy}\left(\frac{t^8}{8!}+\frac{t^9}{9!}\right)$$

……

If we'll consider again an infinite series solution, we write

$$u(x,y,t) \cong \sum_{i=0}^{\infty} v^{(i)}(x,y,t) =$$

$$= e^{xy}\left(\sum_{n=0}^{\infty}(-1)^n \frac{t^{2n+1}}{(2n+1)!} + \sum_{n=0}^{\infty}(-1)^n \frac{t^{2n}}{(2n)!}\right)$$

This is equivalent with the exact solution (32).

4. CONCLUSIONS

In this paper we applied HPM for obtaining exact or approximate solutions of some PDEs arising in wave theory. The basic ideas of the method are presented in a dedicated section. The main conclusions of our study are:

a) It is apparently seen that HPM is very powerful and efficient for solving PDEs arising in wave theory. The obtained solutions are compared with exact solution and the VIM. The five solved examples show that the results of the present method are in excellent agreement with those obtained by the exact solution and VIM. The procedure can be simply extended to solve more complex PDEs;

b) The HPM has many advantages than other methods. For example, this method is to overcome the difficulties arising in calculation of Adomian polynomials. Also, the method does not require complex calculations and avoid linearization and physically unrealistic assumptions. The reliability of the method and the reduction in the size of computational domain gives this method a wider applicability;

c) HPM presents a rapid convergence to the exact solution, only few iterations being enough for a reasonable accuracy. However, for example 3, VIM is better than HPM;

d) Another advantage of HPM is that the method gives an analytical expression as a solution. This is a superiority, when compared to mesh-based numerical methods.

5. REFERENCES

[1] DELEANU, D., MOSCALU, D., *Variational iteration method for approximate solutions of some differential equations arising in vibrational systems*, National Conference on Mechanics of Solids, Bucuresti, sept. 2009

[2] GANJI, J.H., MIRGOLBABAEI, H., MIANSORI, ME., MIANSORI, MO., *Homotopy perturbation technique*, Comput. Math. Applied Mech. Eng., Tome 178(3-4), pg. 257-262, 2008

[3] GANJI, J.H., SAHOULI A.R., FAMOURI, M., *A new modification of He's homotopy perturbation method for rapid convergence of nonlinear undamped oscillators*, J.Appl. Math. Comput, Tome 30, pg. 181-192, 2009

[4] GANJAVI, B., MOHAMMADI, H., GANJI, D.D., BARARI, A., *Homotopy perturbation method and variational iteration method for Zakharov-Kuznetsov equation*, American Journal of Applied Sciences, Tome 5(7), pg. 811-817, 2008

[5] HE, J.H., *Homotopy perturbation technique*, Comput. Meth. Applied Mech. Eng., Tome 178 (3-4), pg. 257-262

[6] HE, J.H., *New interpretation of Homotopy perturbation method*, Int. J. Mod. Phys., B20 (18), pg. 2561-2568

[7] KAYA, D., INC, M., *On the solution of the non-linear wave-equation by the decomposition method*, Bull. Malaysian Math. Soc., 22(1999), pg. 151-155

[8] NOOR, M.A., MOHYUD-DIN, S.T., *Variational homotopy perturbation method for solving higher dimensional initial boundary value problems*, Math. Problems in Engineering, 80(5), pg. 367-378, 2008

ISSN 1582 – 3601

„Nautica" Publishing House,
Constanta Maritime University

Editura
NAUTICA